Experimental approach to the problem of the Navier-Stokes singularities

Paul Debue

NNT : 2019SACLS305

Thèse de doctorat

Experimental approach to the problem of the Navier-Stokes singularities

Thèse de doctorat de l'Université Paris-Saclay
préparée à l'Université Paris-Sud

Ecole doctorale n°564 Physique en Île-De-France (EDPIF)
Spécialité de doctorat : Physique

Thèse présentée et soutenue à Gif-sur-Yvette, le 25/09/2019, par

PAUL DEBUE

Composition du Jury :

Jérémie Bec Directeur de recherche Laboratoire Lagrange, Observatoire de la Côte d'Azur	Rapporteur
Florent Ravelet Maître de Conférences Laboratoire DynFluid, Arts et Métiers ParisTech	Rapporteur
Caroline Nore Professeur LIMSI, Université Paris-Sud	Examinatrice
Mickaël Bourgoin Directeur de recherche CNRS Laboratoire de physique, ENS Lyon	Président du jury
Bérengère Dubrulle Directeure de recherche CNRS SPEC, CEA	Co-directrice de thèse
François Daviaud Directeur de recherche CEA SPEC, CEA	Directeur de thèse

Remerciements

Avant de rentrer dans le vif du sujet, je voudrais préciser que ce travail de thèse est loin d'avoir été un travail solitaire, et donc remercier tous ceux qui ont contribué à son bon déroulement.
Je remercie en premier lieu le jury, en particulier les rapporteurs Jérémie Bec et Florent Ravelet, mais aussi Caroline Nore et Mickaël Bourgoin, qui ont pris le temps de lire beaucoup de ces pages et ont pu me poser des questions ou me faire des commentaires dont certains me turlupinent encore.
Je remercie bien sûr mes encadrants, Bérengère et François, qui m'ont accordé leur confiance et laissé une grande liberté, tout en étant toujours très disponibles. Ils avaient l'avantage d'être complémentaires, non seulement du point de vue de la répartition entre théorie et expérience, Bérengère s'occupant plutôt des aspects théoriques et François de ceux expérimentaux, mais aussi sur la dynamique de la recherche : Bérengère était toujours prompte à maximiser l'entropie, la créativité et le nombre de voies à explorer, tandis que François, plus pragmatique, rappelait l'énergie nécessaire à chaque voie et permettait de trancher entre les différentes possibilités. En quelque sorte, ils personnifiaient cette lutte entre entropie et énergie à la base de la physique statistique.
Il n'y aurait évidemment pas de manip possible sans Cécile et Vincent, chevilles ouvrières de toute thèse expérimentale au SPHYNX. Eux aussi ont toujours été disponibles pour m'aider, que ce soit pour monter ou démonter la manip, débugger Labview ou colmater des fuites.
La mise en place et l'utilisation la TPIV dans les règles de l'art a été rendue possible par l'équipe du LMFL : Jean-Marc, Christophe, Jean-Philippe, ensuite rejoints par Yasar. J'ai énormément appris avec eux. Je remercie également Judith, de Lavision, toujours très réactive.
Un bon environnement de travail est toujours propice au bon déroulement d'un thèse, et je remercie donc mes collègues du SPHYNX d'avoir créé ces bonnes conditions. Ceci inclut mes collègues directs : Vishwanath (I hope you will have learnt French by the time you read this), Hugues et Valentina, mais aussi ceux de l'autre équipe de turbulence, et puis les autres, permanents et non-permanents, pour de l'aide ou des conseils, des pauses ou des footings : Alizée, Arnaud, Basile, Benjamin, Caroline, Daniel, François, Gilbert, Hervé, Ivan, Kakoli, Kanna, Marco, Michel, Paul, Sébastien, Simon, Vadim, Vincent (petit).
Je remercie plus largement le SPEC qui met en place des conditions logistiques remarquables grâce à ses équipes support : l'atelier (Vincent, Jean-Claude, Dominique), le secrétariat (Nathalie, Corinne et Martine), le service informatique (Philippe), la sécurité et les travaux (Roland et Thomas), la propreté et la direction qui coordonne tout ça.
Enfin, je remercie famille et amis pour les week-ends, vacances ou soirées passés ensemble qui m'ont permis de me changer les idées et de garder un certain lien avec le monde extérieur à la recherche.

Contents

Introduction

In the introduction to his « Théorie analytique de la chaleur » (1822), Joseph Fourier states that : « Les causes primordiales ne nous sont point connues ; mais elles sont assujetties à des lois simples et constantes, que l'on peut découvrir par l'observation, et dont l'étude est l'objet de la philosophie naturelle. » A few paragraphs later, he adds : « L'étude approfondie de la nature est la source la plus féconde des découvertes mathématiques. Non seulement cette étude, en offrant aux recherches un but déterminé, a l'avantage d'exclure les questions vagues et les calculs sans issue ; elle est encore un moyen assuré de former l'analyse elle-même, et d'en découvrir les éléments qu'il nous importe le plus de connaître, et que cette science doit toujours conserver : ces éléments fondamentaux sont ceux qui se reproduisent dans tous les effets naturels. » There are two main ideas in these statements. First, Fourier means that the nature is ruled by general principles that can apply to several domains. These principles, usually formulated mathematically, can be inferred from a careful observation of the nature in a particular case, and then used to describe many other problems, in a clear framework that avoids imprecise statements. But Fourier also implies that purely mathematical discoveries can arise from nature observation. For instance, Joseph Fourier himself studied experimentally the propagation of heat and then introduced the heat equation, a diffusion equation which can apply to many other phenomena. But his study also led him to pave the way for a new mathematical tool, the Fourier transform, which has an utmost importance not only in diffusive physics, but in many domains of physics and more generally to many domains implying mathematical modelling.

In the case of turbulence, the general principles ruling the motion of incompressible fluids have been gathered in a mathematical formulation at the mid-19th century : the incompressible Navier-Stokes equations. Compared to the heat equation, the solutions to these incompressible equations are much less known (in 3D). The existence of solutions for a viscous fluid in 3D has been shown by Leray in 1934, but their uniqueness and regularity are still open questions. In the case of an inviscid fluid, for which the Navier-Stokes equations are called Euler equations, the unicity has been proven false but the existence and regularity in the general 3D case also remain open problems. The existence of singularities in these solutions is of major interest ; in particular, it may be related to the dissipation anomaly and to intermittency, two properties of turbulence widely observed both in experimental and numerical results that are not clearly related to the incompressible Navier-Stokes equations yet.

In this thesis, we follow the second idea of Fourier and investigate what can be learnt about such singularities from an experimental study of a turbulent flow. We therefore make the bold assumption that such singularities exist. We do not expect to see such mathematical and abstract objects in a real flow, but we can reasonably expect that the existence of singularities would have an impact on real turbulent flows, and that we should be able to detect prints of them. We can thereupon wonder : how are these prints of singularities distributed ? What does the velocity field around them look like ? How do they appear ? How do they evolve in time ?

These are the questions we try to answer in this thesis. To this aim, we use a detection method based on the mathematical work by Duchon and Robert, which is described in chapter 2, after a general presentation of the problem of the singularities of the 3D incompressible Navier-Stokes and

Euler equations in chapter 1. This detection method is applied to 3D velocity fields measured at the center of an experimental turbulent swirling flow, the von Kármán flow, described in chapter 3. The velocity fields are measured by tomographic particle image velocimetry (TPIV), either time-resolved or not ; this technique is presented in chapter 4. Several tens of thousands of velocity fields have been acquired, with different spatial resolution that vary from the inertial range down to the dissipative range ; the different data sets are detailed in chapter 5. We then present some statistical results in order to characterize the distribution of the detected prints of singularities in chapter 6. Chapter 7 supplements this analysis by establishing a link between the possible prints of singularities and the intermittency. In chapter 8, we report the analysis of the topology of these prints. Finally, chapter 9 gives some preliminary results concerning the time evolution of the prints of singularities.

Part I

Presentation of the problem and method used

Chapter 1

From turbulence to singularities

In this chapter we show how the rather abstract mathematical problem of the Navier-Stokes singularities emerges from the practical issue of understanding and modeling the turbulent motion of fluids.

1 Some properties of turbulence

In this section, we quickly define what is turbulence and present three properties of turbulent flows which are related to the problem of singularities.

1.1 Turbulence ?

Turbulence is the phenomenon happening in a flow when inertial effects prevail over viscous ones. In such a case, viscous forces are too small to hinder the fluid motion. For instance, let us consider the casual situation of a breakfast, involving a cup of coffee and a liquid honey pot. If the coffee is too hot, one might want to add some milk and to stir the mixture to homogeneize the temperature. Doing so, one would notice that even in the case of a simple circular stirring motion, the milk will form interesting complex structures before being quickly homogeneously spread in the coffee. On the contrary, if one thereafter wishes to take some honey, one will notice first that it requires more strength as it is more difficult to stir ; and second that the breadcrumbs left in the pot by the previous user are much more quiet than the milk in the coffee. The flow generated in the coffee is a typical example of turbulent flow : the liquid has a low viscosity, and therefore the motion induced by a relatively weak stirring can develop freely. The motion in the honey pot is very laminar : the liquid honey is very viscous and any motion is damped quickly.
Reynolds showed that this definition of turbulence is relevant in his paper of 1883 [Reynolds, 1883] and that the dimensionless number named after him was the proper control parameter when discussing turbulence. The Reynolds number of a flow involving a fluid of kinematic viscosity ν (expressed in m^2/s) streaming at a global velocity V (in m/s) over a length L (in m) is :

$$Re = \frac{UL}{\nu} \tag{1.1}$$

This ratio indeed compares the inertial effects, in the numerator, and the viscous ones, in the denominator. Thus, the single value of either U, L or ν does not matter, it is their relative amount which is important. In practice, the threshold value or the range of values of the Reynolds number corresponding to the transition from a laminar to a turbulent flow depends on the geometry.

In the breakfast situation studied above, taking the diameters of the coffee cup and of the honey pot equal to 10 cm, the stirring speed equal to 2 rounds per second, the coffee kinematic viscosity to 10^{-6} m^2/s and the honey viscosity equal to 7×10^{-3} m^2/s, we find $Re_{coffee} = 6 \times 10^4$ and $Re_{honey} = 10$: the coffee flow has a large Reynolds number and the honey flow a small one.

1.2 Multiplicity of scales

Turbulent flows are characterized by a multiplicity of scales. Indeed, when looking at a turbulent flow, seeded with bubbles or particles, or when looking at turbulent velocity fields, one can see patterns or structures of different sizes. For instance, figure 1.1 shows two different turbulent velocity fields measured in the von Kármán flow (see chapter 3), a turbulent swirling flow. The Reynolds is 3×10^5 for both velocity fields, but the first one (a) covers the whole height of the flow, whereas the second one (b) covers only a part of it, shown by the white square on figure (a). Note that (b) was acquired at a different time, it is not a zoom on (a) but it could be a zoom on a velocity field acquired in the same conditions as (a). We can see a vortex on (a) around $(x, y) = (-5 \text{ cm}, -2 \text{ cm})$ which has a diameter of a few centimeters, and another on (b) around $(x, y) = (-1 \text{ cm}, -2 \text{ cm})$ which has a diameter of less than 1 cm : these are two similar structures of different sizes.

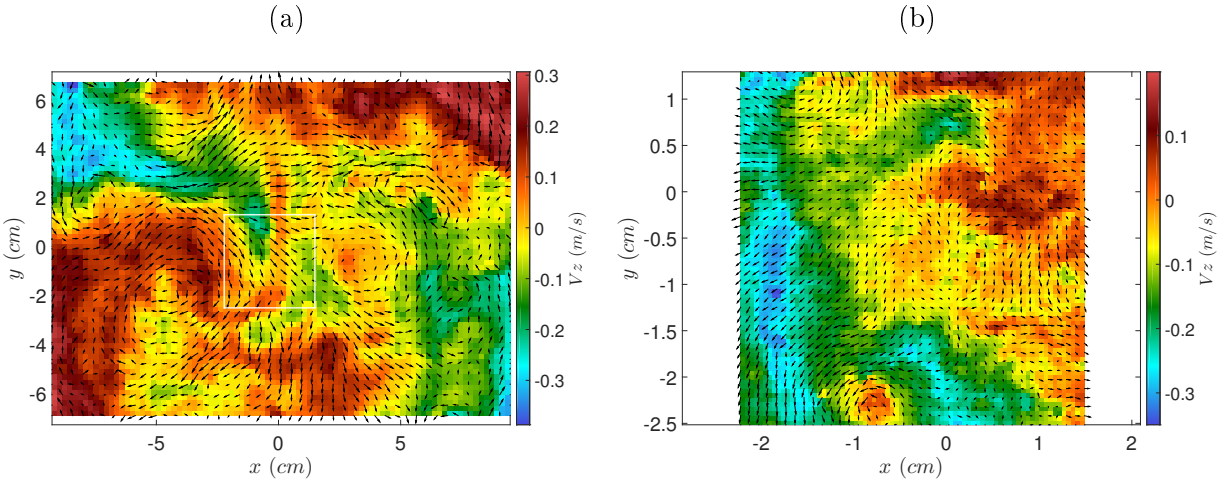

Figure 1.1: Velocity fields measured in the von Kármán flow at Re=3×10^5 with water filling the tank and the impellers rotating at 5 Hz. The arrows correspond to the in-plane velocity components and the color to the out-of-plane velocity component. (a) Velocity field measured in a meridian plane covering the whole height and width of the flow. (b) Velocity field measured at a different time at the center of the flow, in the white square shown on (a).

This multiplicity of scales can also be felt when computing the spatial spectrum of a turbulent velocity field. Such a spectrum is shown in figure 3.11 in chapter 3. It shows that a turbulent velocity field can be splitted in a wide range of modes having a non-negligible energy : indeed, there is a slow algebraic decay in $k^{-5/3}$ covering several decades. This is the famous Kolmogorov law widely observed in experimental and numerical works. To account for this multiplicity of scales, the cascade picture is usually invoked. According to this picture, schematically depicted on figure 1.2, energy is injected in turbulent flows around a large scale L, i.e. small wavenumbers are excited when stirring a fluid. Then, the energy is somehow transferred to smaller scales : larger and larger wave numbers get progressively excited. This "energy cascade" stops at some scale, called dissipative, viscous or Kolmogorov scale : structures whose size matches this scale or modes with

corresponding wavenumbers are damped by viscous effects and have less energy. One therefore distinguishes between the inertial range of scales, in which inertial effects are stronger and energy is transferred towards smaller scales, and the dissipative range of scales, in which dissipative effects become more important and where energy is dissipated by viscous dissipation. In steady state and for an homogeneous flow, this picture allows to derive a power law for the spectrum in the inertial range out of dimensional analysis : in the inertial range, viscous effects are negligible, and the relevant variables are the wavenumber k (in m^{-1}), the energy at this wavenumber $E(k)$ (in m^3/s^2), and the inter-scale energy transfer rate ϵ (in m^2/s^3). In steady state and for a homogeneous flow, ϵ can be considered constant over space and equal to the energy injection rate and to the energy dissipation rate. The only way to relate the three quantities is the following : $E(k) \propto \epsilon^{2/3} k^{-5/3}$. This law for the energy spectrum was obtained by Kolmogorov in a more rigorous way, in his theory of 1941. Extrapolating the cascade image to the limit of zero viscosity, one can imagine that there is no dissipation range and that the inertial range extends towards infinity. Such an algebraic decay towards infinity would imply a singular velocity field.

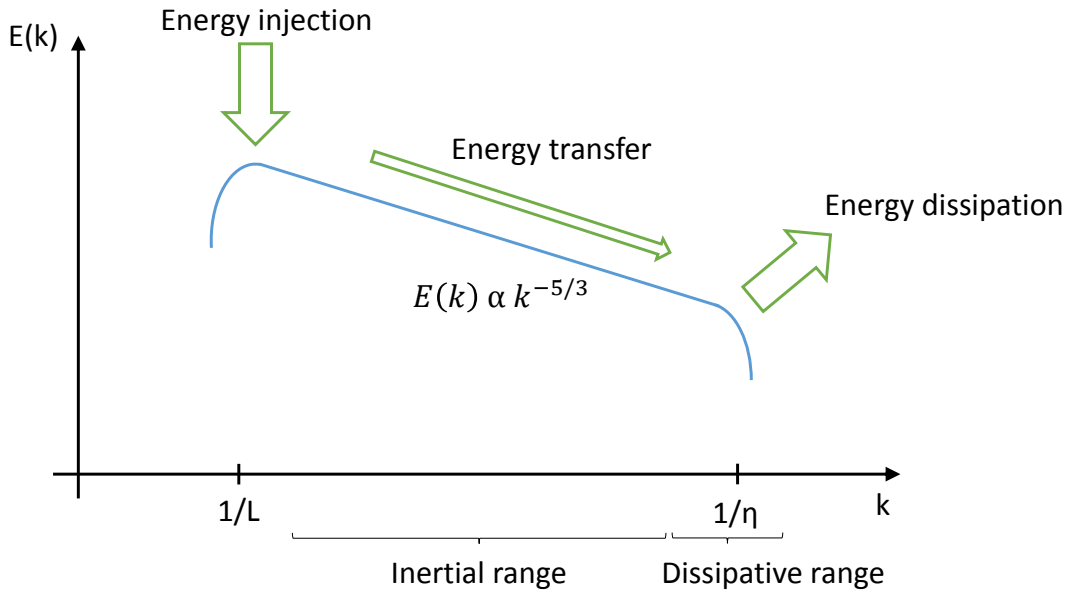

Figure 1.2: Schematic representation of the cascade picture

1.3 Intermittency

However, real turbulence is more complex than a in-space and in-time homogeneous cascade : it features intermittency. A signal is said to be intermittent when it features occasional bursts in a rather low background, and when the bursts becom scarcer and scarcer as the observation resolution is decreased. This is the case for some turbulent quantities. A consequence of intermittency is the fact that these intermittent turbulence statistics are not scale-invariant (see [Frisch, 1995]). Turbulence intermittency can be characterized by the structure functions of the velocity increments. Let $\boldsymbol{v}(\mathbf{x}, t)$ be the velocity at location $\mathbf{x}$ and at time t. The velocity increment over $\mathbf{r}$ is defined by :

$$\boldsymbol{\delta v}(\mathbf{x}, \mathbf{r}, t) = \boldsymbol{v}(\mathbf{x} + \mathbf{r}, t) - \boldsymbol{v}(\mathbf{x}, t) \tag{1.2}$$

The longitudinal structure function of order p is defined by :

$$S_p(\mathbf{x}, \mathbf{r}, t) = \langle \left(\boldsymbol{\delta v} \cdot \frac{\mathbf{r}}{|\mathbf{r}|} \right)^p \rangle \tag{1.3}$$

The brackets correspond to an ensemble average (assuming that a probabilistic description of turbulence is relevant and that the velocity field can be seen as a random function with its own probability measure, see [Frisch, 1995]). For homogeneous isotropic turbulence (i.e. if the velocity increment distribution is independent from space, time and from the increment direction), the arguments $(\mathbf{x}, t)$ can be dropped and the structure function will depend on $r = |\mathbf{r}|$ only. These structure functions will be sensible to intermittency because they involve different powers p of the velocity increments : for large p, only the largest values of the velocity increments (the "bursts") will significantly contribute to the structure function. If there were no intermittency, the structure functions would be self-similar : $S_p(r) \propto r^{\alpha p}$ with α some exponent. This is the prediction of Kolmogorov's 1941 theory (with $\alpha = 1/3$), which is not observed experimentally for large p.
Several models for the structure functions exist, that account for intermittency. For instance, Kolmogorov modified his theory of 1941 and added a space-dependent dissipation rate $\epsilon(\mathbf{x})$ in order to better comply with the experimental results [Kolmogorov, 1962]. Another model, introduced by Parisi and Frisch, is the multifractal model [Parisi and Frisch, 1985]. This model suggests that inviscid flows ($\nu = 0$) can develop singularities which are responsible for intermittency, but this model does not necessarily require these singularities and can be formulated without involving them. Note that a link between intermittency and singularities had already been established : in [Frisch and Morf, 1981], the authors show that singularities in the complex time domain close to the real axis are responsible for the intermittent bursts.

1.4 Dissipation anomaly

Turbulence is a dissipative phenomenon. Joule evidenced it with an experience rather close to the one described in chapter 3 : one propeller is rotating in a calorimeter ; it is driven by a mass falling due to its weight. When falling, the potential energy of the mass is converted into kinetic energy, which is transferred to the propeller and then to the fluid. After some time, Joule notices that the propeller and the fluid are at rest, the mass is still down, but that the temperature of the fluid has increased. It can be concluded that the mechanical energy of the mass was converted into heat by the fluid. This experience was repeated recently in the SHREK set-up [Saint-Michel et al., 2014], which is equipped with a calorimeter and it was found that the injected energy equals the released heat.
In the cascade picture of turbulence, energy dissipation is due to viscous effects that become significant when small-enough modes appear. These viscous effects are responsible for part of the momentum transfer but are irreversible and come along with heat production.
However, a well-known experimental fact questions this explanation : the anomalous dissipation or 0-th law of turbulence. It is the fact that the energy dissipation does not depend on the Reynolds number, and thus on the viscosity, at large Reynolds numbers. This can be seen on figure 3.5, showing the dimensionless time-average of the total dissipation rate plotted as a function of the Reynolds number in a von Kármán flow. This composite curve was obtained with several set-ups. At low Reynolds numbers, the dimensionless dissipation is proportional to the Reynolds to the

power -1, i.e. to the viscosity. However, at high Reynolds number, it becomes constant, at least up to $Re = 10^8$.
The dissipation anomaly may be seen as a hint that singularities occur in the limit of zero viscosity or of infinite Reynolds number. Indeed, the viscous dissipation ϵ is proportional to the square of the velocity gradient : $\epsilon = \nu(\boldsymbol{\nabla u})^2$, or, with dimensionless quantities marked with a * :

$$\epsilon^* = (\boldsymbol{\nabla}^* \boldsymbol{u}^*)^2 / Re$$

The dissipation anomally can therefore be written :

$$\lim_{Re \to +\infty} \int (\boldsymbol{\nabla}^* \boldsymbol{u}^*)^2 / Re = C \tag{1.4}$$

with C independent from Re and where the dissipation is summed over space. Therefore, $\int (\boldsymbol{\nabla}^* \boldsymbol{u}^*)^2$ tends to $+\infty$ like Re when Re tends to $+\infty$: the velocity gradient increases in order to compensate for the increase of Re (this can be explained by a refinement of the flow scales for instance). In the limit $\nu = 0$ or $Re = \infty$, $\int (\boldsymbol{\nabla}^* \boldsymbol{u}^*)^2 = \infty$. Therefore, in this limit and for a finite domain, there is at least one point in the flow where the velocity gradient diverges, i.e. where there is a singularity. Of course, this is not a rigorous proof : the limit of the velocity field when ν tends to 0 may not be equal to the velocity field obtained when $\nu = 0$. But this rather supports the existence of singularities when $\nu = 0$.

2 The incompressible Navier-Stokes equations

The incompressible Navier-Stokes equations are the partial differential equations describing the motion of incompressible fluids. They constitute a mathematical representation of the problem, involving a limited number of physical phenomena ; therefore, they are valid under certain assumptions only. They allow to account for and better understand part of the properties of turbulence detailed in the previous section.

2.1 From the compressible to the incompressible equations : underlying hypotheses

2.1.1 Compressible equations

The compressible Navier-Stokes equations date back to the half of the 19th century. They include two conservation equations : one for the mass and one for the momentum, and they apply for the whole flow described. For a Newtonian fluid following Stokes' hypothesis, they are written as follows :

$$\partial_t \rho + \partial_i (\rho u_i) = 0 \tag{1.5}$$

$$\rho \frac{du_i}{dt} = -\partial_i p + \mu \Delta u_i + \frac{\mu}{3} \partial_i (\partial_j u_j) + f_i \tag{1.6}$$

In these equations,

- $\rho(\mathbf{x}, t)$ is the density of the fluid,
- $u_i(\mathbf{x}, t)$ with $i \in 1, 2, 3$ are the three components of the velocity field,

- $p(\mathbf{x}, t)$ is the pressure field,
- $\mu = \rho\nu$ is the dynamic viscosity of the fluid,
- $f_i(\mathbf{x}, t)$ stands for the possible volumic forces acting on the fluid (gravity or magnetic forces for instance).

The first one is the mass conservation equation, stating that an elementary volume of fluid can be dilated or compressed and that its density will vary accordingly, but that its mass will remain constant.
The second one is the momentum conservation equation, corresponding to Newton's second law applied to an elementary volume of fluid at spatial position $\mathbf{x}$ and at time t. It states that its motion is governed by the forces applied on it. In this equation, the left-hand-side term is the elementary volume acceleration, the first right-hand-side (r.h.s.) corresponds to the pressure forces, the second r.h.s. term to the viscous forces and the third one to other forces.

The compressible Navier-Stokes equations can also be derived with the kinetic theory of gases (see e.g. chapter Ia of [Eyink, 2008]). Such a derivation makes more clear an important hypothesis which should be verified for the Navier-Stokes equation to apply : the separation of scales. This hypothesis states that there should exist a range of scales ℓ between the smallest length scale of the flow $\ell_{min,flow}$ and the scale over which molecular interactions happen ℓ_{mol} :

$$\ell_{mol} << \ell << \ell_{min,flow} \tag{1.7}$$

In other words, the Knudsen number $Kn = \ell_{mol}/\ell_{min,flow}$ should be very small. Usually, the Kolmogorov scale is considered to be the smallest length scale of the flow $\ell_{min,flow}$: it is the scale at which the viscous effects are large enough to absorb the inertial effects and stop the energy cascade. ℓ_{mol} is usually the mean free path for a gas or the distance between molecules for a liquid. This condition ensures that elementary volumes exist, which can both be considered point-like in the flow so that elementary forces apply to them, and which are not subject to molecular effects, these molecular effects happening between the atoms or molecules that constitute the elementary volumes but not between elementary volumes. With this condition, the Navier-Stokes equations are closed : they do not depend on smaller scale variables.
For air at atmospheric pressure, the mean free path is about 70 nm. In water, distance between particles is about 0.1 nm. In this thesis, we use water or water-glycerol mixtures and the smallest Kolmogorov scale we will deal with is 15 μm : this is 150000 times higher than the distance between particles. Therefore, scale separation is effective.

2.1.2 Incompressible equations

If the density of the fluid flowing is constant, the flow is said to be incompressible. In such a case, the compressible Navier-Stokes equations simplify into the incompressible Navier-Stokes equations (INSE) :

$$\partial_j u_j = 0 \tag{1.8}$$

$$\partial_t u_i + u_j \partial_j u_i = -\partial_i p' + \nu \Delta u_i + f_i' \tag{1.9}$$

where $p' = p/\rho$ and $f_i' = f_i/\rho$. The ' will be removed in the following for convenience.

In this case, the pressure field can be deduced from the velocity field, it is not anymore an unknown quantity as in the compressible equations. Indeed, taking the divergence of equation 1.9 and using 1.8, we get a Poisson equation for the pressure :

$$\Delta p = -(\partial_i u_j)(\partial_j u_i) \tag{1.10}$$

A fluid can be considered incompressible in a given flow if the Mach number of this flow is small enough. Indeed, in such a case, the density can be considered constant. The INSE then apply. The Mach number Ma of a flow is the ratio between the reference velocity of the flow v and the sound speed in the considered fluid c :

$$Ma = \frac{v}{c} \tag{1.11}$$

In air at atmospheric pressure, the sound speed is around 340 m/s and in water it is around 1500 m/s. In this thesis, the maximum velocity we will deal with are of the order of 3 m/s ; in water the corresponding Mach number is 2×10^{-3} : the incompressible approximation holds.

2.2 Link with turbulence properties

The analysis of the INSE allows to describe more formally the competition between inertial and viscous terms and thus the energy cascade.

We defined turbulence as the phenomenon occuring when inertial effects dominate the viscous ones, i.e. when the Reynolds number is high. The Reynolds number appears in the dimensionless INSE, obtained using a reference velocity U, a reference scale L and the density of the fluid ρ to make the different quantities dimensionless (reference time is L/U and reference pressure ρU^2) :

$$\partial_t^* u_i^* + u_j^* \partial_j^* u_i^* = -\partial_i^* p^* + \frac{1}{Re}\Delta^* u_i^* + \frac{f_i}{\rho U^2/L} \tag{1.12}$$

In this equation, the * means that the quantities are dimensionless. The role of the Reynolds number is very clear : when it is very high, the viscous term $\Delta^* u_i^*/Re$ becomes negligible compared to the non-linear terms $u_j^* \partial_j^* u_i^*$ and $\partial_i^* p^*$ (except at the places where $\Delta^* u_i^*$ is very large too). In the limit $Re = \infty$, there is no viscous term and the remaining equations are called the Euler equations.

The non-linear terms of the Navier-Stokes equation allows to account for the multiplicity of scales observed in turbulent flows. They may also be responsible for instabilities and divergences. The link with the multiplicity of scales can be seen from the very simple trigonometry formula :

$$\cos(\mathbf{k} \cdot \mathbf{x})^2 = \frac{\cos(2\mathbf{k} \cdot \mathbf{x}) + 1}{2} \tag{1.13}$$

Given an initial velocity field with only one mode of wavevector $\mathbf{k}$, a second mode of wavevector $2\mathbf{k}$ will appear in the Navier-Stokes equation due to the quadratic term. Repeating this process with the new mode, many other modes can appear.

However, viscous dissipation will temper this scenario. It can be estimated from the energy conservation equation, obtained by multiplying equation 1.9 by u_i :

$$\partial_t \frac{u_i^2}{2} + u_j \partial_j \frac{u_i^2}{2} + = -u_i \partial_i p + \nu \Delta \frac{u_i^2}{2} - \nu \partial_j u_i \partial_j u_i + u_i f_i \tag{1.14}$$

Inertial effects correspond to the term $u_j \partial_j u_i^2/2$ and the viscous dissipation is $-\nu \partial_j u_i \partial_j u_i$, always negative. Let u be the amplitude of velocity fluctuations at scale ℓ. The respective order of magnitude of the discussed terms at scale ℓ are u^3/ℓ and $\nu u^2/\ell^2$. u^3/ℓ can be interpreted as the inter-scale energy transfer rate ; let us assume it homogeneous in space and scale, equal to ϵ, as long as the viscous effects are negligible. One then finds that $\nu u^2/\ell^2 \approx u^3/\ell \approx \epsilon$ when $\ell \approx \eta$, η being the Kolmogorov scale defined as follows :

$$\eta = \left(\frac{\nu^3}{\epsilon}\right)^{1/4} \tag{1.15}$$

For $\ell \approx \eta$, $\nu u^2/\ell^2 \approx \epsilon$: the inter-scale energy transfer is equal to the viscous dissipation, whose main contribution is due to the dissipative scales. The Kolmogorov scale is usually considered as the smallest length scale of a turbulent flow.

The analysis of the Navier-Stokes equations improves our understanding of turbulence, and especially of the energy cascade. The non-linearity of the INSE is probably responsible for the intermittency. However, no mechanism leading from the INSE to the observed intermittency, which would go along with a derivation of the expression of the longitudinal structure functions starting from the INSE, exists so far. Likewise, no explanation of the dissipation anomaly using the INSE exists. On the contrary, the dissipation anomaly had to be used as a first principle by Kolmogorov while deriving its famous $4/5^{th}$ law [Kolmogorov, 1941] concerning the third order longitudinal structure function. In brief, two major properties of turbulence possibly related to the existence of singularities still resist the attempts of connection with the turbulence equations, the INSE. From the mathematical side, mathematicians are still struggling to prove or disprove the existence of singularities in the solutions of the 3D incompressible Navier-Stokes and Euler equations.

3 The possible singularities

Singularities are mathematical objects which require a particular handling. In the case of the 3D Euler and Navier-Stokes equations, a lot of work has been done without a final result yet. A singularity cannot occur in a real flow, but the existence of singularities in the mathematical solutions of the Euler or Navier-Stokes equations would probably have consequences on real flows.

3.1 What is a singularity ?

3.1.1 Continuity

Mathematically, a singularity can be defined as opposed to continuity. The continuity is rigorously defined as follows : a function

$$\begin{array}{rccc} f & : & \Omega \subset \mathbb{R}^n & \rightarrow & \mathbb{R}^m \\ & & x & \mapsto & f(x) \end{array}$$

is continuous at a point x_0 if and only if :

$$\forall \epsilon > 0, \exists\ \delta > 0 \mid \forall x \in \mathbb{R}^n, ||x - x_0|| < \delta \implies ||f(x) - f(x_0)|| < \epsilon \tag{1.16}$$

One can say that f features a singularity if it is not continuous on Ω. The singularity is what occurs at the point where f is not continuous.

In the definition of continuity given above, we see that the amplitude variation of the function f cannot be too high for a given variation of the variable x. We can thus say that a singularity occurs in a velocity field when there is an infinite variation of the amplitude of the velocity over a finite distance (figure 1.3 (a)) ; or a finite variation of the amplitude of the velocity over a zero-distance (figure 1.3 (b)). In both cases, the singularity corresponds to a refinement of scales of the velocity field, i.e. a refinement of the sizes of the patterns of the velocity field : there are significant variations of the velocity over very small scales.

3.1.2 Regularity

More generally, one can say that a continuous function features a singularity if one of its derivatives is not continuous. For instance, the function $f : x \mapsto \sqrt{x}$ (defined on $\mathbb{R}^+$) is continuous in 0 but its derivative is not. We can say that it is less smooth than a function whose first derivatives are continous. To characterize the degree of smoothness of a function, one can use the concept of Hölder regularity. The regularity of a function can be characterized by a Hölder exponent h : a function

$$\begin{array}{rccc} f & : & \Omega \subset \mathbb{R}^n & \rightarrow & \mathbb{R}^m \\ & & x & \mapsto & f(x) \end{array}$$

is h-Hölder continuous on Ω if and only if :

$$\exists\, C > 0 \mid \forall x, y \in \Omega, ||f(x) - f(y)|| \leq C||x - y||^h \tag{1.17}$$

If $h \geq 1$, f is differentiable. If $h > 0$, f is continuous. If $h \geq 0$ only, f is bounded but may feature discontinuities like the one in figure 1.3 (b). The larger h, the more regular f and the higher the order of its first discontinuous derivative.

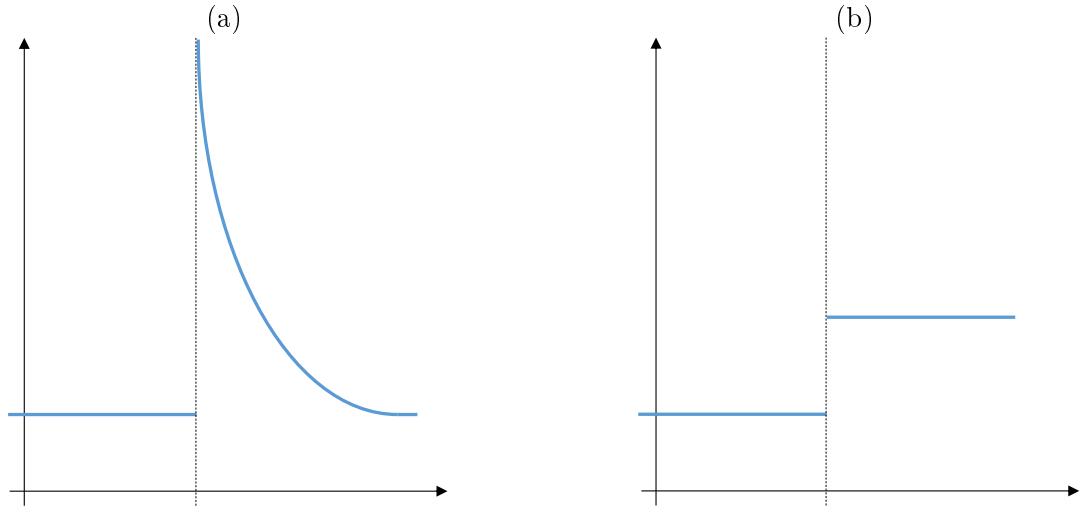

Figure 1.3: Examples of 1D singularities.

3.1.3 Singularities in partial differential equations

Singularities and regularity are well-defined mathematical concepts. However, from a physical point of view, they are not very meaningful : infinite quantities are not compatible with principles such as mass or energy conservation ; a zero-length scale is quite an abstract concept : a scale can be

small compared to another but not absolutely small. Also, singularities are not compatible with numerical simulations, which are discrete representations of a given problem : infinite time- or space-derivatives would require infinitely small time- or space-steps, or at least very small ones, which require huge computing and storage capacities. Therefore, when dealing with a partial differential equation (PDE) coming from physics, it is important to show that it is regular enough, in order to ensure that it is physically relevant and that it can be simulated.
Actually, mathematicians usually try to prove that PDEs follow the three conditions : there is a solution to this PDE, it is unique and it is regular. In order to prove that, the usual strategy consists in showing the existence of a solution in a space including both regular and irregular functions, and then to prove the unicity and the regularity. To this end, the PDE should first be extended to irregular solutions, i.e. given a meaning in the case of irregular solutions : indeed, derivatives are not defined for such solutions. This is achieved with the so-called weak derivatives in the framework of the distribution theory. The extended PDE is called "weak formulation" of the initial PDE, obtained by replacing the derivatives by weak derivatives. Its solutions are called "weak solutions" ; they are usually seeked in Sobolev spaces, in which the functions should have a finite p-norm ($\int ||\mathbf{u}||^p$), with $p > 1$, as well as some of their derivatives.

3.2 Clues on the possible singularities of the 3D incompressible Euler and Navier-Stokes equations

In 2D, it is known that both the incompressible Navier-Stokes equations (see [Ladyzhenskaya, 1969]) and the incompressible Euler equations (see [Yudovich, 1963] for existence and unicity) have a unique solution which is regular. In 3D, the problem seems to be more difficult, and only partial results were obtained, even if these equations date back to the 19^{th} century. In the case of the Navier-Stokes equations, the existence and smoothness is one of the "Millenium problems" for which the Clay Mathematics Institute of Cambridge (Massachusetts) will award 1 million dollars. The problem of singularities motivated not only theoretical works, but also numerical and experimental works which aimed at providing some knowledge on the possible singularities.

3.2.1 Theoretical works

The existence of solutions to the 3D incompressible Navier-Stokes equations was shown by Jean Leray in 1934. He obtained the weak formulation and managed to exhibit weak solutions in the general case [Leray, 1934]. The weak formulation is written as follows :

$$\int_{\mathbb{R}^3}\int_{\mathbb{R}} u_i \partial_t \phi_i + \int_{\mathbb{R}^3}\int_{\mathbb{R}} u_i u_j \partial_j \phi_i = -\int_{\mathbb{R}^3}\int_{\mathbb{R}} p \partial_i \phi_i - \nu \int_{\mathbb{R}^3}\int_{\mathbb{R}} u_i \partial_k \partial_k \phi_i$$

$$\int_{\mathbb{R}^3}\int_{\mathbb{R}} u_i \partial_i \psi = 0$$

for any test functions ϕ and ψ. These test functions are very regular functions that can be differentiated. The derivatives are shifted to these functions by integration by parts, and u and p need not be differentiable anymore ; they should only have integration properties.
However, the uniqueness and regularity of these solutions are still open questions. Concerning the possible singularities, some results have been obtained. If they exist, such singularities will always come along with an unbounded velocity [Constantin, 2008]. This rules out cases of the type of figure 1.3 (b). If they exist, singularities are also very scarce : indeed, a consequence of [Cafarelli et al., 1982] is that Navier-Stokes singularities cannot form space-time continuous curves : therefore, they

would pop-up from time to time but not persist. Stationary singular solutions to the Navier-Stokes equations have been exhibited in [Li et al., 2018]. However, this does not prove that the Navier-Stokes equations could develop a singularity in finite time starting from smooth initial conditions. In particular, these solutions display a singular axis : this is not compatible with the result of [Cafarelli et al., 1982] ; therefore, such velocity fields cannot form from smooth initial conditions. The velocity field of these stationary solutions is given, in spherical coordinates, by :

$$u_r = \frac{1}{r}\left(-1 - \frac{2(\gamma+1)}{(\gamma+1)\ln(\frac{1+\cos(\theta)}{2}) - 2} - \frac{1-\cos(\theta)}{1+\cos(\theta)}\frac{3(\gamma+1)}{\left((\gamma+1)\ln(\frac{1+\cos(\theta)}{2}) - 2\right)^2}\right)$$

$$u_\theta = \frac{1}{r}\left(\frac{1-\cos(\theta)}{\sin(\theta)}\right)\left(1 + \frac{2(\gamma+1)}{(\gamma+1)\ln(\frac{1+\cos(\theta)}{2}) - 2}\right)$$

$$u_\Phi = \frac{1}{r\sin(\theta)}(b\ln(1+\cos(\theta)) + a) \; if \; \gamma = -1$$

$$u_\Phi = \frac{1}{r\sin(\theta)}\left(\frac{b}{\ln(1+\cos(\theta))} + a\right) \; if \; \gamma > -1$$

with a, b and γ parameters. Such velocity fields corresponding to two sets of parameters are shown on figure 1.4.

In the case of the 3D incompressible Euler equations, the general existence and the regularity are still to prove (or disprove). The uniqueness is false [Shnirelman, 1997]. An important result is the fact that singularities occuring in the solution of a Euler equation, if they existed, would always come along with an unbounded vorticity [Beale et al., 1984].

There are also hints that singularities can dissipate energy. Such a dissipation mechanism was suggested by Onsager in [Onsager, 1949], where he conjectures that in the inviscid case, too smooth velocity fields (that are Hölder continuous with $h > 1/3$) cannot dissipate energy in this way. This conjecture was proven for instance in [Duchon and Robert, 2000], where the authors derive an energy budget valid for the weak solutions and which implies an additional dissipation term, stemming from the lack of smoothness of the velocity field. This work is the foundation of this thesis ; it is detailed in chapter 2.

3.2.2 Numerical works

The result of [Beale et al., 1984] on the divergence of the vorticity suggests to look for places where the vorticity is extreme in order to find possible singularities. Several numerical works were carried out in order to study large vorticity structures. Of course, they do not allow to draw a definitive conclusion because of the finite resolution of numerical simulations.
In [Brachet et al., 1992] the Euler equations are simulated on a 256^3 grid with periodic boundary conditions. It is found that large-vorticity zones are pancakes that become thinner and thinner until their thickness reaches the simulation resolution ; it is not known whether they would have become even thinner at later times or not. In this work, the so-called "analyticity strip width" method [Sulem et al., 1983] is also performed. It consists in monitoring the imaginary part of a singularity in the complex space domain, i.e. the distance of the singularity to the real axis. This distance governs the Fourier spectrum of the velocity field ; if a singularity was to occur, then this distance

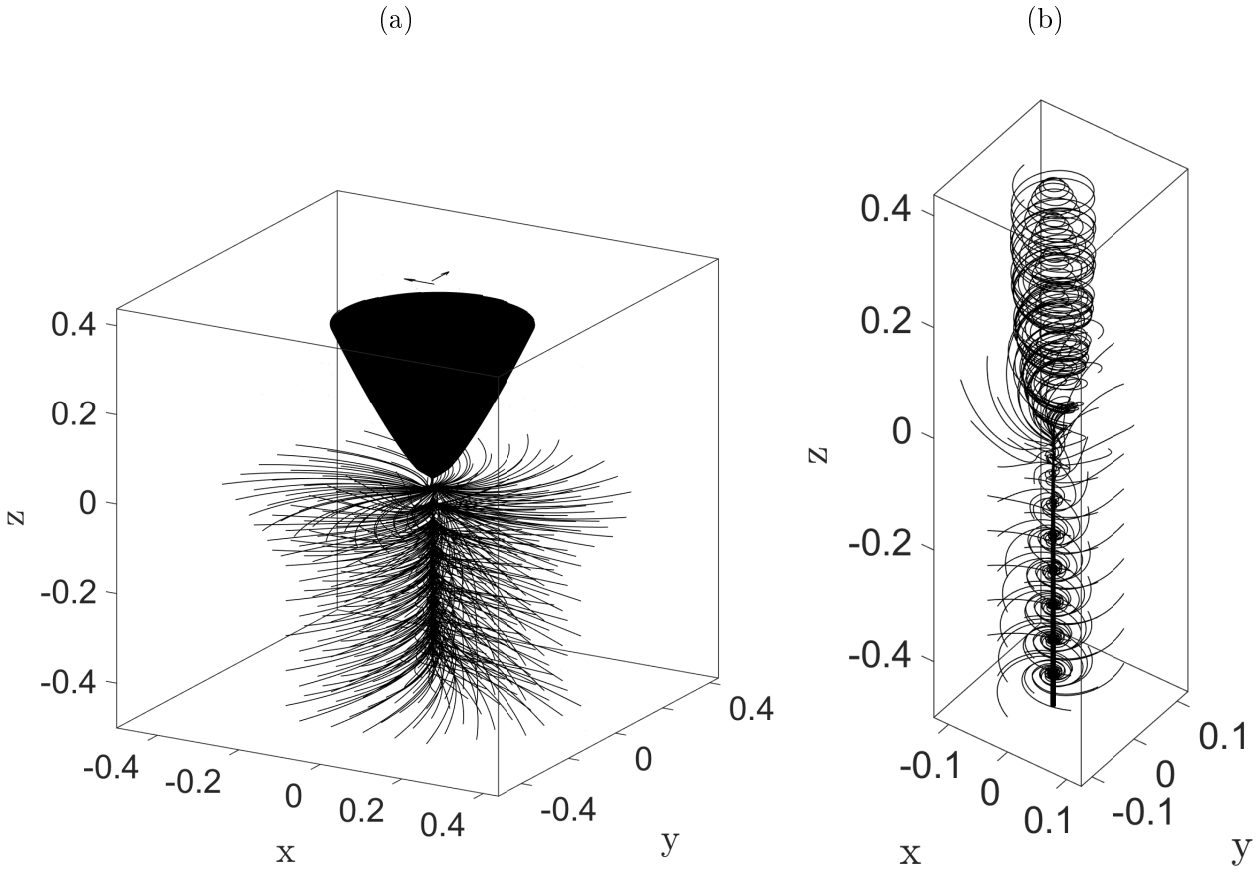

Figure 1.4: Velocity streamlines of two stationary singular solutions of the Navier-Stokes equations exhibited in [Li et al., 2018] with $a = b = 1$. (a) $\gamma = 1/2$. For $z < 0$, streamlines are spiraling towards the semi-axis $z < 0$, and for $z > 0$, they are slowly spiraling away from the semi-axis $z > 0$, forming a bell shape. (b) $\gamma = -1$. For $z > 0$, the streamlines are spiraling downwards to the point $(x, y, z) = (0, 0, 0)$ and for $z < 0$, streamlines are spiraling towards the semi-axis $z < 0$.

would tend to zero. In [Brachet et al., 1992], this method did not allow to conclude to a finite-time blow-up of the 3D incompressible Euler equations. In [Pumir and Siggia, 1990], an adaptative mesh refined 50 to 600 times at relevant places is used ; no evidence of finite-time blow-up is found neither. The fact that in pancake-like structures the quantities depend only on one direction (perpendicular to the pancakes) probably leads to a depletion of non-linearity and prevents any singularity from developing further [Frisch, 1995]. However, a more recent simulation of the 3D incompressible Euler equations on a logarithmic lattice [Campolina and Mailybaev, 2018] strongly suggested that the 3D incompressible Euler equations could develop singularities, and that current computers were not able to simulate them by direct numerical simulations (DNS). It should still be kept in mind that using a logarithmic lattice implies a strong assumption : many modes have to be removed, this is assumed to have no impact on the result.

Large-vorticity structures were also studied in DNS of 3D incompressible Navier-Stokes equations, with continuously increasing resolution and Reynolds number. In [She et al., 1990], these equations are simulated on a 90^3 grid, the Taylor-scale based Reynolds number being $R_\lambda = 90$; in [Vincent and Meneguzzi, 1991], a grid of 240^3 points is achieved, with $R_\lambda = 240$. In both works, the authors noticed that large-vorticity zones were elongated thin tubes. In [Vincent and Meneguzzi, 1994], it

is shown that these tubes result from the rolling-up of sheets of large vorticity and that they are surrounded by zones of large dissipation rate. With the improvement of computational power, it was possible to study larger Reynolds numbers : in [Yeung et al., 2015], a grid of 8192^3 points is achieved, together with a Taylor-scale based Reynolds number $R_\lambda \approx 1300$. At such a large Reynolds number, the authors still observed vorticity tubes, but they found that the very strongest vorticity events were rather blobs, characterized by the colocation of a large vorticity and a large dissipation rate.

3.2.3 Experimental works

A few experimental works tried to tackle the singularities problem, or can be related to it.
For instance, in [Douady et al., 1991], the authors take advantage of the fact that large-vorticity zones are also low pressure zones, which can therefore concentrate small bubbles. The organization of bubbles can be observed with fast cameras. The authors observed that the large-vorticity zones where the bubbles gather are also elongated tubes which appear very quickly and then disappear more slowly.
In [Saw et al., 2016], the authors rely on the work [Duchon and Robert, 2000] and on the fact that singularities may dissipate energy. They analyze 2D-3C velocity fields (3 components of the velocity on a 2D plane) measured by stereoscopic particle image velocimetry (SPIV) and look for places where there could be dissipation due to singularities. They find four kinds of structures : fronts, spirals, jets and cusps, but their 2D measurements do not allow them to know whether they are different slices of a single structure, possibly seen at different times, or not.

The existence of singularities in a solution of the 3D incompressible Euler and Navier-Stokes equations remains an open question. Let us all the same discuss the physical consequences of the possible existence of such singularities.

3.3 Physical consequences of the possible existence of singularities

From a physical point of view, an infinite velocity amplitude or an infinitely small length scale is not meaningful : it breaks conservation principles or it is too abstract : a quantity can be very large or very small compared to another but not infinitely large or small. If singularities cannot occur in real flows, is it physically relevant to study the Euler and Navier-Stokes singularities ? Is it really a physical problem or only mathematical one ? Would the existence of the Navier-Stokes and Euler singularities have an impact on a real turbulent flow ?

3.3.1 Navier-Stokes case

The existence of singularities in a mathematical solution to the 3D incompressible Navier-Stokes equations would lead to the invalidation of the assumptions used to derive those equations from the compressible equations. Therefore, the existence of a singularity in a real flow modelled by such a solution is not implied, even if there would probably be an impact on this real flow.
Indeed, in the case of a singularity occuring in the solution of the 3D INSE, the velocity norm would increase to infinity and a real flow modelled by this solution would become compressible. Therefore, the emergence of a singularity in the real flow is not implied at all as the 3D INSE would stop being a proper model. The real flow would probably be impacted though but would display only prints or remainings of the singularity and not a genuine one. The singularities problem would be shifted to the compressible Navier-Stokes equations, in which the compressible effects would maybe

prevent the apparition of a singularity. Note that even if the compressible Navier-Stokes equations could develop singularities in finite time, they would also stop being a proper model for a real flow as the scale separation assumed to derive them would not be achieved anymore. This suggests that the existence of a singularity in the solution of a mathematical model should be seen as an indication that this model is not physically relevant anymore and that additional physics should be added. Other examples exist : for instance, in fracture mechanics, the elasticity equations and the special boundary conditions near a crack tip lead to a divergence of the stress at the crack tip, the energy remaining all the same bounded. However, in a real material the stress does not take infinite values : when it reaches some threshold value, the material does not follow the linear elastic equations anymore ; damage develops and the material will break. Everything happens as if the singularity was replacing a physical phenomenon not accounted for by the model. In the case of the INSE, the possible singularities would even have their own dissipation term, accounting for the dissipation due to the missing phenomena : Duchon and Robert showed in [Duchon and Robert, 2000] that a new dissipation term appears in the energy budget of the weak solutions of the INSE, which can be non-zero in the case of a singularity.
As a conclusion, the existence of singularities in the solutions of the INSE is of physical importance for two reasons. First, it should have an impact on real flows which would display prints of singularities, and second, it would invalidate the INSE as a proper model for incompressible flows. As the singularities should be very scarce, the INSE would probably remain a proper model most of the time though.

3.3.2 Euler case

Contrary to the 3D INSE, the 3D incompressible Euler equations are not a proper model for real viscous flows, even without singularities, because they do not feature any viscous effect. However, the existence of singularities in the solutions of the 3D incompressible Euler equations may have an impact on the solutions of the 3D INSE, and thus on real flows.
Indeed, in the Navier-Stokes equations, the viscous effects are negligible at large scales. The large-scale behaviour of the 3D incompressible Euler and Navier-Stokes equations should therefore be similar, and, if singularities were developing in the Euler equations, they may also start forming in the INSE before evolving differently. They would therefore have an impact on the INSE that could be measured. The following reasoning, inspired by the multifractal model [Parisi and Frisch, 1985], shows what this impact could be.
Let $\mathbf{u}$ be a solution of the incompressible Navier-Stokes equation 1.9 and assume that it is locally h-Hölder continuous, i.e. behaving as follows :

$$||\boldsymbol{\delta u}|| = ||\boldsymbol{u}(\boldsymbol{x}+\boldsymbol{\ell}) - \boldsymbol{u}(\boldsymbol{x})|| \propto ||\boldsymbol{\ell}||^h \tag{1.18}$$

We can then reproduce the energy cascade reasoning with $\delta u \propto \ell^h$ instead of $\delta u \propto \ell^{1/3}$. The Hölder condition leads to the following estimates of the viscous dissipation and inertial energy terms :

$$\nu \partial_i u_j \partial_i u_j \approx \nu \frac{\delta u^2}{\ell^2} \approx \nu \frac{\ell^{2h}}{\ell^2} \approx \nu \ell^{2h-2} \tag{1.19}$$

$$u_j \partial_j \frac{u_i^2}{2} \approx \frac{\ell^{3h}}{\ell} \approx \ell^{3h-1} \tag{1.20}$$

Both terms are comparable when $\ell^{3h-1} \approx \nu \ell^{2h-2}$ i.e. when $\ell \approx \nu^{1/(1+h)}$. We define $\eta_h = \nu^{1/(1+h)}$. All this can be interpreted as a local cascade with a particular scaling : there is an inertial range with $\delta u \propto \ell^h$ in which viscous effects are negligible and where energy is transferred to smaller scales.

The dissipative scales are of the order of η_h. The viscous dissipation absorbs the inter-scale transfer and no structures smaller than $\approx \eta_h$ can develop ; therefore, the velocity field is smooth below this scale : $\delta u(\ell) \propto \ell$. For $h = 1/3$, we find the usual scaling, in particular, $\eta_{1/3}$ is the Kolmogorov scale. However, for other h, the situation is different ; for $h < 1/3$, η_h is smaller than the Kolmogorov scale.
According to this reasoning, the event $\{\exists A \subset \mathbb{R}^n, \exists \boldsymbol{x} \in A |\ \forall \boldsymbol{y} \in A, ||\boldsymbol{v}(x) - \boldsymbol{v}(y)|| \propto ||\boldsymbol{x} - \boldsymbol{y}||^h\}$ with $-1 < h < 1$ cannot occur in a solution of the 3D INSE : indeed, the viscosity would smooth the velocity field below η_h and the Hölder condition $||\boldsymbol{v}(x) - \boldsymbol{v}(y)|| \propto ||\boldsymbol{x} - \boldsymbol{y}||^h$ would hold only for $||\boldsymbol{x} - \boldsymbol{y}|| > \eta_h$. However, it could occur in a solution to the 3D incompressible Euler equation where there are no viscous effects. We therefore call it a Euler-type singularity, as opposed to a Navier-Stokes-type singularity, if $h = -1$: even viscous effects cannot smooth the velocity field as the regularization scale is $\eta_{-1} = 0$, and the velocity field is therefore singular. The singular fields shown in figure 1.4 are Navier-Stokes-type singularities. Euler-type singularities ($-1 < h < 1$) could be an example of a singularity of the 3D incompressible Euler equations which have an impact on the 3D INSE : such events developing in the 3D INSE would lead to a multiplicity of dissipative scales, in particular smaller than the Kolmogorov scale. This would be quite a change in the classical picture of turbulence. The existence of too small length scales could however question the scale separation required for the derivation of the Navier-Stokes equations. Such events would also lead to a multiplicity of scalings, and would impact the statistics of the velocity field. This is the idea behind the multifractal model, which provides good fit of experimental data. Also, according to this model, the smaller h, the less probable the occurence of a locally h-Hölder continuous velocity field. This suggests that Navier-Stokes-type singularities are very scarce, in accordance with the result of [Cafarelli et al., 1982], and rules out too small η_h, ensuring the scale separation. But it is not known yet whether the previous reasoning corresponds to the reality or not. The multifractal model also has a probabilistic formulation which does not require such a phenomenology. Besides, the organization of the flow as a juxtaposition of places where $\delta u \propto \ell^h$ with different h was never directly evidenced. One should therefore be careful with this representation. In particular, the above reasoning does not constitute a rigorous proof that singularities with $h > -1$ cannot occur in a solution of the Navier-Stokes equations.

Summary

In this chapter we introduced the 3D incompressible Navier-Stokes equations, the partial differential equations which govern the motion of incompressible fluids and which therefore feature turbulence. The regularity of these equations, as well as the 3D incompressible Euler equations, are still open mathematical problems. The possible singularities are incidentally related to intermittency and to the dissipation anomaly, two turbulence features which are not clearly connected with the 3D INSE yet.
Even if singularities have no physical meaning and are not to occur in the physical world, their mathematical existence should have an impact on real flows. Therefore, we claim that studying a real flow allows to give insight into the possible singularities of the Euler and Navier-Stokes equations, or at least their formation. This is detailed in the next chapter.

Chapter 2

The problem of singularities addressed by the experiment

In this chapter we explain how we tackle the problem of singularities with an experimental approach. We use a detection criterion which is based on the work of Duchon and Robert [Duchon and Robert, 2000] in order to detect prints of singularities, i.e. places that might correspond to the formation of singularities or to aborted singularities. This criterion was already introduced in [Kuzzay et al., 2017] and applied to 2D-3C data in [Saw et al., 2016] ; in this thesis we will apply it to 3D-3C data. The detection principle can be applied to any velocity field, obtained either by a numerical simulation or an experimental measurement ; we then compare both approaches and explain why we chose an experimental approach. Finally, we detail the outline of the method used in this thesis.

1 Prints of singularities as extreme events of inter-scale transfer rate at small scale

Our detection method is based on the work by Duchon and Robert [Duchon and Robert, 2000]. A singularity corresponds to an infinite refinement of scales, and this mathematical work states formally that such a singularity may come along with a non-zero inter-scale transfer down to infinitely small scales. This inter-scale transfer interpretation establishes a link with the LES equations.

1.1 Duchon and Robert's paper

1.1.1 An energy budget for the weak solutions

In their paper [Duchon and Robert, 2000], Duchon and Robert derive an energy budget for weak solutions of the INSE, in a rigorous mathematical framework. In the absence of forcing, this energy budget is expressed as follows :

$$\partial_t \frac{u_i^2}{2} + \partial_j[u_j(\frac{u_i^2}{2} + p)] = \nu\Delta\frac{u_i^2}{2} - \nu\partial_j u_i \partial_j u_i + D(\mathbf{u}) \tag{2.1}$$

In this equation, $\mathbf{u}$ is a weak solution of the INSE, and the derivatives should therefore be understood in the weak way, i.e. in the sense of distributions, so that they are well-defined if $\mathbf{u}$ is singular. If $\mathbf{u}$ is regular, the equation also holds with the classical meaning of the derivatives. Compared to the classical energy budget 1.14, there is a new term $D(\mathbf{u})$. Duchon and Robert proved this term to be zero for regular solutions, and greater than or equal to zero for the weak solutions constructed by

Leray to prove the existence of weak solutions. It is not proved however that $D(\mathbf{u})$ is positive in the general case. Anyway, the work by Duchon and Robert gives shape in a mathematical rigorous framework and thus supports the idea of Onsager [Onsager, 1949] that a singularity would generate additional dissipation due to the lack of regularity of the velocity field. Such an energy budget is also obtained in the case of 0 viscosity, i.e. in the case of the Euler equations, with the same consequence (additional dissipation due to a lack of regularity).

1.1.2 The smoothed velocity field

In order to derive this energy budget, Duchon and Robert started from the weak INSE and from a smoothed version of it. The latter is obtained by smoothing (or regularizing, or filtering) the velocity field at a length scale ℓ :

$$\mathbf{u}^\ell(\mathbf{x}) = \phi^\ell * \mathbf{u}(\mathbf{x}) = \int \phi^\ell(\mathbf{y})\mathbf{u}(\mathbf{x}-\mathbf{y})d^3\mathbf{y} \tag{2.2}$$

The smoothed velocity field $\mathbf{u}^\ell$ is the convolution product of the velocity field $\mathbf{u}$ and a smoothing function ϕ^ℓ. The idea of smoothing is to average locally the velocity field in order to remove fluctuations over scales smaller than $\propto \ell$. The velocity field should be less and less smoothed as ℓ is decreased. ϕ^ℓ is then defined from a "mother" function ϕ as follows :

$$\phi^\ell \ : \mathbf{x} \mapsto \frac{\phi(\mathbf{x}/\ell)}{\int \phi(\mathbf{y}/\ell)d^3\mathbf{y}} \tag{2.3}$$

The integral of ϕ^ℓ is equal to 1, the values $\phi^\ell(\mathbf{x})$ can thus be seen as weights in the averaging process. ϕ is usually a simple function such as a hat function or a Gaussian. In this whole thesis, we will use a Gaussian :

$$\phi^\ell(\mathbf{x}) = \frac{\exp\left(-\frac{30\mathbf{x}^2}{2\ell^2}\right)}{\left(2\pi\ell^2/30\right)^{3/2}} \tag{2.4}$$

Figure 2.1 shows $\phi^\ell(\mathbf{x})/\phi^\ell(0)$ for different values of ℓ. The larger ℓ, the wider the filter.

1.1.3 The balance equation for the regularized point-split energy density

Smoothing the INSE 1.8-1.9, one obtains the smoothed incompressible Navier-Stokes equations (the forcing is equal to 0) :

$$\partial_j u_j^\ell = 0$$
$$\partial_t u_i^\ell + \partial_j \left(u_i u_j\right)^\ell = -\partial_i p^\ell + \nu \partial_k \partial_k u_i^\ell$$

This also has a meaning if $\mathbf{u}$ is a weak solution, and combining these equations with the weak INSE, Duchon and Robert then obtained the balance equation for the regularized point-split energy density (valid in the sense of distributions) :

$$\frac{1}{2}\partial_t u_i u_i^\ell + \partial_i T_i^\ell = \frac{1}{2}\nu\partial_j\partial_j(u_i u_i^\ell) - \nu\partial_j u_i \partial_j u_i^\ell - \Pi_{DR}^\ell \tag{2.5}$$

where :

$$T_i^\ell = \frac{1}{2}\left[u_j u_j^\ell u_i + p^\ell u_i + p u_i^\ell\right] + \frac{1}{4}\left[(u_i u_j u_j)^\ell - (u_j u_j)^\ell u_i\right]$$

and :

$$\Pi^\ell_{DR} = \frac{1}{4}\int \nabla\phi^\ell(\xi)\cdot\delta\mathbf{u}(\delta\mathbf{u})^\mathbf{2}\mathbf{d}\xi \tag{2.6}$$

We call Π^ℓ_{DR} the Duchon-Robert term.
Duchon and Robert then showed that the limit of equation 2.5 when $\ell \to 0$ was equation 2.1, with :

$$\lim_{\ell\to 0}\Pi^\ell_{DR} = D(\mathbf{u}) \tag{2.7}$$

In the case of a singularity, $D(\mathbf{u})$ may not be equal to zero, as suggested by Onsager. In such a case, Π^ℓ_{DR} would remain large even for very small ℓ. This provides a new criterion to look for singularities. In practice, "very small" means of the order or smaller than the Kolmogorov scale η, which is usually considered as the smallest length scale of a turbulent flow. In this thesis, we call "prints of singularities" and study the places where the Duchon-Robert term Π^ℓ_{DR} computed at $\ell \approx \eta$ takes very large values. These are prints of singularities in the sense that they may correspond to singularities which start developping and are aborted by physical effects not embedded in the INSE (in the case of experiments) or by a lack of resolution (in the case of numerics). However, it is also possible that such events have nothing to do with singularities : for instance, they may be regular places that are less regular or places where the amplitude of the fluctuations is larger, leading to a larger Π^ℓ_{DR}.

1.2 Physical interpretation and weak Kármán-Howarth-Monin equation

Equation 2.5 can be interpreted as a local, in space and in scale, energy budget, meaning that the variation of energy contained in scales $> \ell$ at a given point $(\partial_t(u_i u_i^\ell)/2)$ is due to :

- spatial transport and pressure terms embedded in the term $\partial_i T_i^\ell$
- viscous diffusion due to scales $> \ell$: $\nu\partial_j\partial_j(u_i u_i^\ell)/2$
- viscous dissipation due to scales $> \ell$: $\nu\partial_j u_i \partial_j u_i^\ell$
- inter-scale energy transfer towards scales $< \ell$: Π^ℓ_{DR}

Strictly speaking, this is not an energy budget as $u_i u_i^\ell$ is not positive-definite and cannot therefore be considered as an energy. However, it resembles the term $u_i^\ell u_i^\ell$ and has the same limit $u_i u_i$ (which is an energy) when ℓ tends to 0. Therefore, we can say that it corresponds to an energy. Similar remarks can be applied to the other terms.
Equation 2.5 is very useful, as it can be used to study locally the energy transfers in a turbulent flow. In the previous chapter, we explained that singularities were characterized by a refinement of the characteristic length scales of the flow. In this scope, the paper of Duchon and Robert becomes more meaningful : the occurence of a singularity would come along with an infinite refinement of scales, and therefore a large inter-scale transfer Π^ℓ_{DR} down to very small scales ℓ. The limit when $\ell \to 0$ would then be non-zero.
Of course, this interpretation is valid only in a mathematical abstract continuum with infinitely small scales. In the physical world, the continuum approximation is valid only down to a finite scale, and we already mentioned that the occurence of a singularity would violate the assumptions of incompressibility and/or of scale separation, therefore bringing additional physics into play. However, if singularities existed in the mathematical world, we can reasonably expect to see their growth in the physical world, characterized by a large inter-scale transfer Π^ℓ_{DR} at very small scales.

In the previous chapter, we mentioned how the competition between inertial and viscous effects was responsible for the different behaviours in the inertial and dissipative ranges. Also, we explained how it could lead to different dissipative scales : the refinement of scales stops when the viscous effects become important enough. This suggests that singularities may not correspond to large values of the Duchon-Robert term itself, but to large values of the ratio between the Duchon-Robert and the viscous dissipation terms.

However, in this thesis we deal with velocity fields measured by experimental means and which can therefore feature some noise. Computing the ratio of noisy quantities leads to noise amplification, especially for a noisy denominator. This is the case of the dissipation term $\nu\partial_j u_i \partial_j u_i^\ell$, which is the product of one smoothed quantity and one unsmoothed quantity. We therefore need a different viscous dissipation term, better suited to experimental data. For instance, the Duchon-Robert term seems to be very suited for the analysis of experimental data. Indeed, it is not directly $-\frac{1}{4}\nabla\cdot\delta\mathbf{u}(\delta\mathbf{u})^\mathbf{2}$ which is computed but a smoothed version of that, with the derivative shifted to the smoothing function, thus avoiding noise amplification due to the derivative. In [Dubrulle, 2019], equation 2.5 is modified by introducing a new viscous dissipation term $\mathscr{D}_\nu^\ell$ inspired by the Duchon-Robert term. The weak Kármán-Howarth-Monin equation is thus obtained.

The new viscous dissipation term is :

$$\mathscr{D}_\nu^\ell = \nu \int \Delta\phi^\ell(\xi) \frac{\delta\mathbf{u}(x,\xi)^2}{2} d\xi = \nu \int \Delta\phi^\ell(\xi) \frac{[\mathbf{u}(x+\xi)-\mathbf{u}(x)]^2}{2} d\xi \tag{2.8}$$

It can be shown that :

$$\mathscr{D}_\nu^\ell = \frac{1}{2}\nu\partial_j\partial_j(u_i u_i)^\ell - \nu\partial_j(u_i\partial_j u_i^\ell) + \nu\partial_j u_i \partial_j u_i^\ell \tag{2.9}$$

Note that :

$$\frac{1}{2}\nu\partial_j\partial_j(u_i u_i)^\ell = \frac{1}{2}\nu(\partial_j\partial_j u_i u_i)^\ell = \nu(\partial_j[u_i\partial_j u_i])^\ell \tag{2.10}$$

so that $\lim_{\ell\to 0}\mathscr{D}_\nu^\ell = \nu\partial_j u_i\partial_j u_i$, for a regular velocity field at least. The limit of $\mathscr{D}_\nu^\ell$ when $\ell \to 0$ is the usual dissipation term, and $\mathscr{D}_\nu^\ell$ is therefore positive for small enough ℓ.

Replacing 2.9 in 2.5, we get the weak Kármán-Howarth-Monin equation :

$$\frac{1}{2}\partial_t u_i u_i^\ell + \partial_i {J_i}^\ell = -\mathscr{D}_\nu^\ell - \Pi_{DR}^\ell \tag{2.11}$$

where :

$${J_i}^\ell = T_i^\ell - \frac{1}{2}\nu\partial_i[(u_j u_j)^\ell + u_j u_j^\ell] + \nu(u_j\partial_i u_j^\ell) \tag{2.12}$$

(the viscous diffusion term is now embedded in J_i^ℓ).

This equation is very close to the balance equation for the regularized point-split energy density 2.5 and can be interpreted similarly ; only, it is better suited to analyze experimental data. It also resembles the Kármán-Howarth-Monin relation (see for instance [Frisch, 1995]), but it features local quantities whereas the Kármán-Howarth-Monin relation deals with average quantities.

1.3 Link with the LES energy equation

When discussing scale-by-scale energy budgets, smoothed (i.e. filtered) Navier-Stokes equations, or inter-scale transfer, it is difficult not to think to Large Eddy Simulations (LES) [Germano, 1992]. LES are numerical simulations of turbulent flows where only part of the inertial scales are resolved, and where the interactions with smaller scales are modelled. The simulated equations are the filtered INSE :

$$\partial_j u_j^\ell = 0$$
$$\partial_t u_i^\ell + \partial_j u_i^\ell u_j^\ell = -\partial_i p^\ell + \nu \partial_k \partial_k u_i^\ell - \partial_j \tau_{ij}^\ell$$

where the so-called subgrid stress tensor $\tau_{ij}^\ell = (u_i u_j)^\ell - u_i^\ell u_j^\ell$ has been introduced. This is the term corresponding to the interactions with smaller scales which should be modelled.
The LES energy equation is obtained by multiplying these filtered incompressible Navier-Stokes equations 1.3 by u_i^ℓ. A budget of the energy contained in the scales larger than $\approx \ell$ is then obtained :

$$\partial_t \frac{(u_i^\ell)^2}{2} + \partial_j \left(u_j^\ell \frac{(u_i^\ell)^2}{2} + u_j^\ell p^\ell - \nu u_i^\ell \partial_j u_i^\ell + u_i^\ell \tau_{sgs}^\ell \right) = -\nu \partial_k u_i^\ell \partial_k u_i^\ell + \partial_j u_i^\ell \tau_{sgs}^\ell \qquad (2.13)$$

In the following, we will use the notations :

$$\mathscr{D}_{\nu,LES}^\ell = \nu \partial_k u_i^\ell \partial_k u_i^\ell \text{ (viscous dissipation at scale } \ell)$$
$$\Pi_{LES}^\ell = -\partial_j u_i^\ell \tau_{sgs}^\ell \text{ (inter} - \text{scale energy transfer to scales smaller than } \ell)$$

Like the weak Kármán-Howarth-Monin equation 2.11, the LES energy equation features a spatial transport and diffusion term, a viscous dissipation term due to scales $> \ell$ ($\mathscr{D}_{\nu,LES}^\ell$) and an inter-scale transfer term towards scales $< \ell$ (Π_{LES}^ℓ). They can be interpreted in the same manner as terms $\mathscr{D}_\nu^\ell$ and Π_{DR}^ℓ, and in this case, $(u_i^\ell)^2/2$ is positive-definite and can really be interpreted as an energy. $\mathscr{D}_{\nu,LES}^\ell$ and Π_{LES}^ℓ seem both suited to the analysis of experimental data as none of them involves the gradient of an unsmoothed quantity. We can therefore wonder whether we should use rather the weak Kármán-Howarth-Monin equation or this LES energy equation for our study, i.e. the pair (Π_{DR}^ℓ, $\mathscr{D}_\nu^\ell$) or the pair (Π_{LES}^ℓ, $\mathscr{D}_{\nu,LES}^\ell$).
There is an argument which suggests to favour the first pair though. Contrary to Π_{DR}^ℓ, Π_{LES}^ℓ is the product of two terms : $\partial_j u_i^\ell$ and τ_{sgs}^ℓ. Assuming that the velocity field is locally h-Hölder continuous, i.e. $\delta u \propto \ell^h$, we can find the scaling of these two terms : $\partial_j u_i^\ell \propto \ell^{h-1}$ and $\tau_{sgs}^\ell \propto \ell^{2h}$. If $h < 1$, the first one will become very large as ℓ becomes small, whereas the second one will also become small. Therefore, the uncertainty on the product of the two terms should be quite large. This may also be the reason why Duchon and Robert used the balance equation for the regularized point-split energy density and Π_{DR}^ℓ rather than the LES energy equation and Π_{LES}^ℓ in order to derive the energy budget of weak solutions. In chapter 6, we compare the two pairs of terms and try to establish a link between the weak Kármán-Howarth-Monin and the LES energy equation.

2 Practical implementation of the detection method

In this section, we discuss some practical issues of the detection method based on the Duchon-Robert term : the scale effectively probed by the smoothing function $\phi^\ell(\mathbf{x}) = \exp(-30\mathbf{x}^2/(2\ell^2))$,

the discretization of this smoothing function, the problem of PIV filtering and the limited thickness of the measurement volume.

2.1 Probed scale

It can be asked whether ℓ is exactly the smallest scale probed by ϕ^ℓ or whether there is a prefactor. For instance, we could say that the probed scale is the Gaussian mid-height width ($\sqrt{2\ln(2)/30}\ell$), because ϕ^ℓ is too small for $|\mathbf{x}|$ above this length, and the local-averaging stops there. Actually, "probing a scale" is not a rigorous well-defined concept, so we can choose how to define it. We chose to define it based on the 2 dB cut-off wavenumber of ϕ^ℓ, seen as a filter. The Fourier transform of ϕ^ℓ is :

$$\widehat{\phi^\ell}(\mathbf{k}) = \exp\left(-\frac{\mathbf{k}^2\ell^2}{2\times 30}\right) \tag{2.14}$$

The 2 dB cut-off (of the energy spectrum) is reached for $|\mathbf{k}| = k_c^\ell = \sqrt{30\ln(2)}/\ell$. According to Shannon's criterion, the smallest period of a signal that can be captured by a mode of wavenumber k_c^ℓ is π/k_c^ℓ. Therefore, we define the smallest scale probed by ϕ^ℓ as :

$$\ell_c = \frac{\pi}{\sqrt{30\ln(2)}}\,\ell \approx 0.69\ell \tag{2.15}$$

In this thesis, we will use ℓ_c most of the time ; it should always be understood as $\ell_c = \ell_c(\ell) = \pi\ell/\sqrt{(30\ln(2))}$.

2.2 Smoothing function discretization

In this thesis, we deal with experimental velocity fields consisting in a discrete sampling of the flow. Therefore, we compute discrete approximations of the integrals involved in the weak Kármán-Howarth-Monin and LES terms. When ℓ is too small, the smoothing function is not well discretized and the integrals cannot be properly computed. This can be seen in figure 2.1 (a) : for $\ell = 1\cdot dx$, ϕ^ℓ is equal to zero everywhere except in 0 ; this is a crude approximation of the Gaussian ϕ^ℓ. We observed on analytical examples that ℓ should be greater than or equal to 6 or 7 dx so that the proper values of the weak Kármán-Howarth-Monin and LES terms are obtained.

2.3 PIV filtering

The choice of the definition of ℓ_c was inspired by the analysis of the filtering effect of Particle Image Velocimetry (PIV, see chapter 4).
In an experiment, the measured velocity field $\widetilde{\boldsymbol{u}}$ can be modelled as the original velocity field $\boldsymbol{u}$ filtered at the resolution scale :

$$\widetilde{\boldsymbol{u}}(\mathbf{x}) = \psi^{exp} * \boldsymbol{u}(\mathbf{x}) = \int \psi^{exp}(\mathbf{r})\mathbf{u}(\mathbf{x}-\mathbf{r})d^3\mathbf{r} \tag{2.16}$$

where ψ^{exp} is a transfer function modeling the effect of the measurement chain. For a PIV measurement with square interrogation windows, this function can be approximated by a top hat function whose width is the interrogation window size X (see chapter 4).
Because of the PIV filtering, we lose all the information about scales smaller than $\approx X$. A first consequence is that it is useless to use smoothing functions ϕ^ℓ filtering less than the PIV filter :

fluctuations over scales smaller than $\approx X$ would have already been filtered. This is achieved if the 2 dB cut-off $k_c^\ell = \pi/\ell_c$ of ϕ^ℓ is less than or equal to the 2 dB cut-off k_c of PIV. For a square interrogation window of size X, the 2 dB PIV cut-off is equal to $2.8/X \approx \pi/X$. Therefore, ℓ_c should be greater than X : the definition of ℓ_c allows to compare it directly to X.
Figure 2.1 allows to compare the filtering due to a square interrogation window (whose size is 4 times the space step for an overlap of 75%, see chapter 4) and to the filtering due to the Gaussian smoothing function we use in this thesis at several scales. Figure (b) clearly shows that ℓ_c is more relevant than ℓ : the filtering due to the PIV and the one due to the Gaussian filter are closer for $\ell_c \approx X = 4dx$ than for $\ell \approx X = 4dx$. It can also be seen that for $\ell_c < X$, the smoothing function ϕ^ℓ is narrower than the top-hat function corresponding to PIV filtering : it is clear that using such filters after the top-hat filter is meaningless.

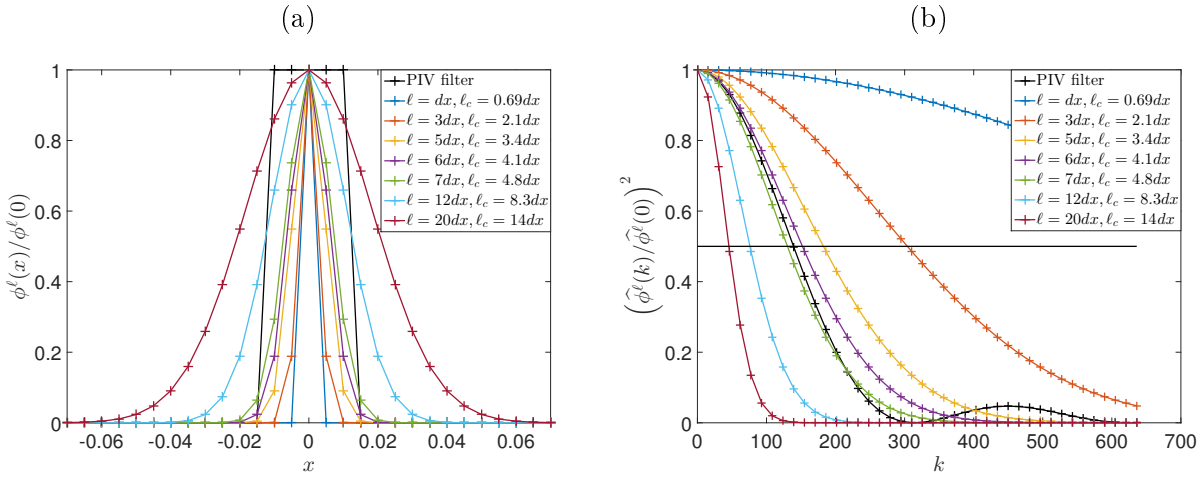

Figure 2.1: (a) Normalized smoothing function $\phi^\ell(x)/\phi^\ell(0) = \exp\left(-30x^2/(2\ell^2)\right)$ for several ℓ (a) and square of the corresponding Fourier transforms (normalized too) (b). The space step is $dx = 0.005$ (dimensionless value), this is the horizontal distance between two consecutive crosses + on (a). The PIV filter is a top-hat filter of width $4dx$.

A second consequence of PIV filtering is that we can only compute the inter-scale transfer and viscous dissipation terms on already coarse-grained velocity fields. For example, we will not compute the Duchon-Robert term :

$$\Pi_{DR}^\ell(\mathbf{x}) = \int \boldsymbol{\nabla}\phi^\ell(\mathbf{r}) \cdot \boldsymbol{\delta u}(\boldsymbol{\delta u})^2 d^3\mathbf{r} \tag{2.17}$$

$$\tag{2.18}$$

but :

$$\int \boldsymbol{\nabla}\phi^\ell(\mathbf{r}) \cdot \widetilde{\boldsymbol{\delta u}}(\widetilde{\boldsymbol{\delta u}})^2 d^3\mathbf{r} \tag{2.19}$$

$$\tag{2.20}$$

This is a priori a problem when ℓ_c is in the inertial range as a lot of scales are filtered, and possibly in the dissipative range if there exists scales smaller than the Kolmogorov scale. However, if $\ell_c >> X$, one can invoke the principle of UV locality introduced by Eyink ([Eyink, 2005], [Eyink, 2008]) and consider that most of the contribution to Π_{DR}^ℓ comes from scales close to ℓ_c. Note that this principle is valid only for places where the local Hölder exponent is larger than 0. It is probably

the case almost everywhere, but not around possible prints of singularities that we are interested in. Π^{ℓ}_{DR} may therefore be underestimated there. In this thesis, we have at most $\ell_c > 1.7X$ for 3D measurements because of the limited thickness of the measurement volume. This may not be enough and this fact should be kept in mind while analyzing the results.

2.4 Finite volume thickness

During this thesis, we performed 3D measurements of the velocity field. A priori, this allows to compute 3D fields of the Duchon-Robert term as well as the other terms. However, in tomographic particle image velocimetry (TPIV), one of the dimensions of the measurement volume is smaller (about 8 times smaller) to ensure a proper volume reconstruction (see chapter 4).
In addition to that, the weak Kármán-Howarth-Monin and LES terms cannot be computed over the whole velocity field. Indeed, they correspond to integrals over space. Fortunately, the integrand is very small over most of the space because ϕ^{ℓ} is a Gaussian ; therefore the integral can be computed even if we do not have access to the whole velocity field. However, all the points where the integrand cannot be neglected should be considered. We empirically observed that the integrand is not negligible over a sphere of radius $\approx 3\ell + dx$ (dx being the space step). This means that the weak Kármán-Howarth-Monin and LES terms cannot be computed over margins as wide as $3\ell + dx$ on the sides of the velocity field : indeed, one does not know the velocity field outside. This is schematized in figure 2.2.

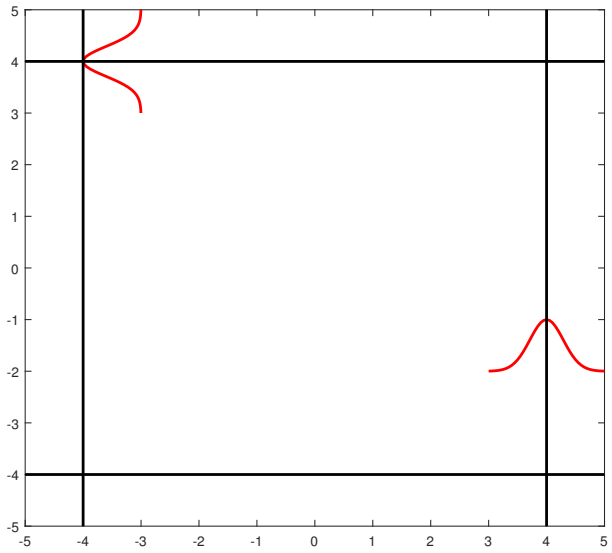

Figure 2.2: Schematic representation of the margins on which the weak Kármán-Howarth-Monin and LES terms cannot be computed. The red curves correspond to the Gaussian filter ϕ^{ℓ} and the black lines to the margins. Outside the margins, the filter cannot be convoluted with the velocity field because the velocity is not available out of the velocity field

On the one hand, ℓ cannot be too small to ensure a proper discretization of the smoothing function and to get enough contribution of the measured scales in the weak Kármán-Howarth-Monin and LES terms ; on the other hand, the volume has a rather small thickness to ensure a proper volume reconstruction in TPIV. The result is that we are left with only one scale ℓ at which the weak

Kármán-Howarth-Monin and LES terms can be properly computed : the largest ℓ such that the corresponding filter width fits in the volume thickness. At this scale, the weak Kármán-Howarth-Monin and LES terms are available on one or two planes only, in the middle of the measurement volume. Therefore, we only have 2D fields of the weak Kármán-Howarth-Monin and LES terms, but compared to the previous work [Saw et al., 2016], we can compute the "full" terms, not a 2D version of them. Indeed, we have access to the velocity out of the plane and can thus compute gradients in the direction perpendicular to the plane ; it was not possible with stereoscopic particle image velocimetry (SPIV) measurements which give access to the three components of the velocity field on a plane only.

2.5 Multi-scale analysis ?

According to what precedes, there is only one length scale ℓ at which the weak Kármán-Howarth-Monin and LES terms can be properly computed. How to perform a multi-scale analysis then ? We will vary the Reynolds number and therefore the Kolmogorov scale so that the ratio ℓ_c/η varies. This is explained in the next chapter.

3 Comparison between the experimental and numerical approaches

The detection method described in the previous sections can be applied to any velocity field, be it analytical, numerical or obtained from the experiment. The analytical approach is to be handled by mathematicians. As for physicists, the numerical and experimental approaches both have their own advantages and limits, and are therefore complementary. In this thesis, we focus on experimental results. Still, it is interesting to discuss here the respective advantages and limits of both approaches. In particular, the experimental limits should be kept in mind while analyzing and interpreting the results.

3.1 Numerical approach

The numerical approach consists in numerically integrating a discretized version of the 3D incompressible Navier-Stokes equations. The obtained velocity field behaves like a solution of the 3D INSE under certain assumptions.
There are mainly two kinds of numerical simulations. Simulations of the first kind do not compute small scale fluctuations and use models to account for their impact on larger scales. They include for instance RANS simulations (Reynolds-Averaged Navier-Stokes) and LES (Large Eddy Simulations). They are not suited at all to study the problem of singularities as they do not simulate small scales. Simulations of the second type, namely DNS (Direct Numerical Simulations), do not involve any such model and are supposed to resolve all the scales. We will therefore only consider DNS here.
In a DNS, the spatial and time resolutions are then necessarily finite. In order to reproduce the behaviour of the 3D INSE, a DNS should have a spatial and a time resolution which are smaller than the smallest flow length- and time-scales.

3.1.1 Usual estimation of the computational and storage costs for a DNS

In the case of the Navier-Stokes equations, it is usually considered that the smallest length scale is the Kolmogorov scale $\eta = (\nu^3/\epsilon)^{1/4}$. Calling respectively L and U the flow large scale and the flow typical velocity at this large scale, we obtain a Reynolds-based expression for the Kolmogorov scale : $\eta = L(Re^3\epsilon^*)^{-1/4}$. In this expression, $\epsilon^* = \epsilon L/U^3$ is the dimensionless average energy

dissipation rate, which is known to be independent from Re in the limit of large Reynolds numbers : this is the dissipation anomaly. Therefore, if one wishes to simulate the flow in a volume of size $\approx L$, one should use a space step $dx \leq \eta$, and there would be more than $(L/\eta)^3 \propto Re^{9/4}$ grid points. The three components of the velocity and the pressure should be computed and stored at each grid point. The total number of operations per time step and the memory should therefore scale like $Re^{9/4}$. Furthermore, the equations have to be integrated with respect to time. To this end, a sufficiently small time step should be used. The smallest time scale of a turbulent flow can be estimated in the same manner as the Kolmogorov scale, by comparing inertial and viscous terms : $\tau = (\nu/\epsilon)^{1/2} = T(Re \cdot \epsilon^*)^{-1/2}$ where $T = L/U$ is the typical time-scale at large scales. To simulate the Navier-Stokes equations over one large time-scale T, one should therefore use more than $T/\tau \propto Re^{1/2}$ space steps. Therefore, the total number of operations needed to simulate the Navier-Stokes over one large time-scale scales like $Re^{9/4} * Re^{1/2} = Re^{11/4}$. As turbulent flows correspond to large Reynolds numbers, the computational cost is huge. To perform the simulations in a reasonable time period, complicated parallelization algorithms have to be used. The storage costs are also important ($\propto Re^{9/4}$ per velocity field), even if not every velocity field has to be recorded.
For instance, a state-of-the-art simulation [Yeung et al., 2015] recently achieved to simulate homogeneous isotropic turbulence (HIT) in a cube of 8192^3 gridpoints. The Taylor-based Reynolds number was 1300, corresponding approximately to a Reynolds number of 640000 in a von Kármán flow (see chapter 3), and the resolution was around η. More than 250 000 cores were used on a machine rated at more than 10 petaflops (10^{15}) in aggregated speed, and a storage capacity of 0.5 petabyte was used. Simulations of real flows are more complex than simulations of HIT. For instance, the largest Reynolds number reached in a DNS of a von Kármán flow by the team of Caroline Nore is 6000. A DNS of ten impeller rotations of the full von Kármán flow at a Reynolds number of 6000, with a resolution equal to the Kolmogorov scale, takes one million computation hours with the SFEMANS code [Cappanera et al., 2019]. This gives around 200000 velocity fields, but only 30 independent ones. Such a DNS took 10 days to complete on a cluster of 2000 cores. For comparison, according to the ranking available at www.top500.org in June 2019, the fastest supercomputer could deliver almost 150 petaflops with slightly less than 250000 cores (requiring a power of 10MW).
Note that in this subsection, we obtained a scaling depending on the Reynolds number, but the prefactor is also important. The Kolmogorov length- and time- scales are estimations of the smallest flow length- and time- scales, but they may involve prefactors ; for instance, the smallest flow length scale could be $\eta/5$ requiring a simulation resolution even smaller : $dx \approx \eta/10$. In [Yeung et al., 2018], the authors point out the influence of the spatial and temporal resolutions on the characteristics of the extreme vorticity events and suggest that the resolution used in [Yeung et al., 2015] was not small enough.

3.1.2 The case of singularities

In the previous chapter, we showed that if singularities existed, they would probably come along with scales smaller than the dissipative scale involved in turbulent flows. Therefore, the space- and time-steps of the DNS should be quite smaller than η and τ. To comply with that, there are two possibilities : either keeping constant space- and time-steps and decreasing the Reynolds number, in order to increase η and τ ; or decreasing the space- and time-steps, which requires to increase the computational power and memory compared to the above estimations.
For instance, using the scaling suggested by the multifractal model, given a minimum Hölder exponent h_{min} in the flow (see previous chapter), the smallest length in the flow should be $\eta_{h_{min}} = LRe^{-1/(1+h_{min})}$. The total number of operations per time step and the memory should then scale

like $Re^{3/(1+h_{min})}$ and the total number of operations needed to simulate the Navier-Stokes over one large time-scale like $Re^{3/(1+h_{min})} * Re^{(1-h_{min})/(1+h_{min})} = Re^{(4-h_{min})/(1+h_{min})}$. However, these scalings are based on the existence of such scaling exponents in turbulent flows, which is still to prove. Also, adaptative meshes can be used with a variable space step for which the above estimations are too conservative : indeed, the mesh is refined only where needed (where the local Hölder exponent is small for instance) and can be coarser elsewhere. In [Pumir and Siggia, 1990], the mesh is thus refined 50 to 600 times at relevant places.

3.2 Experimental approach

The experimental approach consists in measuring velocity fields in a real flow, which is assumed to follow the 3D incompressible Navier-Stokes equations. As detailed in the previous chapter, this is the case if the incompressibility and scale separation hypotheses are valid, i.e. if the flow velocity is smaller than the sound speed in the fluid and if the smallest flow length-scale is much larger than the molecular scale.

3.3 Comparison

3.3.1 Agreement with the Navier-Stokes equations

A DNS allows to study a discretized version of the 3D incompressible Navier-Stokes equations with a finite number of modes ; measuring the velocity in an experiment allows to study a physical phenomenon that can well be accounted for by the 3D INSE. In both cases, the velocity field can be considered as a solution of the 3D INSE only as long as certain assumptions are verified. It is likely not to be the case if a singularity occurs, as such singularities are known to come along with infinitely small scales and infinitely large velocity amplitudes. In a DNS, the obtained velocity field will stop correspond to the 3D INSE when scales smaller than the simulation resolution will be generated. In an experiment, there is also a constraint on the smallest flow length scale, which should be much larger than the molecular scale. However, this is probably much less limiting than in a simulation. For instance, in the von Kármán flow used in this thesis, the Kolmogorov scale is around 15 μm at $Re = 3 \times 10^5$ (and larger at smaller Reynolds numbers), and the molecular scale is around 0.1 nm, i.e. more than 5 orders of magnitude lower. In a DNS, the spatial resolution is usually set around the Kolmogorov scale, and decreasing it requires to decrease the Reynolds number. Therefore, the hypothesis on the smallest flow length scale will probaby hold longer in the case of the experimental approach. The most limiting assumption of the experimental approach is probably the incompressibility assumption.

3.3.2 Sampling

Singularities, if they exist, are scarce. Therefore, a large amount of velocity fields should be collected to have a chance to detect a print of singularity. Simulations are not well suited to that : they produce correlated velocity fields at a huge cost ; producing independent velocity fields would be even more costly. On the contrary, in an experiment, one just needs to use a low enough acquisition rate to be sure that two following velocity fields are uncorrelated ; what happens between these two velocity fields is totally ignored.
However, state-of-the art DNS of homogeneous isotropic turbulence involve velocity fields so large that they allow to gather enough statistics on few frames. For instance, in [Yeung et al., 2015], one velocity field contains $8192^3 \approx 5 \times 10^{11}$ points, separated by a distance around the Kolmogorov scale η. In this thesis, one velocity field contains around $100 \times 150 \times 20 \approx 3 \times 10^5$ points separated

by η, and we collect 30000 such velocity fields, yielding $\approx 10^{10}$ points. The DNS approach seems to allow a better sampling ; this is true only if a resolution of the order of the Kolmogorov scale is enough. If the resolution should be of the order of $\eta/10$, then the number of points separated by η would be only $\approx 800^3 \approx 5 \times 10^8$.

3.3.3 Resolution and Reynolds number

Singularities are characterized by very fine scales ; therefore, a fine resolution is needed when looking for prints of them. Also, their apparition might be conditioned on the Reynolds number, as suggested at the end of [Yeung et al., 2015]. Therefore, large Reynolds numbers should be studied. In this thesis, we obtain an experimental resolution of the order of the Kolmogorov scale for a Reynolds number of 6000. In a close future, we should be able to get down to $\eta/5$ or to increase the Reynolds number up to 50000 while keeping the resolution around the Kolmogorov scale (see chapter G). The DNS of [Yeung et al., 2015] reached a Taylor-based Reynolds of 1300, corresponding to a Reynolds number of 640000 in our von Kármán flow, with a resolution of 1.5η. It seems much better than what can be done in the experiment, but it should be nuanced : if the resolution should be of the order of $\eta/10$, then the Reynolds number would be around 6000, of the order of the Reynolds number reached in the experiment. As for the DNS of the von Kármán flow performed by the team of Caroline Nore at a Reynolds number of 6000, their resolution is around the Kolmogorov length scale too. However, larger Reynolds are out of reach currently.

3.3.4 Measurement error

In numerics, there is no measurement error, contrary to the experiments. However, singularities of the Navier-Stokes equations should come along with large velocities, and singularities of the Euler equations should come along with large vorticities. Therefore, such events should not be hidden in the noise. However, it is possible that spurious measurements lead to the detection of irrelevant events. Furthermore, in the case of Particle Image Velocimetry (PIV) measurements, it is possible that the occurence of prints of singularities breaks down the grounding assumption that the tracked particles follow the fluid. In this case, the event would probably be detected but the velocity field around it would be inaccurate.

3.3.5 Dynamic range

In order to perform scale-by-scale analyses of a flow, the size of the velocity field should be large compared to the space step. In a DNS, all scales from the large scale to the space step are simulated and available. The dynamic range, i.e. the ratio between the largest scale and the space step, is 8192 in the DNS of HIT previously mentioned. In the case of PIV measurements, the dynamic range is limited by the sensor size and the minimum interrogation window size (see chapter 4) ; currently in 2D PIV it is at most a few hundreds. In the case of tomographic PIV, where the thickness of the velocity field is limited and where the seeding particle concentration cannot be too high, implying larger interrogation volume size, the dynamic range based on the smallest dimension is rather of the order of a few tens. Also, we showed in the previous section that for an experimental velocity field, which has a finite width, the weak Kármán-Howarth-Monin and LES terms can only be computed on a restricted almost 2D area. In a DNS of homogeneous isotropic turbulence, this is not the case as these terms can be computed over the boundaries (which are periodic).

3.3.6 Forcing

There is an additional difference between simulations of homogeneous isotropic turbulence (HIT) and experiments : the forcing, i.e. the way the energy is injected. Indeed, in experiments, the forcing comes from the boundary conditions : for instance, an impeller rotating in a fluid will rotate it, but there is no forcing in the bulk of the flow. In the case of a simulation of (HIT), there are periodic boundary conditions so the forcing cannot be due to these boundary conditions ; a volume forcing, local in scale (at large scales) is usually used.
This difference in forcing could impact the formation of a singularity. In the official formulation of the problem of singularities, as stated by the Clay Institute, the considered space is either $\mathbb{R}^3$ or $\mathbb{R}^3/\mathbb{Z}^3$, so there are either no or periodic boundary conditions. The existence and smoothness should be proved for a 0 forcing only.

3.3.7 Conclusion

The comparison between the experimental and numerical approaches shows that both have pros and cons. It is difficult to conclude as it is not clear what the smallest resolution of a DNS should be. The main advantage of the experiment approach is to allow length scales much smaller than the Kolmogorov scale, even if they cannot be measured. Either DNS neglect these smaller scales, which could impact the velocity field and possibly hinder the formation of possible singularities, or they resolve these smaller scales, but cannot reach too large Reynolds numbers.

4 Outline of the method

We will now sum up the goal of the thesis and the strategy used to reach it.

The guideline is the following : analyzing 3D velocity fields obtained by experimental means in a real turbulent flow in order to provide more insight into the possible singularities that might occur in the solutions to the 3D incompressible Navier-Stokes and Euler equations. We look for prints of them, i.e. places where the inter-scale transfer or the ratio of inter-scale transfer to viscous dissipation is extreme. We then examine how these prints are distributed, how they look like and how they evolve with respect to time, assuming that these prints behave to some extent like the possible singularities.

In order to do so, we generate a turbulent flow at several Reynolds numbers using the von Kármán set-up described in chapter 3. We do not resolve the Kolmogorov scale at all Reynolds numbers but we vary it to study different scale ranges, from the inertial one to the dissipative one. The different cases investigated are presented in chapter 5.

We measure the velocity field in this flow by particle image velocimetry methods detailed in chapter 4, either time-resolved or not.

Non-time-resolved measurements allow to get uncorrelated velocity fields and thus to sample more properly the extreme events. We used such measurements to study the distribution of inter-scale transfer and viscous dissipation, and of their extreme values, as reported in chapters 6 and 7. We used both stereoscopic and tomographic particle image velocimetry (resp. SPIV and TPIV), giving access to the three components of the velocity field in repectively two and three dimensions. The latter one can then be used to study the topology of the prints of singularities, this is exposed in chapter 8.

Time-resolved measurements are used to study the time evolution of extreme events, in an Eulerian frame. This is the subject of chapter 9.

The current spatial resolution of our experimental set-up is around the Kolmogorov scale. We showed in the previous chapter that singularities, if they exist, involve scales smaller than this Kolmogorov scale. Therefore, improving the experimental resolution is required to study this kind of events. In appendix G, we present the design of an experimental set-up five times bigger than the one used in this thesis and meant to improve the spatial resolution. The design of this set-up was one of the tasks of this thesis, but the set-up itself was not used during this thesis.

Part II

Description of the experimental set-up and measurements

Chapter 3

Implementation of the von Kármán flow : the VK2 set-up

In this chapter, we describe the turbulent flow used in this thesis, as well as the corresponding experimental set-up. The advantages of using such a flow are then detailed.

1 Flow description

A von Kármán flow is a general type of flow generated between two rotating impellers facing each other. This is quite a wide definition, gathering a lot of flows, since the relative size of the impellers and the distance between them can be varied, as well as their rotation frequencies, the shape of their blades or the boundary conditions. A summary of the scientific work dealing with these flows can be found in [Marié, 2003].

1.1 Geometry

In this thesis, we consider a particular von Kármán flow, whose geometry is shown in figure 3.1. The extension of the flow is finite, limited by a cylinder of radius R. The aspect ratio, defined as the distance between the disks H divided by the cylinder radius, is 1.8.

There are two identical impellers, one at the bottom and one at the top. They are disks supporting eight blades, as depicted on figure 3.2. These blades are circular arcs passing through the center of the impeller and whose radius is such that the exit angle defined on figure 3.2 is 72°. These impellers correspond to the "TP87" or "TM87" impellers described in [Ravelet, 2005] ("P" stands for plastic and "M" for metallic). In this thesis, we only consider the case where they are exactly counter-rotating, their rotation frequency being imposed. We distinguish between the positive direction of rotation, called "contra", when the convex side of the impellers pushes the fluid, and the negative direction, called "anti", when it is the concave side of the impellers which pushes the fluid.

The geometry of our von Kármán flow is invariant by rotations R_θ around the cylinder axis, which we will call vertical axis, with θ a multiple of 45° (the angle between two blades), and by the so-called R_π symmetry : a rotation of π radians around any horizontal axis crossing the center of the cylinder.

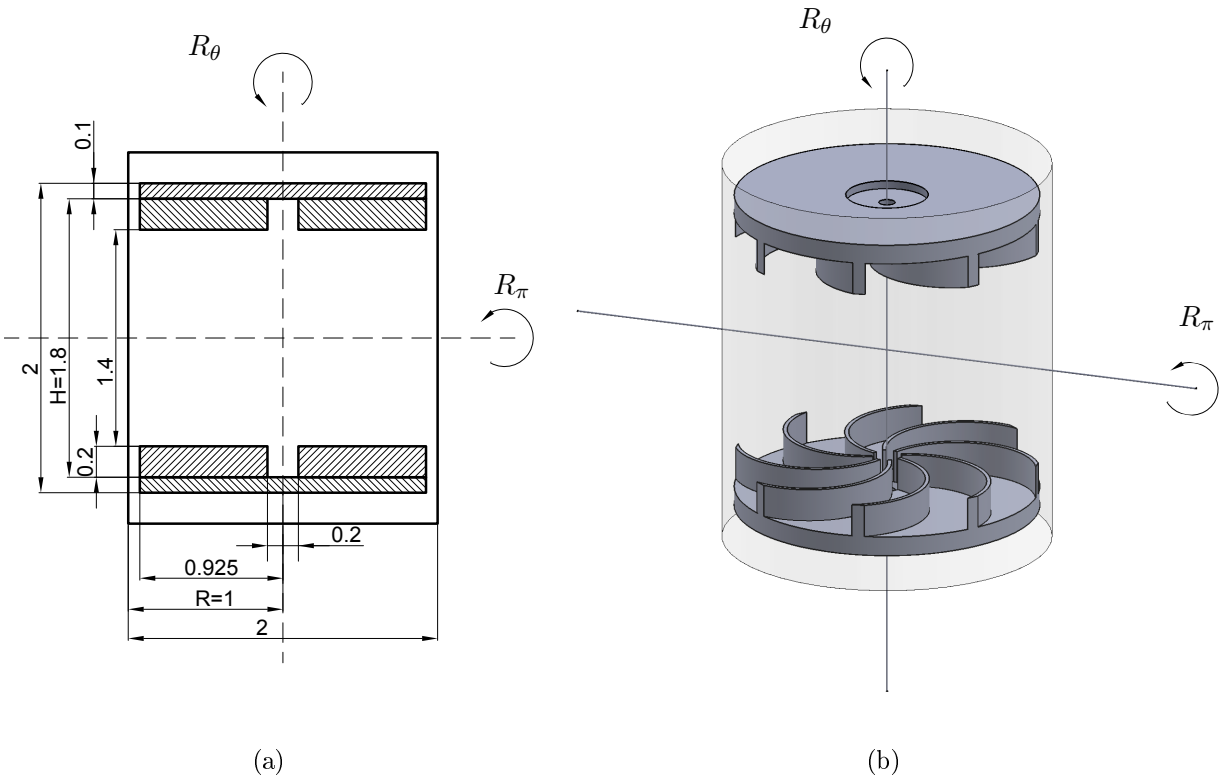

(a) (b)

Figure 3.1: Geometry of the considered von Kármán flow. (a) Vertical cross-section. (b) Perspective. The lengths are in units of the cylinder radius R.

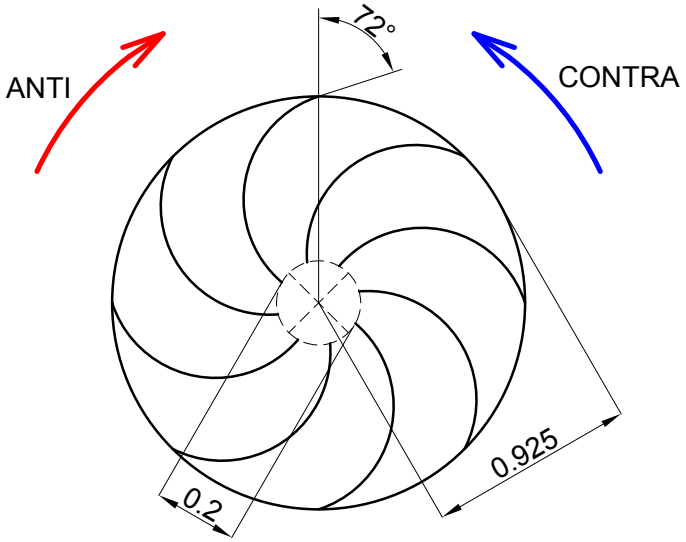

Figure 3.2: Geometry of the TP87 impellers. The lengths are in units of the cylinder radius R.

1.2 Velocity field in laminar and turbulent regimes

The considered von Kármán flow is characterized by a Reynolds number based on the cylinder radius R, the impeller rotation frequency F and the fluid kinematic viscosity ν as follows :

$$Re = \frac{2\pi R^2 F}{\nu} \tag{3.1}$$

The transition to turbulence was studied during the PhD thesis of Florent Ravelet [Ravelet, 2005, Ravelet et al., 2008] (for similar impellers but with twice more blades). It starts around $Re = 150$ and for $Re > 6000$ the flow is fully turbulent. In the laminar regime, the flow is made of two rotating cells corresponding to the two impellers and separated by a mixing layer with a strong shear. Each cell motion can be splitted into two components : a toroidal one, corresponding to the rotational motion of the impeller, in blue on figure 3.3 (a) and a poloidal one, in red, corresponding to a pumping motion : impellers expel fluid towards the cylinder, and therefore the fluid is sucked at the center of the impellers. Both cells are symmetrical with respect to the R_π symmetry and therefore have the same size. There is no qualitative difference between contra and anti directions in the laminar regime, only the direction of rotation is different : for instance, the laminar flow corresponding to the contra direction of rotation can be figured out by reversing the blue arrows of figure 3.3 (a).

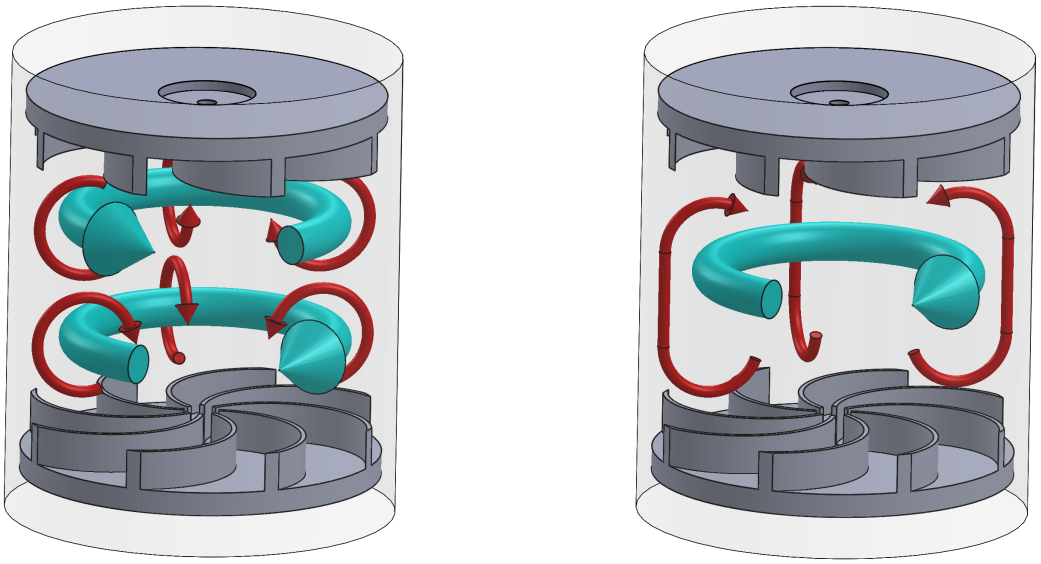

(a) (b)

Figure 3.3: Average flow. (a)Anti direction, symmetrical flow. (b) Anti direction, bifurcated flow (bottom impeller imposing its direction). The blue arrows correspond to the toroidal components and the red arrows to the poloidal components.

When the flow is turbulent, the velocity field is of course much more complex. However, for the contra direction the average velocity field is similar to the laminar one. For the anti direction, the situation is more complicated : when the impellers start counter-rotating at the same frequency, the average velocity field is similar to the laminar velocity field, as depicted on figure 3.3 (a) or 3.4 (a), even if the velocity strongly fluctuates (the rms of the three velocity components are shown on figures 3.4 (b), (c) and (d)). This average velocity field is symmetrical with respect to the R_π symmetry, so the flow is said to be statistically invariant by the R_π symmetry. But after some time,

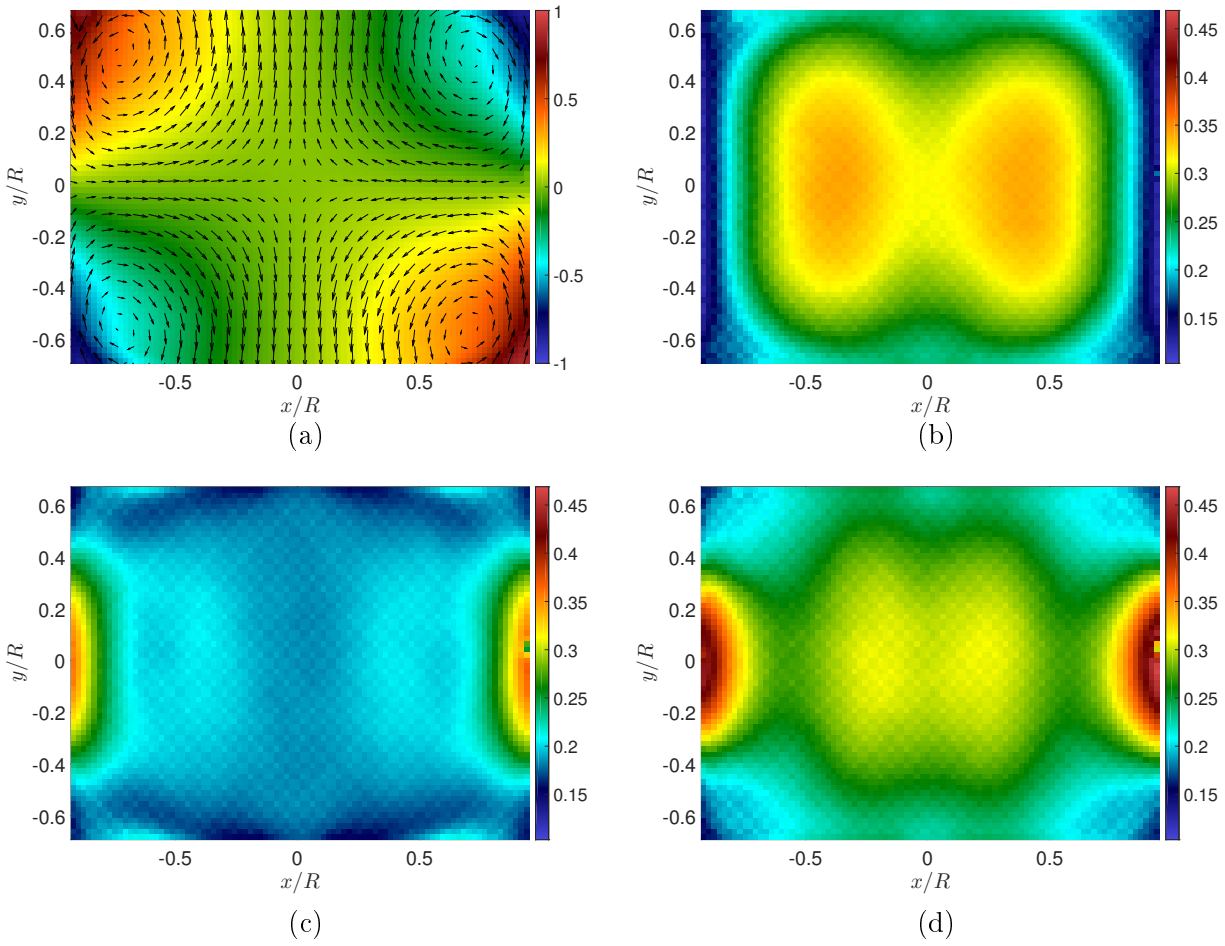

Figure 3.4: Average velocity field and rms fields at $Re = 3 \times 10^5$ for impellers rotating in the anti direction. The flow is symmetric. (a) The arrows correspond to the average in-plane component and the color to the average out-of-plane component (u_z). (b) u_x^{rms}. (c) u_y^{rms}. (d) u_z^{rms}. The color scale corresponds to the velocity normalized by $2\pi RF$, the color scale for (a) is different from the colorscale of (b), (c) and (d).

the average velocity field switches to a state with only one rotating cell, as shown on figure 3.3 (b). The statististical invariance with respect to the R_π symmetry is then broken, and the flow is said to bifurcate. This bifurcation is described in [Ravelet et al., 2004]. One impeller pumps and rotates most of the fluid, while the other one has much less effect. There is not even a second smaller cell confined to the "dominated" impeller : as can be seen in [Cappanera et al., 2019], even very close to the "dominated" impeller, the azimutal velocity has the same direction as the "dominating" impeller. Such a bifurcation happens without modifying the rotation frequency of the impellers, and when the flow is bifurcated, it cannot come back to a symmetrical state. Note that there are two possible bifurcated states : the single rotating cell can either follow the bottom impeller (this is the case shown on figure 3.3 (b)) or the top one. For impellers counter-rotating at the same frequency, the average time before the flow bifurcates is very large : the flow is said to be marginally stable. In practice, this almost never happens, but one must all the same be careful and check whether the flow is symmetrical or not.

The bifurcation can also happen when the rotation frequency of only one of the impellers is increased : this impeller will then "beat" the other and impose its rotation direction to most of the

flow. In contra direction, when increasing only one impeller rotation frequency, there is no bifurcation but the cell corresponding to the faster impeller becomes larger than the other and the mixing layer between the two cells is moved towards the slower impeller.

1.3 Global dissipation rate, dissipation anomaly and characteristic scales

Let us call T the average torque (over time) applied on the fluid by one impeller. The total applied torque is $2T$ and the total power is $2(2\pi F)T$. The dimensionless average torque applied by one impeller on the fluid is called K_p :

$$K_p = \frac{T}{\rho R^5 (2\pi F)^2} \tag{3.2}$$

The behaviour of K_p with respect to the Reynolds number Re was studied in several configurations for TP87 impellers or similar impellers with the same behaviour. The K_p vs. Re curves are plotted in figure 3.5. In the laminar regime, there is no difference between contra and anti directions, and both dimensionless torques behave as $1/Re$: dissipation is proportional to viscosity. However, in the turbulent regime, the laminar curve splits into three different curves, each saturating to a constant value for high Re. The lowest one corresponds to the contra direction, the middle one corresponds to the anti direction in a symmetrical state and the top one to the anti direction in a bifurcated state : in turbulent regime, the applied torque and power are higher for anti direction than for contra one, and higher for a bifurcated state than a symmetrical one in anti direction. In the bifurcated state, the impeller imposing its rotation to most of the fluid applies a higher torque than the other one. The saturation of the dimensionless torque value was observed up to $Re = 10^8$ thanks to VKS and SHREK experiments [Saint-Michel et al., 2014]. It corresponds to the dissipation anomaly mentioned in chapter 1 and widely observed in turbulent flows : the dissipation is independent of viscosity at high Reynolds numbers.
The average energy dissipation rate per unit mass ϵ in our von Kármán flow depends on K_p. In steady state, the energy dissipation rate is equal to the power injected by the impellers. Let us call m the total mass of fluid in the flow. As the aspect ration is 1.8, we have :

$$m = \rho\pi R^2 H = 1.8\rho\pi R^3 \tag{3.3}$$

Therefore :

$$\epsilon = \frac{2(2\pi F)T}{m} = \frac{2\rho R^5 (2\pi F)^3 K_p}{1.8\rho\pi R^3} = \frac{2R^2(2\pi F)^3 K_p}{1.8\pi} \tag{3.4}$$

The dimensionless average energy dissipation rate per unit mass is (the asterisk means that a quantity is dimensionless) :

$$\epsilon^* = \frac{\epsilon}{R^2(2\pi F)^3} = \frac{2K_p}{1.8\pi} \tag{3.5}$$

The dimensionless Kolmogorov length, time and velocity scales of the flow (respectively η^*, τ^* and v_k^*) are :

$$\eta^* = \frac{\eta}{R} = (Re^3\epsilon^*)^{-1/4} \tag{3.6}$$

$$\tau^* = 2\pi F\tau = (Re\cdot\epsilon^*)^{-1/2} \tag{3.7}$$

$$v_k^* = \frac{v_k}{2\pi RF} = (Re/\epsilon^*)^{-1/4} \tag{3.8}$$

$$\tag{3.9}$$

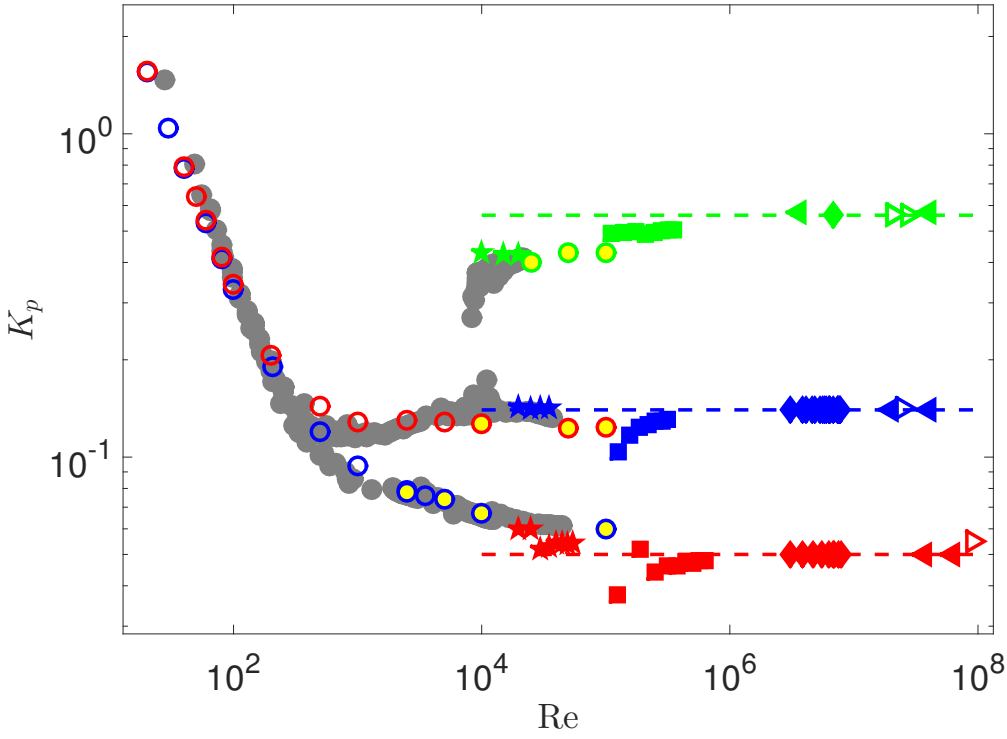

Figure 3.5: Dimensionless torque as a function of the Reynolds number in a von Kármán flow. Grey symbols were obtained with TM60 impellers that are similar to TM87 impellers except that they have 16 blades instead of 8 (see [Ravelet, 2005, Ravelet et al., 2008]) ; all other symbols were obtained with TM87 impellers. Red symbols correspond to the contra direction of rotation whereas blue symbols correspond to the anti direction of rotation with a symmetrical flow and the green symbols correspond also to the anti direction of rotation with a bifurcated flow. Pentagons were obtained with a water-glycerol mixture and squares with only water ; both pentagons and squares correspond to measurements performed in the VK2 set-up. Diamonds correspond to measurements performed in the VKS set-up, the working fluid being liquid sodium (unpublished data, courtesy of the VKS collaboration : M. Faure, N. Bonnefoy, S. Miralles, N. Plihon, J.-F. Pinton, Ph. Odier, G. Verhille, M. Bourgoin, S. Fauve, F. Petrelis, M. Berhanu, N. Mordant, B. Gallet, S. Aumaitre, F. Daviaud, A. Chiffaudel, R. Monchaux, P. Gutierrez). Triangles correspond to measurements performed with liquid helium in the SHREK set-up [Saint-Michel et al., 2014] : left-pointing triangles were obtained with helium-4 at T=2.3 K and right-pointing triangles with helium-4 at T=2 K (superfluid phase). The colourful circles correspond to numerical simulations : empty circles correspond to DNS and yellow-filled circles to LES (courtesy of Caroline Nore). This figure is a compilation of results published in [Dubrulle, 2019] and [Cappanera et al., 2019].

Concerning the injection length scale of our von Kármán flow, it is between the impeller height ($0.2R$) and the cylinder radius (R).

We can also compute the dimensionless Taylor length scale λ^*. Usually, the Taylor length scale is defined by :

$$\frac{(u_i^{rms})^2}{\lambda^2} = (\partial_i u_i)^2 \tag{3.10}$$

where u_i is one of the velocity components and where there is no implicit summation in $\partial_i u_i$. This scale corresponds to the end of the inertial range ([Frisch, 1995]). For homogeneous isotropic

turbulence, it can be shown that :

$$\lambda = \sqrt{\frac{15\nu(u_i^{rms})^2}{\epsilon}} \tag{3.11}$$

with ϵ the average dissipation rate. The von Kármán flow is not homogeneous nor isotropic but if we notice that for homogeneous isotropic turbulence, the total rms of the fluctuations $u_{tot}^{rms2} = \sum_i u_i^{rms2}$ is equal to $3 \cdot u_i^{rms2}$ for any i, we get that :

$$\lambda = \sqrt{\frac{5\nu(u_{tot}^{rms})^2}{\epsilon}} \tag{3.12}$$

This gives a definition which is independent from the velocity component i and that we can use in the case of the von Kármán flow, using the global ϵ computed from torque measurements. Actually, we just replaced u_i^{rms} by the quadratic average of the three u_i^{rms}, which is $u_{tot}^{rms}/\sqrt{3}$. The dimensionless Taylor scale is then :

$$\lambda^* = \lambda/R = \sqrt{\frac{5(u_{tot}^{rms*})^2}{Re \cdot \epsilon^*}} \tag{3.13}$$

The Taylor-scale Reynolds number is therefore given by :

$$R_\lambda = \frac{\lambda u_{tot}^{rms}/\sqrt{3}}{\nu} = \sqrt{\frac{5Re}{3\epsilon^*}}(u_{tot}^{rms*})^2 \tag{3.14}$$

In turbulent regime, at large Reynolds numbers, ϵ^* and u_{tot}^{rms*} are independent of Re. Therefore, the dimensionless Kolmogorov scales, the dimensionless Taylor scale and the Taylor-scale Reynolds number only depend on the Reynolds number.

The Taylor-scale Reynolds number is especially useful to compare the level of turbulence in a von Kármán flow and in a direct numerical simulation (DNS) of homogeneous isotropic turbulence (HIT). Indeed, as the geometry and the forcing are different, it is not really meaningful to compare the integral Reynolds numbers. For a given Taylor scale Reynolds number R_λ obtained in a DNS of HIT, the integral Reynolds number of a von Kármán flow leading to this value of R_λ can be obtained by reversing 3.14, as we know $\epsilon^*(Re)$ and $u_{tot}^{rms*}(Re)$ in our von Kármán flow. It is not a priori equal to the Reynolds number of the DNS computed with the integral scales of the DNS.

2 VK2 set-up description

In this thesis, we used the already existing VK2 set-up to generate the described von Kármán flow. This set-up, shown on figures 3.6 and 3.7, has a total height of about one meter ; the cylinder diameter is 20 cm and the distance between the two impellers is 14 cm. It was already used and described in previous PhD theses [Monchaux, 2007, Saint-Michel, 2013] and works [Saw et al., 2016]. During this thesis, we modified it in order to put 4 or 5 cameras around it despite its smallness, and thus to perform tomographic particle image velocimetry (TPIV).

2.1 The tanks

The VK2 set-up includes two tanks : a cylindrical one where the flow is generated and an outer one, filled with the same liquid and intended to reduce optical deformations. Both are fixed on a structure made of X95 rails and steel plates. This structure is fixed itself on an anti-vibration marble table.

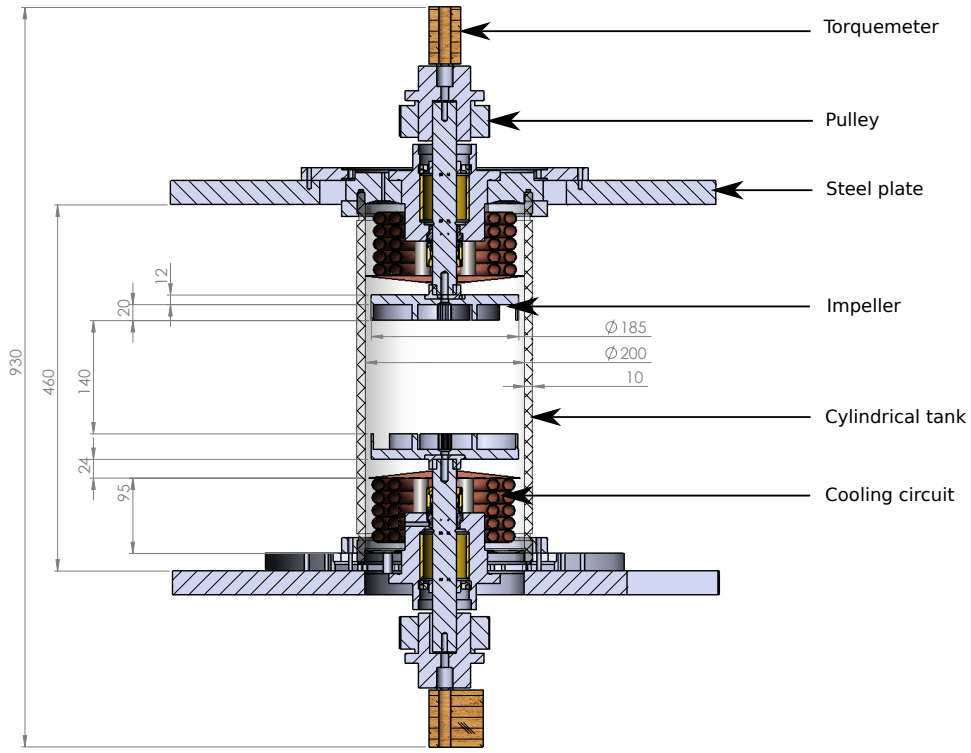

Figure 3.6: Vertical cross-section of the experimental set-up without the outertank.

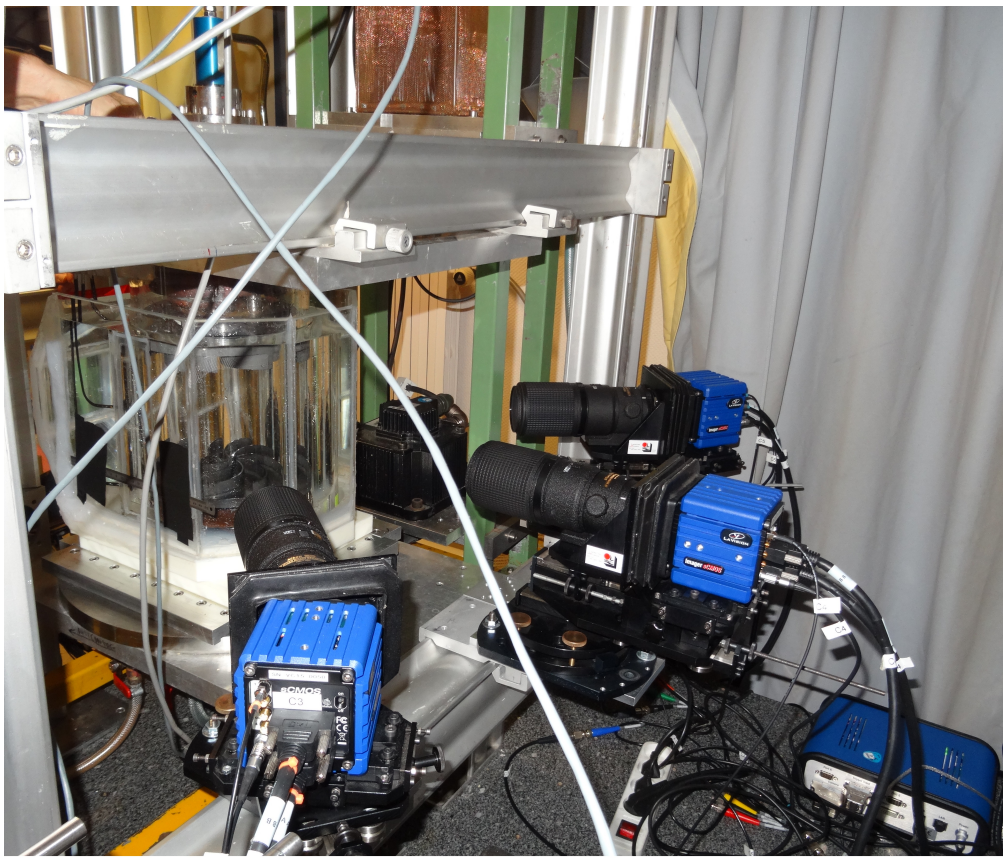

Figure 3.7: Photograph of the VK2 set-up with outer tank A.

2.1.1 The cylindrical tank

In this set-up, the cylinder is one centimeter thick and made of PMMA (polymethyl methacrylate, or Plexiglas). It is transparent (optical index around 1.49) so that one can do optical measurements through it.
It is a closed tank, hermetically sealed with two toric joints (O-ring, one at the bottom and one at the top) so that we can pressurize it. Pressurizing it is needed for two reasons : first, it allows to avoid cavitation and growth of bubbles which could affect the flow and would impact the measurement technique : as bubbles are much bigger than the particles, they scatter much more light and then saturate the cameras, possibly damaging them. The resulting images have big spots which may also deplete the reconstruction and correlation quality (see chapter4). The second reason is the proper functioning of the mechanical sealings which requires a pressure of 1.8 bar.
The cylindrical tank is firmly fixed to the set-up structure at the top and at the bottom by two flanges fitting and pressing in a groove carved out in the tank. These flanges are screwed to the structure with M6 screws. This way, the sealing is ensured. Note that the cylindrical tank, which is made of PMMA, does not hold the top parts of the set-up (steel plate, pulley, impeller and torquemeter). A metallic structure, not shown in figure 3.6 but which can be seen on 3.7, holds these parts and connects them to the bottom parts.

2.1.2 The outertanks

Because of its curvature, direct observations through the cylindrical tank yield important optical deformations. To avoid them, an outertank filled with the same fluid as the inner tank is added so that the observation directions cross the outertank perpendicularly on flat surfaces. In this thesis, we used three different outertanks.
The first one was preexisting [Monchaux, 2007, Saint-Michel, 2013, Saw et al., 2016] and is used for stereoscopic particle image velocimetry (SPIV) which involves only two cameras. It has a square

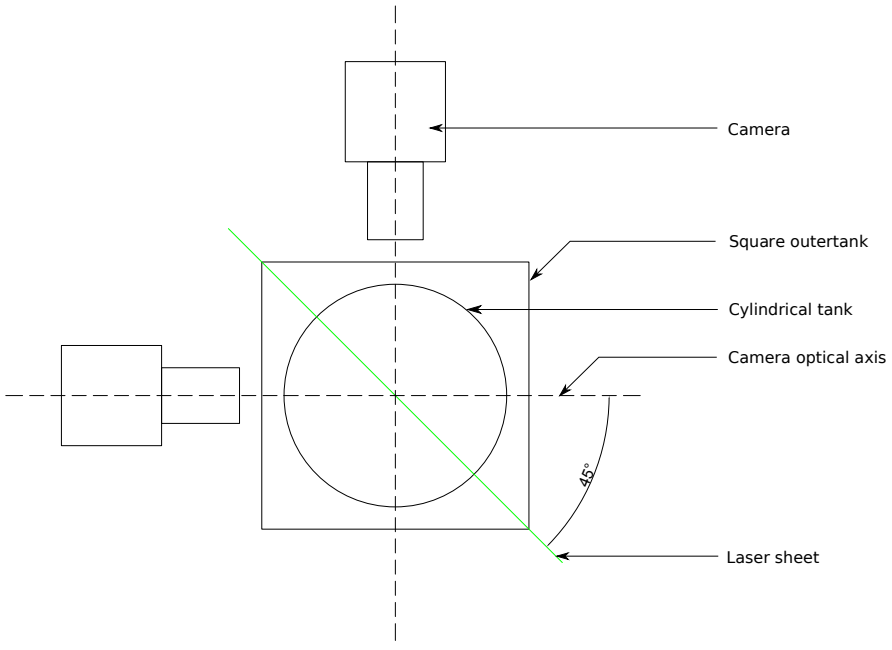

Figure 3.8: SPIV configuration with two cameras

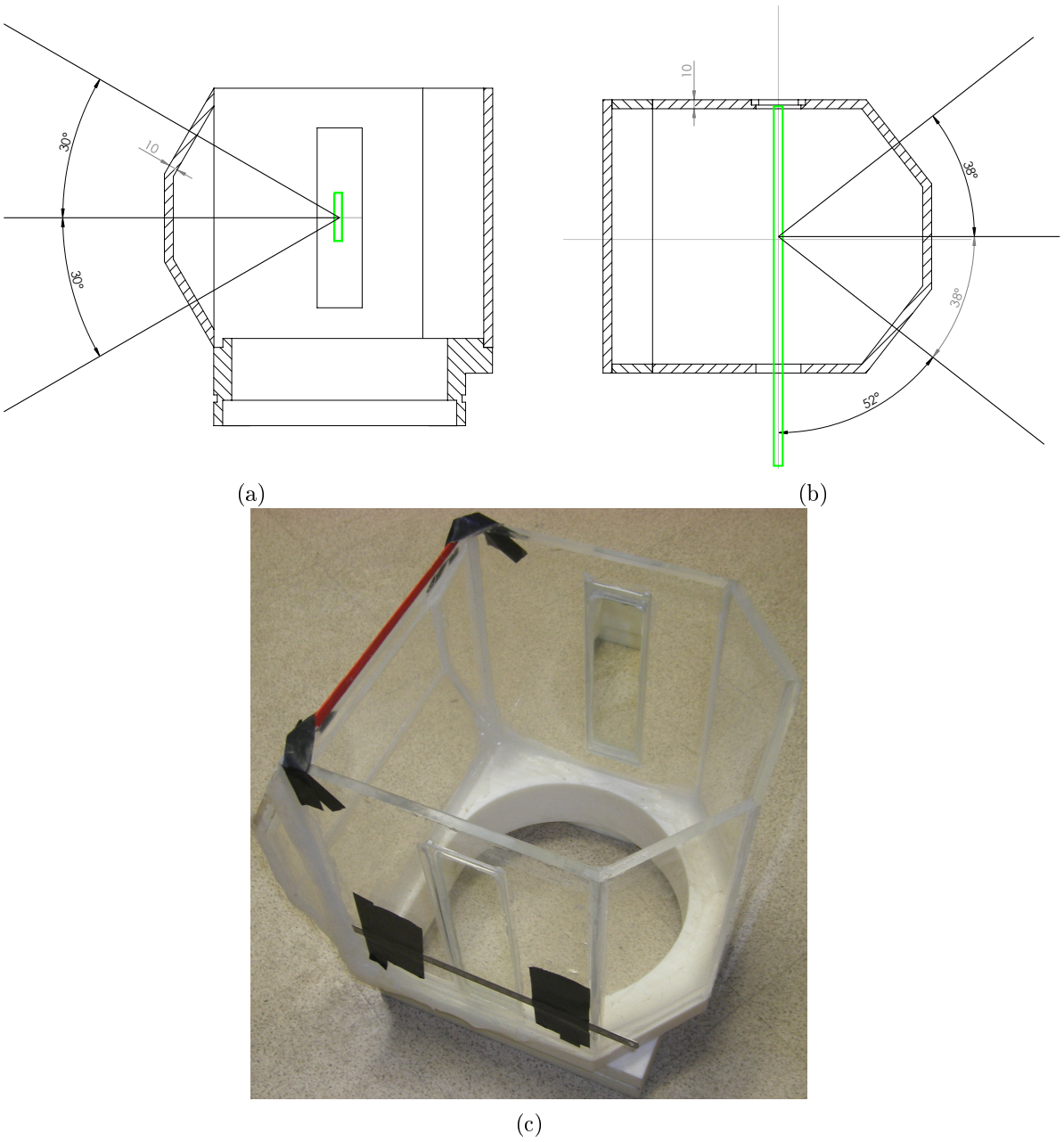

(a) (b)

(c)

Figure 3.9: TPIV outertank A : Vertical (a) and horizontal (b) cross-sections and photograph (c). The green rectangles stand for the laser volume.

section and allows to put two cameras whose optical axes form an angle of 90°, as shown on figure 3.8. The laser sheet is vertical and contains the bisector of these two axes.

The two other tanks were built during this thesis by Vincent Padilla on Jean-Marc Foucaut's advice, in order to install 4 or 5 cameras around the flow and perform TPIV. The first one to be built, which we call outertank A and which is shown on figure 3.9, allows to put five cameras whose optical axes are in two different planes (one vertical and one horizontal). In this configuration, the particle images on cameras 1 and 2 were distorted because the optical axes of these cameras were not perpendicular to the cylinder (see next chapter). Therefore, we built another outertank, outertank

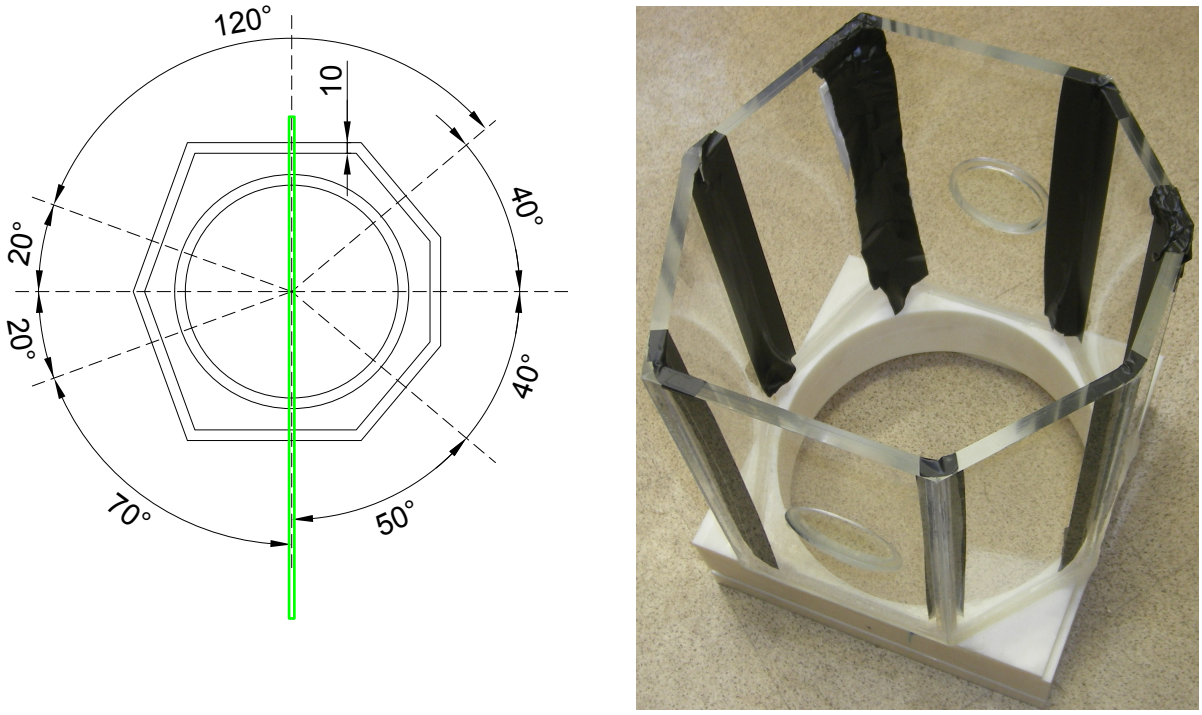

(a) (b)

Figure 3.10: TPIV outertank B : Horizontal (a) cross-section and photograph (b). The green rectangles stand for the laser volume.

B. This outertank, shown in figure 3.10 allows to use five cameras too, but their optical axes are all in the same horizontal plane, and therefore all crossing the (vertical) cylinder perpendicularly. Such a configuration was used in the PhD thesis of [Martins, 2016] in the case of a channel flow. The possible drawback was the possible depletion in reconstruction quality because observation directions are closer to each other in this new configuration. However, it turned out that this configuration allowed good reconstruction too (see section 3.2 and appendix D) and it was finally used for most of the measurements.

Outertanks A and B both have PMMA faces glued on a nylon base which is fixed by flanges on the bottom steel plate. They both have glass windows on the faces through which the laser beam passes, so that it does not spoil the PMMA (for outer tank B, it is even anti-reflective glass). Outer tank A also includes a mirror to reflect the laser volume so that cameras which are in forward and backward scattering receive approximately the same amount of light ; in the case of outer tank B, the beam leaves the outer tank through a second glass window before it is reflected by an external mirror.

2.2 Impellers, transmission and engines

The impellers are TP87 impellers, made of polycarbonate and machined by a 3-axis milling machine. Their geometry is the one shown in figure 3.2. The width of the blades is 2 mm.

They are slotted and screwed by one screw in their rotating shaft through an intermediary hub.

The diameter of the shafts is 30 mm, they are guided by two angular contact ball bearings each. The sealing at the shaft is ensured by mechanical sealings, which require a pressure inside the tank of 1.8 bar for an optimal functioning (see [Saint-Michel, 2013]).
Each shaft is fixed to a pulley at its end, which is rotated by a belt connected by another pulley to the engine. As the pulley fixed to the engine has a diameter twice smaller than the one fixed to the shaft, the rotation frequency of the engines is twice the rotation frequency of the impellers.
The electrical engines are Yaskawa Servopack SGMGH. They can provide a power of 1.8 kW and a torque of 11.5 N.m each. They are controlled by a Labview program developed by Cécile Wiertel-Gasquet, and provide a measure of their rotation frequency and torque. They are fixed on a structure separated from the one holding the tanks, fixed on the floor and therefore independent from the structure supporting the tanks. The only links between the two structures are the anti-vibration table which is placed on the floor, and the belts. With this separation, the tanks are not subject to the engine vibrations.
In order to get a more accurate measurement of the torque and rotation frequency, one SCAIME torquemeter is located on each pulley. The measured torque is thus free from belt contributions, but not from the ones of the bearings and sealings (see [Saint-Michel, 2013] for a deep investigation of this problem).

2.3 Fluid

The fluids used in this thesis were either water or water-glycerol mixtures. Changing the fluid allows to vary the viscosity and then to reach different Reynolds number with a limited frequency range of the impellers. The impeller rotation frequency is limited at lower values by the accuracy of the engine control, and at higher values by the engine power.
At low Reynolds numbers, using a water-glycerol mixture is more suited. Accurate engine control at low frequency is indeed not possible with our equipments, the lower limit of the engine rotation frequency being 0.2 Hz (0.1 Hz on the impeller rotation frequency because of the pulley ratio). At this frequency, the relative amplitude of the frequency variations is 1%. This frequency corresponds in water to a Reynolds number of 6000, i.e. the smallest turbulent Reynolds number of our flow. We could then in principle avoid using glycerol but at such a frequency with water filling the tank, torques are too small to be measured with our system. In addition, we observed sedimentation of particles in water at this frequency, the gravity forces being stronger than inertia forces. This does not affect the measured velocity (see chapter 4) as the fall speed is still lower than the particle velocity, but after few minutes the particles concentration has significantly decreased which requires to stir strongly the liquid to lift the particles again. With a water-glycerol mixture, this sedimentation phenomenon is much less pronounced as the rotation frequencies are higher (for the same Reynolds numbers) and the liquid density is closer to the density of the particles. Also, at low impeller rotation frequencies, the acquisition frequency of the cameras should be smaller in order to get decorrelated frames because the velocity field is longer to decorrelate. This can result in very long acquisition times.
At higher Reynolds number, we use pure water. Indeed, at higher rotation frequencies problems of torque measurement, sedimentation and acquisition frequency do not exist and water remains much more convenient as it does not require dilution nor cleaning.
Table 3.1 gives the densities and viscosities of few water and glycerol mixtures at 20°C, based on the online calculator available at `http://www.met.reading.ac.uk/~sws04cdw/viscosity_calc.html` (accessed January 24th, 2019).
The kinematic viscosity is sensitive to liquid temperature : at 20°C, a variation of 1% of the temperature results in a variation between 0.5% (for pure water) to 2% (for pure glycerol) of the

Glycerol concentration in volume (%)	Density (kg/m^3)	Kinematic viscosity(m^2/s)	Impellers rotation frequency (Hz) at $Re =$			
			6000	3×10^4	6×10^4	3×10^5
0	1.00×10^3	1.01×10^{-6}	0.1	0.5	1	5
43.6	1.12×10^3	5.17×10^{-6}	0.5	2.5	5	25
55.3	1.16×10^3	1.01×10^{-5}	1	5	25	50
100	1.26×10^3	1.12×10^{-3}	500	2500	5000	25000

Table 3.1: Properties of several water-glycerol mixtures at 20° C and the corresponding impeller rotation frequencies in the VK2 set-up for given Reynolds numbers.

viscosity of the mixture.
The refractive index of water is around 1.33 whereas the one of pure glycerol is around 1.47. This is closer to the PMMA refractive index. Using a water-glycerol mixture would then theoretically decrease optical distorsion due to multiple changes of refractive indices but in practice we did not observe any major difference in the measurement quality between the two kinds of liquid.

2.4 Cooling circuit

The energy injected by the impellers into the flow is dissipated by viscous effects (at least) which convert kinetic energy into heat. To keep the flow at a constant temperature and avoid variation of the fluid viscosity with temperature (and thus of the Reynolds number), a cooling circuit is used. It consists in two windings of copper pipe located behind the impellers (a disk is added between the windings and the impeller both at the top and the bottom in order to reduce the impact of the flow generated in the windings on the von Kármán flow). The copper pipes are plugged into a Lauda thermostat allowing to regulate the temperature of the fluid in the cooling circuit with an accuracy of 0.1°C. The studied flow being fully turbulent, we can reasonably assume that the fluid temperature is homogeneous.
With this cooling system, it is also possible to tune the viscosity by modifying the fluid temperature.

3 Why using this flow ?

In this section we detail the advantages of using the von Kármán flow for the particular purposes of this thesis.

In addition to practical advantages, this set-up is well suited for the multi-scale analysis of turbulence as the Reynolds number can be varied easily by playing either on the impeller rotation frequency or on the fluid viscosity. The latter can be tuned either by modifying the glycerol fraction or the temperature of the fluid. When changing the Reynolds number, the Kolmogorov scale η changes too. Therefore, keeping a constant spatial resolution, i.e. without zooming in or out, we can still study different scale ranges as the ratio $\Delta x/\eta$ is modified (Δx being the vector spacing). The ratio $\Delta x/L$ (with L the integral scale) remains constant though, and the scale separation is not very pronounced at small Reynolds numbers.
This principle was already used several times by the group, for example in [Debue et al., 2018a]. In this paper, a composite spectrum covering 3 decades is obtained by combining different spectra obtained at different Reynolds numbers. This spectrum is reproduced in figure 3.11. Velocity measurements in the von Kármán flow at three different Reynolds numbers were needed to achieve

this spectrum : Re=6×10^3, Re=6×10^4 and Re=3×10^5. The corresponding Kolmogorov scales are respectively 0.3 mm, 75 μm and 15 μm. The vector spacing Δx was not exactly the same for all cases. Indeed, the magnification was smaller for the first case, hence a larger Δx ; and the interrogation window sizes (see next chapter) were 16 or 32 pixels, hence the factor 2 between the resolutions of other cases. In order to obtain the composite spectrum, wavenumbers are rescaled by the Kolmogorov scale and the spectra by $\epsilon^{2/3}\eta^{5/3}$. This spectrum features both the inertial and dissipative ranges. This confirms that this method allows to study different scale ranges with a constant or limited range of spatial resolution. This is very important because PIV methods have a finite resolution ; with this method we can still study small scales.

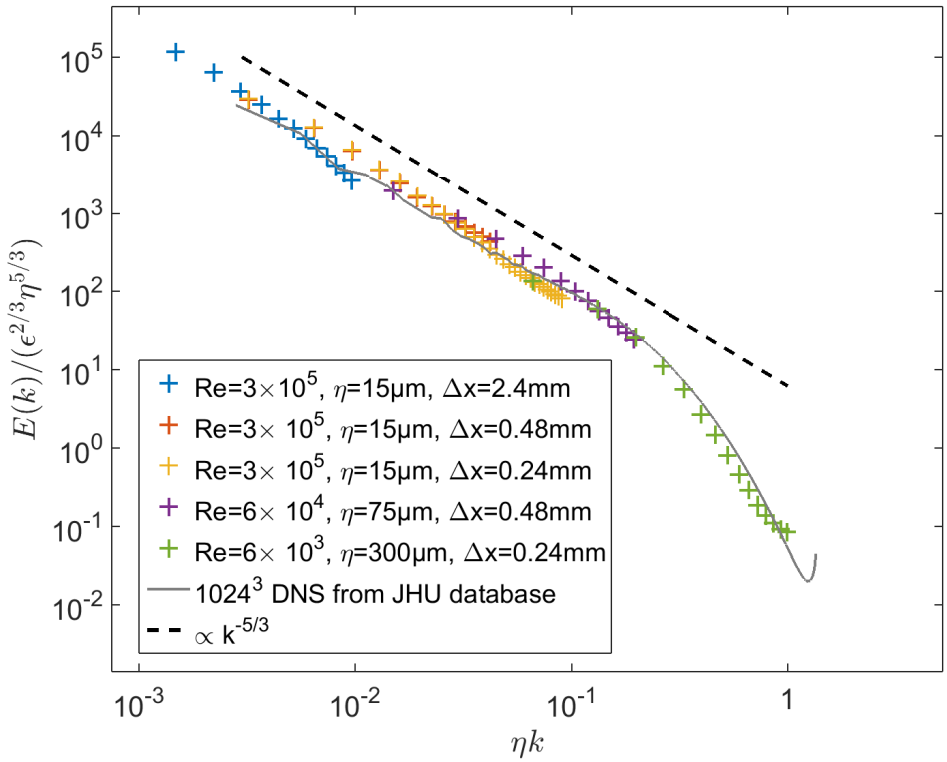

Figure 3.11: Composite spectrum of the von Kármán flow. The different colors correspond to different Reynolds numbers, resolutions and/or magnifications.

Also, the flow itself has been widely studied, especially during the past thirty years, both experimentally and numerically. We therefore have a good knowledge of it : for example we know that it can bifurcate when the TP87 impellers are rotating in the anti direction, or we know how the mean flow looks like as well as the behaviour of other velocity statistics. We can therefore check the consistency of the velocity measurements obtained with the new 3D PIV methods. Concerning the computation of energy transfer and dissipation terms in the special case of the von Kármán flow, no such work already exists but the same analysis we perform is being done by the team of Caroline Nore on the results of von Kármán flow simulations obtained with the SFEMANS code. Comparing our results will again allow to check their consistency.

Another advantage is that the von Kármán flow is not homogeneous. It features different kinds of flows : strong shear in the equatorial plane between the two counter-rotating cells, influence of a wall near the cylinder, simple advection within one cell along the cylinder axis. This allows to study the influence of the flow type. Note that there is always a global swirl though. In this thesis, we only focus on one particular point of the flow, its center, i.e. the intersection between the equatorial plane and the cylinder axis. The turbulence is close to homogeneous and isotropic turbulence (HIT) around this point : indeed, this area is invariant by rotation around the cylinder axis and the R_π symmetry. Variations of the rms of the velocity are small (see C.4). It is not exactly isotropic, as shown in [Ouellette et al., 2006], the vertical direction being different from the others (for instance, it has a rms 30% smaller, see also chapter 5), but it was shown in the appendix of [Debue et al., 2018a] that the slopes of the spectra are the same for the three velocity components. This quasi-homogeneity and -isotropy makes the comparison of our results with others obtained in DNS of HIT more meaningful.

Lastly, the cylindrical geometry of the von Kármán flow is interesting because the presence of swirl may favour the existence of singularities and because the cylinder axis seems to be a preferred place for possible singularities to occur. Indeed, an axisymmetrical flow cannot feature singularities if the swirl component is zero (i.e. if the azimutal component of the velocity is uniformly zero) : the flow is then 2D and the result in [Ladyzhenskaya, 1968] applies. When the swirl is non-zero, it was proven in [Hou and Li, 2008] that axisymmetrical flows are regular for finite time, in a domain excluding the symmetry axis, implying that any singularity would necessarily be located along the symmetry axis (in this case, the dimension is usually considered to be 2.5 because the flow is axisymmetric but there is a non-zero azimutal velocity component). Of course, these theorems do not apply to fully turbulent 3D flows which are not axisymmetric, but they may be interpreted as indications of the favourable conditions for the occurence of singularities.

Chapter 4

Tomographic particle image velocimetry and its application to our set-up

In this thesis, we use Tomographic Particle Image Velocimetry (TPIV) in order to measure turbulent velocity fields at the center of our von Kármán flow. TPIV is an Eulerian measurement method which allows to get the three components of the velocity on a 3D grid (it is said to be a 3D-3C method). Both non-time-resolved and time-resolved TPIV are used. The former allows to obtain a large amount of uncorrelated fields in order to statistically sample the flow and to gather as many extreme events as possible. The latter allows to study the time evolution of the extreme events.
In this chapter, we detail the working principles of TPIV, along with the way to estimate resolution, quality and error of the measurements. Optimization tests for our set-up are then briefly exposed.

1 General principles

TPIV, as well as other laser velocimetry methods, relies on particles seeding the flow, lighted by a laser and whose images are acquired by cameras. Processing of the acquired images allows to get the particle displacements and velocities.

1.1 Typical set-up

A typical PIV set-up, as the one sketched on figure 4.1, involves a laser and one or more cameras. For 2D-2C measurements (yielding two velocity components on a 2D grid), one camera is enough ; more cameras can be used to get an additional component or dimension. The laser beam can be shaped by optics such as lenses and mirrors in order to obtain a laser sheet or volume with a proper thickness and dimensions corresponding to the considered area. PIV lasers are usually pulsed lasers because continuous lasers are less powerful ; they must then be synchronized with the cameras. The considered flow is seeded with particles which scatter the laser light, their images are then recorded by the cameras. Acquisition parameters are set from a computer connected with the laser and the cameras, and the recorded images are transferred to this computer for analysis. The idea is to acquire images with a small interframing time dt and to measure the particle displacements over this small time in order to deduce their velocity. A good synchronization with a high accuracy on dt is then required ; it is handled by a separated device.
PIV analysis consists in measuring the displacement of groups of particles by image correlation at some particular time. In order to get one velocity field, two images are required. The interframing time between the two images should be such that the displacements of the particles can be properly

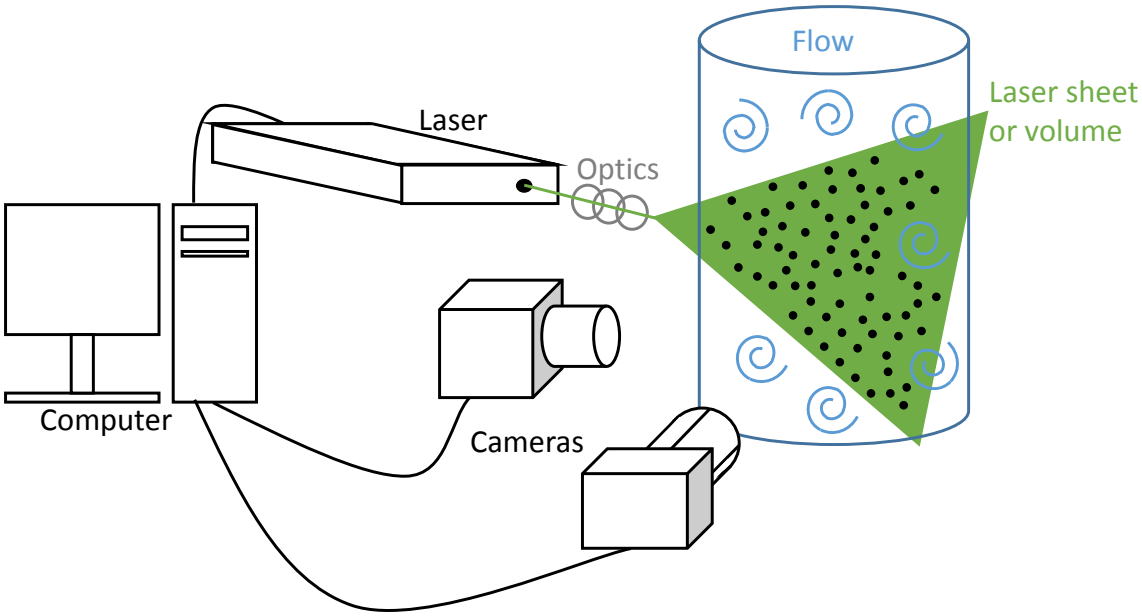

Figure 4.1: Typical PIV set-up.

estimated ; in practice, the maximum displacement of the particles on the images should be of the order of ten pixels. If the interframing time is too small, there is no difference between the two images ; if it is too large, the images are completely decorrelated. In both cases, the velocity field cannot be deduced.

In order to measure uncorrelated velocity fields, i.e. in the case of non-time-resolved PIV, one should wait enough time between two pairs of images. The triggering signal then looks like the upper part of figure 4.2. So-called "slow" or "low-speed" lasers and cameras are usually used for non-time-resolved measurements. "Slow" lasers allow to produce two very close pulses, by using two cavities with a slightly shifted triggering time, but need a longer time to be ready for the next pair of pulses. "Slow" cameras are designed to record a pair of images separated by a very small dt, but need a longer time to be ready to acquire the next pair.

In order to measure correlated velocity fields and perform time-resolved PIV, the time period between two pairs of images should also be small. In this case, the common practice is to acquire a whole set of images separated by a constant interframing time. The corresponding triggering signal is shown on the lower part of figure 4.2. The correlation is then performed on consecutive images : the n^{th} velocity field is obtained by correlating images n and $n+1$. Each image (except the first one and the last one) is therefore used to compute two velocity fields. The time period between two consecutive velocity fields is dt. For time-resolved measurements, so-called "fast" or "high-speed" lasers and cameras are required. These are designed to produce a pulse or acquire an image every interframing time dt. This is more challenging compared to "slow" equipment. Therefore, the features of "fast" equipments are slightly less good compared to "slow" ones. For instance, "fast" cameras have bigger pixels. At very high frequencies, the sensor size of "fast" cameras has to be decreased, because the interframing time dt is too short to store the full image ; therefore, the measurement area is smaller. "Fast" cameras usually have an internal memory as the interframing time dt is too short to transfer images to the computer ; therefore, the acquisition time is limited by the memory

size. "Fast" lasers are less powerful than "slow" ones, this can be a problem when the measured area is too large or too thick (in the case of volumetric measurement) or when particles are too small.

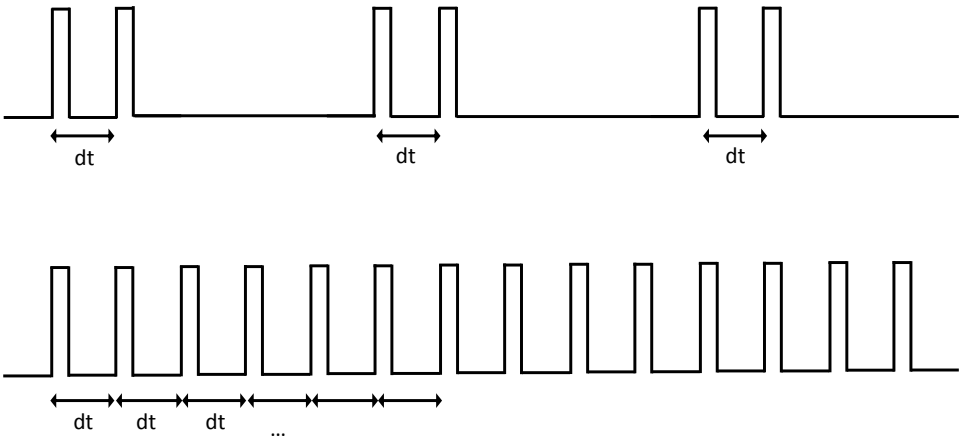

Figure 4.2: Triggering signal. Top : non time-resolved measurements. Bottom : time-resolved measurements.

1.2 Particles

PIV consists in seeding a flow and measuring the average velocity of groups of particles. It therefore relies on two main assumptions : the particles properly follow the fluid and their presence does not modify the flow.

Because of their inertia, particles cannot follow too fast structures. It is possible to estimate whether spherical particles will follow a flow or not. Following [Rhodes, 2008, Boutier, 2012], let us define a Reynolds number Re_p, a Mach number M_p and a Knudsen number K_n characterizing the flow around the particle :

$$Re_p = \frac{|v_p - v_f| d_p}{\nu}, \tag{4.1}$$

$$M_p = \frac{|v_p - v_f|}{c}, \tag{4.2}$$

$$K_n = \frac{L_p}{d_p}, \tag{4.3}$$

where :

- $v_p - v_f$ is the difference between the fluid velocity v_f and the particle velocity v_p,

- d_p is the particle diameter,
- ν is the viscosity of the fluid,
- c is the sound speed in the fluid,
- L_p is the mean free path of the fluid molecules.

When $Re_p << 1$, $M_p << 1$ and $K_n << 1$, Stokes' law is holding : the drag force applied by the fluid on a spherical particle is :

$$\overrightarrow{F_p} = -6\pi\mu\frac{d_p}{2}(\overrightarrow{v_p} - \overrightarrow{v_f}) \tag{4.4}$$

where $\mu = \rho\nu$ is the fluid dynamic viscosity, ρ being its density.
The relaxation time of a spherical particle is the time constant of the differential equation :

$$m_p\frac{d(\overrightarrow{v_p} - \overrightarrow{v_f})}{dt} = -6\pi\mu\frac{d_p}{2}(\overrightarrow{v_p} - \overrightarrow{v_f}) \tag{4.5}$$

where $m_p = \frac{4}{3}\pi\left(\frac{d_p}{2}\right)^3\rho_p$ is the mass of the particle, ρ_p being its density.
It is the typical time needed by the particle to match its velocity with the one of the fluid, equal to :

$$t_p = \frac{\rho_p d_p^2}{18\mu} \tag{4.6}$$

If $t_p << t_f$, t_f being a typical time of the fluid motion, the particle is assumed to follow the flow. The ratio of these two typical times is called the Stokes number :

$$S_t = \frac{t_p}{t_f} = \frac{\rho_p d_p^2}{18\mu t_f} \tag{4.7}$$

It should be much smaller than 1 to ensure that the particles follow the flow in the stated conditions on Re_p, M_p and K_n.
In order to compute S_t, we need to choose which t_f to use. In turbulence, in the inertial range and at the beginning of the dissipative range, the typical level of velocity fluctuations at scale ℓ is $u^\ell \approx U(\ell/L)^{1/3}$, with U and L the integral velocity and length scales (see [Frisch, 1995] for instance). Therefore, the typical time scale of structures at scale ℓ is $t^\ell \approx \ell/u^\ell \approx T(\ell/L)^{2/3}$ with $T = L/U$ the integral time scale. This is a decreasing function of ℓ : smaller structures have smaller typical time scales. Therefore, t_f should be the time scale at the smallest resolved scale of the flow Δ_{res} : for PIV, it would be of the order of the interrogation window size. We have :

$$t_f = T\left(\frac{\Delta_{res}}{L}\right)^{2/3} \tag{4.8}$$

If we consider that there are places in the flow where $u^\ell \approx U(\ell/L)^h$ with $h \in [-1;1]$, as in the phenomenological interpretation of the multifractal model (see chapter 1), then :

$$t_f = T\left(\frac{\Delta_{res}}{L}\right)^{1-h} \tag{4.9}$$

with $1-h$ possibly higher than $2/3$: the corresponding time scale is smaller than for $h = 1/3$ and it is more difficult for the particles to follow the flow. We can estimate the "smallest resolved exponent h", i.e. the smallest exponent h associated with time scales (at the resolution scale Δ_{res})

that are large enough compared to the relaxation time of a spherical particle. In other words, this is the smallest exponent generating structures whose size is of the order of our spatial resolution and that particles can follow. For smaller h, the particles do not follow properly the structures that are spatially resolved. For a given $r \geq 1$, we want $T\left(\frac{\Delta_{res}}{L}\right)^{1-h} \geq r \cdot t_p$. This is achieved for :

$$h \geq h(r) = 1 - \frac{ln(\frac{\rho_p d_p^2 r}{18\mu T})}{ln(\frac{\Delta_{res}}{L})} \tag{4.10}$$

In the next chapter, we compute the Stokes number based on the Kolmogorov scale and of the "smallest resolved h" for the flow parameters considered in this thesis.

Another problem which can occur when the density of the particles is higher than the density of the fluid is sedimentation. It results in a systematic error on the velocity because this adds a "drift" component to the velocity of the particles in addition to the velocity of the fluid. Also, because of this sedimentation, the density of the seeding decreases gradually with time and requires new seeding or strong stirring to suspend them again. This phenomenon can be characterized by the falling speed v_g of the particles in the fluid. In a fluid at rest, once the particles (assumed spherical here) have reached their falling speed, we have :

$$0 = \frac{4}{3}\pi\left(\frac{d_p}{2}\right)^3(\rho_p - \rho)\overrightarrow{g} - 6\pi\mu\frac{d_p}{2}\overrightarrow{v_g} \tag{4.11}$$

with $\overrightarrow{g}$ the acceleration due to gravity. Hence :

$$\overrightarrow{v_g} = \frac{d_p^2(\rho_p - \rho)\overrightarrow{g}}{18\mu} \tag{4.12}$$

In the next chapter, we compute the falling speed of the particles for the flow parameters considered in this thesis.

The falling speed and the Stokes number are both proportional to the square of the particle diameter d_p. However, the size of the particles cannot be arbitrarily decreased ; otherwise, they would not scatter enough light.

1.3 Lighting and light scattering

Lighting is a critical point in PIV. A powerful light source is needed along with cameras featuring a large dynamic range and a low noise level in order to get a good contrast and a fine intensity resolution. This is why lasers are mainly used as they allow to focus the power in a thin sheet or in a finite volume. Mirrors as well as cylindrical and spherical lenses allow to shape the light ; they should minimize the light losses (transmission for mirrors and reflection for lenses).

Diffusion of light by particles is at the heart of PIV. It is well accounted for by Mie's theory which describes the behaviour of an electromagnetic plane wave scattered by a sphere using Maxwell's equations. Main results of Mie's theory are the increase of scattered intensity with the particle size, the anisotropy of scattered intensity and dependance of the scattered intensity with the light polarisation. As a consequence, the particles used in a PIV set-up should not be too small. Sometimes, a metallic coating is used to increase the scattered intensity. Also, when using several cameras placed in different directions, they may receive different light intensities. This may be a problem when gathering the images taken by different cameras as the same particle will have different intensities

on different pictures, and will therefore be more difficult to identify. This problem can be solved by image processing or by experimental means : for example, adding a mirror at the end of the light beam will allow cameras initially receiving only backward scattered light to receive a forward scattered light too, as shown on figure 4.3. This technique is used in this thesis. Note that in the case of figure 4.3 where all cameras are in the same plane, another solution would be to light the measurement volume from the direction perpendicular to the plane containing the cameras ; however, it is not possible in the experimental set-up used in this thesis.

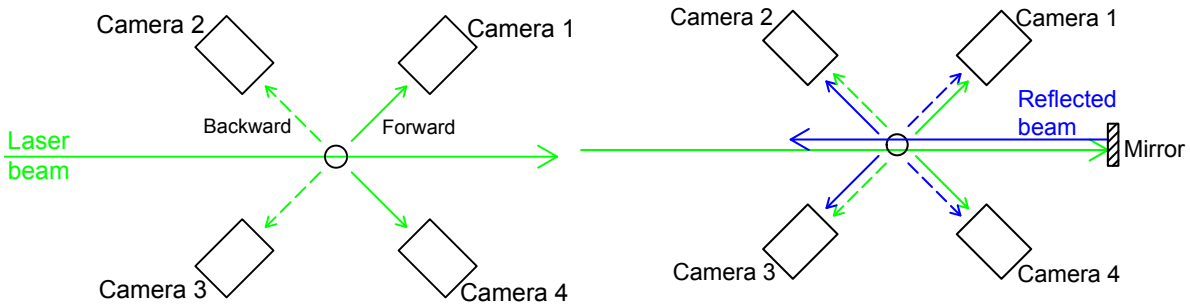

(a) (b)

Figure 4.3: Advantage of using a mirror. (a) Cameras 1 and 4 are in forward scattering whereas cameras 2 and 3 are in backward scattering. (b) All cameras are both in forward and backward scattering.

The light scattered by the particles then reaches the cameras after crossing lenses. Optical settings of the lenses and cameras must follow general guidelines.

1.4 Optical settings

There are two main important guidelines regarding the optical settings. First, the particle image size on the sensor should be between 2 and 3 pixels. It should not be too small to avoid peak locking [Prasad et al., 1992] and to allow subpixel accuracy. Indeed, if the particle image size is smaller than the camera pixel size, then it will be seen as one pixel by the processing algorithms. The measured displacement in pixels will then be an integer. If the particle image size is a few pixels, then the intensity of the diffraction spot can be fitted and the position of the particle determined more accurately, with a sub-pixel resolution. The displacements will then be measured with more accuracy. Usually, three points are enough to fit a diffraction spot. On the contrary, if the size of the particle images is too large, particle images will overlap. This will deplete 3D reconstruction and correlation quality. The seeding concentration could be decreased to avoid that but the space resolution would then be worse. The particle image diameter can be estimated by the Airy disk diameter Φ_d [Adrian, 1997] :

$$\Phi_d = 2.44 f_{\#} \lambda (1 + M) \tag{4.13}$$

where :

- $f_{\#} = \frac{f'}{D}$ is the numerical aperture of the lens, defined as the ratio of its focal length f' over the diaphragm diameter D,
- λ is the wavelength of the scattered light,
- $M = \frac{sensor\ size}{field\ size}$ is the magnification of the set-up, defined as the ratio between the sensor size over the real size of the observed field.

The second guideline concerns the focal depth of the set-up which should be larger than the field depth. This ensures that all particles images are well focused and that their images are not blurred and therefore too large. The focal depth δ is given by the following formula :

$$\delta = 2f_{\#}\Phi_d \frac{1+M}{M^2} = 4.88 f_{\#}^2 \lambda \frac{(1+M)^2}{M^2} \tag{4.14}$$

The previous formula for the focal depth is valid when there is only one optical medium. This is not the case for the experimental set-up used in this thesis, where the light beams scattered by the particles are passing through three different media, as depicted on figure 4.4 (a) : water or water-glycerol mixture, plexiglas, water or water-glycerol mixture again, plexiglas again, and then air. The optical indices are given in the table below :

	Pure water	Pure glycerol	Plexiglas	Air
Optical index	1,33	1,473	1,492	1

This configuration can be modelled by a simpler one where only two optical media are involved, as shown on figure 4.4 (b). Indeed, plexiglas and water or water-glycerol mixture have a relatively close optical index, so that we can assume that the liquid in the cylindrical tank, the cylindrical tank, the liquid in the outertank and the outertank correspond to one single medium. In such a two-media configuration, the formula for the focal depth in the small-angle approximation, derived in the appendix A, is the following :

$$\delta = 4.88 f_{\#}^2 \lambda \frac{n_i}{n_e} \frac{(1+M)^2}{M^2} \tag{4.15}$$

where n_i is the optical index of the medium containing the observed field and n_e is the optical index of the external medium where the camera is located. When $n_i > n_e$, then the focal depth is larger than when both optical indices are equal, for a fixed magnification M. It is then possible to observe a thicker field.

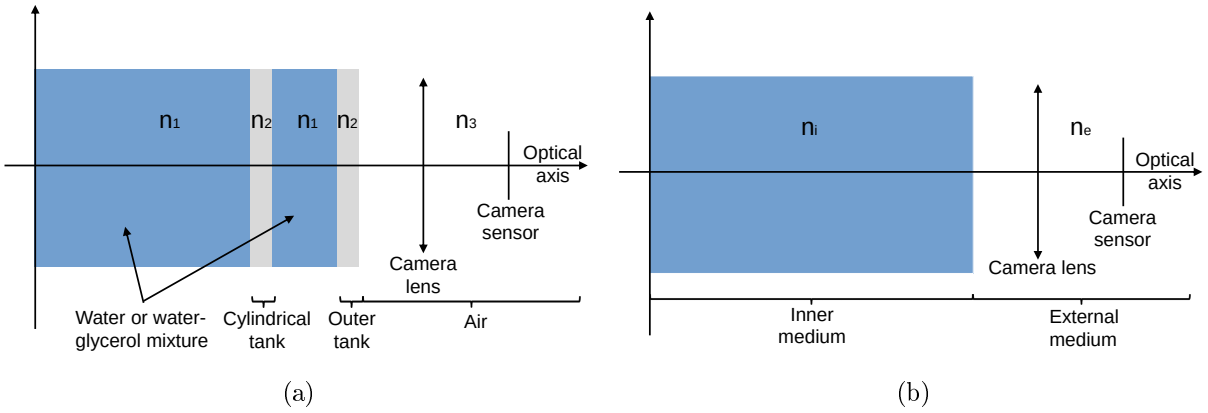

Figure 4.4: Different optical media crossed by the scattered beams in the VK2 set-up. (a) Real configuration. (b) Simplified configuration for computations.

In the case of several cameras observing the same area from different angles, additional devices called Scheimpflugs should be used. Indeed, if there is an angle between the camera sensor and the

light sheet, but no angle between the lens and the camera sensor, then part of the measured area will be out of focus and the corresponding image area will be blurred, as shown on figure 4.5 : even with a non-zero field depth, the focus zone of the camera on the left does not overlap the light sheet whereas the one on the right does. The Scheimpflug condition states that the light sheet, the sensor plane and the lens plane should intersect on a single line so that the whole considered area on the light sheet is in focus. The Scheimpflugs devices achieve this condition by tilting the sensor plane compared to the lens plane. However, this leads to distortion of the images as the magnification will not be the same over the whole image. This should be accounted for in the calibration.

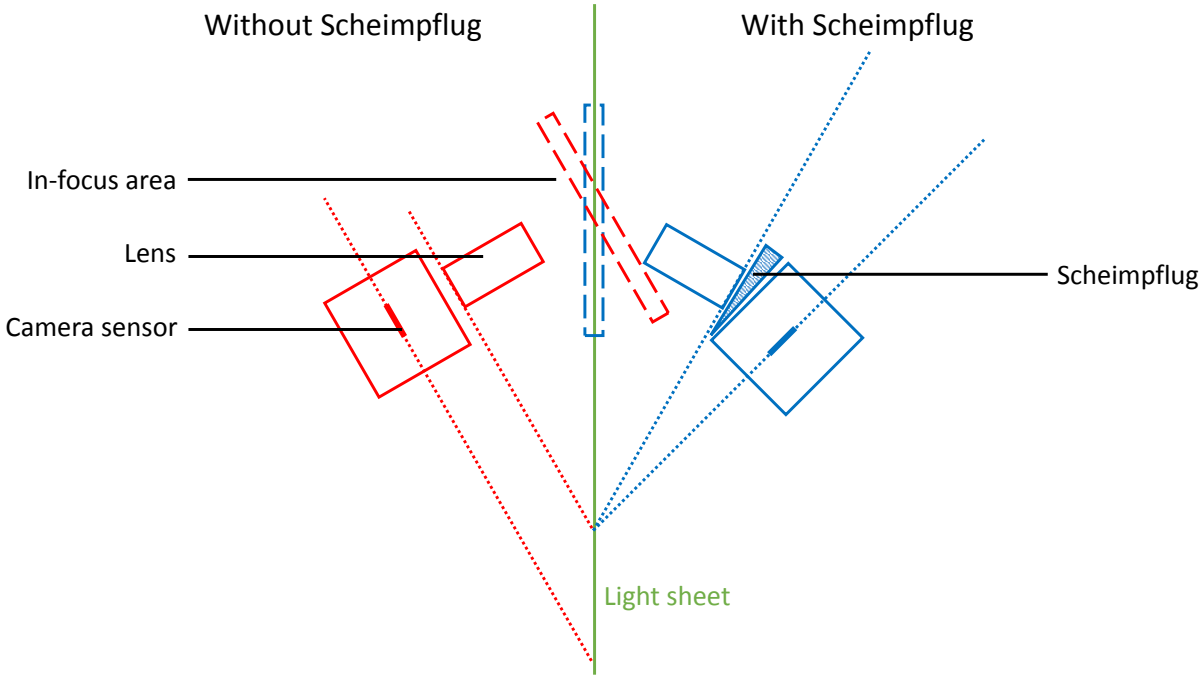

Figure 4.5: Scheimpflug principle.

1.5 Correlation

Once the images are acquired, the velocity field is obtained by image correlation.

1.5.1 Basic 2D-2C correlation

Initially, PIV was a 2D-2C method allowing to compute two components (2C) of the velocity on a 2D plane (the two in-plane components). A single camera was needed. In order to compute a velocity field, two consecutive images separated by an interframing time dt are needed . Both images are splitted into rectangles called interrogation windows. The correlation between two images, i.e. between two consecutive light intensity fields, is then computed window by window. For each window, the displacement corresponding to the maximum of correlation (the correlation peak) is multiplied by a calibration factor in order to get the real displacement and divided by dt to get the corresponding velocity. Such a method is therefore intrinsically filtering : each obtained velocity vector roughly corresponds to an average of the real velocity field over an interrogation window and over dt.

The cross-correlation between two images is done efficiently using fast Fourier transforms. Peak detection can be performed by fitting a function, a Gaussian for instance, on the correlation map. This allows to reach sub-pixel accuracy on the displacements : indeed, the maximum of the fitting function can be located between two pixels. The particle image size should not be too small in order to achieve this sub-pixel accuracy and to avoid peak locking. The quality of the peak detection also depends on the peak shape : it should be well pronounced in order to distinguish it from spurious peaks which can arise in the correlation map. In [Keane and Adrian, 1992], four guidelines allowing to get a proper peak are obtained based on synthetical data :

- There should be at least ten particles in each interrogation window. This can be achieved by tuning the particle concentration and the interrogation window size. Note that when the particle concentration is too high, it is not possible to distinguish between the particles and the correlation peak cannot be detected. Increasing the interrogation window size will result in a worse resolution.
- The maximum displacement over one interframing frame should be smaller than one quarter of the interrogation window size, so that enough particles remain in the same interrogation window during dt. Indeed, particles going out of the interrogation window cannot contribute to the correlation peak, and may contribute to the spurious peaks.
- The out-of-plane displacement during dt should be smaller than one quarter of the light sheet width, so that particles remain in the interrogation window during dt and can be seen in both images.
- The fourth rule concerns the variation of the displacement in one interrogation window : it should be smaller than the particle diameter. Indeed, if the displacement variation over one interrogation window is too large, the correlation peak will also be too large.

1.5.2 Advanced correlation algorithms

Correlation methods have been improved to increase the measurement accuracy, resolution and efficiency. Here, we describe a few advanced features.

Window shifting and deformation consists in shifting, rotating and distorting the interrogation windows based on a first guess of the velocity field, so that the interrogation windows follow the flow. This allows to reduce the amount of particles leaving the interrogation windows during the interframing time dt, and to reduce the interrogation window size as the second rule of [Keane and Adrian, 1992] does not make sense anymore. Actually, this window shifting and deformation method goes along with multipass processing.

In multipass processing, a first guess of the velocity field is realized based on fixed interrogation windows. For this first guess, the rules of [Keane and Adrian, 1992] apply. For the next pass, the interrogation windows are shifted, rotated and distorted and their size can also be decreased. Iterating this procedure allows to improve the accuracy and the resolution of the measurement. To achieve multipass processing, a procedure should be defined to assign a velocity vector to interrogation windows for which the algorithm could not find any peak. This procedure can also be used to detect and replace spurious velocity vectors. Such a procedure is for instance implemented by the general outlier detection filter, described in [Westerweel and Scarano, 2005].
Of course, doing several passes will increase the computation time. In Davis, the software sold by LaVision, pixels are binned together for the first passes. It is equivalent to depleting the pictures

resolution : each packet of $n \times n$ pixels will be replaced by one bigger pixel with intensity equal to the average of the smaller pixels, and the obtained images will have n^2 times less pixels. The computing time for the correlation will then be decreased. Of course, no binning is done for the last pass.

LaVision also uses Gaussian interrogation windows in their software : they are circular, and the light intensity is weighted by a Gaussian function of the window radius. The idea of using weighted functions was already discussed in e.g. [Nogueira et al., 2005]. It allows to reduce the impact of particles that are close to the edges of the interrogation window and which may go out of the interrogation window during the interframing time dt. The amount of outlier vectors is then decreased.

Overlapping of interrogation windows consists in oversampling the pictures. For instance, given an interrogation window size X, the distance between two consecutive interrogation window centers will be X without overlap, X/2 with an overlap of 50% and X/4 with an overlap of 75%. Window overlapping allows to improve the resolution for Gaussian interrogation windows as shown in appendix C but not for square interrogation windows [Foucaut et al., 2004]. It allows to compute the gradients more accurately : for instance, using an order-2 centered scheme, the error will be in $O(X^2)$ without overlap and $O(X^2/4)$ with an overlap of 50%. A priori, adding overlapping windows increases the computation time but in the user manual of Davis, LaVision claims to manage to compute the correlation with or without overlap in the same amount of time.

2 Tomographic Particle Image Velocimetry (TPIV) principles

TPIV is a method based on image correlation. Compared to basic 2D PIV, it involves 3D tomographic reconstruction implying additional steps. In this section, we present the steps of the TPIV method, as well as the related resolution and error. We then discuss the links with other correlation-based methods.

2.1 Volume correlation

The last step of TPIV is the volume correlation. It is very similar to the 2D correlation described in 1.5 but it is performed on 3D light intensity volumes representing the position of the particles in space. The correlation algorithms described in 1.5 all the same apply to such a 3D correlation. Also, in this case, the problem of particles going out of the light sheet is much less important as it concerns only the sides of the volume.
TPIV provides a way to reconstruct such a 3D volume.

2.2 Volume reconstruction

The specificity of TPIV is the tomographic reconstruction of a "3D light intensity volume" from a few 2D images acquired from different cameras. The problem is modelled as pictured on figure 4.6 : the reconstructed light intensity volume is discretized in N_v voxels (3D pixels) of finite size. The j^{th} voxel ($1 \leq j \leq N_v$) has a location (x_j, y_j, z_j) and an intensity E_j. If there is a particle at location (x_j, y_j, z_j) in the measurement volume, then the intensity E_j should be high, otherwise it should be close to zero, as coded by the grey scale on figure 4.6. Therefore, the lower the seeding concentration, the more sparse the vector E_j.

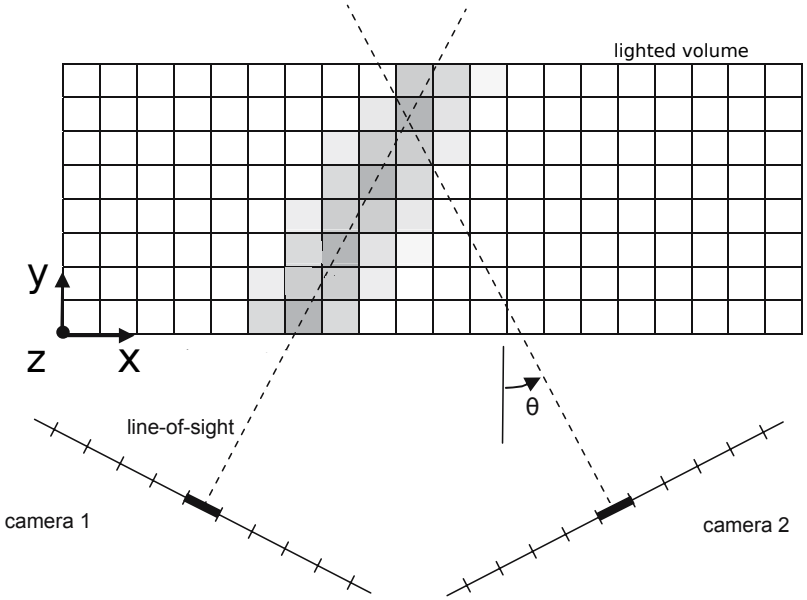

Figure 4.6: Representation of the tomographic reconstruction problem (top view). Adapted from [Elsinga et al., 2006]

A given particle contributes to the intensity of pixels of the cameras, and those pixels should contribute to the intensity of the voxel corresponding to the particle. Let us call N_c the number of cameras and N_r the number of pixels by camera. There are $N_p = N_r \times N_c$ pixels, each having an intensity I_i (with $1 \leq i \leq N_p$). The relation between the pixel intensities and the voxel intensities can be modelled by the following linear equation :

$$\sum_{j=1}^{N_v} w_{i,j} E_j = I_i \tag{4.16}$$

where $w_{i,j}$ is a weighting coefficient corresponding to the contribution of the particle at location (x_j, y_j, z_j) to the intensity of pixel i.
Tomographic reconstruction then consists in solving the inverse problem of deducing E_j for $1 \leq j \leq N_v$ from I_i with $1 \leq i \leq N_p$. It can be achieved by algebraic methods, such as the Multiplicative Algebraic Reconstruction Technique (MART), an iterative method initially developped for medical tomography. This is the method used in this thesis. Starting from a first guess E_j^0, the 3D light intensity field at iteration $k+1$ is deduced from its value at previous iteration as follows :

$$E_j^{k+1} = E_j^k \prod_{i=1} N_p \left(\frac{I_i}{\sum_{j=1}^{N_v} w_{i,j} E_j^k} \right)^{\mu w_{i,j}} \tag{4.17}$$

μ is a relaxation parameter allowing to control the convergence of the algorithm. After 5 iterations, the solution has already a good accuracy [Scarano, 2013].

The reconstruction problem is underdetermined as there are too many voxels in the measurement volume compared to the number of pixels in the N_c cameras. There are therefore several solutions to the problem. As a consequence, the MART algorithm may converge to a solution which does not correspond to the distribution of real particles. It can for instance yield ghost particles, following

the principle sketched on figure 4.7 : two particles, in blue, are observed by two cameras. If the red particles were also there, the intensity seen by the cameras would not be much changed. The MART algorithm could therefore converge to a solution with 4 particles, whereas there are only two : in this case, the red particles would be ghost particles.

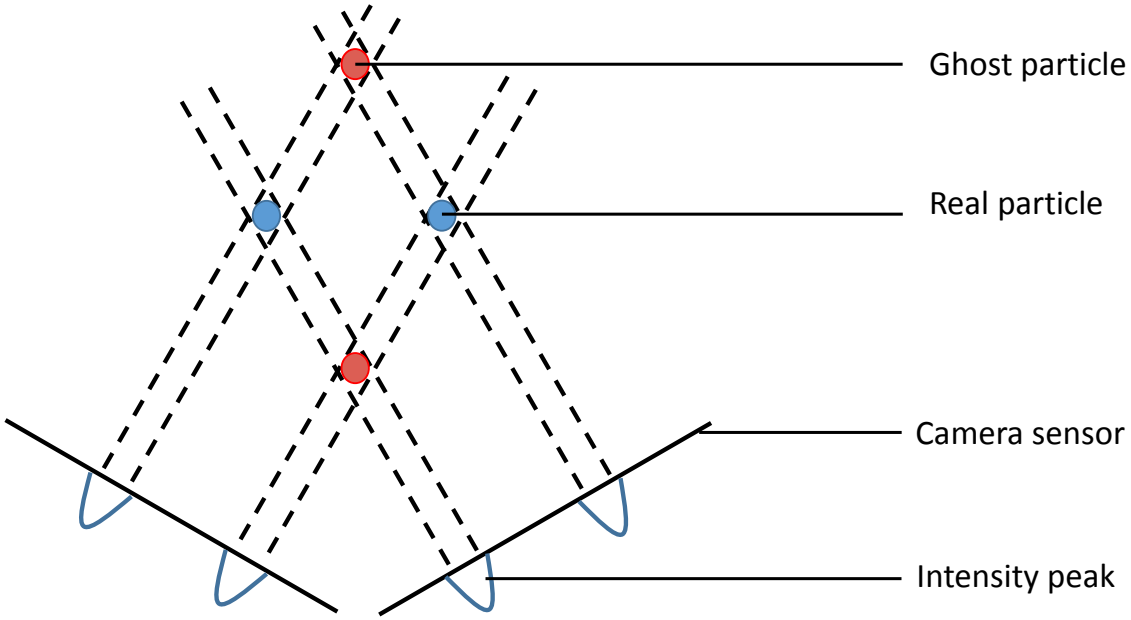

Figure 4.7: Formation of ghost particles. Real particles are in blue and ghost particles in red.

The reconstruction quality is a decreasing function of the number of particles on the camera sensors (usually expressed in particle per pixel, ppp). Indeed, the higher the number of particles on the camera sensors, i.e. the less sparse the I_i vector, the higher the number of possibilities for E_j : the problem is more underdetermined and there will be more ghost particles. Therefore, the solution will have a poorer quality (a lower signal-to-noise ratio). Also, a large concentration in ppp is often due to a large physical concentration (in particle per m^3), which leads to laser light diffusion in all directions and a loss on contrast. However, as the spatial resolution is improving with the physical seeding density, it cannot be decreased to much. Seeding densities up to 0.05 particle by pixel (on camera sensors) can be handled with a 4-cameras system according to [Elsinga et al., 2006]. A technique exists that allows to limit the amount of ghost particles : the Motion Tracking-Enhanced MART [Novara et al., 2010] ; it is quite resource consuming though.

The more cameras, the better the reconstruction because the problem will be less underdetermined. Acceptable reconstruction quality can be reached with 4 or 5 cameras and saturates for higher N_c, as shown in [Elsinga et al., 2006, Scarano, 2013]. The viewing angles of the cameras, i.e. the angles between the axes of the cameras and the smallest volume dimension (y direction on figure 4.6) should be neither too small nor too high. If the viewing angles are too small, reconstructed particles will be elongated. Also, different cameras will give almost redundant information. If the viewing angles are too large, then the lines of sight cross a larger part of the volume and the reconstruction will be more difficult : one pixel will contain information about more voxels. The spatial configuration of

the cameras also matters : in [Scarano, 2013], it is shown that a 3D cross-configuration is relatively better than a planar 2-D configuration.

The reconstruction quality will also depend on the quality of the mapping between cameras pixels and volume voxels, i.e. on the accuracy of matrix $(w_{i,j})$. This matrix is generated during the calibration step.

2.3 Calibration and self-calibration

The aim of the calibration step is to obtain, for each camera, the projection function associating a point on the sensor to a point in the measurement volume. This projection function is coded by the matrix $(w_{i,j})$. After the calibration, the cameras and the lenses should not move at all, otherwise the calibration should be done again. The calibration is done in two steps : first, a rough calibration is done with a 3D calibration plate ; then, it is refined by a method called self-calibration.

2.3.1 Plate calibration

The plate calibration consists in taking, for each camera, one picture of a calibration plate having marks on at least two depth levels. Such a calibration plate is shown on figure 4.8. The calibration plate is placed at the measurement area and the pictures should be taken in the measurement conditions (same fluid, same intermediary optical interfaces) in order to take all the optical path into account. Knowing the real marks position and the position of their images on the cameras sensors allows to fit a 3D mapping function for each camera $\Phi : (x, y, z) \mapsto (x_c, y_c)$. This mapping function can be a pinhole function [Tsai, 1986] or a third-order polynomial [Soloff et al., 1997]. A good accuracy on the position of marks is therefore required ; the higher the number of points, the more accurate the fit. In order to have more points in the direction normal to the plate, it is possible to replace it by a plane with marks and to shift it gradually along the normal direction.

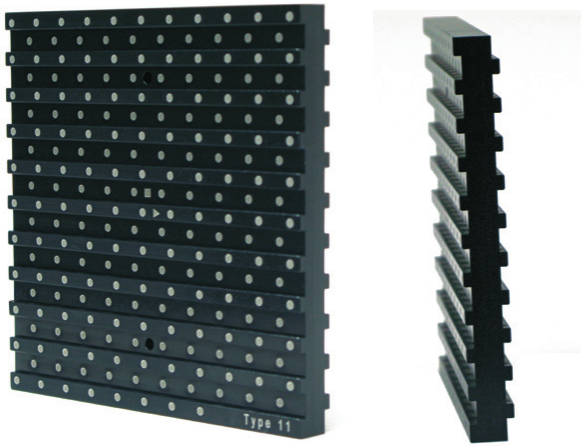

Figure 4.8: 3D calibration plate from LaVision company. Source : LaVision specification sheet.

2.3.2 Volume self-calibration

After the plate calibration, the maximum calibration error is typically above 0.5-2 pixels whereas it should be less than 0.1 pixel to perform proper TPIV [Wieneke, 2008]. A correction of the 3D

mapping obtained during the plate calibration is then required. It can be achieved by the volume self-calibration procedure proposed in [Wieneke, 2008].

This method uses uncorrelated images of particles obtained with a low seeding concentration. The idea is to triangulate particles with some tolerance ϵ using images from all the cameras. ϵ should not be too small, otherwise no particle can be triangulated because the plate calibration is not accurate enough. Each triangulated particle is located at slightly different positions by different cameras, as sketched on figure 4.9 : the lines of sight do not intersect. The average position is considered as the true one, and is reprojected on each camera. The difference between the initial particle image and the reprojected image is called disparity. For example, on figure 4.9, the disparity for camera i is $(x'_i, y'_i) - (x_i, y_i)$.

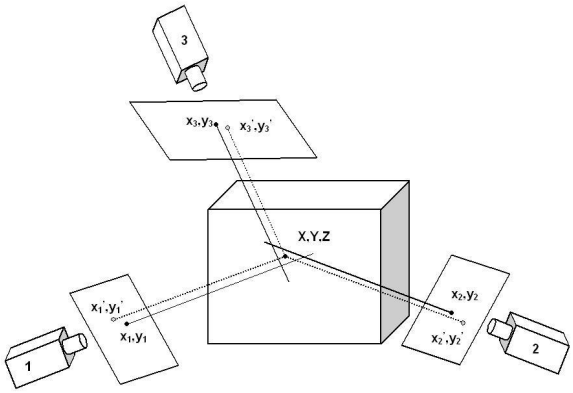

Figure 4.9: Triangulation and reprojection during volume self-calibration. Source : [Wieneke, 2008]

The measurement volume is then divided into subvolumes. For each subvolume, a disparity is computed using several frames (for more details, see [Wieneke, 2008]), and the mapping function is corrected accordingly . The whole process is then iterated until disparities become smaller than 0.1 pixel.

Volume self-calibration allows to get information from the whole measurement volume and not only for a finite number of marks. For instance, when acquiring thousands of pictures, it can be performed every thousand frames to correct the mapping function which may have become wrong because of vibrations or thermal expansion of the cameras and optics. It is a very powerful tool, able to correct a disparity up to 20 pixels.

2.4 Image preprocessing

Volume reconstruction requires good quality images, with a homogeneous light and a good contrast. In principle, raw camera images should be good enough not to do any preprocessing which could impact the result. However, image preprocessing cannot always be avoided to get proper volume reconstruction. Here are a few preprocessings implemented in Davis (the software sold by LaVision) and tested during this thesis (results are exposed in section 3) :

- Backgound subtraction : probably the most important preprocessing that can be done. It consists in subtracting the time-average of the images, i.e. the camera background. This considerably reduces the amount of ghost particles. Sometimes, the minimum (over time) is subtracted instead of the time-average.

- Subtraction of the sliding minimum : another way to remove the image background. The goal is to increase the contrast by subtracting the local minimum (over few pixels) intensity.
- Normalization with local average : it consists in normalizing the intensity by a local average of the intensity, in order to get a homogeneous lighting over the whole image and from an image to the other.
- Gaussian smoothing : the idea is too smooth the particle images in order to get an homogeneous, large enough particle image size. Indeed, according to [Nobach and Bodenschatz, 2009], variations in particle image intensities limit PIV accuracy.

2.5 Summary of the method

The TPIV sequence of steps is summarized in figure 4.10 :

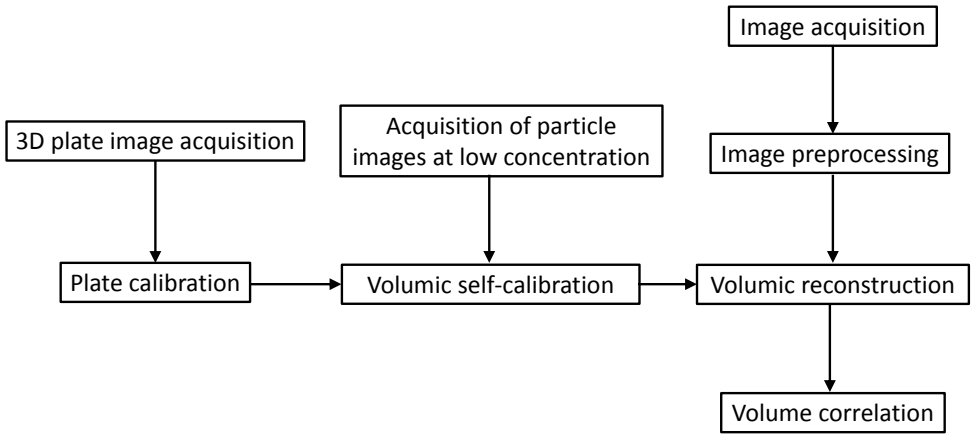

Figure 4.10: TPIV sequence of steps

2.6 TPIV error and quality indicators

Estimating the measurement error in PIV is quite a challenge ; in TPIV it is even more difficult. Here, we analyze the measurement procedure in order to compute the combined uncertainty. This allows to identify critical steps but it is difficult to know exactly the uncertainty corresponding to the reconstruction and correlation steps. Therefore, we then present quality indicators based on the reconstructed intensity volume and methods to estimate the noise and error from the velocity fields.

2.6.1 Measurement procedure analysis following the GUM method

There exists an international consensus on the expression of uncertainty in measurement ; the general method is detailed in the Guide to the expression of uncertainty in measurement (GUM) [Joint Committee for Guides in Metrology-Working Group 1, 2008], developed among others by the Bureau International des Poids et Mesures (BIPM) and the International Standardization Organization

(ISO). In [Gomit et al., 2018], the authors try to apply this method to 2D PIV. Here, largely following this paper and an example seen in a course on 3D-3C PIV given by Laurent David during the 11ème Ecole d'automne de Vélocimétrie et granulométrie laser en mécanique des fluides, we try to apply it to TPIV.

The first step consists in analyzing the measurement procedure in order to establish an estimate of the measurand (the quantity subject to measurement), which is the velocity here. The analysis can be performed via a 5M or Ishikawa diagram, listing the possible causes of uncertainty. This diagram is shown in figure 4.11.

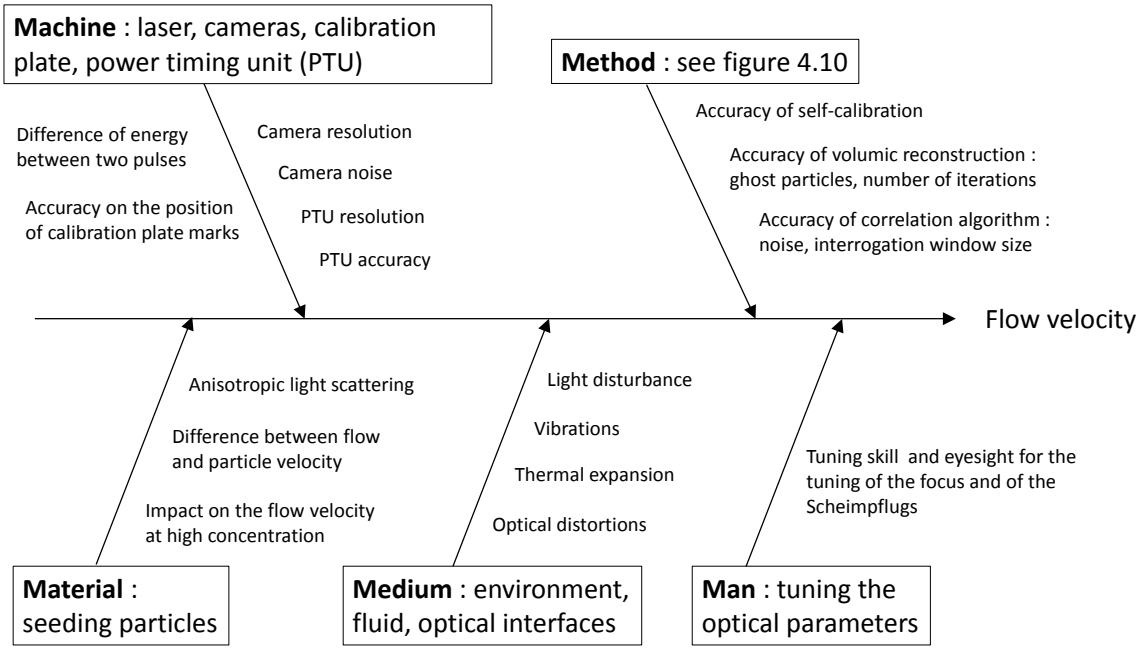

Figure 4.11: 5M diagram for the velocity measurement by TPIV.

Once the possible causes have been identified, the estimate of the measurand can be derived. In our case, the measured velocity u can be modelled as follows :

$$u = \frac{(d_{pix} - e_{recons}) * f}{dt - e_{PTU}} - e_{particles} \tag{4.18}$$

where :

- d_{pix} is the displacement in pixels obtained by the correlation algorithm,
- e_{recons} is the error on d_{pix} due to the inaccuracy of the calibration,
- f is a pixel-to-meter conversion coefficient,
- dt is the interframing time,
- e_{PTU} is the inacurracy of dt due to the fact that the PTU is not perfect (the PTU is the device handling the synchronization between the laser and the cameras),

- $e_{particles}$ is error due to the fact that particles may not follow exactly the flow.

Note that the measured velocity u is filtered over space and time : it is the velocity of a group of particles integrated over dt. We discuss here the uncertainty on the filtered velocity. The effect of the filtering is discussed in next section.

The second step consists in estimating the uncertainty due to the quantities involved in the expression of u.
The uncertainty on d_{pix} (whose value is usually between 5 and 10 pixels) depends on the efficiency of the correlation algorithm, but also on the quality of images and of the 3D reconstruction (ghost particles, shape of the particles) or on the flow itself (in case of large gradients). In the case of 2D PIV, several methods have been proposed to compute the uncertainty on d_{pix} for each velocity vector ; some of them are tested in [Sciacchitano et al., 2015], among which the correlation statistics method [Wieneke, 2015]. However, they are not implemented in 3D yet. A rough general estimation of the error on d_{pix} is 0.1 pixel.
e_{recons} corresponds to the error on the position of the particles due to the inacurracy of the calibration. It also contains errors due to optical distortions. Because of it, the volume correlation is done on an inaccurate light intensity volume. The error due to calibration can be estimated everywhere from the disparity maps. It can even be done for each frame separately thanks to recent advances of the self-calibration [Wieneke, 2018]. For acceptable TPIV, e_{recons} should be below 0.1 pixel.
The error on f is due to the plate calibration and to the self-calibration. f is constant over the whole measurement volume, the error on it too. Considering that the position of the marks on the calibration plate can be estimated with an accuracy of one pixel, and that the distance between two most remote marks is of the order of 1000 pixels on the camera images, we can assume that the relative error on f is around $1/1000^{th}$.
The error on dt is due to the resolution of the PTU. For LaVision's PTU X used in this thesis, it is 10 ns. In this thesis, dt is always larger than 10 μs.
For LaVision's PTU X, e_{PTU} is the jitter time, less than 50 ps.
According to section 1.2, $e_{particles}$ has two components : one due to the fact that particles cannot follow too fast velocity variations and the other due to sedimentation. The latter one corresponds to the falling speed computed in section 1.2. For particles of 10 μm diameter and density 1.2 in water, it is equal to 6 μm/s. The first one is more difficult to estimate. For non-time-resolved measurements, it is not possible to find it as the time evolution of the velocity cannot be known. It can be considered negligible if the Stokes number is low enough.

The next steps of the GUM method consist in determining the combined standard uncertainty and then the expanded uncertainty from the standard uncertainties on each quantities involved in the expression of u. In principle, the GUM method therefore allows to find the rigorous uncertainty on the velocity measurement for each velocity vector. In practice, it is difficult to know the standard uncertainty of each quantity (for d_{pix} it is not yet implemented in 3D, for $e_{particles}$ it implies to know the local flow time scale). Here, we stop after the second step of the GUM method. It nevertheless allows to identify the main sources of uncertainty. The uncertainty on d_{pix} and e_{recons} are of the order of a few percents of d_{pix}. The relative error on dt and f are of the order of $1/1000^{th}$. If $e_{particles}$ can be neglected, it appears that the overall relative error is of the order of a few percents, and mainly due to the reconstruction and correlation steps. It is therefore relevant to express it in pixels ; its value is of the order of 0.2-0.3 pixel [Westerweel et al., 2013].

The GUM method is rigorous but can hardly be applied. However, there exists indicators that do not give the exact error on the measurement but that allow to assess the quality of a volume

reconstruction or of a 3D velocity field.

2.6.2 Quality indicators based on the volume reconstruction

There exists several quality indicators to assess the quality of a volume reconstruction (see e.g. [Martins, 2016]) ; in this thesis we used two of them, presented here.

Ghost level The ghost level is the ratio between the amount of false reconstructed particles, called ghost particles and the amount of real ones. Of course, it is not possible to distinguish between them in the measurement volume. However, when reconstructing a volume larger than the illuminated one, the tomographic algorithm also reconstructs ghost particles outside the illuminated volume. Considering that the concentration of ghost particles is the same inside and outside the illuminated volume, it is possible to compute the ghost level. Let us consider a measurement volume defined by $(x, y, z) \in [-X, X] \times [-Y, Y] \times [-Z, Z]$. The expanded light beam is finite in the z direction and has a thicknesss equal to $2Z$. If a volume reconstruction of the 3D light intensity field $E(x, y, z)$ is performed on an area $(x, y, z) \in [-X, X] \times [-Y, Y] \times [-Z', Z']$ with $Z' > Z$, then the average $\langle E \rangle_{x,y}$ of E over $[-X, X] \times [-Y, Y]$ will be similar to the one depicted on figure 4.12.

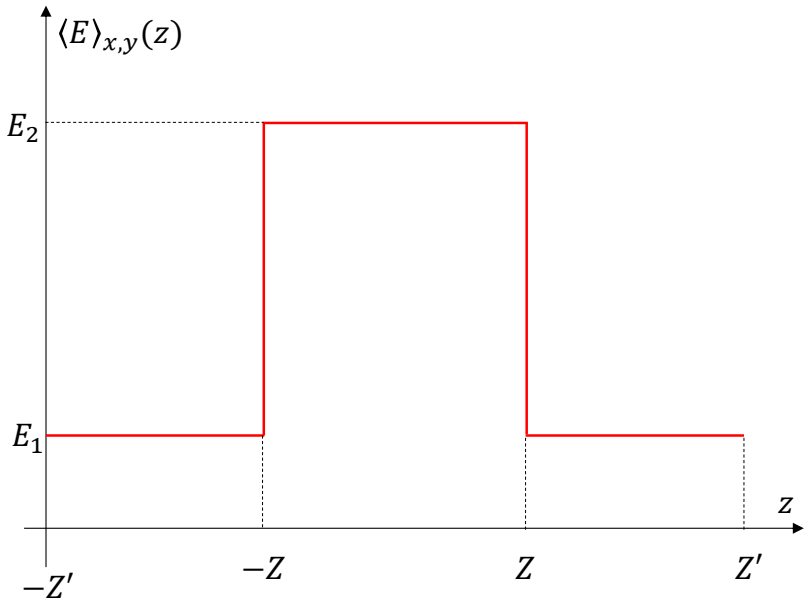

Figure 4.12: Typical intensity z-profile for a volume reconstruction

For $|z| < Z$, there are both real and ghost particles whereas for $Z < |z| < Z'$, there are only ghost particles ; hence a lower average intensity. With $E_1 = \langle E \rangle_{x,y}(Z < |z| < Z')$ and $E_2 = \langle E \rangle_{x,y}(|z| < Z)$, the ghost level can be computed as :

$$\frac{E_1}{E_2 - E_1} \tag{4.19}$$

According to [Scarano, 2013], the ghost level should be smaller than 100% to ensure a good reconstruction quality.

Normalized intensity variance Another indicator is the normalized intensity variance which measures the contrast of the reconstructed light intensity field. It is defined as :

$$\frac{\sqrt{\langle E^2 - \langle E \rangle^2 \rangle}}{\langle E \rangle} \tag{4.20}$$

where the brackets $\langle\rangle$ correspond to the average over the whole lighted volume $[-X, X] \times [-Y, Y] \times [-Z, Z]$. A good reconstruction with few ghosts particles will feature strong intensity peaks corresponding to particles over a low background ; on the contrary, for a bad reconstruction the intensity peaks will be lower, closer to the background level and to the lower intensity peaks corresponding to the ghost particles. According to [Lynch and Scarano, 2014], the normalized intensity variance should be higher than 20 to ensure a good reconstruction quality.

2.6.3 Noise and uncertainty estimation based on the velocity fields

There are also different methods to estimate the noise and the uncertainty on the velocity measurement directly based on the velocity field.

1D Fourier spectrum Computing the 1D Fourier spectrum of the measured velocity field is fruitful as it allows to figure out what is the resolution and what is the noise level (see subsection 2.7.1). Recently, a method was proposed in [Cuvier and Foucaut, 2018] to estimate the noise level from two different analyses of the images with slightly different interrogation window sizes. The method was tested for 2D PIV only but can be applied to 3D PIV as well.

Velocity auto-correlation Computing the 2-point correlation of the velocity $\langle u(x)u(x+r)\rangle$ allows to estimate the noise level. Indeed, as the noise is uncorrelated, the 2-point correlation will feature a spurious peak for $r = 0$. The difference between the peak height and the neighbouring values of the correlation function corresponds to the mean square of the noise.

Velocity divergence For 3D-3C measurements of incompressible flows resolving the smallest scales of the flow, the velocity divergence can be computed and used to estimate the uncertainty on the velocity. Indeed, in such a case, the three components of the velocity are available ; also, their derivatives can be computed in the three directions with low truncature error as the smallest scales of the flow are resolved. There are several ways to use the divergence.

For instance, in [Zhang et al., 1997] and [Worth et al., 2010], the joint pdf of $\partial_x u_x$ and $-\partial_y u_y - \partial_z u_z$ is plotted. For a zero divergence, it should be a straight line of slope 1 ; with uncertainty on the velocity, it rather looks like an ellipsoid around the identity line. In [Zhang et al., 1997], the distribution of $\frac{(\partial_x u_x + \partial_y u_y + \partial_z u_z)^2}{(\partial_x u_x)^2 + (\partial_y u_y)^2 + (\partial_z u_z)^2}$ is also computed.

When using a center scheme for the derivative computation, the uncertainty on the velocity can be directly related to the uncertainty on the divergence. The latter can easily be computed as it is the root mean square of the error on the divergence, equal to the divergence itself as its value should be 0 for an incompressible flow. As shown in [Atkinson et al., 2011], for a space step dx, and assuming that the uncertainties on the three velocity components of the velocity are independent but have the same standard deviation, the uncertainty on one velocity component δu is related to

the uncertainty on the divergence $\delta(\partial_i u_i)$ by :

$$\delta u = \sqrt{\frac{2\ dx^2}{3}}\delta(\partial_i u_i) \tag{4.21}$$

2.7 PIV and TPIV spatial resolution

PIV and TPIV in particular have a finite space resolution : indeed, particles and interrogation volumes have a non-zero size. Here, we discuss the smallest scale resolved by PIV. We then derive a formula relating PIV or TPIV resolution with the optical settings, allowing to estimate the maximum resolution possible and to identify what are the limiting factors.

2.7.1 Resolution considerations

The absolute limit of PIV resolution is the seeding density [Willert and Gharib, 1991]. Indeed, the flow velocity is sampled by the particles, and the fluid velocity between two particles cannot be known. The smallest scale that PIV could resolve is therefore the average distance between two particles. Given a (mean) seeding density d, the average distance between two particles is $1/\sqrt{d\delta}$ for 2D PIV (with δ the laser sheet thickness) and $1/\sqrt[3]{d}$ for 3D PIV (in particular TPIV).

However, on top of this physical limit, PIV resolution is limited by the whole measurement procedure which produces noise and has a filtering effect. In the spirit of [Foucaut et al., 2004], we can write the 1D Fourier spectrum of a velocity field measured by PIV as follows :

$$E_{meas}(k) \propto (E_{real}(k) + E_{noise})|H(k)|^2 \tag{4.22}$$

where :

- E_{meas} is the measured 1D Fourier spectrum
- k is the wavenumber
- E_{real} is the real 1D Fourier spectrum
- E_{noise} is the noise level (constant, not depending on k)
- $H(k)$ is the transfer function of the PIV system

The resolution limit due to noise can be written $k < k_{noise}$ with k_{noise} such that $k < k_{noise} \implies E_{real}(k) > \alpha E_{noise}$, with α a coefficient standing for the stringency on this limit. It means that fluctuations over too small scales, corresponding to $k > k_{noise}$, are considered to be unresolved as they are covered by noise. The noise level depends on several parameters including the interrogation window size X. The larger the interrogation window, the larger the number of particles inside it and remaining inside it during the interframing time ; therefore, the better the correlation peak. For example, for standard square windows, it is shown to be proportional to $1/X$ [Foucaut et al., 2004]. The noise level also depends on the quality of pictures and on the efficiency of the correlation algorithm : for instance, window shifting and deformation improve the noise level because less particles leave the window during the interframing time ; the use of weighting function also improves the noise level as the impact of particles leaving the interrogation windows is decreased.

The resolution limit due to to the filtering can be written $k < k_c$ with k_c such that $k < k_c \implies |H(k)|^2 > \beta$, where β is a coefficient standing for the stringency on this limit. It means that

fluctuations corresponding to $k > k_c$ are considered to be unresolved as they are too filtered ; therefore, they do not contribute significantly to the measured velocity field. Filtering occurs because of the windowing inherent to PIV : the measured velocity vectors are deduced from the time evolution of patterns of several particles, they can be seen as local space-averages of the real velocity. The filtering depends on the shape of the transfer function. For example, for square interrogation windows, it can be well approximated by a sinc function [Foucaut et al., 2004], the Fourier transform of a gate function :

$$H(k) = \frac{sin(kX/2)}{kX/2} \tag{4.23}$$

where X is the interrogation window size. In this case, PIV is roughly the same as a moving average. Using $\beta = 1/2$ gives $k_c \approx 2.8/X$. According to Shannon-Nyquist theorem, properly sampling such a wavenumber requires a sampling period equal to $\pi X/2.8 \approx X$: modes sampled with a space step smaller than X have an energy divided at more than 2. We can then say that the resolution is the interrogation window size. Note that using a larger β would have given a resolution larger than X. For standard square interrogation windows, modifying the window overlap does not impact the resolution, it only has an oversampling effect. It is useful as it gives more vectors to interpolate the velocity field while distorting the windows and may therefore contribute to reduce noise. Also, an overlap of 50% allows to compute the derivatives using the centered scheme with points separated by X instead of $2X$.

Knowing the PIV transfer function would theoretically allow to deconvolute the signal to get only $E_{real}(k) + E_{noise}$. However, the real transfer function of a PIV system is much more complicated than a simple sinc function and it is not possible to deconvolute it directly [Nogueira et al., 2004]. Iterative correlation algorithms can nevertheless be seen as a way to partly deconvolute the signal, under certain conditions, for example if weighting functions are used [Nogueira et al., 2005]. In this case, the resolution can be lower than the interrogation window size (i.e. $k_c > \pi/X$), even with $\beta = 1/2$ [Nogueira et al., 2002]. However, it is not possible to use such weighting functions with too small interrogation windows [Nogueira et al., 2001].

As mentioned in [Foucaut et al., 2004], the optimal X is such that $k_{noise} = k_c$. Indeed, if $k_{noise} < k_c$, noise is the most limiting so X should be increased and if $k_{noise} > k_c$, filtering is limiting so X should be reduced. In [Foucaut et al., 2004], a method is proposed in the case of square interrogation windows to optimize the interrogation window size. In the general case, it is possible to find the cut-off wavenumber of the PIV transfer function for a particular X by analyzing a case with no flow : the obtained velocity field will be only white noise, so that the obtained spectrum is proportional to the transfer function. Knowing the cut-off wavenumber for different X, the real velocity fields can be analyzed with different interrogation window sizes X until the proper X is found, for which the noise level E_{noise} fullfills : $E_{meas}(k_c) = (E_{real}(k_c) + E_{noise})|H(k_c)|^2 = (\alpha + 1)\beta E_{noise}$.

As a conclusion, PIV resolution would ideally be the average distance between particles. However, due to the imperfections of the PIV processing, it is higher. Interpreting this as the need for a given PIV processing chain to use a minimum number N of particles to get a resolution satisfying the α and β criteria, the resolution can be expressed, for 2D PIV, as :

$$\sqrt{\frac{N}{d\delta}} \tag{4.24}$$

with δ the light sheet thickness and d the particle density. For 3D PIV it reads :

$$\sqrt[3]{\frac{N}{d}} \tag{4.25}$$

PIV resolution is thus a decreasing function of the seeding density. However, the seeding cannot be too dense for three reasons : it would modify the flow, it would prevent the light propagation and the density of particles on the camera images cannot be too high, otherwise the correlation algorithm would fail. Relating the PIV resolution to the particle density on cameras allows to identify resolution limits due to optical parameters.

2.7.2 Relation between PIV resolution and optical settings

In this section, we relate the theoretically optimal resolution for 2D PIV and TPIV to the optical settings, using the fact that particle images should not be too close on the cameras. Note that we do not take into account the two other limits on the seeding density (it should be low enough not to impact the flow nor hinder the light).

In this section, the following notations are used :

- s : minimum distance between two particle images, side to side. Typically, $s = 1$ pixel.
- c : camera pixel size. For Image sCMOS cameras, $c = 6.5$ μm and for Miro m340 cameras, $c = 10$ μm.
- $\Phi_d = 2.44 f_\# \lambda (1 + |M|)$: Airy disk diameter.
- $f_\#$: the numerical aperture of the lens.
- λ : wavelength of the laser.
- $|M|$: absolute value of the magnification.
- d : seeding density.
- $\delta = 2 \cdot 2.44 f_\# \lambda \frac{(1+|M|)^2}{M^2}$: camera focal depth, taken equal to the light sheet thickness. In the case of two optical media of indices n_i and n_e, $\delta = 2 \cdot 2.44 f_\# \lambda \frac{n_i}{n_e} \frac{(1+|M|)^2}{M^2}$ (see 1.4).
- N : number of particles per interrogation window.

Each particle should have an area on the camera sensor at least equal to :

$$\frac{\pi(\Phi_d/c + s)^2}{4} \text{ pixel} \tag{4.26}$$

The maximum density on the camera images is therefore :

$$\frac{4}{\pi(\Phi_d/c + s)^2} \text{ particle per pixel (ppp)} \tag{4.27}$$

Case of 2D PIV In the case of 2D PIV, the maximum particle density in the light sheet is then :

$$d\delta = \frac{4|M|^2}{\pi(\Phi_d + cs)^2} \text{ particles per m}^2 \tag{4.28}$$

Replacing in 4.24, we obtain a theoretical 2D resolution equal to :

$$r_{th}^{2D} = \sqrt{\frac{\pi N(\Phi_d + cs)^2}{4|M|^2}} = \sqrt{\pi N}\frac{\Phi_d + cs}{2|M|} \text{ m} \tag{4.29}$$

Φ_d should be between 2 and 3 pixels ; it depends on both $|M|$ and $f_\#$. There is a loose constraint on $f_\#$ in 2D PIV : a small aperture (corresponding to a high numerical aperture $f_\#$) can be balanced by a bright light sheet. Indeed, the laser sheet being thin, the laser energy is not limiting. The constraint on the field depth δ is also loose as the light sheet can be quite thin. Therefore, $|M|$ can be increased without too much care and fine resolution can be reached.
For $N = 10$ (for instance in the case where the resolution is equal to the interrogation window size and where there should be at least 10 particles per interrogation window) and $s = 2$ pixels, the tables B.1 to B.4 of appendix B give the values of r_{th}^{2D}, δ and Φ_d for $c = 6.5$ pixels (Imager sCMOS cameras) and $c = 10$ pixels (Phantom Miro m340 cameras) in the cases $n_i = n_e$ and $n_i = 1.4 \neq n_e = 1$. In all cases, a resolution of 0.1 mm can be reached, with suitable values of Φ_d and δ. For instance, in the case $c = 6.5$ pixels and $n_i = n_e$, $f_\# = 8$ and $M = 0.7$ is a proper set of parameters. For larger pixel size, $|M|$ and/or $f_\#$ should be increased. For $n_i \neq n_e$, the field depth is increased for the same set ($|M|$, $f_\#$) ; to lower it while keeping Φ_d constant, $f_\#$ should be decreased.

Case of 3D PIV In the case of 3D PIV, the maximum density in particle per voxel is obtained by dividing the concentration in ppp by the lighted volume thickness, taken equal to the field depth of the cameras, converted into pixels :

$$\frac{4}{\pi(\Phi_d/c + s)^2|M|\delta/c} \text{ particle per voxel (ppv)} \tag{4.30}$$

The maximum seeding density is then :

$$d = \frac{4|M|^3/c^3}{\pi(\Phi_d/c + s)^2|M|\delta/c} = \frac{4|M|^2}{\pi(\Phi_d + cs)^2\delta} \text{ particles per m}^3 \tag{4.31}$$

The resolution is proportional to at least :

$$r_{th}^{3D} = \sqrt[3]{\frac{\pi N(\Phi_d + cs)^2\delta}{4|M|^2}} \text{ m} \tag{4.32}$$

Compared to 2D PIV, there are more constraints. Φ_d should still be between 2 and 3 pixels, but δ cannot be too small as we want a 3D velocity field ; it should be equal to a few times the resolution. $f_\#$ cannot be too high, otherwise the aperture is very small and requires a strong light intensity on the whole measurement volume, i.e. a very high laser energy.
For $N = 10$ and $s = 2$ pixels, the tables B.5 to B.8 of appendix B give the values of r_{th}^{3D}, δ and Φ_d for $c = 6.5$ pixels (Imager sCMOS cameras) and $c = 10$ pixels (Phantom Miro m340 cameras) in the cases $n_i = n_e$ and $n_i = 1.4 \neq n_e = 1$. Because of the more numerous constraints, the possible resolutions are worse than for 2D PIV. For $c = 6.5$ pixels and $n_i = n_e$, a good set of parameters is $f_\# = 11$ and $|M| = 0.3 - 0.4$. The resolution is then between 0.5 and 0.8 mm and the field

depth between 6 and 7.5 times the resolution. $f_\# = 8$ and $|M| = 0.7 - 0.9$ is also possible, yielding a better resolution of 0.2-0.25 mm but the ratio δ/r_{th}^{3D} is then smaller. For larger pixel size, $|M|$ and/or $f_\#$ should be increased to keep Φ_d between 2 and 3 pixels. In this case, the resolution is a bit worse than for $c = 6.5$ pixels but the ratio δ/r_{th}^{3D} is a bit higher. For $n_i \neq n_e$, the same sets of $f_\#$ and $|M|$ can be used as previoulsy, but the resolution is slightly worse whereas the ratio δ/r_{th}^{3D} is slighty better.

2.8 Comparison with other correlation-based methods

In this section we briefly compare TPIV with two other PIV methods : stereoscopic PIV (SPIV) and scanning PIV.

2.8.1 Stereoscopic PIV

Stereoscopic PIV is a correlation-based method allowing to measure the three components of the velocity field on a 2D grid. It requires only two cameras, but Scheimpflugs and a 3D calibration plate are needed. Volume self-calibration is not required. Less powerful lasers can be used as only a sheet should be lighted and not a volume. The third component of the velocity can also be measured because the cameras look at the flow from different angles ; therefore, the 3D motion of the particles is projected into two different planes, which allows to find the three components of the displacement (the sheet has a small but non-zero width so that the out-of-plane component of the motion does not bring them out of the laser sheet during the interframing time dt).

SPIV was used in our group before this thesis and the implementation of TPIV for the VK2 set-up. Velocity fields measured by SPIV in this set-up are also analyzed in this thesis and were used in several papers [Debue et al., 2018a, Debue et al., 2018b].

Compared to TPIV, SPIV provides only two dimensions and therefore does not allow to compute the gradients in the third direction. It is then impossible to compute the exact Π_{DR}^ℓ, $\mathscr{D}_\nu^\ell$, Π_{LES}^ℓ and $\mathscr{D}_{\nu,LES}^\ell$ terms defined in chapter 2 (only 2D versions can be computed) and difficult to really analyze the flow topology. Also, noise occuring in the correlation step due to out-of-the plane motion is much more important. However, the method is much less time-consuming as it does not require volume reconstruction and as the correlation is performed on 2D arrays only. This allows to compute more velocity fields and to get more converged statistics and more extreme events (of the quantities that can be computed). Also, SPIV allows to reach better spatial resolutions, as seen above and also observed in [Atkinson et al., 2011] for instance.

2.8.2 Scanning PIV

Scanning PIV is another 3D PIV method. It consists in scanning the measurement volume with a thin light sheet, fast enough so that the scanning time is much smaller than the flow smallest time scale. It requires one high-speed camera and a high-speed laser, both synchronized with a mechanical device allowing to shift the light sheet at high frequency.
Compared to TPIV, this method does not require volume reconstruction : indeed, the light intensity volume is obtained by juxtaposing the images acquired in the same scan. Therefore, it is less time-consuming and is free from the noise due to volume reconstruction, and especially the ghost particles. Also, it allows to measure thicker fields. However, scanning PIV may be less accurate due to the fact that one volume is made of pictures acquired at different times. The acquisition frequency of the camera must be very high, but high-speed cameras have smaller sensors and bigger pixels ; the

size of the field and the resolution are then worse than for TPIV. Time-resolved scanning PIV is also hardly possible because far too high frequencies are needed.

3 Test of Davis software and optimization of the TPIV parameters for our set-up

In this thesis, we used TPIV to measure the velocity field at the center of the turbulent von Kármán flow generated in the VK2 set-up described in chapter 2. The location of the measurement volume is shown in figure 5.11 of chapter 5. We used the commercial software Davis developed by LaVision. However, we do not know the exact inner functioning of this software. Also, even if TPIV measurements have already been reported in a von Kármán flow ([Worth et al., 2010] for instance, with set-up description in [Gan et al., 2016]), the corresponding set-up is ten times bigger than ours and has a dodecahedral tank instead of a circular one in our case. We therefore performed some tests to have a better knowledge of the behaviour of Davis and to find the optimal TPIV parameters in the particular case of the VK2 set-up. Here, we just summarize the main results of these tests. More details are provided in the appendices C and D.

3.1 Test of Davis software

During the second part of the time-resolved measurement campaign of 2018, we acquired one batch of images with the fluid at rest (no rotation of the impellers). We analyzed the images with different sets of volume correlation parameters and obtained a so-called "case-control (CC) data set" made of eleven cases. This allowed to test the influence of the different parameters and to have a better knowledge of the whole PIV measurement chain which involves a software that we did not develop. We were especially interested in estimating the measurement noise and the cut-off wavenumbers for different interrogation window sizes, overlaps and shapes.

The main results of these tests of Davis are the following :

- Increasing the overlap of Gaussian interrogation windows has the same impact as decreasing the interrogation window size : the resolution is improved but the noise level increases.
- Compared to a square interrogation window of similar size, using a Gaussian interrogation windows yields a lower noise level but a worse spatial resolution.

The details of the tests can be found in appendix C.

3.2 Optimization of the TPIV parameters for our set-up

In order to optimize the TPIV parameters in the particular case of the VK2 set-up, we studied the impact of :

- the outer tank (outer tank A vs. B),
- the seeding particles (silver-coated vs. lighter non-silver-coated particles),
- the reflecting mirror at the end of the laser line,
- the inter-framing times dt,

- the seeding concentration.

We also studied the impact of the impeller rotation frequency.
We used the quality criteria described above to compare the impact of the different parameters.

Overall, these tests show that TPIV is quite robust and not significantly sensitive to the chosen parameters. In order to get the best results, outer tank B should be used because it avoids astigmatism. Non-silver-coated particles should also be favoured as they yield a better contrast and as there is no effect of the impeller rotation frequency when using these particles. However, a reflecting mirror should be used in addition to these particles so that cameras in backward scattering get enough light. The highest concentration reachable is of the order of 0.09 ppp.
The details of the tests can be found in appendix D.

Chapter 5

Presentation of the experimental data sets

In this chapter we present the three experimental data sets that are used in this thesis, i.e. the conditions in which they were obtained, the equipment used and the statistics of the velocity fields. This will give insight for the interpretation of the results in part III. The three data sets consist in velocity fields measured in the VK2 set-up described in chapter 3.
The first data set was obtained by non-time-resolved stereoscopic PIV before this thesis ; it is a statistically relevant set of independent 2D-3C velocity fields at different Reynolds number in the anti direction of rotation. With such velocity fields, only 2D versions of the Duchon-Robert and viscous dissipation terms can be computed. This data set allowed to start the study of the statistics and extreme events of these terms, before getting the equipment and skills to perform 3D measurements.
The second data set was obtained by non-time-resolved tomographic PIV during two measurement campaigns performed during this thesis ; it is a statistically relevant set of independent 3D-3C velocity fields measured at different Reynolds number in the anti direction of rotation and in the contra direction of rotation for one Reynolds number. It is meant to confirm the 2D analysis and to study the 3D structure of the velocity field around the extreme events of viscous dissipation or of the Duchon-Robert term.
The third data set was obtained by time-resolved tomographic PIV, during another measurement campaign performed during this thesis ; it consists in 40 subsets of time-correlated 3D-3C velocity fields measured at a Reynolds number equal to 6000 with the impellers rotating in the anti direction of rotation. This is the largest Reynolds for which the spatial resolution of the measurement is in the dissipative range. It allows to study the time evolution of the extreme events that we are interested in.

Notations and definitions

In the following, we will deal with Eulerian quantities measured at different spatial locations and at different times. In all cases, such quantities are measured on a rectangular Eulerian grid at regular time intervals. Let x, y and z be the cartesian coordinates and t the time coordinate ; we then call Δx, Δy and Δz the corresponding space steps of the Eulerian grid and Δt the time interval. In this thesis, we always have $\Delta x = \Delta y = \Delta z$. We will also call n_x, n_y and n_z the number of points of the Eulerian grid in the x, y and z directions respectively and n_t the number of time steps. The

Eulerian grid is then :

$$[x_1, x_1+\Delta x, ..., x_1+(n_x-1)\Delta x] \times [y_1, y_1+\Delta y, ..., y_1+(n_y-1)\Delta y] \times [z_1, z_1+\Delta z, ..., z_1+(n_z-1)\Delta z] \tag{5.1}$$

and the different time steps are :

$$[t_1, t_1+\Delta x, ..., t_1+(n_t-1)\Delta t] \tag{5.2}$$

with x_1,y_1 and z_1 the smallest values of the space coordinates at which the quantities are measured and t_1 the smallest time at which they are measured (we usually take $t_1 = 0$).
A measured Eulerian scalar quantity X (for instance a velocity component u_i) can then be stored in a 4-dimension array $(X_{i,j,k,l})$ with $1 \leq i \leq n_x$, $1 \leq j \leq n_y$, $1 \leq k \leq n_z$ and $1 \leq l \leq n_t$ such that $X_{i,j,k,l}$ is the quantity measured at position $(x_1+(i-1)\Delta x, y_1+(j-1)\Delta y, z_1+(k-1)\Delta z)$ and at time $t_1+(l-1)\Delta t$. This is the convention used in this thesis.

Averages

We can then define the time-average of X at position $(x_1+(i-1)\Delta x, y_1+(j-1)\Delta y, z_1+(k-1)\Delta z)$ as :

$$\langle X_{i,j,k} \rangle_t = \frac{1}{n_t} \sum_{l=1}^{n_t} X_{i,j,k,l} \tag{5.3}$$

It can be written $\langle X \rangle_t$, the dependance on space being implicit.
The space-average of X at time $t_1+(l-1)\Delta t$ is defined as :

$$\langle X_l \rangle_{x,y,z} = \frac{1}{n_x n_y n_z} \sum_{i=1}^{n_x} \sum_{j=1}^{n_y} \sum_{k=1}^{n_z} X_{i,j,k,l} \tag{5.4}$$

It can be written $\langle X \rangle_{x,y,z}$, the dependance on time being implicit.
The space-time-average of X is defined as :

$$\langle X \rangle_{x,y,z,t} = \frac{1}{n_x n_y n_z n_t} \sum_{i=1}^{n_x} \sum_{j=1}^{n_y} \sum_{k=1}^{n_z} \sum_{l=1}^{n_t} X_{i,j,k,l} \tag{5.5}$$

These definitions extend easily to quantities X measured at a single spatial point or which do not depend on space ($n_x = n_y = n_z = 1$), or to quantities measured on a single plane ($n_z = 1$).

Root mean squares

In the case of the velocity components u_i, we define the time root-mean-square (rms) of the fluctuations of each component u_i^{rms} and the total time rms u_{tot}^{rms} as follows :

$$u_i^{rms}(x,y,z) = \sqrt{\langle (u_i - \langle u_i \rangle_t)^2 \rangle_t} \tag{5.6}$$

$$u_{tot}^{rms}(x,y,z) = \sqrt{\sum_{i=1}^{3} (u_i^{rms}(x,y,z))^2} \tag{5.7}$$

$$\tag{5.8}$$

We then define the space-time rms as follows :

$$U_i^{rms} = \sqrt{\langle (u_i - \langle u_i \rangle_t)^2 \rangle_{x,y,z,t}} = \sqrt{\langle u_i^{rms}(x,y,z)^2 \rangle_{x,y,z}} \tag{5.9}$$

$$U_{tot}^{rms} = \sqrt{\sum_{i=1}^{3} (U_i^{rms})^2} = \sqrt{\langle u_{tot}^{rms}(x,y,z)^2 \rangle_{x,y,z}} \tag{5.10}$$

$$\tag{5.11}$$

Effective number of independent frames

When the acquisition frequency f_{acq} is too high compared to the typical frequencies of the flow, i.e. when the time step $\Delta t = 1/f_{acq}$ between two consecutive velocity fields is too small, consecutive values of the velocity components measured at the same point $u_i(x,y,z,t)$ and $u_i(x,y,z,t+\Delta t)$ are correlated. This is expected for time-resolved measurements, but should be avoided when the goal is to statistically sample the flow. In the case where consecutive velocity fields are correlated, the total number of time steps n_t does not correspond to the number of independent velocity fields, and it is not a good indication of the amount of statistics. To better account for it, we can compute the effective number $n_{t,eff}$ of independent frames based on the definition in [Sciacchitano and Wieneke, 2016]. For each velocity component u_i at each point $\mathbf{x}$, one can define the auto-correlation coefficient $\rho_i(\mathbf{x}, \Delta t, p)$:

$$\rho_i(\mathbf{x}, \Delta t, p) = \frac{\langle u_i(\mathbf{x},t) u_i(\mathbf{x}, t+p\Delta t) \rangle_t}{\langle u_i(\mathbf{x},t)^2 \rangle_t} \tag{5.12}$$

The corresponding effective number of independent samples of the velocity component i at point $\mathbf{x}$ is then given by :

$$n_{t,eff,i}(\mathbf{x}) = \frac{n_t}{\sum_{p=-\infty}^{+\infty} \rho_i(\mathbf{x}, \Delta t, p)} = \frac{n_t}{\rho_i(\mathbf{x}, \Delta t, 0) + 2\sum_{p=1}^{+\infty} \rho_i(\mathbf{x}, \Delta t, p)} \tag{5.13}$$

Here, we assumed that ρ is an even function of p. In practice, the summation is stopped before the first negative ρ_i.
$n_{t,eff,i}$ is strongly varying through space in the von Kármán flow considered in this thesis (between less than half its space average to twice its space average, see figure 5.3). We noticed that it takes higher values, in average and at the center of the von Kármán flow, for the velocity component along x. Therefore, in the following we give $\langle n_{t,eff,x} \rangle_{x,y,z}$ as a conservative indication of the effective number of independent velocity fields, though the previous remarks should be kept in mind.

1 2D-3C data set

The 2D-3C data set was acquired by Saw et al (see e.g. [Saw et al., 2016]) before this thesis. However, it was used during this thesis for the analysis presented in chapter 7. It consists in 5 cases (A, B, C, D and E) of SPIV measurements obtained at Reynolds numbers ranging from 6000 to 300000 with the impellers rotating in the anti direction of rotation. For each case, several thousands of almost uncorrelated frames were acquired. These cases are the same as the cases studied in [Debue et al., 2018a] and [Debue et al., 2018b].

1.1 Flow parameters

Cases were acquired at different Reynolds numbers in order to vary the Kolmogorov scale and therefore to probe different scale ranges. Cases A to C allow to probe the inertial range, case D allows to probe the transition range between the inertial and dissipative ranges, and case E allows to probe the dissipative range. The Reynolds number of case D is lower than those of cases A to C ; the Kolmogorov scale is then larger and this case thus allows to probe scales closer to the dissipative range. The Reynolds number is the same in cases A to C ; however, these cases allow to probe different scales. Indeed, in case A the measurement area is larger and the magnification is smaller than case B (see 1.3) ; the probed scales are therefore further from the dissipative range. For case C, the interrogation window size is twice as small as in case B (see 1.4), allowing to probe smaller scales than case B.
The Reynolds numbers of the different cases are given in table 5.1, along with the corresponding flow parameters. The liquid used was water at 20°C for cases A to C, water at 5°C for case D and a water-glycerol mixture containing 59% of glycerol in volume at 20°C for case E. For all cases, the impellers used are TP87 impellers rotating in the anti direction. The values of λ and R_λ for cases A to C are different, especially for case A, because the values of the rms are different.

Case		A	B	C	D	E
Rotation frequency (Hz)		5			1	1.2
Normalization velocity V=$2\pi RF$ (m/s)		3.1			0.63	0.75
Liquid	Percentage of glycerol in volume	0				59
	Temperature (°C)	20			5	20
	Kinematic viscosity (m^2/s)	1×10^{-6}			1.5×10^{-6}	1.3×10^{-5}
	Density (kg/m^3)	998			1000	1166
Reynolds number Re		3.1×10^5			4.1×10^4	5.8×10^3
Taylor Reynolds number R_λ		610	920	890	300	72
Kolmogorov length scale η (mm)		0.016			0.073	0.32
Kolmogorov time scale τ_k (s)		2.6×10^{-4}			3.6×10^{-3}	7.9×10^{-3}
Taylor length scale λ (mm)		0.79	0.97	0.96	2.5	5.4

Table 5.1: Flow parameters for the 2D-3C cases.

1.2 Seeding parameters

The particles used were silver-coated glass hollowspheres sold by Dantec. They have a diameter of 10 to 30 μm, the average being 15 μm. Their density is 1.4 g/cm^3.
The Stokes number St_{τ_k} based on the Kolmogorov time scale τ_k, the smallest resolved Hölder exponent h (defined in 4.10 in chapter 4) and the velocity shift v_g (see chapter 4) are given in table 5.2.
For all cases, the Stokes number is smaller than 1. The smallest resolved Hölder exponent $h(10)$, i.e. the smallest Hölder exponent such that the typical time scale corresponding to the resolution scale is ten times larger than the seeding particle reponse time, is varying from one case to another. It is higher for cases B and C compared to case A because the resolution is smaller. Therefore, the typical time scale of the structures having a size of the order of the resolution is smaller than for

Case	A	B	C	D	E
St_{τ_k}	6.7×10^{-2}	6.7×10^{-2}	6.7×10^{-2}	3.3×10^{-3}	1.5×10^{-4}
h(10)	-0.6	-0.1	0.0	-0.6	-0.7
v_g (m/s)	-4.9×10^{-5}	-4.9×10^{-5}	-4.9×10^{-5}	-3.3×10^{-5}	-1.9×10^{-6}

Table 5.2: Seeding parameters for the SPIV cases A to E

case A ; for very low h it will be smaller than the particle response time. In case A, the flow time scales are the same as for cases B and C but as the spatial resolution is worse, the typical time scale of a structure of a given Hölder exponent h at the resolution length scale will be larger. For cases D and E, the flow time scales are larger, allowing to resolve smaller h. Overall, this estimation of the smallest resolved Hölder exponent shows that the scarcity of low Hölder exponents will hinder their study much more than the inertia of the particles.
The velocity shifts are all negative, because the particles are heavier than the fluid. They are smaller than the average velocity components and even smaller than the root mean squares of the fluctuations of the velocity components (see table 5.4). Therefore, the sedimentation does not affect the velocity measurement.

1.3 Acquisition

1.3.1 Laser

The laser used is a Solo II PIV laser sold by New Wave Research. It is a Nd:YAG (neodymium:Yttrium-Aluminium-Grenat) laser producing a green light at 532 nm. It has two cavities, each of them having a repetition rate of 30 Hz and delivering a maximum rated energy of 30 mJ per pulse. The pulse width is between 3 and 5 ns.

1.3.2 Cameras

The cameras used are two Dantec Flow Sense 2M cameras. These cameras have a CCD sensor of 1600×1200 square pixels of 7.4 μm square. Their dynamic range is either 8 or 10 bits and the maximum acquisition frequency is 15 Hz.

1.3.3 Configuration

The spatial arrangement of the cameras and of the laser is shown on figure 5.1. The laser beam is expanded into a vertical sheet by a sheet optics and then reflected by a mirror in order to enter the outer tank through a narrow face. It then crosses the cylindrical tank, passing through the cylinder axis, and is absorbed by a home-made beam dumper. The angle between the laser sheet and the faces of the square outer tank or between the laser sheet and the camera optical axes is 45°. Both cameras are equipped with Scheimpflugs.

1.3.4 Acquisition parameters

The measurement area is contained in a meridian plane of the cylindrical tank. For case A, the measurement area is covering the whole space between the impellers and the walls, whereas for cases B to E it is covering only a smaller area of roughly 4 cm × 4 cm near the center of the flow, as illustrated on figure 5.2. In this thesis, we call x the horizontal direction, y the vertical direction

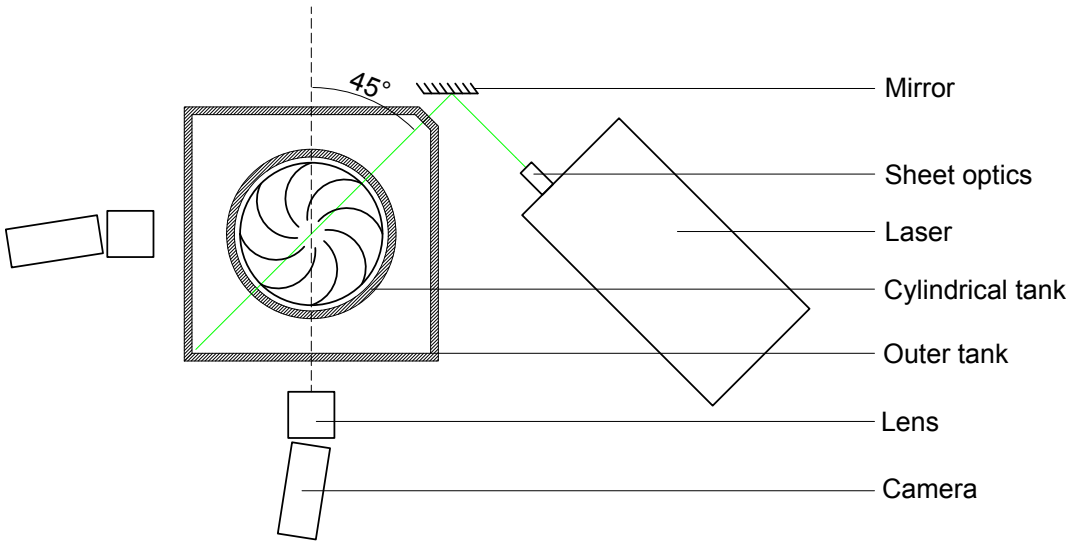

Figure 5.1: Top view of the spatial arrangement of the laser and of the cameras. The green line corresponds to the laser beam.

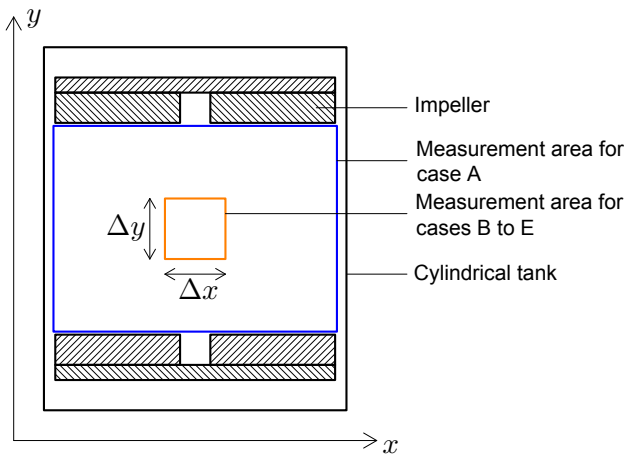

Figure 5.2: Measurement area in the meridian plane for 2D-3C cases.

and z the out-of-plane direction. The exact dimensions of the measurement areas for cases A to E, as well as the corresponding magnifications, are given in table 5.3.
Because of small differences between the rotation frequencies of the impellers, the measurement area was not exactly centered on the mixing layer. Figure 5.5 shows the average velocity fields for cases A to E. For cases B to E, the measurement area is slightly below the mixing layer.
Table 5.3 also gives the number of frames n_t acquired for each case. In all cases, the velocity fields were acquired with an acquisition frequency $f_{acq} = 15$ Hz, meaning that the time interval between two consecutive velocity fields is $\Delta t = 1/f_{acq} \approx 0.067$ s. This acquisition frequency is quite

Case	A	B	C	D	E
Field size (Δx (cm) $\times$ Δy (cm))	18.8×13.6	3.7×3.8	3.9×3.8	3.7×3.9	3.6×4.1
Magnification	0.056	0.25	0.24	0.25	0.25
Number of frames	29999	29228	28000	9999	30188
$\langle n_{t,eff,x} \rangle_{x,y}$	4400	8600	8700	730	2200

Table 5.3: Acquisition parameters for the 2D-3C cases.

large compared to the rotation frequency of the impellers, resulting in a small correlation between consecutive frames.

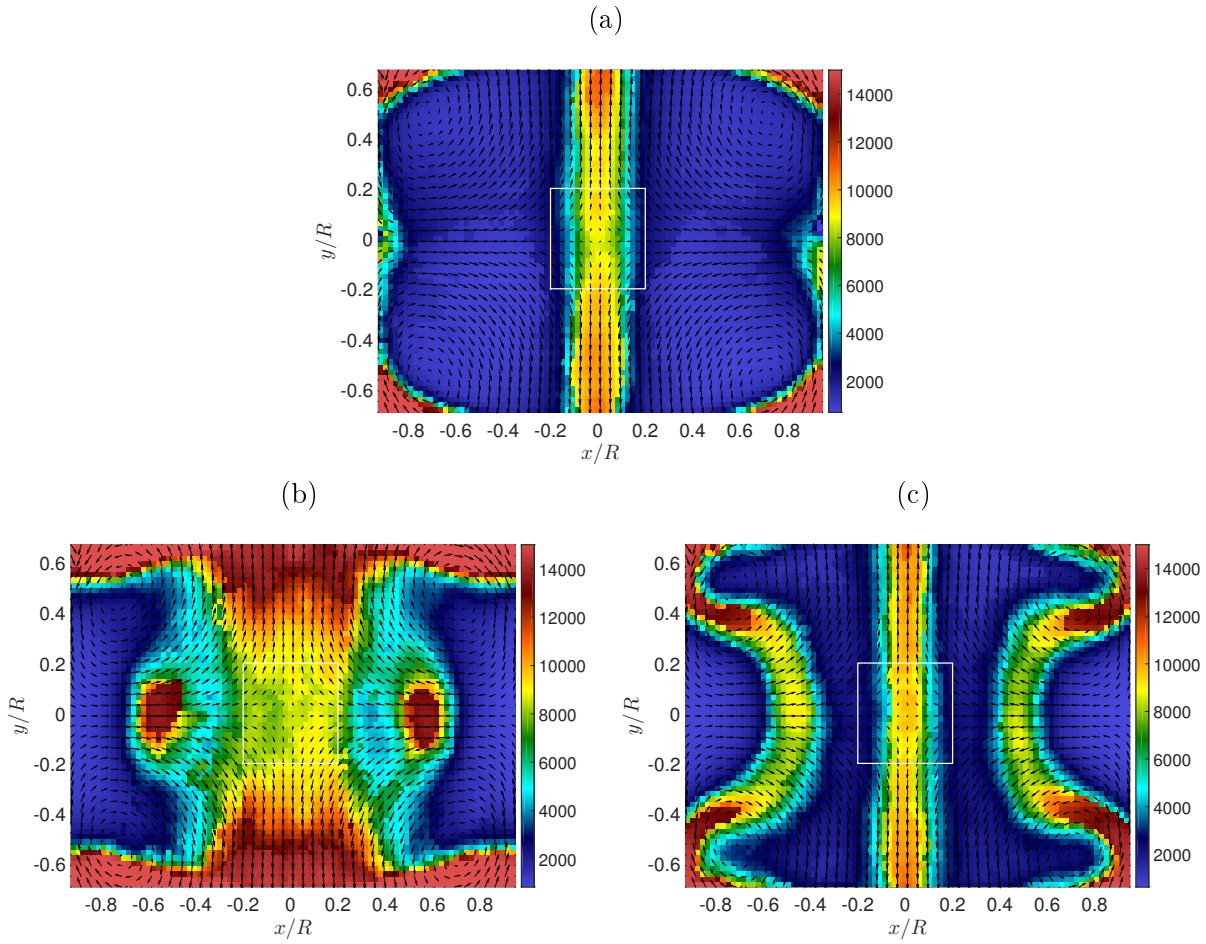

Figure 5.3: Number of independent frames $n_{t,eff}(\mathbf{x})$ as a function of space for case A and the three velocity components. (a) u_x (b) u_y (c) u_z. The white square shows the location of the measurement area for cases B to E.

Figure 5.3 shows the effective number of independent samples $n_{t,eff,i}(\mathbf{x})$ for the three velocity components for case A. The white square shows the measurement area of cases B to E. One can see that $n_{t,eff,i}(\mathbf{x})$ is strongly varying through space, with a factor 7 between the smallest and largest values. Even in the zone at the center where the velocity fields of cases B to E were acquired (represented by a white square), there is a factor 5 between the smallest and largest $n_{t,eff,i}(\mathbf{x})$ for

components along x and z. For the component along y in the center area, the ratio between the largest and smallest values of $n_{t,eff,i}(\mathbf{x})$ is smaller. Note that these ratios are also observed for cases B to E even if the absolute values of $n_{t,eff,i}(\mathbf{x})$ are different. Even if $n_{t,eff,i}(\mathbf{x})$ is strongly varying through space, we still give their space averages for the velocity component along x (the component giving the worst values) in table 5.3 as an indication of the effective number of independent frames. It is smaller for case A than for cases B and C because the space average was done on a larger area including wide domains where the effective number of independent frames is small. For cases D and E, it is smaller than for cases B and C because the impeller rotation frequency is smaller (therefore, the time-scales, including the decorrelation time, are smaller). Also, for case D only, the total number of frames is smaller, resulting in an even smaller$\langle n_{t,eff,x}\rangle_{x,y}$. For all cases, $\langle n_{t,eff,x}\rangle_{x,y}$ seems to be large enough. For case D though, it may be too low, making it more difficult to see extreme events.

1.4 Correlation parameters and velocity statistics

Table 5.4 sums up the main correlation parameters and velocity statistics for cases A to E.

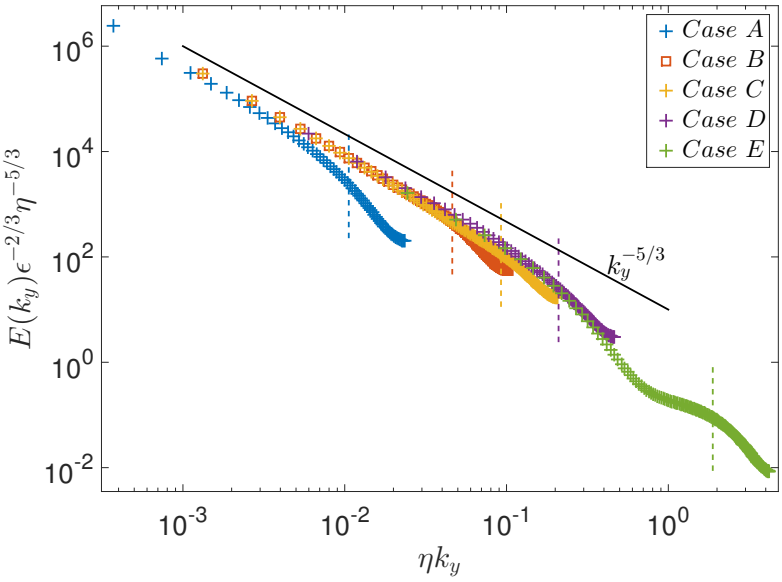

Figure 5.4: 1D Fourier spectrum along the y axis for cases A to E. The vertical dashed lines correspond to the PIV 2 dB cut-off wavenumbers.

In all cases, the overlap is 50%, but for some cases the interrogation window size is 16 pixels whereas for others it is 32 pixels ; the number of points is then respectively of the order of 160 × 160 or 80 × 80. For case E, the interrogation window size is of the order of the Kolmogorov scale ; therefore, the resolved scales belong to the dissipative range, as is clear from the 1D spectra along the y direction on figure 5.4. Note however that the saturation above $\eta k_y \approx 0.7$ corresponds to noise and that the fluctuations above this wavenumber should not be considered. For cases A to D, the resolved scales belong to the inertial range, the interrogation window size being one to two orders of magnitude higher than the Kolmogorov scale. The corresponding spectra on figure 5.4 follow quite well the Kolmogorov $k^{-5/3}$ scaling. They are slightly steeper at smaller wavenumbers ; at larger wavenumbers they become really steeper because of the cut-off due to the windowing inherent to

PIV and arising at values of ηk_y represented by the dashed lines.

Case		A	B	C	D	E
Number of points ($n_x \times n_y$)		89×65	77×79	162×157	77×80	151×174
Overlap		50%				
Interrogation volume size	pix	32	32	16	32	16
	m	4.3×10^{-3}	9.8×10^{-4}	4.9×10^{-4}	9.8×10^{-4}	4.7×10^{-4}
	η	260	60	30	13	1.5
Space step	m	2.1×10^{-3}	4.9×10^{-4}	2.4×10^{-4}	4.9×10^{-4}	2.4×10^{-4}
	η	130	30	15	7	0.7
Average of u_x	m/s	3.8×10^{-4}	2.7×10^{-2}	1.3×10^{-2}	0.7×10^{-2}	1.3×10^{-3}
	adim	1.2×10^{-4}	8.7×10^{-3}	4.1×10^{-3}	1.1×10^{-2}	1.7×10^{-3}
Average of u_y	m/s	5.3×10^{-3}	0.8×10^{-1}	0.8×10^{-1}	1.7×10^{-2}	2.1×10^{-2}
	adim	1.7×10^{-3}	2.5×10^{-2}	2.5×10^{-2}	2.7×10^{-2}	2.8×10^{-2}
Average of u_z	m/s	1.5×10^{-2}	1.3×10^{-2}	1.4×10^{-2}	9.2×10^{-3}	8.3×10^{-3}
	adim	4.8×10^{-3}	4.2×10^{-3}	4.5×10^{-3}	1.5×10^{-2}	1.1×10^{-2}
Rms of u_x fluctuations	m/s	8.5×10^{-1}	1.0×10^{0}	1.0×10^{0}	2.0×10^{-1}	1.9×10^{-1}
	adim	0.27	0.33	0.33	0.32	0.26
Rms of u_y fluctuations	m/s	6.4×10^{-1}	6.6×10^{-1}	6.7×10^{-1}	1.3×10^{-1}	1.3×10^{-1}
	adim	0.20	0.21	0.21	0.20	0.17
Rms of u_z fluctuations	m/s	8.5×10^{-1}	1.1×10^{0}	1.1×10^{0}	2.1×10^{-1}	1.9×10^{-1}
	adim	0.27	0.35	0.35	0.34	0.25
Rms of total fluctuations	m/s	1.4×10^{0}	1.7×10^{0}	1.6×10^{0}	3.2×10^{-1}	3.0×10^{-1}
	adim	0.43	0.53	0.52	0.50	0.40

Table 5.4: Velocity fields characteristics and mean and rms values.

Table 5.4 also gives the space-time average of the velocity components $\langle u_i \rangle_{x,y,t}$, the root-mean-square of the fluctuations of the velocity components U_i^{rms} and the total root-mean-square of the fluctuations U_{tot}^{rms}. For all cases, the rms values are much higher than the average values. This is expected as the average value is 0 at the very center of the flow, and should therefore be small in the surroundings. The dimensionless rms values of cases B to D are very similar, which supports the fact that the dimensionless statistical quantities become independent of the Reynolds number in the limit of high Reynolds numbers. The dimensionless rms values are different for case A because the average is done over a larger area ; for case E they are different probably because the Reynolds number is smaller.
The average velocity fields are shown on figure 5.5. One can see that the measurement area slightly varies around the center of the flow for cases B to E. It can be due to the fact that the cameras were not exactly centered on the center of the flow. The vertical shift can also be explained by a small difference between the rotation frequencies of the bottom and top impellers, resulting in a shift of the mixing layer (through which $\langle u_y \rangle_t$ changes sign). The maps of the rms values are not provided here. The one for case A is shown in chapter 3. For cases B to E, the rms values are varying by less than 10 percent across the measurement area.

The probability density functions of the components are shown in figure 5.6 in semi-logarithmic coordinates. They seem close to Gaussian distributions. For cases B to E, the pdfs of the components along directions x and z are very close to each other. This can be explained by a statistical invariance by rotation around the cylinder axis, as a rotation of 90° around this axis maps the z direction onto the x direction. The pdfs of the component along the y direction are narrower, in accordance with the smaller rms values. For case E, peak locking is observed. In principle, this is due to too small particle images. Here the magnification used for case E is similar to those of cases B to D ; the peak locking may be due to a too small numerical aperture $f_{\#}$ (see chapter 4).

Here are the main informations of this section :

- The 2D-3C data set is made of 5 cases acquired by SPIV in the VK2 set-up. The velocity fields were measured in a meridian plane of the set-up. For case A, the measurement area covers the whole height and width of the set-up whereas for other cases it is a 4×4 cm^2 area at the center of the flow.
- The Reynolds number and/or the spatial resolution is varied from a case to another in order to probe different scale ranges. For case E, the spatial resolution is in the dissipative range. For all cases, the impellers are rotating in the anti direction of rotation.
- Each case provides a statistically relevant set of velocity fields ; for case D the effective number of independent frames is lower.
- For case E, there is peak locking affecting the measurements.

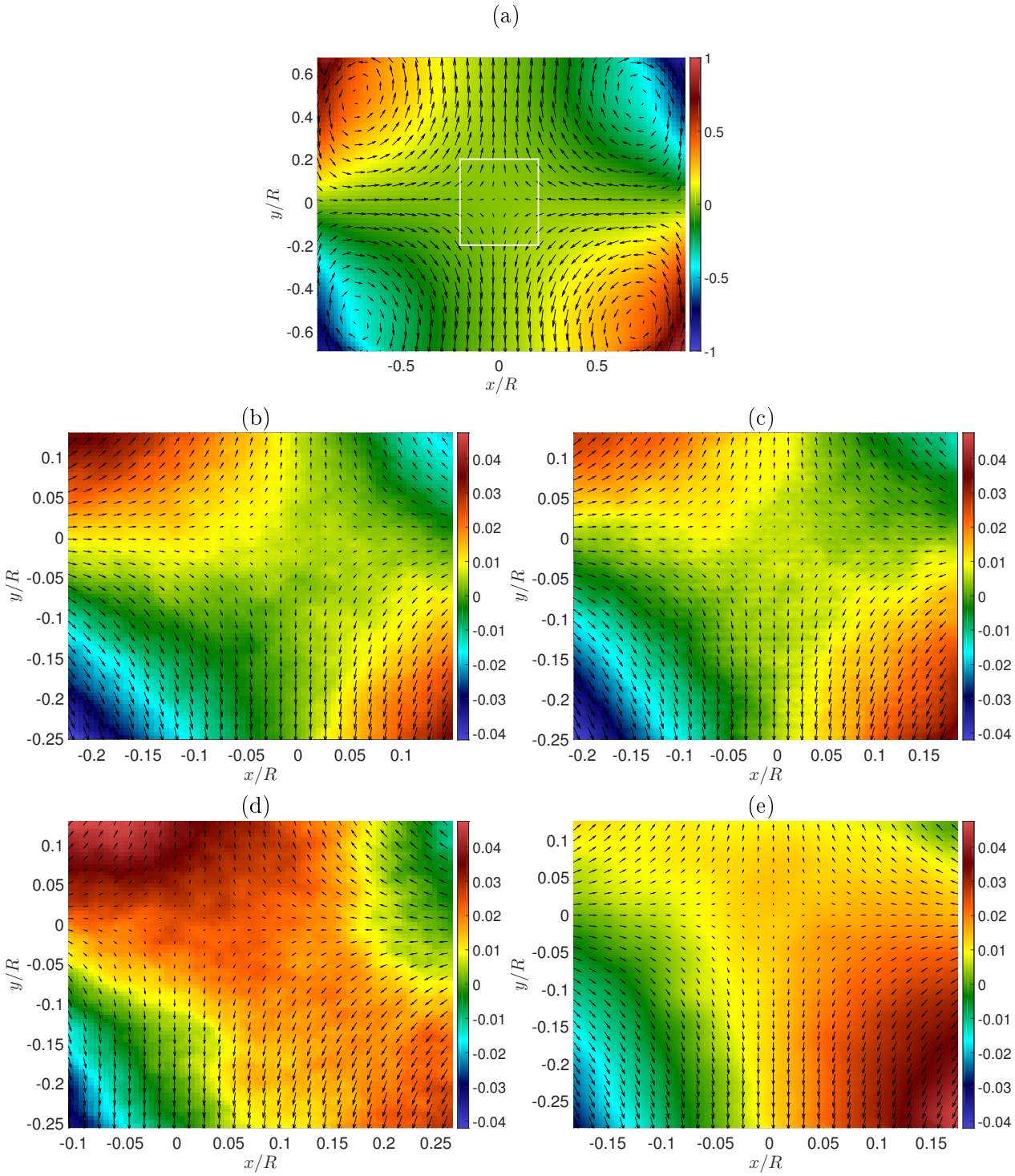

Figure 5.5: Mean flow. The arrows correspond to the in-plane components (u_x and u_y) and the color to the out-of-plane component (u_z) normalized by the reference velocity $2\pi RF$ (R is the tank radius and F the impeller rotation frequency, see chapter 3). (a) Case A. (b) Case B. (c) Case C. (d) Case D. (e) Case E. The white square on (a) corresponds approximately to the measurement area of cases B to E.

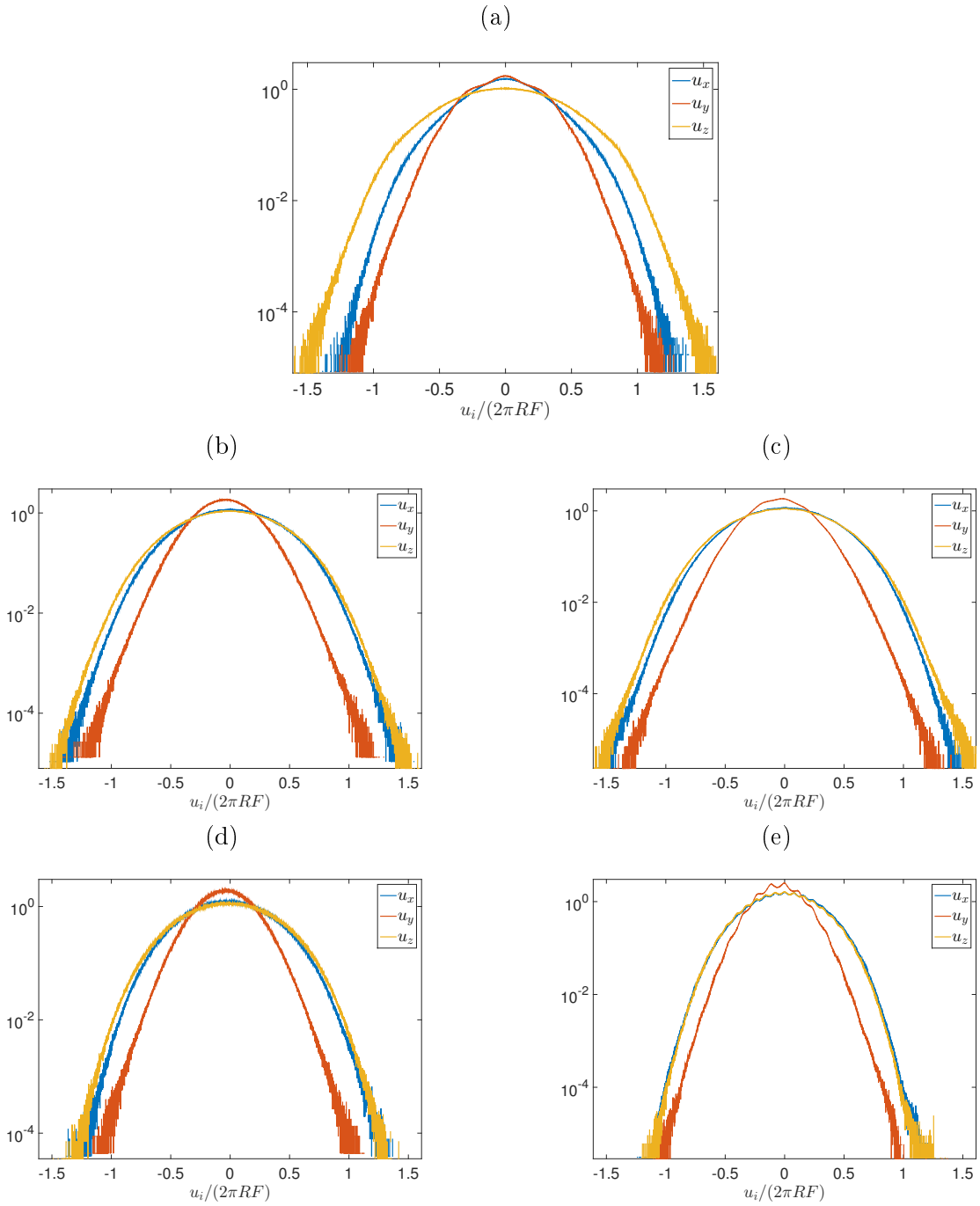

Figure 5.6: Velocity probability density functions (pdfs) of the three velocity components normalized by the reference velocity $2\pi RF$ (R is the tank radius and F the impeller rotation frequency, see chapter 3). The vertical axes correspond to the pdfs, in logarithmic coordinates and the horizontal axes to the velocity component values in linear coordinates. (a) Case A. (b) Case B. (c) Case C. (d) Case D. (e) Case E.

2 3D non-time-resolved data set

The 3D non-time-resolved dataset consists in 6 cases (T1, T2, T3, T4, T5 and T6, T standing for tomographic) of TPIV measurements performed during two measurement campaigns, in January 2017 and in April-May 2018. In all cases, the liquid used was water at T=20°C ; however, the rotation frequency of the impellers was varied in order to vary the Reynolds number from 6000 to 300000 (the Reynolds number of a given case is decreasing with the case number). The campaign of January 2017 was our first campaign of TPIV measurements ; therefore, the acquisition parameters were not optimized. Several cases were acquired but for many of them the quality indicators defined in chapter 4 were not good, and we kept only cases T5 and T6, acquired at a Reynolds number of 6000 with the impellers rotating in the anti and contra direction of rotation respectively. During the campaign of April-May 2018, the acquisition parameters were improved and we acquired cases T1 to T4, at different Reynolds numbers but with the impellers rotating in the anti direction of rotation only. Note that for cases T4 and T5, the flow parameters are exactly the same, only the acquisition parameters (laser, seeding particles, outer tank, field size, magnification) are different. Comparing them then allows to see the impact of these parameters and to check the repeatability of the measurements.

2.1 Flow parameters

Like the 2D-3C data set, cases were acquired at different Reynolds numbers in order to vary the Kolmogorov scale (the Kolmogorov scale is increasing with the case number) and therefore to probe different scale ranges. Cases T1 and T2 allow to probe the inertial range, case T3 allows to probe the transition range between the inertial and dissipative ranges and cases T4 to T6 allow to probe the dissipative range. For case T6, the Kolmogorov scale is slightly larger than cases T4 and T5 because the impellers are rotating in the contra direction of rotation ; therefore the average dissipation rate ϵ is a bit lower.

Case		T1	T2	T3	T4	T5	T6
Campaign		April-May 2018				January 2017	
Rotation frequency (Hz)		5	1	0.5	0.1		
Rotation direction		anti					contra
Normalization velocity V=$2\pi RF$ (m/s)		3.1	0.63	0.31	0.063		
Liquid (water) properties	Temperature (°C)	20					
	Kinematic viscosity (m^2/s)	1.0×10^{-6}					
	Density (kg/m^3)	998					
Reynolds number Re		3.1×10^5	6.3×10^4	3.1×10^4	6.3×10^3		
Taylor Reynolds number R_λ		890	390	250	80	75	100
Kolmogorov length scale η (mm)		0.016	0.054	0.09	0.3		0.4
Kolmogorov time scale τ_k (s)		2.6×10^{-4}	2.9×10^{-3}	8.2×10^{-3}	9.2×10^{-2}		1.6×10^{-1}
Taylor length scale λ (mm)		0.96	2.1	2.8	5.3	5.2	7.9

Table 5.5: Flow parameters for the 2D-3C cases.

The Reynolds numbers of the different cases are given in table 5.5, along with the corresponding

flow parameters. The liquid used was water at 20°C for all cases. The impellers were rotating in the anti direction of rotation for all cases except case T6 (for which it was contra). The fluctuations of frequency (measured by the torquemeters) were of the order of a few percents of the average rotation frequency ; it was even less than one percent for case T1.

2.2 Seeding parameters

The particles used were different in the first and in the second campaign. During the first campaign of January 2017, they were the same as for the 2D-3C data set, i.e. silver-coated glass hollowspheres sold by Dantec, with a diameter of 10 to 30 μm, the average being 15 μm and their density 1.4 g/cm^3. Due to the silver coating, these particles are quite heavy, resulting in more important sedimentation (especially in water) ; and they also scatter a lot of light, generating a strong background and a bad contrast on the images. Therefore, during the second campaign, we tried different, non-silver-coated particles. These particles are borosilicate glass particles sold by LaVision, with a diameter between 9 and 13 μm and a density of 1.1 g/cm^3.

The Stokes number St_{τ_k} based on the Kolmogorov time scale τ_k, the smallest resolved Hölder exponent $h(10)$ and the velocity shift v_g (see chapter 4) are given in table 5.6.

Case	T1	T2	T3	T4	T5	T6
Average particle diameter	10 μm				15 μm	
Particle density	1.1 g/cm^3				1.4 g/cm^3	
Silver coating	no				yes	
St_{τ_k}	2.4×10^{-2}	2.1×10^{-3}	7.5×10^{-4}	6.7×10^{-5}	1.9×10^{-4}	1.1×10^{-4}
$h(10)$	-0.5	-0.8	-1.0	-1.4	-1.0	-1.0
v_g (m/s)	-5.6×10^{-6}				-4.9×10^{-5}	

Table 5.6: Seeding parameters for the SPIV cases T1 to T6.

For all cases, the Stokes number is smaller than 1. Comparing case T1 to case A (2D-3C data set) or case T4 to case T5, we see that the Stokes number is 2 to 3 times smaller with the non-silver coated lighter particles.

The smallest resolved Hölder exponent $h(10)$, i.e. the smallest Hölder exponent such that the typical time scale at the resolved length scale is ten times larger than the seeding particle reponse time, is increasing with the Reynolds number. Indeed, even if the probed scale is higher in terms of the Kolmogorov scale for higher Reynolds number cases, the impeller rotation frequency is higher, so the time scales are smaller and it is more difficult for the seeding particles to follow them.

The velocity shift is negative, because the particles are heavier than the fluid. It is smaller than the average velocity components and even smaller than the root mean squares of the fluctuations of the velocity components (see table 5.9). Therefore, the sedimentation does not affect the velocity measurement. It is also one order of magnitude smaller for the non-silver-coated particles than for the silver-coated particles in water at 20°C ; however it is 3 times larger than for such silver-coated particles in a water-glycerol mixture containing 59% of glycerol in volume (case E of the 2D-3C data set).

2.3 Acquisition

2.3.1 Campaign of January 2017

Laser The laser used is a SpitLight PIV Compact 400 sold by InnoLas and provided by our collaborators of the Laboratoire de Mécanique des Fluides de Lille. It is a Nd:YAG (neodymium:Yttrium-Aluminium-Grenat) laser producing a green light at 532 nm. It has two cavities, each of them having a repetition rate of 10 Hz and delivering a maximum rated energy of 180 mJ. The pulse width is between 4 and 6 ns. The M^2 factor is between 1.5 and 2.

Cameras The cameras used are five Imager sCMOS cameras sold by Lavision and provided by our collaborators of the Laboratoire de Mécanique des Fluides de Lille. These cameras have a CMOS sensor of 2560×2160 pixels of 6.5 μm square. They have a dynamic range of 16 bits and a maximum acquisition frequency of 50 Hz (for full frames). The exposure time of the first frame is 10 μs and the exposure time of the second frame is 20 ms ; the interframing time is 120 ns.
The cameras were mounted on Scheimpflugs designed by our colleagues from Laboratoire de Mécanique des Fluides de Lille. They were equipped with Nikon lenses of focal length 200 mm. The numerical aperture was $f_\# = 22$.

Configuration The spatial arrangement of the cameras and of the laser is shown on figures 5.7, 5.8 and 5.9. The inner cylindrical tank is surrounded by outer tank A described in chapter 3.
The laser beam is first reflected by two dichroic mirrors in order to reach the lenses. It is first expanded in all directions by two spherical lenses forming a telescope, and then expanded only in the vertical direction (y) by two cylindrical lenses. A third dichroic mirror reflects the beam towards a 5 mm-wide slit before it reaches the tanks. It is reflected by a standard mirror so that camera 3, which is in backward scattering with respect to the incoming beam, receives as much light as camera 5, which is in forward scattering. There is a slight angle between the direction of the incident beam and the mirror so that the reflected beam does not come back exactly into the laser, but is deviated towards a beam dumper.
The five cameras are placed in two different planes : cameras 1 and 2 are in a vertical (zy) plane whereas cameras 3, 4 and 5 are in a horizontal (xz) plane. The lines of sight of cameras 1 and 2 are therefore not perpendicular to the walls of the cylindrical tank, which results in astigmatism and distorted particle images.

2.3.2 Campaign of April-May 2018

Laser The laser used is the Solo II PIV laser used for the 2D-3C data set.

Cameras The cameras used were Imager sCMOS cameras, similar to the ones used during the first campaign of January 2017.
They were mounted on Scheimpflugs sold by Lavision and equipped with Zeiss Milvus 2 lenses of focal length 100 mm. The numerical aperture was $f_\# = 11$.

Configuration The spatial arrangement of the cameras and of the laser is shown on figure 5.10. The inner cylindrical tank is surrounded by outer tank B described in chapter 3.
The laser beam is first expanded by a volume optics sold by Lavision and gathering two spherical lenses and a cylindrical one. After this device, the beam is slightly diverging. It is then reflected by three optical mirrors in order to reach the measurement volume, and the edges of the beam are

cut by a slit in order to make the section of the beam rectangular. The beam goes in and out of the outertank by two optical glass windows. It is reflected by an optical mirror in the same manner as for the campaign of January 2017, so that cameras 2 and 3, which are in backward scattering with respect to the incoming beam, receive as much light as cameras 1 and 4, which are in forward scattering.
The five cameras are placed in the same horizontal (xz) plane. The distance between the cameras and the outer tank is around 20 cm. Note that for case T2, one camera did not record all of the pictures for some reason; therefore, we did not use any image of this camera and performed the volume reconstruction with 4 cameras only.

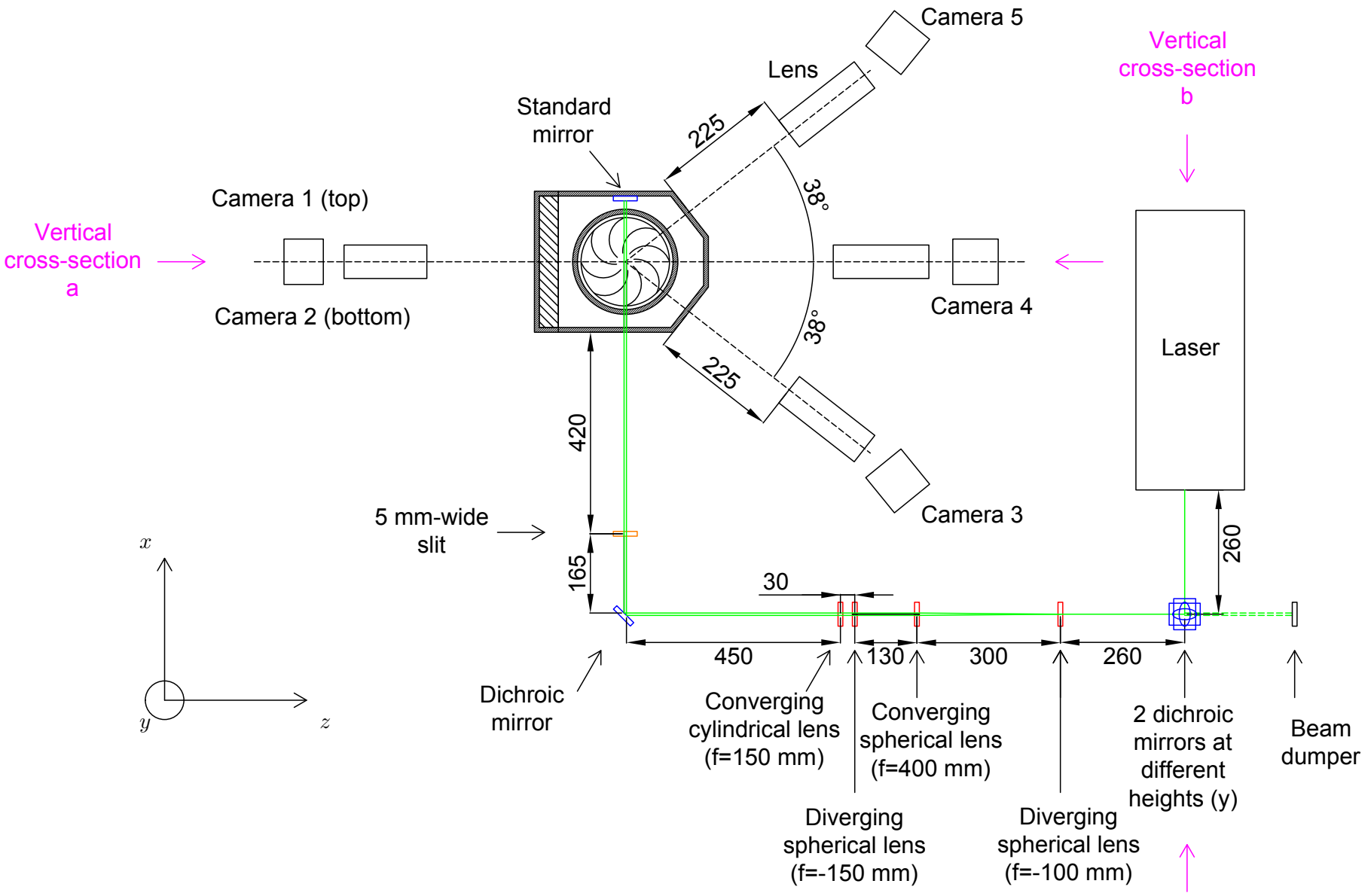

Figure 5.7: Top view of the spatial arrangement of the laser and of the cameras for the campaign of January 2017. The green line corresponds to the laser beam. Mirrors are represented in blue, lenses for the laser beam in red and the slit in orange. Distances are given in mm.

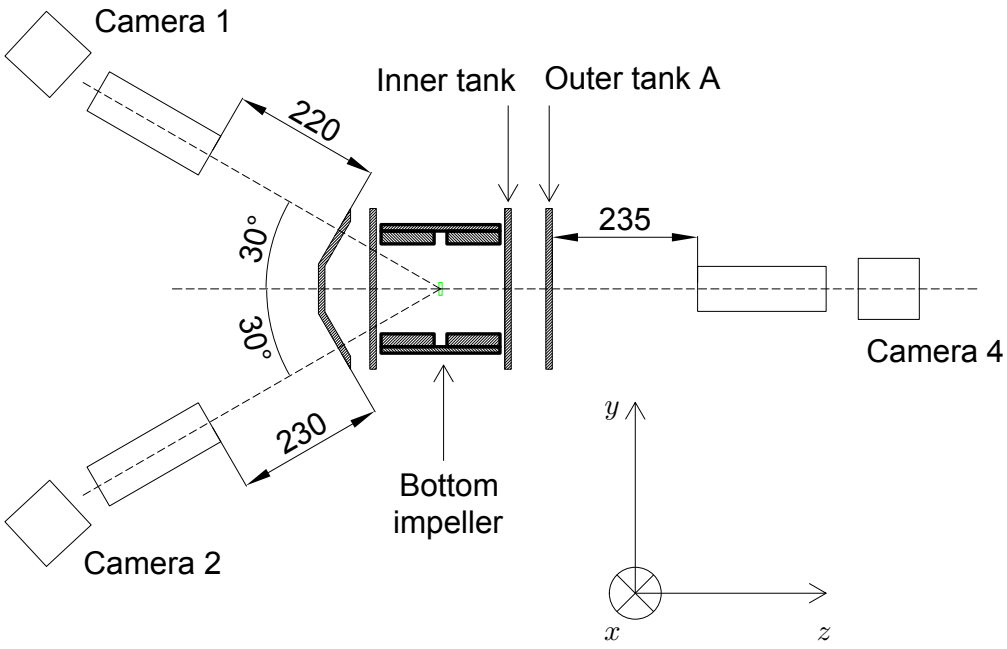

Figure 5.8: Vertical cross-section a of figure 5.7. Distances are given in mm.

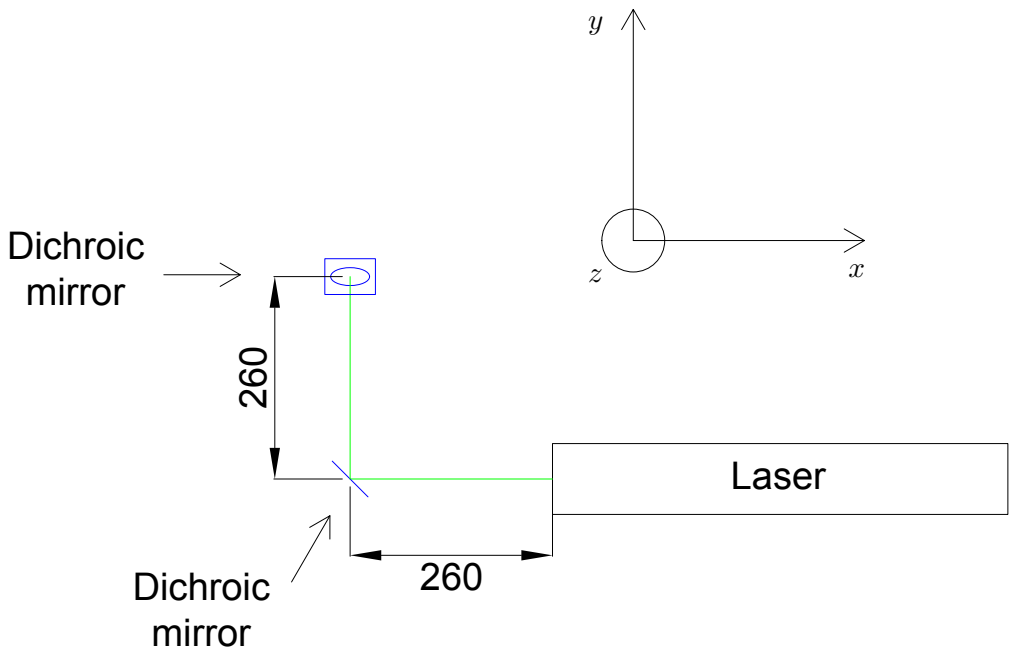

Figure 5.9: Vertical cross-section b of figure 5.7. Mirrors are represented in blue. Distances are given in mm.

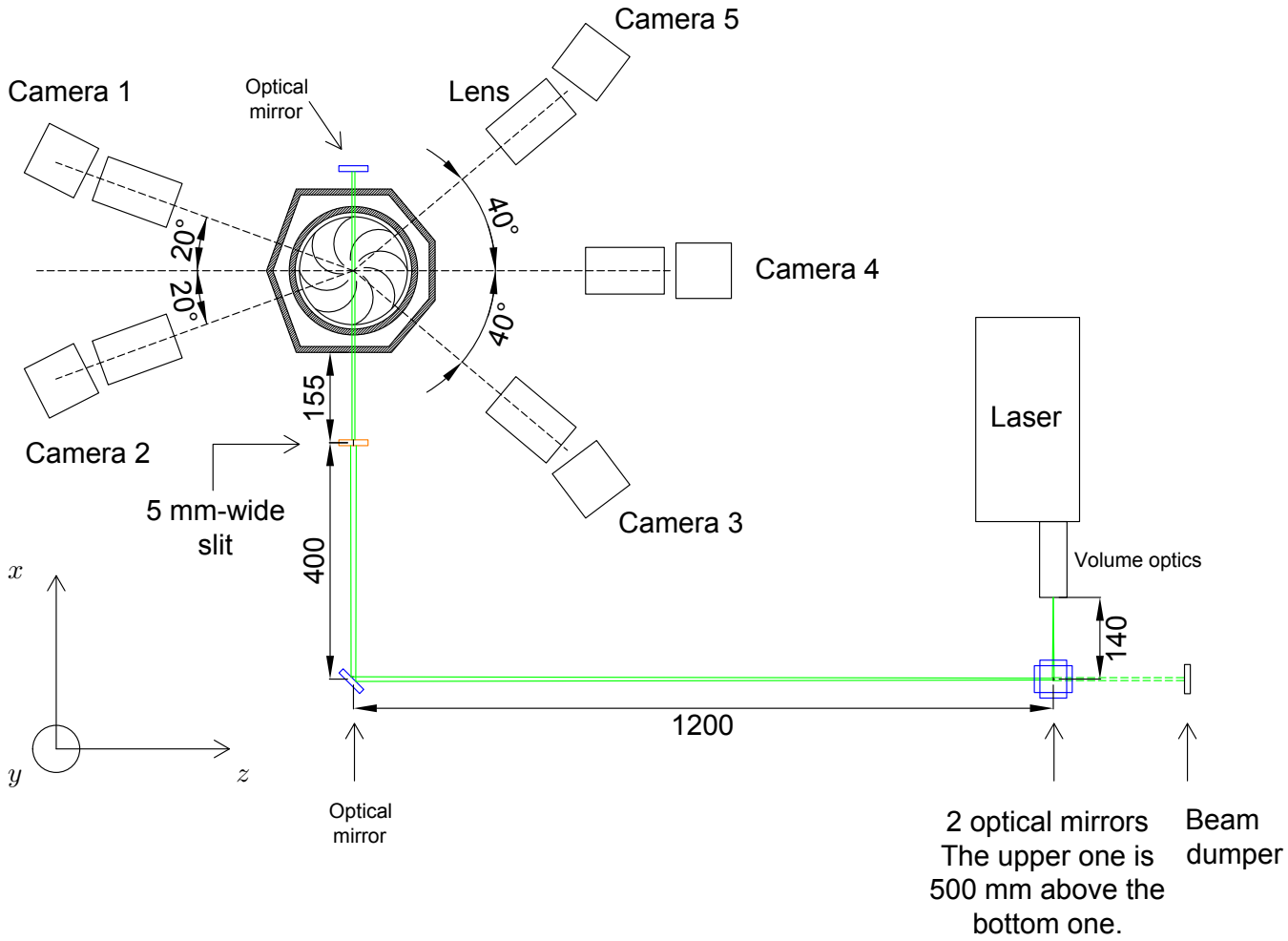

Figure 5.10: Top view of the spatial arrangement of the laser and of the cameras for the non-time-resolved campaign of April-May 2018. The green line corresponds to the laser beam. Mirrors are represented in blue and the slit in orange. Distances are given in mm.

2.3.3 Acquisition parameters

The measurement area is a rectangular volume located at the center of the cylinder. The size in the z direction is smaller because it corresponds to the light beam thickness, and it cannot be too large to ensure an accurate volume reconstruction. For the campaign of January 2017, we tried a very strong magnification, implying a relatively small volume of roughly 2 cm $\times$ 2 cm $\times$ 0.5 cm. However, with such a strong magnification, the particle diffraction spots were too large. Thus, in the campaign of April-May 2018, we used a lower magnification to get a proper particle image diameter. This did not affect significatively the resolution because we could use smaller interrogation volumes ; in addition, it allowed to have a larger field size and more measurement points. Figure 5.11 shows the location and size of the measurement volume for both campaigns. The exact dimensions of the measurement areas, as well as the corresponding magnifications, are given in table 5.7.

This table also gives the number of frames n_t acquired for each case, as well as the acquisition frequency f_{acq} and the space average of the effective number of independent frames (based on the decorrelation of the velocity component along x which is the longer to decorrelate). As already mentioned, the effective number of independent frames is highly fluctuating through space, between one

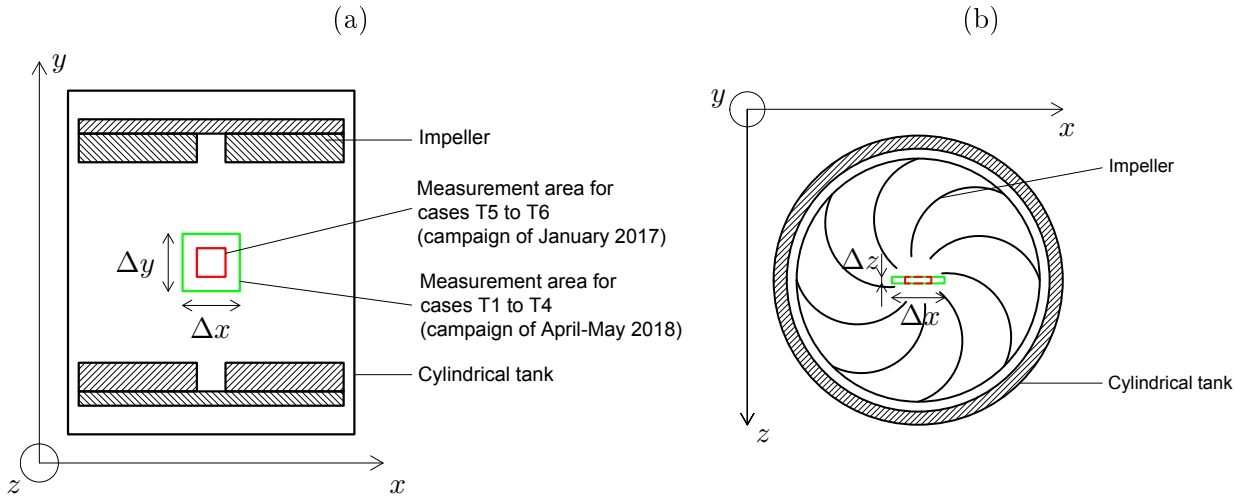

Figure 5.11: Measurement area for cases T1 to T4 (green) and T5 to T6 (red). (a) Vertical cross-section in a meridian plane. (b) Horizontal cross-section in an equatorial plane.

Case		T1	T2	T3	T4	T5	T6
Field size	Δx(cm)	5.2	4.9	5.2	5.2	1.8	1.8
	Δy(cm)	3.6	3.5	3.6	3.5	1.8	1.8
	Δz(cm)	0.67	0.67	0.67	0.67	0.40	0.43
Magnification		0.37				0.75	
Interframing time dt (μs)		100	450	950	6000	3000	3500
Number of frames		10000	10200	10000	30000	20000	18219
Acquisition frequency f_{acq}		5	5	2.5	0.5	5	5
$\langle n_{t,eff,x} \rangle_{x,y,z}$		4800	1600	1300	3800	630	680

Table 5.7: Acquisition parameters for the 3D cases.

half and twice the average value given in the table. Cases T5 and T6 have the lowest $\langle n_{t,eff,x} \rangle_{x,y,z}$; indeed, the acquisition frequency was 5 Hz, which is quite high compared to an impeller rotation frequency of 0.1 Hz. Having noticed that, we chose to reduce the acquisition frequency for the lower Reynolds cases of the campaign of April-May 2018. We thus managed to reach higher effective numbers of independent frames.

The settling of particles does not impact the measured velocity, but results in a decrease of the seeding concentration. Therefore, we had to stir the fluid regularly (every 2000 frame typically, with an impeller rotation frequency of 5 Hz) in order to resuspend the particles. We then waited long enough in order to reach a stationary state back.

2.4 Image preprocessing, calibration and volume reconstruction

For cases T1 to T5 and part of case T6, the image preprocessing only consisted in subtracting the time average of the image, taken over 400 to 2000 images. For case T6, a special image preprocessing consisting in substracting a local average (in an area of 5 pixels square), then normalizing the intensity with a local average (over an area of 300 pixels square), then applying a Gaussian smoothing

(with a kernel of 3 pixels square) and finally applying a sharpening filter was tested on part of the images, without changing significantly the quality of the reconstruction and of the correlation.
The calibration was done in two steps : a first guess was done with a 3D calibration plate with two levels, which was then refined by a few iterations of volume self-calibration using 200 images. For cases T1 to T3, and T5 and T6, the total set of images was splitted in subsets of 2000 images and one self-calibration was done for each subset. For case T4, subsets of 400 images were done and one self-calibration was done for each of them. Table 5.8 gives the average, standard deviation and maximum disparity for each case. The values are quite homogeneous and coherent with what can be found in the literature. The values are smaller for case T2, probably due to the fact that only 4 cameras are used.
Table 5.8 also gives the parameters and quality indicators for the volume reconstruction step. For all cases, 4 MART iterations were used. The ghost ratio is always much smaller than 100%, which is considered in the literature as the maximum acceptable value. The normalized intensity variance is always higher than 20, the minimum recommended value in literature. Note that case T2 has the highest ghost ratio and the smallest normalized intensity variance ; this can be explained by the fact that only 4 cameras were used, instead of 5 for the other cases.

Case		T1	T2	T3	T4	T5	T6
Disparity (pixels)	Average	0.05	0.03	0.04	0.04	0.05	0.07
	Standard deviation	0.03	0.02	0.03	0.03	0.02	0.04
	Maximum	0.3	0.2	0.2	0.2	0.15	0.35
Volume size (voxels)	n_x^{vox}	3204	3204	3260	3140	2713	2530
	n_y^{vox}	2251	2251	2243	2194	2716	2197
	n_z^{vox}	396	396	396	396	509	560
Number of MART iterations		4	4	4	4	4	4
Ghost ratio		5%	10%	5%	6%	7%	4%
Normalized intensity variance		38	35	36	41	39	41

Table 5.8: Volume reconstruction parameters and quality indicators.

2.5 Volume correlation parameters and velocity statistics

Table 5.9 gives the parameters of the volume correlation as well as the main characteristics of the velocity fields for cases T1 to T6.
Cases T1 to T4 have more points than cases T5 and T6 because the interrogation window size is smaller (in pixels). The overlap was 75% for all cases, which is the value recommended by Lavision when using their software (Davis). The interrogation volume size in pixels or in meters is the same for cases T1 to T4, but as the Kolmogorov scale is not the same for these cases, the probed range of scales is different from one case to another, as can be seen on figure 5.12. For cases T1 and T2, the interrogation volume size belongs to the inertial range ; for case T3 it is between the inertial range and the dissipative range and for case T4 it is equal to 4.7 times the Kolmogorov scale. Concerning cases T5 and T6, both have a spatial resolution belonging to the dissipative range ; their interrogation window size is smaller when expressed in units of η because the magnification was larger. It is even smaller for case T6 compared to T5 because for case T6, the impellers are

rotating in contra direction, for which the average dissipation rate is smaller, and the Kolmogorov scale therefore larger.

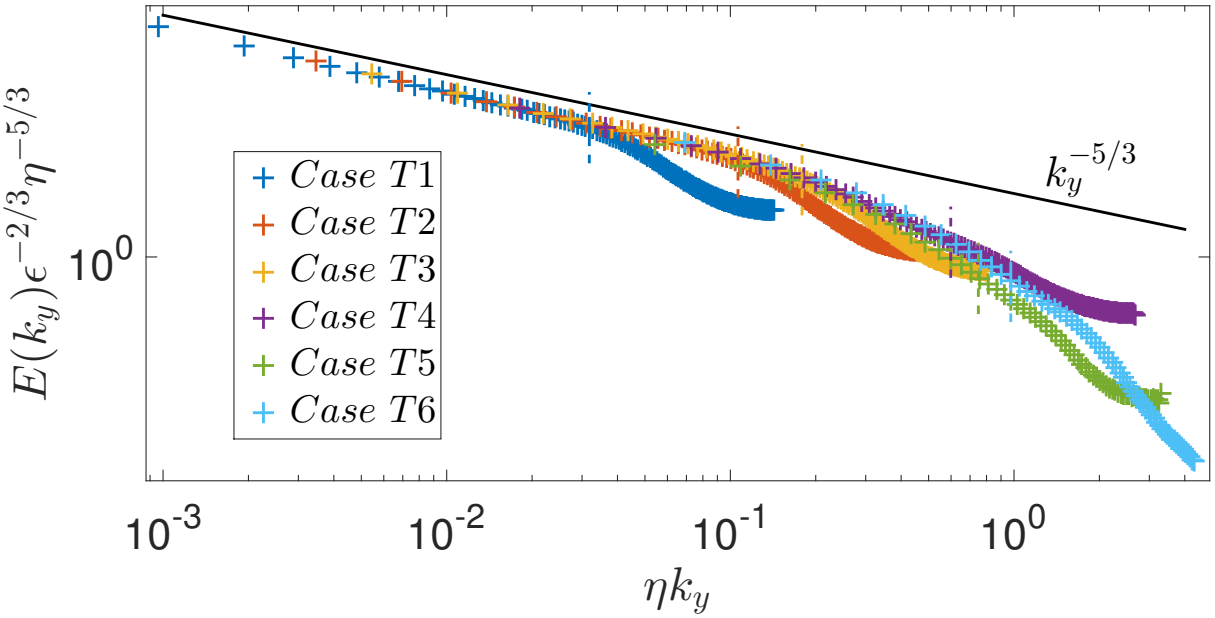

Figure 5.12: 1D Fourier spectrum along the y axis for cases T1 to T6. The vertical dashed lines correspond to the PIV 2 dB cut-off wavenumbers.

Table 5.9 also gives the mean and standard deviation of the correlation value of the volume correlation performed on the images ; the values are high, and higher for the lower Reynolds number cases. As we deal with 3D measurements, an estimation of the uncertainty based on the root mean square of the divergence can be computed, based on the fact that for an incompressible flow the divergence should be zero (see chapter 4). In table 5.9, values were computed based on the square root of the space-time average of the square of the divergence, computed with an order-2 centered scheme. Note that the spatial variations of the square root of the time-average of the square of the divergence are smaller than 10%. For cases T1 to T3, computing such a quantity is not really meaningful as the resolution is above the Kolmogorov scale, so the gradients are not resolved. For case T4, the value is consistent with the maximum disparity. For cases T5 and T6, it is almost five times smaller than for case T4 ; it is of the order of the average disparity and not of the maximum disparity. It is not yet understood why.
Table 5.9 finally gives the values of the space-time averages and the root mean squares of the three velocity components. Values of the space-time averages of the velocity components are of the order of a few percents of the root mean squares, except for case T6 where the velocity component along the y direction is higher than the corresponding space-time average. This is due to the fact that the mixing layer was below the measurement area, probably due to the fact that the top impeller was rotating faster than the bottom one. This can be seen on the average velocity field shown in appendix E. This appendix also shows the average velocity field for cases T1 to T5 ; for these cases the measurement area is not exactly centered on the mixing layer but the mixing layer is contained in the measurement area. The values of the root mean square of the fluctuations are consistent with the values of the 2D-3C data set. Spatial variations of the "root time-mean square" are less than 10% and are not shown there.

Case		T1	T2	T3	T4	T5	T6
Number of points	n_x	149	139	148	149	63	64
	n_y	103	101	103	100	64	65
	n_z	20	20	20	20	15	16
Overlap		75%					
Interrogation volume size	pix	80	80	80	80	128	128
	m	1.4×10^{-3}	1.4×10^{-3}	1.4×10^{-3}	1.4×10^{-3}	1.1×10^{-3}	1.1×10^{-3}
	η	88.0	26.3	15.6	4.7	3.7	2.9
Space step	pix	20	20	20	20	32	32
	m	3.5×10^{-4}	3.5×10^{-4}	3.5×10^{-4}	3.5×10^{-4}	2.8×10^{-4}	2.8×10^{-4}
	η	22.0	6.6	3.9	1.2	0.9	0.7
Correlation value	Average	0.78	0.82	0.89	0.95	0.97	0.96
	std	0.11	0.09	0.07	0.05	0.01	0.02
Uncertainty based on divergence rms	pix	0.65	0.44	0.39	0.27	0.06	0.06
	m/s	1.1×10^{-1}	1.7×10^{-2}	7.2×10^{-3}	8.1×10^{-4}	1.8×10^{-4}	1.4×10^{-4}
	adim	3.7×10^{-2}	2.8×10^{-2}	2.3×10^{-2}	1.3×10^{-2}	2.9×10^{-3}	2.3×10^{-3}
Average of u_x	pix	0.11	0.08	0.11	-0.06	0.15	-0.05
	m/s	2.0×10^{-2}	3.1×10^{-3}	2.0×10^{-3}	-1.7×10^{-4}	4.3×10^{-4}	-1.3×10^{-4}
	adim	6.5×10^{-3}	5.0×10^{-3}	6.3×10^{-3}	-2.7×10^{-3}	6.9×10^{-3}	-2.0×10^{-3}
Average of u_y	pix	-0.16	-0.37	-0.60	0.12	-0.67	4.57
	m/s	-2.8×10^{-2}	-1.5×10^{-2}	-1.1×10^{-2}	3.6×10^{-4}	-2.0×10^{-3}	1.2×10^{-2}
	adim	-8.8×10^{-3}	-2.3×10^{-2}	-3.6×10^{-2}	5.7×10^{-3}	-3.1×10^{-2}	1.8×10^{-1}
Average of u_z	pix	0.19	0.17	0.19	0.13	0.20	0.002
	m/s	3.3×10^{-2}	6.7×10^{-3}	3.6×10^{-3}	3.9×10^{-4}	5.8×10^{-4}	6.1×10^{-6}
	adim	1.0×10^{-2}	1.1×10^{-2}	1.1×10^{-2}	6.2×10^{-3}	9.2×10^{-3}	9.7×10^{-5}
Rms of u_x fluctuations	pix	5.9	5.2	5.4	5.6	5.5	5.7
	m/s	1.0×10^{0}	2.1×10^{-1}	1.0×10^{-1}	1.7×10^{-2}	1.6×10^{-2}	1.4×10^{-2}
	adim	0.33	0.33	0.32	0.27	0.26	0.23
Rms of u_y fluctuations	pix	3.9	3.3	3.4	3.6	3.6	3.7
	m/s	6.9×10^{-1}	1.3×10^{-1}	6.3×10^{-2}	1.1×10^{-2}	1.1×10^{-2}	9.5×10^{-3}
	adim	0.22	0.21	0.20	0.17	0.17	0.15
Rms of u_z fluctuations	pix	6.0	5.2	5.3	5.5	5.5	5.8
	m/s	1.1×10^{0}	2.0×10^{-1}	9.9×10^{-2}	1.6×10^{-2}	1.6×10^{-2}	1.5×10^{-2}
	adim	0.34	0.33	0.31	0.26	0.26	0.23
Rms of total fluctuations	pix	9.2	8.1	8.3	8.7	8.6	9.0
	m/s	1.6×10^{0}	3.2×10^{-1}	1.5×10^{-1}	2.6×10^{-2}	2.5×10^{-2}	2.3×10^{-2}
	adim	0.52	0.51	0.49	0.41	0.40	0.36

Table 5.9: Main parameters of the image correlation and velocity statistics for cases of the 3D non-time-resolved data set.

Figure 5.13 shows the probability density functions of the three velocity components for cases T1 to T6. They are very similar to the pdfs of the 2D-3C data set. One observes a slight peak locking which is more important for lower Reynolds numbers. For case T6, the pdf of the velocity component along y is not centered on 0, in agreement with the larger average value of this component.

Here are the main informations of this section :

- The 3D non-time-resolved data set is made of 6 cases acquired by TPIV in the VK2 set-up. The velocity fields were measured in a thin volume located at the center of the flow.
- The 3D non-time-resolved cases were acquired during two campaigns. Cases T5 and T6 were acquired during the first one for which the acquisition parameters were not optimized.
- The Reynolds number and/or the spatial resolution is varied from a case to another in order to probe different scale ranges. For case T4, the spatial resolution is in the dissipative range. The impellers were rotating in anti direction for all cases but case T6 for which they were rotating in contra direction.
- Each case provides a statistically relevant set of velocity fields ; for cases T5 and T6 the effective number of independent frames is lower though.
- For each case, the volume reconstruction quality is good. The uncertainty on the velocity components (estimated with the rms of the velocity divergence) is between 5 and 10 % of the rms of the fluctuations of the components for case T4 and between 1 and 2 % for cases T5 and T6.

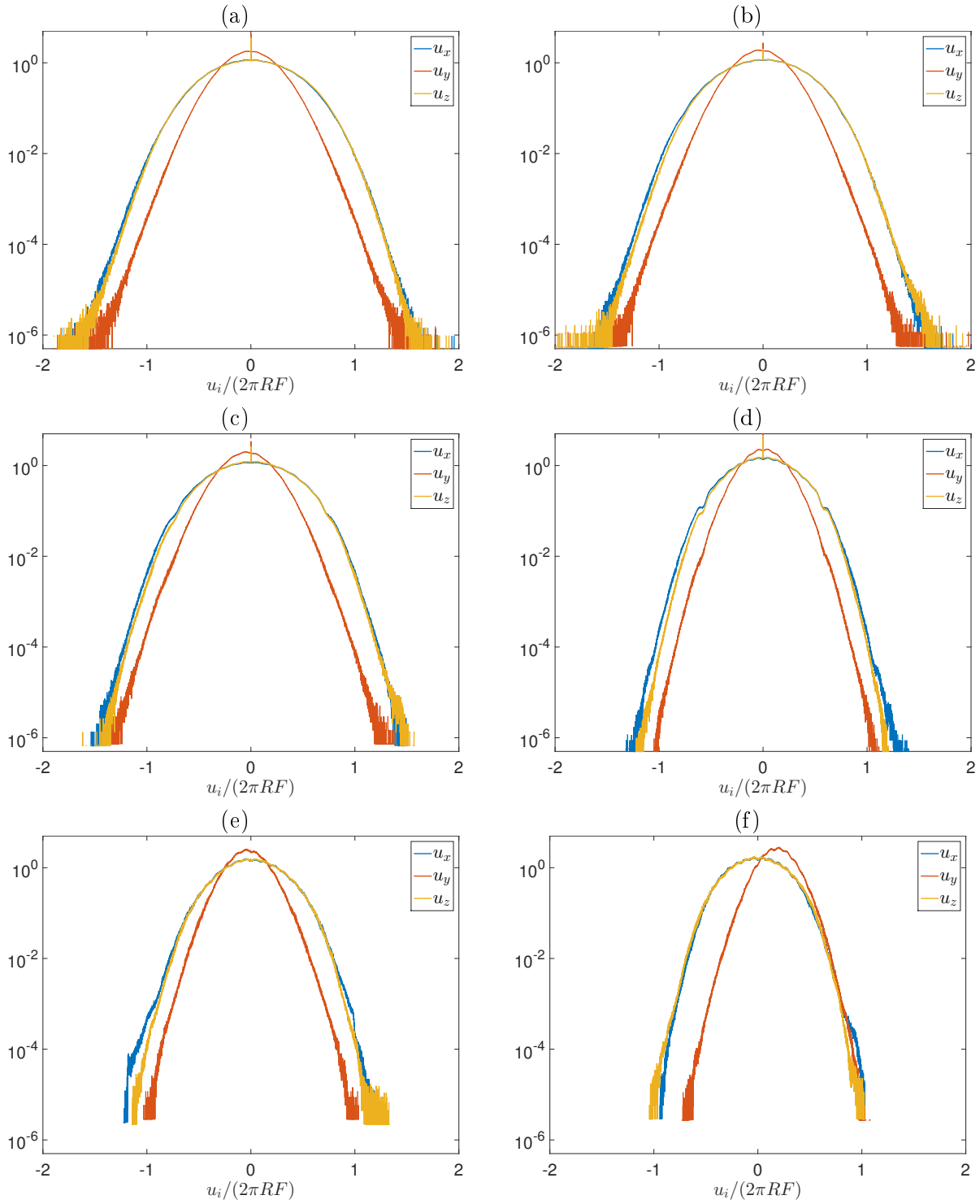

Figure 5.13: Velocity probability density functions (pdfs) of the three velocity components. The vertical axes correspond to the pdfs, in logarithmic coordinates and the horizontal axes to the velocity component values in linear coordinates. (a) Case T1. (b) Case T2. (c) Case T3. (d) Case T4. (e) Case T5. (f) Case T6.

3 3D time-resolved data set

The 3D time-resolved dataset consists in 1 case (T4t, the small t standing for time-resolved) acquired with high-speed laser and cameras during a measurement campaign in May 2018. The liquid used was water at T=20°C ; the rotation frequency of the impellers was 0.1 Hz in order to get a Reynolds number of 6000. Other cases were acquired but not analyzed during this thesis. The flow parameters for case T4t are exactly the same as for case T4 of the non-time-resolved 3D data set (hence the name), but for case T4t the following frames are strongly correlated in time, which allows to study the time-evolution of the velocity field, whereas case T4 is meant to study the statistics of the velocity field.

3.1 Flow parameters

Case T4t was meant to study the time-evolution of the structures on the dissipative range ; hence, the Reynolds number is 6000 in order to get a large enough Kolmogorov scale, of the order of our spatial resolution. The flow parameters are given in table 5.10. The amplitude of the rotation frequency fluctuations was 5% of the average velocity, the standard deviation being 1% of it.

Case		T4t
Rotation frequency (Hz)		0.1
Rotation direction		anti
Normalization velocity V=$2\pi RF$ (m/s)		0.063
Liquid (water) properties	Temperature (°C)	20
	Kinematic viscosity (m^2/s)	1.0×10^{-6}
	Density (kg/m^3)	998
Reynolds number Re		6.3×10^3
Taylor Reynolds number R_λ		80
Kolmogorov length scale η (mm)		0.3
Kolmogorov time scale τ_k (s)		9.2×10^{-2}
Taylor length scale λ (mm)		5.3

Table 5.10: Flow parameters for the 3D time-resolved data set.

3.2 Seeding parameters

The particle used for case T4t are the same as for case T4 ; as the flow parameters are the same, the Stokes number is the same. As the resolution is larger than for case T4, $h(10)$ is slightly lower than for case T4 : $h(10) = -1.6$.

3.3 Acquisition

3.3.1 Laser

The laser used is a Quantronix Darwin Duo provided by our collaborators of the Laboratoire de Mécanique des Fluides de Lille. It is a Nd:YLF (neodymium:Yttrium-Lithium-Fluoride) laser producing a green light at 527 nm. It has two cavities, each of them having a repetition rate between

0.1 and 10 kHz. The energy per cavity is 30 mJ/pulse when the repetition rate is between 0.1 and 1 kHz. It is lower for higher rates ; at 10 kHz the total maximum power is 100 W. The pulse width is smaller than 210 ns. The M^2 factor is smaller than 25.
The energy of the two output beams is tuned by playing on the polarization of the beams in order to get the desired energy and to have the same energy for both pulses. Usually, a Pockels cell is used to modify the polarization of one of the beam so that both beams have the same. However, in this case a $\lambda/2$ polarizer is used instead. It divides by two the wavelength but gives the same polarization to the two beams. Playing on the polarization with the $\lambda/2$ polarizer also allows to get better pictures as it was noticed that PMMA was better transmitting particular polarizations (for some unknown reason). Furthermore, playing on the polarization allows to avoid the light scattered by dusts smaller than the seeding particles, because smaller objects select a polarization due to their smaller size whereas larger ones have a more isotropic scattering.

3.3.2 Cameras

The cameras used are four Phantom Miro m340 provided by our collaborators of the Laboratoire de Mécanique des Fluides de Lille. These cameras have a CMOS sensor of 2560×1600 pixels of 10 μm square. They have a dynamic range of 12 bits, a minimum exposure time of 1 μs and a maximum acquisition frequency at full frame of 800 Hz. They can acquire at a rate of 4 kHz but only 512×512 pixels are then used ; for such small images, it is difficult to do the calibration with our current 3D calibration plate whose dots are too far from each other for such a small field (at the chosen magnification). For case T4t, the sensor size was 1600×1600 pixels. As these cameras have a memory of 38.5 Go, up to 3226 images can be acquired in a row for this sensor size. The exposure time for case T4t is 4997 μs and the interframing time is 3 μs.
The cameras were mounted on Scheimpflugs designed by our colleagues from Laboratoire de Mécanique des Fluides de Lille (the same as for the measurement campaign of January 2017). They were equipped with Nikon Macro lenses of focal length 105 mm. The numerical aperture was $f_{\#} = 11$.

3.3.3 Configuration

The spatial arrangement of the cameras and of the laser is shown on figure 5.14. The inner cylindrical tank is surrounded by outer tank B described in chapter 3, as for the campaign of April-May 2018 (cases T1 to T4).
After the $\lambda/2$ polarizer, the laser beam is reflected by two dichroic mirrors which raise it up to the level of the lenses and of the measurement volume. The distance between the output of the laser and the first lens is 1.11 m. The first lens is a converging spherical lens located at its focal distance of the beam waist (the natural divergence of the beam is used, so no diverging spherical lens is used). The beam is then expanded in the vertical (y) direction by a diverging cylindrical lens, before being cut by a first slit of height Δy =35 mm. The beam is then converged by a converging cylindrical lens ; right after it, the beam height is 42 mm. The beam is then reflected by a dichroic mirror and crosses a second slit of width Δz =5 mm, before entering the outer tank through an anti-reflective glass window. After having crossed the inner cylindrical tank, the beam gets out of outer tank B by another anti-reflective glass and is reflected by a dichroic mirror so that cameras 2 and 3, which are in backward scattering with respect to the incoming beam, receive as much light as cameras 1 and 4, which are in forward scattering. There is a slight angle between the direction of the incident beam and the mirror so that the reflected beam does not come back exactly into the laser, but is deviated towards a beam dumper.

The distance between the cameras and the outer tank is 22.5 cm.

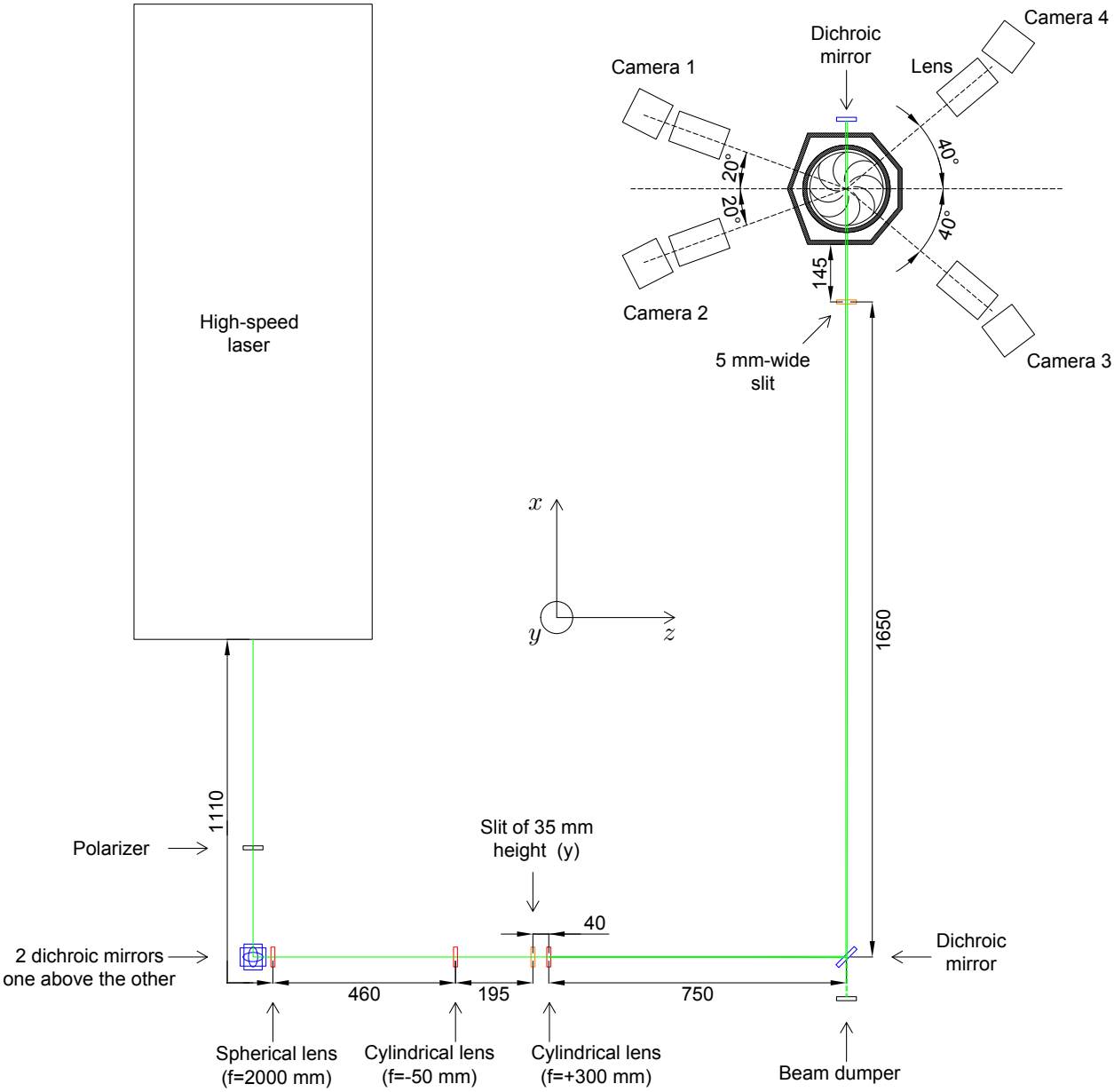

Figure 5.14: Top view of the spatial arrangement of the laser and of the cameras for the time-resolved measurement campaign of May 2018. The green line corresponds to the laser beam. Mirrors are represented in blue, lenses for the laser beam in red and the slit in orange. Distances are given in mm.

3.3.4 Acquisition parameters

The measurement area is a rectangular volume centered on the center of the cylinder, it is almost the same as case for T4 (see figure 5.11). The exact dimensions of the measurement area, as well as the corresponding magnification, are given in table 5.11. With the fast cameras used, the images are stored in the camera memory and then transferred to the computer. The number of correlated

images that one can acquire is then limited by the camera memory. For case T4t, we acquired the images by sets (called "runs") of 3226 images (allowing to compute 3225 velocity fields or frames). The images of one run are correlated between them, but the images of different runs are not. It takes about half a run for the velocity field to decorrelate, hence an effective number of independent frames of the order of twice the number of runs. Compared to case T4, the velocity fields are thinner.

Case		T4t
Field size	Δx(cm)	4.1
	Δy(cm)	3.8
	Δz(cm)	0.42
Magnification		0.39
Acquisition frequency f_{acq} (Hz)		200
$1/f_{acq}$	μs	5000
	τ_k	0.05
Number of runs		40
Number of images per run		3226
Total number of frames		129000
$\langle n_{t,eff,x} \rangle_{x,y,z}$		110

Table 5.11: Acquisition parameters for the time-resolved 3D data set.

3.4 Image preprocessing, calibration and volume reconstruction

For case T4t, the image preprocessing only consisted in computing the time average of the images for each run and subtracting it to the images of the corresponding run.
The calibration was done in two steps : a first guess was done with a 3D calibration plate with two levels, which was then refined by a few iterations of volume self-calibration using 200 images. One self-calibration was done for each run. Table 5.12 gives the average, standard deviation and maximum disparity for case T4t. They are comparable to those for case T4, but slightly lower. Table 5.12 also gives the parameters and quality indicators for the volume reconstruction step. 4 MART iterations were used. The ghost ratio and the normalized intensity variance are both correct ; they are slightly worse than for case T4. This can be explained by the fact that one more camera is used for case T4.

3.5 Volume correlation parameters and velocity statistics

Table 5.13 gives the parameters of the volume correlation as well as the main characteristics of the velocity fields for case T4t. The velocity fields of this case have less points than for case T4 because the fast cameras have less pixels than the slow ones. The overlap is 75%, as for cases T1 to T4. The interrogation volume size in pixels is the same as for case T4, but the interrogation volume size in meters is slightly larger than for case T4 because the pixels of the fast cameras are larger than for case T4. However, it is still in the dissipative range. The mean and standard deviation of the correlation value for case T4t are similar to those for case T4. The estimation of the uncertainty based on the rms of the divergence is lower than for case T4.

Case		T4t
Disparity (pixels)	Average	0.03
	Standard deviation	0.02
	Maximum	0.2
Volume size (voxels)	n_x^{vox}	1678
	n_y^{vox}	1641
	n_z^{vox}	207
Number of MART iterations		4
Ghost ratio		8%
Normalized intensity variance		28

Table 5.12: Volume reconstruction parameters and quality indicators for case T4t.

Table 5.13 also gives the values of the space-time averages and the root mean squares of the fluctuations of the three velocity components. Values of the space-time average are different but this is probably a problem of convergence as there are less independent frames for case T4t. However, the values of the rms are coherent. The pdfs of the velocity components for case T4t are shown on figure 5.15. They are very similar to those of case T4. A slight peak locking can also be seen.

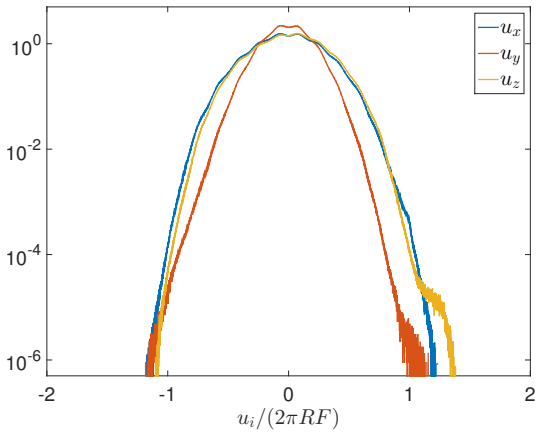

Figure 5.15: Velocity probability density functions (pdfs) of the three velocity components for case T4t. The vertical axes correspond to the pdfs, in logarithmic coordinates and the horizontal axes to the velocity component values in linear coordinates. .

Here is the main information of this section :

- Case T4t is the counterpart of case T4 with correlated frames. It therefore allows to study the time-evolution of the velocity fields with resolved dissipative scales.

Case		T4t
Number of points	n_x	79
	n_y	73
	n_z	9
Overlap		75%
Interrogation volume size	pix	80
	m	2.1×10^{-3}
	η	6.9
Space step	pix	20
	m	5.2×10^{-4}
	η	1.7
Correlation value	Average	0.93
	std	0.03
Uncertainty based on divergence rms	pix	0.08
	m/s	4.1×10^{-4}
	adim	6.5×10^{-3}
Average of u_x	pix	-0.15
	m/s	-7.7×10^{-4}
	adim	-1.2×10^{-2}
Average of u_y	pix	-0.12
	m/s	-6.3×10^{-4}
	adim	-1.0×10^{-2}
Average of u_z	pix	0.14
	m/s	7.5×10^{-4}
	adim	1.2×10^{-2}
Rms of u_x fluctuations	pix	3.1
	m/s	1.6×10^{-2}
	adim	0.26
Rms of u_y fluctuations	pix	2.2
	m/s	1.2×10^{-2}
	adim	0.18
Rms of u_z fluctuations	pix	3.1
	m/s	1.6×10^{-2}
	adim	0.26
Rms of total fluctuations	pix	4.9
	m/s	2.6×10^{-2}
	adim	0.41

Table 5.13: Main parameters of the image correlation and velocity statistics for case T4t.

Part III

Results

Chapter 6

Statistics of the inter-scale energy transfer and viscous dissipation terms

The aim of this thesis is to characterize the extreme events of the Duchon-Robert term Π^ℓ_{DR}, interpreted as extreme events of energy transfer term through scales and which may be prints of the singularities possibly developed by the 3D Euler or Navier-Stokes incompressible equations. In this chapter, we characterize the amplitude of the extreme events of Π^ℓ_{DR} in different scale ranges, by comparing them to the average behaviour of Π^ℓ_{DR}, by analyzing the distribution of this term and by comparing its statistics to the ones of the viscous dissipation term $\mathscr{D}^\ell_\nu$. We also show that using the pair (Π^ℓ_{LES}, $\mathscr{D}^\ell_{\nu,LES}$) instead of ($\Pi^\ell_{DR}$, $\mathscr{D}^\ell_\nu$) leads to overall similar results, though some discrepancies reveal that they have slightly different physical meanings.

1 Global behaviour of Π^ℓ_{DR} and $\mathscr{D}^\ell_\nu$ with respect to scales

Before analyzing the extreme values of the Duchon-Robert term Π^ℓ_{DR}, we studied the average values and the standard deviation of this term and their behaviour with respect to scales.

1.1 Space-time average

The space-time averages of the Duchon-Robert term Π^ℓ_{DR} and of the viscous dissipation term $\mathscr{D}^\ell_\nu$, normalized by the global dissipation rate ϵ (computed from measurements of the rotation frequency and of the torque applied on the impellers) are plotted on figure 6.1 for cases T1 to T5. They are plotted as a function of the scale ℓ_c defined in chapter 2, normalized by the Kolmogorov scale η. The average of Π^ℓ_{DR} is plotted in blue and the average of $\mathscr{D}^\ell_\nu$ is plotted in red. The different cases can be distinguished by different symbols ; also, they correspond to different ranges of ℓ_c/η : therefore, the curves corresponding to the highest Reynolds number case (T1) are at the right and the ones corresponding to the lowest Reynolds number cases (T4 and T5) are at the left.
Overall, the space-time average of the Duchon-Robert term is increasing with the ratio ℓ_c/η whereas the viscous dissipation is decreasing with it ; both terms are equal for $\ell_c \approx 20\eta$. For cases T4 and T5, the viscous dissipation is much larger than the Duchon-Robert term whereas for case T1 it is the contrary : this confirms that cases T4 and T5 allow to study the dissipative range whereas case T1 corresponds to the inertial range ; cases T2 and T3 are in-between.
It can be noticed that the curves corresponding to cases T2 and T3 do not overlap, and more generally that the different curves corresponding to either Π^ℓ_{DR} or $\mathscr{D}^\ell_\nu$ cannot be connected smoothly. It is especially striking for the Duchon-Robert term, but it is also true for the viscous dissipation

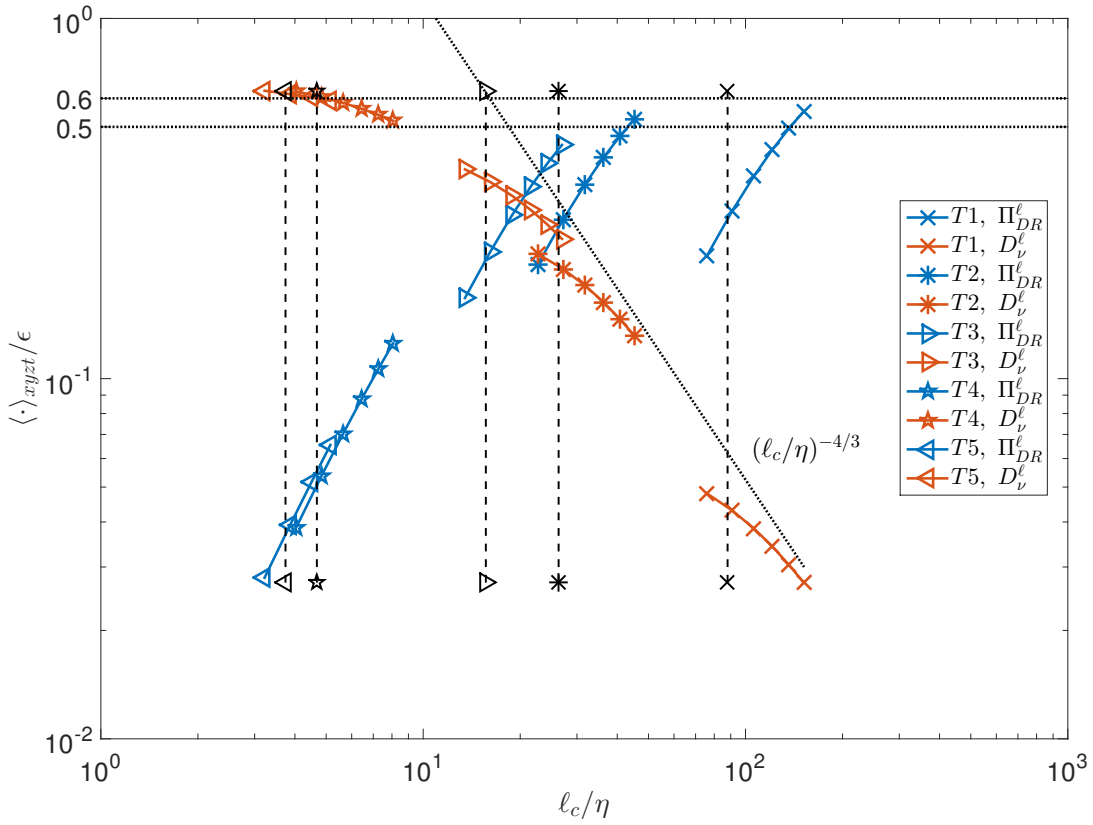

Figure 6.1: Space-time average of Π^ℓ_{DR} and $\mathscr{D}^\ell_\nu$ terms wrt. scales. The curves corresponding to Π^ℓ_{DR} are plotted in blue whereas those corresponding to $\mathscr{D}^\ell_\nu$ are plotted in red. The vertical dashed lines correspond to the values of the interrogation volume size. ϵ is the average dissipation rate computed from torque measurements. η is the Kolmogorov scale.

whose curves feature a kind of saturation at low values. This is probably due to the filtering inherent to PIV discussed in chapter 2 : when ℓ_c is too close to the interrogation volume size (which is represented by a vertical dashed line for each case), the UV locality principle does not hold because most of the scales contributing to Π^ℓ_{DR} or $\mathscr{D}^\ell_\nu$ have been filtered. The values of Π^ℓ_{DR} and $\mathscr{D}^\ell_\nu$ are therefore significantly decreased. The effect is stronger for the Duchon-Robert term which involves the velocity increments to the cube whereas the viscous dissipation term only involves the velocity increments to the square. According to this reasoning, one should consider only the rightmost point of each curve, or the two rightmost points, for which there are enough contributions from the smaller scales. Also, one should not compare the first rightmost point to the second one in a same curve as they correspond to a different filtering. For cases T1 to T4, the first (resp. second) rightmost point of a given curve should be compared to the first (resp. second) rightmost points of the other curves ; indeed, the acquisition (except for the interframing time dt), correlation and processing parameters were exactly the same for these four cases ; therefore, the differences between those points are only due to physical effects and not to measurement nor processing. As case T5 was acquired and processed in different conditions, the comparison is more difficult. We can see that the curves corresponding to cases T4 and T5 almost overlap (both for Π^ℓ_{DR} and $\mathscr{D}^\ell_\nu$), but is it is difficult to interpret, as the acquisition and processing parameters are different.

In the following, we will present only results (pdfs, joint pdfs, extremes) corresponding to the rightmost points of the curves corresponding to cases T1 to T4. Indeed, these points correspond to the lowest impact of PIV filtering and to the same acquisition and processing parameters from one case to another. Differences are then only due to the physics, and the comparison is therefore meaningful. For these rightmost points, ℓ_c is equal to 1.7 times the interrogation window size. For case T4, $\ell_c/\eta = 8$; for case T3, $\ell_c/\eta = 27$; for case T2, $\ell_c/\eta = 45$ and for case T1, $\ell_c/\eta = 150$.

When considering only the rightmost point of each curve, it can be seen that the space-time average of the viscous dissipation term follows fairly well a power law of exponent $-4/3$ for $\ell_c > 30\eta$. This is the scaling for the inertial range that can be derived from the theory of Kolmogorov of 1941. For lower scales, it seems to saturate at a value higher than 0.5ϵ. This saturation is in agreement with a regularization of the velocity field by the viscous effects and with increments δu_ℓ over a distance ℓ scaling like ℓ. However, the saturation value can hardly be estimated here as we do not have enough points to see the saturation plateau (the leftmost points are too affected by PIV filtering). Note that here, ϵ is the global dissipation rate corresponding to the power dissipated in the whole von Kármán flow. It is probably different from the local dissipation rate corresponding to the measurement area and which is the theoretical limit of $\mathscr{D}^\ell_\nu$ when ℓ_c/η tends to 0. Note that using either ϵ or the saturation value of $\mathscr{D}^\ell_\nu$ does not affect much the value of the Kolmogorov scale which depends on the dissipation to the power -1/4 only : a dissipation twice smaller would generate a Kolmogorov scale 1.2 times larger. The Duchon-Robert term which corresponds to non-linear effects and which can be interpreted as inter-scale transfer seems to saturate for $\ell_c > 50\eta$. Such a saturation corresponds to the 1941 Kolmogorov scaling in the inertial range. Again, it is difficult to estimate accurately the saturation value but it is consistent with the viscous dissipation saturation value in the dissipative range. In this dissipative range, the curve of the space-time average of the Duchon-Robert term is steeper. The expected scaling corresponding to a regularized velocity field is ℓ^2 ; however, we do not have enough data points to really see it. The curve corresponding to case T4 seems to be increasing as ℓ^2 but it is not due to physical effects only : the PIV filtering effect is also involved so it cannot be concluded that the Duchon-Robert term is actually scaling like ℓ^2 in the dissipative range.

The influence of the forcing on the space-time average of the Duchon-Robert term and of the viscous dissipation can be studied based on figure 6.2 (for the dissipative range only). On this figure, the space-time averages of these terms have been plotted for cases T4 and T5 again, and for case T6. They are normalized by the space-time average of the viscous dissipation term obtained at the smallest possible scale, which is the closest value to the exact viscous dissipation. Such a normalization is better to compare the ANTI and CONTRA cases, compared to the normalization involving the global dissipation rate estimated from torque measurements : indeed, the dissipation rate is a priori not homogeneous and its spatial distribution is not a priori the same for ANTI or CONTRA directions. For cases T4 and T5, the impellers are rotating in the ANTI direction of rotation whereas for case T6 they are rotating in the CONTRA direction ; the rotation frequency is the same for the three cases. The acquisition and correlation parameters for cases T5 and T6 are exactly the same. As the average dissipation rate is lower for the CONTRA direction compared to the ANTI direction, the Kolmogorov scale is larger and smaller ratios of ℓ_c/η can be studied. No difference can be seen on figure 6.2. One could have perhaps expected that curves corresponding to cases T5 and T6 would not overlap due to the same PIV filtering effect which prevents curves of cases T2 and T3 from overlapping. This effect is probably mitigated by the normalization by a value which is itself filtered.

As a conclusion, we confirmed that our different cases allow to study scales from the dissipative range to the inertial one. The space-time averages of the Duchon-Robert term and of the viscous

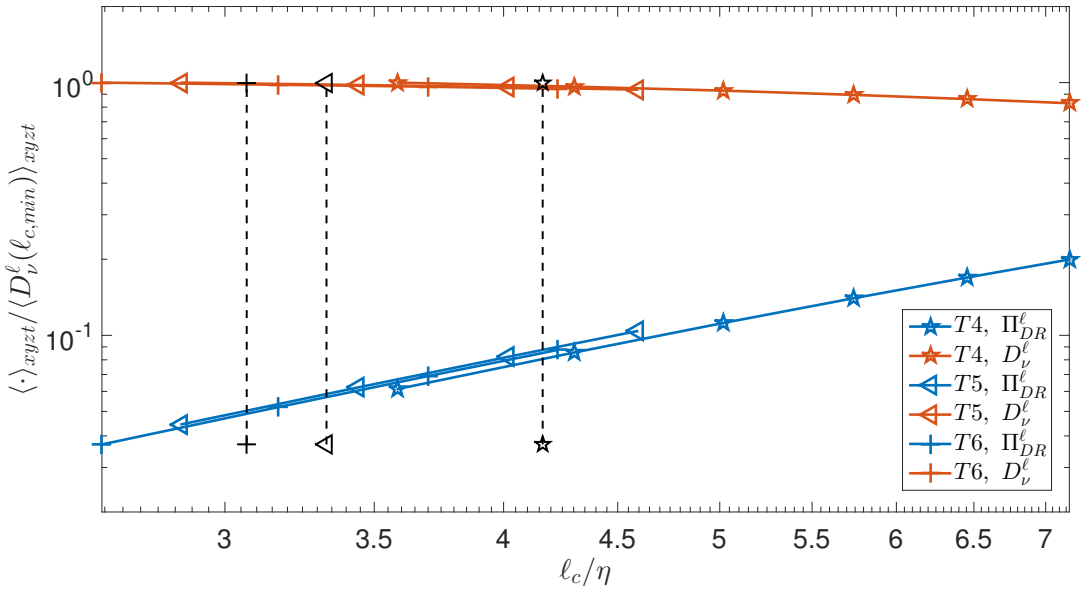

Figure 6.2: Space-time average of Π_{DR}^ℓ and $\mathscr{D}_\nu^\ell$ terms wrt. scales for different directions of rotation. The curves corresponding to Π_{DR}^ℓ are plotted in blue whereas those corresponding to $\mathscr{D}_\nu^\ell$ are plotted in red. The vertical dashed lines correspond to the values of the interrogation volume size. For cases T4 and T5, the impellers are rotating in the ANTI direction whereas for case T6 they are rotating in the CONTRA direction. $D_\nu^\ell(\ell_{c,min})$ is the viscous dissipation term computed at the smallest value of ℓ_c.

dissipation show a behaviour very close to the classical cascade picture (see chapter 1) and to Kolmogorov 1941 theory : in the dissipative range, the inter-scale transfer is increasing with scales but remains much smaller than the viscous dissipation which is quite constant. In the inertial range, the inter-scale transfer is constant and the viscous dissipation is fairly well decreasing like $\ell^{-4/3}$. The forcing does not seem to impact the ratio between the space-time averages of Π_{DR}^ℓ and $\mathscr{D}_\nu^\ell$.

1.2 Standard deviation (computed over space and time)

We now analyze the behaviour of the standard deviation, computed over space and time, of the Duchon-Robert and viscous dissipation terms. This allows to quantify the dispersion of these two terms.

Figure 6.3 shows the standard deviations, computed over space and time, for cases T1 to T5. The global behaviour with respect to scale is the same as for the space-time averages : Π_{DR}^ℓ is increasing and saturating at the largest values, whereas $\mathscr{D}_\nu^\ell$ seems to saturate at the lowest values and then decreases, roughly following the $(\ell_c/\eta)^{-4/3}$ scaling. However, the saturation value of Π_{DR}^ℓ at large ℓ_c/η is around three times the saturation value of $\mathscr{D}_\nu^\ell$ at low ℓ_c/η. Also, the standard deviations of the Duchon-Robert term are three to four times higher than its space-time averages whereas the standard deviation of the viscous dissipation term are of the same order as its space-time averages. The impact of filtering seems to be weaker for the standard deviations than for the space-time averages. We do not understand why. On the contrary, there is a more pronounced difference between the standard deviation of the Duchon-Robert term of cases T4 and T5. For a given value of ℓ_c/η, the distribution of the Duchon-Robert term will be more spread for case T4 than for case T5. This may be due to different acquisition or correlation parameters, or to a lack of statistics for case T5. This shows that one should be careful while comparing such a quantity as the Duchon-Robert

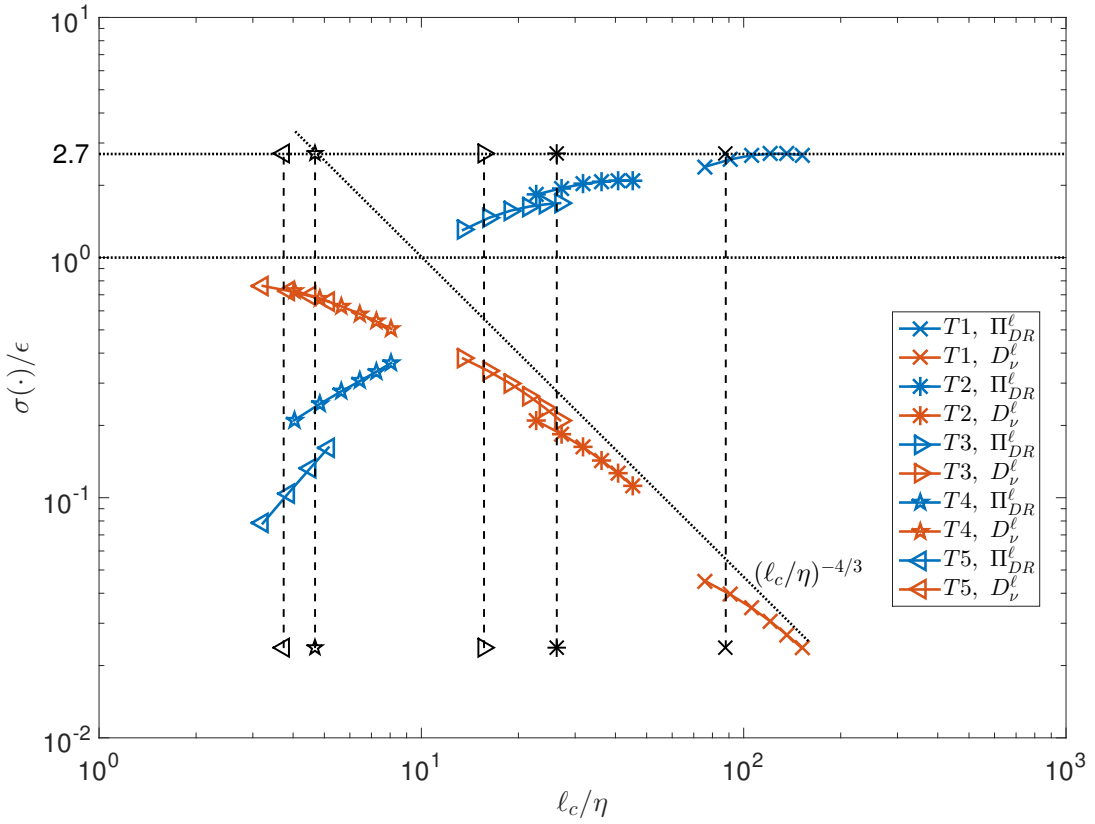

Figure 6.3: Standard deviation (computed over space and time) of Π^ℓ_{DR} and $\mathscr{D}^\ell_\nu$ terms wrt. scales. The curves corresponding to Π^ℓ_{DR} are plotted in blue and those corresponding to $\mathscr{D}^\ell_\nu$ are plotted in red. The vertical dashed lines correspond to the values of the interrogation volume size. ϵ is the average dissipation rate computed from torque measurements.

term for cases obtained in different conditions. The standard deviation of the viscous dissipation of cases T4 and T5 still agrees ; this is perhaps due to the fact that it is a smaller order quantity that converges faster.

Again, the impact of the forcing can be studied (in the dissipative range only) by comparing the standard deviations of the Duchon-Robert term and of the viscous dissipation of cases T4 to T6. The standard deviations are normalized by the space-time average of the viscous dissipation term obtained at the lowest scale as it is the closest to the real dissipation rate. No difference can be noted between the two directions of rotation.

As a conclusion, the behaviour of the standard deviations (computed over space and time) with respect to scales is similar to the one of the space-time averages. The standard deviation of the viscous dissipation is of the same order as its space-time average whereas the standard deviation of the Duchon-Robert term is three to four times higher than its space-time average.

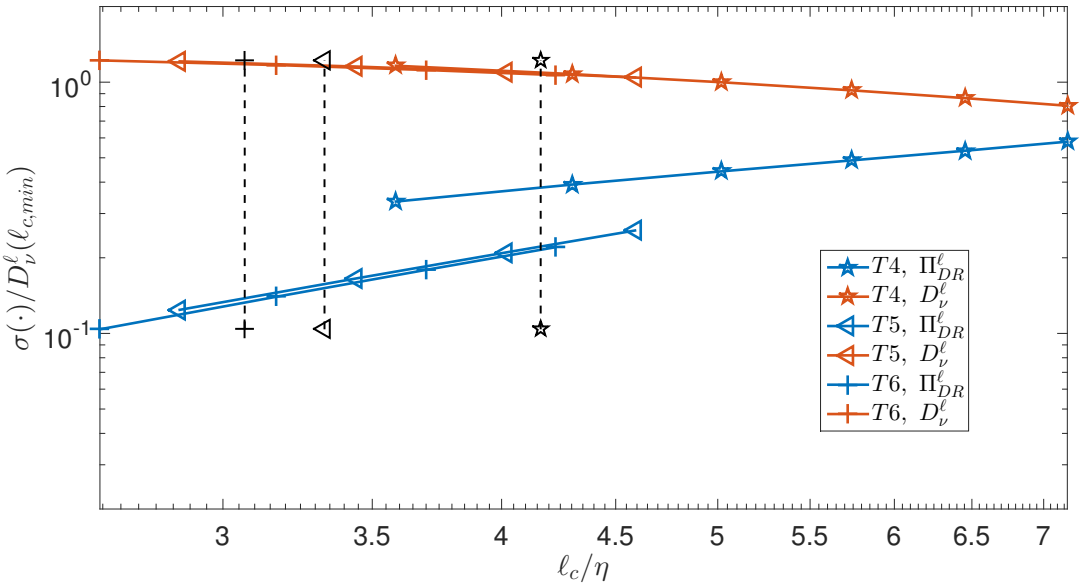

Figure 6.4: Standard deviation (computed over space and time) of Π_{DR}^ℓ and $\mathscr{D}_\nu^\ell$ terms wrt. scales for different impeller rotation directions. The curves corresponding to Π_{DR}^ℓ are plotted in blue and those corresponding to $\mathscr{D}_\nu^\ell$ are plotted in red. The vertical dashed lines correspond to the values of the interrogation volume size. For cases T4 and T5, the impellers are rotating in the ANTI direction whereas for case T6 they are rotating in the CONTRA direction.

2 Probability density functions and extreme values of Π_{DR}^ℓ and $\mathscr{D}_\nu^\ell$: a subtler behaviour

The global behaviour of Π_{DR}^ℓ and $\mathscr{D}_\nu^\ell$ with respect to scales as described by their space-time averages and standard deviations is in line with the classical picture of turbulence. We now study more in details the behaviour of Π_{DR}^ℓ and $\mathscr{D}_\nu^\ell$ by analyzing their probability density functions (pdfs) and their extreme values.

2.1 Evolution of the pdfs of Π_{DR}^ℓ and $\mathscr{D}_\nu^\ell$ with respect to ℓ_c/η

Figure 6.5 (a) shows the pdfs of the Duchon-Robert term at different values of ℓ_c/η corresponding to the rightmost points of the space-time average or standard-deviation curves (figures 6.1 and 6.3). Each pdf was obtained from one different case among T1, T2, T3 and T4. However, ℓ_c is always equal to 1.7 times the interrogation window size : indeed, the four pdfs were obtained with exactly the same acquisition (except for the interframing time dt), correlation and processing parameters, therefore only ℓ_c/η varies from one pdf to another. The horizontal axis is normalized by the global dissipation rate ϵ obtained from torque measurements. It can be seen that the pdfs have wide tails, the width of the tails increasing with ℓ_c/η. This is coherent with the increase of the space-time average and standard deviation of the Duchon-Robert term with this ratio. It is interesting to note that even in the dissipative range, Π_{DR}^ℓ can take values larger than 50ϵ. More interesting is the behaviour of the centered-reduced pdf of the Duchon-Robert term shown in figure 6.5 (c) : it becomes more skewed towards positive values in the dissipative range, and it also has a wider positive tail. The larger skewness means that direct inter-scale transfer is favoured in the dissipative

range. The wider positive tails suggest that extreme events "resist" better in the dissipative range than medium-amplitude events, i.e. that their probability decreases less. To summarize, there are still very strong events of the Duchon-Robert term in terms of ϵ in the dissipative range, and they seem to be less impacted by the viscous effects than weaker events. Interpreting the Duchon-Robert term as inter-scale transfer, this strongly supports the fact that the flow has scales smaller than our resolution, which is in the dissipative range (see figure 6.1). This suggests that there is not only one dissipative scale, but a range of dissipative scales. This is in line with the multifractal model and the mechanism exposed in chapter 1, and thus supports the existence of local Hölder exponents smaller than 1/3.

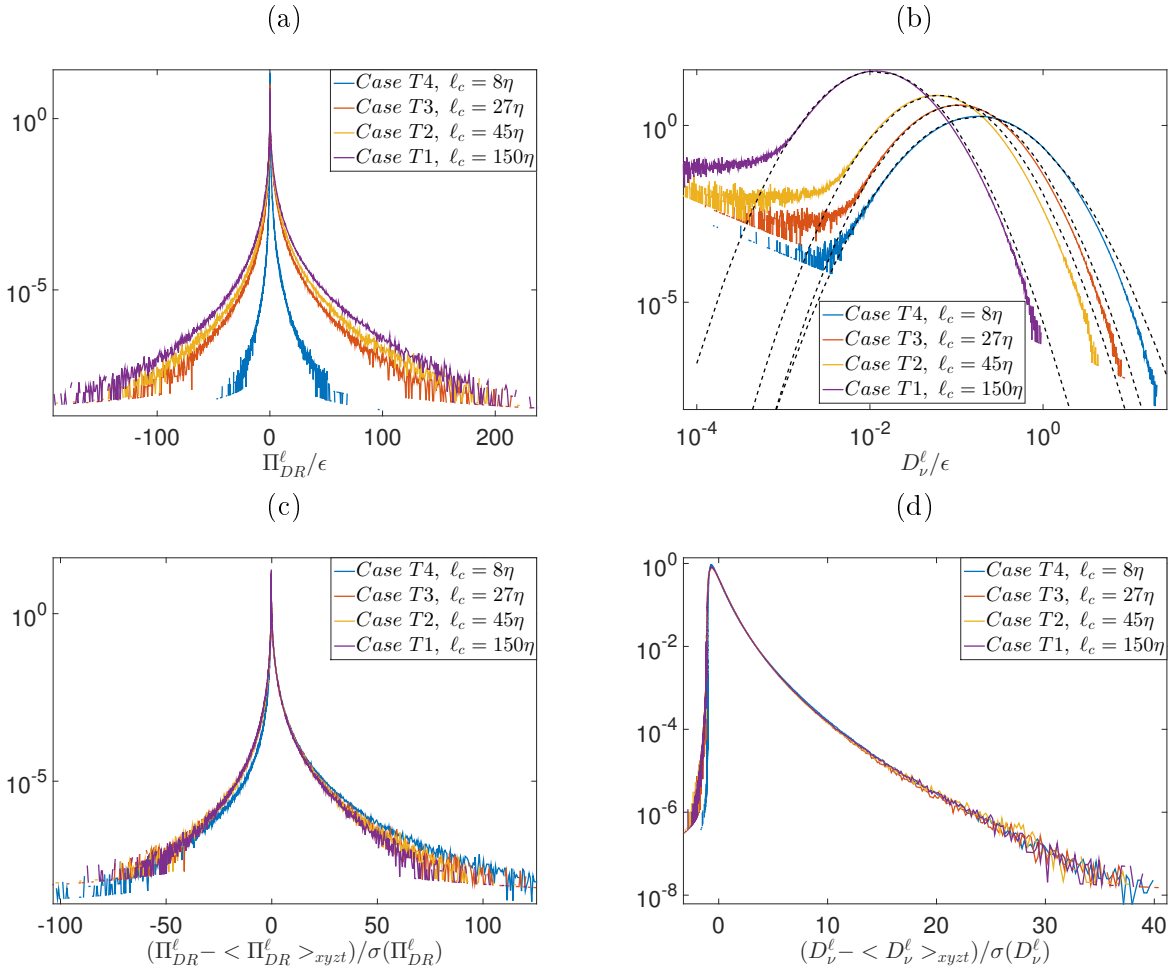

Figure 6.5: Probability density functions of the Duchon-Robert term Π^ℓ_{DR} and of the viscous dissipation term $\mathscr{D}^\ell_\nu$ for cases T1 to T4. In all cases, ℓ_c is equal to 1.7 times the interrogation volume size. The vertical axes are in logarithmic coordinates and the horizontal axes in linear coordinates except for (b) where it is in logarithmic coordinates. (a) Pdf of Π^ℓ_{DR} normalized by the global dissipation rate ϵ (computed from torque measurements). (b) Pdf of $\mathscr{D}^\ell_\nu$ normalized by the global dissipation rate ϵ. The dashed lines correspond to log-normal distributions. (c) Centered-reduced pdf of Π^ℓ_{DR}. (d) Centered-reduced pdf of $\mathscr{D}^\ell_\nu$.

This behaviour of the Duchon-Robert term is especially striking when compared to the one of the viscous dissipation. Pdfs of $\mathscr{D}^\ell_\nu$ are shown on figure 6.5 (b) in log-log coordinates, the horizontal axis being normalized by the global dissipation rate ϵ. They are obtained from the same values of ℓ_c/η as the pdfs of Π^ℓ_{DR} on figure 6.5 (a). As expected, the right tail becomes larger as ℓ_c/η is decreased :

indeed, viscous dissipation is more important in the dissipative range. Note that the shape of these pdfs is very close to a parabola (the dashed lines) with a slightly smaller right tail (the left tail which saturates is probably spurious). We performed Lilliefors tests on these pdfs to check whether they corresponded to log-normal distributions or not ; this hypothesis was always rejected at the 5% level. When centered-reduced, these pdfs collapse : unlike the Duchon-Robert term, the shape of the distribution does not seem to vary with ℓ_c/η, only the amplitude is varying. Even if the Lilliefors tests were negative, suggesting that $\mathscr{D}_\nu^\ell$ does not follow a log-normal distribution, the fact that the pdf of $\mathscr{D}_\nu^\ell$ is only characterized by its average and standard-deviation reminds much of K62 theory.
This behaviour of the tails can be well accounted for by computing the skewness S and the kurtosis K defined as follows :

$$S(X) = \frac{\langle (X - \langle X \rangle)^3 \rangle}{\langle (X^2 - \langle X \rangle^2) \rangle^{3/2}} \tag{6.1}$$

$$K(X) = \frac{\langle (X - \langle X \rangle)^4 \rangle}{\langle (X^2 - \langle X \rangle^2) \rangle^2} \tag{6.2}$$

Table 6.1 gives the skewness and the kurtosis of the pdfs of the Duchon-Robert and viscous dissipation terms shown in figure 6.5. In agreement with figure 6.5 (d), the skewness and the kurtosis of the viscous dissipation do not depend on ℓ_c/η. However, the skewness and kurtosis of the Duchon-Robert term are both increasing when decreasing ℓ_c/η : in the dissipative range, even if the values of the Duchon-Robert term are overall smaller than in the inertial range, its distribution is much more skewed (towards positive values) and pinched.

ℓ_c/η	Case	Skewness		Kurtosis	
		Π_{DR}^ℓ	$\mathscr{D}_\nu^\ell$	Π_{DR}^ℓ	$\mathscr{D}_\nu^\ell$
150	T1	4.3	3.3	190	25
45	T2	5.1	3.2	240	25
27	T3	6.2	3.1	330	25
8	T4	11	3.4	590	26

Table 6.1: Skewness and kurtosis of Π_{DR}^ℓ and $\mathscr{D}_\nu^\ell$ at several values of ℓ_c/η.

2.2 Evolution of the extreme values of Π_{DR}^ℓ and $\mathscr{D}_\nu^\ell$ with respect to ℓ_c/η

We now focus on the very extreme values of Π_{DR}^ℓ and $\mathscr{D}_\nu^\ell$.
For each case T1, T2, T3 and T4, we computed the maxima over space of the absolute value of the Duchon-Robert term and of the viscous dissipation :

$$\tilde{M}_{DR}^\ell(t) = \max_{xyz}(|\Pi_{DR}^\ell(x,y,z,t)|) \tag{6.3}$$

$$\tilde{M}_\nu^\ell(t) = \max_{xyz}(|\mathscr{D}_\nu^\ell(x,y,z,t)|) \tag{6.4}$$

We ordered them :

$$\tilde{M}^\ell_{DR}(t_{i_1}) > \tilde{M}^\ell_{DR}(t_{i_2}) > ... > \tilde{M}^\ell_{DR}(t_{i_{n_t}}) \tag{6.5}$$
$$\tilde{M}^\ell_{\nu}(t_{j_1}) > \tilde{M}^\ell_{\nu}(t_{j_2}) > ... > \tilde{M}^\ell_{\nu}(t_{j_{n_t}}) \tag{6.6}$$

We then define the nth highest maxima as follows :

$$M^\ell_{DR}(n) = \tilde{M}^\ell_{DR}(t_{i_n}) \tag{6.7}$$
$$M^\ell_{\nu}(n) = \tilde{M}^\ell_{\nu}(t_{j_n}) \tag{6.8}$$

Thereafter, the nth highest maximum over space is called abusively "nth highest extreme event". It is abusive because if there are two extreme events on the same instantaneous velocity field, one of them will be omitted by this technique. However, it is unlikely as these events are rare and the velocity fields are not very large ; this will therefore not affect the results significantly. Also, we will analyze the velocity fields corresponding to the ten highest extreme events in chapter 8 ; if the joint apparition of two maxima is an important feature, we will notice it.

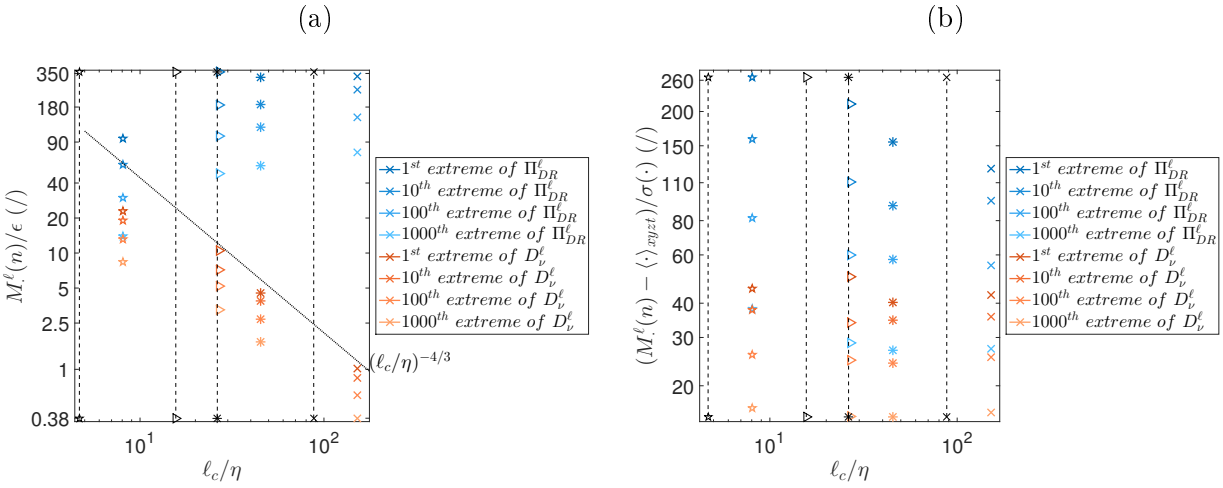

Figure 6.6: Values of the nth highest extreme event of the Duchon-Robert term and of the viscous dissipation term with n $\in \{1,\ 10,\ 100,\ 1000\}$. Pentagons correspond to $\ell_c/\eta = 8$ (obtained with case T4), triangles to $\ell_c/\eta = 27$ (obtained with case T3), stars to $\ell_c/\eta = 45$ (obtained with case T2) and crosses to $\ell_c/\eta = 150$ (obtained with case T1). The vertical dashed lines correspond to the interrogation volume size of each case. (a) Values are normalized by ϵ. (b) Values are centered-reduced.

Figure 6.6 gives the values of $M^\ell_{DR}(n)$ and of $M^\ell_\nu(n)$ for n $\in \{1,\ 10,\ 100,\ 1000\}$ and for $\ell_c/\eta \in \{8,\ 27,\ 45,\ 150\}$ (as the pdfs shown in figure 6.5). The extremes of $\mathscr{D}^\ell_\nu$ all correspond to positive values ; however, $M^\ell_{DR}(10)$ and $M^\ell_{DR}(100)$ correspond to negative values of Π^ℓ_{DR}. The extreme events of Π^ℓ_{DR} are mainly positive ; the amount of negative extreme events is decreasing when ℓ_c/η is lowered. For instance, there are 223 negative events among the 1000 most extreme events at $\ell_c/\eta = 150$ and only 90 at $\ell_c/\eta = 8$.
When normalized by the global dissipation rate ϵ, the behaviour of $M^\ell_{DR}(n)$ and of $M^\ell_\nu(n)$ is similar to the behaviour of the corresponding space-time averages shown on figure 6.1 : $M^\ell_{DR}(n)$ is increasing and $M^\ell_\nu(n)$ decreasing with ℓ_c/η. However, it can be noticed that $M^\ell_{DR}(n)$ is larger

than $M_\nu^\ell(n)$ for all n in the dissipative range, contrary to the space-time averages. When centered-reduced (i.e. when subtracting the space-time average and normalizing by the standard deviation computed over space and time), we observe a different behaviour which corresponds to the behaviour of the centered-reduced pdfs and of the skewness and kurtosis : $(M_\nu^\ell(n) - \langle \mathscr{D}_\nu^\ell \rangle_{xyzt})/\sigma(\mathscr{D}_\nu^\ell)$ is hardly varying with scales, whereas $(M_{DR}^\ell(n) - \langle \Pi_{DR}^\ell \rangle_{xyzt})/\sigma(\Pi_{DR}^\ell)$ is decreasing with scales, especially when considering the first extremes. In the dissipative range, the extremes of Π_{DR}^ℓ are more extreme than in the inertial range in that sense that they deviate more from the average behaviour.

3 Relation between Π_{DR}^ℓ and $\mathscr{D}_\nu^\ell$: the highlight of the joint pdfs and of the extreme ratios

As discussed in chapter 2, the prints of singularities may rather correspond to extreme values of the ratio between the Duchon-Robert and the viscous dissipation terms than to extreme values of the Duchon-Robert term itself. Indeed, we are mainly interested by the events for which the inertial effects are large compared to the viscous effects ; a priori, this could happen at places where the Duchon-Robert term is large compared to the viscous dissipation at this particular point, but not compared to other values of the Duchon-Robert term at other points. In order to determine whether these two criteria are equivalent or not, we analyze here the joint distributions of Π_{DR}^ℓ and $\mathscr{D}_\nu^\ell$ and the distribution of the ratio between these two terms.

3.1 Joint pdfs of Π_{DR}^ℓ and $\mathscr{D}_\nu^\ell$

Four joint pdfs of Π_{DR}^ℓ and $\mathscr{D}_\nu^\ell$ are shown in figure 6.7. Each one corresponds to a different value of ℓ_c/η. The considered values of ℓ_c/η correspond again to the rightmost points of figures 6.1 and to the values considered on figure 6.5.
It can be observed that the shape of the joint pdf is an upside down triangle in all cases. The isolines of the joint pdf can be fairly approximated either by the equation $\mathscr{D}_\nu^\ell = a$ for the top edge of the triangle or by the equation $\mathscr{D}_\nu^\ell = \pm b * \left(\Pi_{DR}^\ell\right)^\alpha$ with α close to 1 for the side edges. This means that the rare events correspond either to very large values of $\mathscr{D}_\nu^\ell$ or to very large values of the ratio $|\Pi_{DR}^\ell/\mathscr{D}_\nu^\ell|$, and not only very large values of $|\Pi_{DR}^\ell|$. Another consequence is that the most extreme events of the Duchon-Robert term also correspond to extreme events of viscous dissipation ; however, an extreme event of the ratio $|\Pi_{DR}^\ell/\mathscr{D}_\nu^\ell|$ is not necessarily an extreme event of the Duchon-Robert term. This suggests that the prints of singularities may be extreme events of the ratio $|\Pi_{DR}^\ell/\mathscr{D}_\nu^\ell|$ rather than extreme events of $|\Pi_{DR}^\ell|$, which come along large values of $\mathscr{D}_\nu^\ell$ and would therefore be regularized. This motivates a study of the extreme events of the ratio $|\Pi_{DR}^\ell/\mathscr{D}_\nu^\ell|$ in addition to the extreme events of the Duchon-Robert term.
When increasing ℓ_c/η, the joint pdfs are moving below the identity lines corresponding to $\Pi_{DR}^\ell = \pm\mathscr{D}_\nu^\ell$. This corresponds to a decrease of the a and b coefficients. It means that $\mathscr{D}_\nu^\ell$ takes overall larger values than Π_{DR}^ℓ in the dissipative range, whereas it is the contrary in the inertial range ; this is in line with behaviour of the space-time averages 6.1. However, it is noticeable that the ratio $\Pi_{DR}^\ell/\mathscr{D}_\nu^\ell$ can be lower than 1 in the inertial range, or larger than 1 in the dissipative range (with a small probability though). Also, when increasing ℓ_c/η, the side edges seem to become more curved. At all values of ℓ_c/η, the bottom angle of the triangle, corresponding to the small values of $\mathscr{D}_\nu^\ell$, is very wide compared to the others. This is in agreement with the saturation of the pdfs of $\mathscr{D}_\nu^\ell$ at small values shown on figure 6.5(b). This phenomenon happens only for low-enough values of the Duchon-Robert term. The observation of the corresponding velocity fields did not reveal any interesting features. These low values of ratio $\mathscr{D}_\nu^\ell$ may appear during the computation of this term.

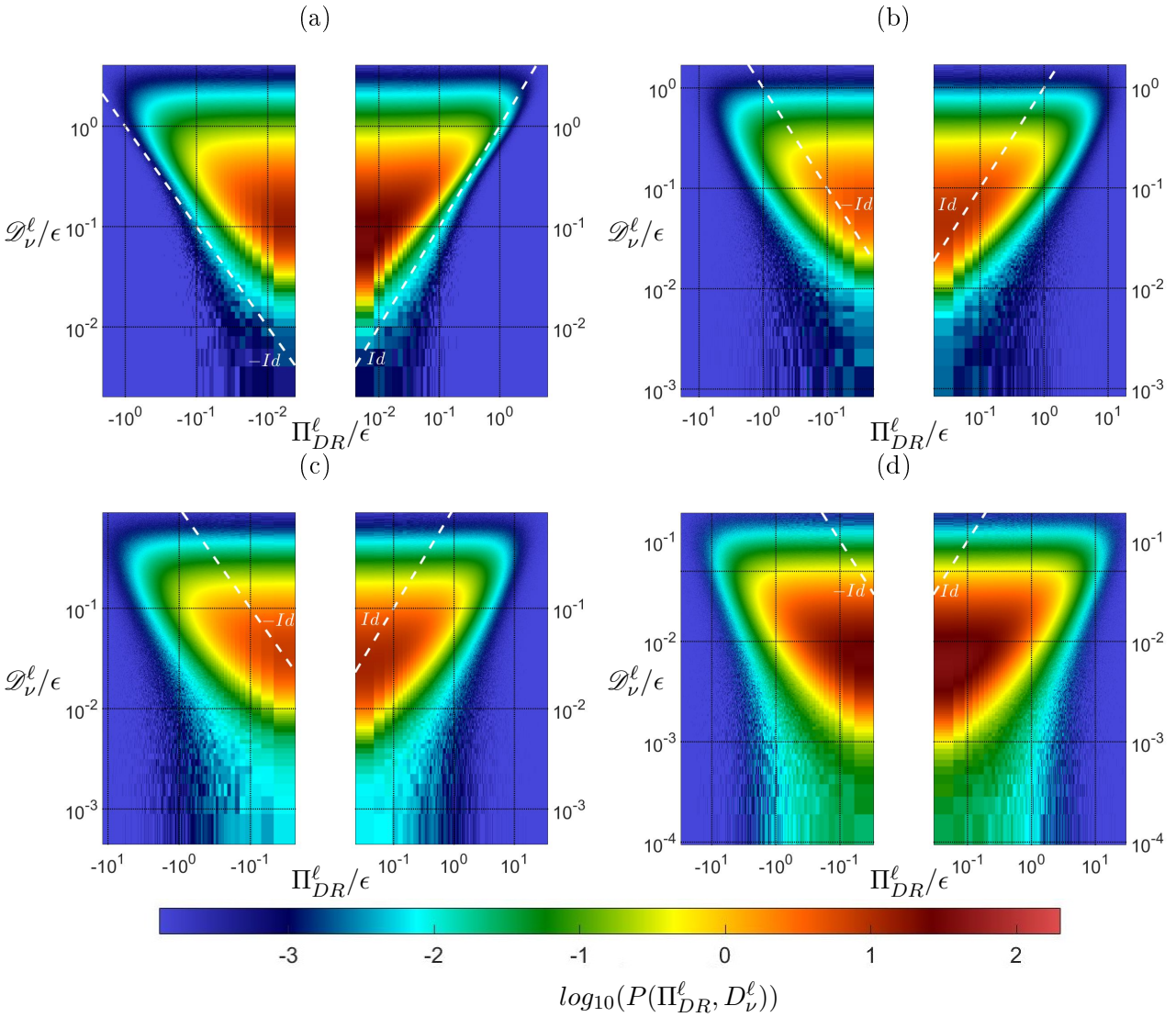

Figure 6.7: Logarithm of the joint probability density function of the Duchon-Robert and viscous dissipation terms. The vertical and horizontal axes are in logarithmic coordinates. (a) $\ell_c/\eta = 8$ (obtained with case T4). (b) $\ell_c/\eta = 27$ (obtained with case T3). (c) $\ell_c/\eta = 45$ (obtained with case T2). (d) $\ell_c/\eta = 150$ (obtained with case T1). The white dashed lines correspond to the identity lines $\Pi^\ell_{DR} = \mathscr{D}^\ell_\nu$.

They probably do not have any physical meaning as they are not observed for the $\mathscr{D}^\ell_{\nu,LES}$ term. However, one must take these values into account when studying the ratio $|\Pi^\ell_{DR}/\mathscr{D}^\ell_\nu|$: low values of viscous dissipation will result in very high values of this ratio which do not correspond to physical phenomena. To avoid these spurious very high values, a threshold on $\mathscr{D}^\ell_\nu$ should be used.

All the joint pdfs are slightly asymmetric with respect to the axis $\Pi^\ell_{DR} = 0$, the right part (corresponding to positive values of the Duchon-Robert term) being wider than the left part (corresponding to the negative ones). This is in agreement with the positive skewness of the pdf of the Duchon-Robert term. The right part is also slightly lower : overall, direct inter-scale transfer is associated with smaller values of dissipation.

3.2 Distribution of the ratio $\Pi^\ell_{DR}/\mathscr{D}^\ell_\nu$

The analysis of the joint pdfs showed that the extreme events of the Duchon-Robert term are not necessarily the same as the extreme events of the ratio $\Pi^\ell_{DR}/\mathscr{D}^\ell_\nu$. Here, we characterize the behaviour of this ratio by studying its distribution for different values of ℓ_c/η.

Figure 6.8 shows the pdfs of the logarithm of the absolute value of the ratio $\Pi^\ell_{DR}/\mathscr{D}^\ell_\nu$ for four different values of ℓ_c/η in semi-logarithmic coordinates (the horizontal axis correspond to the logarithm of the absolute value of the ratio, shown in linear coordinates). The considered values of ℓ_c/η correspond again to the rightmost points of figure 6.1 and to the joint pdfs considered on figure 6.7. For each value of ℓ_c/η, we show three joint pdfs : a pdf conditioned on positive values of the ratio (i.e. on positive values of the Duchon-Robert term since the viscous dissipation is always positive), a pdf conditioned on the negative values of the ratio and an unconditioned pdf. This allows to detect a possible different behaviour between direct and indirect energy transfer. The arrows indicate the absolute value of the ratio $\Pi^\ell_{DR}/\mathscr{D}^\ell_\nu$ at the maximum of the two conditioned pdfs.

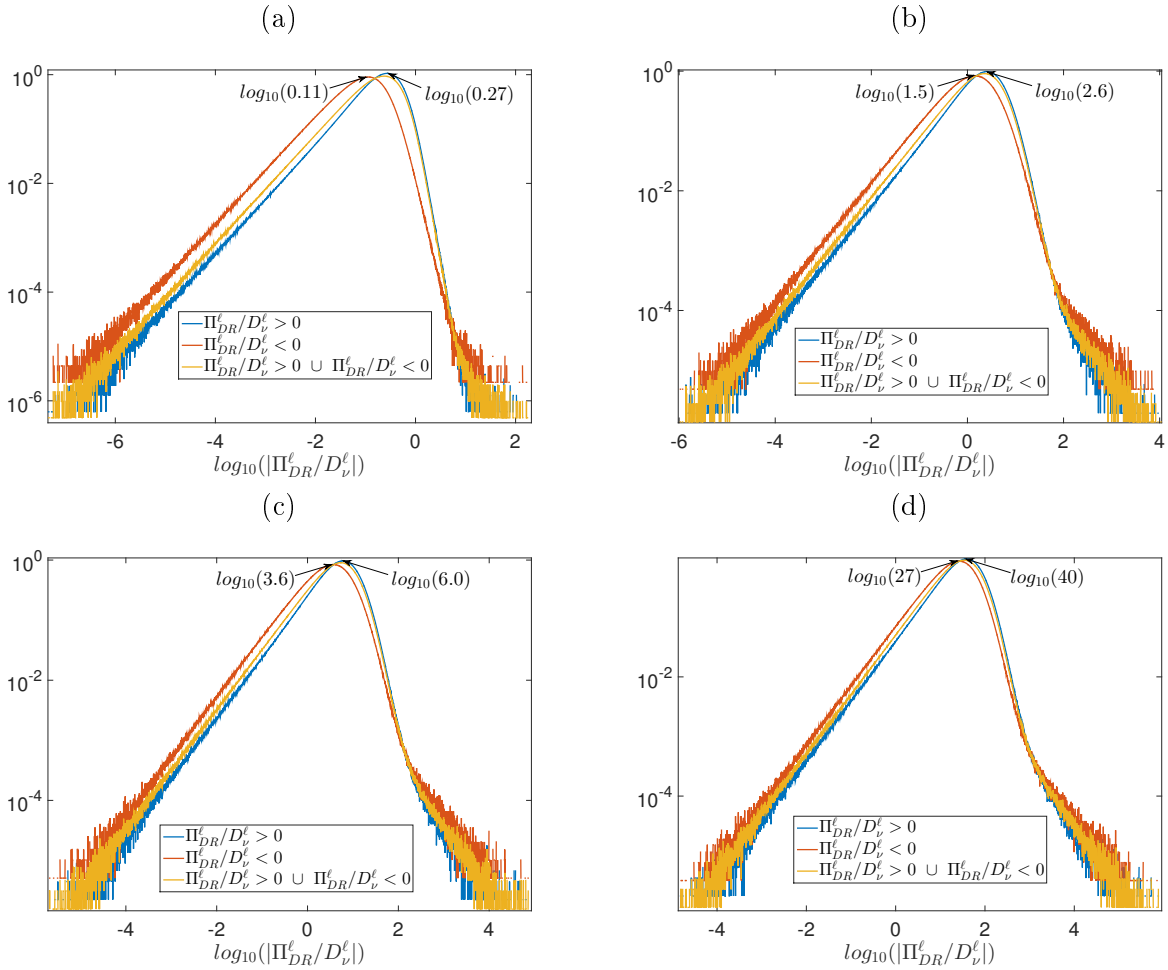

Figure 6.8: Probability density function of the logarithm of the absolute value of the ratio $\Pi^\ell_{DR}/\mathscr{D}^\ell_\nu$. Blue curves correspond to the pdf conditioned on positive values of the ratio, red curves to the pdf conditioned on negative values of the ratio and yellow curves to unconditioned pdf. The arrows show the maxima of the blue and red curves. (a) $\ell_c/\eta = 8$ (obtained with case T4). (b) $\ell_c/\eta = 27$ (obtained with case T3). (c) $\ell_c/\eta = 45$ (obtained with case T2). (d) $\ell_c/\eta = 150$ (obtained with case T1).

The shape of the three pdfs are the same for a given value of ℓ_c/η, and also for different values of ℓ_c/η : there is a wide exponential tail on the left and a sharply decreasing tail on the right. At the extreme right, the pdfs seem to widen but this is probably linked with the saturation of the pdfs of the viscous dissipation term at small values which we do not understand and believe to have no physical meaning. The strong asymmetry of these pdfs means that extremely high values of the ratio $\Pi^{\ell}_{DR}/\mathscr{D}^{\ell}_{\nu}$ are much rarer than extremely small values, whatever ℓ_c/η. This asymmetry was not very obvious from the joint pdfs.

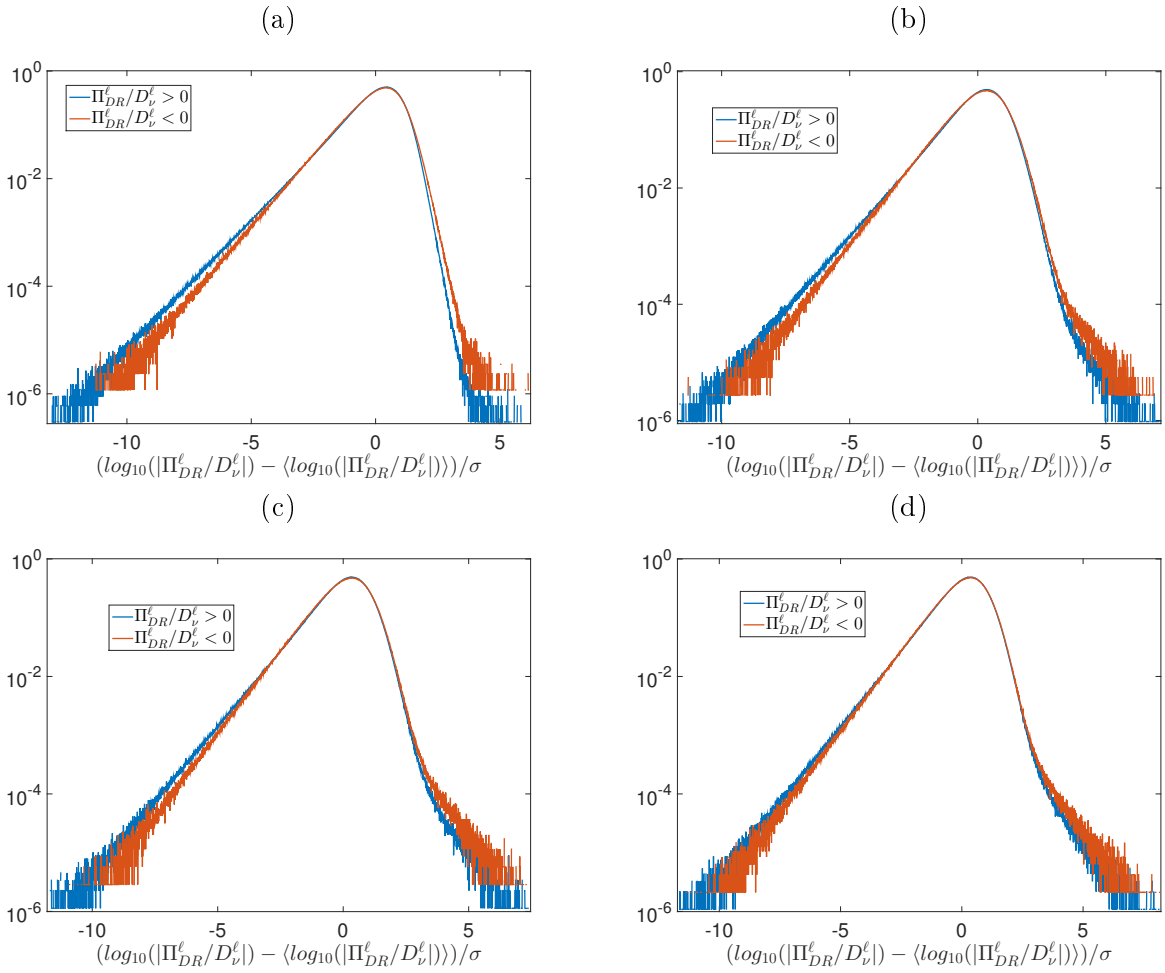

Figure 6.9: Centered-reduced probability density function of the logarithm of the absolute value of the ratio $\Pi^{\ell}_{DR}/\mathscr{D}^{\ell}_{\nu}$. Blue curves correspond to the pdf conditioned on positive values of the ratio, red curves to the pdf conditioned on negative values of the ratio. (a) $\ell_c/\eta = 8$ (obtained with case T4). (b) $\ell_c/\eta = 27$ (obtained with case T3). (c) $\ell_c/\eta = 45$ (obtained with case T2). (d) $\ell_c/\eta = 150$ (obtained with case T1).

For a given value of ℓ_c/η, the maximum of the pdf conditioned on negative values of the ratio is achieved for a lower value of the ratio compared to the pdf conditioned on positive values of the ratio. The two maxima however become closer when ℓ_c/η is increased. This corresponds to a more symmetrical behaviour of forward and backward inter-scale transfer in the inertial range compared to the dissipative range. This phenomenon also appears in the centered-reduced pdfs of the ratio $\Pi^{\ell}_{DR}/\mathscr{D}^{\ell}_{\nu}$, conditioned on positive and negative values, which is shown on figure 6.9. In the dissipative range, the pdfs conditioned on positive values of the ratio are more skewed towards smaller values of the ratio than pdfs conditioned on negative values. When ℓ_c/η increases, the centered-reduced

pdfs conditioned on positive and negative values of the ratio progressively overlap. Note that the unconditioned pdf is very close to the pdf conditioned on the positive values of the ratio ; this is due to the fact that there are many more positive values of the ratio $\Pi^\ell_{DR}/\mathscr{D}^\ell_\nu$.

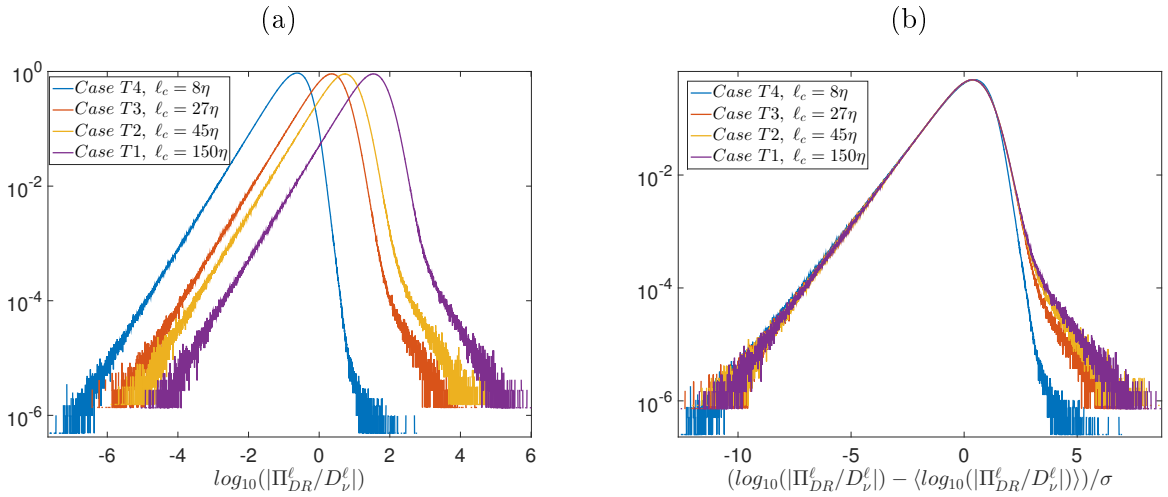

Figure 6.10: (Unconditioned) probability density functions of the logarithm of the absolute value of the ratio $\Pi^\ell_{DR}/\mathscr{D}^\ell_\nu$ at several scales. (a) Raw pdfs. (b) Centered-reduced pdfs.

Figure 6.10 allows to see better the behaviour of the ratio pdfs when ℓ_c/η is varied. This figure shows the unconditioned raw pdfs on the left and the unconditioned centered-reduced pdfs on the right. The conditioned pdfs feature the same behaviour. When increasing ℓ_c/η, the maximum of the pdf is shifted towards the right, i.e. towards larger values of the ratio, which is expected : in the dissipative range, viscous dissipation is stronger than inertial effects, whereas it is the contrary in the inertial range. Note that values of $|\Pi^\ell_{DR}/\mathscr{D}^\ell_\nu|$ around 10 can all the same be found in the dissipative range. More interesting is the behaviour of the centered-reduced pdfs of $log_{10}(|\Pi^\ell_{DR}/\mathscr{D}^\ell_\nu|)$: they become more skewed towards negative values in the dissipative range compared to the inertial range ; this is not very obvious in figure 6.10 for the left tail but much more clear for the right one. This behaviour of the raw and centered-reduced pdfs of $log_{10}(|\Pi^\ell_{DR}/\mathscr{D}^\ell_\nu|)$ should be compared to the behaviour of their counterparts for Π^ℓ_{DR}. Indeed, both $|\Pi^\ell_{DR}/\mathscr{D}^\ell_\nu|$ and $|\Pi^\ell_{DR}|$ take smaller values in the dissipative range, with still very strong extremes ($|\Pi^\ell_{DR}/\mathscr{D}^\ell_\nu|$ around 10, $|\Pi^\ell_{DR}|$ around 100ϵ). However, whereas the centered-reduced pdfs of Π^ℓ_{DR} have a wider positive tail in the dissipative range, indicating that the extreme events "resist" better the viscous effects than medium-amplitude events, the centered-reduced pdfs of $log_{10}(|\Pi^\ell_{DR}/\mathscr{D}^\ell_\nu|)$ become more skewed towards negative values in the dissipative range, indicating that extreme events of $|\Pi^\ell_{DR}/\mathscr{D}^\ell_\nu|$ are more impacted by the viscous effects that medium-amplitude ones, i.e. that their probability decreases more in the dissipative range.

3.3 Extreme events of the ratio $\Pi^\ell_{DR}/\mathscr{D}^\ell_\nu$

As we defined the highest maxima of the Π^ℓ_{DR} and $\mathscr{D}^\ell_\nu$ dissipation terms, we now define the highest maxima and lowest minima of the ratio $\Pi^\ell_{DR}/\mathscr{D}^\ell_\nu$. We condition the highest maxima on values of $\mathscr{D}^\ell_\nu$ higher than a threshold T^ℓ, whose choice is based on the joint pdfs, in order to avoid very small values of $\mathscr{D}^\ell_\nu$ which we believe to be spurious. The thresholds used are given in table 6.2.

For each case T1, T2, T3 and T4, we computed the maxima and minima over space of the logarithm of the absolute value of the ratio $\Pi^\ell_{DR}/\mathscr{D}^\ell_\nu$:

Case	ℓ_c/η	T^ℓ
T1	150	0.025ϵ
T2	45	0.1ϵ
T3	27	0.16ϵ
T4	8	0.3ϵ

Table 6.2: Thresholds used to compute the maxima of the ratio $\Pi^\ell_{DR}/\mathscr{D}^\ell_\nu$. ϵ is the global average dissipation rate computed from torque measurements.

$$\tilde{M}^\ell_{ratio}(t) = \max_{xyz}(|\Pi^\ell_{DR}(x,y,z,t)/\mathscr{D}^\ell_\nu(x,y,z,t)| \mid \mathscr{D}^\ell_\nu(x,y,z,t) > T^\ell) \tag{6.9}$$
$$\tilde{m}^\ell_{ratio}(t) = \min_{xyz}(|\Pi^\ell_{DR}(x,y,z,t)/\mathscr{D}^\ell_\nu(x,y,z,t)|) \tag{6.10}$$

We ordered them :

$$\tilde{M}^\ell_{ratio}(t_{i_1}) > \tilde{M}^\ell_{ratio}(t_{i_2}) > ... > \tilde{M}^\ell_{ratio}(t_{i_{n_t}}) \tag{6.11}$$
$$\tilde{m}^\ell_{ratio}(t_{j_1}) < \tilde{m}^\ell_{ratio}(t_{j_2}) < ... < \tilde{m}^\ell_{ratio}(t_{j_{n_t}}) \tag{6.12}$$

We then define the nth highest maxima and n th lowest minima as follows :

$$M^\ell_{ratio}(n) = \tilde{M}^\ell_{ratio}(t_{i_n}) \tag{6.13}$$
$$m^\ell_{ratio}(n) = \tilde{m}^\ell_{ratio}(t_{j_n}) \tag{6.14}$$

Thereafter, the nth highest maximum over space is called abusively "nth highest extreme event of the ratio $|\Pi^\ell_{DR}(x,y,z,t)/\mathscr{D}^\ell_\nu(x,y,z,t)|$" and the nth lowest minimum over space "nth lowest extreme event of the ratio $|\Pi^\ell_{DR}(x,y,z,t)/\mathscr{D}^\ell_\nu(x,y,z,t)|$". As for the extreme events of $\Pi^\ell_{DR}(x,y,z,t)$ and $\mathscr{D}^\ell_\nu(x,y,z,t)$, it is abusive because if there are two extreme events on the same instantaneous velocity field, one of them will be omitted by this technique. However, it is unlikely as these events are rare and the velocity fields are not very large ; this will therefore not affect the results significantly. Also, we will analyze the velocity fields corresponding to the ten highest extreme events in chapter 8 ; if the joint apparition of two maxima is an important feature, we will notice it.
Figure 6.11 shows the values of the logarithm of the 1^{st}, 10^{th}, 100^{th} and 1000^{th} highest and lowest extreme events of the ratio $|\Pi^\ell_{DR}(x,y,z,t)/\mathscr{D}^\ell_\nu(x,y,z,t)|$ for different values of ℓ_c/η. In line with the pdfs of the logarithm of the ratio, both the minimum and the maximum are increasing with scales. The centered-reduced values of the maximum and minimum seem to be quite independent from ℓ_c/η. For the minimum value, this corresponds to the collapse of the left tails of the pdfs of the ratio. For the maximum values, this may be related to the use of a threshold. Also, even if the centered-reduced maximum seems independent from ℓ_c/η, it is much less probable at lower values of ℓ_c/η.

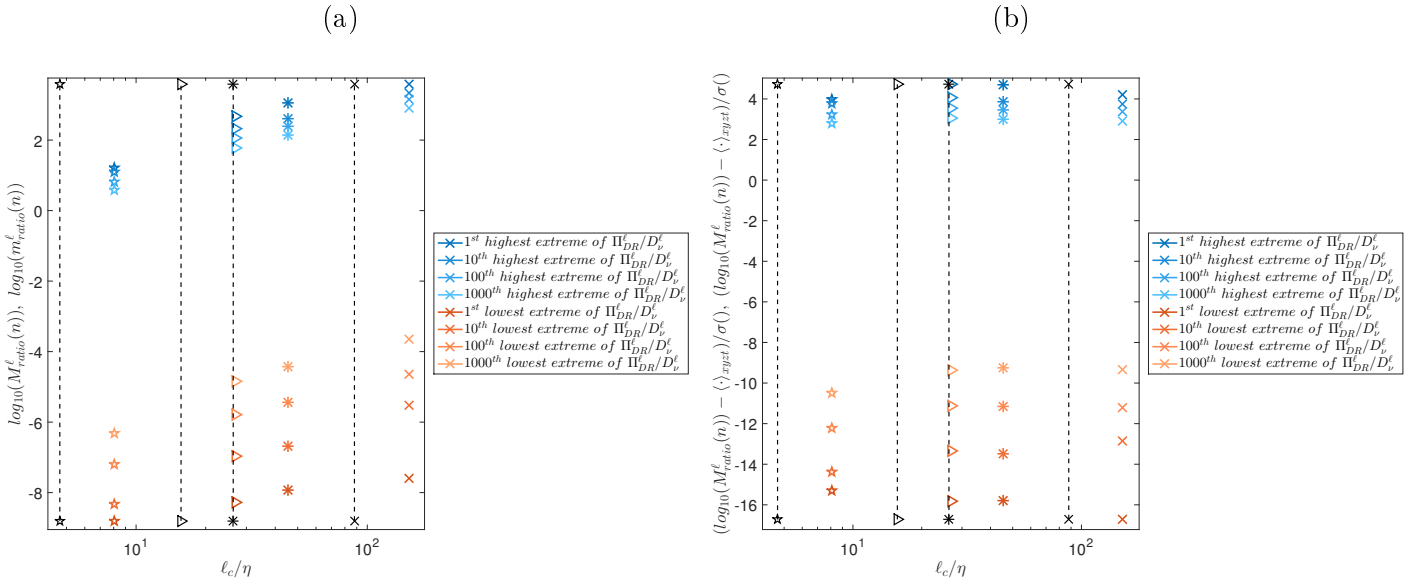

Figure 6.11: Values of the logarithm of the nth highest and lowest extreme event of the ratio $|\Pi^{\ell}_{DR}(x,y,z,t)/\mathscr{D}^{\ell}_{\nu}(x,y,z,t)|$ with n $\in \{1,\ 10,\ 100,\ 1000\}$. Pentagons correspond to $\ell_c/\eta = 8$ (obtained with case T4), triangles to $\ell_c/\eta = 27$ (obtained with case T3), stars to $\ell_c/\eta = 45$ (obtained with case T3) and crosses to $\ell_c/\eta = 150$ (obtained with case T1). The vertical dashed lines correspond to the interrogation volume size of each case.(a) Raw values. (b) Values are centered-reduced.

4 Comparison with the statistics of the terms coming from the LES equations

In chapter 2, we mentioned that using the pair $(\Pi^\ell_{LES}, \mathscr{D}^\ell_{\nu,LES})$ instead of $(\Pi^\ell_{DR}, \mathscr{D}^\ell_{\nu})$ would probably give similar results as it is another way of measuring the inter-scale transfer and the viscous dissipation ; only, Π^ℓ_{DR} should be more suited than Π^ℓ_{LES} when the velocity field is not very regular. We performed the same statistical analyses as previously with these other terms and computed joint statistics in order to check this assertion. We found that overall, the picture of the energy transfer and dissipation is the same but that there are small differences though. We tried to explain these differences and it appears that they are due to slightly different physical meanings of the terms of the two pairs. We first report the experimental results and then provide an attempt of explanation.

4.1 Global behaviour with respect to scales

Figures 6.12 shows the space-time average of the four terms Π^ℓ_{DR}, $\mathscr{D}^\ell_{\nu}$, Π^ℓ_{LES}, and $\mathscr{D}^\ell_{\nu,LES}$. The behaviour is qualitatively the same for the inter-scale transfer terms Π^ℓ_{DR} and Π^ℓ_{LES} on the one

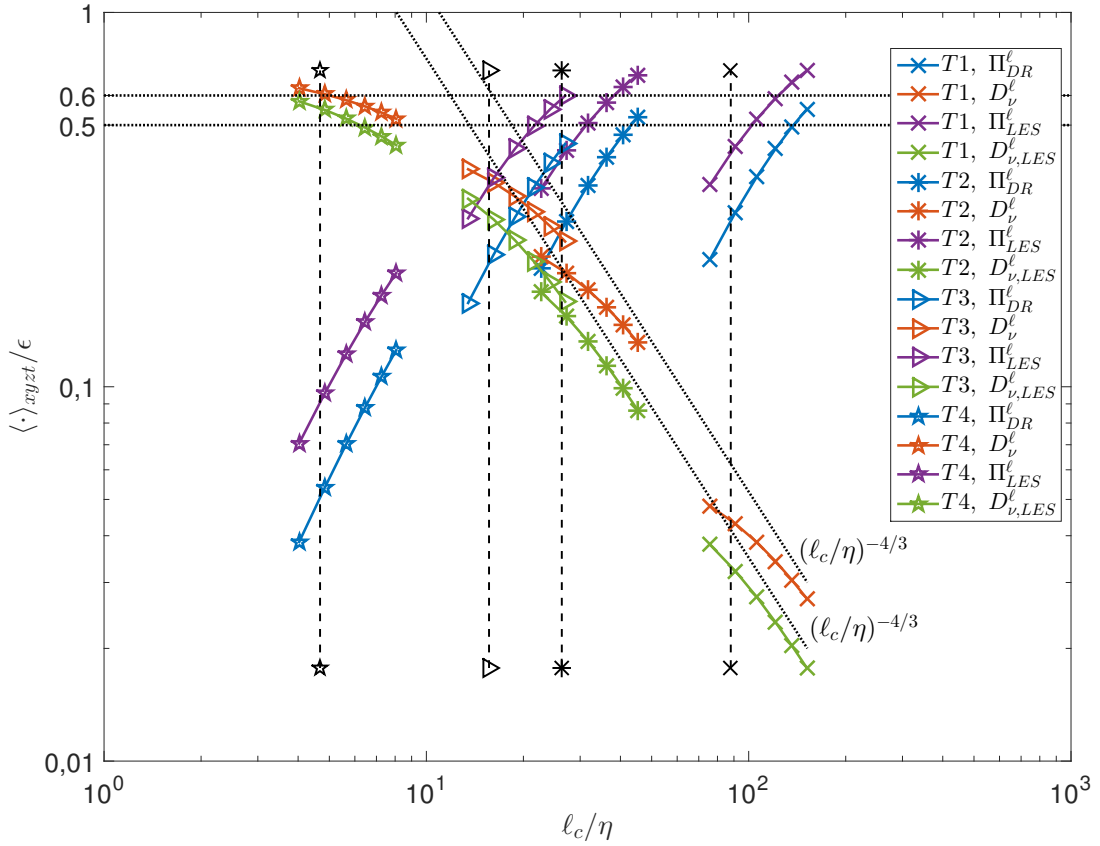

Figure 6.12: Space-time average of Π^ℓ_{DR}, $\mathscr{D}^\ell_{\nu}$, Π^ℓ_{LES} and $\mathscr{D}^\ell_{\nu,LES}$ terms wrt. scales. The curves corresponding to Π^ℓ_{DR} are plotted in blue, those corresponding to $\mathscr{D}^\ell_{\nu}$ are plotted in red, those corresponding to Π^ℓ_{LES} are plotted in purple and those corresponding to $\mathscr{D}^\ell_{\nu,LES}$ are plotted in green. The vertical dashed lines correspond to the values of the interrogation volume size.

hand, and for the viscous dissipation terms $\mathscr{D}_\nu^\ell$ and $\mathscr{D}_{\nu,LES}^\ell$ on the other hand, except that they differ from a multiplicative coefficient between 1.2 and 1.8. For the viscous terms this coefficient is close to 1.2 in the dissipative range and to 1.8 in the inertial range ; for the inter-scale tranfer terms, it is the contrary.

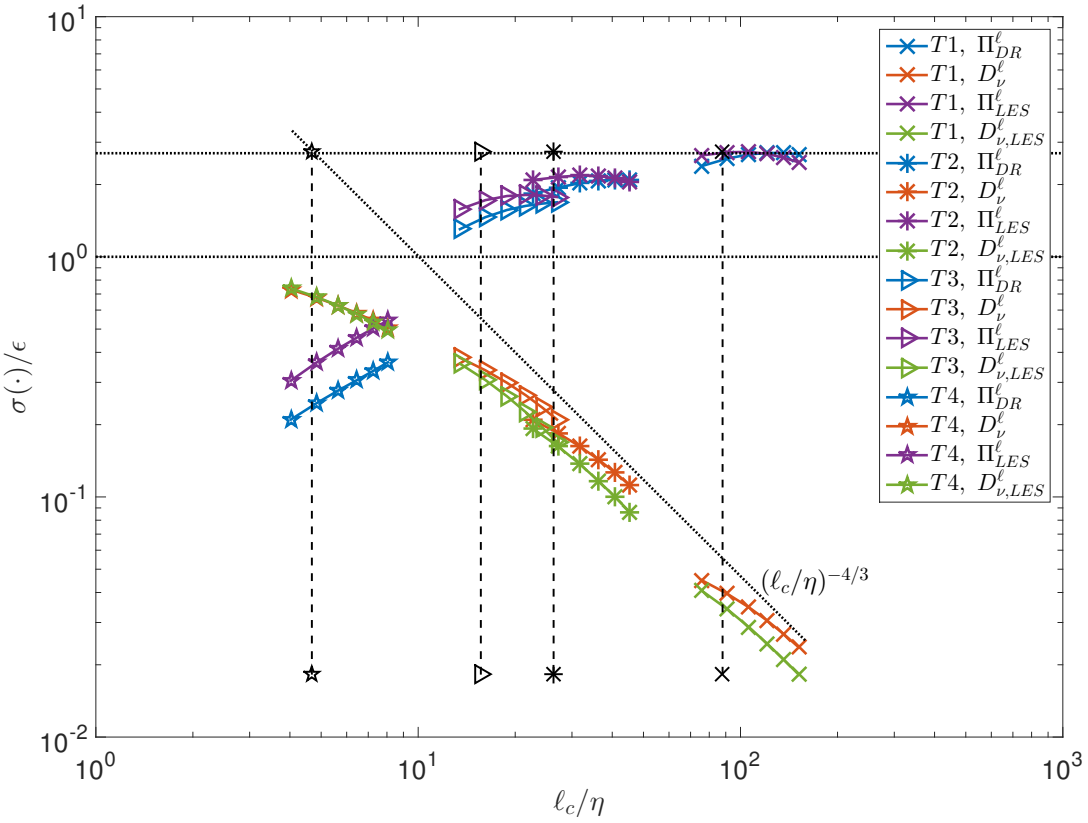

Figure 6.13: Standard deviation (computed over space and time) of Π_{DR}^ℓ, $\mathscr{D}_\nu^\ell$, Π_{LES}^ℓ and $\mathscr{D}_{\nu,LES}^\ell$ terms wrt. scales. The curves corresponding to Π_{DR}^ℓ are plotted in blue, those corresponding to $\mathscr{D}_\nu^\ell$ are plotted in red, those corresponding to Π_{LES}^ℓ are plotted in purple and those corresponding to $\mathscr{D}_{\nu,LES}^\ell$ are plotted in green. The vertical dashed lines correspond to the values of the interrogation volume size.

Concerning the standard deviation (computed over space and time) shown on figure 6.13, there is no qualitative difference either. The standard deviations of the corresponding terms of each pair are even closer than the space-time averages, overlapping exactly for the viscous terms in the dissipative range and for the inter-scale transfer terms in the inertial range. In the inertial range, we have $\langle \mathscr{D}_\nu^\ell \rangle \approx 1.3 \langle \mathscr{D}_{\nu,LES}^\ell \rangle$ and in the dissipative range, we have $\langle \Pi_{LES}^\ell \rangle \approx 1.5 \langle \Pi_{DR}^\ell \rangle$.

As a conclusion, when considering global quantities, using either one or the other of the pairs (inter-scale transfer, viscous dissipation) does not lead to significantly different conclusions. The ratio between the global quantities is however scale dependent.

4.2 Probability density functions

For either the inter-scale transfer or the viscous dissipation terms, the pdfs have the same shape and behaviour when ℓ_c/η is varied. For the viscous dissipation terms, the pdfs of $\mathscr{D}^\ell_{\nu,LES}$ do not feature a saturation at low values, compared to the pdfs of $\mathscr{D}^\ell_\nu$.
As there is no major difference between the pdfs of $\mathscr{D}^\ell_{\nu,LES}$ and Π^ℓ_{LES} compared to those of $\mathscr{D}^\ell_\nu$ and Π^ℓ_{DR} , we do not show them here. However, we give the skewness and kurtosis of these pdfs instead. As the pdfs, they feature the same behaviour with respect to scales as the skewness and kurtosis of $\mathscr{D}^\ell_\nu$ and Π^ℓ_{DR}. It can still be noted that the kurtosis of Π^ℓ_{DR} is quite higher than the one of Π^ℓ_{LES}, especially at $\ell_c/\eta = 8$, in the dissipative range, where it is more than twice higher. The kurtosis of $\mathscr{D}^\ell_{\nu,LES}$ is constant, but 1.4 times larger than the one of $\mathscr{D}^\ell_\nu$.

ℓ_c/η	Case	Skewness		Kurtosis	
		Π^ℓ_{LES}	$\mathscr{D}^\ell_{\nu,LES}$	Π^ℓ_{LES}	$\mathscr{D}^\ell_{\nu,LES}$
150	T1	5.8	3.9	150	35
45	T2	6.3	3.7	150	34
27	T3	7.4	3.6	240	30
8	T4	8.9	4.0	260	36

Table 6.3: Skewness and kurtosis of Π^ℓ_{LES} and $\mathscr{D}^\ell_{\nu,LES}$ at several values of ℓ_c/η.

4.3 Joint behaviour of Π^ℓ_{LES} and $\mathscr{D}^\ell_{\nu,LES}$

Overall, the joint behaviour of Π^ℓ_{LES} and $\mathscr{D}^\ell_{\nu,LES}$ is the same as the joint behaviour of Π^ℓ_{DR} and $\mathscr{D}^\ell_\nu$: the joint pdfs have the same triangular shape meaning that a strong viscous dissipation can occur for any value of the inertial transfer whereas a strong inter-scale transfer is always correlated to a strong viscous dissipation.
The ratio $\Pi^\ell_{LES}/\mathscr{D}^\ell_{\nu,LES}$ is taking higher values when ℓ_c/η is increased, as can be seen from figure

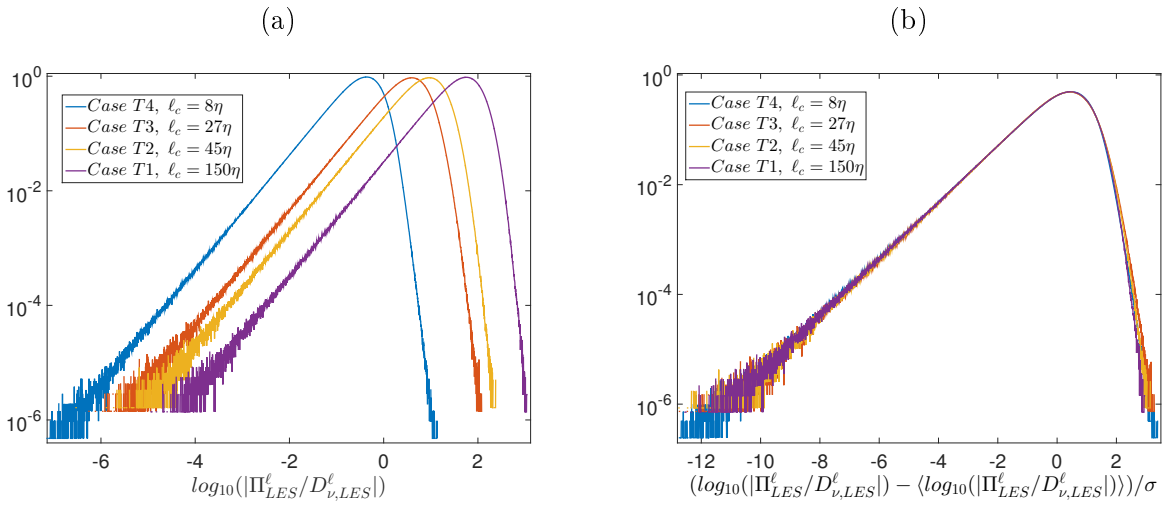

Figure 6.14: (Unconditioned) probability density functions of the logarithm of the absolute value of the ratio $\Pi^\ell_{DR}/\mathscr{D}^\ell_\nu$ at several scales. (a) Raw pdfs. (b) Centered-reduced pdfs.

6.14 (a) : the pdfs of the ratio $\Pi^{\ell}_{LES}/\mathscr{D}^{\ell}_{\nu,LES}$, which have the same shape as the pdfs of the ratio $\Pi^{\ell}_{DR}/\mathscr{D}^{\ell}_{\nu}$, are shifted towards the right. We also analyze the pdfs of the ratio Π^{ℓ}_{LES} and $\mathscr{D}^{\ell}_{\nu,LES}$ conditioned on positive and negative values of this ratio. The same behaviour as for the pdfs of the ratio $|\Pi^{\ell}_{DR}/\mathscr{D}^{\ell}_{\nu}|$ is observed : the maximum of the pdf conditioned on the negative values is slightly lower than the maximum of the pdf conditioned on positive values, but both maxima are coming closer as ℓ_c/η is increased.

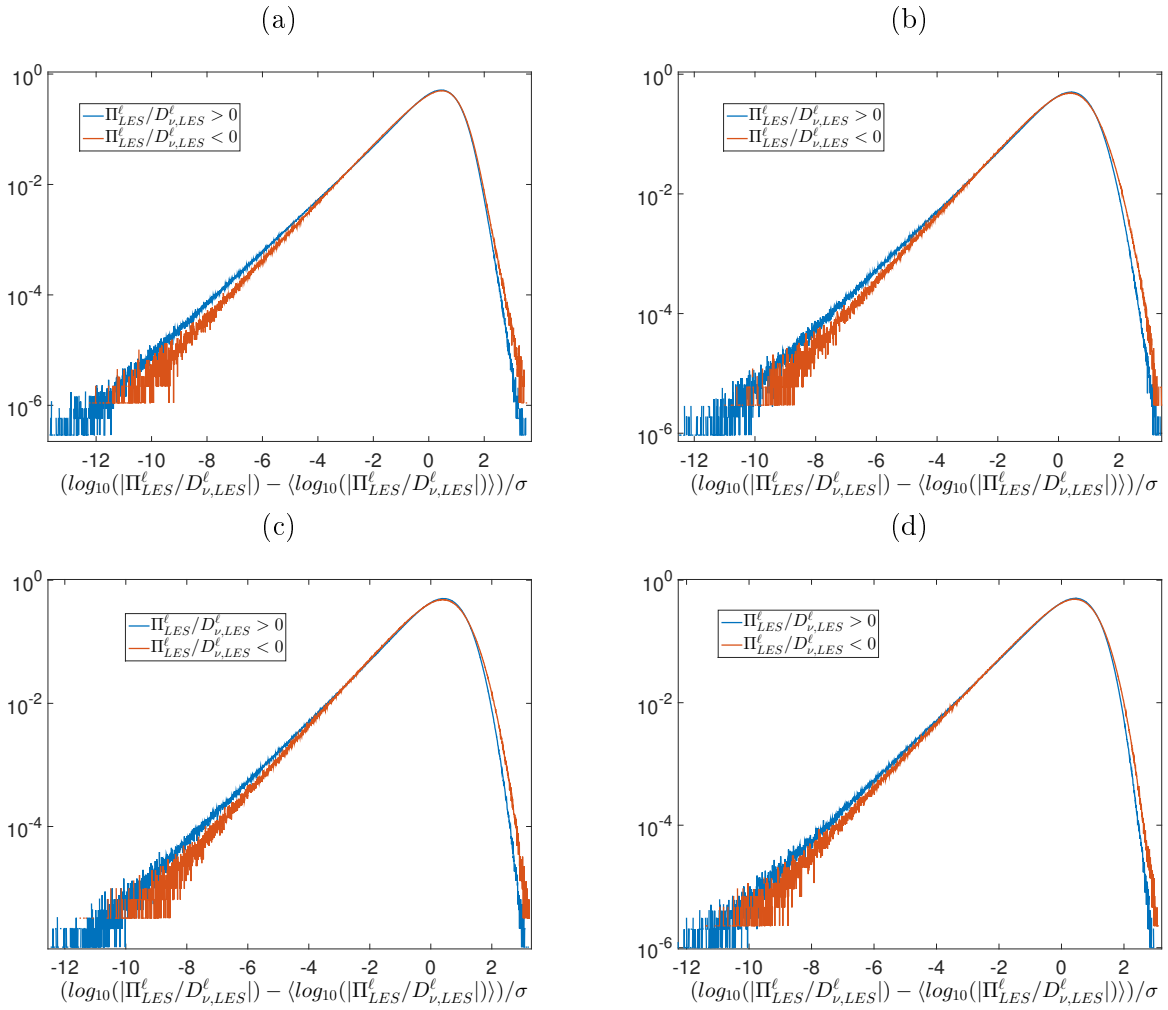

Figure 6.15: Centered-reduced probability density function of the logarithm of the absolute value of the ratio $\Pi^{\ell}_{DR}/\mathscr{D}^{\ell}_{\nu}$. Blue curves correspond to the pdf conditioned on positive values of the ratio, red curves to the pdf conditioned on negative values of the ratio. (a) $\ell_c/\eta = 8$ (obtained with case T4). (b) $\ell_c/\eta = 27$ (obtained with case T3). (c) $\ell_c/\eta = 45$ (obtained with case T2). (d) $\ell_c/\eta = 150$ (obtained with case T1).

When considering the centered-reduced pdfs, we can notice two differences though. First, the centered-reduced pdfs of the ratio $\Pi^{\ell}_{LES}/\mathscr{D}^{\ell}_{\nu,LES}$ conditioned on positive values of the ratio and the one conditioned on negative values are not collapsing when ℓ_c/η is increased, as can be shown on figure 6.15. This is at variance with the behaviour of the corresponding pdfs for the ratio $\Pi^{\ell}_{DR}/\mathscr{D}^{\ell}_{\nu}$. This means that the asymmetry between positive and negative values of Π^{ℓ}_{LES} holds both in the inertial and in the dissipative range. Second, both the left and right tails of the unconditioned centered-reduced pdfs of $log_{10}(|\Pi^{\ell}_{LES}/\mathscr{D}^{\ell}_{\nu,LES}|)$ seem to be independent from ℓ_c/η (as can be seen

on figure 6.14(b)), whereas the right tail of the pdf of $log_{10}(|\Pi^\ell_{DR}/\mathscr{D}^\ell_\nu|)$ is shrinking when ℓ_c/η is decreased. Depending on the ratio considered, we are led to different conclusions : either the extreme events of the ratio of the inter-scale transfer over the viscous dissipation are less probable in the dissipative range than in the inertial range, or they are as probable.

4.4 Joint behaviour of Π^ℓ_{DR} and Π^ℓ_{LES}

In order to investigate further the difference between the two pairs (Π^ℓ_{LES}, $\mathscr{D}^\ell_{\nu,LES}$) and ($\Pi^\ell_{DR}$, $\mathscr{D}^\ell_\nu$), we study here the distribution of the ratio between the two inter-scale transfer terms as well as their joint pdf.

4.4.1 Pdfs of the ratio $\Pi^\ell_{DR}/\Pi^\ell_{LES}$

Figure 6.16 shows the pdfs of the logarithm of the ratio $|\Pi^\ell_{DR}/\Pi^\ell_{LES}|$ for the values of ℓ_c/η studied previously. The pdfs conditioned on negative values of the ratio as well as pdfs conditioned on positive values of the ratio are shown in addition to the unconditioned pdfs.
All the pdfs are shifted towards higher values of the ratio when ℓ_c/η is increased. This is in accordance with the behaviour of the space-time averages and standard deviations : the difference between these quantities for Π^ℓ_{DR} and Π^ℓ_{LES} was smaller in the inertial range than in the dissipative range.
The pdfs conditioned on negative values of the ratio reach their maximum for a value of $|\Pi^\ell_{DR}/\Pi^\ell_{LES}|$ which is slightly higher than for the pdfs conditioned on positive values. It is not very clear whether the difference between the maxima is decreasing or not when ℓ_c/η is increased. The pdfs conditioned on negative values of the ratio are flatter than the ones conditioned on positive values in that sense that the maximum is lower but the tails are higher. They are also more symmetrical, especially at $\ell_c/\eta = 8$: the pdf conditioned on positive values of the ratio is very skewed towards higher values. This skewness of the pdf of the ratio is decreasing when ℓ_c/η is increasing : values higher than the most probable ones are not anymore favoured in the inertial range.

4.4.2 Joint pdfs of Π^ℓ_{LES} and Π^ℓ_{DR}

The joint behaviour of Π^ℓ_{DR} and Π^ℓ_{LES} can also be captured by their joint pdf, shown on figure 6.17. These joint pdfs spread around the lines corresponding to the most probable ratio. For $\ell_c/\eta = 8$, the asymmetry of the pdf of $log_{10}(|\Pi^\ell_{DR}/\Pi^\ell_{LES}|)$ can be seen in the joint pdf which is not symmetrical with respect to the line corresponding to the most probable ratio.

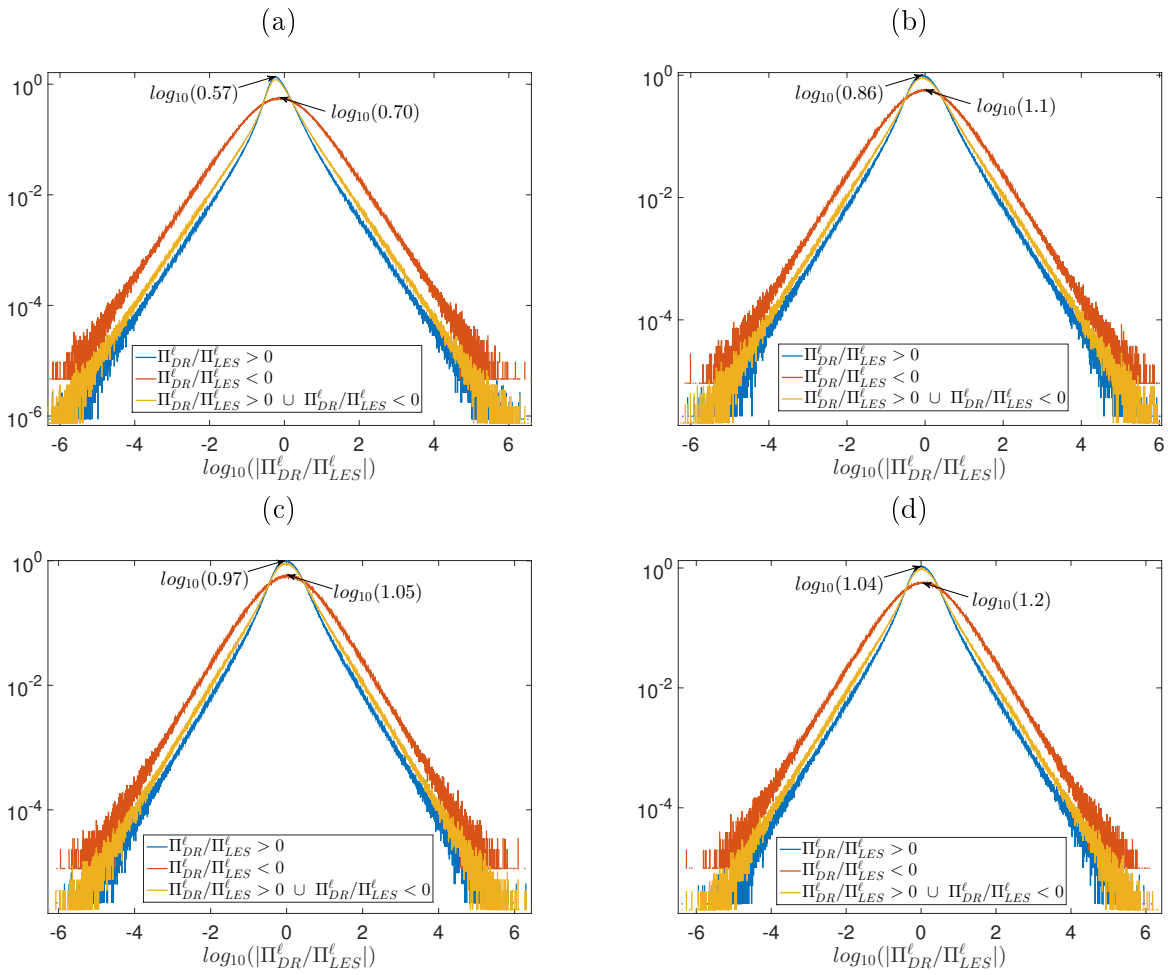

Figure 6.16: Probability density function of the logarithm of the absolute value of the ratio $\Pi^\ell_{DR}/\Pi^\ell_{LES}$. Blue curves correspond to the pdf conditioned on positive values of the ratio, red curves to the pdf conditioned on negative values of the ratio and yellow curves to unconditioned pdf. The arrows show the maxima of the blue and red curves. (a) $\ell_c/\eta = 8$ (obtained with case T4). (b) $\ell_c/\eta = 27$ (obtained with case T3). (c) $\ell_c/\eta = 45$ (obtained with case T2). (d) $\ell_c/\eta = 150$ (obtained with case T1).

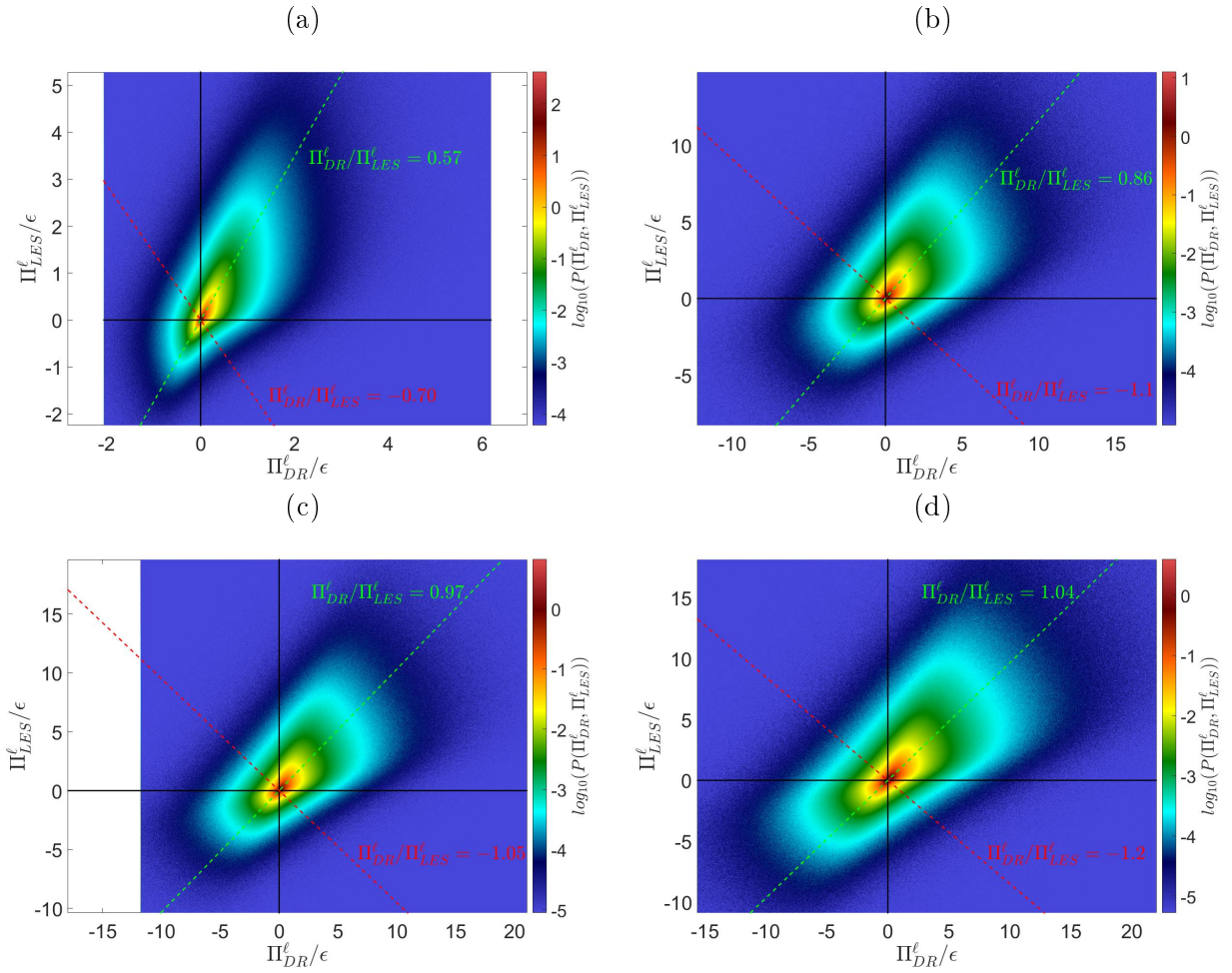

Figure 6.17: Logarithm of the joint probability density function of Π^ℓ_{DR} and Π^ℓ_{LES}. The vertical and horizontal axes are in linear coordinates. The black lines correspond to $\Pi^\ell_{DR} = 0$ and $\Pi^\ell_{LES} = 0$. The dashed lines correspond to the most probable ratio $\Pi^\ell_{DR}/\Pi^\ell_{LES}$, for positive values of this ratio (green) or negative values (red). The axis and color scales are different from a figure to another. (a) $\ell_c/\eta = 8$ (obtained with case T4). (b) $\ell_c/\eta = 27$ (obtained with case T3). (c) $\ell_c/\eta = 45$ (obtained with case T2). (d) $\ell_c/\eta = 150$ (obtained with case T1).

4.5 Joint behaviour of $\mathscr{D}_\nu^\ell$ and $\mathscr{D}_{\nu,LES}^\ell$

Differences observed between the pairs $(\Pi_{LES}^\ell, \mathscr{D}_{\nu,LES}^\ell)$ and $(\Pi_{DR}^\ell, \mathscr{D}_\nu^\ell)$ may also be due to differences between the dissipation terms. Such differences may be studied from the joint pdf of the two viscous dissipation terms, shown on figure 6.18 for different values of ℓ_c/η.
These pdfs have a kind of a plume shape. At $\ell_c/\eta = 8$, it is oriented along the line $\mathscr{D}_\nu^\ell = \mathscr{D}_{\nu,LES}^\ell$. At higher values of ℓ_c/η, it falls under this line, in accordance with the behaviour of the space-time averages and standard deviations computed over space and time. Indeed, these statistical quantities are larger for $\mathscr{D}_\nu^\ell$ than for $\mathscr{D}_{\nu,LES}^\ell$. Also, the aspect ratio of the plume seems larger at $\ell_c/\eta = 8$ than at larger values. This means that $\mathscr{D}_\nu^\ell$ and $\mathscr{D}_{\nu,LES}^\ell$ have a closer behaviour at $\ell_c/\eta = 8$.

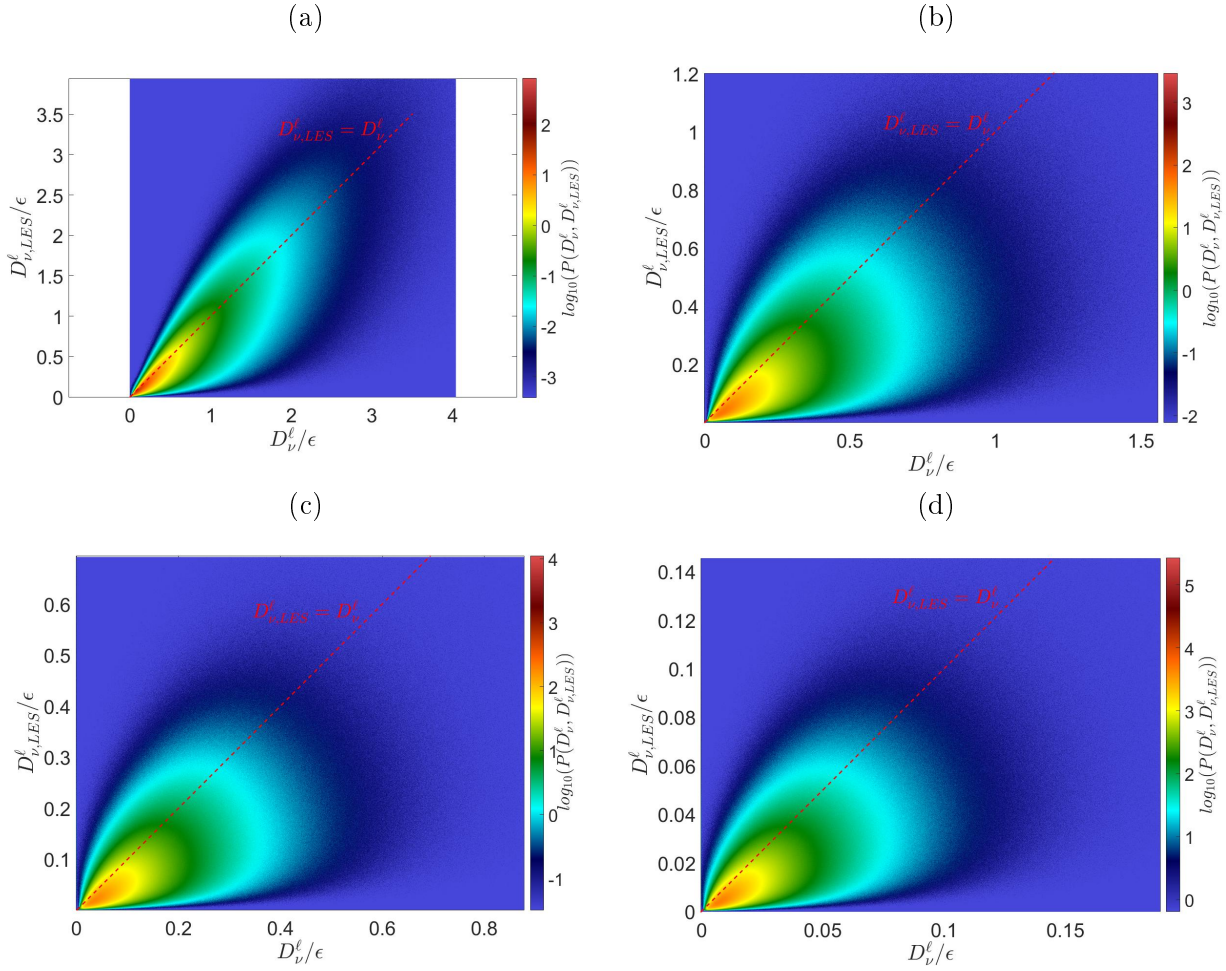

Figure 6.18: Logarithm of the joint probability density function of $\mathscr{D}_\nu^\ell$ and $\mathscr{D}_{\nu,LES}^\ell$. The vertical and horizontal axes are in linear coordinates. The red dashed line corresponds to $\mathscr{D}_\nu^\ell = \mathscr{D}_{\nu,LES}^\ell$. The axis and color scales are different from a figure to another. (a) $\ell_c/\eta = 8$ (obtained with case T4). (b) $\ell_c/\eta = 27$ (obtained with case T3). (c) $\ell_c/\eta = 45$ (obtained with case T2). (d) $\ell_c/\eta = 150$ (obtained with case T1).

4.6 Possible explanation for the differences between the two pairs of terms

Here, we try to provide a physical explanation for the differences between the two pairs of inter-scale transfer and viscous dissipation terms. First, we highlight the subtle difference between the inter-scale transfer terms ; then we analyze the expression for $\mathscr{D}_\nu^\ell$ in order to see how it differs from $\mathscr{D}_{\nu,LES}^\ell$.

4.6.1 Different roles of Π_{DR}^ℓ and Π_{LES}^ℓ

The different roles of the inter-scale transfer terms Π_{DR}^ℓ and Π_{LES}^ℓ are highlighted when one considers the transport equation of the energy contained in the filtered velocity field $\mathbf{u}^\ell$, the transport equation of the energy contained in the subgrid fluctuations $\mathbf{u}-\mathbf{u}^\ell$, and the transport equation of the scalar product $\mathbf{u}^\ell \cdot (\mathbf{u}-\mathbf{u}^\ell)$. These equations are derived in appendix F. We recall them here :

$$\partial_t \frac{{u_i^\ell}^2}{2} + \partial_j[u_j^\ell \frac{{u_i^\ell}^2}{2} + u_i^\ell \tau_{ij}^\ell + u_j^\ell p^\ell] = \nu\Delta\frac{{u_i^\ell}^2}{2} - \mathscr{D}_{\nu,LES}^\ell - \Pi_{LES}^\ell \tag{6.15}$$

$$\begin{aligned} &\partial_t \frac{(u_i-u_i^\ell)^2}{2} + \partial_j[u_j \frac{(u_i-u_i^\ell)^2}{2} - (u_j-u_j^\ell)\frac{{u_i^\ell}^2}{2}] \\ &+\partial_j[u_i^\ell \tau_{ij}^\ell - \frac{1}{2}(u_j u_i u_i)^\ell + \frac{1}{2}u_j(u_i u_i)^\ell + (u_j-u_j^\ell)(p-p^\ell)] \\ &= \nu\Delta\frac{(u_i-u_i^\ell)^2}{2} - \nu\partial_j(u_i-u_i^\ell)\partial_j(u_i-u_i^\ell) - \Pi_{LES}^\ell + 2\Pi_{DR}^\ell \end{aligned} \tag{6.16}$$

$$\begin{aligned} &\partial_t u_i^\ell(u_i-u_i^\ell) + \partial_j[u_j u_i u_i^\ell - u_j^\ell u_i^\ell u_i^\ell + 2\tau_{ij}^\ell] \\ &+\partial_j[\frac{1}{2}(u_j u_i u_i)^\ell - \frac{1}{2}u_j(u_i u_i)^\ell + u_j^\ell(p-p^\ell) + (u_j-u_j^\ell)p^\ell] \\ &= \nu\Delta(u_i^\ell(u_i-u_i^\ell)) - \nu\partial_j u_i^\ell \partial_j(u_i-u_i^\ell) + 2\Pi_{LES}^\ell - 2\Pi_{DR}^\ell \end{aligned} \tag{6.17}$$

Note that the sum of these three equations is the transport equation 1.14 of the total energy of the velocity field $\mathbf{u}$ obtained in chapter 1. Indeed :

$$\frac{{u_i}^2}{2} = \frac{{u_i^\ell}^2}{2} + \frac{(u_i-u_i^\ell)^2}{2} + u_i^\ell(u_i-u_i^\ell) \tag{6.18}$$

These equations show that the time variation of the energy contained in the filtered velocity field at scale ℓ, of the energy contained in the subgrid fluctuations and of the scalar product $\mathbf{u}^\ell \cdot (\mathbf{u}-\mathbf{u}^\ell)$ are all due to spatial transport (the term in $\partial_j[]$), viscous diffusion (the term in $\nu\Delta()$), viscous dissipation (the term in $\nu\nabla()\nabla()$) and inter-scale transfer terms (the remaining terms of the right-hand-side). Analyzing these equations allows to make a fine difference between Π_{DR}^ℓ and Π_{LES}^ℓ : Π_{LES}^ℓ only appears in the transport equation of the energy contained in the filtered velocity field at scale ℓ. Therefore, it can be considered as the rate of energy leaving the scales larger than ℓ. However, in the transport equation for the energy contained in the subgrid fluctuations, the incoming energy transfer term is $-\Pi_{LES}^\ell + 2\Pi_{DR}^\ell$. The Duchon-Robert term is involved here. As for the scalar product $\mathbf{u}^\ell \cdot (\mathbf{u}-\mathbf{u}^\ell)$, the inter-scale energy transfer term is $2\Pi_{LES}^\ell - 2\Pi_{DR}^\ell$, i.e. the difference between the transfer coming from the large scale Π_{LES}^ℓ and the transfer arriving to the small scales $-\Pi_{LES}^\ell + 2\Pi_{DR}^\ell$. This suggests that the energy transfer between the scales larger than ℓ and the

scales smaller than ℓ (the so-called fluctuations) happens in two steps, as sketched in figure 6.19 : first, energy is transferred from scales larger than ℓ to the scalar product $\mathbf{u}^\ell \cdot (\mathbf{u} - \mathbf{u}^\ell)$, then it is transferred from the scalar product to scales smaller than ℓ. The two inter-scale transfers are not a priori equal, and therefore Π^ℓ_{DR} and Π^ℓ_{LES} are not equal (note that if $\Pi^\ell_{DR} = \Pi^\ell_{LES}$, then the energy transfer from scales larger than ℓ to the scalar product $\mathbf{u}^\ell \cdot (\mathbf{u} - \mathbf{u}^\ell)$, and the energy transfer from the scalar product to scales smaller than ℓ are equal too). Hence, differences between Π^ℓ_{DR} and Π^ℓ_{LES} may be due to this two-step energy transfer.

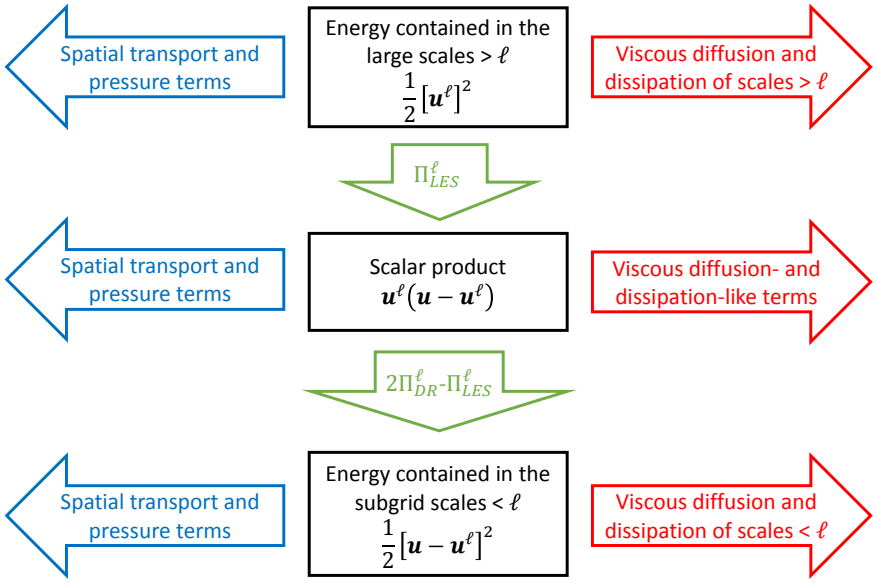

Figure 6.19: Schematic representation of the 2-step energy transfer. Spatial transport and pressure terms are represented by blue arrows, viscous effects by red arrows and inter-scale transfer terms by green arrows.

These equations allow to explain why the space-time averages Π^ℓ_{DR} and Π^ℓ_{LES} differ on average from a factor close to 2 in the dissipative range, but tend to be overall equal in the inertial range. Indeed, averaging the equations 6.16 and 6.17 over space and time and assuming homogeneity (in space and time) leads to :

$$\langle \Pi^\ell_{LES} \rangle - 2\langle \Pi^\ell_{DR} \rangle = \nu \langle \Delta \frac{(u_i - u_i^\ell)^2}{2} \rangle - \nu \langle \partial_j (u_i - u_i^\ell) \partial_j (u_i - u_i^\ell) \rangle \tag{6.19}$$

$$\langle \Pi^\ell_{DR} \rangle - \langle \Pi^\ell_{LES} \rangle = -\nu \frac{\langle \Delta [u_i^\ell (u_i - u_i^\ell)] \rangle}{2} + \nu \langle \partial_j u_i^\ell \partial_j (u_i - u_i^\ell) \rangle \tag{6.20}$$

The brackets stand for space-time averages.
In the dissipative range, u_i^ℓ tends to u_i. The right-hand-side terms of equation 6.19 are terms of second order whereas terms of equation 6.20 are of order one. This suggests to neglect the r.h.s. terms of equation 6.19, leading to $\langle \Pi^\ell_{LES} \rangle = 2\langle \Pi^\ell_{DR} \rangle$. In the inertial range, the r.h.s. terms of equation 6.19 involve the laplacian of $(u_i - u_i^\ell)^2$ and the gradient of $u_i - u_i^\ell$, whereas the r.h.s. terms of equation 6.20 involve the laplacian of $u_i(u_i - u_i^\ell)$ and the gradients of u_i^ℓ and $u_i - u_i^\ell$.

As $u_i - u_i^\ell$ contains the small scales, and u_i^ℓ the large scales, we can reasonably assume that the derivatives of $u_i - u_i^\ell$ are larger than those of u_i^ℓ : the viscous effects are important only for the small scales. If we neglect the r.h.s terms of equation 6.20, we then get $\langle \Pi_{LES}^\ell \rangle = \langle \Pi_{DR}^\ell \rangle$.

Further, we also noticed that the most probable ratio $\Pi_{DR}^\ell / \Pi_{LES}^\ell$ was about 0.5 in the dissipative range with a strong skewness of the pdf of the logarithm of the ratio favouring values higher than 0.5, and that this most probable ratio was increasing to close to 1 in the inertial range. This can be interpreted in the scope of equation 6.16 : the energy transfer received by the scales smaller than ℓ is $2\Pi_{DR}^\ell - \Pi_{LES}^\ell$. Favouring values of $\Pi_{DR}^\ell / \Pi_{LES}^\ell$ larger than 0.5 is equivalent to favouring direct inter-scale transfer to small scales.

4.6.2 Link between $\mathscr{D}_\nu^\ell$ and $\mathscr{D}_{\nu,LES}^\ell$.

The differences between the two viscous dissipation terms can be understood by analyzing the definition of $\mathscr{D}_\nu^\ell$. We have :

$$\begin{aligned}
\mathscr{D}_\ell^\nu &= \nu \int \nabla^2 \phi^\ell(\xi) \frac{\delta \mathbf{u}(x,\xi)^2}{2} d\xi \\
&= \nu \int \nabla^2 \phi^\ell(\xi) \frac{\mathbf{u}(x+\xi)^2 - 2\mathbf{u}(x+\xi)\mathbf{u}(x) + \mathbf{u}(x)^2}{2} d\xi \\
&= \nu \int \nabla^2 \phi^\ell(\xi) \frac{\mathbf{u}(x+\xi)^2}{2} d\xi - \nu \int \nabla^2 \phi^\ell(\xi) \mathbf{u}(x)\mathbf{u}(x+\xi) d\xi + \nu \int \nabla^2 \phi^\ell(\xi) \frac{\mathbf{u}(x)^2}{2} d\xi \\
&= \nu \partial_i \partial_i (u_j u_j)^\ell / 2 - \nu u_i \partial_j \partial_j u_i^\ell \\
&= \nu (\partial_i u_j \partial_i u_j)^\ell + \nu (u_j \partial_i \partial_i u_j)^\ell - \nu u_i \partial_j \partial_j u_i^\ell
\end{aligned}$$

The first term of the last line is the total viscous dissipation filtered at scale ℓ (the one involved in the K62 theory). The second one corresponds to the total power of viscous forces (which can be splitted in viscous diffusion and viscous dissipation) filtered at scale ℓ. The last one also resembles the power of viscous forces, but it is mixing the total velocity field and the filtered velocity field. When ℓ tends to 0, the last two terms cancel, and the first term tends to the total viscous dissipation, as $\mathscr{D}_{\nu,LES}^\ell = \nu \partial_i u_j^\ell \partial_i u_j^\ell$. However, for ℓ in the inertial range, there is no reason why both terms should be equal.

Summary of chapter 6

The main results of this chapter are the following :

- Using either the pair (Π_{LES}^ℓ, $\mathscr{D}_{\nu,LES}^\ell$) or the pair ($\Pi_{DR}^\ell$, $\mathscr{D}_\nu^\ell$) leads to the same, expected picture of the global behaviour of energy transfers : in the dissipative range, the average viscous dissipation term is more important than the inertial one ; in the inertial range, the average viscous dissipation term is decreasing following the Kolmogorov 1941 scaling ($\propto \ell^{-4/3}$) whereas the inertial term becomes more important and seems to saturate, also in accordance with the Kolmogorov 1941 scaling ($\propto \ell^0$).
- The shape of the pdfs of the viscous dissipation term seems to be independent from the scale whereas the pdf of the inertial term is more skewed and pinched in the dissipative range than in the inertial one, meaning that direct inter-scale transfer is favoured in the dissipative range, and that the probability of extreme events decreases less than the one of medium-amplitude events when ℓ_c/η is decreased.

- However, the extreme events of the inertial term are always correlated to extreme events of the viscous dissipation term. This potentially hinders the formation of singularities. This also motivates the study of extreme events of the ratio of the inertial term over the viscous dissipation term. This ratio takes smaller values in the dissipative range compared to the inertial one, with still largest values around 10.

- There are some differences in the statistics of the pair of terms (Π^ℓ_{LES}, $\mathscr{D}^\ell_{\nu,LES}$) compared to the pair of terms (Π^ℓ_{DR}, $\mathscr{D}^\ell_\nu$). In particular, the extreme events of the ratio $\Pi^\ell_{DR}/\mathscr{D}^\ell_\nu$ are less probable in the dissipative range than in the inertial range, whereas the extreme events of the ratio $\Pi^\ell_{LES}/\mathscr{D}^\ell_{\nu,LES}$ are as probable in the dissipative range as in the inertial range. The differences between both pairs of terms are probably due to the fact that the terms have slightly different physical meanings : Π^ℓ_{LES} corresponds to the inter-scale transfer leaving the scales larger than ℓ whereas Π^ℓ_{DR} is part of the inter-scale transfer reaching the scales smaller than ℓ ; $\mathscr{D}^\ell_{\nu,LES}$ corresponds to the viscous dissipation of the scales larger than ℓ whereas $\mathscr{D}^\ell_\nu$ corresponds to the sum of the total viscous dissipation filtered at scale ℓ and diffusive terms. Though Π^ℓ_{DR} and Π^ℓ_{LES} have different definitions and meanings, their behaviour is similar. In the dissipative range, their behaviour is more different than in the inertial range. This may be a sign that some lack of regularity affects Π^ℓ_{LES}, as explained in chapter 2, and encourages to use Π^ℓ_{DR} only.

Chapter 7

Link with intermittency

In this chapter, we reproduce an article published in PRE in 2018. This article aims at showing the link between the prints of singularities that we study in this thesis and the intermittency in turbulence. It starts with statistical analyses of 2D versions of the Duchon-Robert term and of a viscous term, very similar to those performed in the previous chapter on the 3D terms. There is also an analysis of the tail of the pdf of the (2D) Duchon-Robert term by means of a Generalized Pareto Distribution fit. The impact of extreme events of the (2D) Duchon-Robert term on the structure functions of the velocity increment is then highlighted : the prints of singularities seem to be responsible for the intermittency. This strongly supports the phenomenological interpretation of the multifractal model which invokes the existence of a finite set of Hölder exponents in the flow in order to explain the intermittent scalings of the structure functions. Indeed, the extreme events of the Duchon-Robert term mark in principle the low regularity areas of the flow ; these areas could be characterized by a low Hölder exponent.

1 A posteriori remarks

Before reproducing the PRE article, we make some remarks allowing to compare the results of the paper with the other results of this thesis that have been obtained later with improved methods or techniques.

1.1 Data set parameters

The data set used in this paper is the 2D data set presented in chapter 5 ; the cases have the same name. However, one could be surprised to find slightly different values of the Kolmogorov scale in table I of the paper. This is due to the fact that in the paper, they are computed with the value of the average dissipation rate obtained in [Saw et al., 2018] by a fit of the structure functions, wherea in this thesis we use the average dissipation rate based on the torque measurements. This also explains why the Taylor-scale Reynolds numbers are different. However, this does not affect the meaning of the paper.

1.2 Viscous term

In this paper, we used a viscous term slightly different from the one used in this thesis because the latter one had not been derived yet.

The viscous dissipation term used in the paper is :

$$\mathscr{D}^{\ell}_{\nu,PRE} = -\nu \int \nabla^2 \phi^{\ell}(\xi) u_i(x) u_i(x+\xi) d\xi \tag{7.1}$$

whereas the one used in this thesis is :

$$\mathscr{D}^{\ell}_{\nu} = \nu \int \nabla^2 \phi^{\ell}(\xi) \frac{\delta \mathbf{u}(x,\xi)^2}{2} d\xi = \nu \int \nabla^2 \phi^{\ell}(\xi) \frac{[\mathbf{u}(x+\xi) - \mathbf{u}(x)]^2}{2} d\xi \tag{7.2}$$

It can be shown that :

$$\mathscr{D}^{\ell}_{\nu} = \nu \partial_i \partial_i (u_j u_j)^{\ell}/2 + \mathscr{D}^{\ell}_{\nu,PRE} \tag{7.3}$$

Actually, $\mathscr{D}^{\ell}_{\nu,PRE}$ rather corresponds to a viscous diffusion term than a viscous dissipation term. This is why it can take negative values. Also, the joint pdfs of Π^{ℓ}_{DR} and $\mathscr{D}^{\ell}_{\nu}$ are different from the joint pdfs of Π^{ℓ}_{DR} and $\mathscr{D}^{\ell}_{\nu,PRE}$. However, this does not appear clearly in the paper as linear coordinates are used whereas logarithmic coordinates were preferred in chapter 6.

In addition to using a different viscous dissipation term, only 2D versions of this term and of the Duchon-Robert term were studied in the PRE article.

1.3 2D vs. 3D

The main difference between the PRE article and the other results of this thesis is the fact that only 2D versions of the Duchon-Robert term and of the viscous term are computed in the article. Indeed, the paper was written based on the 2D data set, i.e. on 2D-3C velocity fields obtained by stereoscopic PIV (SPIV). It is not possible to compute the derivative in the direction perpendicular to the measurement plane. In the 2D versions of the Duchon-Robert and of the viscous terms, all derivatives along this direction are set to 0.
This may explain the differences between the space-time averages of the 2D and 3D terms, plotted on figure 7.1. On this figure, the space-time averages of Π^{ℓ}_{DR} and $\mathscr{D}^{\ell}_{\nu}$ for SPIV cases A to E and TPIV cases T1 to T5 are plotted. Note that in 2D, we used a smoothing function ϕ^{ℓ} such that $\phi^{\ell}(\mathbf{x}) \propto \exp(-\mathbf{x}^2/(2\ell^2))$ so that $\ell_c = \pi\ell/\sqrt{\ln(2)} \approx 3.8\ell$. In 2D, ℓ_c is not limited by the thickness of the measurement volume, therefore we have access to larger scales. The difference between ℓ_c and X (interrogation window size) is large enough and the principle of UV locality applies (see second part of chapter 2). This probably explains why there is not any bend of the SPIV curves at small ℓ_c (contrary to TPIV curves), and this allows to compare the different points of a given curve with each other. In 3D, ℓ_c is closer to the interrogation volume size X so that the contributions from smaller scales are more filtered, and the 3D terms are underestimated too (see second section of chapter 2). Also, there is a strong difference of filtering between two points of the same curve ; however, the filtering is the same for the rightmost (or n^{th} rightmost) points of two different curves, and two such points can be compared. For the rightmost point, ℓ_c/X is the largest so that the impact of PIV filtering is the lowest. These rightmost points are surrounded by a circle on figure 7.1.
On figure 7.1, we can see that the average 2D terms are lower than the average 3D terms, especially in the case of the Duchon-Robert term. A consequence is that the saturation value of the 2D viscous term in the dissipative range is larger than the saturation value of the 2D Duchon-Robert term in the inertial range. On the contrary, they seem almost equal for the 3D terms. In principle, both

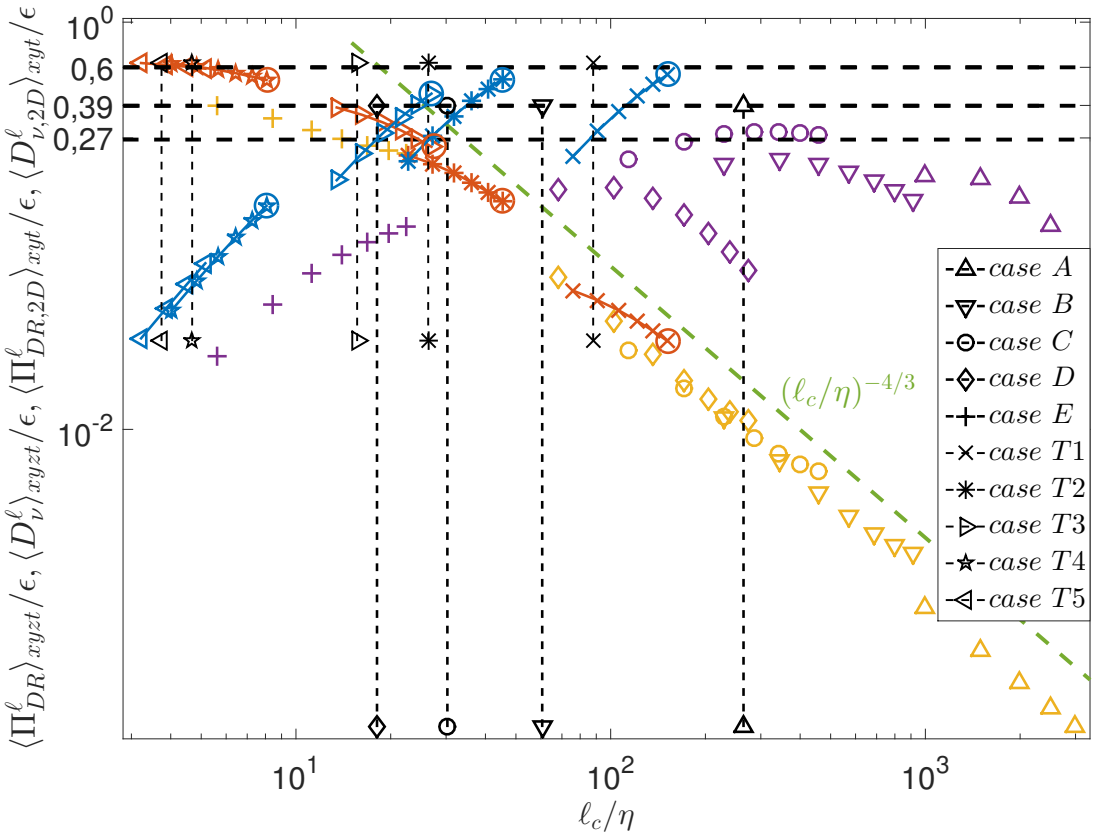

Figure 7.1: Space-time averages of Π^ℓ_{DR} and $\mathscr{D}^\ell_\nu$ for SPIV cases A to E and TPIV cases T1 to T5. For SPIV cases, Π^ℓ_{DR} is in purple and $\mathscr{D}^\ell_\nu$ is in yellow, whereas for TPIV cases Π^ℓ_{DR} is in blue and $\mathscr{D}^\ell_\nu$ is in red. Different cases have different symbols. The vertical black dashed lines correspond to the interrogation window or volume size of the different cases ; for case E, it is outside the figure, at $\ell_c/\eta = 1.5$. The surrounded points are the rightmost points of the curves corresponding to TPIV cases ; for these points the impact of PIV filtering is the lowest.

should be equal to the average dissipation rate (equal to the average inter-scale transfer rate in steady state). This 2D effect is probably due to the missing out-of-plane derivative in 2D cases. This suggests that the underestimation due to the missing derivative in 2D is stronger than the underestimation due to the strong filtering of small scales in 3D. For the viscous dissipation term, the difference in the definition is also probably involved.

The 2D effect may also explain the differences between the pdfs of the Duchon-Robert term : the increase of intermittency in the dissipative range is hardly seen on the 2D data (figure 2 of the paper).

Though there are differences, the main statistical behaviour is captured by the 2D terms. This allows to trust to some extent the results of the paper that have not been re-evaluated in 3D. As for the re-evaluated results, it is of course better to consider the 3D ones, presented in chapter 6.

2 PRE article

We now reproduce the following article : [Debue et al., 2018b], available at : `https://journals.aps.org/pre/abstract/10.1103/PhysRevE.97.053101`.

Dissipation, intermittency, and singularities in incompressible turbulent flows

P. Debue,[1] V. Shukla,[1] D. Kuzzay,[1,2] D. Faranda,[3,4] E.-W. Saw,[1] F. Daviaud,[1] and B. Dubrulle[1,*]

[1]*DSM/IRAMIS/SPEC, CNRS UMR 3680, CEA, Université Paris-Saclay, 91190 Gif sur Yvette, France*

[2]*LESIA, Observatoire de Paris, Université PSL, CNRS, Sorbonne Université, Univ. Paris Diderot, Sorbonne Paris Cité, 5 place Jules Janssen, 92195 Meudon, France*

[3]*DSM/LSCE, CNRS UMR 8212, CEA, Université Paris-Saclay, 91190 Gif sur Yvette, France*

[4]*London Mathematical Laboratory, 14 Buckingham Street, London WC2N 6DF, United Kingdom*

(Received 31 August 2017; revised manuscript received 28 March 2018; published 3 May 2018)

We examine the connection between the singularities or quasisingularities in the solutions of the incompressible Navier-Stokes equation (INSE) and the local energy transfer and dissipation, in order to explore in detail how the former contributes to the phenomenon of intermittency. We do so by analyzing the velocity fields (a) measured in the experiments on the turbulent von Kármán swirling flow at high Reynolds numbers and (b) obtained from the direct numerical simulations of the INSE at a moderate resolution. To compute the local interscale energy transfer and viscous dissipation in experimental and supporting numerical data, we use the weak solution formulation generalization of the Kármán-Howarth-Monin equation. In the presence of a singularity in the velocity field, this formulation yields a nonzero dissipation (inertial dissipation) in the limit of an infinite resolution. Moreover, at finite resolutions, it provides an expression for local interscale energy transfers down to the scale where the energy is dissipated by viscosity. In the presence of a quasisingularity that is regularized by viscosity, the formulation provides the contribution to the viscous dissipation due to the presence of the quasisingularity. Therefore, our formulation provides a concrete support to the general multifractal description of the intermittency. We present the maps and statistics of the interscale energy transfer and show that the extreme events of this transfer govern the intermittency corrections and are compatible with a refined similarity hypothesis based on this transfer. We characterize the probability distribution functions of these extreme events via generalized Pareto distribution analysis and find that the widths of the tails are compatible with a similarity of the second kind. Finally, we make a connection between the topological and the statistical properties of the extreme events of the interscale energy transfer field and its multifractal properties.

DOI: 10.1103/PhysRevE.97.053101

I. INTRODUCTION

A defining feature of any turbulent field is the existence of fluctuations varying across a wide range of spatial and temporal scales. The shape of the energy spectrum of these fluctuations has been derived by Kolmogorov for a stationary, isotropic, homogeneous, and mirror-symmetric turbulence [1]. The starting point is the incompressible Navier-Stokes equations (INSE):

$$\partial_t u_i + u_j \partial_j u_i = -\frac{1}{\rho}\partial_i p + \nu \partial_j \partial_j u_i + f_i, \tag{1a}$$

$$\partial_j u_j = 0, \tag{1b}$$

where u_i is the d-dimensional velocity field, p the kinematic pressure, ρ the density (which we set to 1), f_i a d-dimensional forcing, and ν the molecular viscosity. The second moment of the INSE with the local homogeneity (HH) assumption gives the classical Kármán-Howarth-Monin equation (hereafter KHM):

$$\tfrac{1}{2}\partial_t E(\ell) - \epsilon = \tfrac{1}{4}\boldsymbol{\nabla}_\ell \cdot \langle \delta\boldsymbol{u}(\delta\boldsymbol{u})^2\rangle + \nu\nabla_\ell^2 E,$$

where $\langle\ \rangle$ denotes the statistical average, $\epsilon = \langle \boldsymbol{u}\cdot[\boldsymbol{f}(\boldsymbol{r}+\boldsymbol{\ell}) + \boldsymbol{f}(\boldsymbol{r}-\boldsymbol{\ell})]\rangle/2$ is a measure of the mean energy injection rate, $\delta\boldsymbol{u} = \boldsymbol{u}(\boldsymbol{x}+\boldsymbol{\ell}) - \boldsymbol{u}(\boldsymbol{x})$ is the velocity increments over a distance ℓ, and $E(\ell) = \langle \boldsymbol{u}(\boldsymbol{x})\cdot\boldsymbol{u}(\boldsymbol{x}+\boldsymbol{\ell})\rangle = \langle \boldsymbol{u}^2\rangle - \langle(\delta\boldsymbol{u})^2\rangle/2$ is a measure of the kinetic energy at scale ℓ. Assuming isotropy and looking for stationary self-similar solutions in the inertial range $\nu^{3/4}\epsilon^{-1/4} \ll \ell \ll L$, Kolmogorov obtained $\langle \delta u^2\rangle = C\epsilon^{2/3}\ell^{2/3}$, or equivalently $E(k) = C_K\epsilon^{2/3}k^{-5/3}$, where C_K is the Kolmogorov constant, k is the wave number, and $\langle(\delta\boldsymbol{u}\cdot\boldsymbol{\ell}/\ell)^3\rangle = -4\epsilon\ell/5$.

The resulting standard phenomenological description (K41) is that of a cascade process, in which the energy driving the flow, injected at the large length scales $\ell \sim L$ comparable to the system size, is transferred to the smaller scales in a *self-similar* manner down to the Kolmogorov length scale $\eta = \nu^{3/4}\epsilon^{-1/4}$, where it is dissipated by the viscous processes. In a steady state, the mean rate of energy injection equals the inter-length-scale energy transfer rate at each scale down to the Kolmogorov scale, where it becomes the viscous energy dissipation ϵ. This self-similar picture was challenged by Landau, as one of the basic assumptions of the K41, namely that ϵ is constant, is flawed. Measurements show that it exhibits short bursts in the time series or intense fluctuations over localized regions. The breaking of exact self-similarity was subsequently confirmed by the scaling properties of the velocity structure functions $S_p = \langle[\delta u(x,\ell)]^p\rangle$, which deviate from the self-similar law $S_p \sim \ell^{p/3}$. This led Kolmogorov to formulate in 1962 a refined scaling hypothesis [2,3] to bridge the large-scale and small-

*Corresponding author: berengere.dubrulle@cea.fr

scale behavior using the quantity ϵ_ℓ, characterizing viscous dissipation averaged over a ball of size ℓ, as

$$\epsilon_\ell \sim \frac{[\delta u(x,\ell)]^3}{\ell}. \tag{2}$$

This results in $S_p = \langle \epsilon_\ell^{p/3} \rangle \ell^{p/3} \sim \ell^{\tau(p)+p/3} \sim \ell^{\zeta(p)}$, showing that all the corrections to self-similarity are given by the statistics of ϵ_ℓ, via the function $\tau(p)$.

However, Kraichnan [4] suggested that if such a relation holds, then ϵ_ℓ should represent some well-defined local energy flux Π_ℓ rather than a local energy dissipation averaged over a volume of linear dimension ℓ. The problem of defining the local subscale-energy-flux was considered by Meneveau [5] by employing wavelets to measure the energy transfer to scales smaller than ℓ at any space point $\boldsymbol{x}$, but this analysis was shown to be flawed [6]. Eyink used the coarse-graining approach to obtain a local energy balance in space and scale from the INSE and thereby was able to identify the *local energy flux* from the large scales to the small scales as

$$\Pi_\ell(\boldsymbol{x}) \equiv -\mathrm{Tr}[(\nabla \boldsymbol{u}^\ell)\boldsymbol{\tau}^\ell], \tag{3a}$$

$$\tau_{ij}^\ell = (u_i u_j)^\ell - u_i^\ell u_j^\ell, \tag{3b}$$

where the superscript refers to a coarse-grained field at scale ℓ and τ represents a stress tensor (because of the small-scale components $<\ell$). Physically we can view $\Pi_\ell(\boldsymbol{x})$ as the effective dissipation of the energy contained in the scales larger than ℓ by the action of the stress, coming from scales smaller than ℓ, on the gradients of the large-scale motion [6].

As discussed in Ref. [6], the above definition guarantees that whenever $\delta u(x,\ell) = O(\ell^h)$, then $\Pi_\ell = O(\ell^{3h-1})$. Such a formulation then allows us to link the occurrence of intermittency to the local scaling and regularity properties of the velocity field. Indeed, we find that if $h > 1/3$, Π_ℓ vanishes as $\ell \to 0$ and the weak solutions to the Euler equations do conserve energy; conversely, if $h < 1/3$, then there may exist solutions which dissipate energy, i.e., even in the absence of viscosity $\nu = 0$. This behavior of the weak solutions was conjectured by Onsager in 1949 [7]. Now, if such a solution starts to develop in a viscous fluid, it will be regularized at a scale $\eta_h \propto \nu^{1/(1+h)}$, at which h becomes 1. We refer to this behavior of the solution as an instance of a quasisingularity. The viscous dissipation becomes dominant and constant below η_h, while the energy flux vanishes like ℓ^2. For $h \leqslant 1/3$, this results in a "spot" of large energy dissipation at the location of the quasisingularity and this explains the intermittency.

Another way of interpreting the above behavior is at the probabilistic level, in which case we postulate that the solutions of the INSE obey the scaling $\delta u(x,\ell) \sim \ell^h$ only in a statistical sense [8]. The probability of occurrence of such an event then varies as $P(h,\ell) \sim \ell^{C(h)}$ [8]. In Ref. [9] Eyink used a simple Borel-Cantelli argument to show that such a statistical interpretation implies, almost with certainty, that the velocity field realizations are singular. Moreover, a precise connection between structure function scaling exponents and intermittency can be made by using the multifractal formalism, i.e., in the form of the spatial dimension of the singularity set by means of an explicit variational formula [10]. The latter yields $\tau(p) = \min_h[p(3h-1) + C(h)]$, whereas in the deterministic interpretation, $C(h)$ has the meaning of the codimension of the set of points where a quasisingularity of exponent h occurs.

Irrespective of the interpretation, we see that to understand intermittency, it is interesting to study the local energy transfer $\Pi_\ell(\boldsymbol{x})$. However, a closer examination of the expression for the local flux in Eq. (3) shows that it is a sum of products of two terms: (a) $\nabla_j u_i^\ell = O(\ell^{h-1})$ and (b) $\tau_{ij}^\ell = O(\ell^{2h})$. Therefore, if we take the case of $h = 1/3$ as an illustrative example, then in the limit $\ell \to 0$ the term (a) is unbounded and the term (b) goes to zero smoothly. So, even though the product is theoretically bounded, it is very likely that any attempt to determine Π_ℓ at small scales by using the data from experiments will be prone to unavoidable noise issues, thereby resulting in values which are either too large or small compared to the exact value.

In this paper, we discuss another expression of the local flux, which is devoid of the above-mentioned potential flaw. A weak formulation has been used to derive the local energy balance equation for the three-dimensional (3D) incompressible Euler and NS equations in Ref. [11]. This local energy balance is similar to the classical Kármán-Howarth-Monin (KHM) relation, but it is local in space and does not require the velocity field to be homogeneous or regular. It describes the temporal evolution of the point-split kinetic energy at a given scale ℓ and position $\boldsymbol{x}$. It has three main constituent terms: (1) a spatial flux term, describing how the input energy is transported within the flow; (2) a local energy transfer $\mathscr{D}_\ell^{\mathrm{I}}$ describing how the energy is transferred locally through scales by nonlinear interactions; (3) a term describing the energy transfer and dissipation by viscosity. The $\ell \to 0$ limit of $\mathscr{D}_\ell^{\mathrm{I}}$ gives the contribution to the local dissipation stemming from the eventual lack of smoothness in the solution (singularities), also known as inertial dissipation, $\mathscr{D}^{\mathrm{I}}$.

Such a generalization of the classical KHM relation allows us to handle possible singularities and quasisingularities and to study their impact on the energy transfer and dissipation; it also puts Kolmogorov's 1962 refined similarity hypothesis in a natural framework. This motivates us to explore the statistics of the interscale flux and viscous terms in a fully developed turbulence as the scale ℓ is varied from in the inertial range down to the dissipation scale and analyze how they relate potential singularities or quasisingularities with intermittency.

In the present paper, we perform an experimental study of the connection between the local energy flux and intermittency by analyzing the velocity fields measured via stereo particle image velocimetry (SPIV) in the turbulent von Kármán swirling flow. We generate turbulence at very high Reynolds numbers in a cylindrical vessel filled with fluid by using two independently rotating impellers. Our experimental setup allows us to perform experiments for a long duration of time (ranging from minutes to hours), so as to accumulate sufficient statistics for a reliable data analysis. We also perform direct numerical simulations of the INSE at a moderate resolution to compare with the trends from the analysis of the experimental data.

We connect the high-order statistics of the interscale transfer with the statistics of the velocity field and show that they are compatible with the refined similarity hypothesis. We condition the velocity structure functions on the regions of large or small inertial dissipation and show that the intermittency corrections are governed by the extreme events of the inertial

dissipation. Furthermore, we characterize the statistics of these extreme events via *generalized Pareto distribution* analysis (a peak over threshold approach) and discuss its link with the multifractal analysis.

In Sec. II we give a brief overview of the mathematical background and present details of the experimental setup and the numerical simulations. We present the results of our study in Sec. III and provide a discussion and the conclusions in Sec. IV.

II. METHODS

A. Mathematical background

In this section we briefly review the mathematical framework which we use to analyze the data from the experiments and the supporting numerical simulations. In our discussion we closely follow the material in Refs. [11,12]. We consider a weak solution $\boldsymbol{u}$ of the NS equation Eq. (1a) in the absence of forcing, i.e., $\boldsymbol{f} = 0$, to keep the analysis simple. We now introduce a regularized velocity field

$$\boldsymbol{u}^\ell(\boldsymbol{x},t) = \phi^\ell * \boldsymbol{u}(\boldsymbol{x},t), \tag{4}$$

where

$$\phi^\ell(\boldsymbol{\xi}) = \frac{1}{\ell^3}\phi(\boldsymbol{\xi}/\ell) \tag{5}$$

is an infinitely differentiable function with compact support on $\mathbb{R}^3$, even, non-negative with integral one. The regularized velocity field obeys regularized NS equations given by

$$\partial_t u_i^\ell + \partial_j (u_i u_j)^\ell = -\partial_i p^\ell + \nu \partial_k \partial_k u_i^\ell, \tag{6a}$$

$$\partial_j u_j^\ell = 0. \tag{6b}$$

We remark that we can regard $\boldsymbol{u}^\ell$ as a continuous wavelet transform of the velocity field $\boldsymbol{u}$ with respect to the wavelet ϕ, provided the latter has the correct properties [13].

We multiply Eq. (1a) and Eq. (6a) by $\boldsymbol{u}^\ell$ and $\boldsymbol{u}$, respectively, and add them together; after the rearrangement of terms we obtain the following balance equation:

$$\begin{aligned} \partial_t u_i u_i^\ell + \partial_i T_i &= \mathcal{E}^\ell - 2\nu \partial_j u_i^\ell \partial_j u_i, \\ T_i &= u_j u_j^\ell u_i + p^\ell u_i + p u_i^\ell - \nu \partial_i u_j u_j^\ell, \\ \mathcal{E}^\ell &= u_i u_j \partial_i u_j^\ell - \partial_i (u_i u_j)^\ell u_j. \end{aligned} \tag{7}$$

We rewrite $\mathcal{E}^\ell$ as

$$\begin{aligned} -2\mathcal{E}^\ell = &\int \nabla \phi^\ell(\xi) \cdot \delta \boldsymbol{u} (\delta \boldsymbol{u})^2 d\xi - \partial_i (u_i u_j u_j)^\ell \\ &+ \partial_i [u_i (u_j u_j)^\ell], \end{aligned} \tag{8}$$

where $\delta \boldsymbol{u}$ is the velocity increment over a distance ξ and ∇ the gradient over $\boldsymbol{\xi}$ [11]. Also,

$$\begin{aligned} \nu \partial_j u_i^\ell \partial_j u_i = &-\nu \int \nabla^2 \phi^\ell(\xi) u_i(\boldsymbol{x}) u_i(\boldsymbol{x}+\boldsymbol{\xi}) d\xi \\ &- \nu \partial_j \int \nabla_j \phi^\ell(\xi) u_i(\boldsymbol{x}) u_i(\boldsymbol{x}+\boldsymbol{\xi}) d\xi. \end{aligned} \tag{9}$$

Finally, we note that $2E^\ell(\boldsymbol{x}) \equiv u_i u_i^\ell = \int \phi^\ell(\boldsymbol{\xi}) u_i(\boldsymbol{x}) u_i(\boldsymbol{x}+\boldsymbol{\xi}) d\boldsymbol{\xi}$. Therefore, we have

$$\begin{aligned} \partial_t E^\ell(\boldsymbol{x}) + \partial_j J_j &= \frac{1}{4}\int \nabla \phi^\ell(\xi) \cdot \delta \boldsymbol{u} (\delta \boldsymbol{u})^2 d\boldsymbol{\xi} \\ &\quad + \nu \int \nabla^2 \phi^\ell(\xi) \boldsymbol{u}(\boldsymbol{x}) \cdot \boldsymbol{u}(\boldsymbol{x}+\boldsymbol{\xi}) d\boldsymbol{\xi} \\ &\equiv -\mathscr{D}_\ell^{\mathrm{I}} - \mathscr{D}_\ell^{\nu}, \end{aligned} \tag{10}$$

where

$$\begin{aligned} J_i = &u_i E^\ell + \frac{1}{2}\left(p^\ell u_i + p u_i^\ell\right) \\ &- \frac{1}{4}[(u_i u_j u_j)^\ell - u_i (u_j u_j)^\ell] - \nu \partial_i E^\ell \\ &+ \nu \int \nabla_i \phi^\ell(\xi) u_j(\boldsymbol{x}) u_j(\boldsymbol{x}+\boldsymbol{\xi}) d\boldsymbol{\xi}. \end{aligned} \tag{11}$$

Equation (10) is a local nonrandom form of the classical KHM equation and describes the evolution of the point-split kinetic energy at scale ℓ and at position $\boldsymbol{x}$ through three main ingredients: (1) a spatial flux term $\nabla \cdot \boldsymbol{J}$, which describes how the input energy is transported within the flow; (2) an interscale flux $\mathscr{D}_\ell^{\mathrm{I}}$, which describes how the energy cascades locally across the length scales; and (3) $\mathscr{D}_\ell^{\nu}$, which describes space transfer and dissipation of energy by viscosity. Note that the main assumption in the derivation of the weak Kármán-Howarth-Monin (WKH) equation, namely the existence of a singularity or quasisingularity, breaks the homogeneity assumption; however, if the singularities fluctuate in time and space, homogeneity may be recovered, albeit in a statistical sense [8].

The contribution to the local dissipation because of the possible lack of smoothness of the velocity field is given by

$$\mathscr{D}^{\mathrm{I}} = \lim_{\ell \to 0} \left(\lim_{\nu \to 0} \mathscr{D}_\ell^{\mathrm{I}} \right); \tag{12}$$

note that the order of limits is important: we first take the high Reynolds number limit $\nu \to 0$ and then $\ell \to 0$. The sign of $\mathscr{D}^{\mathrm{I}}$ depends on the space dimension. In one dimension, for the Burgers equation $\mathscr{D}^{\mathrm{I}} \geqslant 0$. In two dimensions $\mathscr{D}^{\mathrm{I}} = 0$. In 3D, the condition of existence of a suitable weak solution only implies that the spatial average $\langle \mathscr{D}^{\mathrm{I}} \rangle \geqslant 0$, while the instantaneous local $\mathscr{D}^{\mathrm{I}}$ depends on the regularity of the velocity field. It is zero if the velocity field is regular and nonzero in the presence of a singularity of the Euler equation. As long as $h < 1/3$, the local energy transfer, which scales like ℓ^{3h-1}, is prone to increase locally with decrease in the scale ℓ until reaching $\ell = \eta_h$ where it is dissipated. This results in a huge variation of the local energy dissipation and intermittency [14]. Such a scenario has already been validated on the shell models of turbulence [15]. This suggests that a natural analog of the quantity ϵ_ℓ is $\mathscr{D}_\ell^{\mathrm{I}}$ [14]. In the present paper we show conclusively by making use of the analytical, numerical, and experimental analysis that it is indeed the case.

B. Experimental setup and the description of the flow field

We use the von Kármán flow setup at SPEC to conduct experiments for this study. Here we briefly describe the experimental setup and refer to Appendix A 1 and Refs. [16,17]

TABLE I. Parameters describing the five experimental data sets (A, B, C, D, and E) and the DNS run. F is the rotation frequency of the impellers in Hz; Re is the Reynolds number based on the radius of the tank; Re_λ is the Taylor-microscale Reynolds number; ϵ is the dimensionless energy dissipation, reported in Ref. [17] for the data sets A–E; η is the Kolmogorov dissipation length scale; and Δx represents the spatial resolution in the measurements and the DNS. The second to last column, Samples, indicates the number of velocity field samples over which the statistical averaging is performed (product of number of time frames and number of spatial points), and the last column shows the symbols used to represent the experimental data sets.

Case	F (Hz)	Glycerol content	Re	Re_λ	ϵ	η (mm)	Δx (mm)	Samples	Symbol
A	5	0%	3×10^5	1870	0.0254	0.02	2.4	$29999 \times 89 \times 65$	○
B	5	0%	3×10^5	2750	0.0450	0.02	0.48	$29228 \times 77 \times 79$	□
C	5	0%	3×10^5	2510	0.0502	0.02	0.24	$28000 \times 162 \times 157$	◇
D	1	0%	4×10^4	917	0.0413	0.08	0.48	$9999 \times 77 \times 80$	△
E	1.2	59%	6×10^3	214	0.0275	0.37	0.24	$30188 \times 151 \times 174$	⋆
DNS		512^3		138	0.0182	0.0091	$2\eta/3$	24×512^3	

for more details. The setup consists of a cylindrical tank of height $H = 20$ cm and radius $R = 10$ cm to hold the test fluid. We drive the fluid to and maintain it in a turbulent state at high Reynolds numbers by means of two independently rotating impellers at frequency F, located at the top and the bottom of the cylindrical tank. We measure the radial u_r, axial u_z, and azimuthal u_ϕ components of the velocity fields by using high-zooming lenses coupled to a standard particle image velocimetry (SPIV) technique. We perform our measurements within a 4 cm × 3 cm region located on the meridian plane, around the symmetry point of the experimental setup (see Fig. 16 in Appendix A 2). At this location, a shear layer induced by the differential rotation produces a strong turbulent motion [18,19]. We used the SPIV data from these experiments in Ref. [17] to present an extensive characterization of the intermittency by using the velocity structure functions in such a flow configuration. However, in this study our goal is more fundamental and we want to trace the origin of the intermittency corrections and connect them with extreme events of local dissipation $\mathscr{D}_\ell^\mathrm{I}$ and $\mathscr{D}_\ell^\nu$.

The Reynolds number based on the radius of the tank is $\mathrm{Re} = 2\pi R^2 F/\nu$, where ν is the kinematic viscosity of the fluid in the tank. The local energy injection rate ϵ has been computed in [17]. In our experiments, we use a mixture of water and glycerol and by varying their proportion we can control the viscosity of the fluid; this in turn allows us to tune the Kolmogorov scale η. This feature coupled with the use of the multiscale imaging method in our experiments enables us to access scales in the range of η to 5000η (i.e., three decades of inertial range) in a fully turbulent flow. Table I summarizes the parameters corresponding to the different data sets used throughout this paper.

C. Direct numerical simulations

In our analysis of the experimental data, we check for the influence of experimental errors, anisotropy, inhomogeneity, finite boundaries, and projection effects (our measurements are on a plane and not over a volume). We implement these checks by comparing the results from the analysis of the experimental with those from the direct numerical simulations (DNS) of the 3D NS Eq. (1a). To carry out the DNS, we use the NSE solver VIKSHOBHA, an efficient, parallel numerical code based on a pseudospectral method. We use this to determine the fluid velocity $\boldsymbol{u}$ on a cubic, triply periodic domain with sides $L = L_\mathrm{x} = L_\mathrm{y} = L_\mathrm{z} = 2\pi$.

The use of the periodic boundary conditions allow us to express $\boldsymbol{u}$ as a Fourier series. However, in any DNS only a finite number of Fourier modes can be used. Therefore, to limit the number of Fourier modes, we make use of a Galerkin truncation and solve the NSE in Fourier space with N_c^3 modes. The velocity field is now given by $\boldsymbol{u}(\boldsymbol{x},t) = \Sigma_{\boldsymbol{k}} \hat{\boldsymbol{u}}_{\boldsymbol{k}} \exp[i\boldsymbol{k}\cdot\boldsymbol{x}]$, where $\boldsymbol{k} = (n_1,n_2,n_3)2\pi/L$ and $n_\mathrm{i} \in [-N_\mathrm{c}, N_\mathrm{c}-1]$. In other words, we discretize the computational domain and use an N_c^3 number of grid points to represent $\boldsymbol{u}$ in the real (physical) space. We use the incompressibility condition $\boldsymbol{\nabla}\cdot\boldsymbol{u}$ to eliminate the pressure by introducing a transverse projection operator $\mathbb{P}_{\mathrm{i,k}}(\boldsymbol{k}) = \delta_{\mathrm{i,j}} - k_\mathrm{i}k_\mathrm{j}/k^2$, which projects the nonlinear term $\boldsymbol{u}\cdot\boldsymbol{\nabla}\boldsymbol{u}$ on the plane perpendicular to $\boldsymbol{k}$. To implement the pseudospectral method, we compute the linear terms in Fourier space and the nonlinear term in real space, which we then transform to Fourier space; to remove aliasing errors we use a 2/3-dealiasing rule, so that the maximum wave number in our simulations is $k_\mathrm{max} = N_\mathrm{c}/3$. We evolve the NS equations in time by using a second-order Runge-Kutta scheme, while exactly solving the linear part.

In the present work, we take $N_\mathrm{c} = 512$ and use the Taylor-Green forcing at wave number $\tilde{k}_f = 1$ with an amplitude $f_0 = 0.12$ (see Appendix A 7 for more details). We use several independent velocity samples to compute the same diagnostics as for the experimental flow field, but now in a 3D volume rather than on a plane.

III. RESULTS

We now present the results from our analysis of the experimental flow field and the numerical simulations.

A. Wavelet structure functions

The local energy transfers are computed by using the wavelet transforms. Therefore, it is natural to make a link between the intermittency of the velocity field and the local energy transfer via the wavelet structure functions, rather than the classical structure functions. They are defined by using the

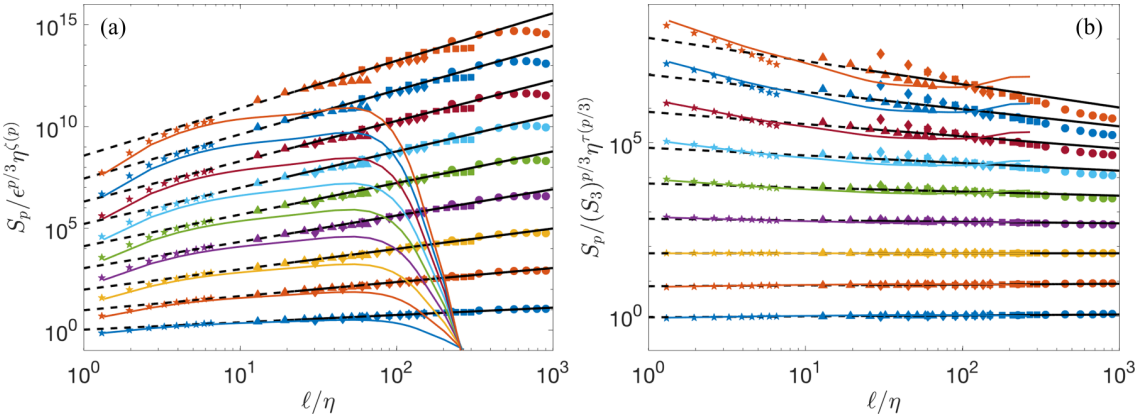

FIG. 1. Wavelet structure functions. (a) Plots of $S_p/\epsilon^{p/3}\eta^{\zeta(p)}$ vs ℓ/η for the first nine orders: $p = 1$ (light blue), $p = 2$ (orange), $p = 3$ (yellow), $p = 4$ (purple), $p = 5$ (green), $p = 6$ (pale blue), $p = 7$ (red), $p = 8$ (strong blue), and $p = 9$ (deep orange). The black dashed lines indicate the power-law behavior $(\ell/\eta)^{\zeta(p)}$ [see Table II for the values of $\zeta(p)$]. (b) Plots of the rescaled structure functions $S_p/S_3^{p/3}$ vs ℓ/η. The black dashed lines indicate the power law $(\ell/\eta)^{\zeta(p)-p/3}$. η is the Kolmogorov dissipation length scale and ϵ is the dimensionless energy injection rate. The structure function of any order p is obtained by combining the five different experimental data sets, shown here by using different symbols: A (circles), B (squares), C (diamonds), D (triangles), and E (stars). A comparison with the DNS results is shown by plotting S_p of different orders as solid curves with the same color scheme as used for the experimental data sets. The structure functions have been shifted by multiplying with an arbitrary factor for visual clarity.

following quantities:

$$G_{ij}(\boldsymbol{x},\boldsymbol{\ell}) = \int d\boldsymbol{y}\nabla_j\Phi_\ell(\boldsymbol{y})u_i(\boldsymbol{x}+\boldsymbol{y}),$$
$$S_{ij}(\boldsymbol{x},\boldsymbol{\ell}) = \frac{1}{2}[G_{ij}(\boldsymbol{x},\boldsymbol{\ell}) + G_{ji}(\boldsymbol{x},\boldsymbol{\ell})],$$
$$A_{ij}(\boldsymbol{x},\boldsymbol{\ell}) = \frac{1}{2}[G_{ij}(\boldsymbol{x},\boldsymbol{\ell}) - G_{ji}(\boldsymbol{x},\boldsymbol{\ell})], \tag{13}$$

where $\Phi_\ell(x) = \ell^{-d}\Phi(x/\ell)$ is a Gaussian function and d is the space dimension. We then compute the wavelet velocity increments as

$$\delta W(\boldsymbol{u})(\boldsymbol{x},\boldsymbol{\ell}) = \left(\delta_L^2 + \delta_\perp^2\right)^{1/2}, \tag{14}$$

where

$$\delta_L(\ell) = \ell \max_{ij}|S_{ij}(\boldsymbol{x},\boldsymbol{\ell})|,$$
$$\delta_\perp(\ell) = \ell \max_{ij}|A_{ij}(\boldsymbol{x},\boldsymbol{\ell})|, \tag{15}$$

respectively. We use the increments $\delta W(\boldsymbol{u})(\boldsymbol{x},\boldsymbol{\ell})$ to infer the general scaling properties of the velocity fields by defining the structure functions as

$$S_p(\ell) = \langle|\delta W(\boldsymbol{u})(\boldsymbol{x},\boldsymbol{\ell})|^p\rangle, \tag{16}$$

where $\langle\ \rangle$ denotes an average over space and time. This way of defining the structure functions has some similarities with those based on the principal values of $|G_{ij}^R(\boldsymbol{x})|$ as reported by Kestener and Arneodo in Ref. [20]. Like in Ref. [20], our approach does not involve the derivatives of the velocity field, nor does it introduce any additional noise. Moreover, our definition is free of singular values computation, a procedure which may generate some noise. Therefore, ours is the smoothest possible definition of the structure functions, which enables us to quantify the scaling properties of a given velocity field.

We first check that this definition provides a description of the intermittency that is compatible with what is obtained by using the classical velocity increments. In Fig. 1(a) we plot the structure functions $S_p(\ell)$, $p \in (1,9)$ for the five experimental flows A to E (see Table I for more details). We observe that the plots of $S_p(\ell)$ rescaled by $\epsilon^{p/3}\eta^{\zeta(p)}$ vs ℓ/η collapse on a universal curve for the cases A to E, which are different for different p. In Table II we summarize the exponents $\zeta(p)$, which we obtain for the different orders of $S_p(\ell)$. The scaling behavior is similar to what is observed for the structure functions computed by directly using velocity increments [17]. Also, the scaling exponents are in good agreement with those computed by using extended self-similarity [21]. Moreover, we find that these structure functions compare well with those computed from the DNS velocity field; in particular, we have a good agreement with the experimental data set E, which has similar Re_λ.

We note that the structure functions from different experimental data sets deviate significantly, by being systematically lower, from those at higher Re_λ. In [17], this difference between

TABLE II. Values of the multiscaling exponents $\zeta(p)$, $\tau(p)$, and $\gamma(p)$ for the velocity, the local transfers, and viscous dissipation structure functions, respectively, of different orders (see text for more details). The values of $\zeta(p)$ listed here have been taken from Ref. [17].

Exponent/Order p	1	2	3	4	5	6	7	8	9
$\zeta(p)$	0.36	0.69	1	1.29	1.55	1.78	1.98	2.17	2.33
$\tau(p/3)$	0.03	0.02	0	−0.04	−0.12	−0.22	−0.30	−0.50	−0.67
$\gamma(p/3)$	0.01	0.01	0	−0.02	−0.06	−0.10	−0.16	−0.22	−0.30

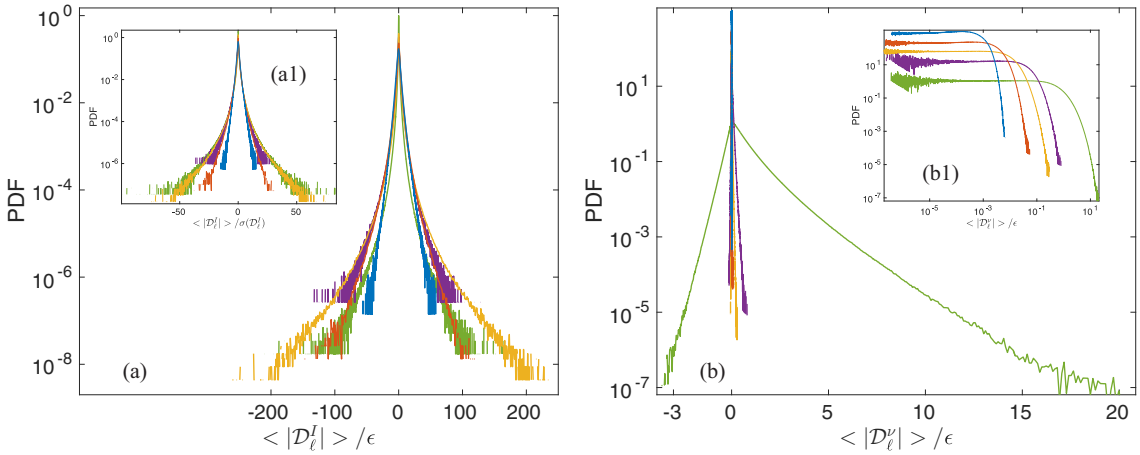

FIG. 2. Plots of the probability distribution function of the instantaneous values of the (a) local energy transfer $\mathscr{D}_\ell^{\mathrm{I}}/\epsilon$ and (b) viscous dissipation $\mathscr{D}_\ell^{\nu}$ at different scales. The PDFs at the different scales are shown by using different colors: $\ell/\eta = 680$ blue curve (data set A), $\ell/\eta = 240$ red curve (data set B), $\ell/\eta = 90$ yellow curve (data set C), $\ell/\eta = 30$ purple curve (data set D), and $\ell/\eta = 3$ green curve (data set E). η is the Kolmogorov dissipation length scale and ϵ is the dimensionless energy injection rate. Inset (a1): Same as in panel (a) but $\mathscr{D}_\ell^{\mathrm{I}}$ normalized with the standard deviation of the distribution. Inset (b1): A log-log plot of the PDF of viscous dissipation $\mathscr{D}_\ell^{\nu}$ at different scales for the positive values only.

different experimental cases was attributed to inhomogeneities of the dissipation. A way to test this hypothesis is to consider *rescaled* wavelet structure functions, i.e., $S_p(\ell)/[S_1(\ell)]^{n/3}$, since in such a case the dependence with respect to ϵ cancels. We plot these rescaled structure functions in Fig. 1(b) and find an improvement in their collapse on the universal curves for all the data sets A to E. Now they follow the expected scaling law $\ell^{\tau(p/3)}$, which is compatible with the scaling $S_3(\ell) \sim \ell$. Also, the agreement with the control DNS is also improved.

B. Spatiotemporal statistics of the local energy transfer and viscous dissipation

We now explore the connection between the intermittency study presented above and the statistics of the local energy transfer and viscous dissipation. We compute $\mathscr{D}_\ell^{\mathrm{I}}$ and $\mathscr{D}_\ell^{\nu}$ for the experimental data sets A to E. Note that in our experimental setup, the velocity fields are such that their fluctuations have spatially homogeneous statistics; they do not depend on space.

1. Probability distribution functions

In Figs. 2(a) and 2(b) we show the probability distribution functions (PDFs) of the local interscale transfer $\mathscr{D}_\ell^{\mathrm{I}}$ and the viscous dissipation $\mathscr{D}_\ell^{\nu}$, respectively, at different scales, by accumulating data from the instantaneous fields. Both quantities are very intermittent in space and time. $\mathscr{D}_\ell^{\nu}$ is predominantly positive; the percentage of the positive values varies between 67% and 90%, as we move from the large length scales to small length scales close to η, respectively. The existence of negative values is due to the fact that $\mathscr{D}_\ell^{\nu}$ is the sum of a transport term and a dissipation term, both originating from the viscous part [see Eq. (9)]. The relative importance of the latter increases with the decreasing scales. This also explains the difference with the traditional viscous dissipation term $\epsilon_\nu = \nu \partial_i u_j \partial_i u_j$ (see Fig. 3), whose PDF is close to the log-normal form. In the inset Fig. 2(b1) we plot the PDFs of the positive values of $\mathscr{D}_\ell^{\nu}$, which show a clear impact of the viscous dissipation at the smaller scales. In contrast, the PDFs of $\mathscr{D}_\ell^{\mathrm{I}}$ are rather symmetric with both large positive and negative values representing direct and inverse (backscatter) energy transfer, respectively. These PDFs display wide tails, irrespective of whether we choose the total dissipation ϵ or the standard deviation of $\mathscr{D}_\ell^{\nu}$ to normalize $\mathscr{D}_\ell^{\nu}$. The tail width of the PDFs of $\mathscr{D}_\ell^{\mathrm{I}}/\epsilon$ initially increases and then decreases, as we move from large to small scales. If $\mathscr{D}_\ell^{\mathrm{I}}$ is normalized by its standard deviation, we observe that the decrease of the tail width of the PDFs is less pronounced at small scales; this results in the overlap of the PDF tails for the length scales 90η and 3η. This suggests that the behavior of

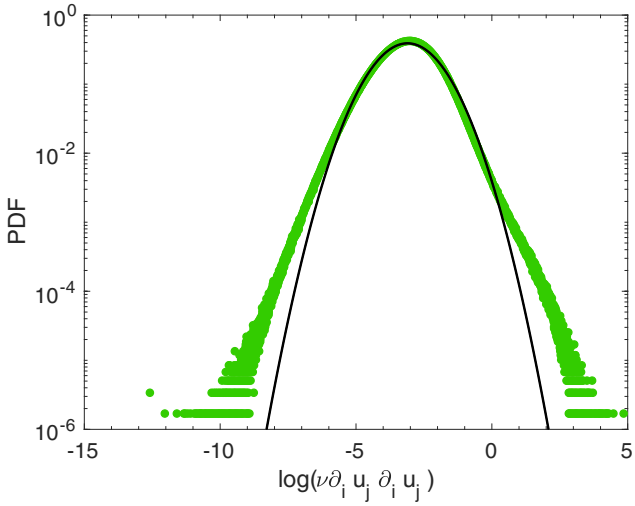

FIG. 3. Plot of the probability distribution function of the instantaneous values of $\log(\epsilon_\nu = \nu \partial_i u_j \partial_i u_j)$ for the experimental data set E. The black curve indicates a Gaussian with the mean and variance obtained from the experimental data set.

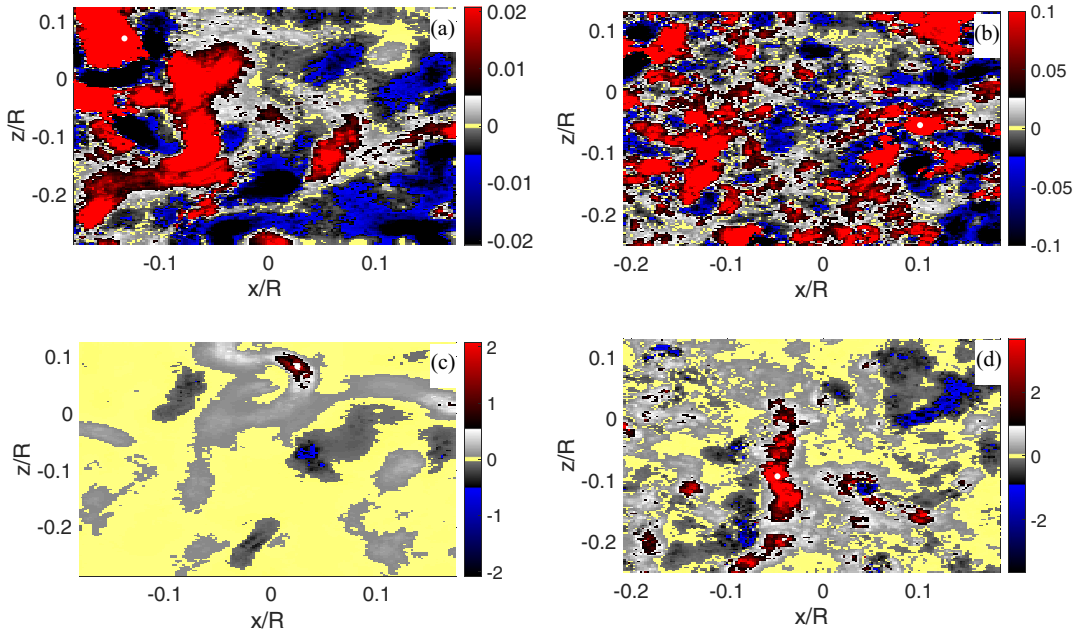

FIG. 4. Pseudocolor plots of the instantaneous $\mathscr{D}_\ell^{\mathrm{I}}$ field in the plane of measurement from the experimental data sets E and C at the scales $\ell = \eta$ and $\ell = 12\,\eta$, respectively. Top panels (a) data set E and (b) data set C: extreme events are absent and the location of the maximal local dissipation is shown by a white dot. Bottom panels (c) data set E and (d) data set C: in the presence of the extreme events, the white dot indicates the location of an extreme event, where the local energy transfer is 100 times larger than the mean. The measurement domain is shown in units of the radius of the cylindrical tank R.

$\mathscr{D}_\ell^{\mathrm{I}}$ in the dissipation range can be as intermittent as it is in the inertial range.

A quantitative measure of the above effect is given by the number of "extreme events" of interscale transfer, i.e., instances when $\mathscr{D}_\ell^{\mathrm{I}}/\langle\mathscr{D}_\ell^{\mathrm{I}}\rangle \geqslant 1000$ over the measurement area. In our analysis, we count the number of such events in one data set of 3×10^4 snapshots. We do not find any extreme event satisfying the above criterion at scale $\ell \approx 160\eta$; only 4 extreme events at scale $\ell \approx 80\eta$; 18 extreme events at scale $\ell \approx 40\eta$; and 36 extreme events at scale $\ell \approx 2\eta$. In Fig. 4 we show the pseudocolor plots of the instantaneous $\mathscr{D}_\ell^{\mathrm{I}}$ for the data sets E and C at scales $\ell \approx \eta$ and $\ell \approx 12\eta$, respectively. In particular, we show these typical maps of local energy transfer in the absence and presence of the extreme events in the upper and lower panels, respectively.

The characterization of the flow topology around the extreme events of inertial dissipation is an important question and it has been suggested that it differs from that associated with the viscous dissipation [16]. The pseudocolor plots of $\mathscr{D}_\ell^{\mathrm{I}}$ Figs. 4(c) and 4(d) show that these extreme events are located within the coherent structures. Moreover, another important feature which is evident from Fig. 4(c) is the presence of these extreme events of energy transfers at the scales of the order of the dissipation length scale. As a result, the local energy balance has a significant contribution from the interscale transfer, irrespective of how it is dissipated at small scales (viscous dissipation or lack of smoothness of the velocity fields [16,22]). This behavior is compatible with the multifractal description of turbulence [10], in which the singularities with exponent $h < 1/3$ dissipate energy at scales $\eta_h \sim \mathrm{Re}^{-1/(1+h)} < \eta$. Even though the number of extreme events increases with decreasing scale, their contribution to the total energy dissipation decreases with it. This is clear from the comparison of Fig. 2(a) and its inset. For example, if we look for events which are larger than 500 times the average dissipation rate ϵ, we find only 3 such events at $\ell \sim \eta$ as compared to 306 events at $\ell \sim 12\eta$.

The above discussion highlights the need to identify the correlation between $\mathscr{D}_\ell^{\mathrm{I}}$ and $\mathscr{D}_\ell^{\nu}$. We do so by computing the logarithm of the joint PDFs of these two quantities at different scales; we show them in Fig. 5. The logarithm of the joint PDFs is such that the maxima of $|\mathscr{D}_\ell^{\mathrm{I}}|$ coincide with minima of $|\mathscr{D}_\ell^{\nu}|$ (and vice versa). This suggests that the extreme events of interscale transfer correspond to the minima of viscous dissipation (and vice versa).

2. Behavior of the spatiotemporal averages

The mean of $\mathscr{D}_\ell^{\mathrm{I}}$ converges very slowly, if at all, perhaps because of the presence of the extreme events of both positive and negative signs in its distribution. Also, the convergence is more difficult at the large length scales than at the small length scales of a given data set; this is so because any statistical analysis of the former involves a lower number of independent blocks of data compared to the latter. In Appendix A 5 we give the details of the convergence tests, which we have performed on the following quantities, namely, $\mathscr{D}_\ell^{\mathrm{I}}$, $\mathscr{D}_\ell^{\nu}$, and $|\mathscr{D}_\ell^{\mathrm{I}}|$ at different scales (see Figs. 19, 20, and 21, respectively). In summary, the mean is in general not converged for any of the scales we considered for the data sets B, C, and D, even over 3×10^4 frames. We observe a satisfactory convergence of the mean only for the first few scales for the data sets C and E. However, if we consider the absolute values of $\mathscr{D}_\ell^{\mathrm{I}}$, this

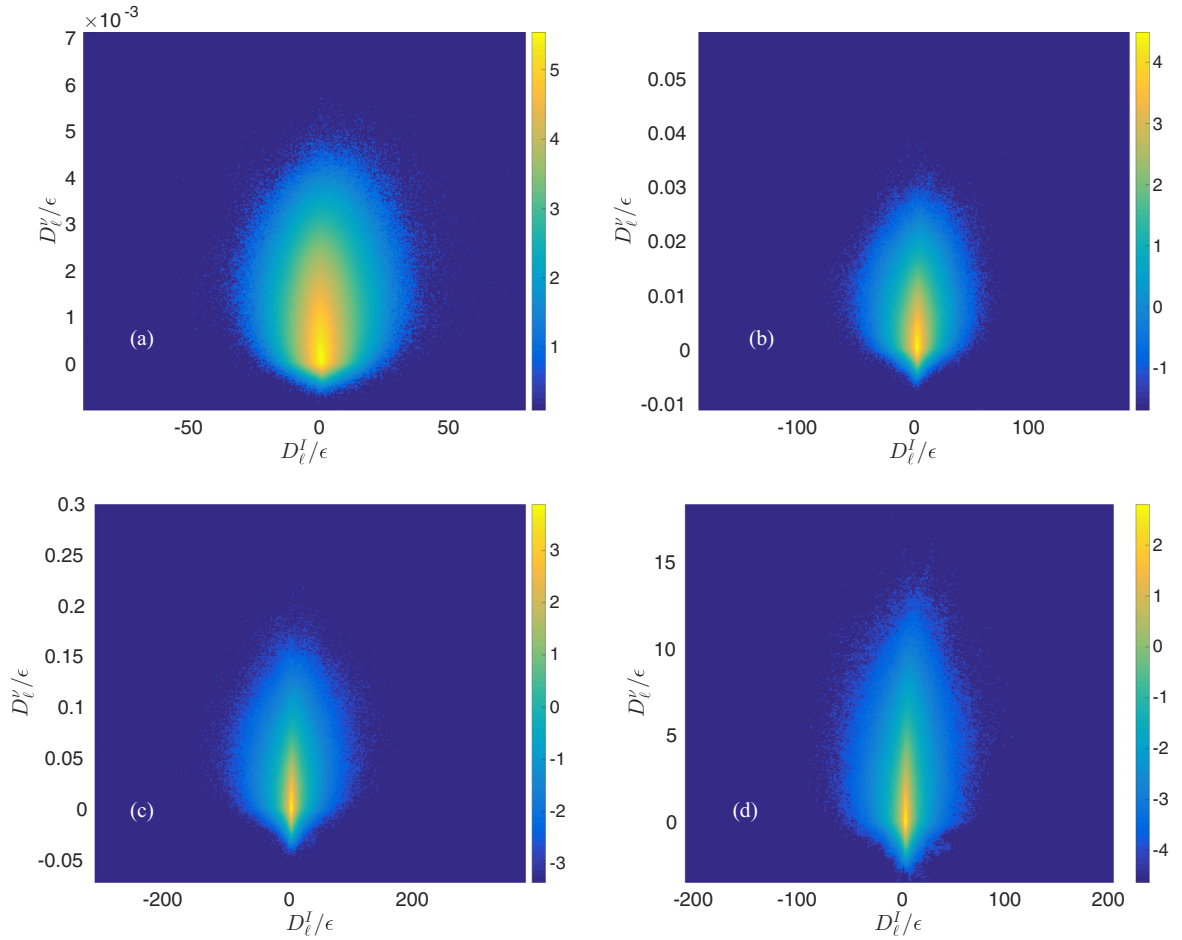

FIG. 5. Plots of the logarithm of the joint probability distribution function of the local energy transfer $\mathscr{D}^{\mathrm{I}}_\ell$ and the viscous dissipation $\mathscr{D}^{\nu}_\ell$ at different scales: (a) $\ell/\eta = 540$, (b) $\ell/\eta = 250$, (c) $\ell/\eta = 70$, and (d) $\ell/\eta = 3$. η is the Kolmogorov dissipation length scale and ϵ is the dimensionless energy injection rate.

problem is absent and the convergence of the mean is ensured at all scales for all the data sets A–E (over 3×10^4 frames).

In Figs. 6(a) and 6(b) we plot the spatiotemporal average of $\mathscr{D}^{\mathrm{I}}_\ell/\epsilon$ and $|\mathscr{D}^{\mathrm{I}}_\ell|/\epsilon$ versus universal coordinates ℓ/η, respectively, for the different experimental data sets (we use different symbols to represent them). We also show the variation of the mean energy dissipation $\langle\mathscr{D}^{\nu}_\ell\rangle$ with scale ℓ/η on these plots. We remark that $\langle\mathscr{D}^{\nu}_\ell\rangle$ is second order in velocity increments and is also everywhere positive; therefore, it does not suffer from the convergence issues (see Fig. 20). Moreover, if we plot $\langle\mathscr{D}^{\nu}_\ell\rangle$ vs ℓ/η, its values from different data sets collapse on a single curve. It displays $\ell^{-4/3}$ power-law scaling down to 30η and it tends to ϵ at small scales. We observe that compared to $\langle\mathscr{D}^{\nu}_\ell\rangle$ the data collapse is not so good for $\langle\mathscr{D}^{\mathrm{I}}_\ell\rangle$ and results in scatter, a signature of the lack of convergence of this quantity for some data sets.

The behavior of absolute value of the local energy transfer $\langle|\mathscr{D}^{\mathrm{I}}_\ell|\rangle$ is significantly different from that of $\langle\mathscr{D}^{\mathrm{I}}_\ell\rangle$. The former reaches a value of about 2 to 3 times ϵ for scales $\ell > 30\eta$, whereas the latter stays below $\epsilon/3$. This large difference can attributed to the fact that our measurements are on a plane, which prevents us from computing the contribution of the velocity increments in the azimuthal direction. This may change the proportion of the events with positive signs compared to that with negative signs, especially the extreme ones.

To check the above arguments, we compare our results with the data from the homogeneous, isotropic 3D DNS. For the DNS run we expect the sum of $\langle\mathscr{D}^{\mathrm{I}}_\ell\rangle$ and $\langle\mathscr{D}^{\nu}_\ell\rangle$ to be equal to the mean energy dissipation ϵ. Figure 7 shows that such a relation is very well satisfied for the scales $\ell < 40\eta$, beyond which the finite-size effects lead to deviation. As expected, the relation is not satisfied for $\langle|\mathscr{D}^{\mathrm{I}}_\ell|\rangle$, which makes the sum exceed ϵ, as now both positive and negative instances contribute without cancellations. From these plots, we can infer that the inertial range exists, if at all, for scales larger than, but close to, 10η. We observe that $\langle\mathscr{D}^{\nu}_\ell\rangle$ obtained from the DNS agrees well with the experimental data, whereas $\langle\mathscr{D}^{\mathrm{I}}_\ell\rangle$ obtained from the DNS is 3 times larger than that from the experiments. This observation is in agreement with the arguments about the projection effects related with SPIV, which highlights the limitation of the experimental measurements.

C. Higher order statistics and refined similarity hypothesis

We explore the higher order statistics of the local energy transfer and viscous dissipation by defining the following

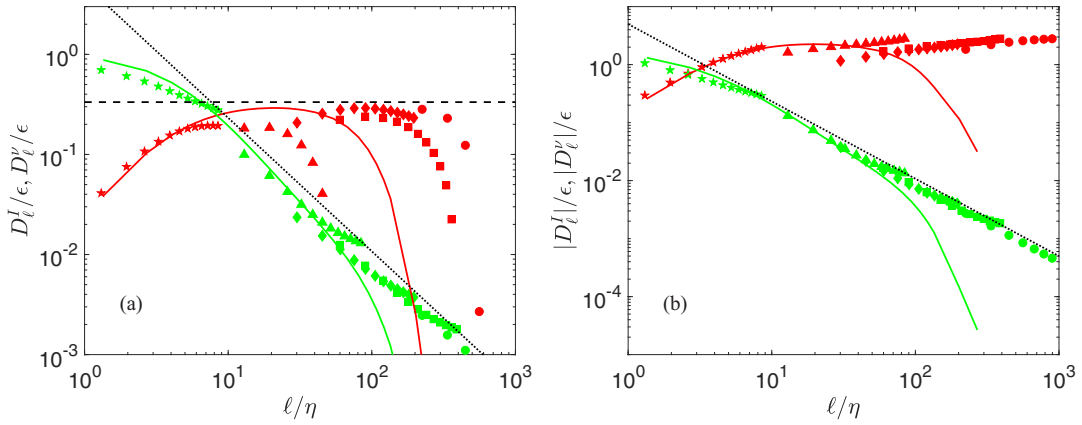

FIG. 6. Spatiotemporal averages of the local energy transfer and viscous dissipation: (a) plots of $\langle \mathscr{D}_\ell^{\mathrm{I}} \rangle/\epsilon$ (red symbols) and $\langle \mathscr{D}_\ell^{\nu} \rangle/\epsilon$ (green symbols) vs ℓ/η. (b) Analogous plots for the absolute values of the local energy transfer and the viscous dissipation. The black horizontal dashed line indicates a constant value of 1/3. The black dotted line indicates the power law $\ell^{-4/3}$. A comparison with DNS is shown by plotting in (a) $\frac{1}{3}\langle \mathscr{D}_\ell^{\mathrm{I}} \rangle/\epsilon$ (red curve) and $\langle \mathscr{D}_\ell^{\nu} \rangle/\epsilon$ (green curve) vs ℓ/η; (b) $2\langle |\mathscr{D}_\ell^{\mathrm{I}}| \rangle/\epsilon$ (red curve) and $\langle |\mathscr{D}_\ell^{\nu}| \rangle/\epsilon$ (green curve) vs ℓ/η. η is the Kolmogorov dissipation length scale and ϵ is the dimensionless energy injection rate. The different experimental data sets are represented by different symbols: A (circles), B (squares), C (diamonds), D (triangles), and E (stars).

structure functions:

$$\Sigma_p^{\mathrm{I}} = \left\langle |\mathscr{D}_\ell^{\mathrm{I}}|^p \right\rangle, \tag{17}$$

$$\Sigma_p^{\nu} = \left\langle |\mathscr{D}_\ell^{\nu}|^p \right\rangle, \tag{18}$$

respectively. We compute these structure functions for $p = i/3$, where $i \in (1,9)$, and plot them in Fig. 8. We observe that for a given order p, Σ_p^{I} and Σ_p^{ν} from different data sets rescaled by $(\Sigma_1^{\mathrm{I}})^p \eta^{\tau(p)}$ and $(\Sigma_1^{\nu})^p \eta^{\gamma(p)}$, respectively, collapse on a single universal curve. For a given order p, the universal curve is a power law with exponent $\tau(p/3) = \zeta(p) - p/3$ and $\gamma(p/3)$ for $\Sigma_{p/3}^{\mathrm{I}}$ and $\Sigma_{p/3}^{\nu}$, respectively. The computation of the exponent $\gamma(p/3)$ from the multifractal theory is postponed to Sec. III F. We find that the magnitude of $\gamma(p/3)$ is always smaller than the exponent $\tau(p/3)$, which we obtain for the intermittency correction to the structure functions.

These results are in agreement with a refined similarity hypothesis, that had been suggested in [23]:

$$\frac{S_p(\ell)}{(S_3(\ell))^{p/3}} \sim \frac{\Sigma_{p/3}^{I}}{\left(\Sigma_1^{I}\right)^{p/3}}. \tag{19}$$

We compute these structure functions for the data from the DNS run and plot them in Fig. 8. Σ_p^{I} and Σ_p^{ν} from the DNS are in agreement with the experimental data sets for orders up to $p = 4/3$, but show increasing deviations both at small and large length scales. We find that the agreement is better for Σ_p^{ν} than it is for Σ_p^{I}, which may be attributed to the aforementioned projection effects related to SPIV.

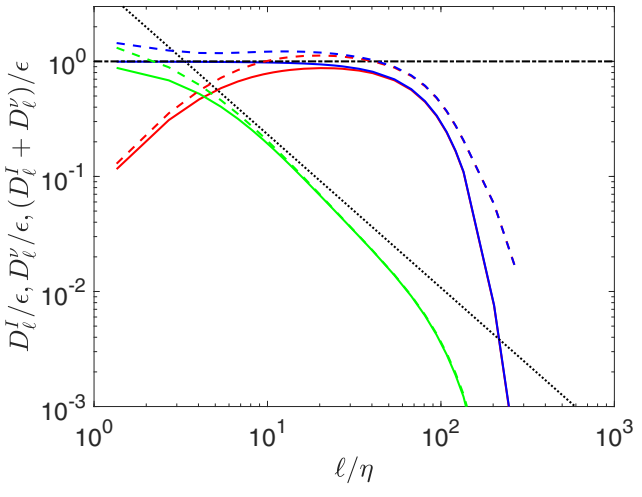

FIG. 7. Spatiotemporal averages of the local energy transfer and viscous dissipation from the DNS: plots of $\langle \mathscr{D}_\ell^{\mathrm{I}} \rangle/\epsilon$ (red curve) and $\langle \mathscr{D}_\ell^{\nu} \rangle/\epsilon$ (green curve) vs ℓ/η. Analogous plots for the average of the absolute values of local energy transfer and the viscous dissipation are shown by dashed red and green curves, respectively. The black horizontal dashed line indicates a constant value of 1. The black dotted line indicates the power law $\ell^{-4/3}$. η is the Kolmogorov dissipation length scale and ϵ is the dimensionless energy injection rate.

D. Conditioned wavelet structure functions: The role of extreme events of inertial dissipation

The discussion in the previous section allows us to draw an important conclusion that in the turbulent regime the intermittency corrections are governed by the local energy transfers. This motivates us to explore this connection further by conditioning the structure functions on the regions of high or low inertial dissipation (i.e., local energy transfers at the resolution scale). We implement this for each of the data sets A to E by defining two special sets of points $\mathcal{A}$ and $\mathcal{B}$ corresponding to the locations of low and high values of $|\mathscr{D}_{\Delta x}^{\mathrm{I}}|$, respectively. We divide the PDF of $|\mathscr{D}_{\Delta x}^{\mathrm{I}}|$ at the smallest scale of a given experimental data set (A to E) into 10 deciles: the set of points forming the first decile (the spatial regions with $|\mathscr{D}_{\Delta x}^{\mathrm{I}}|$ being in the 10% lower values of the inertial dissipation, that is, values close to 0) are assigned to the set $\mathcal{A}$ and the points forming the last decile (the spatial regions with $|\mathscr{D}_{\Delta x}^{\mathrm{I}}|$ in the highest 10% in magnitude) are assigned to the set $\mathcal{B}$. Therefore, the extreme events of $\mathscr{D}_{\Delta x}^{\mathrm{I}}$ are in set $\mathcal{B}$. We then

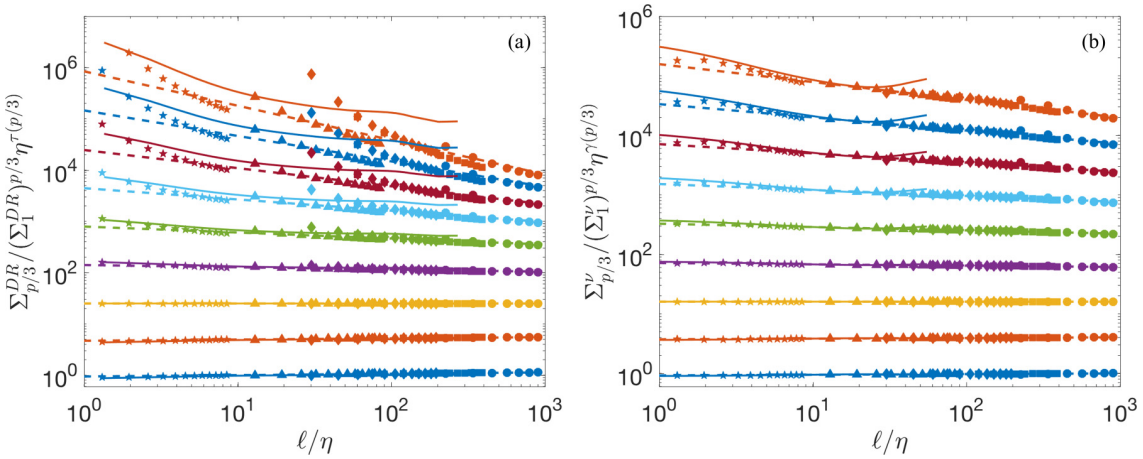

FIG. 8. Plots of the structure function of the (a) local energy transfer Σ^{I}_p vs ℓ/η and (b) viscous dissipation Σ^{ν}_p vs ℓ/η. Different orders of the structure functions are distinguished by using different colors: $p = 1/3$ (light blue), $p = 2/3$ (orange), $p = 1$ (yellow), $p = 4/3$ (purple), $p = 5/3$ (green), $p = 2$ (pale blue), $p = 7/3$ (red), $p = 8/3$ (strong blue), and $p = 3$ (deep orange). For the structure function of a given order, the DNS result is represented by a continuous line, while different experimental data sets are represented by different symbols: A (circles), B (squares), C (diamonds), D (triangles), and E (stars). The dotted lines indicate the power law $\ell^{\tau(p/3)}$ (for Σ^{I}_p) and $\ell^{\gamma(p/3)}$ (for Σ^{ν}_p); see Table II for the values of $\tau(p/3)$ and $\gamma(p/3)$. Note: The structure functions shown in (a) and (b) have been rescaled by $(\Sigma^{DR}_1)^{p/3}\eta^{\tau(p/3)}$ and $(\Sigma^{\nu}_1)^{p/3}\eta^{\gamma(p/3)}$, respectively; η is the Kolmogorov dissipation scale.

compute the wavelet structure functions defined by

$$S^C_n(\ell) = \langle |\delta W(\boldsymbol{u})(\boldsymbol{x},\ell)|^p \rangle_{\mathcal{A},\mathcal{B}}, \tag{20}$$

where the average is taken on either set $\mathcal{A}$ or set $\mathcal{B}$. We show these structure functions in Fig. 9 for orders $p \in (1,9)$ and compare them with the original, unconditioned, wavelet-based structure functions. We observe that the structure functions conditioned on the events of small inertial dissipation are less intermittent than the unconditioned ones and display $\ell^{p/3}$ power-law scaling behavior. In contrast, the structure functions conditioned on the extreme values of the inertial dissipation have intermittency, which is similar to those that are unconditioned. This clearly shows that the intermittency is essentially governed by the extreme events of the inertial dissipation.

E. Extreme value analysis of the spatiotemporal probability distribution functions

We now know from the detailed study of the various structure functions presented in the previous sections that the extreme events of $\mathscr{D}^{\mathrm{I}}_\ell$ control the intermittency and their PDFs are strongly non-Gaussian. Also, these extreme events are located in the tails of the PDFs. Therefore, we now use the tools of the extreme value analysis to further explore the statistical properties of these extreme events. We characterize the tails of the PDFs by using the generalized Pareto distribution (GPD) given by

$$f_{GPD}(x;\mu,\sigma,\xi) = \frac{1}{\sigma}\left[1 + \xi\frac{x-\mu}{\sigma}\right]^{-1-1/\xi}, \tag{21}$$

where $\mu \in \mathbb{R}$ is the location parameter representing the chosen threshold, $\sigma > 0$ is the scale parameter representing the typical order of extreme fluctuations, and ξ is the tail shape parameter, representing the rate of decay of extremes in the tail.

We apply this analysis to the PDFs of $\mathscr{D}^{\mathrm{I}}_\ell$ at different scales (based on 3×10^4 samples) and obtain fits by using the maximum likelihood estimation criterion (implemented in the MATLAB routine "gpfit"). We fit in each case the parameters μ, σ, and ξ for the quantiles 0.975, 0.99, and 0.995 indicating strong, rare, and extreme events, respectively. As a result, we obtain the spatial and scale dependence of these three parameters $\mu(\ell)$, $\sigma(\ell)$, and $\xi(\ell)$ for the above-mentioned three types of events. We varied the series size and find that these indicators have better convergence properties than the moments of $\mathscr{D}^{\mathrm{I}}_\ell$; thus, they are better suited for interpreting the behavior of the tails.

In our use of the GPD analysis, we are also motivated by the possible links it can provide with the multifractal properties of the local energy transfer field $\mathscr{D}^{\mathrm{I}}_\ell(\boldsymbol{x},t)$. The GPD analysis of a multifractal field, characterized by a spectrum $D(h)$, yields the following scale dependence for the three parameters:

$$\mu(\ell) \sim \ell^{h_{\min}}, \quad \sigma(\ell) \sim \ell^{h_{\min}}, \quad \xi \sim 1/p_*, \tag{22}$$

where $h_{\min} = \min[h/D(h) = 0]$ and $p_* = \frac{dD(h)}{dh}|_{h_{\min}}$ (see Refs. [24,25] for additional details).

1. *Quantile value parameter μ*

The parameter μ describes the value at which a given quantile is achieved, i.e., the typical value of an extreme event that has the probability given by the quantile. In Figs. 10(a) and 10(b) we show the variation of μ normalized by ϵ as a function of ℓ/η from the negative and positive tails of the PDF, respectively. We observe that for the positive tails [see Fig. 10(b)], the normalized quantile threshold μ/ϵ follows a smooth curve, which is almost flat over the range of scales $(10\eta, 300\eta)$ coinciding with the inertial range. This behavior corresponds to the value $h_{\min} = 0$. We also find that outside the above-mentioned range of scales, both at the small and large length scales, μ decreases to zero rather sharply. For the

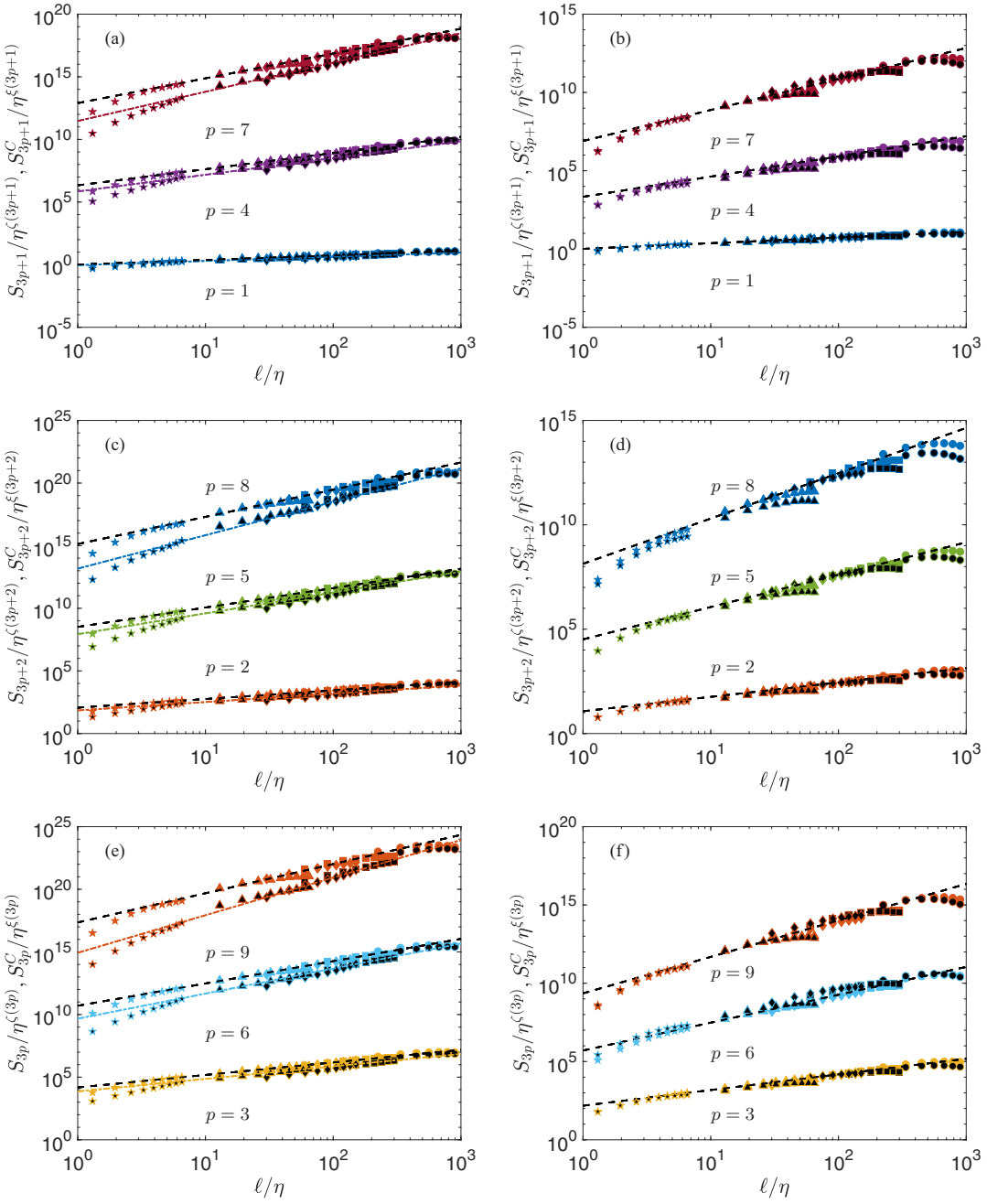

FIG. 9. Role of the extreme events of inertial dissipation. Plots of the structure functions: S_p^C vs ℓ/η conditioned (symbols with black filling) either on the set $\mathcal{A}$ (less intense events of $\mathscr{D}_\Delta^{\mathrm{I}} x$; shown in the left panel) or $\mathcal{B}$ (extreme events of $\mathscr{D}_\Delta^{\mathrm{I}} x$, shown in the right panel) and the unconditioned S_p vs ℓ/η. The black dashed lines indicate $\ell^{\zeta(n)}$. The colored lines show $\ell^{p/3}$: $p = 1$ (light blue), $p = 2$ (orange), $p = 3$ (yellow), $p = 4$ (purple), $p = 5$ (green), $p = 6$(pale blue), $p = 7$ (red), $p = 8$ (strong blue), and $p = 9$ (deep orange). The structure functions have been shifted by multiplying with an arbitrary factor for visual clarity.

negative tails [see Fig. 10(a)], the plots of μ do not follow a smooth curve and are more scattered. This difference between the behavior of the positive and negative tails may be an indication of the fact that the positive and negative events of $\mathscr{D}_\ell^{\mathrm{I}}(\boldsymbol{x},t)$ are not equivalent and correspond to different processes. Moreover, we notice discontinuities on moving from one experimental data set to another, thereby implying that μ is sensitive to the Reynolds number. In Fig. 10(c) we show the plots of μ_-/ϵ versus μ_+/ϵ and we find that on average the μ_+ is larger than μ_-, tracing the asymmetry of the distribution towards positive values.

2. *Intermittency parameter σ*

The parameter σ quantifies the "width" of the tails of a PDF; therefore, it is an indicator of the importance of the extreme events. In Figs. 11(a) and 11(b) we plot the σ normalized by ϵ versus ℓ/η for the negative and the positive tails of the PDFs,

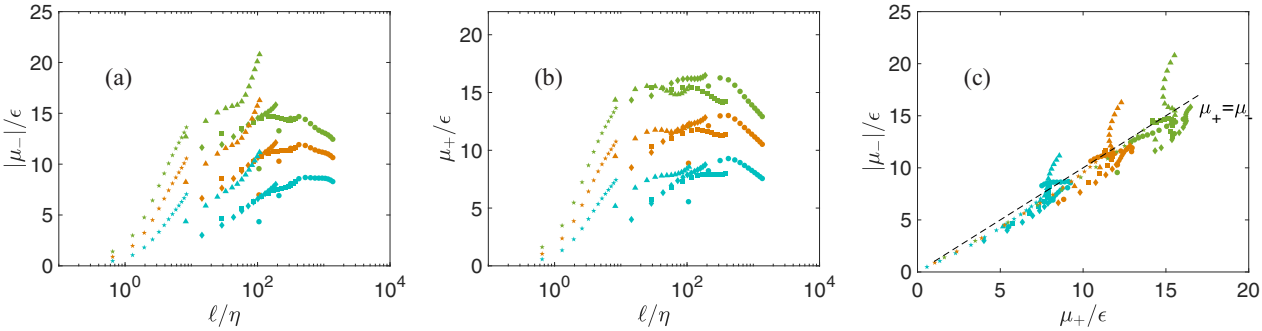

FIG. 10. Quantile threshold parameter from the GPD analysis: (a) μ_-/ϵ vs ℓ/η and (b) μ_+/ϵ vs ℓ/η from the negative and positive tails of the PDF of $\mathscr{D}_\ell^{\mathrm{I}}$, respectively. (c) Parametric plot of μ_-/ϵ vs μ_+/ϵ. Different colors indicate different quantile values: 0.975 (cyan), 0.99 (orange), and 0.995 (green). The dotted line indicates $|\mu_+| = |\mu_-|$. Different experimental data sets are indicated by different symbols: A (circles), B (squares), C (diamonds), D (triangles), and E (stars). η is the Kolmogorov length scale.

respectively. We observe that, when plotted in this manner, only the lowest or the lower two quantiles follow a universal curve for the different experimental data sets A to E and this behavior is independent of whether we choose the positive or the negative tail. For the highest quantile, we notice a Reynolds number dependence in the form of sharp discontinuities on moving from one data set to the next. We may attribute the observation of this behavior to the lack of statistics—the higher the quantile the lower the number of events—therefore, resulting in a poor fit. However, at the highest quantile, we can improve the data collapse of different experimental data sets by explicitly introducing the Reynolds number dependence. This is based on the assumption that the intermittency parameter follows a shape governed by the similarity of second kind, first suggested by Castaing [26,27] and derived by Dubrulle and Graner from finite scale invariance [28]:

$$\ln\sigma = \beta(\exp[\alpha\ln(\ell/L)] - 1), \tag{23}$$

where $\beta = \beta_0\ln(\mathrm{Re})$ and $\alpha = \alpha_0/\ln(\mathrm{Re})$, and L is a large scale ($L = 1$ in our nondimensional units). In the limit $\ln(\mathrm{Re}) \to 0$, we recover the classical similarity $\ln(\sigma) \propto \ln(\ell/L)$, but at finite Re we have to include corrections to the similarity. In the present case, this assumption implies that $\ln(\sigma)/\ln(\mathrm{Re})$ versus $\ln(\ell)/\ln(\mathrm{Re})$ should collapse on a universal curve for the different data sets. We show this in the insets Figs. 11(a.1) and 11(b.1) for the negative and the positive tails of the PDFs, respectively. As we expected, the collapse between the different data sets is better for the highest quantile. Moreover, the curve is a straight line, as required by the shape relation Eq. (23). However, the slope of the straight line, which traces $h_{\min}$, depends on the quantile: it increases from 0 to -0.25 as the quantile changes from 0.975 to 0.995, respectively. This means that $h_{\min}$ decreases with the value of the quantile. We find that in all the cases the value of $h_{\min}$ is smaller than those inferred by using the parameter μ.

In Fig. 12 we show the plots of σ_-/ϵ vs σ_+/ϵ, where σ_- and σ_+ denote the intermittency parameters for the negative and positive tails of the PDFs, respectively. We observe that these parametric curves display some curvature, indicating that the two quantities are not correlated in a simple way. In addition, we find that the intermittency parameter of the positive tail has the tendency to be higher than the negative tails; this implies that the positive extreme events are more intermittent than those with negative sign.

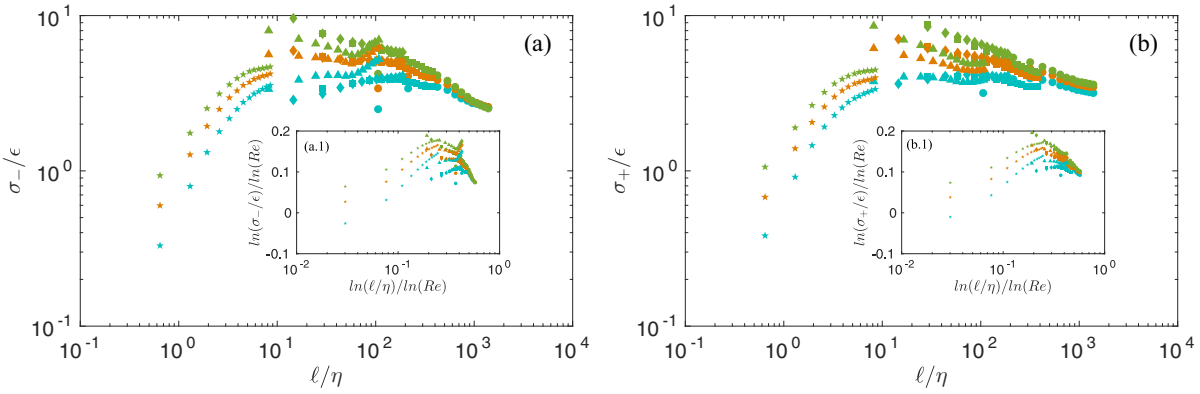

FIG. 11. Intermittency parameter from the GPD analysis: (a) σ_-/ϵ vs ℓ/η and (b) σ_+/ϵ vs ℓ/η for the negative and positive tails of the PDF of $\mathscr{D}_\ell^{\mathrm{I}}$, respectively. Insets: (a.1) and (b.1) show the analogous plots of σ obtained by using the self-similarity of the second kind, i.e., plots of $\ln(\sigma/\epsilon)/\ln(\mathrm{Re})$ vs $\ln(\ell/\eta)/\ln(\mathrm{Re})$, where Re is the Reynolds number. Different colors indicate different quantile values: 0.975 (cyan), 0.99 (orange), and 0.995 (green). Different experimental data sets are indicated by different symbols: A (circles), B (squares), C (diamonds), D (triangles), and E (stars). η is the Kolmogorov length scale.

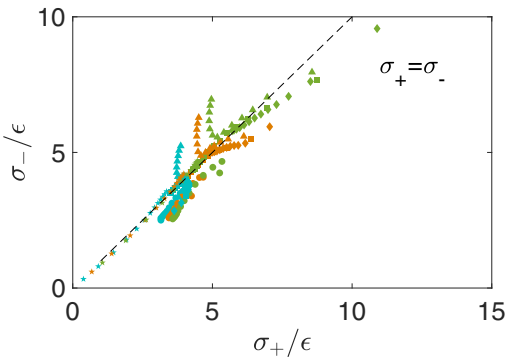

FIG. 12. Intermittency parameter: Parameteric plot of σ_-/ϵ vs σ_+/ϵ. Different colors indicate different quantile values: 0.975 (cyan), 0.99 (orange), and 0.995 (green). Different experimental data sets are indicated by different symbols: A (circles), B (squares), C (diamonds), D (triangles), and E (stars). σ_- (σ_+) denotes the intermittency parameter for the negative (positive) tail of the PDF of $\mathscr{D}_\ell^{\mathrm{I}}$.

3. Power-law parameter ξ

The parameter ξ quantifies the index of the power law of an equivalent GPD. If $\xi \leqslant 0$, this indicates that the distribution is bounded and well behaved. The $\xi > 0$ implies a pathological distribution with diverging moments: if the shape parameter $\xi > 1/n$, the moments of order n and greater do not exist [29]. In Figs. 13(a) and 13(b) we plot the parameter ξ vs ℓ/η for the negative and positive tails of the PDFs, respectively; we show analogous plots in the insets Figs. 13(a.1) and 13(b.1) for this parameter vs ℓ/R for the negative and positive tails of the PDFs, respectively, where R is the radius of the cylindrical tank. Figures 13(a.1) and 13(b.1) show that the curves for different quantiles collapse on each other indicating that the Kolmogorov length scale is not the relevant scale to explain the behavior of this parameter. ξ is close to zero at large length scales and increases continuously as we decrease the scale; at the smallest scale in our data sets its value is close to 0.6 for the highest quantile. This means that the second-order moments are not defined and it also explains why it is so difficult to achieve the convergence of the mean.

The steepening of ξ vs ℓ implies that the parameter $p_* = 1/\xi$ decreases as a function of scale. Moreover, at the Kolmogorov scale, we do not observe any indication of the saturation of the power-law parameter, which means that we are potentially exploring more and more singular regions.

Figure 14 shows that the correlation plot of ξ from the negative tail (ξ_-) vs that from the positive tail (ξ_+) of the PDFs is roughly linear; we also observe that ξ_- has a tendency to be larger than ξ_+. This means that the convergency to a singularity, if any, is faster for the extreme events of $\mathscr{D}_\ell^{\mathrm{I}}$ with negative sign.

F. Compatibility with multifractal analysis

The above GPD analysis has provided us with two important pieces of information regarding the multifractal spectrum of the local energy transfer: (1) $h_{\min}$ is between -0.25 and 0 with dependence on the quantity and quantile considered; (2) p_* changes between 1.67 and ∞, if we move from the Kolmogorov scale to the injection scale. We compare this prediction with the direct estimates of these quantities obtained from the scaling exponents $\tau(p)$ listed in Table II. We use the Legendre transform formula

$$\tau(p) = \min_h [ph + 2 - D(h)] \tag{24}$$

to obtain the values of $D(h)$, which we show in Fig. 15. We obtain $h_{\min} = -0.88$ and $p_* = 4$. This value of $h_{\min}$ is much smaller than that obtained from the GPD analysis, which suggests that the latter requires higher quantile to converge this quantity. The value of p_* obtained by using $D(h)$ is obtained in the GPD analysis for scales close to $\ell = 10^{-2}R$ (=1 mm), which sets the characteristic size of the structure. We recall that the local energy transfer scales as $h = 3h_v - 1$, where h_v is the scaling exponent of the velocity. This suggests that the above structures correspond to those with $h_v \approx 0$. This estimate is compatible with the observations of Saw *et al.* [16] of extreme events of inertial dissipation, that look as shock- or front-like

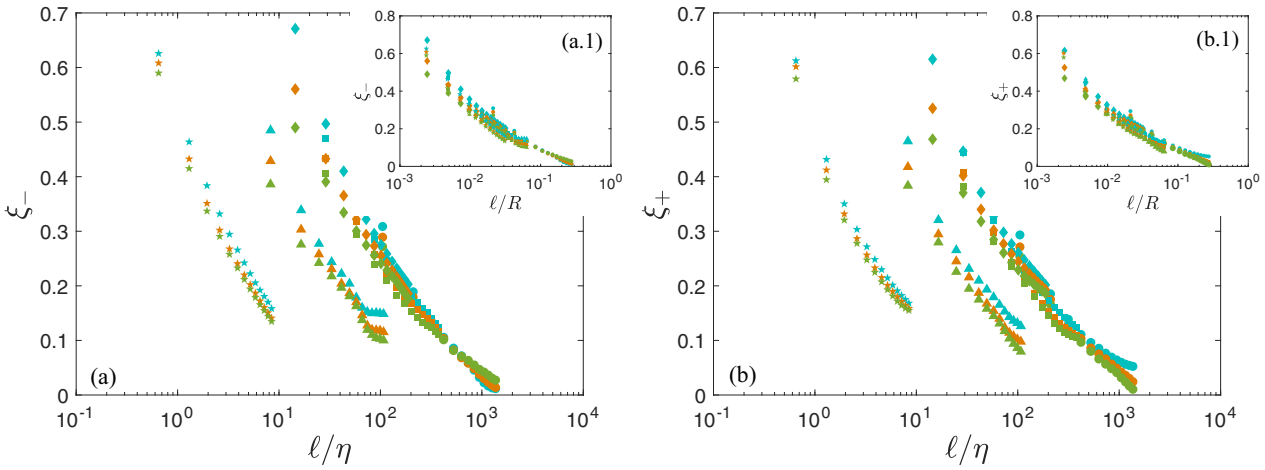

FIG. 13. Power-law parameter from the GPD analysis: (a) ξ_- vs ℓ/η and (b) ξ_+ vs ℓ/η for the negative and positive tails of the PDF of $\mathscr{D}_\ell^{\mathrm{I}}$, respectively. Insets: (a.1) and (b.1) show the analogous plots of ξ vs ℓ/R, where R is the radius of the cylindrical tank. Different colors indicate different quantile values: 0.975 (cyan), 0.99 (orange), and 0.995 (green). Different experimental data sets are indicated by different symbols: A (circles), B (squares), C (diamonds), D (triangles), and E (stars). η is the Kolmogorov length scale.

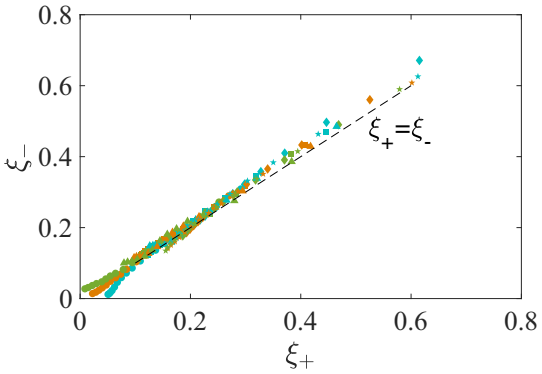

FIG. 14. Power-law parameter from the GPD analysis: Parametric plot of ξ_- vs ξ_+. Different colors indicate different quantile values: 0.975 (cyan), 0.99 (orange), and 0.995 (green). Different experimental data sets are indicated by different symbols: A (circles), B (squares), C (diamonds), D (triangles), and E (stars). ξ_- (ξ_+) is the power-law parameter for the negative (positive) tail of the PDF of $\mathscr{D}_\ell^{\mathrm{I}}$.

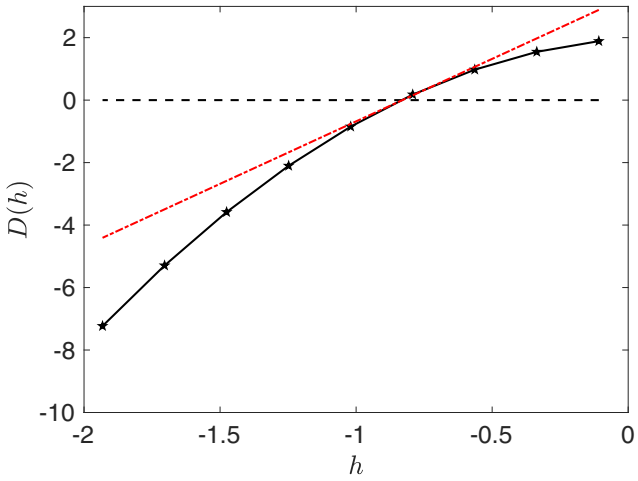

FIG. 15. Multifractal spectrum: Plot of $D(h)$ vs h computed by using the values of the $\tau(p)$, scaling exponents of the local energy transfer structure functions (see Table II), in Eq. (24). The red dash-dot line indicates the tangent $f(h) = 4(h - h_{\min})$, where $h_{\min} = -0.88$.

structures with elongated shape, of about 10 Δx in the direction perpendicular to the front.

The obtained $D(h)$ can also be used to compute other quantities of interest, like the exponent γ. Indeed, since $\mathscr{D}_\ell^\nu$ scales like $2h - 2$, we get

$$\langle|\mathscr{D}_\ell^\nu|^p\rangle \sim \ell^{\xi_\nu(p)},$$
$$\xi_\nu(p) = \min_h[p(2h-2) + 2 - D(h)]. \tag{25}$$

Approximating $C(h) = 2 - D(h)$ by a parabola $C(h) = (h - a)^2/2b$, with $a = 1/3 + 3b/2$ to ensure that $\zeta(3) = 1$, we get

$$\xi_\nu(p) = 2p(a-1) - 2bp^2,$$
$$\gamma(p/3) = \frac{2}{3}bp - \frac{2}{9}bp^2. \tag{26}$$

Using $b = 0.025$, we get the value of Table II.

IV. DISCUSSION AND CONCLUSIONS

We know that at small scales turbulence displays strong deviations from the homogeneity and self-similarity assumptions of Kolmogorov's phenomenological theory. In this work, we have carried out a detailed exploration of the idea that these strong deviations are linked to the existence of singularities or quasisingularities in the turbulent flows, which produce extremely localized and violent events of dissipation [14,15]. Therefore, both the homogeneity and the regularity conditions have to be relaxed and the weak formulation approach needs to be adopted to describe the local energy transport and dissipation [11]. We discuss in detail the local energy balance equation derived by using the weak solution formulation (see Refs. [11,12]). In particular, we elaborate on the expressions for the local energy transfers and local energy dissipation; we show how in our approach they generalize the average quantities in the Kármán-Howarth-Monin equation. We call this framework the weak Kármán-Howarth-Monin (WKH) equation.

We emphasize that this approach offers several interesting possibilities, as we describe below. WKH provides a natural framework to study possible quasisingularities and singularities (see Ref. [22] for more details). In the presence of a quasisingularity or a singularity in the velocity field, it yields a nonzero inertial dissipation term $\mathscr{D}^{\mathrm{I}}$ in the limit $\ell \to 0$. Moreover, even after we perform a coarse-graining on the velocity field, the signatures of quasisingularities and singularities are present at finite resolutions in the form of $\mathscr{D}_\ell^{\mathrm{I}}$ being nonzero along the lines in the scale space that originate from the singularity at $\ell = 0$. We can use the study of the velocity field at the dissipation scales around the extreme events of $\mathscr{D}_\ell^{\mathrm{I}}(\boldsymbol{u},\boldsymbol{x},t)$ to classify the possible quasisingularities and singularities [16]. Therefore, WKH provides a concrete description of the multifractal framework. Also, the analysis of the tail of the PDFs of $\mathscr{D}_\ell^{\mathrm{I}}(\boldsymbol{u},\boldsymbol{x},t)$ provides information about the topology of the quasisingularities.

The main advantage of the WKH framework is to localize in space and time the different terms, which contribute to the energy cascade at any scale ℓ and associate them with special topologies of the velocity fields. This approach can be then used far beyond the Kolmogorov scale, e.g., to study energy transfers in geophysical flows [30]. We find this to be complementary to the traditional methods used in turbulence, which focus only on the structures associated with enstrophy or viscous dissipation (these were thought be the only relevant entities as the end product of the energy cascade). In our framework, the local energy transfer and inertial dissipation term appears as the most relevant quantity, which may be used to devise and validate new models of turbulence. Also, we can compute the main terms describing the local energy transfers $\mathscr{D}_\ell^{\mathrm{I}}$ and $\mathscr{D}_\ell^\nu$, once the velocity field is known. Interestingly, as discussed in Ref. [22], it is now possible to explore these concepts in experiments since the advent of the particle image velocimetry methods. Moreover, the weak formulation introduces a natural smoothing that makes the computation of these quantities much less sensitive to the noise than the original direct formulation.

Motivated by these considerations, we use the experimental measurements in a turbulent swirling flow to provide a study of the statistics and the scaling properties of $\mathscr{D}_\ell^{\mathrm{I}}$ and $\mathscr{D}_\ell^\nu$. We

find that the energy transfers are very intermittent because of the presence of extreme events at the dissipative scale, which may be regarded as the footprints of the quasisingularities or singularities existing at sub-Kolmogorov scale [16]. We show that these extreme events govern the intermittency corrections of the velocity field and follow from a refined similarity analysis based on local energy transfers [6,31]. We characterize the distribution of these extreme events by using the generalized Pareto distribution (GPD) analysis. The width of the tails is shown to be compatible with a similarity of the second kind, first proposed by Castaing [27]. Finally, we make a connection between the topological and the statistical properties of the extreme events of the inertial dissipation field and its multifractal properties.

In our analysis we are constrained to use the velocity fields measured on a plane because of the experimental limitations. We recognize that it is important to perform the same analysis on the velocity field measured over a volume, but the latter is still an experimental challenge because of the extreme refinement needed for such an analysis. We partly fill this gap by performing a 3D DNS at a moderate resolution and check that our results are not affected by the measurement constraints. Given that the numerical simulations of the INSE are performed over a finite resolution, it is yet not clear whether the extreme events of the local energy transfer will still be present, if they are indeed triggered by the potential sub-Kolmogorov scale Navier-Stokes singularities or quasisingularities. In the absence of these extreme events, we expect a different behavior of the tails of the distributions of the local energy transfers. However, an elaborate validation of our experimental results in numerical simulations requires very large simulations, which is a challenging task.

ACKNOWLEDGMENTS

This work has been supported by the Labex PALM (project Interdist), by EuHIT, a project funded by the European Community Framework Programme 7, Grant Agreement No. 312778, and by the ANR EXPLOIT, Grant Agreement No. ANR-16-CE06-0006-01. We thank the anonymous referee for very constructive remarks that helped to improve substantially the paper.

APPENDIX: METHODS

1. Experimental setup

We visualize turbulent von Kármán flows in a plexiglass cylinder of radius $R = 100$ mm, filled with water at a controlled temperature of 20 °C. The flows are driven by two counter-rotating curve-bladed impellers at a frequency F, rotating with their blades concave face pushing forward (called ANTI in previous publications of our group). The setup is oriented with its axis of symmetry in the vertical direction. Using high-zooming lenses coupled to standard stereo particle image velocimetry (PIV), we obtain 3-component velocity fields (radial u_r, axial u_z, azimuthal u_ϕ) of the flows in a vertical plane containing the symmetric axis, with nominal spatial resolution between $\Delta x = 0.24$ mm and $\Delta x = 3.4$ mm (the laser sheet that defines the measurement plane is $\sim$1 mm thick). The torque and frequency of each impeller is measured using a torque meter (SCAIME Inc.). More details on the setup can be found in [16]. The Reynolds number of the flow is given by $\mathrm{Re} = 2\pi R^2 F/\nu$, where ν is the fluid's kinematic viscosity. We use different mixtures of glycerol and water in order to vary the viscosity of the working fluid, and thus the Reynolds number. Monitoring the torques C_1 and C_2 applied to each impeller, we obtain the dimensionless energy injection rate as

$$\epsilon = \frac{2\pi(C_1 + C_2)F}{\rho\pi H R^4 (2\pi F)^3}. \tag{A1}$$

We have checked in a scale 4:1 heat-insulated version of our experiment in helium that in the stationary regime, the global energy input is balanced by a global heat output, so that ϵ also measures the energy dissipated in the flow. Due to flow inhomogeneity, however, the energy dissipation is not homogeneous within the whole flow. Therefore, we use in this paper local estimates, derived from second-order structure functions in [17]. From this, we can compute the Kolmogorov dissipative scale as $\eta = (\epsilon/\nu^3)^{-1/4}$.

We have further shown that in our experimental setup the dimensionless energy dissipation rate saturates towards a constant value $\epsilon = 0.05$ above $\mathrm{Re}_c = 3500$ [32], corresponding to the critical Reynolds number for the onset of fully developed turbulence [33]. Varying the viscosity while keeping $\mathrm{Re} > 3500$ thus enables us to monitor the size of the dissipative scale, while remaining in the regime where the flow is fully turbulent. Measurements at different values of $\Delta x/\eta$ were then obtained by acting on the frequency F, the mixture composition, and the zooming lens. Table I summarizes the parameters corresponding to the different cases. In cases A and B, the SPIV system has been zoomed on a 4 cm × 3 cm zone at the center of the experiment; see Fig. 16.

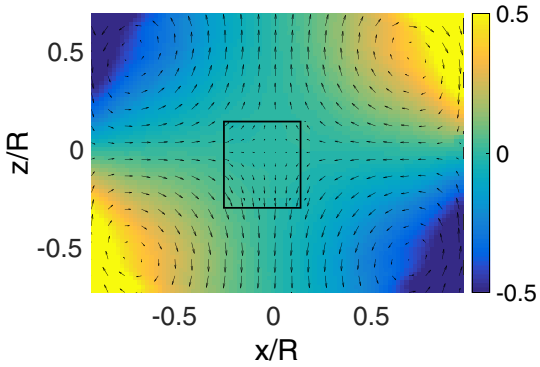

FIG. 16. Patchwork of mean velocity field in experiments A and C (in the black square). Color codes u_y, while u_x and u_z are in arrows. The coordinates have been nondimensionalized by R the radius of the cylinder.

2. Velocity fields

The results of this paper are based on series of SPIV measurements taken at frequency 15Hz (3 to 12 times the eddy turnover time) over 35 to 40 minutes, resulting in samples of 30 000 frames that can be considered as statistically independent. For each sample, the velocity field is reconstructed using peak correlation performed over 50% overlapping windows of size 16 to 32 pixels. As a result, we get instantaneous

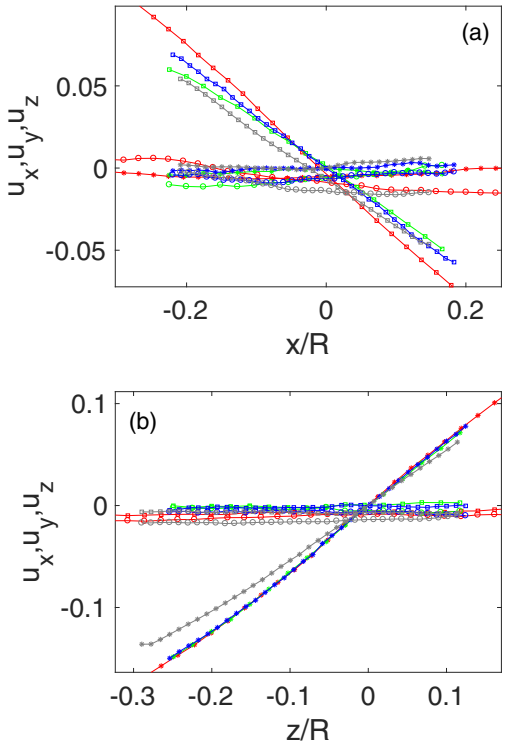

FIG. 17. Radial (a) and vertical (b) velocity profiles at $z = 0$ (resp. $x = 0$). Red: case A; green: case B; blue: case C; gray: case E. Square: u_r; circles: u_y; stars: u_z. The coordinates have been nondimensionalized by R the radius of the cylinder.

snapshots of the three components of the velocity field on a grid of approximate size 90×70. In the sequel, we work with dimensionless quantities, using the radius of the vessel R as the unit of length, and the impeller rotation period $(2\pi F)^{-1}$ as the unit of time. A typical map of the time-averaged velocity fields for the global experiments is provided in Fig. 16 for the cases A and C, showing the location of the zoom window. One observes a continuity in the flow topology between the zoomed and unzoomed case, showing that the calibration is consistent in between the two cases. To quantify further the discrepancy between the different zoomed and unzoomed field and estimate error bars, we plot in Fig. 17 mean radial and vertical profiles near the stagnation point. From this comparison, we can estimate a relative error on velocity measurements of 10%, resulting in an uncertainty of 30% for third-order quantities.

3. Wavelet spectrum

Given that the weak formulation was derived using continuous wavelet transform, it is informative to first compute the wavelet power spectrum of our velocity fields, given by

$$E^W(k) = \frac{1}{C_\Psi k_\Psi} \int d^2b \left| WT_i\left(\Psi, \boldsymbol{u}, \frac{k_\Psi}{k}, b\right)\right|^2, \qquad \text{(A2)}$$

where

$$W_i(\Psi, \boldsymbol{u}, a, b) = \int u_i(x) \Psi\left(\frac{x-b}{a}\right) \frac{d^2x}{a} \qquad \text{(A3)}$$

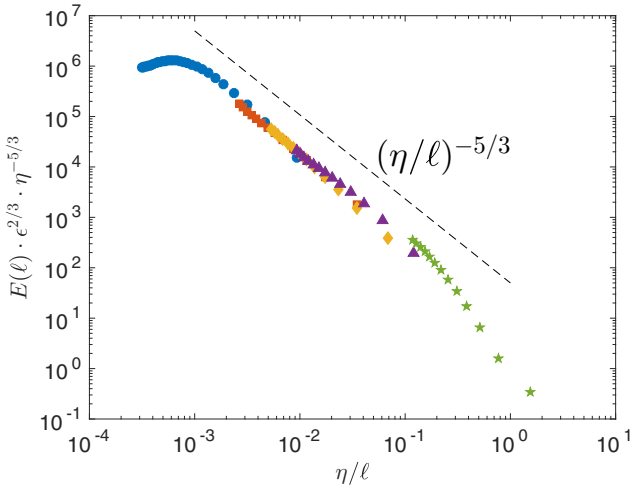

FIG. 18. Wavelet spectrum for the 5 different cases of Table I: blue circle: case A; red square: case B; yellow diamond: case C; purple triangle: case D; green stars: case E. The dotted line is $(\eta/\ell)^{-5/3}$. The spectrum and the the scale ℓ have been made nondimensional using η, the Kolmogorov scale, and ϵ, the energy dissipation.

is the 2D continuous wavelet transform of u_i with respect to the Mexican hat wavelet Ψ (Laplacian of a Gaussian), C_Ψ is a normalizing coefficient, and k_Ψ is the centroid velocity wave number, defined through the Fourier transform of Ψ as

$$k_\Psi = \frac{\int k|\hat{\Psi}(k)|dk}{\int |\hat{\Psi}(k)|dk}. \qquad \text{(A4)}$$

As discussed in [13], this global wavelet spectrum converges towards the Fourier energy spectrum provided Ψ has enough vanishing moments. Its advantage is that it is less noisy than the Fourier energy spectrum, since it can be interpreted as a moving average of the energy spectrum over the wave number space [13]. The wavelet spectrum is provided in Fig. 18 following a "universal" representation $E^W(\ell)/\epsilon^{2/3}/\eta^{5/3} = F(\eta/\ell)$, with $\ell = k_\Psi/k$, for the cases we considered in the paper. One sees that the superposition of the 5 cases follows a $\ell^{-5/3}$ law over a large interval of wave number, that can be interpreted as an inertial range. Case A corresponds to injection scales, cases B, C, and D correspond to inertial range, while case E is in the dissipative range.

4. Diagnostics for energy transfer and dissipation

Given any instantaneous velocity field, we can compute the 2D-3C velocity increments $\delta\vec{u}(\vec{r}) = \vec{u}(\vec{x}^{2D} + \vec{r}^{2D}) - \vec{u}(\vec{x}^{2D})$, $\vec{x}^{2D}$, and $\vec{r}^{2D}$ being the coordinates onto the plane of measurements. In this paper, for simplicity, we omit the ^{2D} superscript.

Following Eq. (10), we may then use our measurements to compute the quantity $\mathscr{D}_\ell^{\mathrm{I}}$ and $\mathscr{D}_\ell^{\nu}$:

$$\mathscr{D}_\ell^{\mathrm{I}} = \frac{1}{4} \int \nabla\phi^\ell(\xi) \cdot \delta\boldsymbol{u}(\delta u)^2,$$

$$\mathscr{D}_\ell^{\nu} = -\nu \int \nabla^2\phi^\ell(\xi)\boldsymbol{u}(x) \cdot \boldsymbol{u}(x+\xi)d\xi. \qquad \text{(A5)}$$

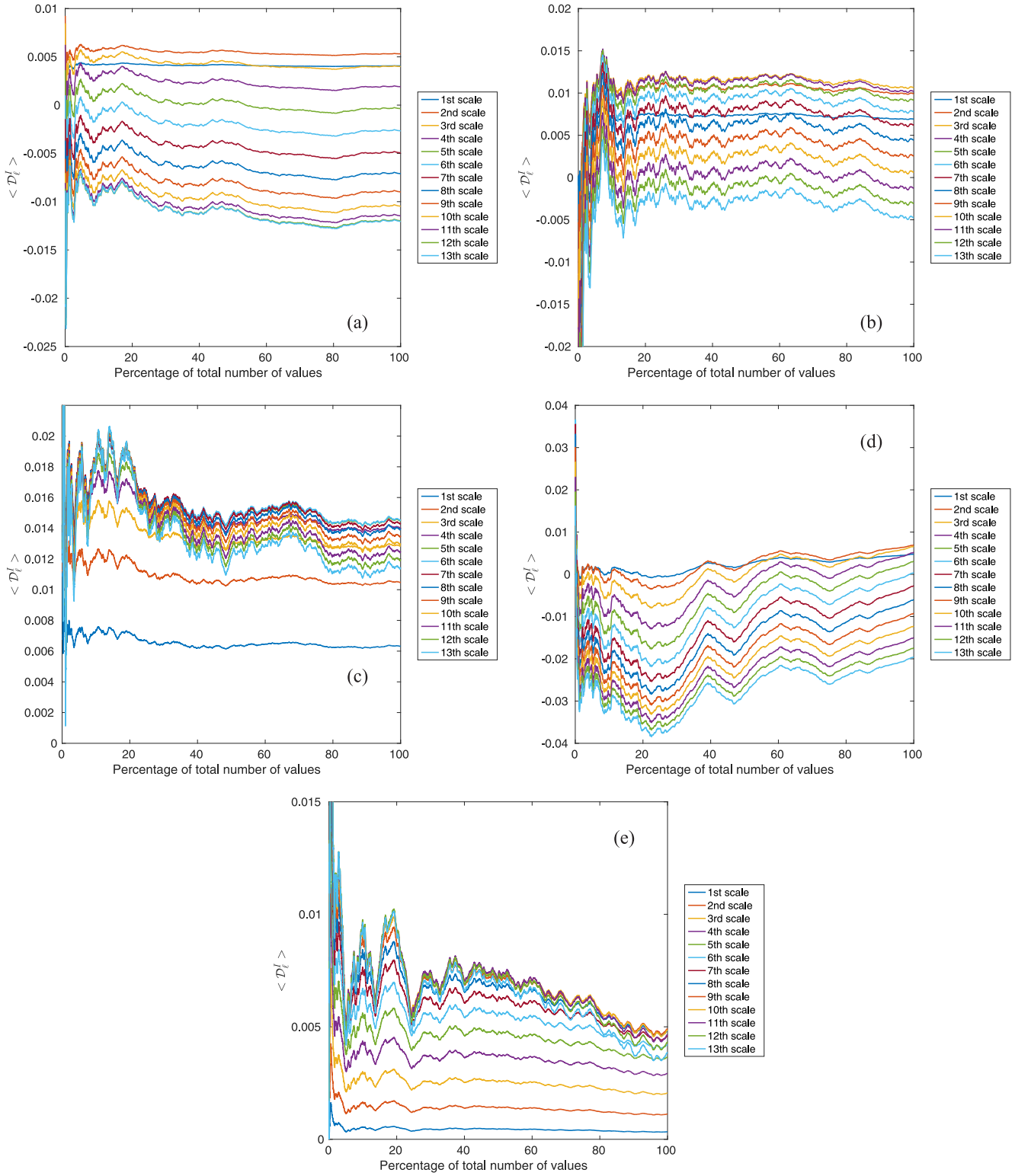

FIG. 19. Convergence of $\mathscr{D}_\ell^{\mathrm{I}}$ for cases A (a), B (b), C (c), D (d), and E (e).

For this, we use a simple shift in the definition of $\mathscr{D}_\ell^v$ to write it in term of a continuous wavelet transform as

$$\mathscr{D}_\ell^v(\boldsymbol{x}) = -\nu u_i(\boldsymbol{x}) WT_i(\Psi, \boldsymbol{u}, \ell, \boldsymbol{x}), \tag{A6}$$

where $WT_i(\Psi, \boldsymbol{u}, \ell, \boldsymbol{x})$ is the continuous wavelet transform of u_i with respect to the wavelet $\Psi = \nabla^2\phi$. Taking ϕ as a Gaussian transforms Ψ into the Mexican hat wavelet. The advantage of such a formulation is that it transforms the problem of computation of $\mathscr{D}_\ell^v(\boldsymbol{x})$ into the problem of computing 3 continuous wavelet transform, which is very fast using algorithms based on FFT. In the sequel, we use the 2D continuous wavelet MATLAB package provided by the toolbox YAWTB [35].

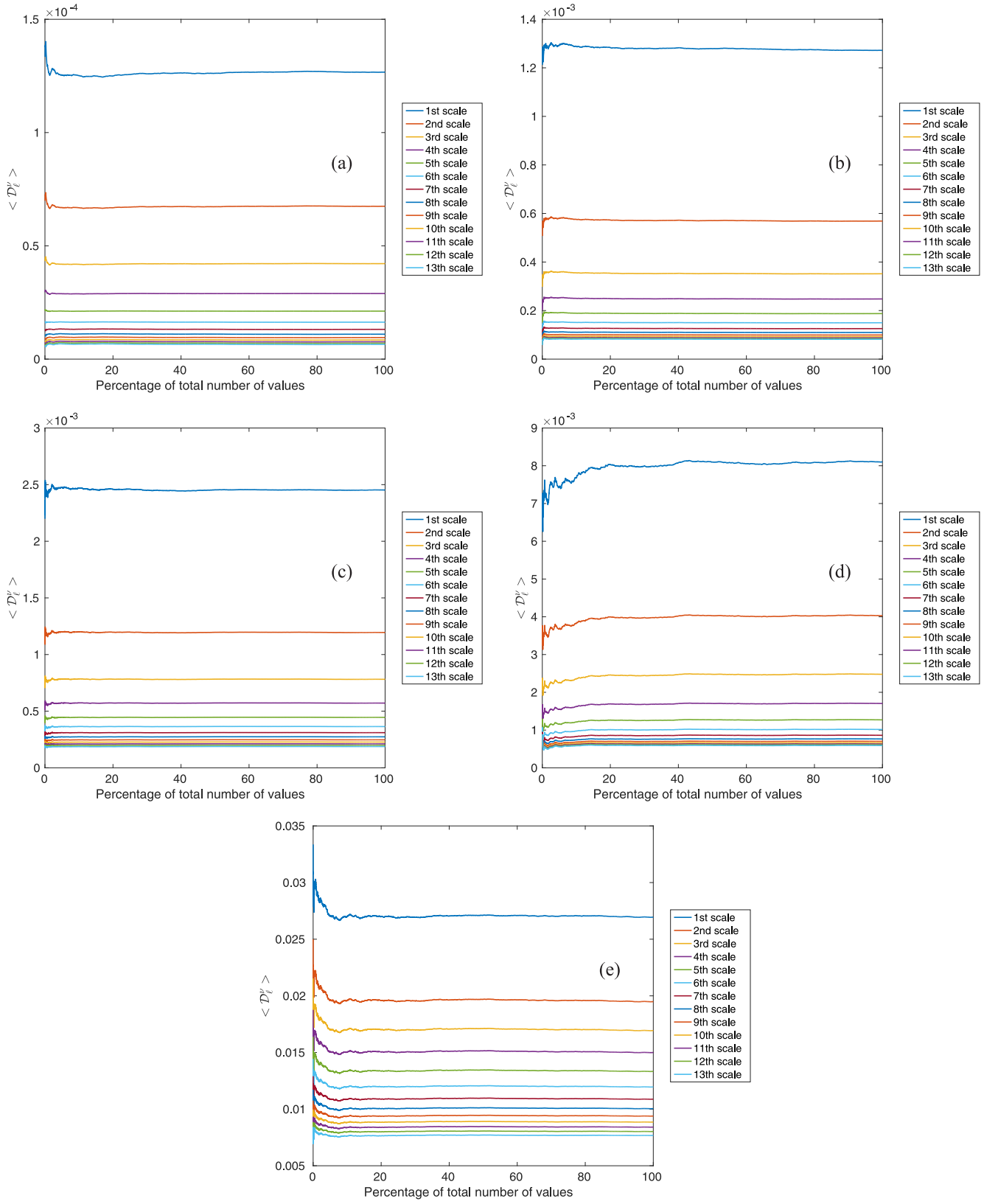

FIG. 20. Convergence of $\mathscr{D}_\ell^v$ for cases A (a), B (b), C (c), D (d), and E (e).

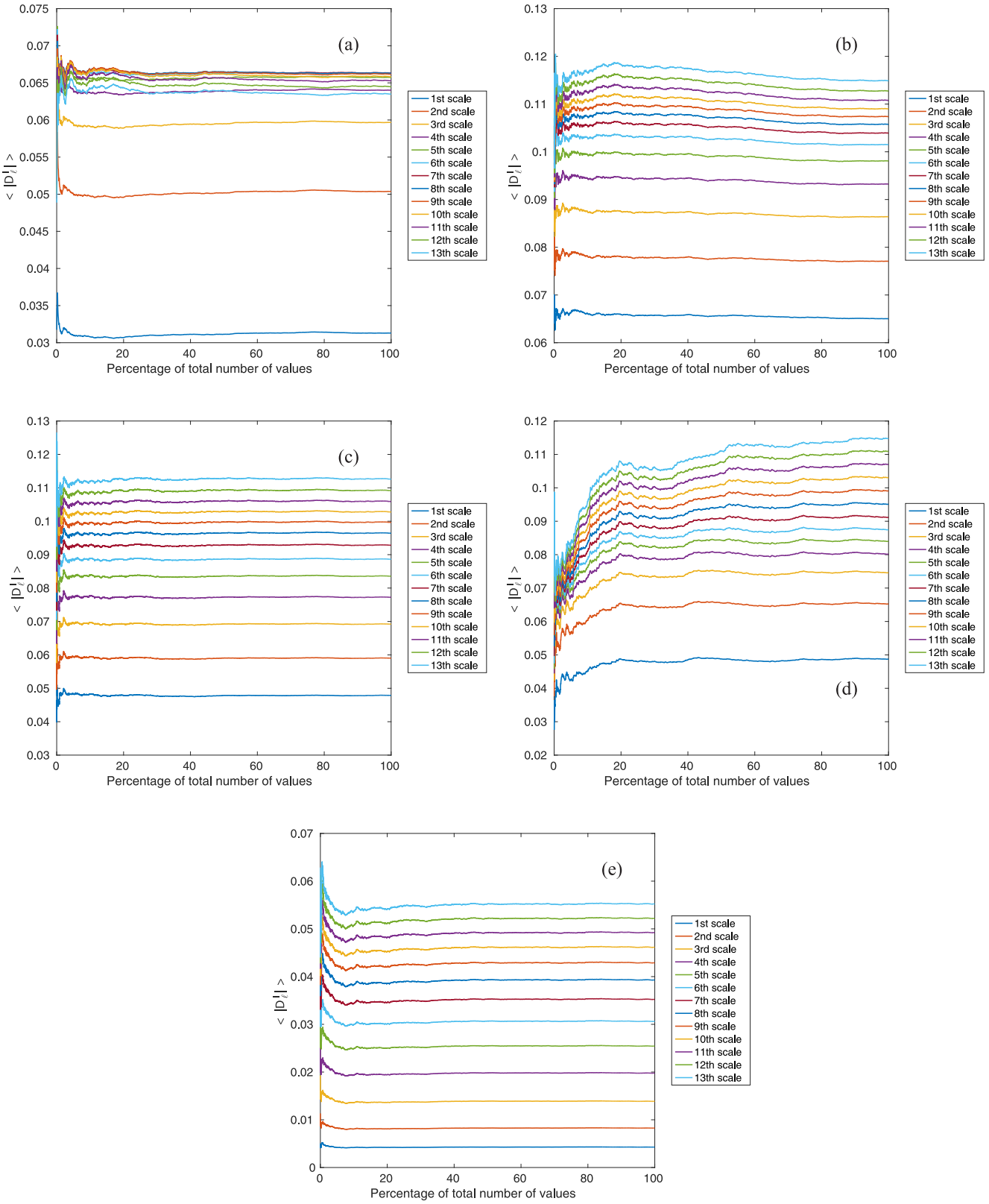

FIG. 21. Convergence of $|\mathscr{D}_\ell^{\mathrm{I}}|$ for cases A (a), B (b), C (c), D (d), and E (e).

In the same way, one can use continuous wavelet transforms to compute efficiently $\mathscr{D}_\ell^{\mathrm{I}}$. Indeed, developing its expression, we get 18 terms looking typically like

$$T_{11} = \frac{1}{4}\int \nabla_1 \phi^\ell(\xi) u_1(x+\xi)|u(x+\xi)|^2, \tag{A7}$$

which can be expressed as

$$T_{11} = \tfrac{1}{4} W T_1(\nabla_1\phi, \boldsymbol{u}|u|^2, \ell, \boldsymbol{x}). \tag{A8}$$

Using complex wave numbers and complex wavelet transforms, we can then compute the whole term $\mathscr{D}_\ell^{\mathrm{I}}$ using only 9 complex continuous wavelet transforms.

For the DNS, we have used the same method, using the 3D continuous wavelet MATLAB package provided by the toolbox YAWTB.

5. Convergency analysis

To check the convergency of the quantity $\mathscr{D}_\ell^{\mathrm{I}}$ and $\mathscr{D}_\ell^{v}$, we have computed the running average of a variable ensemble of velocity fields, ranging from 0% of the total number of frames to 100% of the total number. The results are displayed in Figs. 19 and 20. One sees that the average is converged in all cases and for all scales for $\mathscr{D}_\ell^{v}$, and only for the first scales for the high-resolution data set C and E for $\mathscr{D}_\ell^{\mathrm{I}}$. For all other cases and scales, the average of $\mathscr{D}_\ell^{\mathrm{I}}$ is not converged within our statistics. If one looks for the average of the absolute value of $\mathscr{D}_\ell^{\mathrm{I}}$, the convergency is ensured for all cases and scales, as can be seen in Fig. 21.

6. Generalized Pareto distribution analysis

To perform the extreme value analysis we have chosen the so-called peak-over-threshold approach formalized by Pickands [34]. In this approach one considers a series of independent and identically distributed variables $X_1, X_2, \ldots, X_n$ and studies the probability $P(X > t)$ of exceeding a threshold t corresponding to a large quantile. The Pickands theorem states that such exceedings asymptotically obey a generalized Pareto distribution (GPD) distribution with cumulative distribution function:

$$F_G(x;\mu,\sigma,\xi) = 1 - \left[1 + \xi\left(\frac{x-\mu}{\sigma}\right)\right]^{-1/\xi}, \tag{A9}$$

where $\mu \in \mathbb{R}$ is the *location parameter* representing the chosen threshold and $\sigma > 0$ is the *scale parameter*, representing the typical order of extreme fluctuations. The sign of ξ discriminates the kind of tail decay of the parent distribution: When $\xi = 0$, the distribution is of Gumbel type with exponentially decaying tail and Eq. (A9) reduces to

$$F_G(x;\mu,\sigma,\xi) = 1 - \exp\left(-\frac{x-\mu}{\sigma}\right). \tag{A10}$$

The case $\xi > 0$, corresponds to a Fréchet distribution with a fat tail decaying as a power law. Conversely, the case $\xi < 0$ corresponds to the Weibull distribution with a bounded tail. In the Fréchet $\xi > 0$ case, only the moments up to $1/\xi$ exist, meaning that there is a nonzero probability of observing infinite values for the observable analyzed. The parameters are estimated using the MATLAB function gpfit that use a maximum likelihood estimator.

7. Direct numerical simulations: Initial data and forcing

To start the DNS run, we use the Taylor-Green initial velocity field given by

$$u_x = \sin(x)\cos(y)\cos(z), \tag{A11a}$$
$$u_y = -\cos(x)\sin(y)\cos(z), \tag{A11b}$$
$$u_z = 0. \tag{A11c}$$

We obtain turbulent steady states of the INSE by using the Taylor-Green forcing:

$$f_x = f_0 \sin(\tilde{k}_{\mathrm{f}} x)\cos(\tilde{k}_{\mathrm{f}} y)\cos(\tilde{k}_{\mathrm{f}} z), \tag{A12a}$$
$$f_y = -f_0 \cos(\tilde{k}_{\mathrm{f}} x)\sin(\tilde{k}_{\mathrm{f}} y)\cos(\tilde{k}_{\mathrm{f}} z), \tag{A12b}$$
$$f_z = 0, \tag{A12c}$$

where f_0 and $\tilde{k}_{\mathrm{f}}$ are the forcing amplitude and wave number, respectively. We define $k_{\mathrm{f}} = \sqrt{3}\tilde{k}_{\mathrm{f}}$ as the amplitude of the forcing wave vector $\mathbf{k}_{\mathrm{f}} = (\tilde{k}_{\mathrm{f}}, \tilde{k}_{\mathrm{f}}, \tilde{k}_{\mathrm{f}})$.

[1] A. N. Kolmogorov, Dokl. Akad. Nauk SSSR **30**, 301 (1941).
[2] A. N. Kolmogorov, J. Fluid Mech. **13**, 82 (1962).
[3] A. M. Oboukhov, J. Fluid Mech. **13**, 77 (1962).
[4] R. H. Kraichnan, J. Fluid Mech. **62**, 305 (1974).
[5] C. Meneveau, J. Fluid Mech. **232**, 469 (1991).
[6] G. L. Eyink, J. Stat. Phys. **78**, 335 (1995).
[7] L. Onsager, Il Nuovo Cimento **6**, 279 (1949).
[8] U. Frisch, *Turbulence: The Legacy of A. N. Kolmogorov* (Cambridge University Press, Cambridge, 1995).
[9] G. L. Eyink, J. Stat. Phys. **78**, 353 (1995).
[10] U. Frisch and G. Parisi, in *Turbulence and Predictability in Geophysical Fluid Dynamics and Climate Dynamics*, edited by M. Gil, R. Benzi, and G. Parisi (Elsevier, Amsterdam, 1985), pp. 84–88.
[11] J. Duchon and R. Robert, Nonlinearity **13**, 249 (2000).
[12] G. L. Eyink, Turbulence Theory, course notes, The Johns Hopkins University, 2007-2008, http://www.ams.jhu.edu/~eyink/Turbulence/notes/ChapterIIIb.pdf.
[13] M. Farge and K. Schneider, https://www2.warwick.ac.uk/fac/sci/physics/research/cfsa/people/sandrac/lectures/farge_wavelets_turb2002.pdf.
[14] T. D. Drivas and G. L. Eyink, Commun. Math. Phys. **359**, 733 (2018).
[15] A. A. Mailybaev, Phys. Rev. E **87**, 053011 (2013).
[16] E. W. Saw *et al.*, Nat. Commun. **7**, 12466 (2016).
[17] E. W. Saw *et al.*, J. Fluid Mech. **837**, 657 (2018).
[18] J. F. Pinton and R. Labbé, J. Phys. II **4**, 1461 (1994).
[19] G. Zocchi, P. Tabeling, J. Maurer, and H. Willaime, Phys. Rev. E **50**, 3693 (1994).
[20] P. Kestener and A. Arneodo, Phys. Rev. Lett. **93**, 044501 (2004).

[21] A. Arneodo *et al.*, Europhys. Lett. **34**, 411 (1996).
[22] D. Kuzzay *et al.*, Nonlinearity **30**, 2381 (2017).
[23] B. Dubrulle, Phys. Rev. Lett. **73**, 959 (1994).
[24] J. F. Muzy, E. Bacry, and A. Kozhemyak, Phys. Rev. E **73**, 066114 (2006).
[25] P. Abry, V. Pipiras, and H. Wendt, in *Proc. GRETSI Symposium Signal and Image Processing, Troyes, France* (GRETSI, 2007).
[26] B. Castaing, J. Phys. **50**, 147 (1989).
[27] B. Castaing, Y. Gagne, and E. J. Hopfinger, Phys. D (Amsterdam, Neth.) **46**, 177 (1990).
[28] B. Dubrulle and F. Graner, Phys. Rev. E **56**, 6435 (1997).
[29] M. R. Leadbetter, G. Lindgren, and H. Rootzén, *Extremes and Related Properties of Random Sequences and Processes* (Springer Science & Business Media, New York, Berlin, Heidelberg, 2012).
[30] D. Faranda, V. Lembo, M. Iyer, D. Kuzzay, S. Chibbaro, F. Daviaud, and B. Dubrulle, J. Atmos. Sci. (2018), doi:10.1175/JAS-D-17-0114.1.
[31] R. H. Kraichnan, Adv. Math. **16**, 305 (1975).
[32] B. Saint-Michel *et al.*, Phys. Fluids **26**, 125109 (2014).
[33] F. Ravelet, A. Chiffaudel, and F. Daviaud, J. Fluid Mech. **601**, 339 (2008).
[34] J. Pickands, Ann. Stat. **3**, 119 (1975).
[35] The toolbox YAWTB is available freely at http://sites.uclouvain.be/ispgroup/yawtb

Chapter 8

Topology of the extreme events of the Duchon-Robert term

In this chapter, we analyze the structure of the flow around the extreme events of the Duchon-Robert term, raw (Π^ℓ_{DR}) or normalized by the viscous dissipation term ($\Pi^\ell_{DR}/\mathscr{D}^\ell_\nu$). Indeed, these events may be prints of the possible singularities developed by the 3D incompressible Euler or Navier-Stokes equations. The chapter is splitted into two parts : first, we analyze the topology of the flow using the invariants of the velocity gradient tensor which allow to identify four types of topologies. This analysis can easily be implemented on a computer in order to process a large amount of data ; however, it does not reveal the complexity of the flow around a given point. Therefore, in the second part we describe the structure of the velocity field around the extreme events based on direct visual observation of the corresponding velocity fields.

1 First "blind" approach using the velocity gradient tensor invariants

In this section, we use the velocity gradient tensor invariants to characterize the topology of the velocity field. We first recall the principle of this method, and then present the global distribution of the topologies in the von Kármán flow. Thereafter, we analyze the global behaviour of Π^ℓ_{DR} and $\mathscr{D}^\ell_\nu$ with respect to the invariants before giving the distribution of the topologies among the extreme events.

1.1 The velocity gradient tensor invariants method

The velocity gradient tensor (VGT) invariants method (see [Chong et al., 1990]) consists in studying the velocity streamline pattern at a given point and at a given time. For an incompressible flow, only four categories of topologies (i.e. velocity streamlines configurations) can be found.
Let us consider an instantaneous velocity field $\mathbf{u}(\mathbf{x})$. A streamline $\mathbf{x}(t)$ is defined by $\dot{\mathbf{x}} = \mathbf{u}(\mathbf{x})$. Let us consider a particular point $\mathbf{x_0}$ where the velocity is $\mathbf{u_0}$. If the velocity field is regular enough to be expanded in Taylor series, then for $\delta\mathbf{x}$ small enough, $\mathbf{u}(\mathbf{x_0}+\delta\mathbf{x}) \approx \mathbf{u_0} + \nabla\mathbf{u}\cdot\delta\mathbf{x}$ where $\cdot$ corresponds to the product between a matrix and a vector : with $(\nabla\mathbf{u})_{ij} = \partial_j u_i$, $(\nabla\mathbf{u}\cdot\delta\mathbf{x})_i = \sum_j \partial_j u_i \delta x_j$. Therefore, the streamline equation in the neighbourhood of $\mathbf{x_0}$ is $\dot{\mathbf{x}} \approx \mathbf{u_0} + \nabla\mathbf{u}\cdot(\mathbf{x}-\mathbf{x_0})$. In the inertial frame initially centered on $\mathbf{x_0}$ and moving at constant speed $\mathbf{u_0}$, the streamline equation becomes $\dot{\mathbf{x}} \approx \nabla\mathbf{u}\cdot(\mathbf{x})$. This is a linear differential equation whose solution depends on the eigenvalues of $\nabla\mathbf{u}$, or equivalenty on its three invariants, i.e. the coefficients of its characteristic polynomial.

Depending on whether the eigenvalues are real or not, degenerated or not, and positive, negative or null, only a finite number of configurations are possible, described in [Chong et al., 1990]. In the particular case of an incompressible flow, there is an additional constraint on the eigenvalues : their sum should be 0. Hence, there are only four possible topologies. Calling the three eigenvalues λ_1, λ_2, and λ_3 ; and the VGT invariants P, Q and R (so that the characteristic polynomial is $\lambda^3 + P\lambda^2 + Q\lambda + R$), we have in the particular case of incompressible flows :

- $P = \lambda_1 + \lambda_2 + \lambda_3 = 0$,
- $Q = \lambda_1\lambda_2 + \lambda_1\lambda_3 + \lambda_2 + \lambda_3 = -tr((\nabla \mathbf{u})^2)/2$,
- $R = -\lambda_1\lambda_2\lambda_3 = -tr((\nabla \mathbf{u})^3)/3 = -det(\nabla \mathbf{u})$.

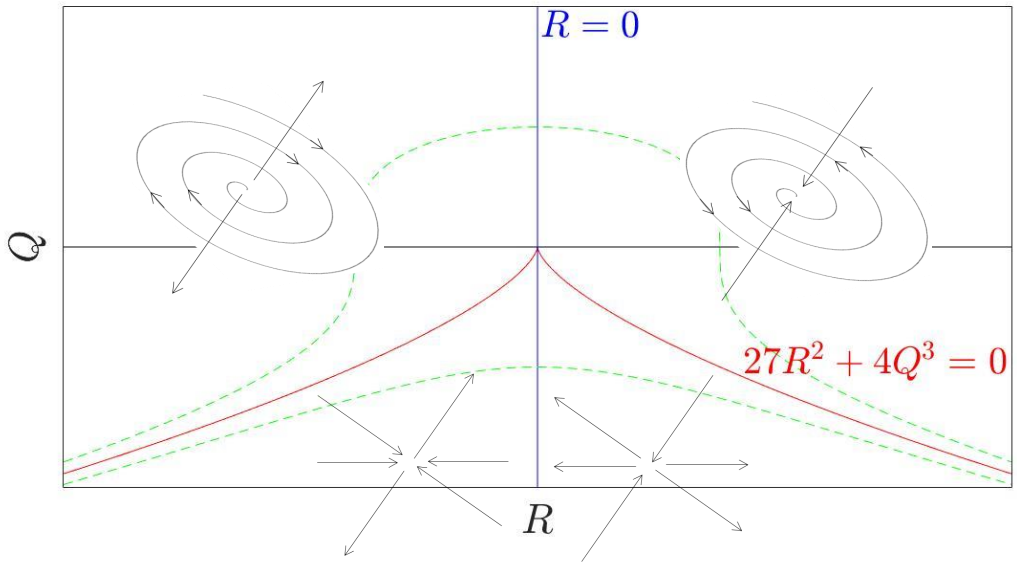

Figure 8.1: Q-R plane and schemes of the different topologies. The red line and the green dashed lines are Vieillefosse lines.

The four different possible topologies in the case of an incompressible flow, shown in figure 8.1, are the following :

- the "filament" (F), or stable node/saddle/saddle, when $27R^2 + 4Q^3 < 0$ and $R < 0$. All three eigenvalues are then real, only one of them being positive. The fluid is compressed in two directions and stretched in the third one.
- the "sheet" (S), or unstable node/saddle/saddle, when $27R^2 + 4Q^3 < 0$ but $R > 0$. All three eigenvalues are then real, but two of them are positive. The fluid is compressed in one direction and stretched in the two others.
- the "vortex stretching" (VS), or stable focus/stretching, when $27R^2 + 4Q^3 > 0$ and $R < 0$. There are then two complex eigenvalues that are conjugated ; the real eigenvalue is positive, resulting in the stretching. In one plane, the motion of the fluid is a converging spiral ; in the remaining direction the fluid is stretched.

- the "vortex compressing" (VC), or unstable focus/compressing, when $27R^2 + 4Q^3 > 0$ but $R > 0$. There are then two complex eigenvalues that are conjugated but the real eigenvalue is negative, resulting in the compressing. The fluid is compressed in one direction ; in the plane containing the two other directions, its motion is a diverging spiral.

In the Q-R plane, the $R = 0$ line distinguishes between stable (converging in two directions and diverging in one) and unstable (diverging in two directions) topologies ; the line $27R^2 + 4Q^3 = 0$ separates the cases with complex eigenvalues (which will feature rotation) from the cases with only real eigenvalues. Note that Vieillefosse [Vieillefosse, 1983] showed that for an elementary fluid particle in an inviscid fluid and not subject to the action of the remaining fluid (i.e. without pressure anisotropic effects), Q and R follow the equations :

$$\dot{Q} = -3R/2 \tag{8.1}$$

$$\dot{R} = Q^2/3 \tag{8.2}$$

where $\dot{X}$ corresponds to the material derivative of X. Integrating these equations leads to :

$$3\dot{Q}^2 + Q^3 = Q_0^3 \tag{8.3}$$

or :

$$27R^2 + 4Q^3 = 4Q_0^3 \tag{8.4}$$

where Q_0 is a constant. The lines $27R^2 + 4Q^3 = 4Q_0^3$ are usually called "Vieillefosse lines". Two of them with $Q_0 \neq 0$ are shown in green in figure 8.1 ; the one corresponding to $Q_0 = 0$ is shown in red.
Therefore, Q diverges towards $-\infty$ and R towards $+\infty$ in finite time and a singularity occurs, on the right branch of the $27R^2 + 4Q^3 = 0$ line.
In some works, for instance in [Danish and Meneveau, 2018], the vortex stretching and compressing zones are further splitted into two sub-zones each : $Q < 0$ and $Q > 0$. The former corresponds to the strain-dominated zone whereas the latter corresponds to the enstrophy-dominated zone. Indeed, splitting the VGT $\nabla \mathbf{u}$ in its symmetrical and antisymmetrical parts S and A, we have :

$$tr((\nabla \mathbf{u})^2) = tr(S^2 + AS + SA + A^2) = tr(S^2) + tr(A^2) \tag{8.5}$$

because the traces of AS and SA are zero, as they are the product of one symmetrical and one antisymmetrical matrix. As S is the strain rate tensor, $tr(S^2)$ measures the strain ; furthermore, it can be shown that $tr(A^2) = -\omega^2/2$. Therefore, $Q = -tr((\nabla \mathbf{u})^2)/2 = \frac{\omega^2/2 - tr(S^2)}{2}$ and $Q < 0 \implies \omega^2 < 2 \cdot tr(S^2)$: the strain dominates the enstrophy.
Usually, it is considered that the VGT is properly computed, and therefore that the "true" topology of the flow is obtained only if the Kolmogorov scale is resolved, as it is generally assumed to be the smallest scale of the flow. Also, the VGT invariants method can only apply to points where the velocity is regular enough to be expanded in Taylor series. In this thesis, we are looking for prints of singularities, where the velocity field is unlikely to be expanded in Taylor series and around which the smallest scale of the flow should be smaller than the Kolmogorov scale, and therefore than our resolution (we resolve the Kolmogorov scale only for cases T4 and T4t, but not lower scales). However, we still think that using the VGT invariants method is relevant because we have a finite experimental resolution, i.e. we work with velocity fields filtered at the experimental resolution.

These fields are therefore regular and the method can be applied. We then do not claim to obtain the exact topology of the flow, but the topology "at the experimental resolution". This is interesting as it can give informations about the way singularities appear.
The VGT invariants method is very practical as it can be implemented on a computer and applied to a wide number of points. It allows to study the global distribution of the topologies in our von Kármán flow in order to compare it with the distribution of the topologies among the extreme events of inter-scale transfer.

1.2 Global topology study in the von Kármán flow

1.2.1 Global topology distribution

Before studying the topologies of the extreme events of inter-scale transfer, we computed the global distribution of the topologies in the von Kármán flow. It is needed to have a reference when studying how the topologies are distributed among the extreme events. Also, the distribution of the topologies (obtained with the VGT invariants method) in a turbulent flow is one of the noticeable features of turbulence (see [Elsinga and Marusic, 2010] for references) : the Q-R joint pdf has a tear-drop shape. Though it can be accounted for by a stochastic model [Chevillard and Meneveau, 2006, Chevillard et al., 2008], it is not yet related to the Navier-Stokes equations. Therefore, it was interesting to see whether we could observe it in the particular case of the von Kármán flow which has a particular geometry.
Figure 8.2 shows the Q-R joint pdf for cases T1 to T4. The gradients were computed with a second-order centered scheme. For case T4, the joint pdf has the well-known tear-drop shape, with the bottom-right tail following the Vieillefosse line with $R > 0$. This shape indicates that the most probable topology is the vortex stretching, followed by the vortex compressing, then the sheet and finally the filament. This shape also suggests that very large values of the gradient happen on the Vieillefosse line with $R > 0$, at the interface between the vortex compressing and the sheet zones.
When X/η is increased (X being the interrogation volume size), the tear-drop shape is progressively blurred, evolving towards an almost square shape. The evolution is due to the fact that the Kolmogorov scale is not resolved anymore, i.e. that only larger (inertial) scales are probed. The square shape means that Q and R are more independent for higher values of X/η. Also, as the Q-R joint pdf is more symmetrical with respect to the $R = 0$ axis, the proportions of vortex stretching and compressing are closer to each other, and so do the proportions of sheet and filament.
We are now interested to see whether particular topologies favour extreme events of the Duchon-Robert term. A first approach is to study the behaviour of the Duchon-Robert term with respect to Q and R, i.e. to compute the conditional average of the Duchon-Robert term, conditioned on Q and R.

1.2.2 Average behaviour of Π^ℓ_{DR} and $\mathscr{D}^\ell_\nu$ with respect to Q and R

The conditional averages of the Duchon-Robert term for the different values of ℓ_c/η previously studied are shown in figure 8.3. For large values of Q and R, that are rare, the conditional averages are scattered : indeed, the averages are not converged because there are not enough points with such (Q, R).
The most striking feature of the average of Π^ℓ_{DR} conditioned on Q and R is the evolution of the zone of negative values of Π^ℓ_{DR} (delimited by the red line) when ℓ_c/η is varied. Indeed, for case T4 (for which the resolution is in the dissipative range), this zone is restricted to a part of the vortex compressing area, with positive but not too high Q. However, when ℓ_c/η is increased, the

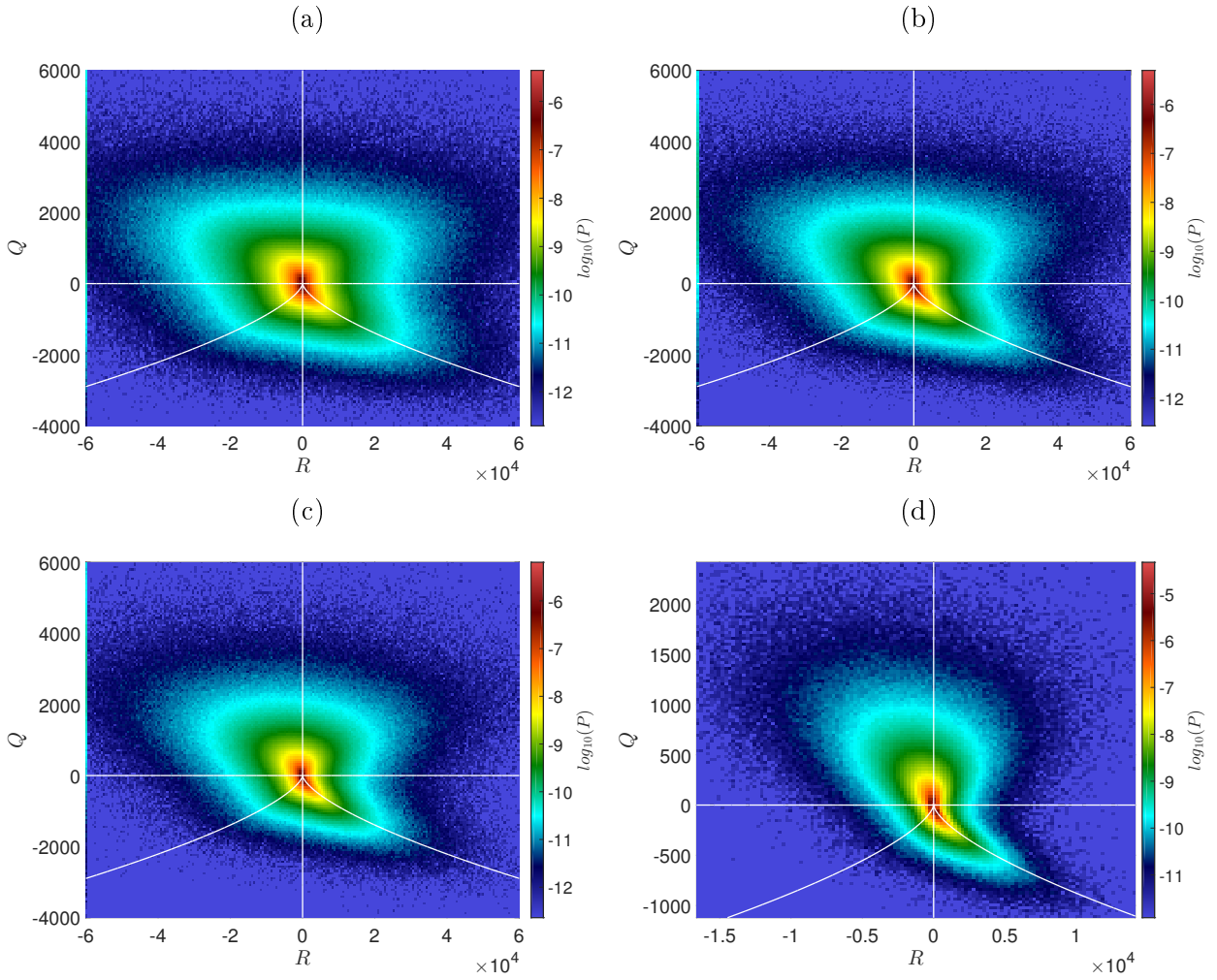

Figure 8.2: Q-R joint pdfs of cases T1 (a), T2 (b), T3 (c) and T4 (d). The white lines correspond to the lines $Q = 0$, $R = 0$ and to the Vieillefosse line $27R^2 + 4Q^3 = 0$. The axis limits are the same for (a), (b) and (c) but not for (d).

negative zone disappears (only zones of low but non-negative Π^ℓ_{DR} can be seen), and reappears at the largest value of ℓ_c/η studied, but it is now in a part of the VS area. The existence of a zone with negative values of the Duchon-Robert term in the vortex compressing area is in agreement with the existence of a negative zone of the so-called energy transfer term in this same area, obtained in [Chevillard et al., 2008]. It can be understood if Π^ℓ_{DR} is interpreted as inter-scale transfer towards smaller scales. Indeed, as vortex compressing is the motion opposite to vortex stretching, which is a mechanism often invoked to explain the energy transfer towards small scales, it is natural to see vortex compressing as a mechanism to transfer energy towards larger scales. However, according to this reasoning, the whole vortex compressing zone should correspond to negative Π^ℓ_{DR}, which is not the case. The negative zone stops at the $Q = 0$ line, distinguishing between strain- and rotation dominated zones ; this suggests that there is a link between the strain-rotation competition and the sign of the inter-scale transfer. However, the other boundary of the negative zone, at large Q, does not correspond to such a particular line. Note that in [Chevillard et al., 2008], the negative zone of the energy transfer does not correspond exactly to the zone of negative Π^ℓ_{DR} that we obtained ; it corresponds to larger values of Q. When the resolution is in the inertial range, backward energy

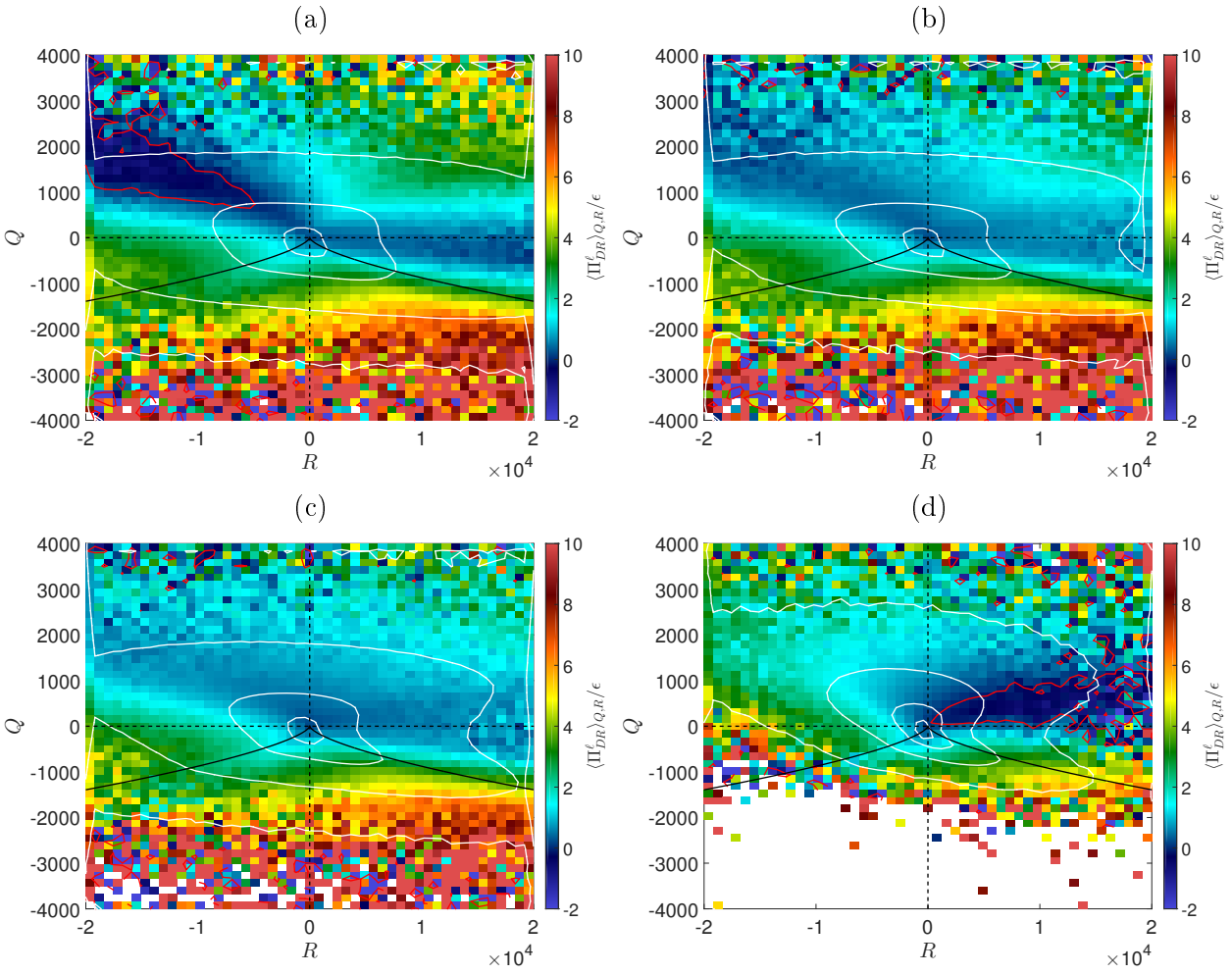

Figure 8.3: Conditional average of the Duchon-Robert term Π^{ℓ}_{DR}. ℓ_c is equal to 1.7 times the interrogation volume size. The white lines correspond to the isolines of the Q-R joint pdfs. The black plain lines correspond to the Vieillefosse line $27R^2 + 4Q^3 = 0$. The black dashed lines correspond to the axes $Q = 0$ and $R = 0$. The red lines correspond to the isoline corresponding to a conditional average equal to 0. (a) $\ell_c = 150\eta$ (obtained with case T1). (b) $\ell_c = 45\eta$ (case T2). (b) $\ell_c = 27\eta$ (case T3). (b) $\ell_c = 8\eta$ (case T4).

transfer is associated with vortex stretching. This contradicts the previous reasoning and suggests that the topology (obtained by the VGT invariants method) "at a given scale" alone cannot explain the inter-scale transfer at this scale ; either other scales are needed, which is unlikely if the energy cascade is local in scale, or other mechanisms are needed to explain the sign of the inter-scale transfer.

Figure 8.3 was obtained for $\ell_c = 1.7X$ (X being the PIV interrogation volume size), the largest ℓ_c we can reach on the current data. As explained in chapter 2, the ratio ℓ_c/X should not be too small, otherwise most of the contributions to Π^{ℓ}_{DR} are filtered. However, with a too large ℓ_c, Π^{ℓ}_{DR} can only be computed on a small area (see chapter 2). Therefore, there are less samples and the statistics may be less converged. Therefore, we present in figure 8.4 the conditional averages of Π^{ℓ}_{DR} obtained for $\ell_c = 1.2X$, for which the statistics are better converged (there are almost five times more points for $\ell_c = 1.2X$ compared to $\ell_c = 1.7$), even if there are less contributions from the smaller scales. On this figure, we can see that the negative Π^{ℓ}_{DR} zone does not disappear for any

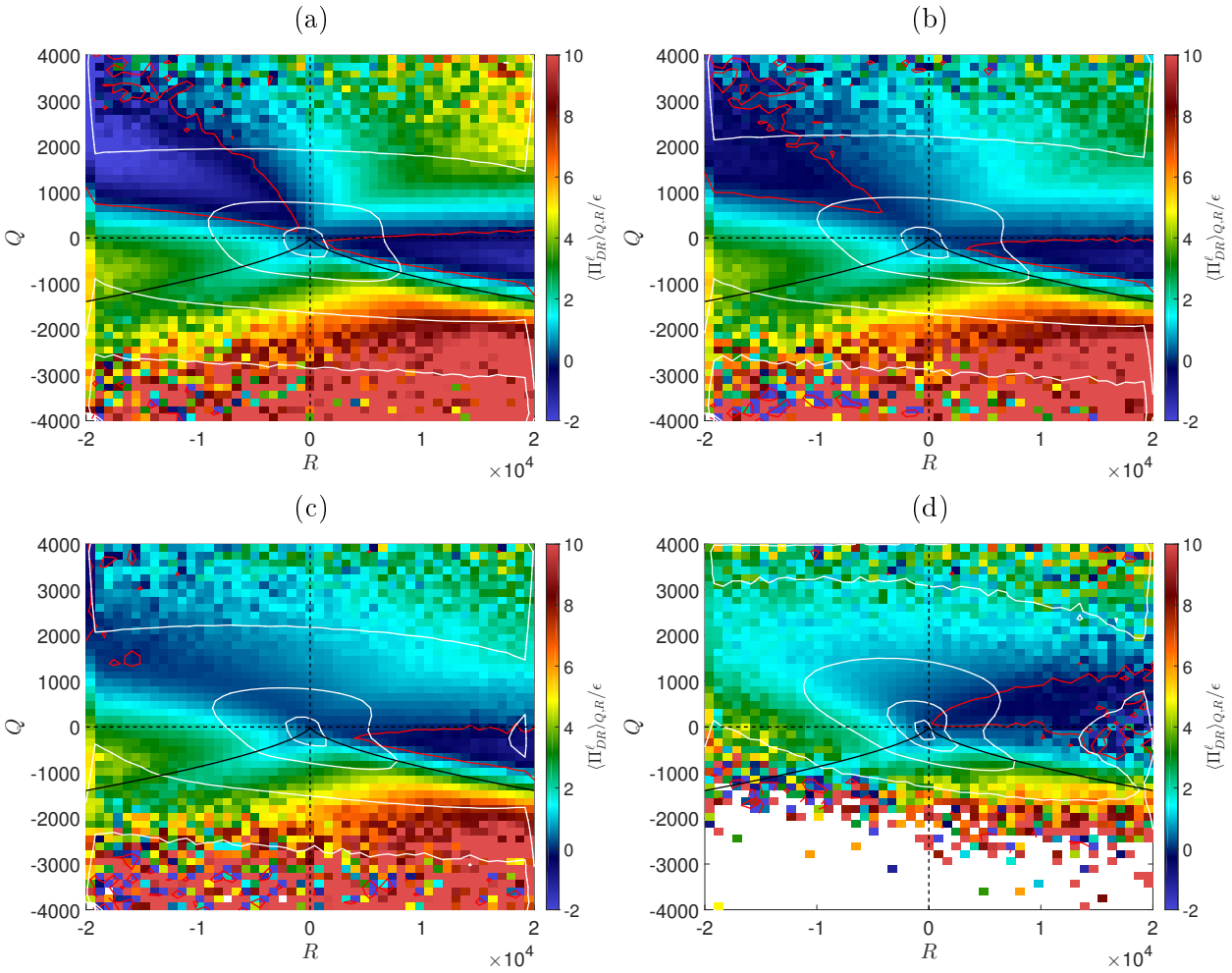

Figure 8.4: Conditional average of the Duchon-Robert term Π^{ℓ}_{DR}. ℓ_c is equal to 1.2 times the interrogation volume size. The white lines correspond to the isolines of the Q-R joint pdfs. The black plain lines correspond to the Vieillefosse line $27R^2 + 4Q^3 = 0$. The black dashed lines correspond to the axes $Q = 0$ and $R = 0$. The red lines correspond to the isoline corresponding to a conditional average equal to 0. (a) $\ell_c = 150\eta$ (obtained with case T1). (b) $\ell_c = 45\eta$ (case T2). (b) $\ell_c = 27\eta$ (case T3). (b) $\ell_c = 8\eta$ (case T4).

value of ℓ_c/η. Also, in the inertial range, there is not only a negative zone which appears in the VS area, but there is still a negative zone in the VC area, which is shifted to $Q < 0$ compared to the dissipative range.

A second feature of these conditional averages of Π^{ℓ}_{DR} is the spreading of the zone of low values (still positive though, at least with the amount of statistics we have) along the left part of the Vieillefosse line, at the boundary between the vortex stretching and the filament zones. This spreading becomes more important when ℓ_c/η is increased.

Lastly, the conditional average of Π^{ℓ}_{DR} gives us a hint of the topology associated with the extreme events. Indeed, whatever ℓ_c/η, the largest values of the conditional average of Π^{ℓ}_{DR} are found in the lower right part of the Q-R plane, i.e. in the sheet zone. There is also a secondary zone of large values for large negative R, around $Q = 0$ in the dissipative range and for $Q < 0$ in the inertial range ; it is less pronounced though. Of course, the extreme events may not follow the average trend ; this is just an indication.

It is also interesting to compare the conditional average of Π^ℓ_{DR} with the one of $\mathscr{D}^\ell_\nu$, in order to see whether there is some topology for which, in average, Π^ℓ_{DR} is high and $\mathscr{D}^\ell_\nu$ is small. The conditional average of $\mathscr{D}^\ell_\nu$ is shown in figure 8.5 for cases T1 to T4. It is striking to see that, for the four cases, the isolines of the conditional average of $\mathscr{D}^\ell_\nu$ are close to the isolines of the Q-R joint pdf (the white lines). This suggests that the joint pdf of Q and R could be expressed as $P(Q,R) = f(\langle\mathscr{D}^\ell_\nu\rangle_{QR})$ where ℓ is taken close to the scale at which the velocity field is filtered. f is a decreasing function. Therefore, the largest values of $\langle\mathscr{D}^\ell_\nu\rangle_{QR}$ are obtained for small $P(Q,R)$ i.e. large values of $|Q|$ and $|R|$. This suggests that extreme events of the ratio $\Pi^\ell_{DR}/\mathscr{D}^\ell_\nu$ should rather have a sheet topology ; indeed, the sheet zone is the zone where large values of $\langle\Pi^\ell_{DR}\rangle_{QR}$ are closer to the center of the plane and large values of $\langle\mathscr{D}^\ell_\nu\rangle_{QR}$ further from it.

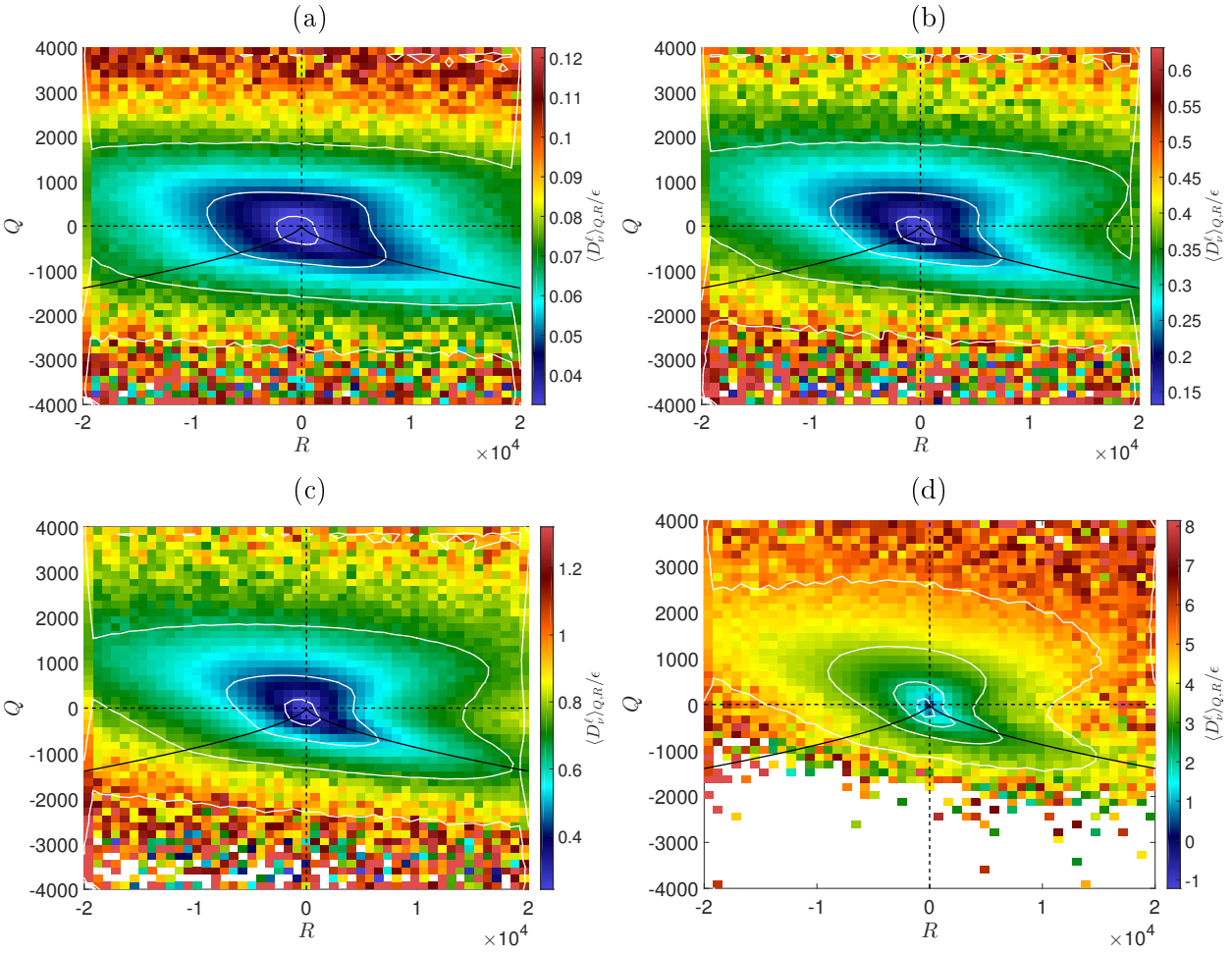

Figure 8.5: Conditional average of the viscous dissipation term $\mathscr{D}^\ell_\nu$. ℓ_c is equal to 1.7 times the interrogation volume size. The white lines correspond to the isolines of the Q-R joint pdfs. The black plain lines correspond to the Vieillefosse line $27R^2+4Q^3=0$. The black dashed lines correspond to the axes $Q=0$ and $R=0$. (a) $\ell_c = 150\eta$ (obtained with case T1). (b) $\ell_c = 45\eta$ (case T2). (b) $\ell_c = 27\eta$ (case T3). (b) $\ell_c = 8\eta$ (case T4).

The analysis of the conditional averages of Π^ℓ_{DR} and $\mathscr{D}^\ell_\nu$ suggests that the extreme events of Π^ℓ_{DR} or $\Pi^\ell_{DR}/\mathscr{D}^\ell_\nu$ should rather have a sheet topology. However, the conditional averages only give the trend, the extreme events could behave differently. Therefore, we now compute directly the topologies (with the VGT invariants method) at the extreme events of Π^ℓ_{DR} or $\Pi^\ell_{DR}/\mathscr{D}^\ell_\nu$.

1.3 Topology of the extreme events

Tables 8.1 to 8.4 give the percentage of each topology (computed with the VGT invariants method) in the whole flow, and among the 1000 strongest extreme events of Π^ℓ_{DR}, $\mathscr{D}^\ell_\nu$ and $\Pi^\ell_{DR}/\mathscr{D}^\ell_\nu$, for cases T1 to T4. The number 1000 is a compromise between the need to have enough events to get relevant statistics and the wish to consider only the very strongest events.
Tables 8.1 and 8.2 show that in the inertial range (i.e. when the dissipative scales are not resolved, or filtered), the distribution of the topologies among the extreme events of Π^ℓ_{DR} is close to the distribution in the whole flow ; only the rotating topologies are slightly favoured, at the expense of the others. This tendency is stronger for the extreme events of $\mathscr{D}^\ell_\nu$. For the extreme events of $\Pi^\ell_{DR}/\mathscr{D}^\ell_\nu$, the situation is different : the proportion of vortex compressing is lower whereas the proportion of sheet is larger (the proportion of the filament and vortex stretching remaining almost constant).

Topology	Whole flow	1000 first extreme events of		
		Π^ℓ_{DR}	$\mathscr{D}^\ell_\nu$	$\Pi^\ell_{DR}/\mathscr{D}^\ell_\nu$
Vortex stretching	40%	44%	51%	42%
Vortex compressing	36%	37%	39%	28%
Sheet	14%	11%	6%	21%
Filament	10%	8%	4%	9%

Table 8.1: Distribution of the topologies obtained with the VGT invariants method for case T1.

Topology	Whole flow	1000 first extreme events of		
		Π^ℓ_{DR}	$\mathscr{D}^\ell_\nu$	$\Pi^\ell_{DR}/\mathscr{D}^\ell_\nu$
Vortex stretching	39%	47%	47%	43%
Vortex compressing	34%	30%	38%	28%
Sheet	17%	16%	8%	21%
Filament	10%	7%	7%	9%

Table 8.2: Distribution of the topologies obtained with the VGT invariants method for case T2.

Topology	Whole flow	1000 first extreme events of		
		Π^ℓ_{DR}	$\mathscr{D}^\ell_\nu$	$\Pi^\ell_{DR}/\mathscr{D}^\ell_\nu$
Vortex stretching	38%	48%	50%	45%
Vortex compressing	33%	31%	36%	26%
Sheet	19%	13%	9%	20%
Filament	10%	8%	5%	9%

Table 8.3: Distribution of the topologies obtained with the VGT invariants method for case T3.

Table 8.3 shows the distributions of the topologies when the resolution is in the transition range between the inertial and the dissipative ranges, and table 8.4 shows them when the dissipative scales are resolved. Whereas the proportion of rotating topologies has decreased for the benefit of the sheet

Topology	Whole flow	1000 first extreme events of		
		Π^ℓ_{DR}	$\mathscr{D}^\ell_\nu$	$\Pi^\ell_{DR}/\mathscr{D}^\ell_\nu$
Vortex stretching	37%	60%	68%	47%
Vortex compressing	31%	21%	27%	15%
Sheet	22%	13%	4%	31%
Filament	10%	6%	2%	8%

Table 8.4: Distribution of the topologies obtained with the VGT invariants method for case T4.

topology in the whole flow, the amount of sheet topology among the extreme events of Π^ℓ_{DR} is the same as in the inertial range, and is therefore relatively smaller than the amount of sheet topology in the whole flow. Vortex stretching seems to be really favoured whereas the proportion of vortex compressing topology is smaller than in the whole flow. Among the extremes of $\mathscr{D}^\ell_\nu$, it is also the vortex stretching topology which is really favoured, the vortex compressing topology being slightly less probable than in the whole flow and the proportion of sheet and filament topologies being very small. Concerning the extremes of $\Pi^\ell_{DR}/\mathscr{D}^\ell_\nu$, the vortex stretching and the sheet topologies are favoured ; however, the proportion of vortex stretching topology is similar to what is observed in the inertial range, whereas the proportion of sheet topology is 1.5 times higher.
These results are partly at variance with what could be inferred from the conditional averages : as expected, the extremes of $\mathscr{D}^\ell_\nu$ correspond mainly to rotating topologies, and especially to vortex stretching in the dissipative range. On the contrary, the extremes of Π^ℓ_{DR} do not favour the sheet topology as could be expected from the conditional average behaviour, but rather the vortex stretching topology. These extremes most probably correspond to the zone of large $\langle\Pi^\ell_{DR}\rangle_{QR}$ located in the vortex stretching zone for Q around or less than zero and for large negative R. The sheet topology is favoured by extremes of $\Pi^\ell_{DR}/\mathscr{D}^\ell_\nu$, as expected, along with the vortex stretching topology.

1.4 Limitations of the VGT invariants method

The VGT invariants method is efficient as it can be implemented on a computer and applied to a large number of points ; however, it does not account for the complexity of the velocity field around a given point. Therefore, some information is lost. Also, it does not distinguish between events that are fully in the observation volume and for which the maximum Π^ℓ_{DR} can be observed, and events which are only partly in the observation volume and for which only a local maximum of Π^ℓ_{DR} can be observed, the maximum over the whole structure being outside the field of view. Furthermore, the result of the method is quite scattered.
For instance, figure 8.6 shows the velocity field around the 4^{th} strongest Π^ℓ_{DR} event of case T4, as well as the Π^ℓ_{DR} field and the topology obtained with the VGT invariants method in a plane perpendicular to the axis of the vortex which seems to form. The extremum is at the intersection between the black lines in figures (a) and (b) and at the intersection of the white lines in figure (d). Overall, a vortex seems to form between one mass of fluid coming from the right (in figures (b), (c) and (d)) and one other coming from the top-left. The extreme of Π^ℓ_{DR} is just below the vortex, at a place where the fluid which wrapped around the vortex hits the fluid coming from the right. According to the VGT invariants method, the topology is a sheet (it is not clear from the figure because of the way the colors are plotted, but the method indeed returns a sheet topology). This does not account for the vortex which is above ; also, Π^ℓ_{DR} cannot be computed at the center of

the vortex where the topology is vortex stretching (because of limited thickness of the observation volume, see chapter 2), it could be higher there. Lastly, in figure (d), it can be seen that the topology is quite scattered, and that the extreme point is between a sheet zone, a vortex stretching zone and a vortex compressing zone ; it is therefore not obvious that the topology obtained with the VGT invariants method is the proper one.
The results obtained with the VGT invariants methods are probably not wrong because they were obtained with a large number of points ; therefore, even if the wrong topology is obtained for some points, it does not impact the overall result. Indeed, the obtained Q-R joint pdf has the typical tear-drop shape which was already largely observed ; also, the conditional averages feature some clear trends which have little chance to be random. But looking at the whole velocity field around the extreme events allows to have more information, for instance to give indications on how they can form. For that reason, we also observed directly the velocity field around the few strongest extreme events (as it takes much more time, only few of them could be studied).

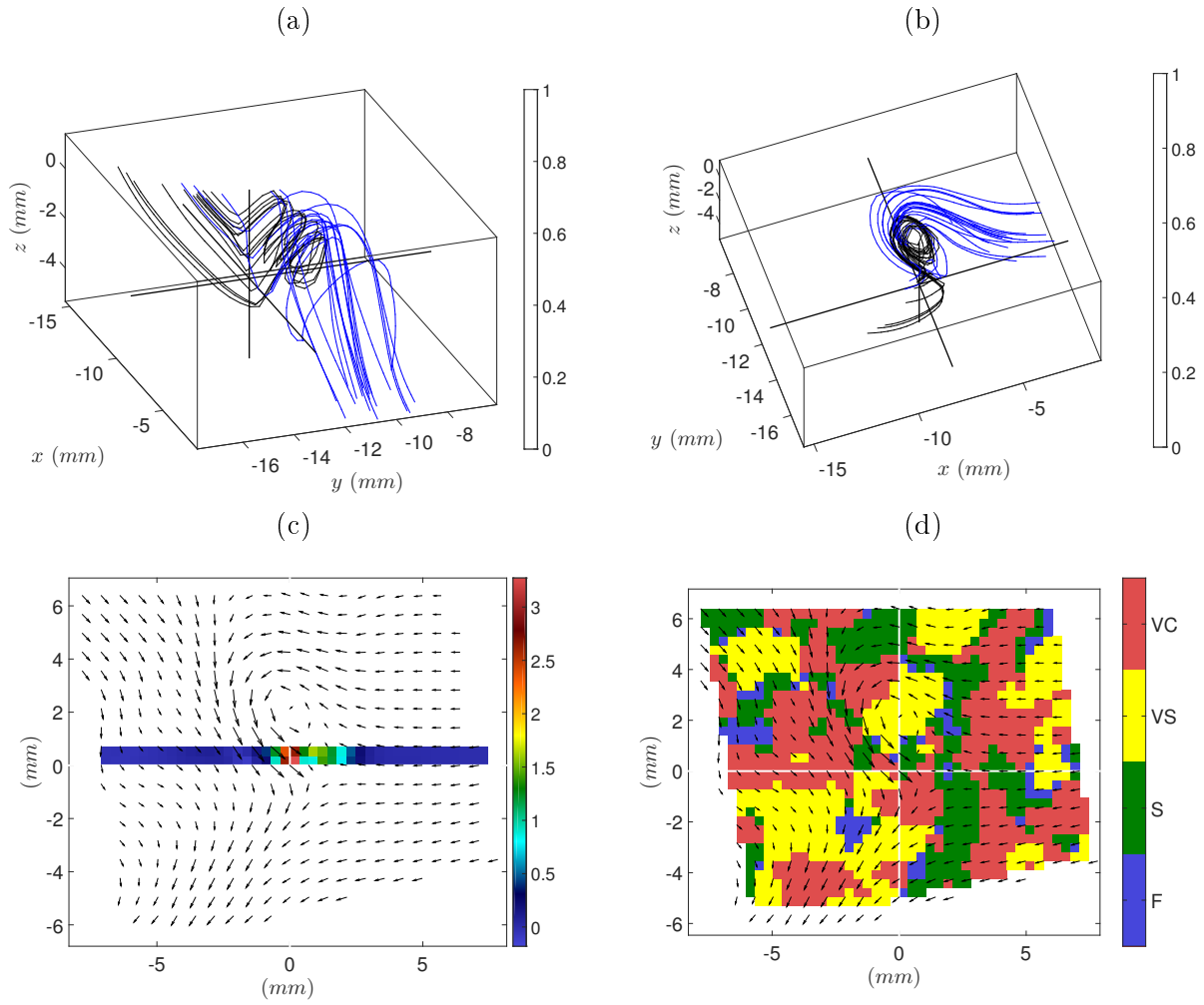

Figure 8.6: Velocity field around the 4^{th} extreme event of Π^{ℓ}_{DR} of case T4. (a) Velocity streamlines. (b) Velocity streamlines from another point of view. (c) In-plane velocity field and Π^{ℓ}_{DR} field in the plane perpendicular to the observation direction of (b) and containing the extreme event. (d) Topology obtained with the VGT invariants method in the same plane as (c). Blue streamlines are arriving around the largest values of Π^{ℓ}_{DR} whereas black ones are leaving this zone.

2 Direct observation of the velocity field around the extreme events

In this section, we report the main features of the velocity fields observed around the very extreme events of $|\Pi^\ell_{DR}|$, $\mathscr{D}^\ell_\nu$ and $|\Pi^\ell_{DR}/\mathscr{D}^\ell_\nu|$ (defined in chapter 6), for cases T1 to T4. We also had a look at the extremes of the vorticity norm. In each case and for each term, we analyzed only the ten strongest extreme events, as well as few events around the 100^{th} and the 1000^{th} ones. Viewing a 3D velocity field is not an easy task, and can lead to biased or flawed interpretation depending on the choice of the variables plotted. For each extreme, we chose to plot the following objects :

- Velocity streamlines starting from or arriving at the zones where the term considered is the highest (higher than a threshold which depends on the event). Velocity streamlines arriving at the zone were plotted in blue whereas velocity streamlines leaving the zone were plotted in black ; this allows to see the flow direction.
- Velocity streamlines starting from or arriving at the highest vorticity zones (with the vorticity higher than a threshold depending on the event). This allowed to better see the vortices but the risk was to see vortices everywhere ; it was therefore necessary to analyze the first kind of streamlines too.
- In-plane components of the velocity (represented by arrows) in the three (xy), (xz) and (yz) planes containing the extreme point, together with either Π^ℓ_{DR}, $\mathscr{D}^\ell_\nu$, the log of $|\Pi^\ell_{DR}/\mathscr{D}^\ell_\nu|$, the velocity divergence or the topology computed with the VGT invariants method. These terms were plotted only on the part of these planes where they were available.
- Isosurface of the vorticity norm corresponding to a given threshold (depending on the extreme)
- Isosurface of the velocity norm corresponding to a given threshold (depending on the extreme)

We forced the streamline step of the matlab function "stream3" to be 1 ; indeed, the default value is 0.1 and leads to sub-resolution structures obtained by interpolation and that may not correspond to the real velocity field.

2.1 Observations in the dissipative range

We now focus on the extreme events of case T4, for which the dissipative scales are resolved.

2.1.1 Extremes of $|\Pi^\ell_{DR}|$

Among the velocity fields we analyzed, we could identify three kinds of structures leading to very high values of the Duchon-Robert term Π^ℓ_{DR} (in absolute value). In these structures, the very extreme point is almost never at the center of the structure or at a particular point ; given two points where the velocity field has apparently the same configuration, it is often not clear why $|\Pi^\ell_{DR}|$ is very large at one of them and not at the other.
The three identified structures are the following :

- the "screw-vortex", as shown in figure 8.7 or 8.15 (a) : the velocity streamlines spiral in one single direction (the vortex axis), the incoming velocity being more or less oriented in this direction. In figure 8.7, they spiral from $z > 0$ to $z < 0$ and in figure 8.15 (a), they spiral from $x < 0$ to $x > 0$, as can be guessed from the two-tone streamlines.

- the "roll-vortex", as shown in figure 8.8 : a sheet or a thick sheet of streamlines rolls up, and the streamlines then spiral along the rolling axis either in one or the other direction. The incoming velocity is perpendicular to the vortex axis.
- the "U-turn" or sharp bend, as shown in figure 8.9 : the velocity streamlines suddenly change their direction. This kind of structure was observed only for some of the ten strongest negative events (6 of them), i.e.events for which $|\Pi^\ell_{DR}|$ is very high but where Π^ℓ_{DR} is negative; however, there is also large positive Π^ℓ_{DR} in these structures.

For one of the extremes, the 3^{rd} strongest extreme, the extreme point is between two such vortices, as shown in figure 8.10. It is not very clear whether the extreme occurs because of the interaction between them or if it is linked with only one of them.
For all extreme events, Π^ℓ_{DR} is large (in absolute value) along most of the structure, but the very extreme zone which is quite localized, does not have a particular location. For instance, in the case of the vortices, it is near the vortex center but never exactly at the center. Therefore, it does not follow the symmetry of the structure (which is at variance with $\mathscr{D}^\ell_\nu$, see below). As a consequence, it is difficult to understand exactly how the extreme occurs ; it seems to come along with the described structures but to be only a by-product, not the main feature of the structure. This is at variance with analytical stationary solutions like the Burgers vortex or the singular velocity fields obtained by [Li et al., 2018], as discussed later. We often noticed that the extreme was correlated with more curvated or twisted streamlines, or to strongly diverging or converging streamlines, but a more systematical analysis should be carried out to confirm that.
For most of the events, the sign of Π^ℓ_{DR} changes in the neighbourhood of the extreme event. In addition to the fact that only negative events were corresponding to sharp changes of direction, we noticed another difference between positive and negative zones of Π^ℓ_{DR} : most of the time, the velocity streamlines or beams of velocity streamlines seem to diverge in negative Π^ℓ_{DR} zones and to converge in positive Π^ℓ_{DR} zones. This is probably related to the divergence operator involved in the expression of Π^ℓ_{DR}.
All the extreme events of Π^ℓ_{DR} correspond to large values of both the velocity norm and of the vorticity norm : measured velocities are around twice the total rms of the velocity, i.e. of the order of the velocity at the tip of the impeller ; vorticities reach values close to the maximum vorticity measured in the flow, between 20 and 30 times the standard deviation of the vorticity norm. This is reminiscent of the results of [Constantin, 2008] (divergence of the velocity norm in the case of a singularity occuring in the 3D INSE) and of [Beale et al., 1984] (divergence of the vorticity norm in the case of a singularity occuring in the 3D incompressible Euler equations). In the case of the vortices, the vorticity is large in the core of the vortex, its isosurfaces being tubes sharing the same axis as the vortex ; the velocity is large just outside the vortex, its isosurfaces being often tubes too, parallel to the vortex but outside it. In the case of the sharp bends, the vorticity isosurfaces are either tubes or pancakes.
$\mathscr{D}^\ell_\nu$ also reaches very high values in the neighbourhood of the extremes of $|\Pi^\ell_{DR}|$, in accordance with the joint pdf of Π^ℓ_{DR} and $\mathscr{D}^\ell_\nu$ shown in chapter 6. Most of the time, the maximum of $\mathscr{D}^\ell_\nu$ is slightly shifted compared to the maximum of $|\Pi^\ell_{DR}|$. For instance, in the case of vortices, the maximum of $\mathscr{D}^\ell_\nu$ is often further from the center of the vortex than the maximum of $|\Pi^\ell_{DR}|$. The zones of large $\mathscr{D}^\ell_\nu$ seem to better follow the symmetries of the structures : for instance, in the case of vortices, the zone of large $\mathscr{D}^\ell_\nu$ seems to be a zone defined by $r_1 < r < r_2$, r being the distance to the center of the vortex. This gives two characteristics bands of high $\mathscr{D}^\ell_\nu$ when the vortex is contained in or close to the observation plane.

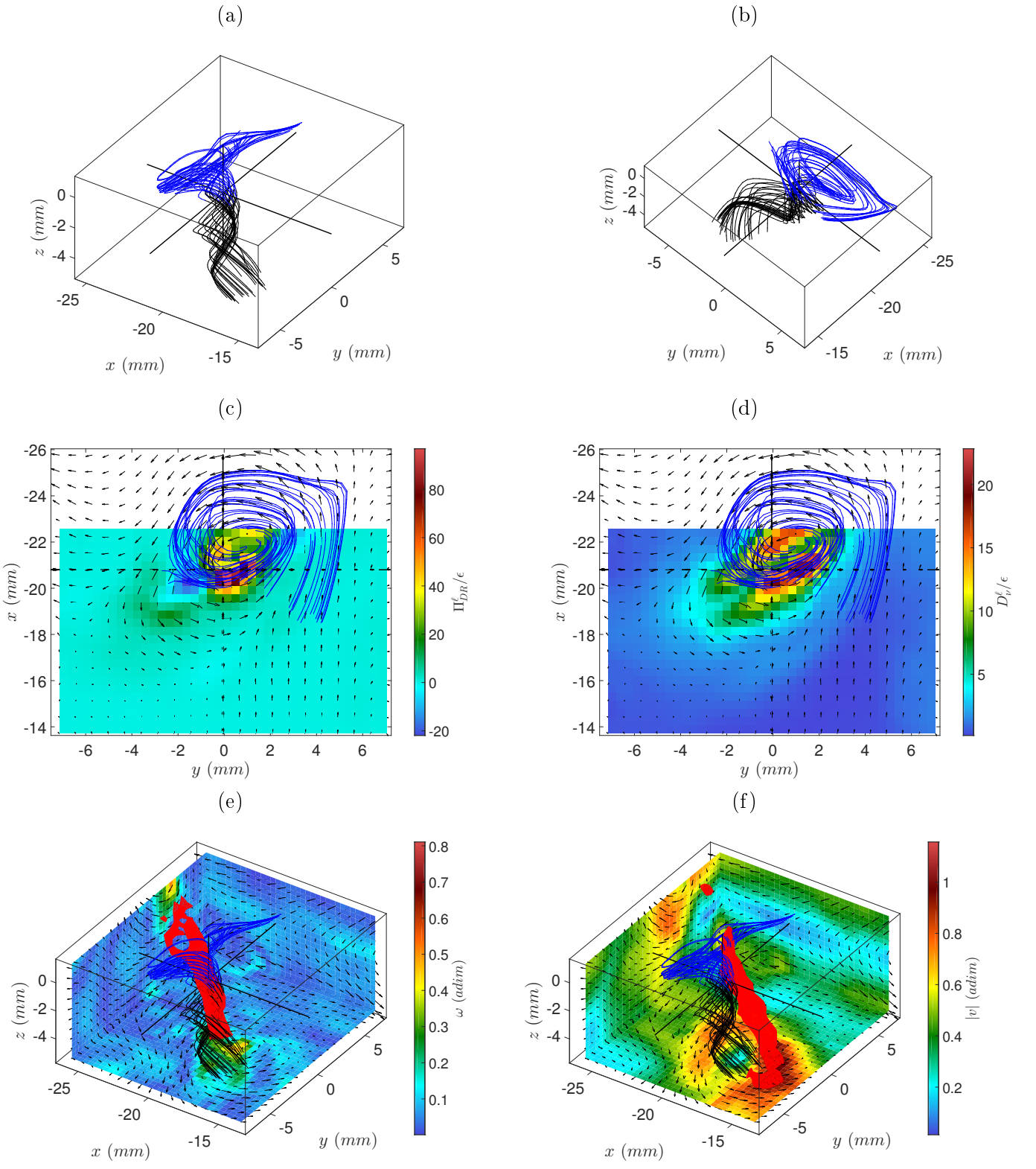

Figure 8.7: Velocity field around the 1^{st} extreme event of Π^{ℓ}_{DR} of case T4. (a) Velocity streamlines. (b) Velocity streamlines from another point of view. (c) In-plane velocity field (arrows) and Π^{ℓ}_{DR} field (color) in the (xy) plane containing the extreme event. (d) In-plane velocity field (arrows) and $\mathscr{D}^{\ell}_{\nu}$ field (color) in the (xy) plane containing the extreme event. (e) In-plane velocity field (arrows) in three (xy), (xz) and (yz) planes bounding the observed area, vorticity norm (color on these planes), velocity streamlines and isosurface of the vorticity norm (isolevel : 0.41). (f) In-plane velocity field (arrows) in three (xy), (xz) and (yz) planes bounding the observed area, velocity norm (color on these planes), velocity streamlines and isosurface of the velocity norm (isolevel : 0.92). Blue streamlines are arriving around the extreme event of Π^{ℓ}_{DR} whereas black ones are leaving the extreme zone.

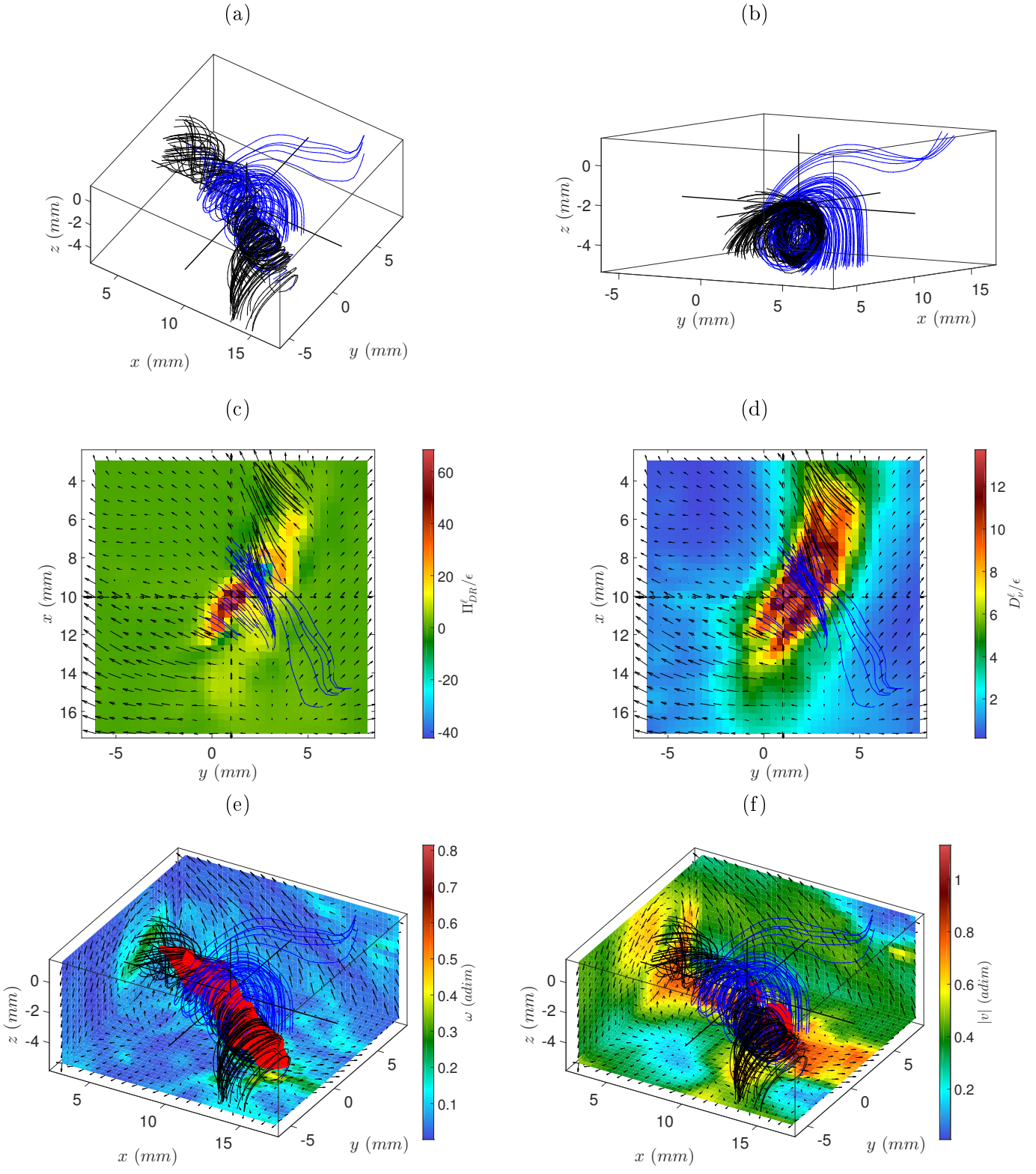

Figure 8.8: Velocity field around the 5^{th} extreme event of Π^{ℓ}_{DR} of case T4. (a) Velocity streamlines. (b) Velocity streamlines from another point of view. (c) In-plane velocity field (arrows) and Π^{ℓ}_{DR} field (color) in the (xy) plane containing the extreme event. (d) In-plane velocity field (arrows) and $\mathscr{D}^{\ell}_{\nu}$ field (color) in the (xy) plane containing the extreme event. (e) In-plane velocity field (arrows) in three (xy), (xz) and (yz) planes bounding the observed area, vorticity norm (color on these planes), velocity streamlines and isosurface of the vorticity norm (isolevel : 0.33). (f) In-plane velocity field (arrows) in three (xy), (xz) and (yz) planes bounding the observed area, velocity norm (color on these planes), velocity streamlines and isosurface of the velocity norm (isolevel : 0.77). Blue streamlines are arriving at zones of large vorticity whereas black ones are leaving such zones.

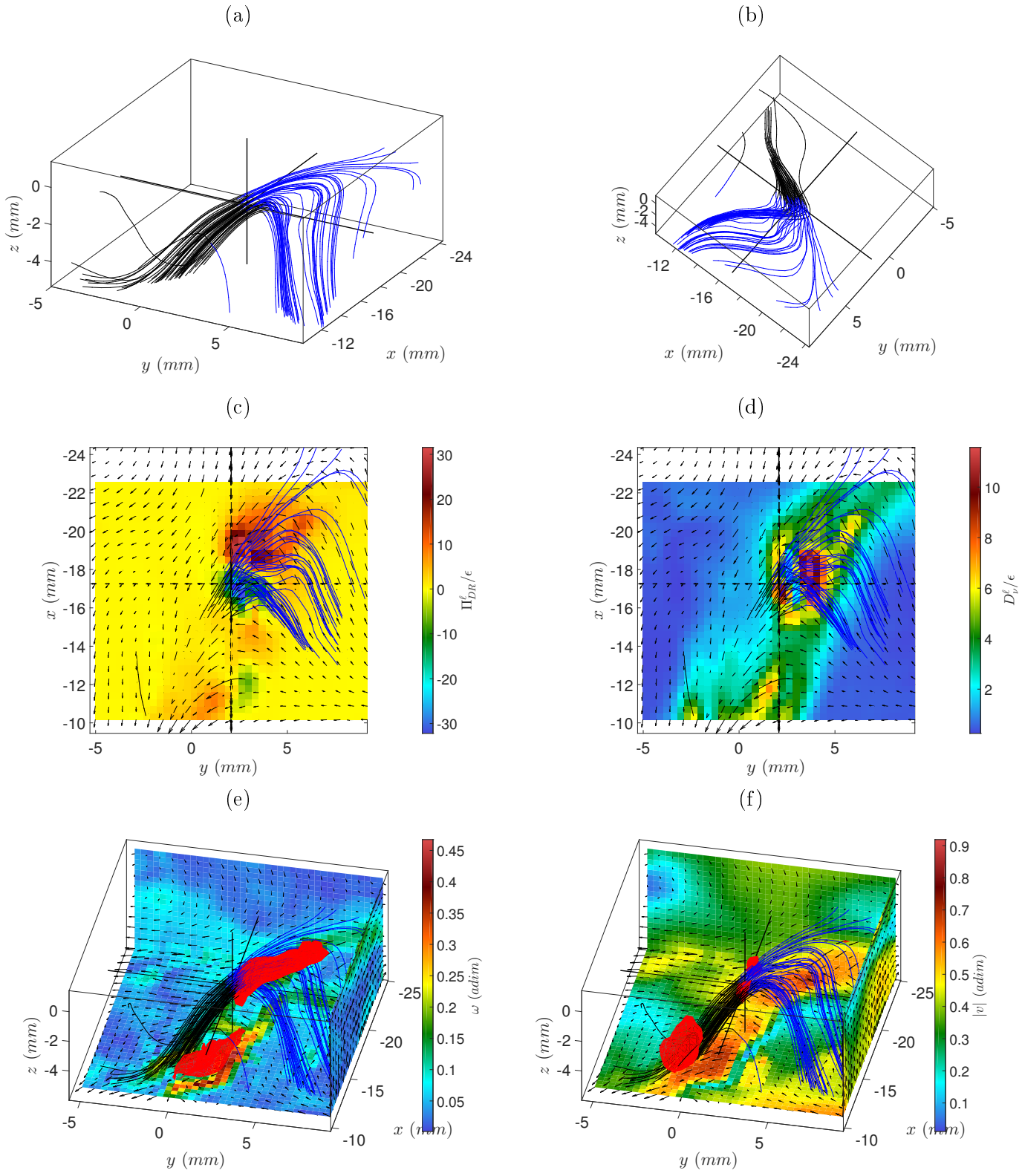

Figure 8.9: Velocity field around the 5^{th} negative extreme event of Π^{ℓ}_{DR} of case T4. (a) Velocity streamlines. (b) Velocity streamlines from another point of view. (c) In-plane velocity field (arrows) and Π^{ℓ}_{DR} field (color) in the (xy) plane containing the extreme event. (d) In-plane velocity field (arrows) and $\mathscr{D}^{\ell}_{\nu}$ field (color) in the (xy) plane containing the extreme event. (e) In-plane velocity field (arrows) in three (xy), (xz) and (yz) planes bounding the observed area, vorticity norm (color on these planes), velocity streamlines and isosurface of the vorticity norm (isolevel : 0.33). (f) In-plane velocity field (arrows) in three (xy), (xz) and (yz) planes bounding the observed area, velocity norm (color on these planes), velocity streamlines and isosurface of the velocity norm (isolevel : 0.77). Blue streamlines are arriving around the extreme event of Π^{ℓ}_{DR} whereas black ones are leaving the extreme zone.

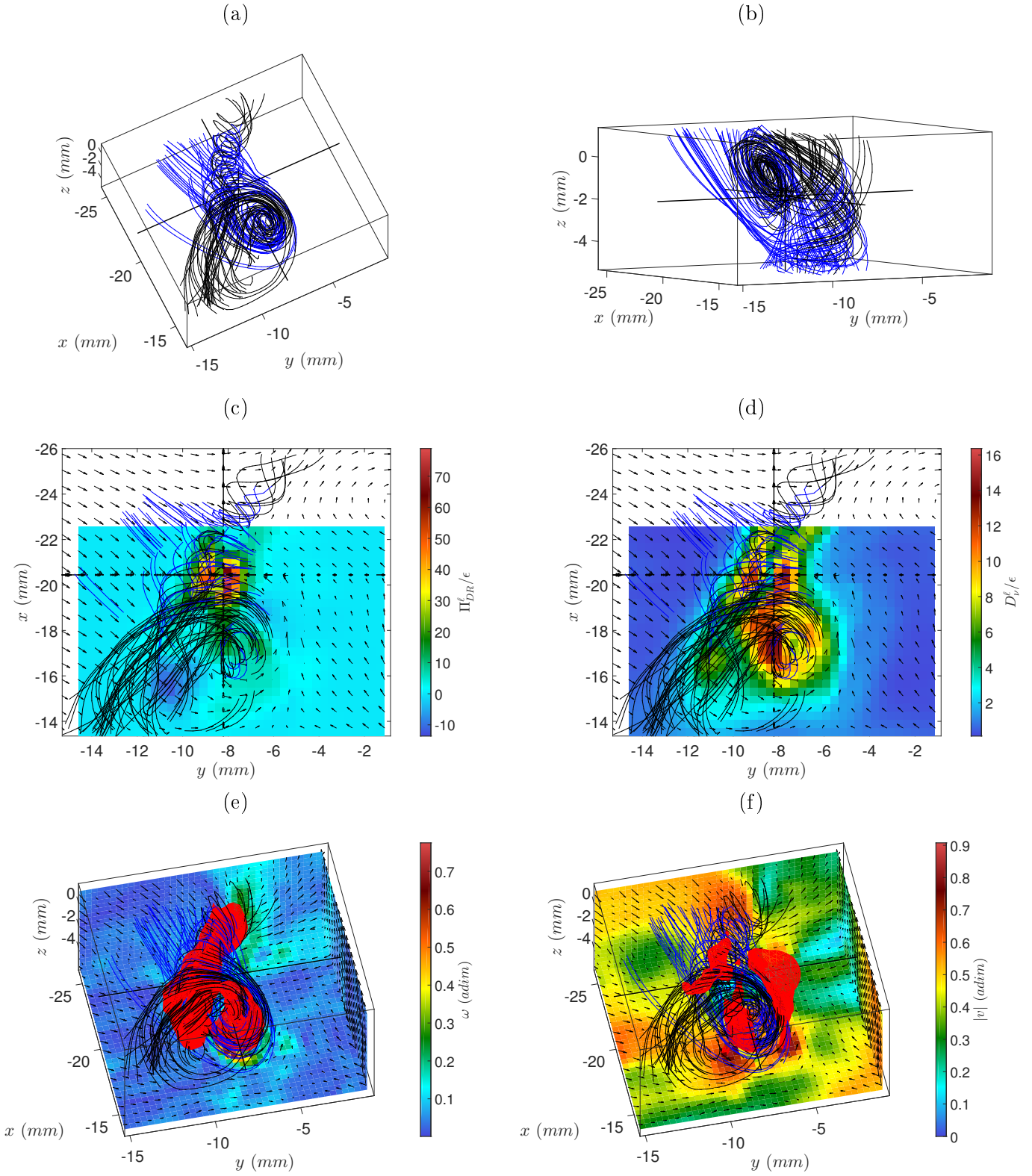

Figure 8.10: Velocity field around the 3^{rd} extreme event of Π^{ℓ}_{DR} of case T4. (a) Velocity streamlines. (b) Velocity streamlines from another point of view. (c) In-plane velocity field (arrows) and Π^{ℓ}_{DR} field (color) in the (xy) plane containing the extreme event. (d) In-plane velocity field (arrows) and $\mathscr{D}^{\ell}_{\nu}$ field (color) in the (xy) plane containing the extreme event. (e) In-plane velocity field (arrows) in three (xy), (xz) and (yz) planes bounding the observed area, vorticity norm (color on these planes), velocity streamlines and isosurface of the vorticity norm (isolevel : 0.26). (f) In-plane velocity field (arrows) in three (xy), (xz) and (yz) planes bounding the observed area, velocity norm (color on these planes), velocity streamlines and isosurface of the velocity norm (isolevel : 0.77). Blue streamlines are arriving around the zones of large vorticity whereas black ones are leaving such zones.

We also computed the divergence of the velocity field around the extreme events of $|\Pi^{\ell}_{DR}|$, as shown in figure 8.11 for the extreme events of $|\Pi^{\ell}_{DR}|$ shown in figures 8.7 to 8.10. On this figure, it is multiplied by $\sqrt{2/3} \cdot dx$ in order to compare it with the estimation of the error based on the divergence rms computed in chapter 5. We can see that near the extreme point, the divergence is 10 to 20 times higher than the rms value (see chapter 5). These high values correspond to the fact that particles do not follow properly the flow around the extreme events. Indeed, for an incompressible flow the divergence should be zero, and in the unlikely case where the flow was locally compressible, the velocity should be locally so large (because of a large Mach number) that the particles could not follow the flow. In the case of the vortices they are most often concentrated in the vortex core (the velocity divergence being negative in the vortex core and positive outside, as shown in figure 8.11 (a) and (b)). The velocity fields around the extreme events are therefore inaccurate ; they correspond to the velocity field of the particles rather than the fluid. We should consider it as an

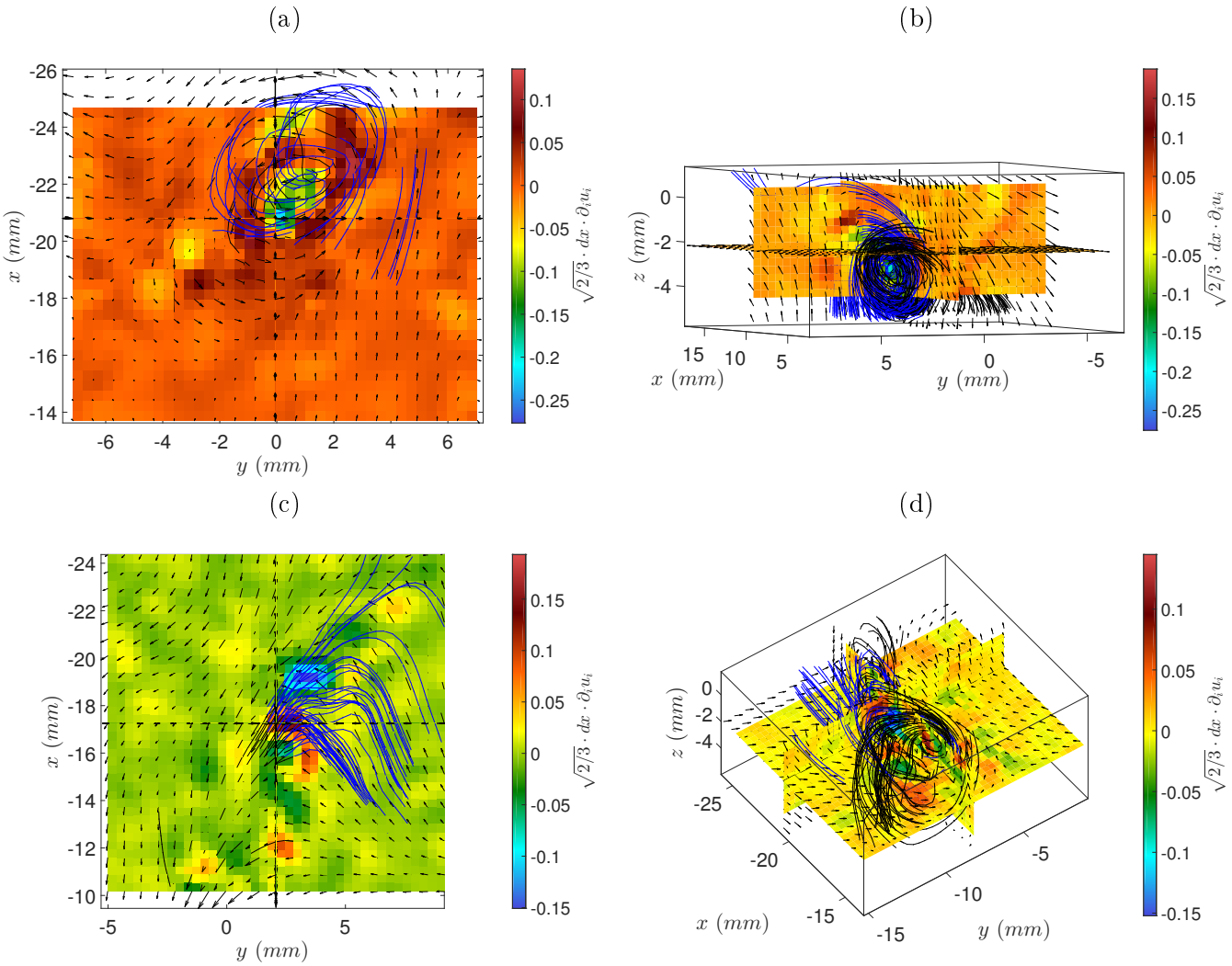

Figure 8.11: In-plane velocity field, velocity streamlines and divergence (multiplied by $\sqrt{2/3}dx$, dx being the space step) around four extreme events of Π^{ℓ}_{DR} for case T4. (a) 1^{st} extreme event. (b) 5^{th} extreme event. (c) 5^{th} negative extreme event. (d) 3^{rd} extreme event. Blue streamlines are arriving around the zones of large vorticity or large Π^{ℓ}_{DR} whereas black ones are leaving such zones.

approximation of the real velocity field. They still reveal the existence of extreme events, otherwise the particles would properly follow the flow and the divergence would remain low. It is interesting to see that the sign of the divergence and the sign of Π^ℓ_{DR} are anti-correlated most of the time. Splitting Π^ℓ_{DR} as follows may explain this observation :

$$\Pi^\ell_{DR}(\mathbf{x}) = \frac{1}{4}\int \boldsymbol{\nabla}\phi^\ell(\mathbf{r})\cdot\boldsymbol{\delta u}(\boldsymbol{\delta u})^2 d^3\mathbf{r} \tag{8.6}$$

$$= -\frac{1}{4}\int \phi^\ell(\mathbf{r})\boldsymbol{\nabla}\left[\boldsymbol{\delta u}(\boldsymbol{\delta u})^2\right] d^3\mathbf{r} \tag{8.7}$$

$$= -\frac{1}{4}\int \phi^\ell(\mathbf{r})(\boldsymbol{\nabla}\cdot\boldsymbol{\delta u})(\boldsymbol{\delta u})^2 d^3\mathbf{r} - \frac{1}{4}\int \phi^\ell(\mathbf{r})\boldsymbol{\delta u}\cdot\boldsymbol{\nabla}(\boldsymbol{\delta u})^2 d^3\mathbf{r} \tag{8.8}$$

We integrated by parts and expanded the divergence term in order to obtain the above results. As the divergence applies only on $\boldsymbol{r}$, the first right-hand-side term can be rewritten :

$$-\frac{1}{4}\int \phi^\ell(\mathbf{r})(\boldsymbol{\nabla}\cdot\boldsymbol{u})(\boldsymbol{\delta u})^2 d^3\mathbf{r}$$

If the second rhs term is small compared to the first one, it is clear that the signs of Π^ℓ_{DR} and of the divergence are opposite.

2.1.2 Extremes of $\mathscr{D}^\ell_\nu$, $|\omega|$ and $|\Pi^\ell_{DR}/\mathscr{D}^\ell_\nu|$

We also analyzed the velocity field around the first extremes of $\mathscr{D}^\ell_\nu$, $|\omega|$ and $|\Pi^\ell_{DR}/\mathscr{D}^\ell_\nu|$ in order to compare with the extremes of Π^ℓ_{DR}. We did not notice significant differences of the global structures ; some extremes of $\mathscr{D}^\ell_\nu$ and $|\omega|$ even correspond to the same velocity fields as extremes of Π^ℓ_{DR}.
The first extremes of $\mathscr{D}^\ell_\nu$ occur in vortices similar to those described previously while considering the extremes of Π^ℓ_{DR}, but no U-turn was observed. They also correspond to large values of $|\omega|$ and Π^ℓ_{DR}. The extreme value of $\mathscr{D}^\ell_\nu$ does not necessarily correspond to the maximum local value of Π^ℓ_{DR}. Some extreme events of $\mathscr{D}^\ell_\nu$ occur in the same velocity structure as extreme events of Π^ℓ_{DR} : the 1^{st}, 2^{nd}, 4^{th},7^{th},9^{th}, and 10^{th} extremes of $\mathscr{D}^\ell_\nu$ occur respectively in the neighbourhood of the 1^{st}, 4^{th}, 11^{th},8^{th},6^{th}, and 2^{nd} extreme events of $|\Pi^\ell_{DR}|$.
The situation is the same for the first extremes of $|\omega|$, a sharp U-turn was also observed. The 7^{th} and 8^{th} extreme events of $|\omega|$ correspond respectively to the 5^{th} and 1^{st} extreme events of Π^ℓ_{DR}, and the 4^{th} extreme event of $|\omega|$ corresponds to the 5^{th} extreme event of $\mathscr{D}^\ell_\nu$ (they are in the neighbourhood of each other, they do not occur exactly at the same point).
The 10 first extreme events of the ratio $|\Pi^\ell_{DR}/\mathscr{D}^\ell_\nu|$ conditioned on large enough values of $\mathscr{D}^\ell_\nu$ correspond to either positive or negative values of Π^ℓ_{DR}. The maximum values of $|\Pi^\ell_{DR}|$ and $\mathscr{D}^\ell_\nu$ found around the extremes are strong but not extreme, the maximum of the ratio arises because the zone of high $|\Pi^\ell_{DR}|$ and the zone of high $\mathscr{D}^\ell_\nu$ are shifted with respect to each other ; we never observed a zone with only high $|\Pi^\ell_{DR}|$ and small $\mathscr{D}^\ell_\nu$. Among the observed structures, a few are similar to those observed for the extreme of Π^ℓ_{DR}, but most of them are characterized by a bend in the streamlines, not very sharp (at most a 90° bend) and which can be in the surroundings of a vortex or not. Figure 8.12 shows the 2^{nd}, 3^{rd} and 7^{th} extreme events of the ratio $|\Pi^\ell_{DR}/\mathscr{D}^\ell_\nu|$ conditioned on large enough values of $\mathscr{D}^\ell_\nu$. The 2^{nd} and 3^{rd} extremes occur near a vortex, the 7^{th} does not.

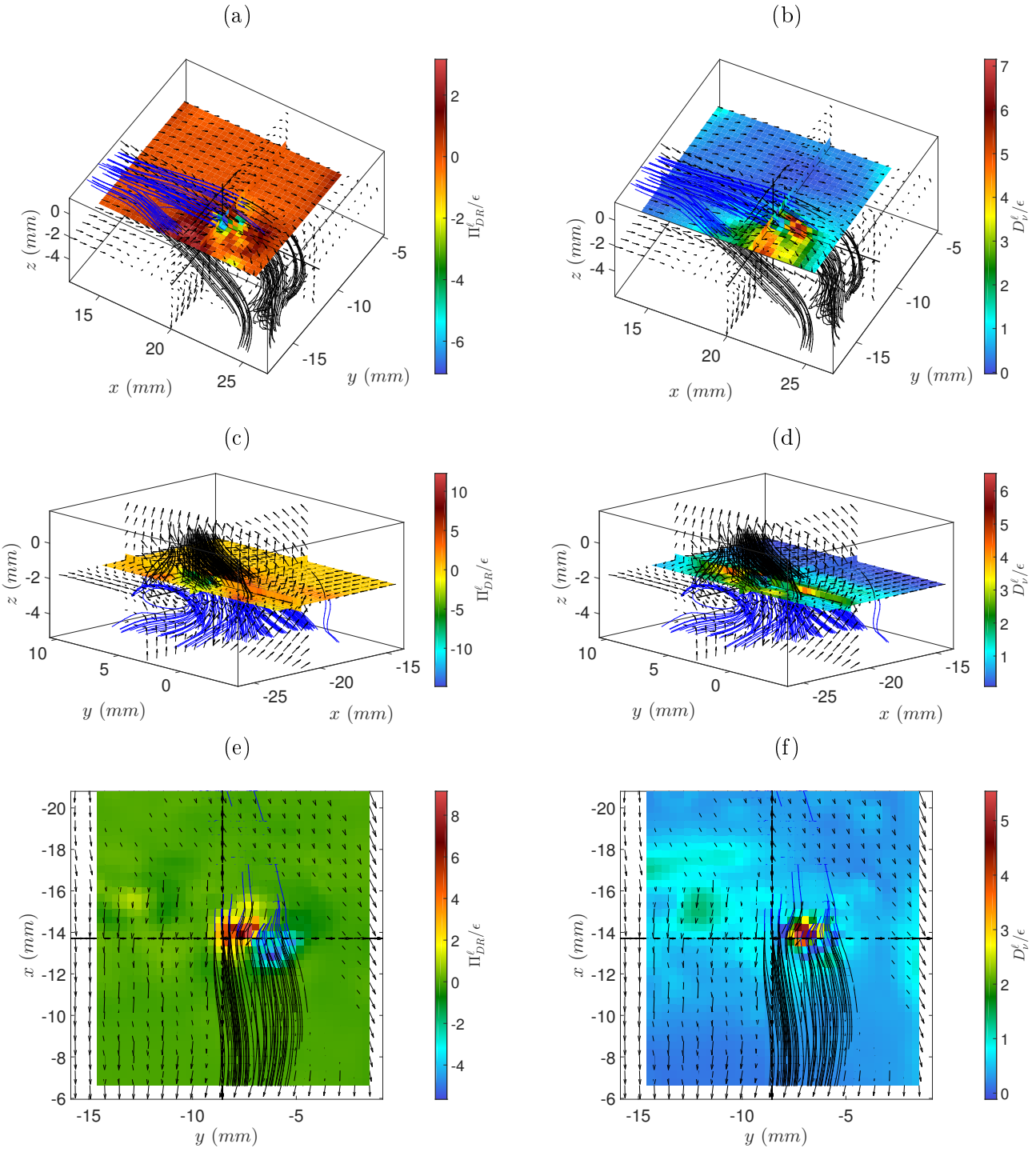

Figure 8.12: Velocity streamlines, in-plane velocity field, Π^{ℓ}_{DR} field and $\mathscr{D}^{\ell}_{\nu}$ field around 3 extreme events of $|\Pi^{\ell}_{DR}/\mathscr{D}^{\ell}_{\nu}|$. Blue streamlines are arriving around the zones of large $|\Pi^{\ell}_{DR}/\mathscr{D}^{\ell}_{\nu}|$ whereas black ones are leaving such zones. (a) Π^{ℓ}_{DR} field for the 2^{nd} extreme event. (b) $\mathscr{D}^{\ell}_{\nu}$ field for the 2^{nd} extreme event. (c) Π^{ℓ}_{DR} field for the 3^{rd} extreme event. (d) $\mathscr{D}^{\ell}_{\nu}$ field for the 3^{rd} extreme event. (e) Π^{ℓ}_{DR} field for the 7^{th} extreme event. (f) $\mathscr{D}^{\ell}_{\nu}$ field for the 7^{th} extreme event.

2.2 Observations in the inertial range

We also analyzed the first extreme events of Π^ℓ_{DR}, $\mathscr{D}^\ell_\nu$, $|\omega|$ and $|\Pi^\ell_{DR}/\mathscr{D}^\ell_\nu|$ for cases T1 to T3 in order to compare the structures corresponding to these events with the ones corresponding to extreme events in the dissipative range.
Overall, we found the same structures, except that they are distorted and therefore seem more complex. For instance, figures 8.13 and 8.14 respectively show a roll-vortex and a screw-vortex observed around extreme events of case T1. The overall structure can be recognized but the vortex axis is distorted ; the streamlines sometimes form beams which themselves are bent or twisted. When only inertial range scales are resolved, the measurement error or lack of resolution is more present : we observed several oscillations of the streamlines or discontinuities in the velocity field that are probably due to the finite resolution of PIV. The fact that we find the same kinds of structures is probably due to the fact that we only vary the Kolmogorov scale from one case to another and not the injection length scale ; therefore, the spatial resolution becomes closer to the Kolmogorov scale for case T4, but remains as close to the injection length scale as for case T1. The structures which develop are therefore the same, but get more distorted for cases T1 to T3 because the inertial effects are more important than the viscous effects. We noticed more extremes corresponding to sharp bends or twists, with no vortices around (except for the extremes of $|\omega|$). This is probably also related to the stronger inertia of the flow which may prevent the fluid to completely roll up.
Concerning the extremes of $|\Pi^\ell_{DR}|$, there are more negative extreme events among the 10 first extremes in the inertial range than in the dissipative range. This is in agreement with the tendency of the flow to favour direct inter-scale transfer in the dissipative range compared to the inertial range : we saw in chapter 6 that the pdf of Π^ℓ_{DR} is more skewed in the dissipative range ; also, in the previous section, we observed that only vortex compressing topologies can lead to negative Π^ℓ_{DR} in the dissipative range whereas some vortex stretching topologies can also lead to negative Π^ℓ_{DR} in the inertial range.
The extremes of $\mathscr{D}^\ell_\nu$ feature large values of Π^ℓ_{DR} in their surrounding, as in the dissipative range. For each one of the cases T1 to T3, we can find 2 or 3 extreme events of $\mathscr{D}^\ell_\nu$ among the ten strongest that occur close to one of the ten strongest extreme events of Π^ℓ_{DR}.
On the contrary, we could not find structures including both one of the ten strongest events of $|\omega|$ and one of the ten strongest events of Π^ℓ_{DR}. Extreme events of $|\omega|$ all the same correspond to high values of Π^ℓ_{DR} and $\mathscr{D}^\ell_\nu$. We only observed vortices among the ten strongest events of $|\omega|$, no sharp bend nor twist.
Concerning the extreme events of $|\Pi^\ell_{DR}/\mathscr{D}^\ell_\nu|$, we found no vortex, only bends or twists of the streamlines.

2.3 Discussion

We found only three different structures leading to extreme events of either Π^ℓ_{DR}, $\mathscr{D}^\ell_\nu$, $|\omega|$ or $|\Pi^\ell_{DR}/\mathscr{D}^\ell_\nu|$. We can wonder whether this set can be further reduced to two or even one structure. Indeed, the two vortical structures are close to each other, and the screw-vortex may be only a part of the roll-vortex, or a part of it a little time after, once the rolling is over but when the fluid leaving the structure is still spiraling. Concerning the U-turn, the link with the vortices is less obvious : maybe a vortex can form in the bend, or the U-turn is a distorted vortex which "opens". Another possibility is that the three structures all correspond to a single structure which is advected at different speeds. Indeed, the velocity fields we analyzed are obtained in the laboratory frame of reference ; they would have a different aspect in another frame of reference, even if it is also an iner-

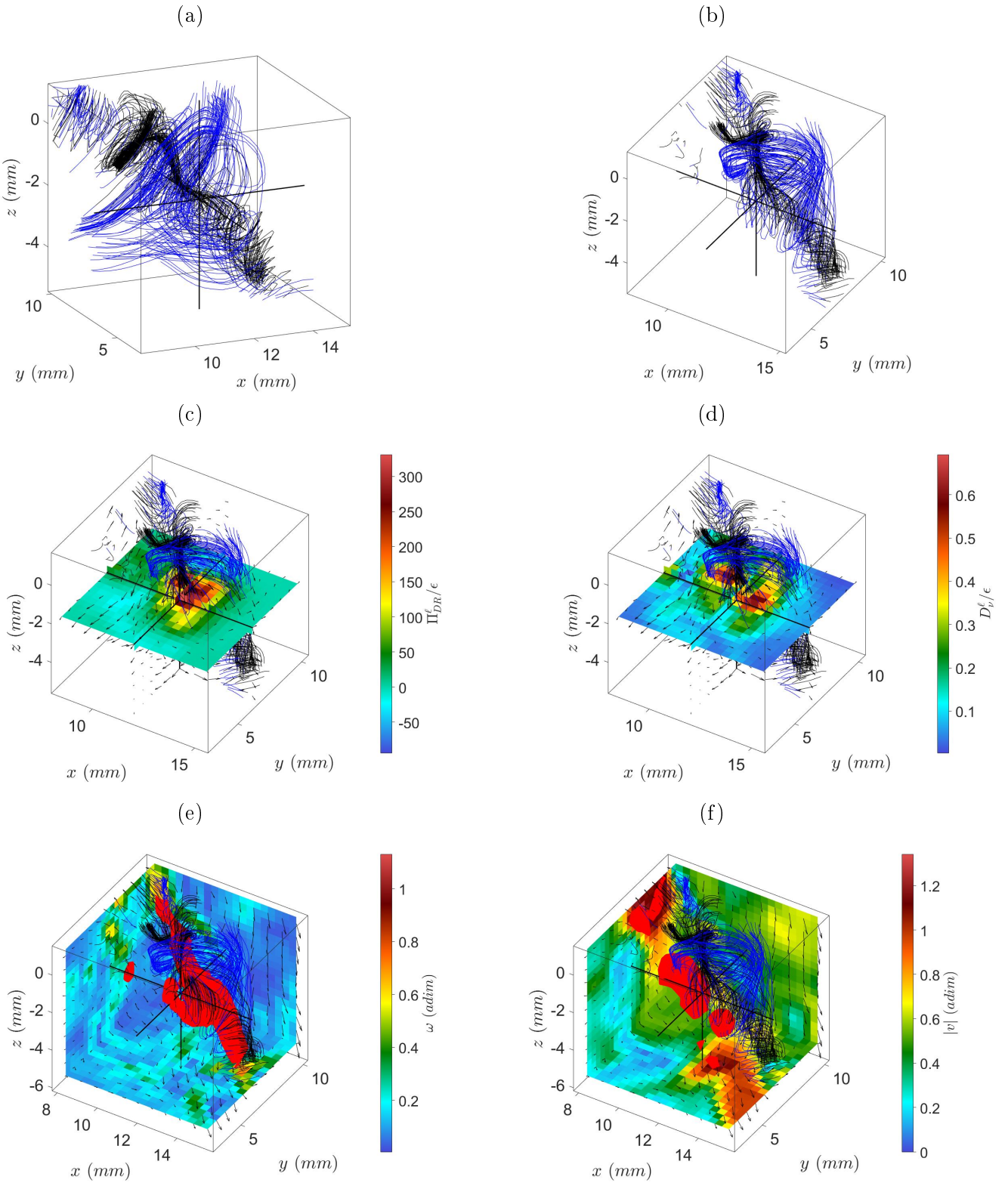

Figure 8.13: Velocity field around the 1^{st} extreme event of Π^{ℓ}_{DR} of case T1. (a) Velocity streamlines. (b) Velocity streamlines from another point of view. (c) In-plane velocity field (arrows) and Π^{ℓ}_{DR} field (color) in the (xy) plane containing the extreme event. (d) In-plane velocity field (arrows) and $\mathscr{D}^{\ell}_{\nu}$ field (color) in the (xy) plane containing the extreme event. (e) In-plane velocity field (arrows) in three (xy), (xz) and (yz) planes bounding the observed area, vorticity norm (color on these planes), velocity streamlines and isosurface of the vorticity norm (isolevel : 0.68). (f) In-plane velocity field (arrows) in three (xy), (xz) and (yz) planes bounding the observed area, velocity norm (color on these planes), velocity streamlines and isosurface of the velocity norm (isolevel : 1.13). Blue streamlines are arriving around the zones of large Π^{ℓ}_{DR} whereas black ones are leaving such zones.

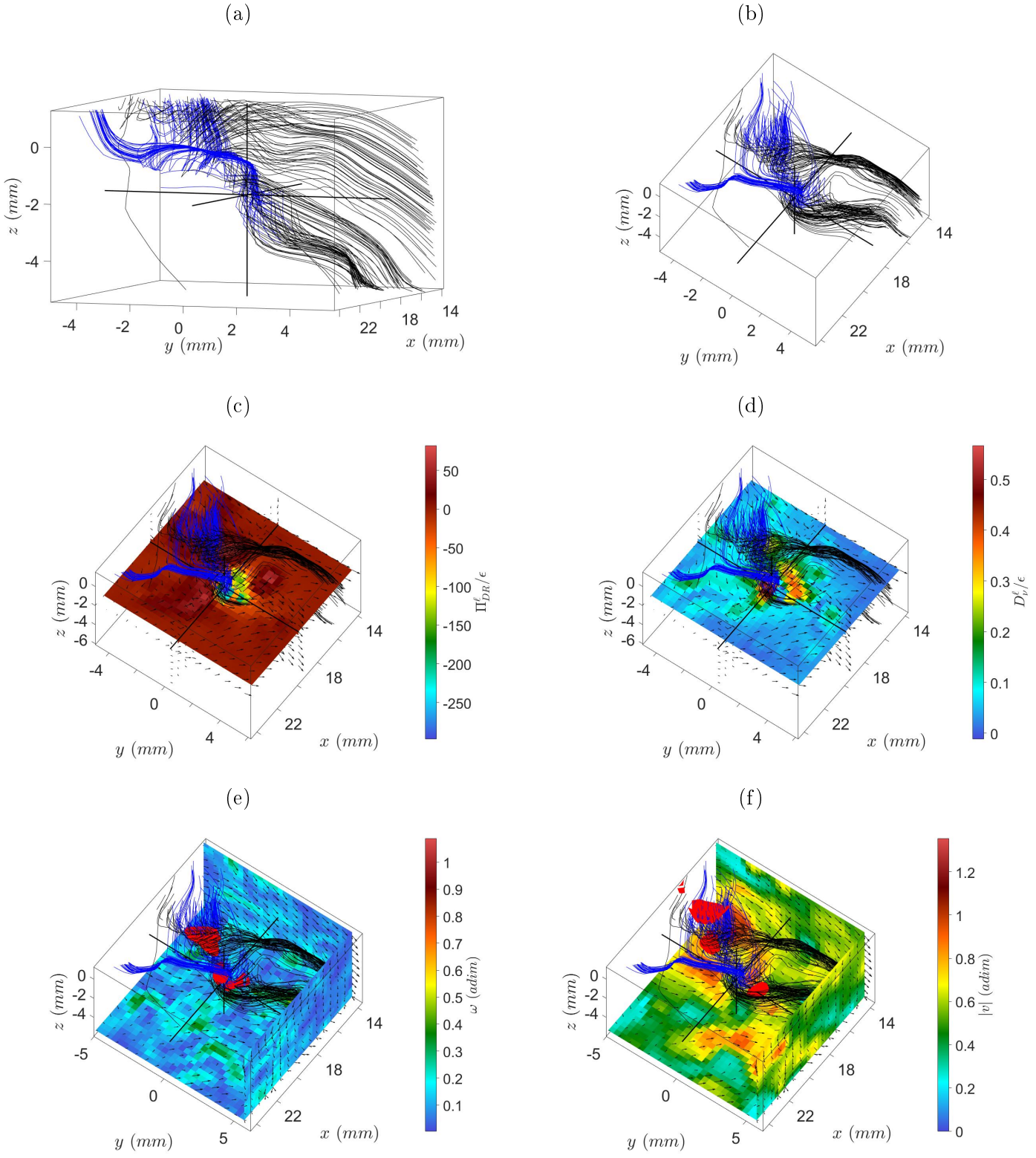

Figure 8.14: Velocity field around the 2^{rd} extreme event of Π^{ℓ}_{DR} of case T1. (a) Velocity streamlines. (b) Velocity streamlines from another point of view. (c) In-plane velocity field (arrows) and Π^{ℓ}_{DR} field (color) in the (xy) plane containing the extreme event. (d) In-plane velocity field (arrows) and $\mathscr{D}^{\ell}_{\nu}$ field (color) in the (xy) plane containing the extreme event. (e) In-plane velocity field (arrows) in three (xy), (xz) and (yz) planes bounding the observed area, vorticity norm (color on these planes), velocity streamlines and isosurface of the vorticity norm (isolevel : 0.65). (f) In-plane velocity field (arrows) in three (xy), (xz) and (yz) planes bounding the observed area, velocity norm (color on these planes), velocity streamlines and isosurface of the velocity norm (isolevel : 1.0). Blue streamlines are arriving around the zones of large vorticity whereas black ones are leaving such zones.

tial frame moving at a constant speed with respect to the laboratory frame. For instance, figure 8.15 shows the velocity streamlines for two extreme events, obtained either in the laboratory frame of reference ((a) and (c)) or in another frame of reference ((b) and (d)). In the laboratory frame, (a) looks like a screw-vortex and (c) like a U-turn, but in the other inertial frames, they both look like a roll-vortex. The roll-vortex would then be the only structure, which can be directly observed in the laboratory frame when it is slowly advected, but which looks like a screw-vortex when it is advected with a larger velocity oriented along the vortex axis, or like a U-turn when it is advected with a large velocity oriented perpendicularly to the vortex axis. This should be tempered : it

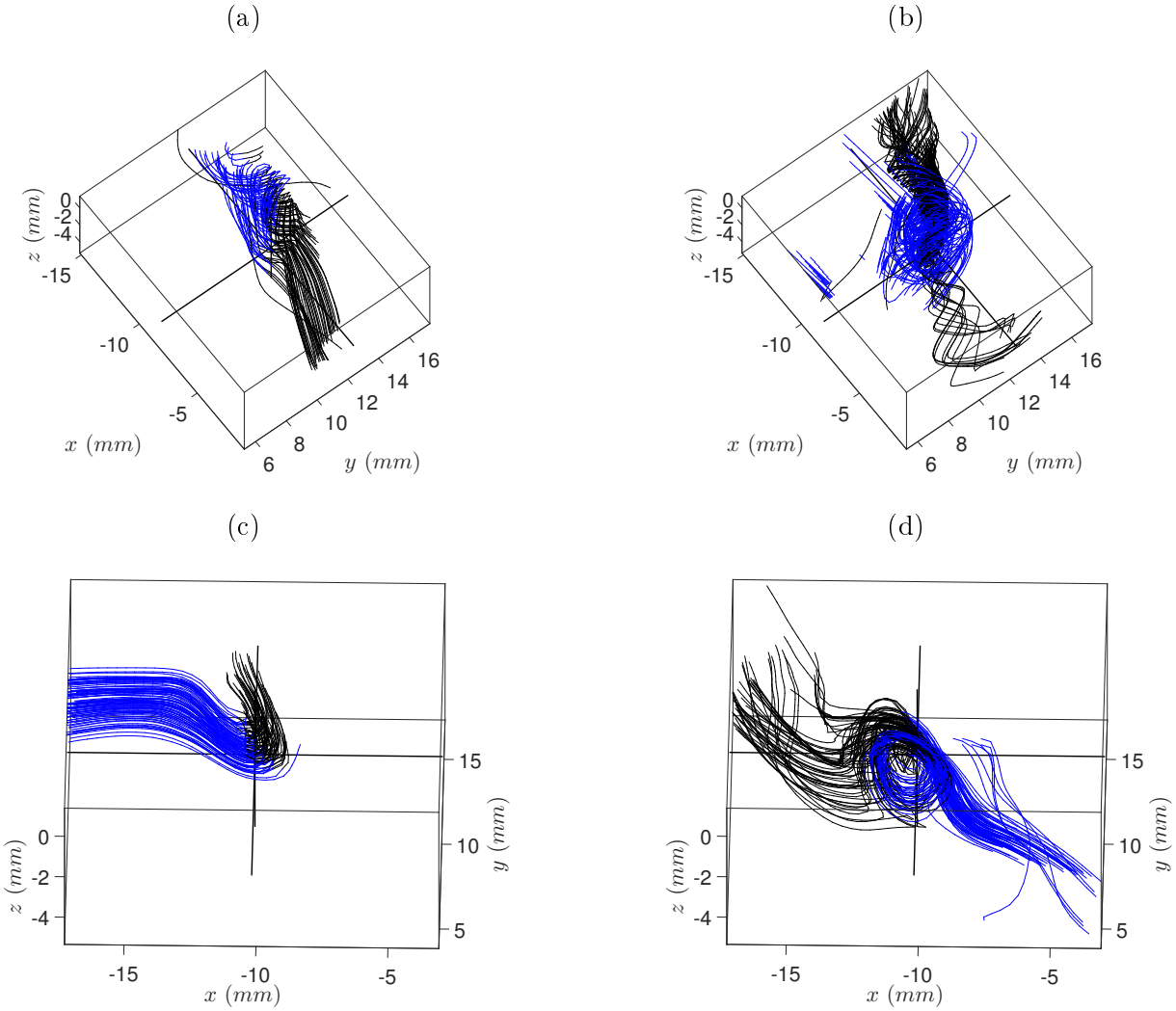

Figure 8.15: Impact of the frame of reference on the velocity field aspect. (a) Velocity streamlines around the 2^{nd} extreme event of Π^{ℓ}_{DR} of case T4 seen in the laboratory frame of reference. (b) Velocity streamlines around the same event but in the frame of reference having a constant velocity (equal to the spatial average of the velocity over the observed field) with respect to the laboratory frame. (c) Velocity streamlines around the 2^{nd} negative extreme event of Π^{ℓ}_{DR} of case T4 seen in the laboratory frame of reference. (b) Velocity streamlines around the same event but in the frame of reference having a constant velocity (equal to the velocity at the extreme point) with respect to the laboratory frame. Blue streamlines are arriving towards zones of high vorticity whereas black ones are leaving such zones. The three black lines intersect at the point where Π^{ℓ}_{DR} is maximum.

is sometimes difficult to find a frame of reference in which the velocity field structure looks like a vortex. For instance, for the velocity field shown in figure 8.9, changing the inertial frame only leads to a very flat vortex which does not look much like a roll-vortex. Incidentally, in this case the vorticity isosurfaces are flat whereas they rather look like tubes for vortices. Anyway, the two examples show that only looking at the velocity fields gives a frame dependent analysis which may lack generality. Studying spatial derivatives, such as the vorticity (which can be captured either by vorticity lines or isosurfaces) would provide more general information. Note that the VGT invariants method is frame independent as it is based on the velocity gradient.

It is interesting to compare our findings with previous works. The closest work to ours is described in [Saw et al., 2016] ; it consists in a study of the topology around the extreme events of a 2D version of Π^{ℓ}_{DR} in the same von Kármán flow studied here. In this work, the velocity was measured by SPIV, which only gives access to the three components of the velocity field in a plane ; therefore

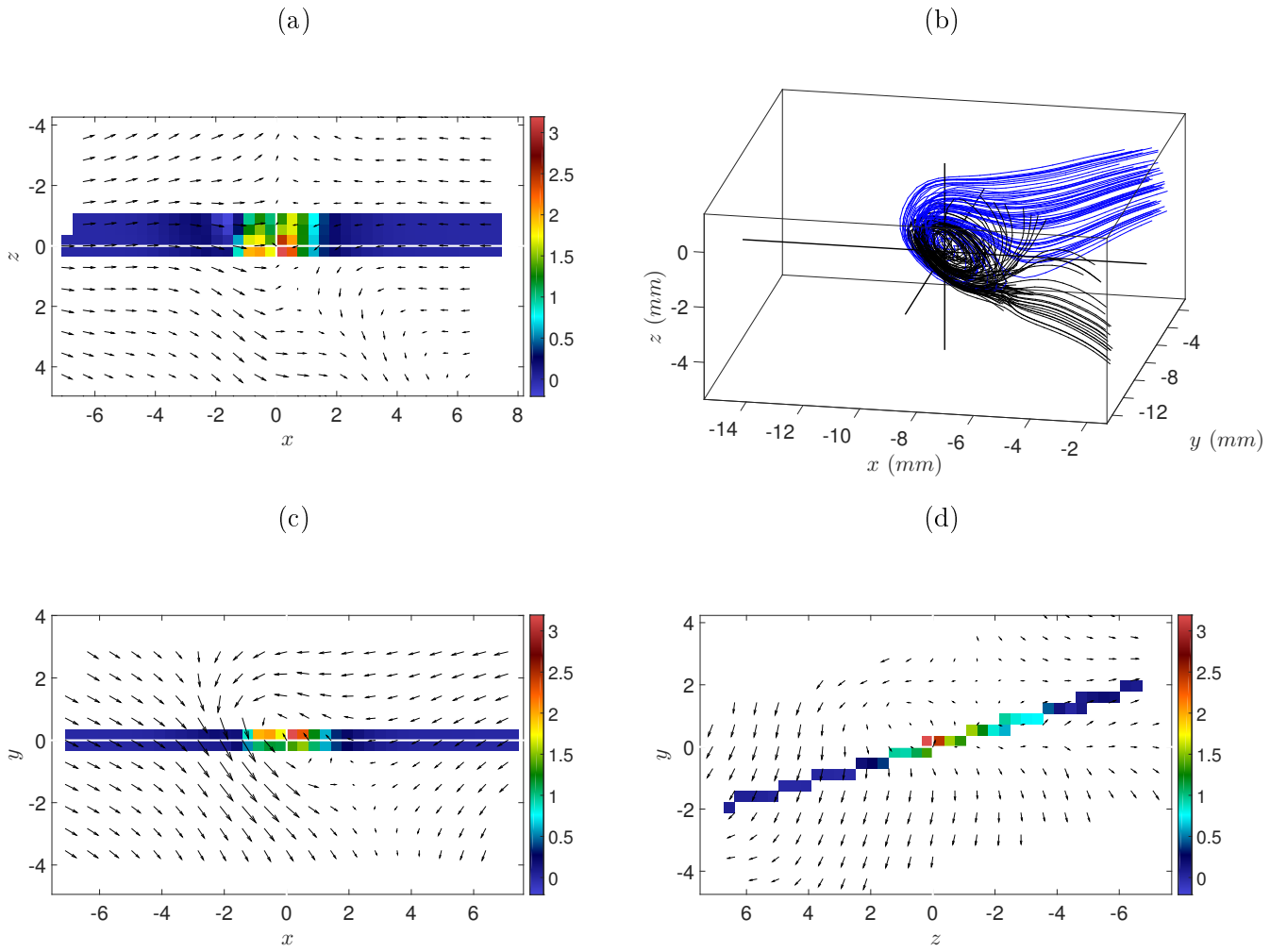

Figure 8.16: Velocity field around the 6^{th} extreme event of Π^{ℓ}_{DR} of case T4. (a) View from the top. (b) Velocity streamlines. (c) View in the observation direction of (b). (d) View from the right. The arrows correspond to the in-plane velocity field and the color to the Duchon-Robert term Π^{ℓ}_{DR}. Blue streamlines are arriving around the zones of large vorticity whereas black ones are leaving such zones.

the gradients in the direction perpendicular to the plane cannot be computed. According to this study, the 2D cross-section of the velocity field around an extreme event of (the 2D projection of) Π^{ℓ}_{DR} is either a front, a jet, a cusp or a spiral. Of course, we also observed spirals or cusps : a cross-section of a roll- or screw-vortex perpendicular to the vortex axis will yield a spiral, and it is easy to figure out that the cross-section of a U-turn or sharp bend will yield a cusp. Inspecting more carefully our extreme events, we could also find fronts : they can be seen in cross-sections of roll-vortices containing the vortex axis. Indeed, in a roll-vortex, a mass of fluid rolls up and is then expelled along the vortex axis in two opposite directions. The 2D projection of the velocity on a plane containing the vortex axis does not show the rotation but the separation of the flow in two directions. Figure 8.16 shows an example of roll-vortex observed and the 2D-projection of the velocity on three perpendicular planes crossing at the extremes. When looking in the vortex

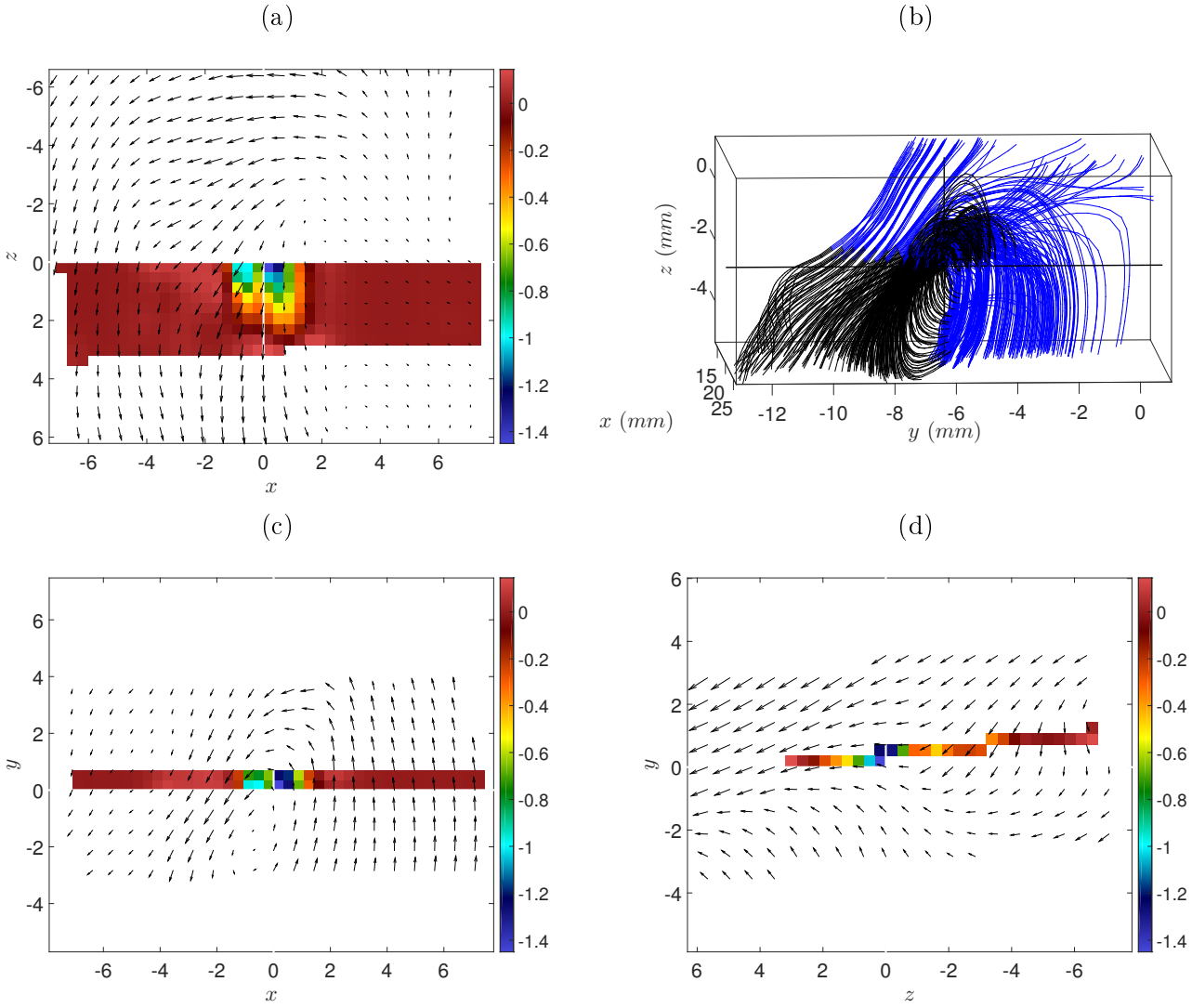

Figure 8.17: Velocity field around the 8^{th} extreme negative event of Π^{ℓ}_{DR} of case T4. (a) View from the top. (b) Velocity streamlines. (c) View in the observation direction of (b). (d) View from the right. The arrows correspond to the in-plane velocity field and the color to the Duchon-Robert term Π^{ℓ}_{DR}. Blue streamlines are arriving around the zones of large vorticity whereas black ones are leaving such zones.

axis direction, one sees a spiral (c) whereas a front appears when looking from the top (a). A front should also appear when looking from the right (d), as this view also corresponds to a plane containing the vortex axis, but it is not really the case ; the flow separates without a front. It may be due to the observation frame or to the position of the (yz) plane. We could also observe one jet, around the 8^{th} negative extreme of Π^{ℓ}_{DR}. The velocity structure around this extreme is in-between the U-turn and the screw-vortex ; it seems to be a U-turn with a strong shear along the bend axis which gives a small swirl to the whole structure. This shear gives the jet topology, which can be seen on the top view (a) of figure 8.17.

Our work can also be compared with previous works studying the large vorticity zones in turbulent flows : indeed, we noticed that extreme events of Π^{ℓ}_{DR}, $\mathscr{D}^{\ell}_{\nu}$ or $\Pi^{\ell}_{DR}/\mathscr{D}^{\ell}_{\nu}$ always come along with a large vorticity, the large vorticity zones being mostly tubes and sometimes (especially for negative Π^{ℓ}_{DR}) flatter (pancakes). For instance, in the numerical study [Vincent and Meneguzzi, 1994], the authors suggest that the formation of the vorticity tubes results from a shear instability and report that first, the zones of high vorticity that appear are pancake-like, they then flatten, bend and finally roll-up. This mechanism is in very good agreement with the roll-vortex topology that we widely observed in our results. This supports the idea that vortices (corresponding to vorticity tubes) correspond to the same structure as the sharp bends or U-turns which feature pancake-like vorticity zones : the U-turns probably evolve towards vortices. Also, the authors show that this mechanism of vorticity tube formation has an important role in the energy cascade ; this is exactly how we detected these events : we looked for extreme values of Π^{ℓ}_{DR} or $\Pi^{\ell}_{DR}/\mathscr{D}^{\ell}_{\nu}$, which can be interpreted as extreme events of inter-scale transfer. We however noticed that Π^{ℓ}_{DR} took both large positive and negative values around these events, which suggest that the energy transfer is a complex mechanism. Finally, the authors also mention that the large dissipation zones are located in the vicinity but outside the vortex cores, as was also noticed in [Brachet, 1991]. We also observed this configuration. As these authors explain, this shows that the observed structures are not spirals. Therefore, they are unlikely to be the singular velocity fields obtained in [Li et al., 2018].

The 3D fields of the Duchon-Robert term, viscous dissipation term, velocity norm and vorticity norm corresponding to these singular, stationary velocity fields are shown in figures 8.18 and 8.19. The velocity streamlines are really converging towards the singular axis $z < 0$ in both cases. We could not observe such a spiraling behaviour in our results ; we could see streamlines coming closer to each other but not converging systematically towards an axis. Also, on these singular velocity fields, all the plotted quantities (Duchon-Robert term, viscous dissipation term, velocity norm and vorticity norm) are increasing when coming closer to the $z = 0$ axis, and take very high values around it. In our observations, this was the case only for the vorticity. It is not due to the fact that the velocity field is singular on the semi-axis $z < 0$: in the case of the Burgers vortex (figure 8.20), a stationary axisymmetrical but regular solution to the Navier-Stokes equations (see [Burgers, 1948]), all the plotted quantities increase when coming closer to the $z = 0$ axis. The singular velocity fields obtained by [Li et al., 2018] and the Burgers vortex are idealized stationary solutions of the INSE, with a lot of symmetries ; this may explain the fact that we do not observe similar configurations in a real flow. It may also be due to the fact that our Reynolds number is not high enough. Indeed, in [Yeung et al., 2015], the authors analyze a DNS of homogeneous isotropic turbulence at a Reynolds number larger than ours by two orders of magnitude. Events of enstrophy and viscous dissipation up to 10000 times the mean are observed, whereas we only observe events of the order of 420 times the mean for the enstrophy and 45 times the mean for the viscous dissipation. The authors report that the maxima of vorticity and viscous dissipation are very close to each other at these very extreme events, whereas at lower Reynolds number, for which the largest events are not as strong, the maxima of vorticity and viscous dissipation are not colocated. Unfortunately, the velocity fields

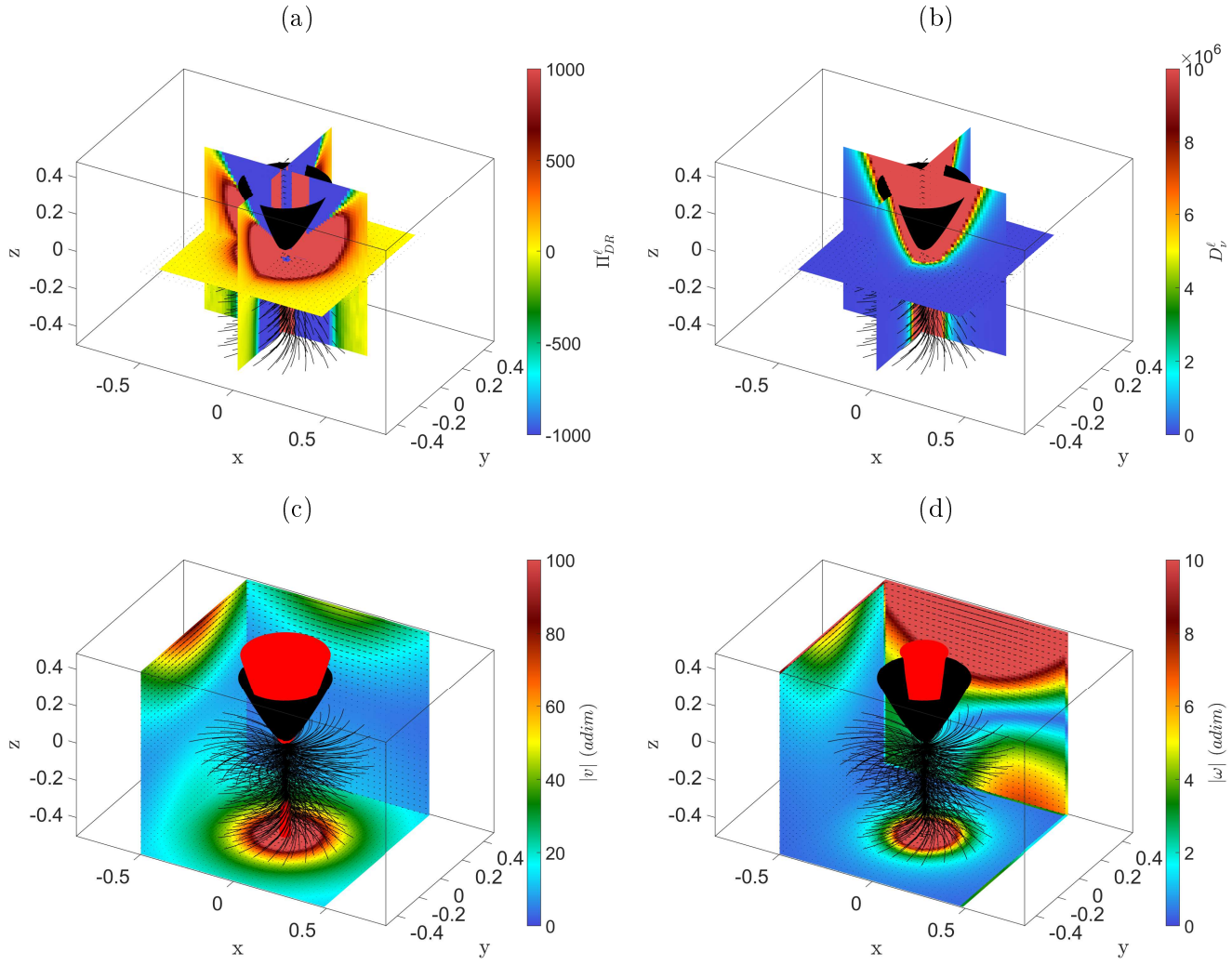

Figure 8.18: Singular velocity field obtained in [Li et al., 2018] with $a = b = 1$ and $\gamma = 1/2$ (see chapter 1). For $z < 0$, streamlines are spiraling towards the semi-axis $z < 0$ and for z > 0, they are slowly spiraling away from the semi-axis $z > 0$, forming a bell shape. (a) Duchon-Robert field. (b) Viscous dissipation field. (c) The color corresponds to the velocity norm, the isosurface corresponds to a constant velocity norm. (d) The color corresponds to the vorticity norm, the isosurface corresponds to a constant vorticity norm. Units are arbitrary.

are not displayed in this article, but this suggests that spiraling structures such as the singular velocity fields of figures 8.18 and 8.19, or structures similar to the Burgers vortex, characterized by the colocation of all the maxima (Duchon-Robert term, viscous dissipation term, velocity norm and vorticity norm) may appear at larger Reynolds numbers.

We will now discuss the link with the topology analysis based on the VGT invariants method presented in the first section of this chapter. Unfortunately, there is not one global observed structure corresponding to each one of the four topologies returned by the VGT invariants method. Actually, all of these elementary topologies are involved in the global structures we observed, as can be seen in figure 8.21. This figure shows the topology obtained with the VGT invariants method at each spatial point for the extreme events shown in figures 8.7 to 8.10. In the case of vortices the vortex core is always made of vortex stretching (VS) topology, more or less mixed with vortex compressing (VC)

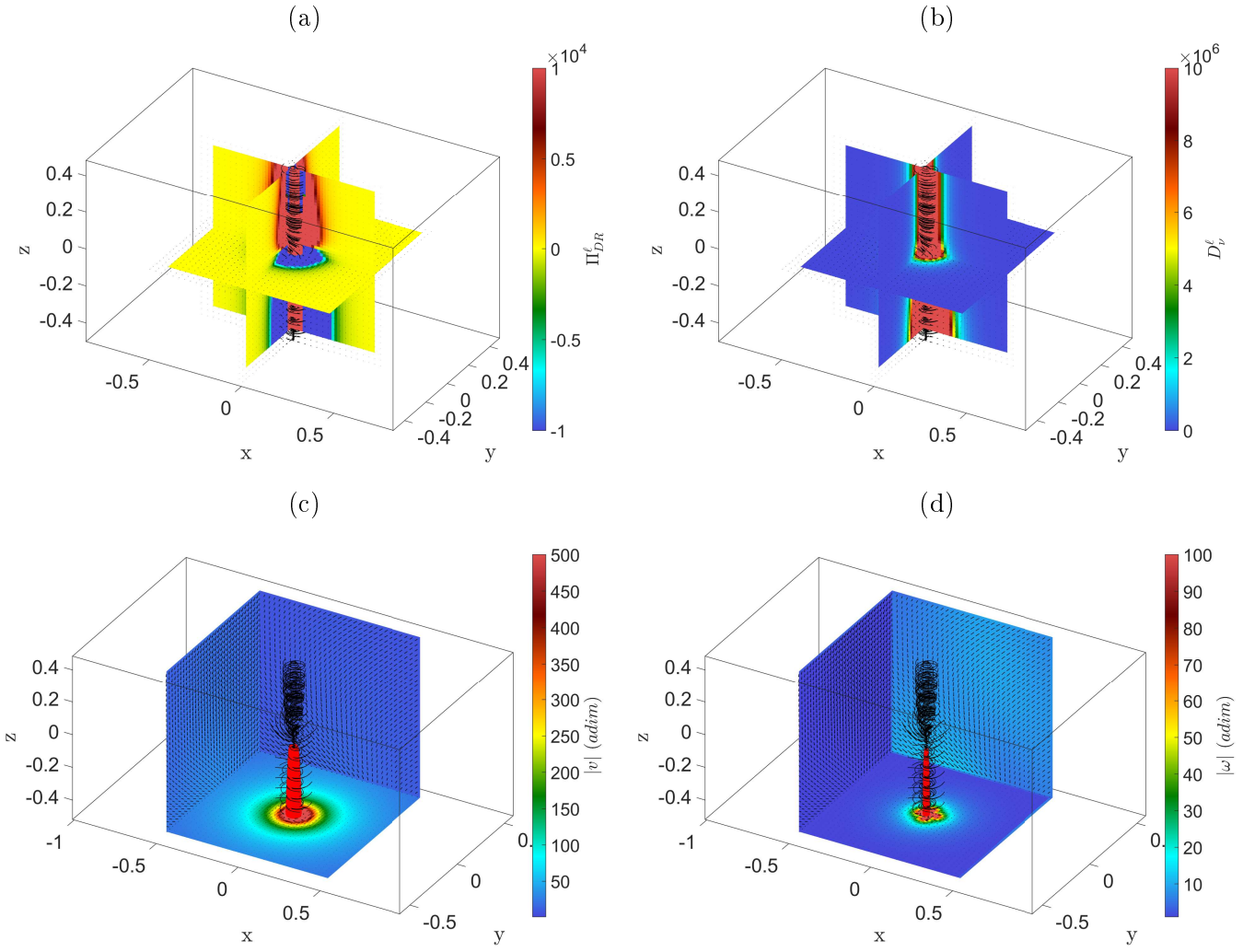

Figure 8.19: Singular velocity field obtained in [Li et al., 2018] with $a = b = 1$ and $\gamma = -1$ (see chapter 1). For $z > 0$, streamlines are spiraling downwards to the point $(x, y, z) = (0, 0, 0)$ and for $z < 0$, streamlines are spiraling towards the semi-axis $z < 0$. (a) Duchon-Robert field. (b) Viscous dissipation field. (c) The color corresponds to the velocity norm, the isosurface corresponds to a constant velocity norm. (d) The color corresponds to the vorticity norm, the isosurface corresponds to a constant vorticity norm. Units are arbitrary.

topology. This is quite natural as they are rotating topologies. The vortices are then surrounded by VC or sheet (S) areas, and sometimes small areas of filaments (F). Concerning the U-turn (figure 8.21 (c)), it is more difficult to relate the elementary topologies to their location in the global structure, but it shows that a VS or VC topology returned by the VGT invariants method does not necessarily corresponds to a global vortex. The observed structures (roll-vortex, screw-vortex and U-turn) may be characterized by a pattern in the Q-R space ; this could be seen by computing the Q-R joint pdf conditioned on the extreme events of a given type.

In the first section of this chapter, we also found that negative values of Π^{ℓ}_{DR} were obtained mainly in a zone of the VC area. We did not notice such a systematic distribution in the few velocity fields we analyzed.

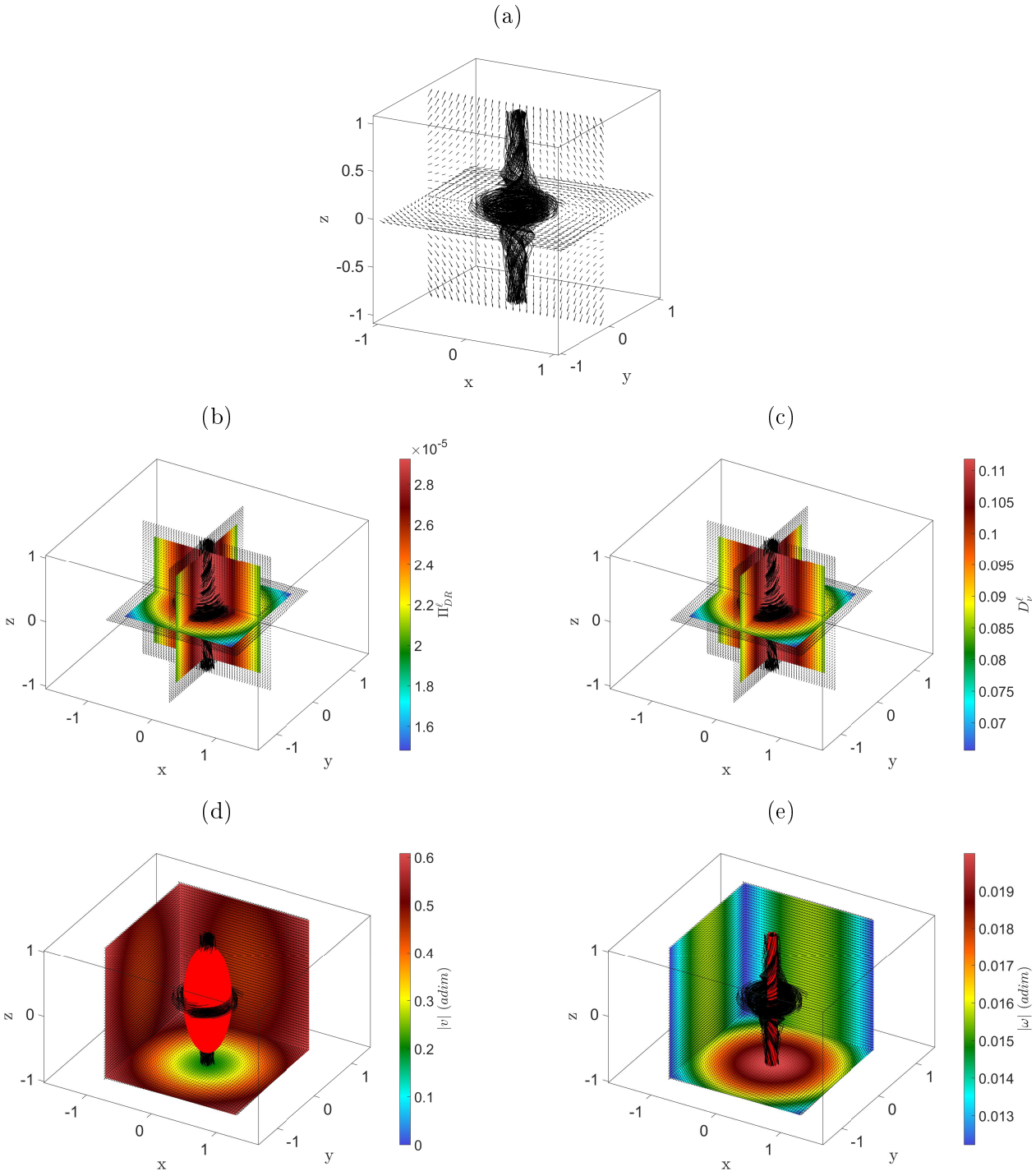

Figure 8.20: Velocity field corresponding to the Burgers vortex [Burgers, 1948]. (a) Streamlines ; they start from large x and y and end at large $|z|$. (b) Duchon-Robert field. (c) Viscous dissipation field. (d) The color corresponds to the velocity norm, the isosurface corresponds to a constant velocity norm. (e) The color corresponds to the vorticity norm, the isosurface corresponds to a constant vorticity norm. Units are arbitrary.

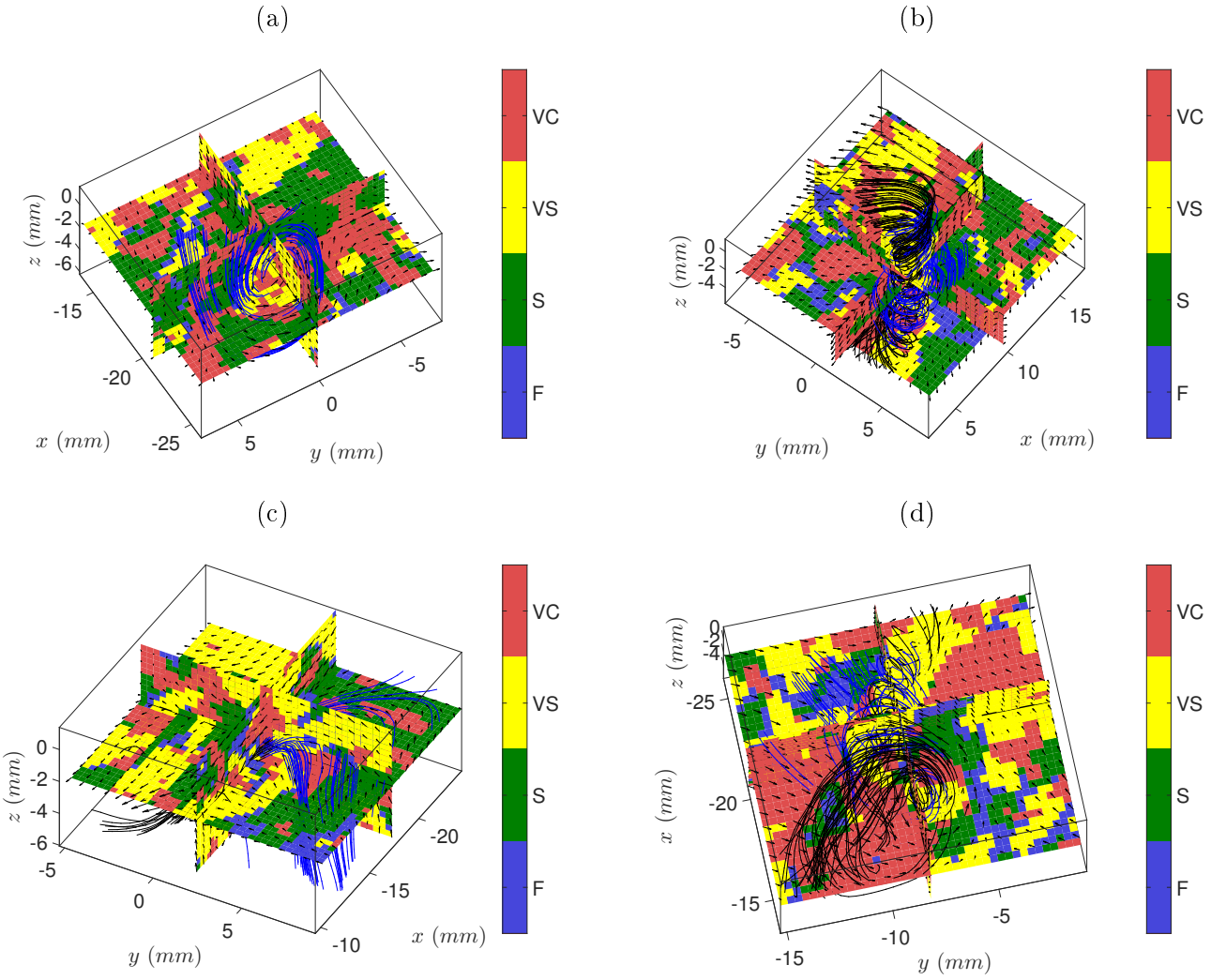

Figure 8.21: In-plane velocity field, velocity streamlines and topology returned by the VGT invariants method around four extreme events of Π^ℓ_{DR} for case T4. (a) 1^{st} extreme event. (b) 5^{th} extreme event (view from below compared to figure 8.8). (c) 5^{th} negative extreme event. (d) 3^{rd} extreme event. Blue streamlines are arriving around the zones of large vorticity or large Π^ℓ_{DR} whereas black ones are leaving such zones. Units are arbitrary.

Summary of chapter 8

In this chapter, we analyzed the topologies around the extreme events of the Duchon-Robert term Π^ℓ_{DR} and of the ratio $\Pi^\ell_{DR}/\mathscr{D}^\ell_\nu$, both with a method based on the invariants of the velocity gradient tensor (VGT) and by direct observation of the velocity fields.

The VGT invariants method is a statistical method which can be easily implemented on a computer and applied to a large number of points. For an incompressible flow, it allows to distinguish between four different elementary topologies. We showed that the global distribution of these topologies at the center of the von Kármán flow is characterized by a tear-drop shape of the Q-R joint pdf, which becomes slightly blurred when the resolution becomes much higher than the Kolmogorov scale. The averages of Π^ℓ_{DR} and $\mathscr{D}^\ell_\nu$, conditioned on the invariants of the VGT, show that large values of Π^ℓ_{DR} are mostly obtained in the sheet zone, and to a lesser extent in the vortex stretching zone

for large negative R, whereas large values of the $\mathscr{D}^\ell_\nu$ are obtained either in the vortex stretching (VS) or vortex compressing (VC) zones. Also, there is a particular area of the vortex compressing zone where Π^ℓ_{DR} is negative in average, when ℓ is in the dissipative range. When ℓ is increased in the inertial range, a new negative area appears in the VS zone. The extreme events of Π^ℓ_{DR} and $\mathscr{D}^\ell_\nu$ mainly favour the vortex stretching topology compared to the global distribution ; the vortex compressing topology is the second most probable topology around them. Some extreme events of Π^ℓ_{DR} still feature sheet topology whereas this topology is very scarce among extreme events of $\mathscr{D}^\ell_\nu$. Extreme events of $\Pi^\ell_{DR}/\mathscr{D}^\ell_\nu$ favour not only the VS topology but also the sheet topology, compared to the global distribution of topologies in the flow.
The VGT invariants method does not account for the complexity of the velocity field around the extreme events, we therefore also analyzed the velocity fields around these events by direct observation. We found mainly three kinds of structures of the velocity field arond extreme events of Π^ℓ_{DR} : the roll-vortex, the screw-vortex and the U-turn or sharp bend. We also noticed that these extreme events correspond to very large values of $\mathscr{D}^\ell_\nu$ and of the velocity and vorticity norms. This is also true for extreme events of $\mathscr{D}^\ell_\nu$ and vorticity norm. Concerning the extreme events of the ratio $\Pi^\ell_{DR}/\mathscr{D}^\ell_\nu$, we found that in addition to these structures, there are also less pronounced structures like bends or twists of the velocity field. In the inertial range, we did similar observations, except that the structures were more distorted and complex. Our results are in agreement with previous experimental and numerical works concerning turbulent velocity fields at similar Reynolds numbers ; however they are quite far from analytical stationary solutions to the incompressible Navier-Stokes equations and to numerical result obtained at a larger Reynolds number.

Chapter 9

An Eulerian point of view on the temporal evolution of extreme events of the Duchon-Robert term

In this last chapter, we report some preliminary results about the temporal evolution of extreme events of the Duchon-Robert term Π^ℓ_{DR}, studied from an Eulerian point of view.
All the results of this chapter were obtained from experimental case T4t, for which the Reynolds number is 6.3×10^3 ; therefore, the dissipative scales are resolved : indeed, the largest ℓ_c is equal to 6η (it was equal to 8η for case T4). However, because the observation volume was thinner, the largest ℓ_c is equal to 0.9 times the interrogation volume size (1.7 times for case T4), which is slightly small. This results in underestimating Π^ℓ_{DR} and $\mathscr{D}^\ell_\nu$ as the contributions from smaller scales are all filtered (see second section of chapter 2).
We did observe extreme events of Π^ℓ_{DR}, both positive and negative, even if time-resolved measurements do not provide a proper statistical sampling of the flow compared to non-time-resolved measurements, for a given amount of data (there are 129000 velocity fields in case T4t and 30000 in case T4, but the effective number of independent frames is about 35 times larger for case T4 than for case T4t, see chapter 5). Indeed, the strongest event of Π^ℓ_{DR} (at $\ell_c = 6\eta = 0.9X$, X being the interrogation volume size) measured in case T4t is larger than 40ϵ (the average dissipation rate computed from torque measurements), and the five strongest events of Π^ℓ_{DR} that we consider in this chapter are all larger than 28ϵ. For comparison, the strongest extreme event of Π^ℓ_{DR} (at $\ell_c = 8\eta = 1.7X$) measured in case T4 was equal to almost 97ϵ, the ten strongest being all larger than 57ϵ.
Also, our acquisition frequency was large enough to observe the time evolution of the extreme events. However, because the measurement volume was too thin, we could only compute Π^ℓ_{DR} and $\mathscr{D}^\ell_\nu$ on a plane (see second section of chapter 2). Therefore, it was not possible to track the extreme events through space. It is nevertheless possible :

- to study the temporal evolution of the 3D velocity field around the extreme event location (the measured velocity field is 3D, only the computation of Π^ℓ_{DR} or $\mathscr{D}^\ell_\nu$ reduces it to a plane),
- to track the maximum of Π^ℓ_{DR} over the computation plane,
- to study the temporal evolution of the flow at the points where the extreme events occur, i.e. to study the time evolution from an Eulerian point of view.

In this thesis, we only had time to start with the third option. We report the first observations here, in two parts. First, we analyze the temporal evolution of Π^ℓ_{DR}, $\mathscr{D}^\ell_\nu$, ω and $|v|$ at the location of the five strongest extreme events of Π^ℓ_{DR} of case T4t. Second, we analyze the temporal evolution of the velocity gradient invariants at the location of these five strongest extreme events and compare them to the average evolution.

1 Temporal evolution of Π^ℓ_{DR}, $\mathscr{D}^\ell_\nu$, ω and $|v|$

Figure 9.1 (a) shows the temporal evolution of Π^ℓ_{DR}, $\mathscr{D}^\ell_\nu$, ω and $|v|$ at the location of the strongest event of Π^ℓ_{DR}, over the whole run (3225 time steps) containing this event. ω is squared and multiplied by ν to be compared with Π^ℓ_{DR} and $\mathscr{D}^\ell_\nu$; their axis is on the left. The axis for $|v|$ is on the right. Figure 9.1 (b) shows the temporal evolution of the maximum and minimum of Π^ℓ_{DR}, computed over the plane where Π^ℓ_{DR} is available.
It can be seen that Π^ℓ_{DR}, $\mathscr{D}^\ell_\nu$ and ω are quite intermittent : they are low most of the time, with some bursts from time to time. The small bursts of these three quantities are not always correlated. Few events characterized by the simultaneous occurence of a peak of $\nu\omega^2$ and a deep of $|v|$ can be observed, they probably correspond to a vortex crossing the observation point, the vorticity being high in its core while the velocity is low.

We now concentrate on the temporal evolution when the extreme events of Π^ℓ_{DR} occur. Figures 9.2 and 9.3 are obtained in the same way as 9.1 but each one of them is focussed on the instant at which one of the 5 strongest extreme events of Π^ℓ_{DR} occurs. The largest negative value of Π^ℓ_{DR} is obtained in the neighbourhood of the third extreme event, ten time-steps later.
The five figures are different ; there is not a common pattern which emerges. However, some common features can be found :

- All the events last 400 to 500 ms, except the fourth one which is shorter. This is of the order of the Kolmogorov time scale (90 ms).
- In all cases except the 4^{th} extreme, a large vorticity, with the maximum of $\nu\omega^2$ of the order of the maximum of Π^ℓ_{DR}, precedes or is preceded by the extreme event of Π^ℓ_{DR}. The 2^{nd} and 5^{th} extremes of Π^ℓ_{DR} correspond to a sharp increase of $\nu\omega^2$; the negative peak of Π^ℓ_{DR} preceding the 1^{st} extreme corresponds to a sharp decrease of $\nu\omega^2$.
- The second extreme of Π^ℓ_{DR} corresponds to a sharp decrease of the velocity norm, whereas the fourth one corresponds to a sharp increase of $|v|$.
- The maximum of $\mathscr{D}^\ell_\nu$ is always smaller than about half the maximum of Π^ℓ_{DR}.

2 Temporal evolution of the velocity gradient tensor invariants

We supplement the above analysis by studying the temporal evolution of the velocity gradient tensor (VGT) invariants, i.e. of the local topology. We insist here on the fact that our data allows to perform only an Eulerian analysis of the time evolution next to the extreme event. We are not able to track the extreme and to study the evolution of the topology during its formation, as does Vieillefosse in [Vieillefosse, 1983] where he shows the occurence of a singularity in idealized conditions. But we can study what happens at the fixed spatial point where the extreme occurs : it is equivalent to looking at the extreme event going by.

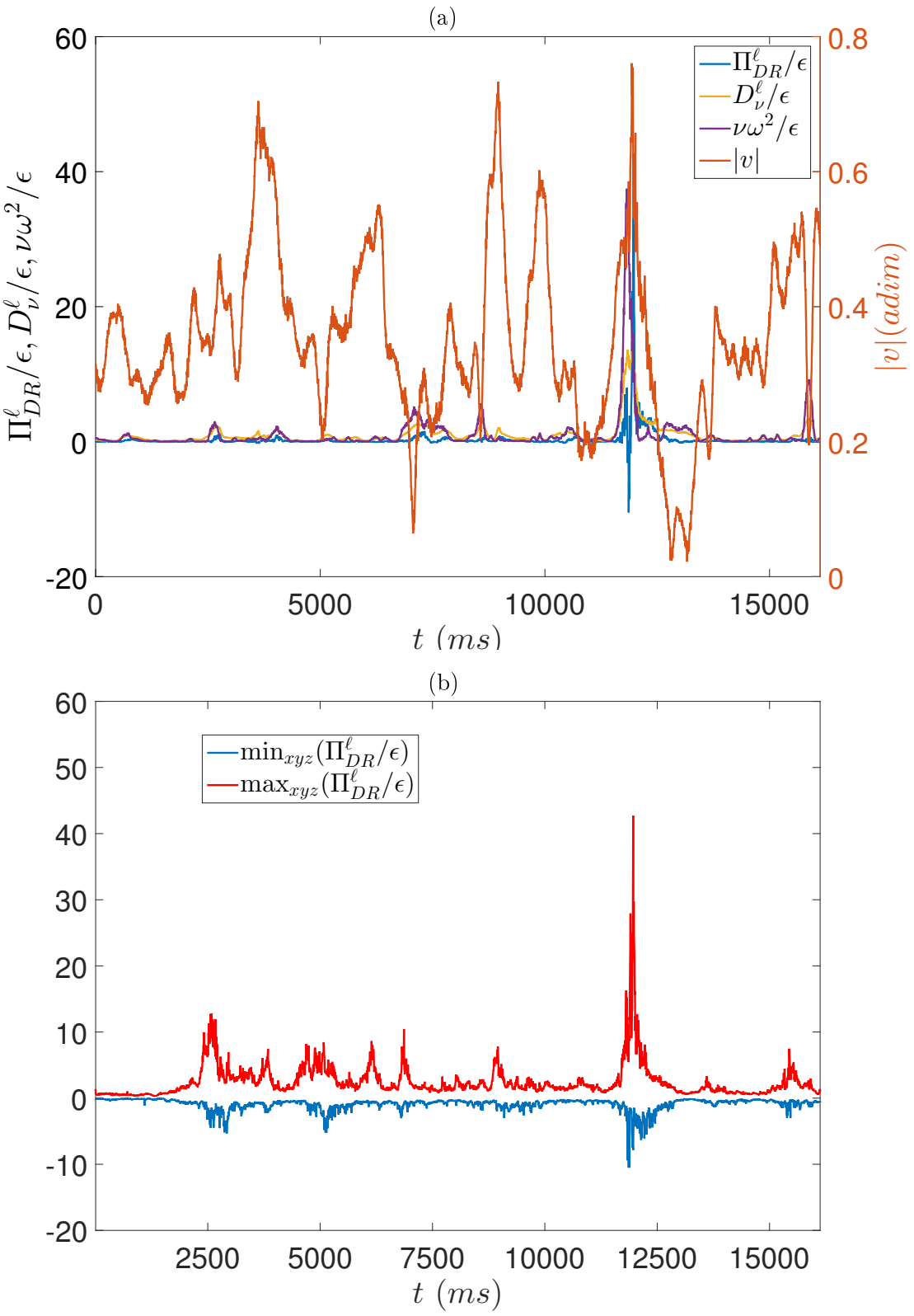

Figure 9.1: Time evolution of several quantities over the whole run where the first strongest extreme event of Π^ℓ_{DR} of case T4t occurs. (a) Time evolution of Π^ℓ_{DR}, $\mathscr{D}^\ell_\nu$, $\nu\omega^2$ (axis on the left) and $|v|$ (axis on the right) at the location where the extreme event occurs. (b) Time evolution of the maximum and minimum of Π^ℓ_{DR} on the plane where Π^ℓ_{DR} can be computed.

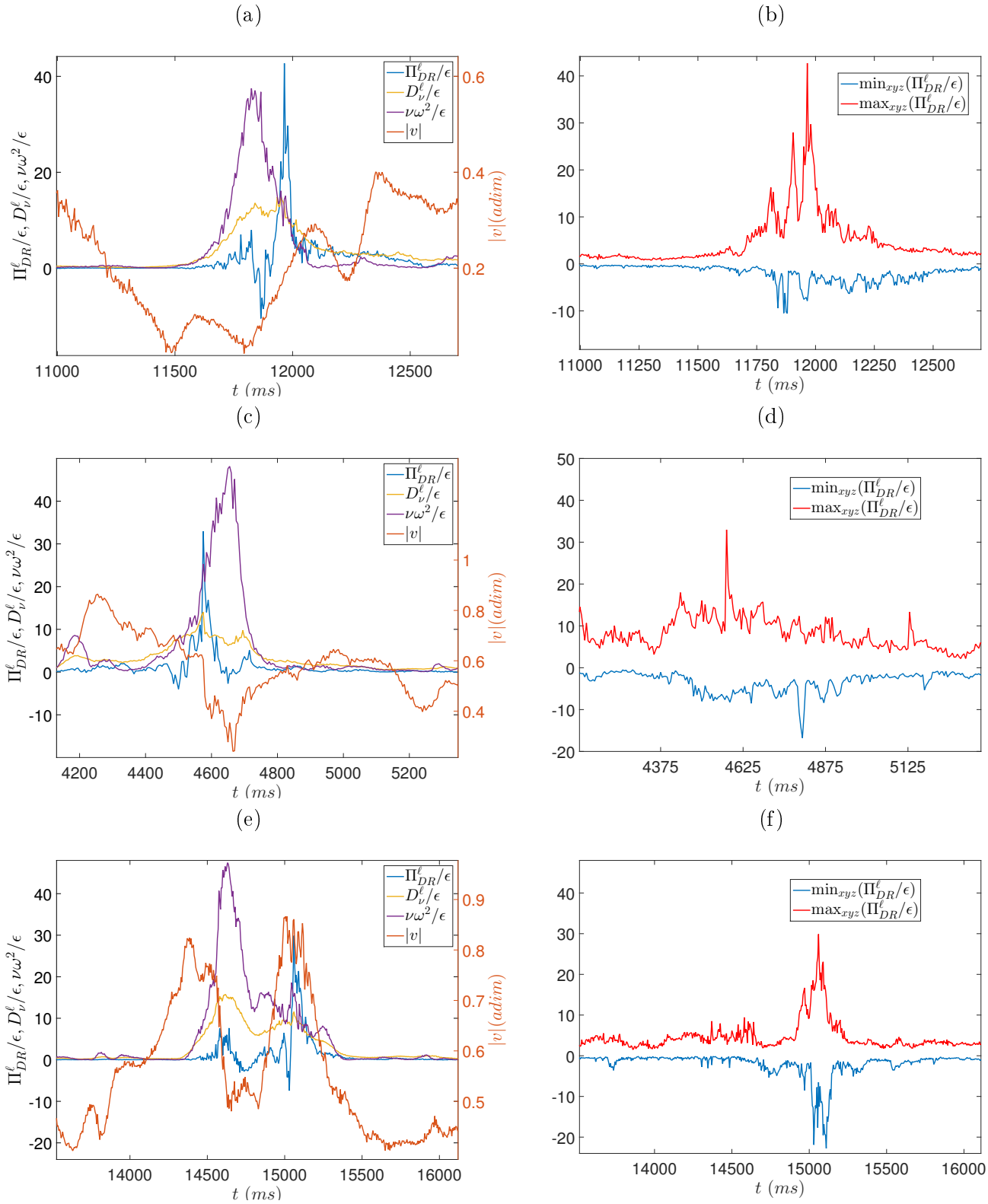

Figure 9.2: Time evolution of several quantities when extreme events of Π^ℓ_{DR} of case T4t occurs. (a) First extreme event, time evolution of Π^ℓ_{DR}, $\mathscr{D}^\ell_\nu$, $\nu\omega^2$ and $|v|$ at the location where the extreme event occurs. (b) First extreme event, time evolution of the maximum and minimum of Π^ℓ_{DR} on the plane where Π^ℓ_{DR} can be computed. (c) Second extreme event, time evolution of Π^ℓ_{DR}, $\mathscr{D}^\ell_\nu$, $\nu\omega^2$ and $|v|$ at the location where the extreme event occurs. (d) Second extreme event, time evolution of the maximum and minimum of Π^ℓ_{DR} on the plane where Π^ℓ_{DR} can be computed. (e) Third extreme event, time evolution of Π^ℓ_{DR}, $\mathscr{D}^\ell_\nu$, $\nu\omega^2$ and $|v|$ at the location where the extreme event occurs. (f) Third extreme event, time evolution of the maximum and minimum of Π^ℓ_{DR} on the plane where Π^ℓ_{DR} can be computed.

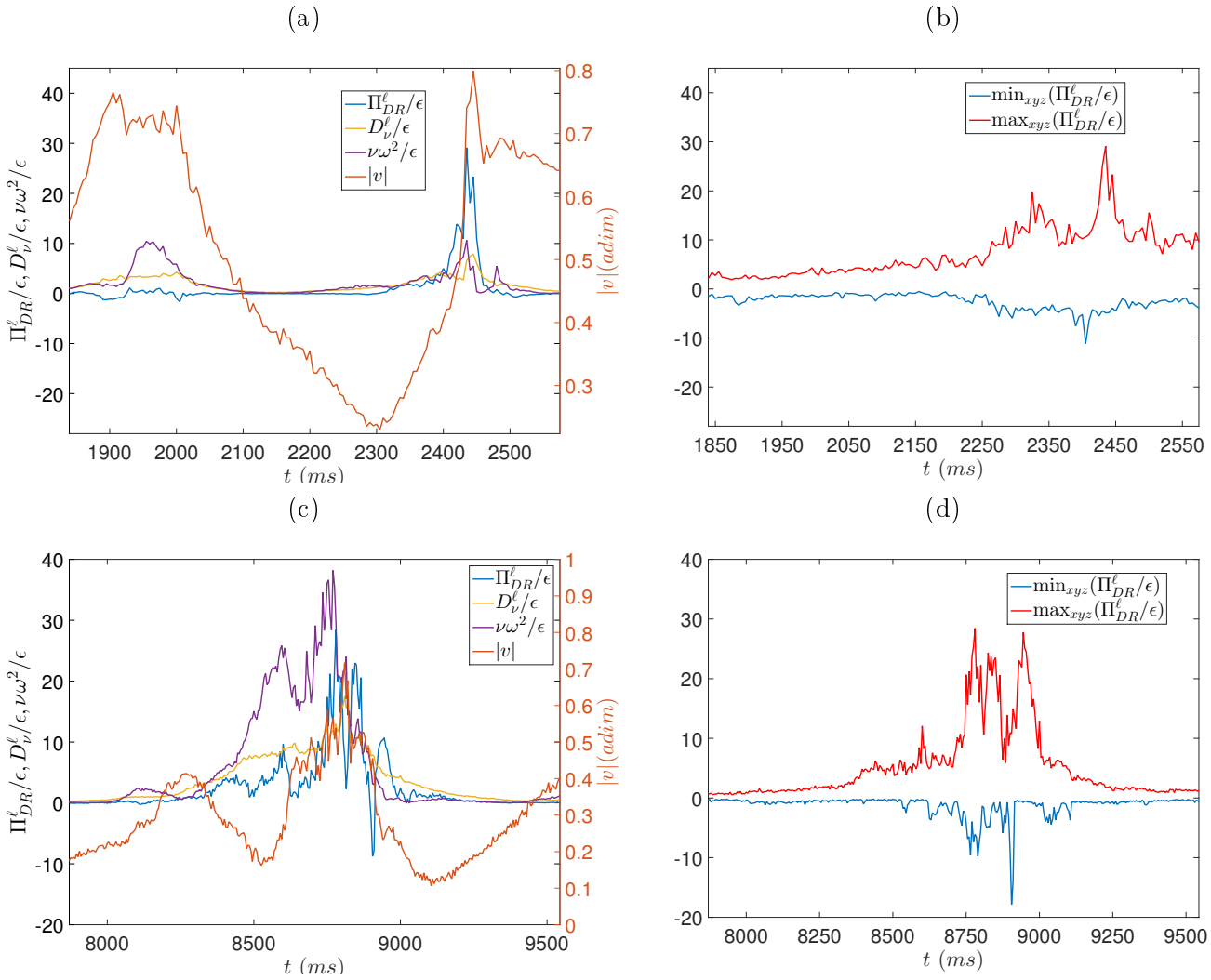

Figure 9.3: Time evolution of several quantities when extreme events of Π^ℓ_{DR} of case T4t occurs. (a) Fourth extreme event, time evolution of Π^ℓ_{DR}, $\mathscr{D}^\ell_\nu$, $\nu\omega^2$ and $|v|$ at the location where the extreme event occurs. (b) Fourth extreme event, time evolution of the maximum and minimum of Π^ℓ_{DR} on the plane where Π^ℓ_{DR} can be computed. (c) Fifth extreme event, time evolution of Π^ℓ_{DR}, $\mathscr{D}^\ell_\nu$, $\nu\omega^2$ and $|v|$ at the location where the extreme event occurs. (d) Fifth extreme event, time evolution of the maximum and minimum of Π^ℓ_{DR} on the plane where Π^ℓ_{DR} can be computed.

2.1 Average behaviour

We will study the trajectories ($Q(t)$,$R(t)$) in the (Q,R) plane. Here, $Q(t)$ and $R(t)$ are respectively the second and third VGT invariants computed at the fixed location where an extreme event of Π^{ℓ}_{DR} occurs. Inspired by [Danish and Meneveau, 2018], we first computed the conditional average of $\partial Q/\partial t$ and $\partial R/\partial t$, conditioned on Q and R to check whether there was an average behaviour. Here, $\partial/\partial t$ stands for the Eulerian, local derivative with respect to time, different from d/dt, the material or Lagrangian derivative. As we have $d/dt = \partial/\partial t + \mathbf{v} \cdot \boldsymbol{\nabla}$, we are also able to compute the conditional averages of dQ/dt and dR/dt : indeed, we have access to $\partial Q/\partial t$, $\partial R/\partial t$, $\mathbf{v}$, $\boldsymbol{\nabla} Q$ and $\boldsymbol{\nabla} R$.
Figure 9.4 shows both the conditional averages of the Lagrangian time derivatives (a) and Eulerian time derivatives (b) of Q and R. They are represented by arrows : the horizontal component corresponds to the derivative of R and the vertical one to the derivative of Q. The color corresponds to the $Q - R$ joint pdf, which has the well-known tear-drop shape. Concerning the Lagrangian derivative, the arrows follow the isolines of the joint pdf, except in the vortex compressing zone just above the right part of the Vieillefosse line. In this area, they are oriented towards the lower values of R. This is consistent with the concavity of the joint pdf in the vortex compressing zone but also questions the existence of the tail of the joint pdf which spreads along the right part of the Vieillefosse line : how do such values of (Q,R) occur if they are in average brought back to smaller R ? This is necessarily explained by deviations to the mean behaviour. This is quite interesting because the (unphysical) singularity of Vieillefosse occurs precisely on this part of the Vieillefosse line.
The conditional average of the Eulerian derivative is quite noisier than in the Lagrangian case. It may be due to insufficient statistics, or simply to the fact that such an average does not exist. The arrows are not always following the isolines. In particular, in the vortex stretching zone, they are oriented towards large values of Q and $|R|$. Just above the left part of the Vieillefosse line, this generates a kind of recirculation, with arrows parallel to the isolines of the joint pdf but in the opposite direction compared to the Lagrangian case. Around the concavity of the joint pdf, in the vortex compressing zone, the arrows are also not following the isolines ; they are oriented towards low values of R, as in the Lagrangian case. However, just above the right part of the Vieillefosse line, some arrows are oriented towards the tail of the joint pdf.

2.2 Eulerian trajectories around extremes in the $Q - R$ plane

We now compare the average behaviour of the Eulerian time derivatives of Q and R with the temporal evolution of Q and R at the location of some extreme events of Π^{ℓ}_{DR}, i.e. of the Eulerian temporal evolution of Q and R. Figure 9.5 shows the trajectories corresponding to this Eulerian temporal evolution, i.e. the Eulerian trajectory, for the five strongest events of Π^{ℓ}_{DR} (the same that are analyzed in the previous section). The trajectories are made of 100 points. The first part of the trajectory is the black dashed line and the second one is the black dotted line. The red triangle corresponds to the first point, the red star to the largest value of Π^{ℓ}_{DR} and the red square to the last point. The colorful contours correspond to the logarithm of the $Q - R$ joint pdf. The black plain line is the Vieillefosse line.
The trajectories are quite discontinuous ; this may be due to noise and a too large time step. We do not observe a behaviour common to the five trajectories. Only the first one (corresponding to the first extreme event of Π^{ℓ}_{DR}) and the fifth one (corresponding to the fifth...) are quite similar : they start in the vortex stretching zone and then go towards the tail of the $Q - R$ joint pdf. The second one has the opposite behaviour. The third one remains mostly in the vortex stretching zone and the fourth one is mainly confined to a zone of low values of Q and R. None of the trajectories completely follows or completely opposes the conditional average of the Eulerian derivatives.

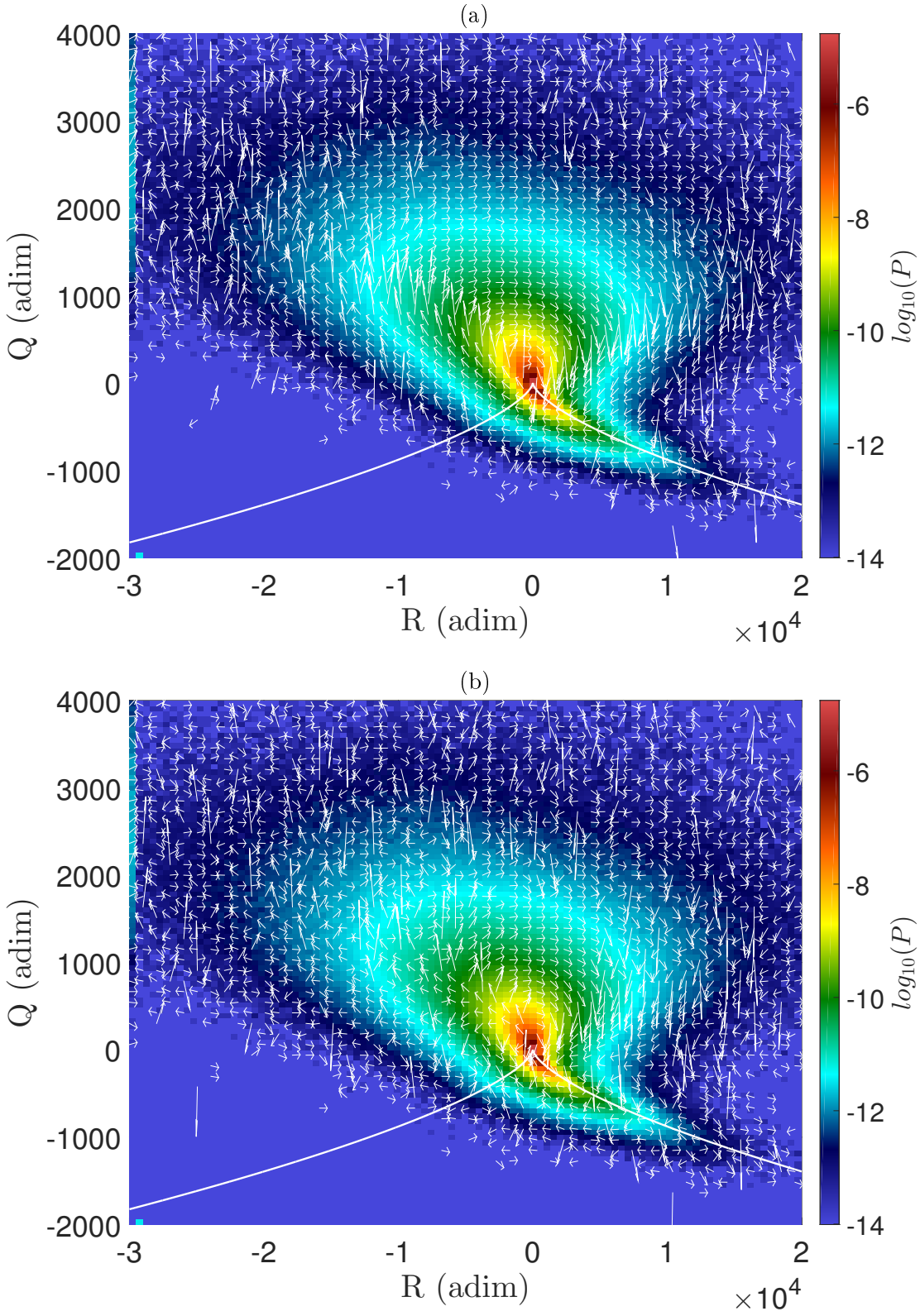

Figure 9.4: Conditional average of the time derivatives of the second and third VGT invariants Q and R, conditioned on Q and R. The coordinates of the arrows are proportional to the derivatives. The color corresponds to the logarithm of the $Q-R$ joint pdf. The white line is the Vieillefosse line. (a) Lagrangian derivative. (b) Eulerian derivative.

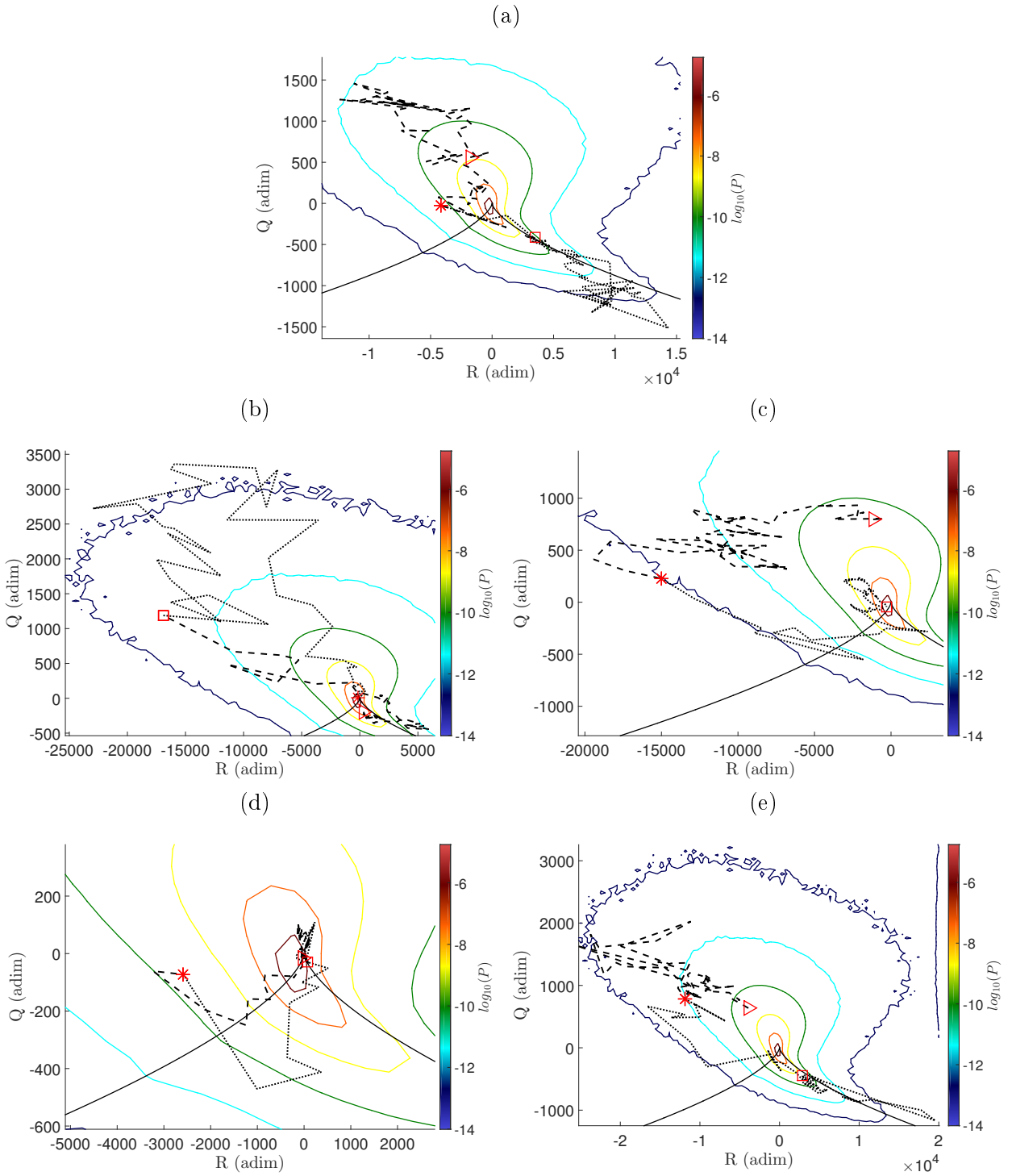

Figure 9.5: Temporal evolution of Q and R at the fixed location of an extreme event of Π^{ℓ}_{DR} in the $Q-R$ plane. The first part of the trajectory is the black dashed line and the second one is the black dotted line. The red triangle corresponds to the first point, the red star to the largest value of Π^{ℓ}_{DR} and the red square to the last point. The colorful contours correspond to the logarithm of the $Q-R$ joint pdf. The black plain line is the Vieillefosse line. (a) First extreme event. (b) Second extreme event. (c) Third extreme event. (d) Fourth extreme event. (e) Fifth extreme event.

3 Perspectives

It is difficult to draw any conclusion from this short analysis based on 1D signals corresponding to only 5 events. These preliminary results however show the feasibility of studying the time evolution of extreme events of the Duchon-Robert term. A higher acquisition frequency may be more appropriate for subsequent measurements : indeed, we do not lack extreme events and it would allow to better follow the events. Also, a larger measurement volume should be used in order to track Π^{ℓ}_{DR} and $\mathscr{D}^{\ell}_{\nu}$ in space. This is quite a challenge because the volume reconstruction quality is decreasing with the volume thickness in TPIV. As for scanning PIV, it allows larger measurement volumes as no volume reconstruction is required but time-resolved scanning PIV would require very high acquisition frequencies, which, if reachable, come along with a smaller sensor size, i.e. a smaller measurement volume.
Better than 1D analyses, studies of the in-plane evolution of Π^{ℓ}_{DR} and $\mathscr{D}^{\ell}_{\nu}$ and of the 3D evolution of the velocity and vorticity fields will allow to characterize the temporal evolution of the extreme events. They will be coupled with Lagrangian analyses based on a different processing of the images used to obtain the velocity fields by TPIV : indeed, Shake-The-Box [Schanz et al., 2016] analyses are currently in progress.

Conclusion and perspectives

In this thesis, we analyzed 3D velocity fields measured by tomographic particle image velocimetry (TPIV) in an experimental turbulent swirling flow, in order to infer some knowledge on the possible singularities developed by solutions to the 3D incompressible Navier-Stokes and Euler equations. We looked for extreme values of the Duchon-Robert term, or of the ratio between the Duchon-Robert term and a viscous dissipation term, computed around the Kolmogorov scale. Indeed, the Duchon-Robert term can be interpreted as inter-scale transfer and singularities are characterized by very small characteristic scales, smaller than the Kolmogorov scale, not smoothed out by viscous effects.

We first studied the statistics of the Duchon-Robert term, including its extreme values, and compared them to those of the viscous dissipation term and of the LES inter-scale transfer term. We showed that though the Duchon-Robert term was overall smaller in the dissipative range compared to the inertial one, its distribution was more intermittent with extreme events up to 100 times the global average dissipation rate. This suggests that a turbulent velocity field does not involve a single typical dissipative scale but several ones, or a range of dissipative scales. This should be confirmed by better spatially resolved measurements. We observed that this behaviour of the Duchon-Robert term is similar to the behaviour of the LES inter-scale transfer term but at variance with the behaviour of the viscous dissipation term, whose centered-reduced pdfs are scale-independent. The study of the joint pdf of the Duchon-Robert term and of the viscous dissipation term showed that the large values of the Duchon-Robert term come along with large values of the viscous dissipation term, though the converse is not true. This should in principle hinder the formation of possible singularities. The ratio between the Duchon-Robert term and the viscous dissipation term can all the same reach values around 10 in the dissipative range.
We then showed, with a 2D-3C analysis, that the extreme events of the Duchon-Robert term are responsible for the intermittent scaling of the velocity increment structure functions. This supports the phenomenological interpretation of the multifractal model, which assumes the existence of low regularity zones to explain the intermittency.

The second part of the results concerns the topological study of the prints of singularities, enabled by the implementation, in the von Kármán flow set-up, of a 3D measurement technique, the TPIV. We first made a systematic study of the topology based on the invariants of the velocity gradient tensor, which allowed to compare the topology distribution among the extreme events to the global distribution. We found that extreme events of the Duchon-Robert term favour the vortex stretching topology whereas the extreme events of the ratio between the Duchon-Robert term and the viscous dissipation term favour both the vortex stretching and the sheet topologies. This is somewhat at variance with the conditional average of the Duchon-Robert term whose largest values are reached for sheet topologies. We then broadened the topology study by the direct observation of the velocity fields corresponding to the very extreme events. This revealed three kinds of structures : roll-vortices, screw-vortices and U-turns that may correspond to a single structure, seen at different times or in different inertial frames. These structures correspond to previous experimental and numerical observations at similar Reynolds numbers. The extreme events of the Duchon-Robert

term come along with a large velocity norm and a large vorticity norm. They also display a large velocity divergence, suggesting that the particles do not follow properly the flow around these events. Also, observations of extreme events at larger Reynolds numbers showed that they feature the same structures, but more distorted ; this may be the sign that there is not enough separation between the dissipative scale and the integral scale at the Reynolds number for which we resolve the dissipative scales.

The third and last part of the results consists in a preliminary study of the time-evolution of the prints of singularities. We were able to detect very large events of the Duchon-Robert term even if time-resolved measurements do not provide a good statistical sampling of the flow and we could resolve them. We found that they last a few Kolmogorov time scales.

This thesis is a proof of concept of the experimental approach to the problem of the Navier-Stokes singularities using the criterion based on the Duchon-Robert term. We showed that it was possible to implement TPIV in the von Kármán set-up, and then to apply the detection method based on the Duchon-Robert term in a reasonable amount of time. We then detected very strong events, even among the time-resolved data. The 3D velocity fields allow to study the flow topology, as expected, and give promising results, as they agree with previous experimental and numerical observations. We also showed that we could follow the time evolution of the extreme events, even if we did not have time to investigate this point further ; it opens interesting perspectives for both Eulerian and Lagrangian measurements.
However, in order to talk about prints of singularities with more confidence, our experimental resolution should be improved and decreased below the Kolmogorov scale. Indeed, this could allow to distinguish between dissipative structures (whose size is of the order of the Kolmogorov scale) and possible singular structures (which should be smaller). Furthermore, studying larger Reynolds numbers is important as the occurence of possible singularities might be conditioned on this parameter ; this would also ensure a proper scale separation between integral and dissipative scales. During this thesis, a new experimental set-up, five times bigger than VK2, was designed in order to divide by 5 our spatial resolution at constant Reynolds number, or to multiply by 8 the Reynolds number at constant resolution. The conception of this set-up, which was not used during this thesis, is reported in appendix G.
A few other points should be addressed too. The relation between vorticity and the Duchon-Robert term should be investigated : is it equivalent to look for extreme events of vorticity or of the Duchon-Robert term ? Or are there large vorticity events which do not involve a large Duchon-Robert term ? The relation of the Duchon-Robert term with helicity and curvature and torsion of the streamlines should also be investigated. Concerning the experimental aspects, increasing the thickness of the velocity fields would be really useful as it would give access to more scales and would allow the study of the 3D structure of the Duchon-Robert field. TPIV may not be the most suited method in that respect. Better particles should also be used as we showed that they were not following the fluid properly around the extreme events. Concerning the post-treatment, $\mathscr{D}_\nu^\ell$ may not be the most suited dissipation term as its pdf saturates at low values, it is especially a problem when studying the ratio $\Pi_{DR}^\ell/\mathscr{D}_\nu^\ell$. Some work should also be done on the visualization and analysis of 3D fields : we showed that the interpretation could depend on the frame of reference or on the choice of the streamlines ; in the case of time-resolved data, the issue is even more troublesome as there is the time dimension to manage too. Using quantities which are independent from the frame of reference should be more suited. More generally, finding a way to classify automatically the structures of the velocity field around the extreme events would be useful as it would allow to analyze more velocity fields without human bias.

Appendices

Appendix A

Focal depth of a lens in the case of two different optical indices

In this appendix, we compute the focal depth of a camera, located in an optical medium of optical index n_e, which is focused on a field contained in an other optical medium of larger optical index $n_i > n_e$. The problem is modelled on figure A.1 : the observed field has a width Δ and is centered on a point A in the medium characterized by the optical index n_i. The camera lens is modelled by a lens of focal length f' located at point O and the camera sensor is located at point A' ; both are in the same medium of optical index $n_e < n_i$. The distance between the camera sensor and the camera lens is p' ; the distance between the optical interface and the camera lens is p_e and the distance between the center of the field and the optical interface is p_i so that the total distance between the center of the field and the optical interface is $p = p_e + p_i$. The distances are signed, the optical axis being directed from the field to the camera (from the left to the right of the figure). Seen from the external medium of optical index n_e, everything happens as if the lengths parallel to the optical axis and inside the medium of optical index n_i were multiplied by n_e/n_i. Therefore, if $n_e < n_i$, the objects inside the medium seem to be closer than what they are ; therefore, they also seem bigger.

1 Small-angle approximation

As $n_e < n_i$, the observed field seems to be closer from the interface, as is sketched on figure A.2. This figure shows the astigmatism of such a set-up : beams coming from the same point do not seem to come from the same point ; however, we work in the small-angle approximation so that they appear to have approximately the same origin. This visible origin is closer to the optical interface than their real origin. In the VK2 set-up, the small-angle approximation is verified as the maximum angle θ_{max} between a beam and the optical axis will be such that $tan(\theta_{max}) = \frac{max(lens\ diameter, fieldsize)}{|p|} \approx 0.1$, hence $\theta_{max} \approx 6°$.

In this approximation, we can show that all beams issued from a single point on the optical axis in the optical medium characterized by an optical index n_i converge to a single point after the lens. Indeed, consider figure A.3. The represented beam starts from a point at height h in the optical medium i with an angle θ_i with the optical axis. Here, we take $h = 0$. At a distance x after the lens, the beam height is :

$$h'(x) = -p_i \tan(\theta_i) - p_e \tan(\theta_e) + x \tan(\alpha) \tag{A.1}$$

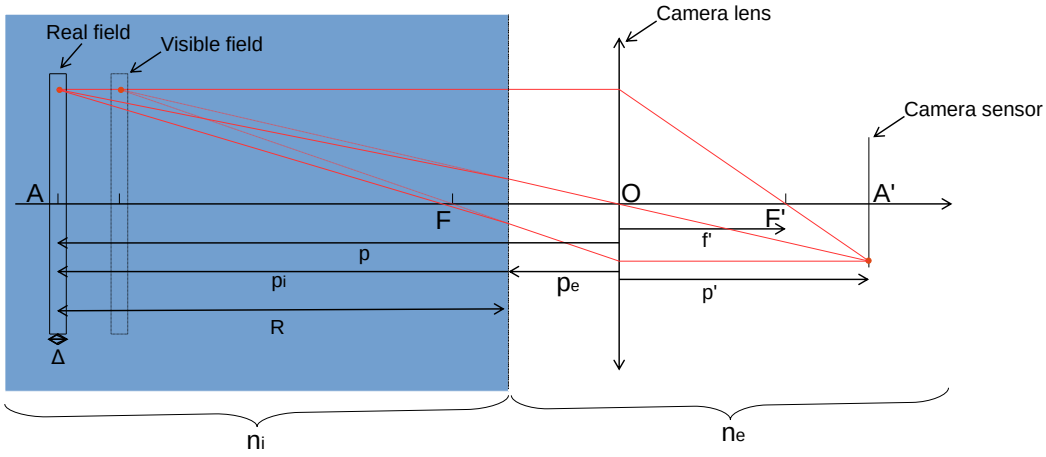

Figure A.1: Representation of the problem.

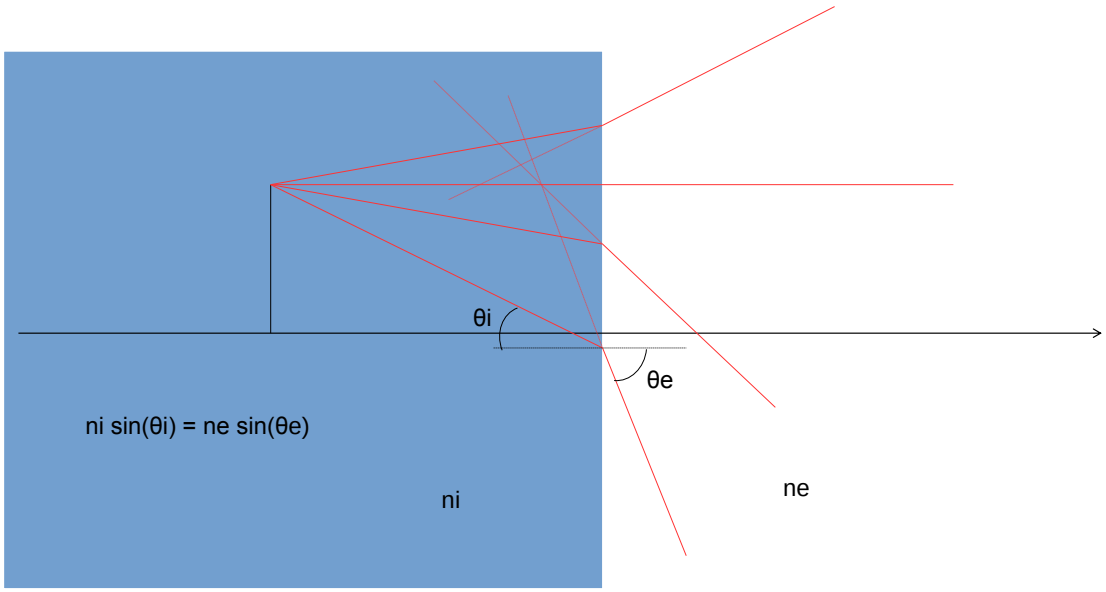

Figure A.2: Astigmatism

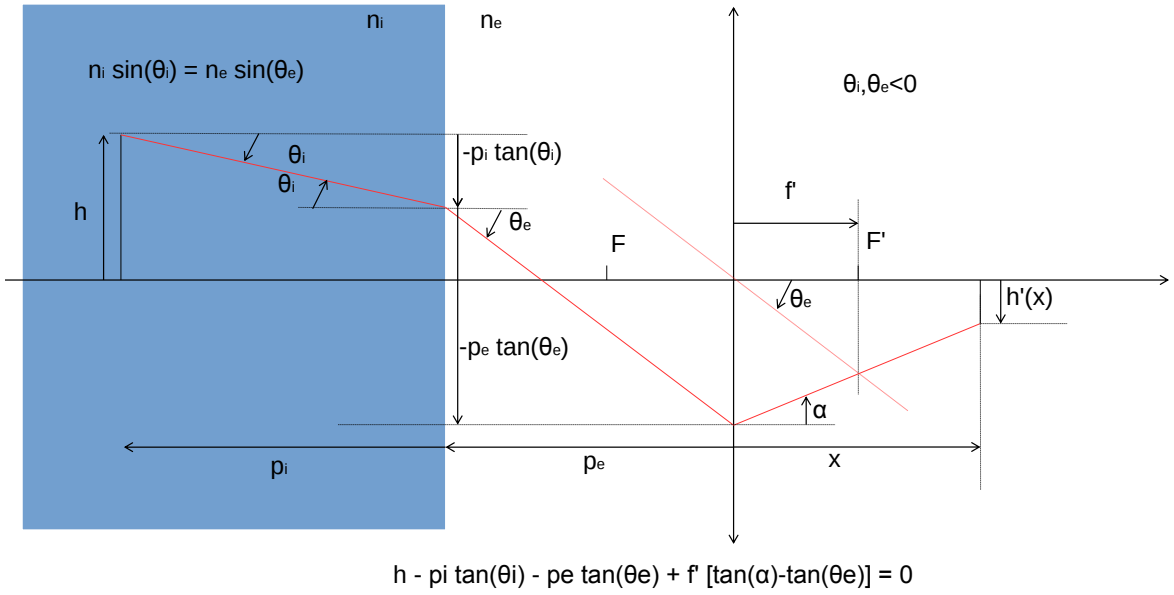

Figure A.3: Heights of a beam.

i.e :

$$h'(x) = -p_i \tan(\theta_i) - p_e \tan(\theta_e) + x \frac{(f' \tan(\theta_e) - (-p_i \tan(\theta_i) - p_e \tan(\theta_e))}{f'} \tag{A.2}$$

where θ_e is such that

$$n_i \sin\theta_i = n_e \sin\theta_e \tag{A.3}$$

In the small-angle approximation, we have :

$$h'(x) = -p_i \theta_i - p_e n_i / n_e \theta_i + x \frac{(f' n_i / n_e \theta_i - (-p_i \theta_i - p_e n_i / n_e \theta_i)}{f'} \tag{A.4}$$

For any θ_i, $h' = 0$ for :

$$x = \frac{f'(n_e p_i + p_e n_i)}{f' n_i + n_e p_i + p_e n_i} = p' \tag{A.5}$$

We showed that all beams coming from a single point on the optical axis converge to a single point on the optical axis at abscissa $x = p'$. The sensor should be at this location so that the images are focused.

2 Magnification

Knowing $p' = x$, we can deduce the magnification : by definition,

$$M = \frac{f' - p'}{f'} = \frac{f' n_i}{f' n_i + n_e p_i + p_e n_i} = \frac{f'}{f' + n_e / n_i p_i + p_e} \tag{A.6}$$

Let us now consider the beam sketched on figure A.3 with $h \neq 0$. It is issued from a point located in the optical medium i at a distance $p = p_i + p_e$ from the lens and at a distance h from the optical

axis. The angle between this beam and the optical axis is θ_i. Let us compute the height h' of the beam at a distance p' of the lens. As previously, we have :

$$h'(x) = h - p_i\theta_i - p_e n_i/n_e\theta_i + x\frac{(f' n_i/n_e\theta_i - (h - p_i\theta_i - p_e n_i/n_e\theta_i)}{f'} \tag{A.7}$$

Therefore :

$$h'(p') = h(1 - \frac{p'}{f'}) = hM \tag{A.8}$$

The size of the observed object is multiplied by M.

3 Focal depth

In the small-angle approximation, a point located at $p = p_i + p_e$ on the optical axis has an image located on the optical axis at :

$$x = p' = \frac{f'(p_i + p_e n_i)}{f' n_i + p_i + p_e n_i} \tag{A.9}$$

Other points located on the optical axis slightly before or after p, i.e. at $p \pm dp$, will have images on the optical axis slightly before or after p', as shown on figure A.4. Therefore, beams coming from these points do not converge to the focal plane at abscissa p' and create a blurred spot in this focal plane. The cameras settings should be such that the size of the blurred spot thus created is smaller than the particle image modelled by an Airy disk of diameter Φ_d, so that the particle image diameter does not increase. In other words, the focal depth is the length of the segment of the optical axis whose points will create a blurred spot smaller than the Airy disk.

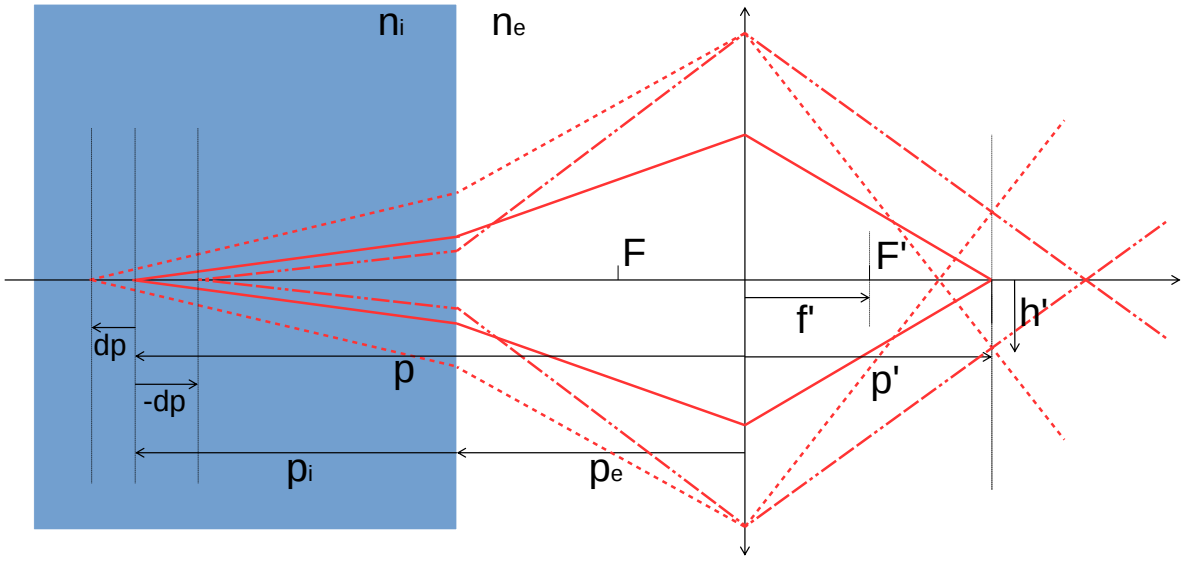

Figure A.4: Focal depth. Out-of-focus points will create a blurred spot whose diameter depends on the distance to the focus.

A beam issued from the abscissa $p \pm dp$ and forming an angle θ_i with the optical axis has a height h' at abscissa p' given by :

$$h' = (-p_i \pm dp)\theta_i - p_e n_i/n_e\theta_i + p'\frac{(f' n_i/n_e\theta_i - ((-p_i \pm dp)\theta_i - p_e n_i/n_e\theta_i)}{f'} = (1 - p'/f')\theta_i(\pm dp) \tag{A.10}$$

Extreme values of h' are reached for $\theta_i = \theta_i^{min} = \frac{-D/2}{-p_i \pm dp - n_i/n_e p_e}$ or $\theta_i = \theta_i^{max} = \frac{D/2}{-p_i \pm dp - n_i/n_e p_e}$ and are equal to (at leading order) :

$$h'_{max/min}(dp) = \pm(1 - p'/f')\frac{D}{2(p_i + n_i/n_e p_e)}dp \tag{A.11}$$

Writing the definition of the focal depth δ yields :

$$\Phi_d = |h'_{max}(|dp| = \delta/2) - h'_{min}(|dp| = \delta/2)| \tag{A.12}$$

Hence, as $D = f'/f_\#$:

$$\Phi_d = (1 - p'/f')\frac{f'}{2f_\#(p_i + n_i/n_e p_e)}\delta = \frac{(f' - p')\delta}{2f_\#(p_i + n_i/n_e p_e)} \tag{A.13}$$

i.e. :

$$\delta = \frac{2\Phi_d f_\#(p_i + n_i/n_e p_e)}{f' - p'} \tag{A.14}$$

As :

$$p_i + n_i p_e = \frac{f' n_i/n_e}{M} - f' n_i/n_e = f' n_i/n_e(\frac{1}{M} - 1) \tag{A.15}$$

we have :

$$\delta = \frac{2\Phi_d f_\# f' n_i/n_e(\frac{1}{M} - 1)}{f' - p'} = 2\Phi_d f_\# n_i/n_e\frac{1 - M}{M^2} = 2 \cdot 2,44 f_\# \lambda\ n_i/n_e \left(\frac{1 - M}{M}\right)^2 \tag{A.16}$$

or :

$$\delta = 2 \cdot 2,44 f_\# \lambda\ \frac{n_i}{n_e}\left(\frac{1 + |M|}{|M|}\right)^2 \tag{A.17}$$

Seen from the external medium, the focal depth is $\delta \cdot n_e/n_i$, but in the medium of optical index n_i it is δ.

Appendix B

Resolution, field depth and Airy disk diameter tables

Tables and figures corresponding to formula in section 2.7.2. All tables were obtained for $\gamma_{2D} = 1$ or $\gamma_{3D} = 1$, $N = 10$ and $c = 2$ pixels.

1 2D PIV

1.1 $\mathbf{n_i = n_e}$

$f_{\#}$	|M|	r_{th}^{2D}(mm)	δ(mm)	Φ_d(pixels)
4	0.1	0.5	5.0	0.9
	0.3	0.2	0.8	1.0
	0.5	0.1	0.4	1.2
	0.7	0.1	0.2	1.4
	0.9	0.1	0.2	1.5
	1.1	0.1	0.2	1.7
	1.3	0.1	0.1	1.8
	1.5	0.0	0.1	2.0
5.6	0.1	0.6	9.9	1.2
	0.3	0.2	1.5	1.5
	0.5	0.1	0.7	1.7
	0.7	0.1	0.5	1.9
	0.9	0.1	0.4	2.1
	1.1	0.1	0.3	2.3
	1.3	0.1	0.3	2.6
	1.5	0.1	0.2	2.8
8	0.1	0.7	20.1	1.8
	0.3	0.2	3.1	2.1
	0.5	0.2	1.5	2.4
	0.7	0.1	1.0	2.7
	0.9	0.1	0.7	3.0
	1.1	0.1	0.6	3.4
	1.3	0.1	0.5	3.7
	1.5	0.1	0.5	4.0
11	0.1	0.8	38.0	2.4
	0.3	0.3	5.9	2.9
	0.5	0.2	2.8	3.3
	0.7	0.1	1.9	3.7
	0.9	0.1	1.4	4.2
	1.1	0.1	1.1	4.6
	1.3	0.1	1.0	5.1
	1.5	0.1	0.9	5.5
16	0.1	1.0	80.4	3.5
	0.3	0.4	12.5	4.2
	0.5	0.2	6.0	4.8
	0.7	0.2	3.9	5.4
	0.9	0.2	3.0	6.1
	1.1	0.1	2.4	6.7
	1.3	0.1	2.1	7.3
	1.5	0.1	1.8	8.0

Table B.1: $c = 6.5$ pixels (cameras Imager sCMOS)

$f_\#$	|M|	r_{th}^{2D}(mm)	δ(mm)	Φ_d(pixels)
4	0.1	0.7	5.0	0.6
	0.3	0.2	0.8	0.7
	0.5	0.2	0.4	0.8
	0.7	0.1	0.2	0.9
	0.9	0.1	0.2	1.0
	1.1	0.1	0.2	1.1
	1.3	0.1	0.1	1.2
	1.5	0.1	0.1	1.3
5.6	0.1	0.8	9.9	0.8
	0.3	0.3	1.5	0.9
	0.5	0.2	0.7	1.1
	0.7	0.1	0.5	1.2
	0.9	0.1	0.4	1.4
	1.1	0.1	0.3	1.5
	1.3	0.1	0.3	1.7
	1.5	0.1	0.2	1.8
8	0.1	0.9	20.1	1.1
	0.3	0.3	3.1	1.4
	0.5	0.2	1.5	1.6
	0.7	0.2	1.0	1.8
	0.9	0.1	0.7	2.0
	1.1	0.1	0.6	2.2
	1.3	0.1	0.5	2.4
	1.5	0.1	0.5	2.6
11	0.1	1.0	38.0	1.6
	0.3	0.4	5.9	1.9
	0.5	0.2	2.8	2.1
	0.7	0.2	1.9	2.4
	0.9	0.1	1.4	2.7
	1.1	0.1	1.1	3.0
	1.3	0.1	1.0	3.3
	1.5	0.1	0.9	3.6
16	0.1	1.2	80.4	2.3
	0.3	0.4	12.5	2.7
	0.5	0.3	6.0	3.1
	0.7	0.2	3.9	3.5
	0.9	0.2	3.0	3.9
	1.1	0.2	2.4	4.4
	1.3	0.1	2.1	4.8
	1.5	0.1	1.8	5.2

Table B.2: $c = 10$ pixels (cameras Phantom Miro m340)

1.2 $\mathbf{n_i = 1.4 \neq n_e = 1}$

$f_{\#}$	|M|	r_{th}^{2D}(mm)	δ(mm)	Φ_d(pixels)
4	0.1	0.5	7.0	0.9
	0.3	0.2	1.1	1.0
	0.5	0.1	0.5	1.2
	0.7	0.1	0.3	1.4
	0.9	0.1	0.3	1.5
	1.1	0.1	0.2	1.7
	1.3	0.1	0.2	1.8
	1.5	0.0	0.2	2.0
5.6	0.1	0.6	13.8	1.2
	0.3	0.2	2.1	1.5
	0.5	0.1	1.0	1.7
	0.7	0.1	0.7	1.9
	0.9	0.1	0.5	2.1
	1.1	0.1	0.4	2.3
	1.3	0.1	0.4	2.6
	1.5	0.1	0.3	2.8
8	0.1	0.7	28.1	1.8
	0.3	0.2	4.4	2.1
	0.5	0.2	2.1	2.4
	0.7	0.1	1.4	2.7
	0.9	0.1	1.0	3.0
	1.1	0.1	0.8	3.4
	1.3	0.1	0.7	3.7
	1.5	0.1	0.6	4.0
11	0.1	0.8	53.2	2.4
	0.3	0.3	8.3	2.9
	0.5	0.2	4.0	3.3
	0.7	0.1	2.6	3.7
	0.9	0.1	2.0	4.2
	1.1	0.1	1.6	4.6
	1.3	0.1	1.4	5.1
	1.5	0.1	1.2	5.5
16	0.1	1.0	112.6	3.5
	0.3	0.4	17.5	4.2
	0.5	0.2	8.4	4.8
	0.7	0.2	5.5	5.4
	0.9	0.2	4.1	6.1
	1.1	0.1	3.4	6.7
	1.3	0.1	2.9	7.3
	1.5	0.1	2.6	8.0

Table B.3: $c = 6.5$ pixels (cameras Imager sCMOS)

$f_\#$	|M|	r_{th}^{2D}(mm)	δ(mm)	Φ_d(pixels)
4	0.1	0.7	7.0	0.6
	0.3	0.2	1.1	0.7
	0.5	0.2	0.5	0.8
	0.7	0.1	0.3	0.9
	0.9	0.1	0.3	1.0
	1.1	0.1	0.2	1.1
	1.3	0.1	0.2	1.2
	1.5	0.1	0.2	1.3
5.6	0.1	0.8	13.8	0.8
	0.3	0.3	2.1	0.9
	0.5	0.2	1.0	1.1
	0.7	0.1	0.7	1.2
	0.9	0.1	0.5	1.4
	1.1	0.1	0.4	1.5
	1.3	0.1	0.4	1.7
	1.5	0.1	0.3	1.8
8	0.1	0.9	28.1	1.1
	0.3	0.3	4.4	1.4
	0.5	0.2	2.1	1.6
	0.7	0.2	1.4	1.8
	0.9	0.1	1.0	2.0
	1.1	0.1	0.8	2.2
	1.3	0.1	0.7	2.4
	1.5	0.1	0.6	2.6
11	0.1	1.0	53.2	1.6
	0.3	0.4	8.3	1.9
	0.5	0.2	4.0	2.1
	0.7	0.2	2.6	2.4
	0.9	0.1	2.0	2.7
	1.1	0.1	1.6	3.0
	1.3	0.1	1.4	3.3
	1.5	0.1	1.2	3.6
16	0.1	1.2	112.6	2.3
	0.3	0.4	17.5	2.7
	0.5	0.3	8.4	3.1
	0.7	0.2	5.5	3.5
	0.9	0.2	4.1	3.9
	1.1	0.2	3.4	4.4
	1.3	0.1	2.9	4.8
	1.5	0.1	2.6	5.2

Table B.4: $c = 10$ pixels (cameras Phantom Miro m340)

2 3D PIV

2.1 $\mathbf{n_i = n_e}$

$f_\#$	|M|	r_{th}^{3D}(mm)	δ(mm)	δ/r_{th}^{3D}	Φ_d(pixels)
4	0.1	1.11	5.03	4.5	0.9
	0.3	0.30	0.78	2.6	1.0
	0.5	0.17	0.37	2.2	1.2
	0.7	0.12	0.24	2.0	1.4
	0.9	0.10	0.19	1.9	1.5
	1.1	0.08	0.15	1.8	1.7
	1.3	0.07	0.13	1.8	1.8
	1.5	0.06	0.12	1.8	2.0
5.6	0.1	1.51	9.85	6.5	1.2
	0.3	0.41	1.53	3.8	1.5
	0.5	0.24	0.73	3.1	1.7
	0.7	0.17	0.48	2.8	1.9
	0.9	0.14	0.36	2.7	2.1
	1.1	0.12	0.30	2.6	2.3
	1.3	0.10	0.25	2.5	2.6
	1.5	0.09	0.23	2.5	2.8
8	0.1	2.11	20.10	9.5	1.8
	0.3	0.58	3.12	5.4	2.1
	0.5	0.34	1.50	4.4	2.4
	0.7	0.25	0.98	4.0	2.7
	0.9	0.20	0.74	3.8	3.0
	1.1	0.17	0.61	3.6	3.4
	1.3	0.15	0.52	3.5	3.7
	1.5	0.13	0.46	3.4	4.0
11	0.1	2.91	38.01	13.1	2.4
	0.3	0.80	5.90	7.4	2.9
	0.5	0.47	2.83	6.0	3.3
	0.7	0.35	1.85	5.4	3.7
	0.9	0.28	1.40	5.0	4.2
	1.1	0.24	1.14	4.8	4.6
	1.3	0.21	0.98	4.6	5.1
	1.5	0.19	0.87	4.5	5.5
16	0.1	4.33	80.42	18.6	3.5
	0.3	1.20	12.48	10.4	4.2
	0.5	0.72	5.98	8.4	4.8
	0.7	0.53	3.92	7.4	5.4
	0.9	0.43	2.96	6.9	6.1
	1.1	0.37	2.42	6.6	6.7
	1.3	0.33	2.08	6.3	7.3
	1.5	0.30	1.85	6.1	8.0
22	0.1	6.18	152.04	24.6	4.8
	0.3	1.73	23.60	13.6	5.7
	0.5	1.03	11.31	10.9	6.6
	0.7	0.77	7.41	9.7	7.5
	0.9	0.63	5.60	8.9	8.3
	1.1	0.54	4.58	8.5	9.2
	1.3	0.48	3.93	8.1	10.1
	1.5	0.44	3.49	7.9	11.0

Table B.5: $c = 6.5$ pixels (cameras Imager sCMOS)

$f_\#$	|M|	r_{th}^{3D}(mm)	δ(mm)	δ/r_{th}^{3D}	Φ_d(pixels)
4	0.1	1.38	5.03	3.7	0.6
	0.3	0.37	0.78	2.1	0.7
	0.5	0.21	0.37	1.8	0.8
	0.7	0.15	0.24	1.7	0.9
	0.9	0.12	0.19	1.6	1.0
	1.1	0.10	0.15	1.5	1.1
	1.3	0.09	0.13	1.5	1.2
	1.5	0.08	0.12	1.5	1.3
5.6	0.1	1.82	9.85	5.4	0.8
	0.3	0.49	1.53	3.1	0.9
	0.5	0.28	0.73	2.6	1.1
	0.7	0.20	0.48	2.4	1.2
	0.9	0.16	0.36	2.3	1.4
	1.1	0.13	0.30	2.2	1.5
	1.3	0.12	0.25	2.2	1.7
	1.5	0.10	0.23	2.2	1.8
8	0.1	2.50	20.10	8.0	1.1
	0.3	0.67	3.12	4.6	1.4
	0.5	0.39	1.50	3.8	1.6
	0.7	0.28	0.98	3.5	1.8
	0.9	0.22	0.74	3.3	2.0
	1.1	0.19	0.61	3.2	2.2
	1.3	0.17	0.52	3.1	2.4
	1.5	0.15	0.46	3.1	2.6
11	0.1	3.36	38.01	11.3	1.6
	0.3	0.91	5.90	6.4	1.9
	0.5	0.53	2.83	5.3	2.1
	0.7	0.39	1.85	4.8	2.4
	0.9	0.31	1.40	4.5	2.7
	1.1	0.26	1.14	4.3	3.0
	1.3	0.23	0.98	4.2	3.3
	1.5	0.21	0.87	4.1	3.6
16	0.1	4.88	80.42	16.5	2.3
	0.3	1.34	12.48	9.3	2.7
	0.5	0.79	5.98	7.6	3.1
	0.7	0.58	3.92	6.8	3.5
	0.9	0.47	2.96	6.3	3.9
	1.1	0.40	2.42	6.1	4.4
	1.3	0.35	2.08	5.9	4.8
	1.5	0.32	1.85	5.7	5.2
22	0.1	6.81	152.04	22.3	3.1
	0.3	1.89	23.60	12.5	3.7
	0.5	1.12	11.31	10.1	4.3
	0.7	0.82	7.41	9.0	4.9
	0.9	0.67	5.60	8.4	5.4
	1.1	0.57	4.58	8.0	6.0
	1.3	0.51	3.93	7.7	6.6
	1.5	0.47	3.49	7.5	7.1

Table B.6: $c = 10$ pixels (cameras Phantom Miro m340)

2.2 $\mathbf{n_i = 1.4 \neq n_e = 1}$

$f_\#$	|M|	r_{th}^{3D}(mm)	δ(mm)	δ/r_{th}^{3D}	Φ_d(pixels)
4	0.1	1.25	7.04	5.6	0.9
	0.3	0.33	1.09	3.3	1.0
	0.5	0.19	0.52	2.7	1.2
	0.7	0.14	0.34	2.5	1.4
	0.9	0.11	0.26	2.4	1.5
	1.1	0.09	0.21	2.3	1.7
	1.3	0.08	0.18	2.3	1.8
	1.5	0.07	0.16	2.2	2.0
5.6	0.1	1.68	13.79	8.2	1.2
	0.3	0.45	2.14	4.7	1.5
	0.5	0.26	1.03	3.9	1.7
	0.7	0.19	0.67	3.5	1.9
	0.9	0.15	0.51	3.3	2.1
	1.1	0.13	0.42	3.2	2.3
	1.3	0.11	0.36	3.1	2.6
	1.5	0.10	0.32	3.1	2.8
8	0.1	2.36	28.15	11.9	1.8
	0.3	0.64	4.37	6.8	2.1
	0.5	0.38	2.09	5.5	2.4
	0.7	0.27	1.37	5.0	2.7
	0.9	0.22	1.04	4.7	3.0
	1.1	0.19	0.85	4.5	3.4
	1.3	0.17	0.73	4.4	3.7
	1.5	0.15	0.65	4.3	4.0
11	0.1	3.25	53.21	16.4	2.4
	0.3	0.90	8.26	9.2	2.9
	0.5	0.53	3.96	7.5	3.3
	0.7	0.39	2.59	6.7	3.7
	0.9	0.31	1.96	6.3	4.2
	1.1	0.27	1.60	6.0	4.6
	1.3	0.24	1.38	5.8	5.1
	1.5	0.22	1.22	5.6	5.5
16	0.1	4.84	112.59	23.2	3.5
	0.3	1.35	17.47	13.0	4.2
	0.5	0.80	8.37	10.5	4.8
	0.7	0.59	5.49	9.3	5.4
	0.9	0.48	4.15	8.6	6.1
	1.1	0.41	3.39	8.2	6.7
	1.3	0.37	2.91	7.9	7.3
	1.5	0.34	2.58	7.7	8.0
22	0.1	6.91	212.86	30.8	4.8
	0.3	1.93	33.03	17.1	5.7
	0.5	1.16	15.83	13.7	6.6
	0.7	0.86	10.38	12.1	7.5
	0.9	0.70	7.84	11.2	8.3
	1.1	0.61	6.41	10.6	9.2
	1.3	0.54	5.51	10.2	10.1
	1.5	0.50	4.89	9.9	11.0

Table B.7: $c = 6.5$ pixels (cameras Imager sCMOS)

$f_\#$	|M|	r_{th}^{3D}(mm)	δ(mm)	δ/r_{th}^{3D}	Φ_d(pixels)
4	0.1	1.54	7.04	4.6	0.6
	0.3	0.41	1.09	2.7	0.7
	0.5	0.23	0.52	2.2	0.8
	0.7	0.17	0.34	2.1	0.9
	0.9	0.13	0.26	2.0	1.0
	1.1	0.11	0.21	1.9	1.1
	1.3	0.10	0.18	1.9	1.2
	1.5	0.08	0.16	1.9	1.3
5.6	0.1	2.04	13.79	6.8	0.8
	0.3	0.55	2.14	3.9	0.9
	0.5	0.31	1.03	3.3	1.1
	0.7	0.22	0.67	3.0	1.2
	0.9	0.18	0.51	2.9	1.4
	1.1	0.15	0.42	2.8	1.5
	1.3	0.13	0.36	2.7	1.7
	1.5	0.12	0.32	2.7	1.8
8	0.1	2.79	28.15	10.1	1.1
	0.3	0.75	4.37	5.8	1.4
	0.5	0.44	2.09	4.8	1.6
	0.7	0.31	1.37	4.4	1.8
	0.9	0.25	1.04	4.1	2.0
	1.1	0.21	0.85	4.0	2.2
	1.3	0.19	0.73	3.9	2.4
	1.5	0.17	0.65	3.8	2.6
11	0.1	3.76	53.21	14.1	1.6
	0.3	1.02	8.26	8.1	1.9
	0.5	0.60	3.96	6.6	2.1
	0.7	0.43	2.59	6.0	2.4
	0.9	0.35	1.96	5.6	2.7
	1.1	0.30	1.60	5.4	3.0
	1.3	0.26	1.38	5.3	3.3
	1.5	0.24	1.22	5.2	3.6
16	0.1	5.46	112.59	20.6	2.3
	0.3	1.50	17.47	11.7	2.7
	0.5	0.88	8.37	9.5	3.1
	0.7	0.65	5.49	8.5	3.5
	0.9	0.52	4.15	7.9	3.9
	1.1	0.45	3.39	7.6	4.4
	1.3	0.40	2.91	7.4	4.8
	1.5	0.36	2.58	7.2	5.2
22	0.1	7.62	212.86	27.9	3.1
	0.3	2.11	33.03	15.6	3.7
	0.5	1.25	15.83	12.6	4.3
	0.7	0.92	10.38	11.3	4.9
	0.9	0.75	7.84	10.5	5.4
	1.1	0.64	6.41	10.0	6.0
	1.3	0.57	5.51	9.6	6.6
	1.5	0.52	4.89	9.4	7.1

Table B.8: $c = 10$ pixels (cameras Phantom Miro m340)

Appendix C

Test of Davis software

During the second part of the time-resolved measurement campaign of 2018, we acquired one run of 4575 images with the fluid at rest (no rotation of the impellers). We analyzed the images with different sets of volume correlation parameters and obtained a so-called "case-control (CC) data set" made of eleven cases named from CC1 to CC11. This allowed to test the influence of different correlation parameters and to have a better knowledge of the whole PIV measurement chain which involves a software that we did not develop. We were especially interested in estimating the measurement noise and the cut-off wavenumbers for different interrogation window sizes, overlaps and shapes.

1 Presentation of the case-control data set

1.1 Flow parameters

The liquid filling the tank was a water-glycerol mixture containing 55.3% of glycerol in volume. After a previous measurement during which the impellers had been rotating at 1 Hz in contra direction for two hours and a half, both engines were turned off and unplugged to avoid residual rotation. We then waited for a few minutes before acquiring the images. In these conditions, the fluid is almost at rest, but natural convection can still occur due to temperature gradients. Also, particles may have a motion due to brownian motion or Archimedes' principle. These contributions will be included in the noise measured with these cases.

Case		CC1 to CC11
Rotation frequency (Hz)		0
Liquid (water) properties	Temperature (°C)	20
	Kinematic viscosity (m^2/s)	1.0×10^{-5}
	Density (kg/m^3)	1156

Table C.1: Flow parameters for the case-control data set.

1.2 Seeding parameters

The particles used for the case-control data set are the same as for cases T1 to T4 and T4t. Their density is 1.1 ± 0.05 g/cm^3, which is very close to the liquid density. It is slightly lower, so that particles should go up due to Archimedes' principle. The velocity shift in this liquid is $v_g = 2.6 \times 10^{-7}$ m/s.

1.3 Acquisition

The acquisition set-up is exactly the same as for the time-resolved 3D data set, except for the exposure time which was 622 μs.

1.3.1 Acquisition parameters

The measurement area is a rectangular volume centered on the center of the cylinder, it is smaller than for case T4t (see figure 5.11). The exact dimensions of the measurement area, as well as the corresponding magnification, are given in table C.2. Images were acquired in one run. For the chosen acquisition frequency, the sensor size is smaller than for case T4t and one run contains more images (4575, allowing to compute 4574 velocity fields).

Case		CC1 to CC11
Field size	Δx(cm)	3.3
	Δy(cm)	3.1
	Δz(cm)	0.50
Magnification		0.40
Acquisition frequency f_{acq} (Hz)		1600
Interframing time dt (μs)		625
Number of runs		1
Number of images per run		4575
Total number of frames		4574
$\langle n_{t,eff,x} \rangle_{x,y,z}$		4400 (130)

Table C.2: Acquisition parameters for the time-resolved 3D data set.

This table also gives the number of frames n_t acquired for each case, as well as the acquisition frequency f_{acq} and the space average of the effective number of independent frames (based on the decorrelation of the velocity component along x which seems to be the longer to decorrelate). Here, the effective number of frames is not very meaningful and cannot be really compared to the ones of the cases with a turbulent flow. Indeed, two following frames are anti-correlated because the measured velocity corresponds to the lighting difference between the two pulses. As the time step is very small compared to the typical time scales of the flow, the difference between two images is mainly due to the intensity difference between two pulses. The n^{th} image is very close to the $(n+2)^{th}$ image (as they correspond to the same pulse), so that the correlation between images n and (n+1) will give a velocity almost opposite to the correlation between images (n+1) and (n+2). When summing the correlation values ρ_i, the negative correlation values will cancel the positive ones ; hence, the resulting $n_{t,eff,x}$ will be higher than for positive correlation values only. To get a more meaningful value of $n_{t,eff,x}$, one can use only one velocity field out of two, such that the correlation values are always positive. We then get a value of 130 effectively independent frames.

1.4 Image preprocessing, calibration and volume reconstruction

The image preprocessing was the same as for case T4t.
The calibration was done in two steps : a first guess was done with a 3D calibration plate with two levels, which was then refined by a few iterations of volume self-calibration using 200 images acquired previously with the impellers rotating (the acquired frames were too correlated for the

disparity map to converge). Table C.3 gives the average, standard deviation and maximum disparity for the case-control data set.
Table C.3 also gives the parameters and quality indicators for the volume reconstruction step. Four MART iterations were used. The ghost ratio and the normalized intensity variance both have acceptable values, comparable to the other cases.

Case		CC1 to CC11
Disparity (pixels)	Average	0.03
	Standard deviation	0.02
	Maximum	0.2
Volume size (voxels)	n_x^{vox}	1566
	n_y^{vox}	1388
	n_z^{vox}	220
Number of MART iterations		4
Ghost ratio		10%
Normalized intensity variance		25

Table C.3: Volume reconstruction parameters and quality indicators for the case-control data set

2 Comparison of the volume correlation parameters

The first goal of the case-control data set was to improve our knowledge of the PIV processing done by the software we used (Davis, from LaVision) but did not develop. We wanted to study the impact of the interrogation window size, overlap, and interrogation window shape. The second goal of the case-control data set was to carry out a case-control study of our analyses. To achieve this, we needed cases with the same volume correlation parameters as the "real" cases.
The case parameters were defined in order to fullfill the above objectives :

- cases CC1, CC2, CC5, CC7 and CC10 are used to study the impact of the interrogation window size
- cases CC3, CC4 and CC5 on the one hand (interrogation volume side of 64 pixels), and cases CC8, CC9 and CC10 on the other hand (interrogation volume side of 32 pixels) are used to study the impact of the overlap
- cases CC5 and CC6 on the one hand (interrogation volume side of 64 pixels), and cases C10 and CC11 on the other hand (interrogation volume side of 32 pixels) are used to study the impact of the interrogation window type

Table C.4 gives the main characteristics of the velocity fields of the case-control data set. The field sizes are varying with the interrogation volume size and with the overlap. The correlation values are similar to cases obtained at low Reynolds number (T4 to T6) but slightly higher than the other "real" cases. The uncertainty computed from the square root of the space-time average of the square of the divergence is not very useful here as the noise level can be estimated directly from the value of the rms of the fluctuations, which corresponds to measurement noise. However, it is interesting to see that both estimations of the noise level are coherent with each other.

Case		CC1	CC2	CC3	CC4	CC5	CC6	CC7	CC8	CC9	CC10	CC11
Number of points	n_x	39	65	21	43	84	84	114	42	87	172	172
	n_y	37	63	20	39	77	77	105	41	79	161	160
	n_z	7	11	3	7	14	14	18	7	14	26	27
Overlap (%)		75	75	0	50	75	75	75	0	50	75	75
Interrogation volume type		Gaussian	Gaussian	Gaussian	Gaussian	Gaussian	Square	Gaussian	Gaussian	Gaussian	Gaussian	Square
Interrogation volume size	pix	128	80	64	64	64	64	48	32	32	32	32
	m	3.2×10^{-3}	2.0×10^{-3}	1.6×10^{-3}	1.6×10^{-3}	1.6×10^{-3}	1.6×10^{-3}	1.2×10^{-3}	8.1×10^{-4}	8.1×10^{-4}	8.1×10^{-4}	8.1×10^{-4}
Space step	pix	32	20	64	32	16	16	12	32	16	8	8
	m	8.1×10^{-4}	5.0×10^{-4}	1.6×10^{-3}	8.1×10^{-4}	4.0×10^{-4}	4.0×10^{-4}	3.0×10^{-4}	8.1×10^{-4}	4.0×10^{-4}	2.0×10^{-4}	2.0×10^{-4}
Correlation value	avg.	0.96	0.97	0.97	0.97	0.97	0.97	0.97	0.97	0.96	0.97	0.93
	std.	0.01	0.02	0.01	0.02	0.02	0.03	0.02	0.02	0.04	0.03	0.13
Uncertainty based on divergence rms	pix	0.02	0.04	0.02	0.04	0.04	0.07	0.05	0.06	0.11	0.14	0.24
	m/s	7×10^{-4}	2×10^{-3}	7×10^{-4}	2×10^{-3}	2×10^{-3}	3×10^{-3}	2×10^{-3}	2×10^{-3}	4×10^{-3}	6×10^{-3}	10×10^{-3}
Average of u_x	pix	2×10^{-4}	1×10^{-5}	5×10^{-4}	7×10^{-5}	6×10^{-4}	8×10^{-4}	7×10^{-4}	4×10^{-5}	7×10^{-4}	1×10^{-3}	5×10^{-3}
	m/s	8×10^{-6}	6×10^{-7}	2×10^{-5}	3×10^{-6}	2×10^{-5}	3×10^{-5}	3×10^{-5}	2×10^{-6}	3×10^{-5}	6×10^{-5}	2×10^{-4}
Average of u_y	pix	-0.03	-0.03	-0.03	-0.03	-0.03	-0.03	-0.03	-0.03	-0.03	-0.03	-0.03
	m/s	-1×10^{-3}	-1×10^{-3}	-1×10^{-3}	-1×10^{-3}	-1×10^{-3}	-1×10^{-3}	-1×10^{-3}	-1×10^{-3}	-1×10^{-3}	-1×10^{-3}	-1×10^{-3}
Average of u_z	pix	-3×10^{-5}	-4×10^{-4}	1×10^{-4}	-2×10^{-5}	-5×10^{-4}	1×10^{-4}	-2×10^{-4}	1×10^{-4}	2×10^{-4}	-7×10^{-5}	4×10^{-3}
	m/s	-1×10^{-6}	-2×10^{-5}	4×10^{-6}	-8×10^{-7}	-2×10^{-5}	6×10^{-6}	-10×10^{-6}	5×10^{-6}	6×10^{-6}	-3×10^{-6}	2×10^{-4}
Rms of u_x fluctuations	pix	0.02	0.04	0.02	0.03	0.05	0.07	0.06	0.05	0.10	0.16	0.25
	m/s	7×10^{-4}	2×10^{-3}	6×10^{-4}	1×10^{-3}	2×10^{-3}	3×10^{-3}	3×10^{-3}	2×10^{-3}	4×10^{-3}	6×10^{-3}	1×10^{-2}
Rms of u_y fluctuations	pix	0.02	0.04	0.01	0.04	0.05	0.08	0.07	0.05	0.11	0.18	0.24
	m/s	8×10^{-4}	2×10^{-3}	6×10^{-4}	1×10^{-3}	2×10^{-3}	3×10^{-3}	3×10^{-3}	2×10^{-3}	4×10^{-3}	7×10^{-3}	10×10^{-3}
Rms of u_z fluctuations	pix	0.03	0.06	0.02	0.05	0.07	0.09	0.09	0.07	0.13	0.18	0.31
	m/s	1×10^{-3}	2×10^{-3}	9×10^{-4}	2×10^{-3}	3×10^{-3}	4×10^{-3}	3×10^{-3}	3×10^{-3}	5×10^{-3}	7×10^{-3}	1×10^{-2}
Rms of total fluctuations	pix	0.04	0.08	0.03	0.07	0.10	0.14	0.13	0.10	0.19	0.30	0.47
	m/s	2×10^{-3}	3×10^{-3}	1×10^{-3}	3×10^{-3}	4×10^{-3}	6×10^{-3}	5×10^{-3}	4×10^{-3}	8×10^{-3}	1×10^{-2}	2×10^{-2}

Table C.4: Correlation parameters and velocity field characteristics of the case-control cases.

Table C.4 also gives the values of the space-time averages and the root mean squares of the three velocity components. Values of the space-time averages of the velocity components along x and z are two or three orders of magnitude lower than the corresponding rms. They are varying from one case to the other. On the contrary, the space-time average of the velocity component along the y direction, i.e. the vertical direction, is the same for all cases. It is of the order of the corresponding rms or lower (down to one tenth for case CC11) for cases with higher noise. However, considering that the convergence of the average is proportional to the rms divided by the square-root of the effective number of independent samples, the obtained value can be considered as relevant. It is nevertheless four orders of magnitude higher than the computed velocity shift v_g, and the sign is the opposite. We measured the diameter of the seeding particle and estimated the particle density and found that they were similar to the characteristics given by the provider. The measured displacement may be due to remaining motion (we may not have waited enough after switching off the engines) or to convection. Indeed, the liquid may be warmer than the cooling circuit or than the air outside the tank. The order of magnitude of the velocity due to convection can be estimated as $\sqrt{\alpha \Delta T g l}$ with α the expansion coefficient, ΔT the temperature difference, g the gravitational acceleration and l the typical length. With $\alpha \approx 2e-4$ K^{-1}, $\Delta T \approx 0.1$ K and $l \approx 1$ cm, one finds a velocity of the order of 1 mm/s, i.e. the value measured along the y axis. This value is two orders of magnitude below the rms of the fluctuations when the impellers are rotating at 1 Hz.

The rms values correspond to the noise level. Indeed, for a uniformly zero velocity field, they should all be equal to zero. Therefore, the values found correspond to the measurement noise. One can see that the noise is increasing when the interrogation volume size is decresing, and when the overlap is increasing, as expected. It can also be seen that the so-called Gaussian windows contribute to decrease the noise level, by a factor 1/3 roughly. Compared to the average disparity values, the rms of the total fluctuations is always higher, except for case CC3 for which it is equal. It is expected as the disparity corresponds to the error due to the volume reconstruction step, whereas the rms of the total fluctuations corresponds to the total error. It can also be noticed that the rms of the fluctuations along the z axis is larger than the others.

It is interesting to compare the rms value of case CC2 to the uncertainty estimated from the divergence for case T4t. Indeed, the set-up was exactly the same, except that water was filling the tanks instead of the water-glycerol mixture for case T4t. For case $T4t$, it is 0.4 mm/s compared to 2 mm/s for case CC2 which is five times larger. This suggests that using the divergence of the velocity field to estimate the uncertainty leads to an underestimated uncertainty. This may be due to the approximations inherent to the divergence approach. This comparison is not as relevant for cases CC1 and T5 and T6, or cases CC2 and T4, because the cameras were not the same. Also, for cases T5 and T6, the magnification and the numerical aperture were much different.

Figures C.1, C.2 and C.3 show the spectra of some cases, normalized by their first value in order to better see the cut-off. As expected, increasing the window size decreases the cut-off value, as shown in figure C.1. More interestingly, the shape of the spectra are close to the square sinc function, which is the expected spectrum for square interrogation windows (see [Foucaut et al., 2004]). These sinc functions are represented by the continuous lines on the spectrum figures. This means that the analytical value of the 2 dB cut-off for square interrogation windows can be used as a good approximation of the value of the 2 dB cut-off for Gaussian interrrogation windows. Figures C.2 and C.3 show the normalized spectra for interrogation volume sizes of 64 and 32 pixels respectively. They both reveal that for Gaussian interrogation volumes, increasing the overlap decreases the cut-off wavenumber. This is at variance with square interrogation windows, for which the overlap does not impact the cut-off wavenumber [Foucaut et al., 2004]. These figures also show that the cut-off wavenumber corresponding to square interrogation volumes is larger than the

one corresponding to Gaussian interrogation volumes of the same (effective) size. Surprisingly, the square sinc function does not fit well the spectra obtained for square interrogation windows, and in the case of an interrogation volume size of 64 pixels, it is closer to the spectrum obtained with a Gaussian interrogation window.
The probability density functions of cases CC1 to CC11 are given in figure C.5. The pdfs of the velocity component along y have a maximum shifted towards the negative values, corresponding to the non-zero average. The pdfs of the velocity component along the z direction are similar to the ones of the component along the x direction, except that they are more spread. This corresponds to the larger rms values.

The main results of these tests of Davis are the following :

- Increasing the overlap of Gaussian interrogation windows has the same impact as decreasing the interrogation window size : the resolution is improved but the noise level increases.
- Compared to a square interrogation window of the same (effective) size, using a Gaussian interrogation windows yields a lower noise level but a worse spatial resolution.

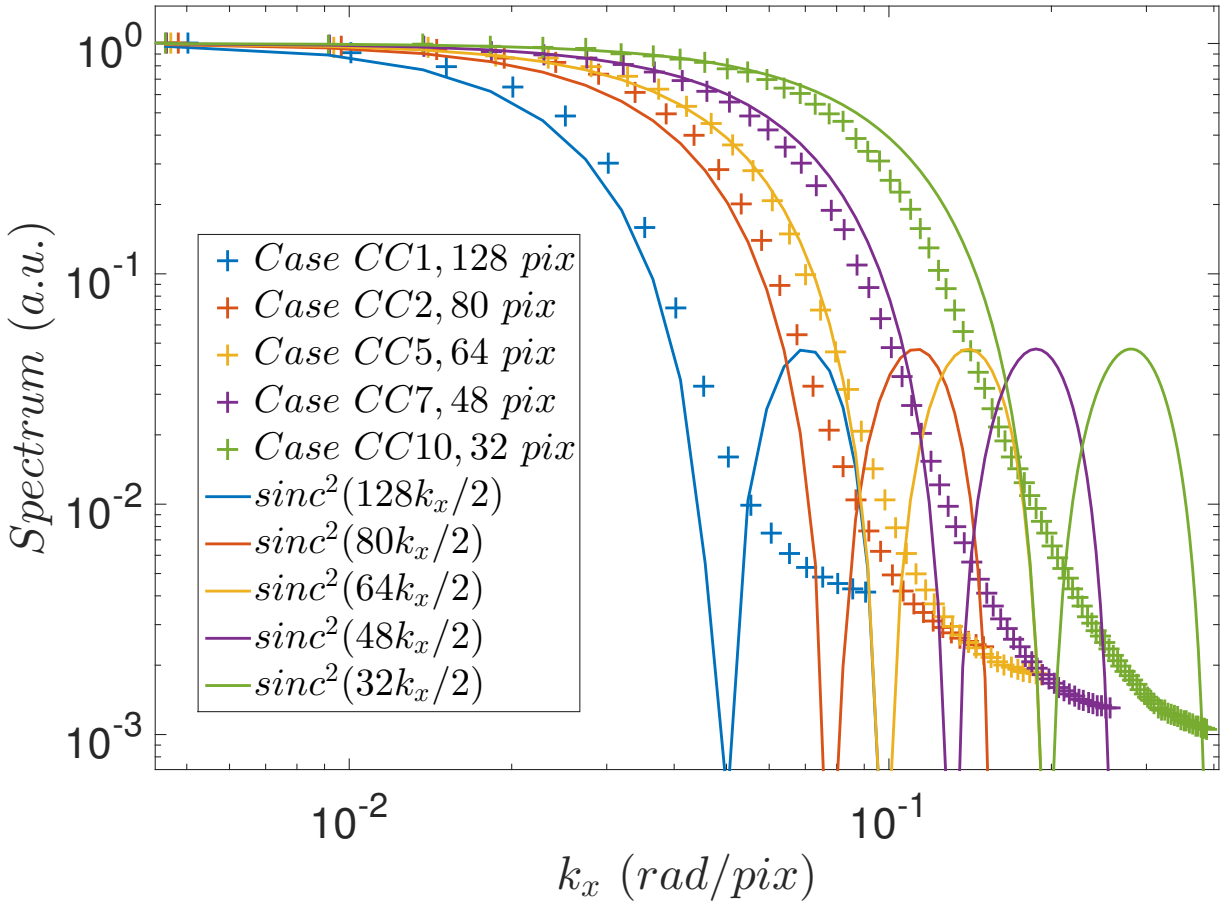

Figure C.1: Fourier spectra for cases CC1, CC2, CC5, CC7 and CC10 normalized to their first values and corresponding square sinc functions.

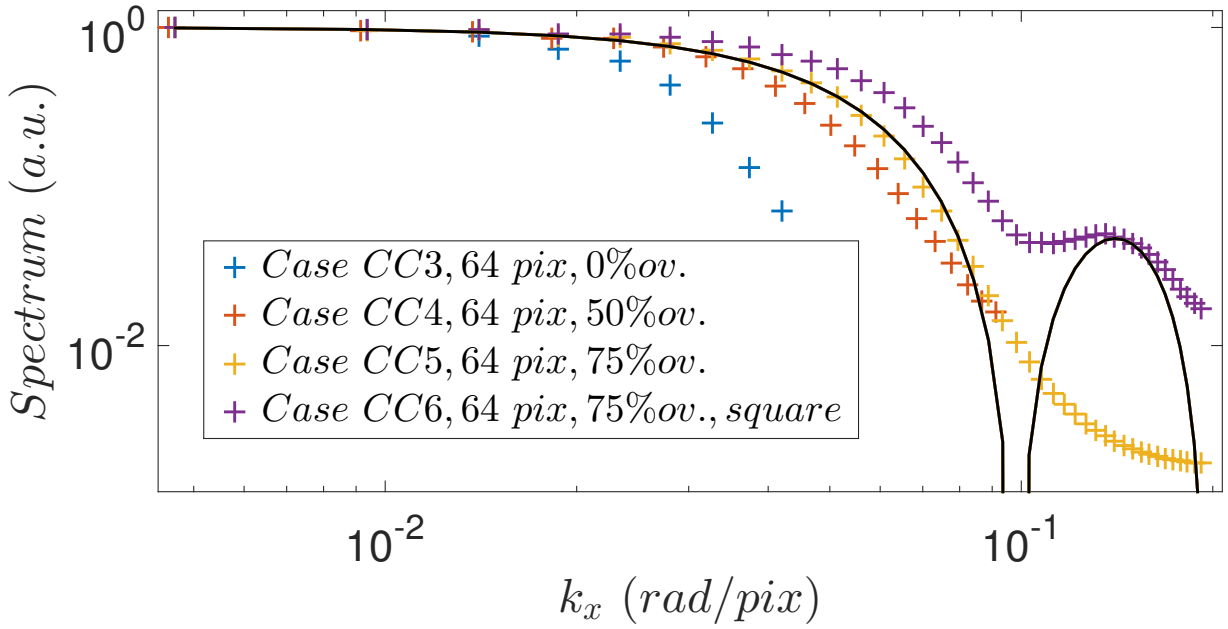

Figure C.2: Fourier spectra for cases CC3, CC4, CC5 and CC6 normalized to their first values and the corresponding square sinc function $sinc^2(64k_x/2)$.

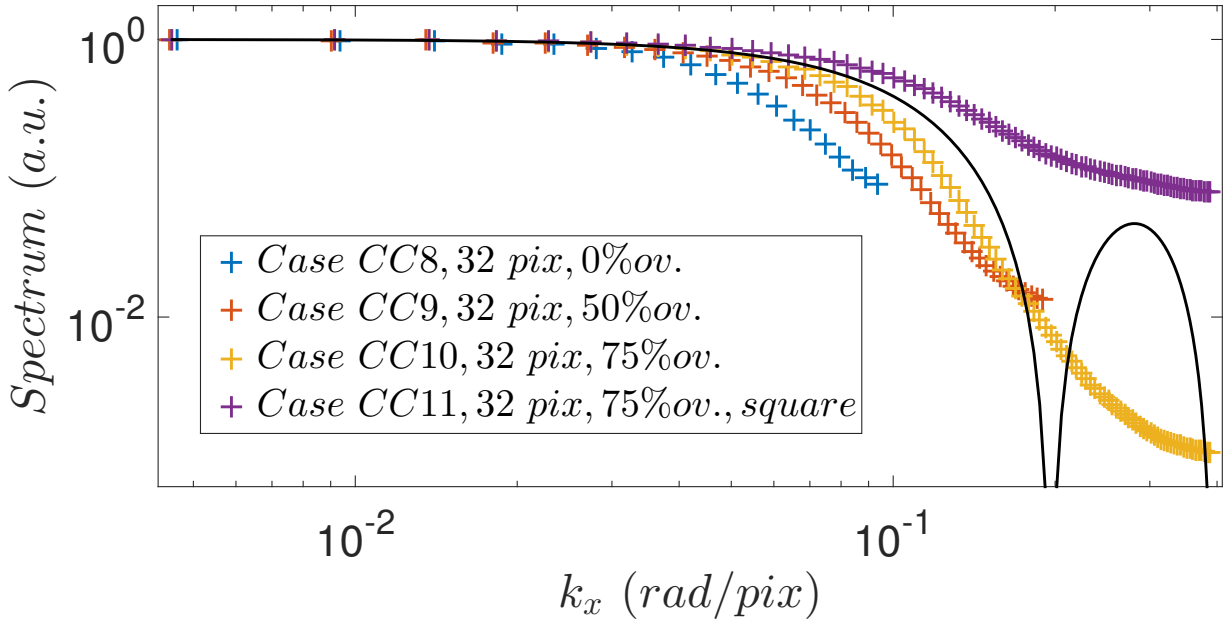

Figure C.3: Fourier spectra for cases CC8, CC9, CC10 and CC11 normalized to their first values and the corresponding square sinc function $sinc^2(32k_x/2)$.

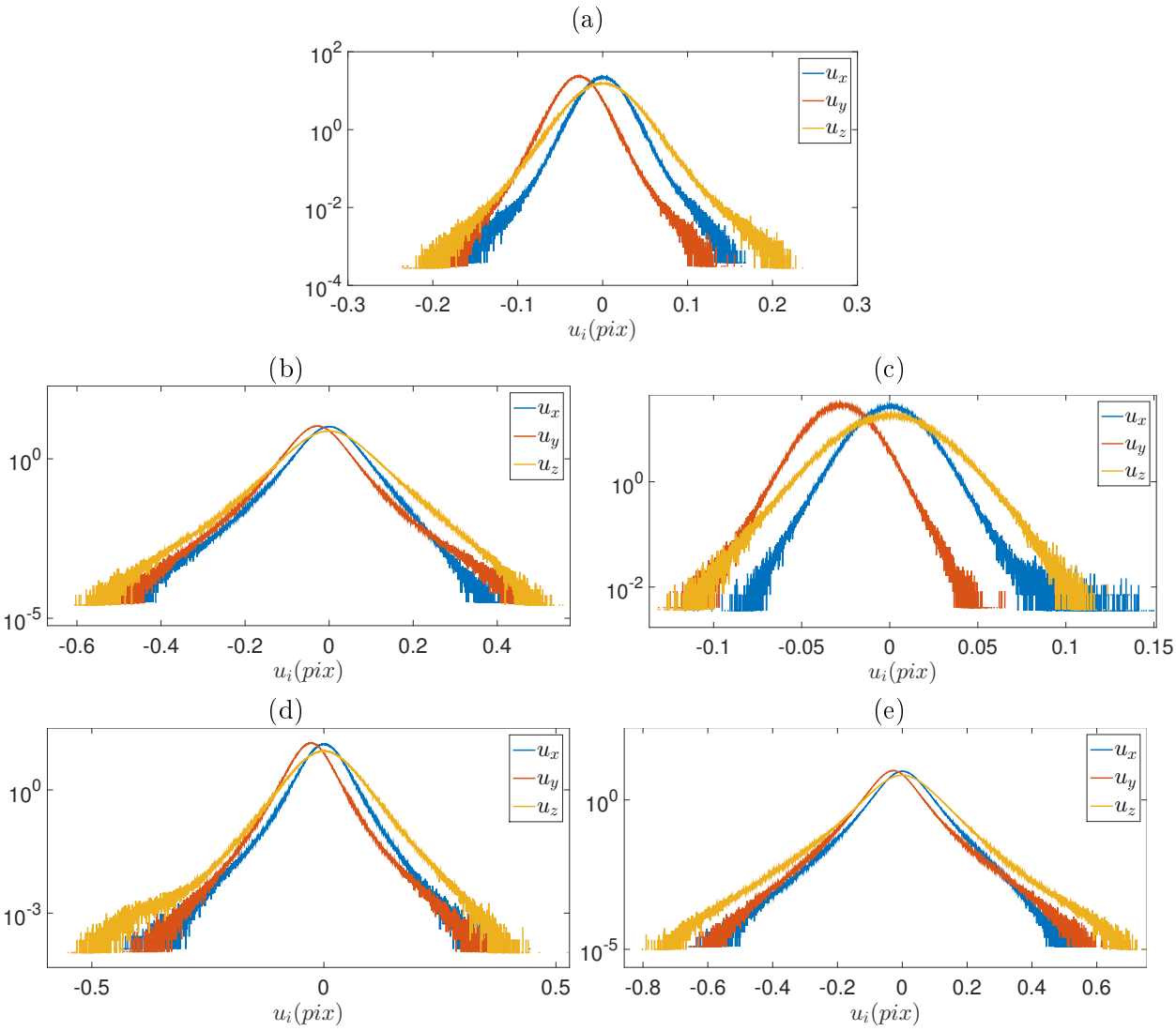

Figure C.4: Pdfs of cases CC1 to CC5. The vertical axis is in logarithmic coordinates. (a) Case CC1. (b) Case CC2. (c) Case CC3. (d) Case CC4. (e) Case CC5.

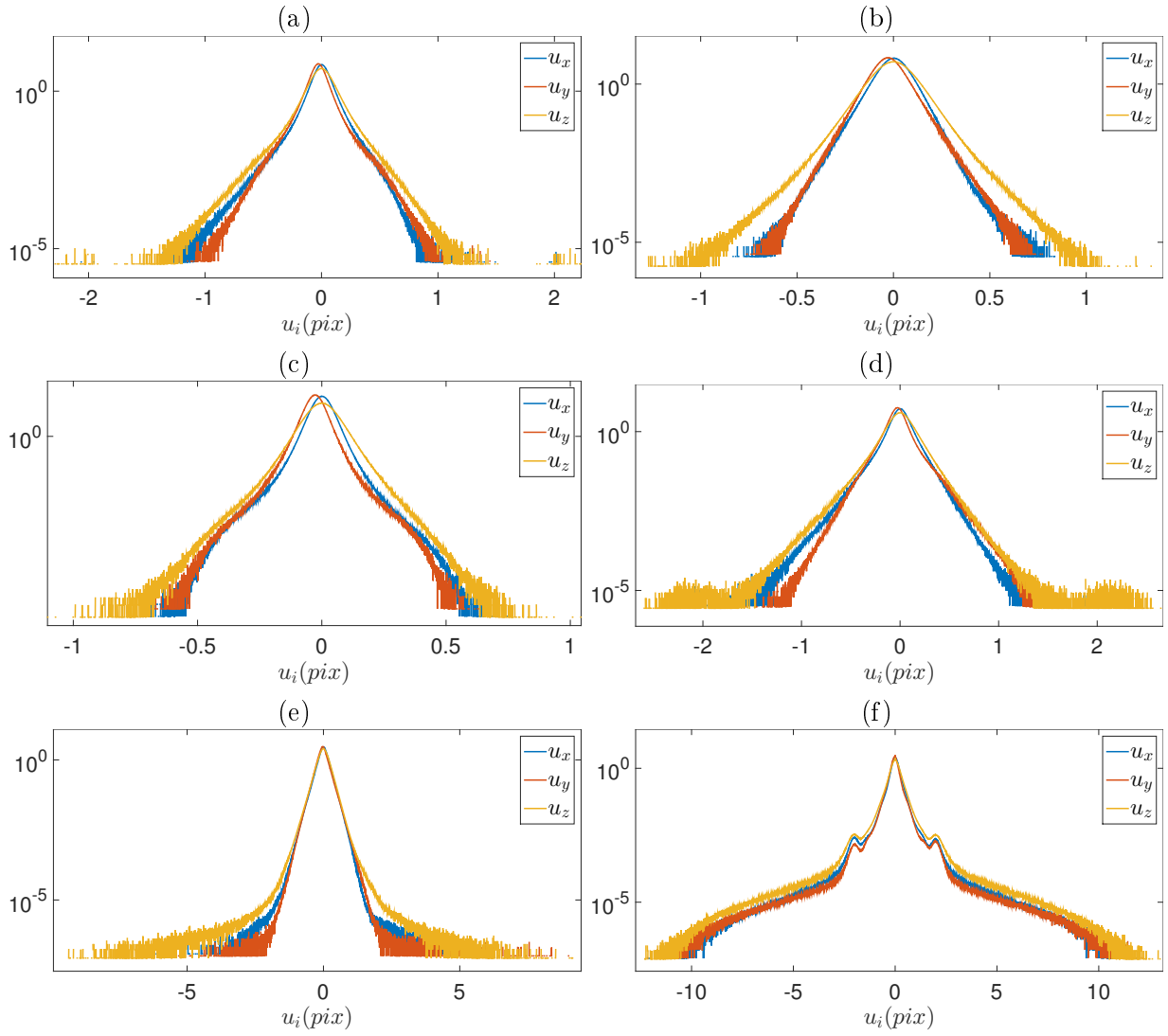

Figure C.5: Pdfs of cases CC6 to CC11. The vertical axis is in logarithmic coordinates. (a) Case CC6. (b) Case CC7. (c) Case CC8. (d) Case CC9. (e) Case CC10. (f) Case CC11.

Appendix D

Optimization of the TPIV parameters for our set-up

In this thesis, we used TPIV to measure the velocity field at the center of the turbulent von Kármán flow generated in the VK2 set-up described in chapter 2. The location of the measurement volume is shown in figure 5.11 of chapter 5. TPIV measurements have already been reported in a von Kármán flow ([Worth et al., 2010] for instance, with set-up description in [Gan et al., 2016]). However, the corresponding set-up is ten times bigger than ours and has a dodecahedral tank instead of a circular one in our case. We therefore tested several TPIV parameters in order to find an optimal configuration in the particular case of the VK2 set-up.

1 Test cases

All test cases were acquired with the same cameras and laser used for the slow campaign of 2018 described in section 2 of chapter 5 : a New Wave Research Solo II PIV laser and five Imager sCMOS cameras. The laser energy was 15 mJ/pulse for all cases. The numerical aperture of all the lenses is $f_{\#} = 11$. In all cases, 200 (double-)frames were acquired and the results were processed with Davis 8. There was 16 different test cases, whose parameters are summarized in table D.1. These cases are splitted into two sets :

- set A : Test cases of this set were all done with the outer tank A described in chapter 2 and Dantec silver-coated particles of average diameter 15 μm and of density 1.4. The camera configuration is the same as the slow campaign of 2017 (see chapter 5).
- set B : Test cases were all done with the outer tank B described in chapter 2 and LaVision (non-silver-coated) hollow spheres of average diameter 10 μm and of density 1.1. The camera configuration is the same as the slow campaign of 2018 (see chapter 5).

Ideally, we should have tested both particles with both outer tanks but because of the limited time we chose not to test all the possible combinations. For each set,

- Case 1 is the reference case, obtained with both impellers rotating in contra direction at 1Hz.
- Case 2 is obtained by varying the dt to test the impact of this parameter on the correlation.
- Case 3 is obtained by removing the mirror reflecting the laser beam (the goal of this mirror is to avoid intensity differences between cameras in forward scattering and cameras in backward scattering, see section 1.3).

- Case 4 is obtained by rotating the impellers in contra direction at 5Hz. This case was added to the list because it was noticed that for impellers rotating at 5Hz, and with silver-coated seeding the flow, there was a strong background noise. We wanted to test whether it was due to the particles or to the rotation frequency, even if the reason was not obvious.
- Cases 5 to 8 are obtained by modifying the seeding concentration. It is difficult to set accurately the concentration in our set-up, because particles can get stuck in several parts (bearings, cooling circuit). Hence it is not proportional to the amount of particles put in the flow.

The particle concentration was measured in three ways : counting by eye on a finite area and dividing by the area, using the 2D peak detection on camera images implemented in the self-calibration operation of Davis, or counting the particles in the 3D reconstructed light intensity volume, using the "particle density 3D" operation of Davis. Results were different from a method to another. Concentrations given in table D.1 were obtained with the third one. The concentration in ppp is obtained by multiplying the concentration in ppv by the volume thickness in pixels.

Case name	outer tank	Particles	Seeding density (ppv)	(ppp)	dt (μs)	Average displacement (pix)	Standard deviation of displacement (pix)	Mirror	Impeller rotation frequency (Hz)
A1	A	Dantec silver-coated 15 μm density : 1.4	3×10^{-5}	0.01	550	6.8	2.8	With	1
A2			5×10^{-5}	0.017	1050	11.7	5.0		
A3			4.2×10^{-5}	0.014	550	6.0	2.4	Without	
A4			6.7×10^{-5}	0.022	120	6.6	2.8	With	5
A5			0.6×10^{-5}	0.002	1050	10.9	4.3		1
A6			4.3×10^{-5}	0.014		11.9	4.6		
A7			2.7×10^{-4}	0.023		11.9	4.7		
A8			1.1×10^{-3}	0.09		11.3	4.5		
B1	B	LaVision non-silver-coated 10 μm density : 1.1	6.4×10^{-5}	0.022	900	10.4	4.4	With	1
B2			2.5×10^{-5}	0.008	700	8.2	3.4		
B3			1.6×10^{-4}	0.052	900	10.4	4.2	Without	
B4			4.3×10^{-5}	0.015	180	10.2	4.3	With	5
B5			1.7×10^{-4}	0.06	900	10.5	4.3		1
B6			1.8×10^{-4}	0.06		11.1	4.5		
B7			1.8×10^{-4}	0.06		10.2	4.2		
A8			2.4×10^{-4}	0.08		11.0	4.3		
C	A	Dantex silver-coated	2.4×10^{-5}	0.012	3500	9.5	3.4	With	0.1

Table D.1: Summary table of the test parameters

2 Test results

The test cases were compared using criteria based either on the camera images, on the volume reconstruction or on the velocity fields.

2.1 Quality of images

For each test case, the following quantities were computed :

- The average intensity over all camera images. It can be seen as an indicator of the background noise as particles cover only between 10% and 20% of the images. Note that the intensity on cameras whose optical axis is at 90° with respect to the laser beam (cameras 1, 2 and 4 for cases of set A, camera 4 for cases of set B) have a lower intensity. However, for cases of set A, the intensity was similar for cameras 3 and 5 (respectively in backward and forward scattering) with or without mirror used. For cases of set B, the intensity was lower for cameras 2, 3 and 4 than for cameras 1 and 5 in the case 3 where there is no mirror.

- The standard deviation of the intensity, computed over all camera images. It can be considered as an indicator of the contrast. Indeed, for strong intensity peaks corresponding to particle images, the standard deviation of the intensity will be high, whereas for bad contrast and small difference between the particle image and background intensity, it will be small. As for the average intensity, the standard deviation was smaller for cameras whose optical axis is at 90° with respect to the laser beam.

- the ratio of the standard deviation of the intensity over the average intensity

- the average particle diameter, estimated by eye. Particle size was not very homogeneous. For cases of set A, particle images on cameras 1 and 2 were elongated in the vertical direction. This is probably due to astigmatism : the optical axis of these cameras are not crossing the cylindrical tank perpendicularly as they are not in a horizontal plane. Therefore, the cylindrical tank acts as a lens and the particle images are distorted.

The above quantities are given in table D.2.
Cases of set A have higher values of average and standard deviation of intensity than cases of set B. This is easily explained by the silver-coating of the used Dantec particles. However, the ratio $\sigma(I)/\langle I\rangle$ is comparable for both sets, it is even better at higher concentration for cases of set B.
Without a mirror, the average and standard deviation of intensity is lower both in sets A and B (for set B, it is better to compare case B3 to case B5 as the reference case B1 has a lower particle concentration than case B3), as expected. The $\sigma(I)/\langle I\rangle$ ratio is smaller without mirror only in set B. This may be due to the silver-coating, or to the higher concentration of cases B3 and B5 compared to cases A1 and A3.
For an impeller rotation frequency of 5 Hz, we notice that the values of average and standard deviation of intensity are higher than for 1 Hz for set A (cases A4 and A7 for comparison with constant concentration). The $\sigma(I)/\langle I\rangle$ ratio is a bit better at 5Hz. The reason is not very clear, it may be a lack of statistics. In set B, the rotation frequency has no effect on the intensity.
For cases of set A, increasing the particle concentration results in an increase of the values of average and standard deviation of intensity but a decrease of the $\sigma(I)/\langle I\rangle$ ratio. For cases of set B, the values of average and standard deviation of intensity decrease with concentration but $\sigma(I)/\langle I\rangle$ is constant or even increasing.

Case name	Average intensity $\langle I \rangle$	Standard deviation of intensity $\sigma(I)$	$\frac{\sigma(I)}{\langle I \rangle}$
A1	600	670	1.1
A2	630	570	0.9
A3	540	520	1
A4	840	740	0.9
A5	400	420	1.2
A6	480	600	1.2
A7	660	460	0.7
A8	960	700	0.7
B1	350	250	0.7
B2	360	320	0.9
B3	340	240	0.7
B4	370	320	0.9
B5	400	450	1.1
B6	420	470	1.1
B7	500	600	1.2
B8	550	630	1.1

Table D.2: Average, standard deviation and corresponding ratio of the light intensity on camera images.

As a conclusion, this analysis of the camera images shows that configuration of set B is better, provided there is a mirror, as the contrast is better, particles are not distorted due to astigmatism and there is no strange effect for an impeller rotation frequency of 5Hz.

2.2 Volume reconstruction quality

To assess the quality of the volume reconstruction, we compared the mean, standard deviation and maximum of the disparity obtained after the self-calibration, as well as the normalized intensity variance and the ghost level. The corresponding values can be found in the table D.3.
Overall, for all cases the disparity values, normalized intensity variance and ghost level are good and in the proper range allowing good volume reconstruction, there are only small differences between cases. For the highest concentrations of both sets A and B, the ghost level is higher and the normalized intensity variance smaller, reaching the threshold value (20). For case B3, where there is no mirror, the ghost level is higher than comparable cases of set B.

As a conclusion, the comparison based on self-calibration and volume reconstruction does not allow to identify a significantly better configuration. It confirms the advantage of using a mirror in the configuration of set B. It shows that the maximum concentration is around 0.09 ppp ; for higher concentration, the normalized intensity variance is too low.

2.3 Velocity field quality

To assess the quality of the correlation step, we compared the correlation value, the rms of the divergence of the velocity and the smallest possible interrogation volume size. The corresponding values can be found in the table D.4.
Overall, the results are homogeneous and no case gives significantly different results than the others.

Case name	Disparity (pixels)			Normalized intensity variance	Ghost level (%)
	Average	Standard deviation	Maximum		
A1	0.04	0.04	0.4	33	3
A2	0.05	0.03	0.2	31	3
A3	0.04	0.04	0.4	32	3
A4	0.04	0.04	0.4	29	5
A5	0.06	0.06	0.8	46	2.5
A6	0.04	0.03	0.7	48	3
A7	0.04	0.04	0.8	20	20-30
A8	0.04	0.04	0.7	19	25-35
B1	0.03	0.02	0.1	40	11
B2	0.03	0.03	0.3	41	7
B3	0.04	0.03	0.2	40	25
B4	0.04	0.03	0.2	40	8
B5	0.09	0.05	0.3	32	13
B6	0.04	0.03	0.3	28	13
B7	0.08	0.04	0.3	25	13
B8	0.04	0.04	0.5	22	25

Table D.3: Disparity values, normalized intensity variance and ghost level.

Case name	Correlation value		Uncertainty based on divergence rms		Smallest possible interrogation volume size	
	Average	Standard deviation	(pix)	(% of U_{tot}^{rms})	(pix)	(mm)
A1	0.86	0.11	0.5	8	64	1.2
A2	0.8	0.16	0.6	10	56	1.0
A3	0.78	0.14	0.4	7	56	1.0
A4	0.76	0.15	0.7	10	48	0.86
A5	0.66	0.11	0.7	6.8	152	2.7
A6	0.89	0.11	0.8	7.4	64	1.1
A7	0.76	0.13	0.6	5.1	44	0.8
A8	0.76	0.12	0.6	5.1	48	0.9
B1	0.87	0.16	0.9	10	52	0.93
B2	0.89	0.12	0.7	10	64	1.2
B3	0.83	0.21	0.8	9	40	0.72
B4	0.83	0.16	1	11	56	1.0
B5	0.9	0.12	0.5	5.7	40	0.72
B6	0.85	0.17	0.6	5.9	32	0.6
B7	0.86	0.12	0.5	5.3	40	0.72
B8	0.82	0.13	0.5	5.2	40	0.72

Table D.4: Correlation value (average and standard deviation), uncertainty based on the rms of divergence and smallest possible interrogation window size. The uncertainty based on the divergence is expressed both in pixels and in % of the root mean square of the velocity in the flow (U_{tot}^{rms}). The interrogation window size is expressed both in pixels and in millimeters.

The values of uncertainty based on the rms of divergence are higher than what can be found in the literature.
For both sets A and B, the correlation value is a bit lower for higher concentration cases but the resolution is better and the uncertainty is similar or better than lower concentration cases.
For both sets A and B, increasing the dt results in slightly better uncertainty and resolution.

As a conclusion, the comparison based on the velocity fields does not allow to identify a significantly better configuration

Finally, these tests show that TPIV is quite robust and not significantly sensitive to the chosen parameters. It is better to use a mirror in the configuration of set B. The highest concentration reachable is of the order of 0.09 ppp.

Appendix E

Average velocity fields of the 3D velocity data sets

The average velocity fields of the cases of the non-time-resolved 3D data set and of case T4t are shown in this appendix. The representation is always the same : the top-left figure corresponds to the top view of a mid-height (mid-y) plane ; the arrows correspond to the in-plane velocity (i.e. to the components along x and z directions) and the color to the out-of-plane velocity (i.e. to the component along y). The bottom-left figure corresponds to the front view of a mid-z plane ; the arrows correspond to the in-plane velocity (i.e. to the components along x and y directions) and the color to the out-of-plane velocity (i.e. to the component along z). The bottom-right figure corresponds to the right view of a mid-x plane ; the arrows correspond to the in-plane velocity (i.e. to the components along z and y directions) and the color to the out-of-plane velocity (i.e. to the component along x). The color scale and the vector scale are the same for the three figures ; the color scale is in units of the reference velocity $2\pi RF$ (see chapter 3) and the vector scale is such that the space between two vectors correspond to one tenth of the reference velocity $2\pi RF$ (see chapter 3). The white lines on each figure correspond to the location of the two other planes.

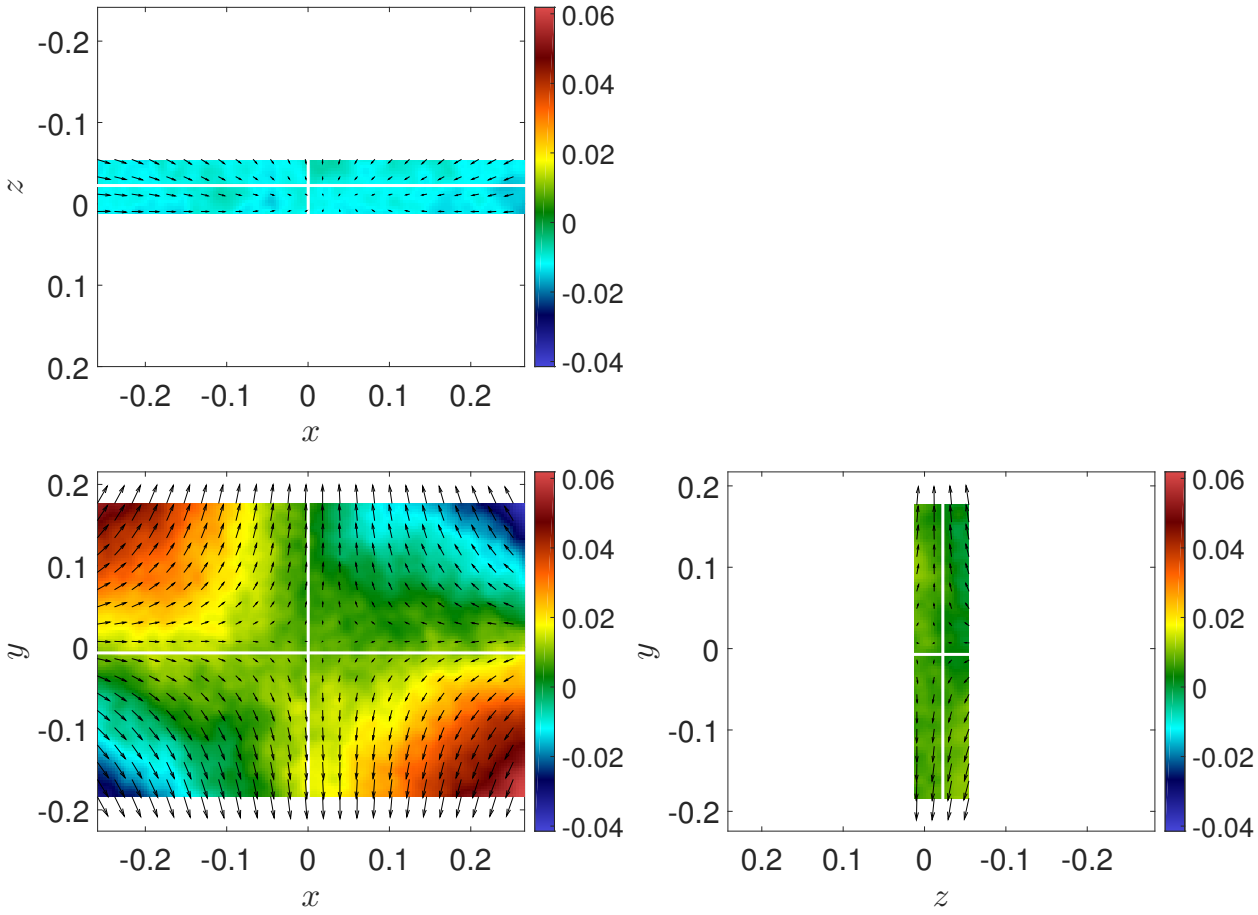

Figure E.1: Average velocity field for case T1.

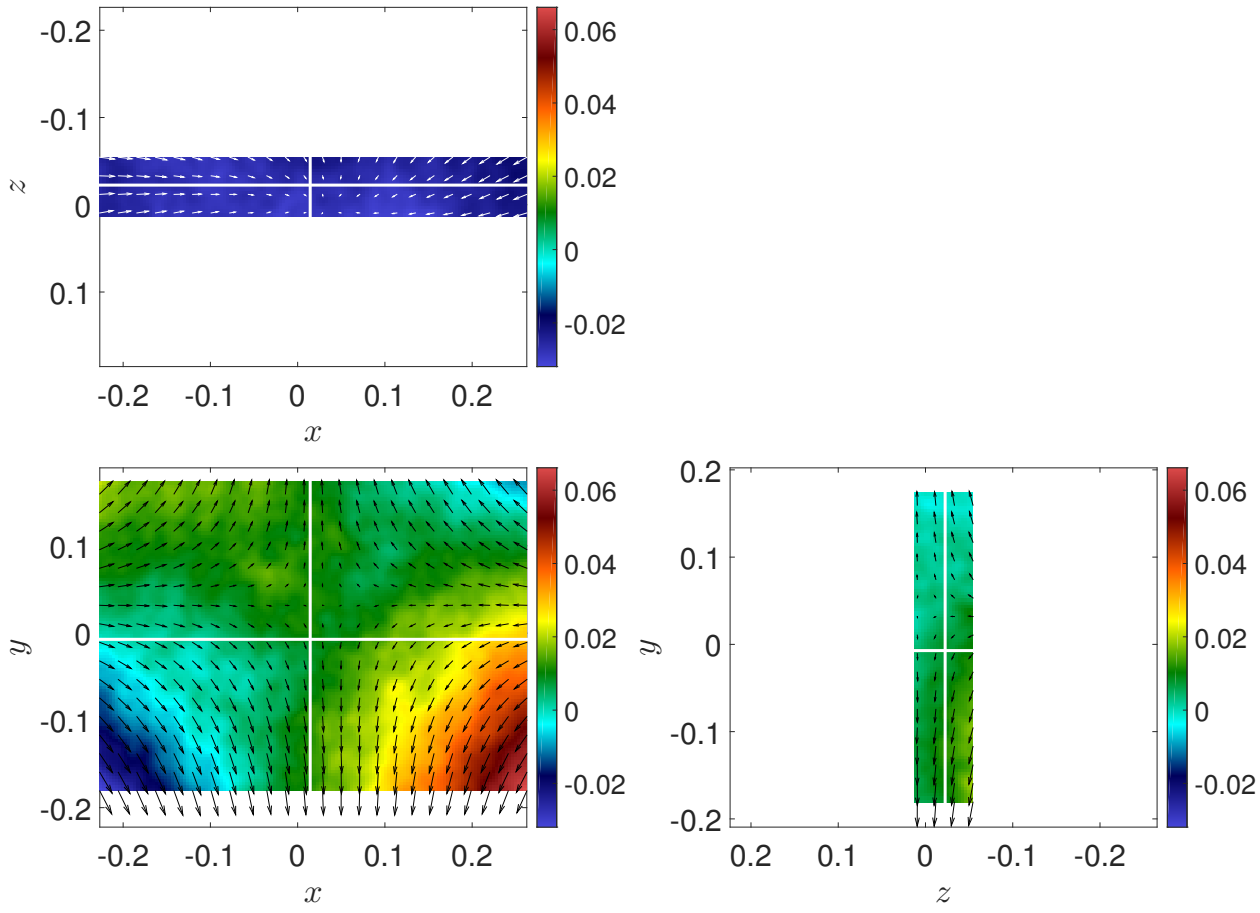

Figure E.2: Average velocity field for case T2.

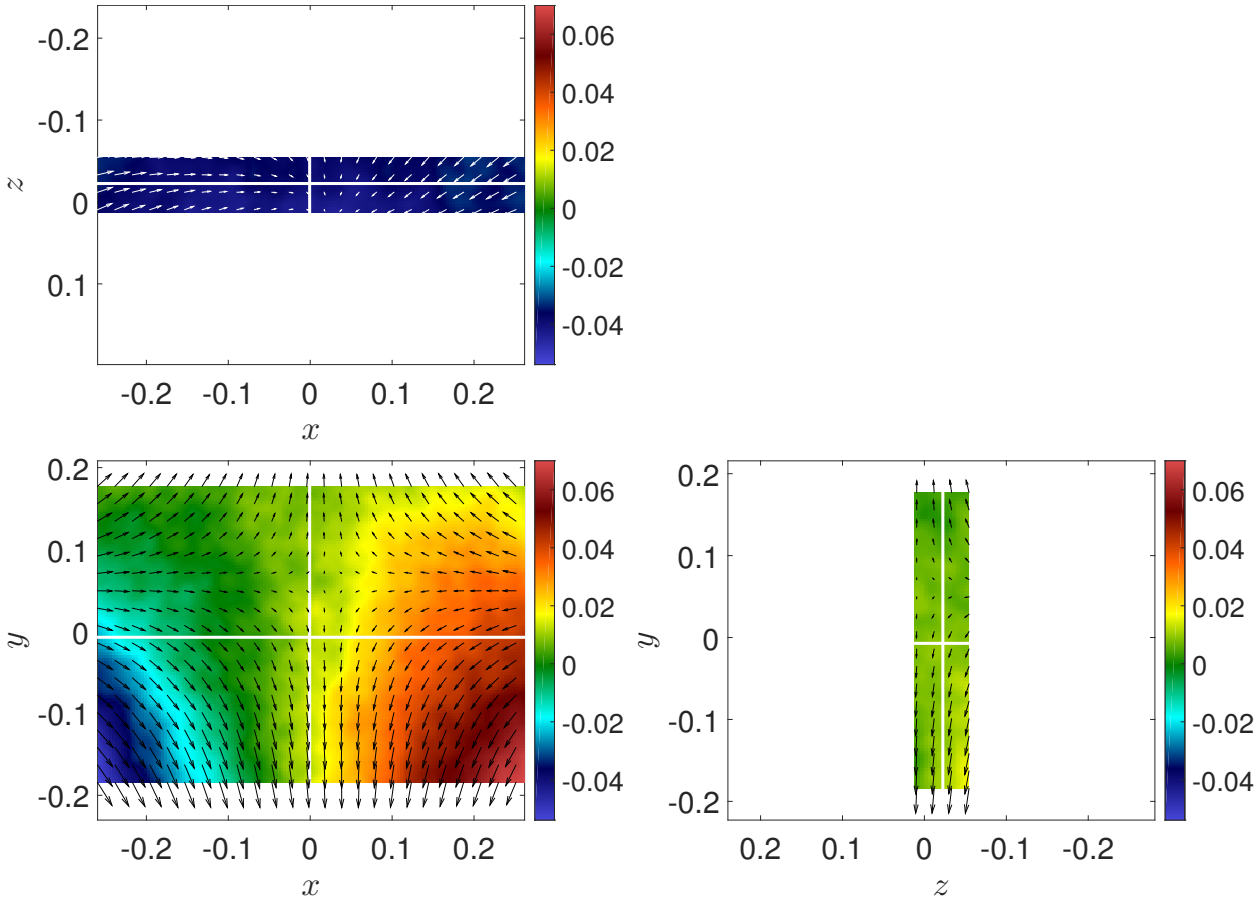

Figure E.3: Average velocity field for case T3.

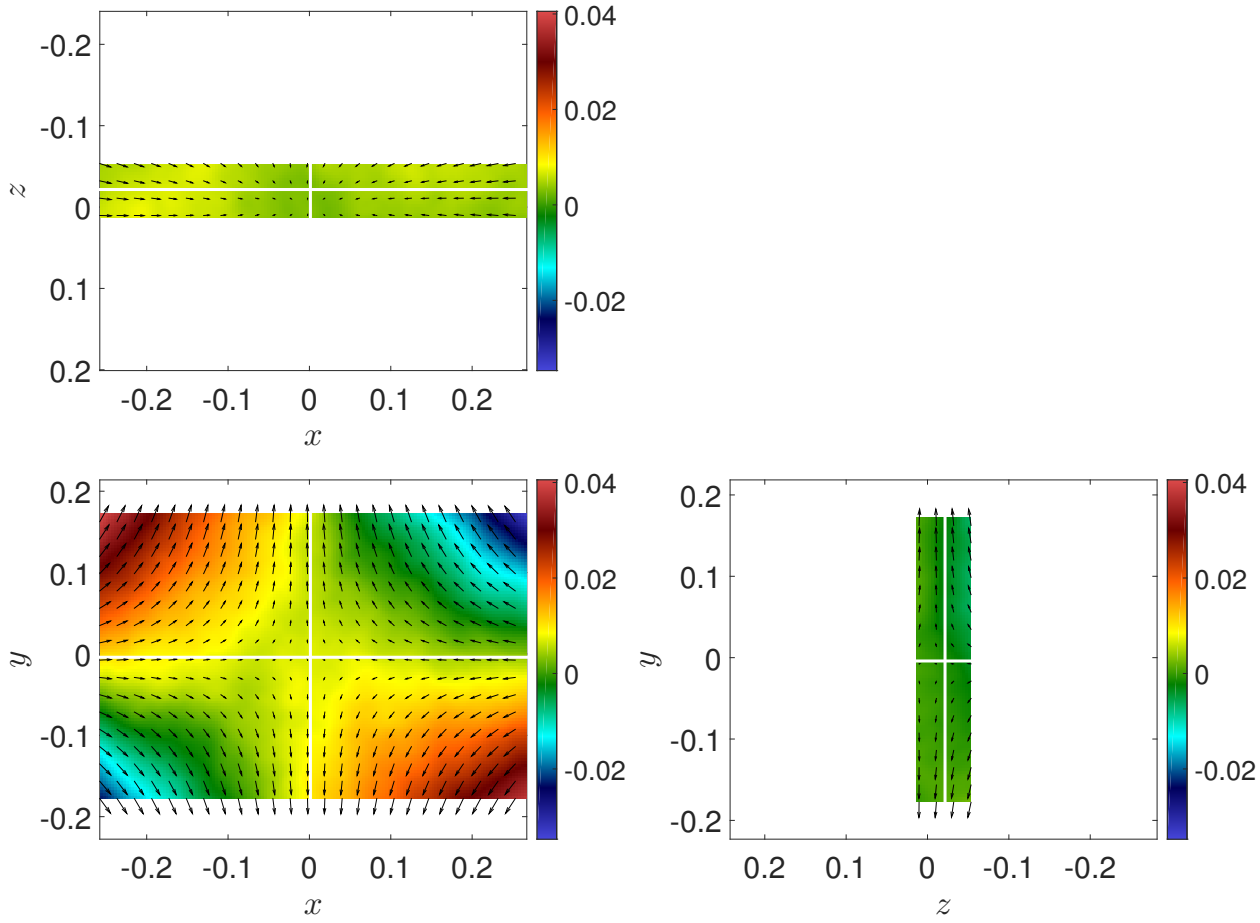

Figure E.4: Average velocity field for case T4.

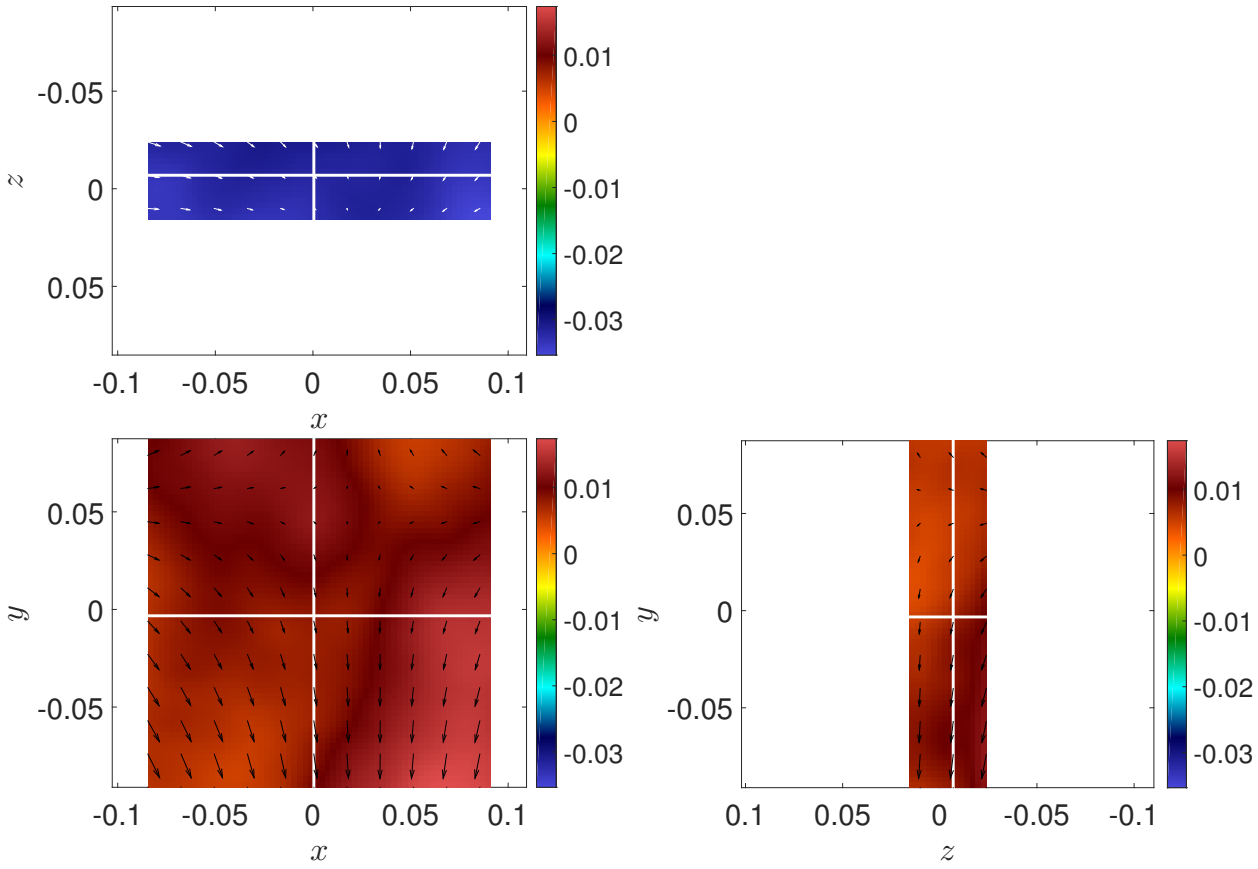

Figure E.5: Average velocity field for case T5.

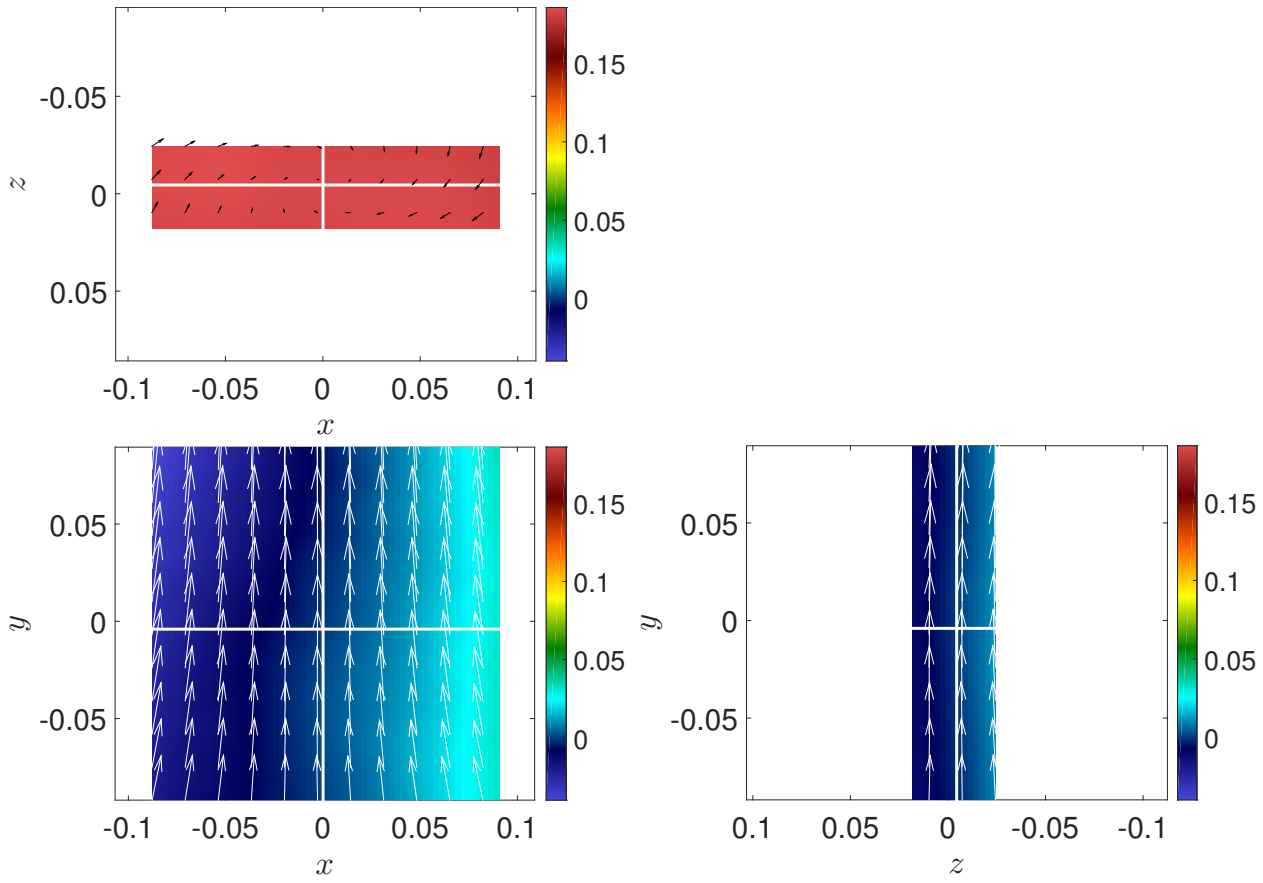

Figure E.6: Average velocity field for case T6.

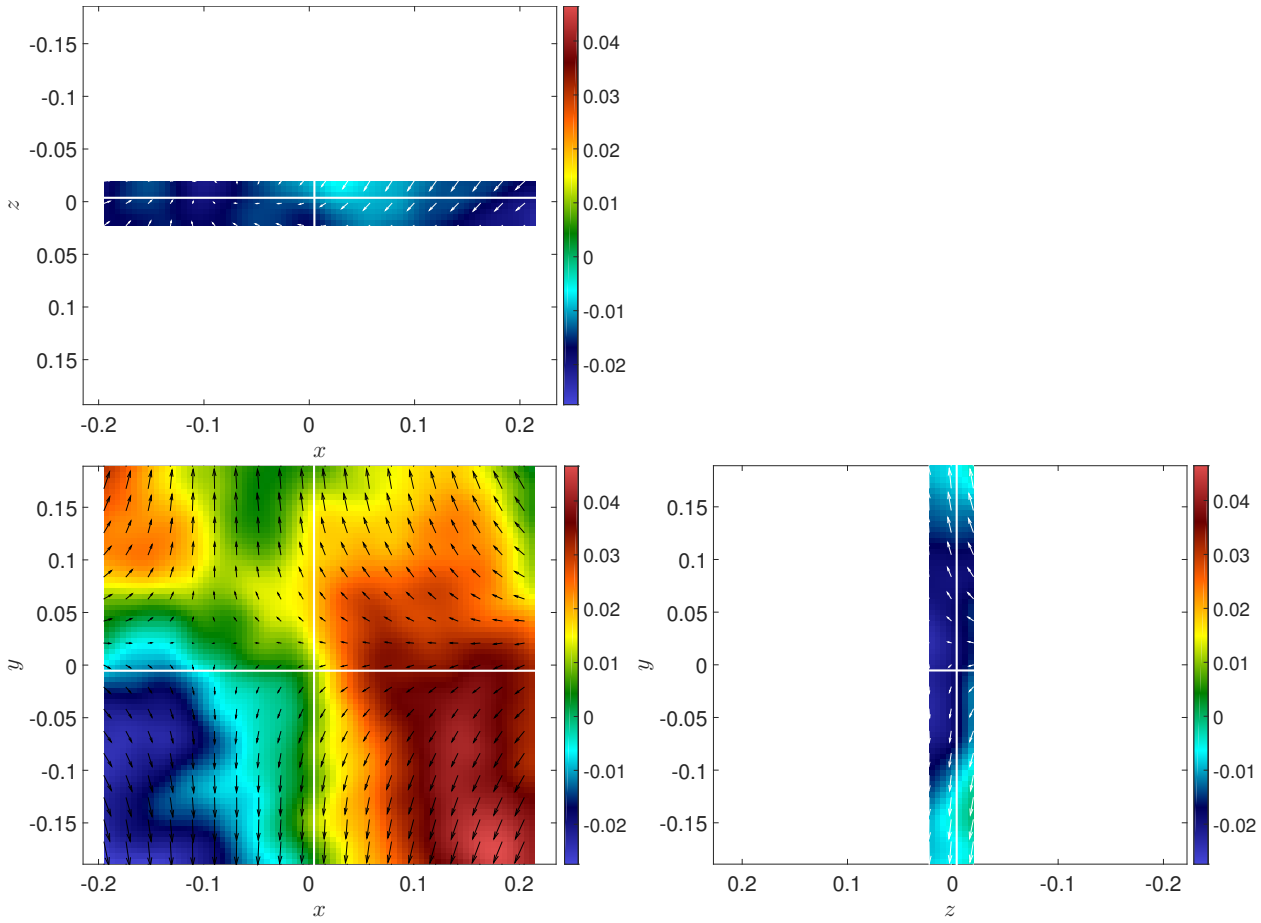

Figure E.7: Average velocity field for case T4t.

Appendix F

Transport equations of the energy contained in the filtered velocity field and in the fluctuations

In this appendix, we derive the transport equations for the energy contained in the filtered velocity field $\mathbf{u}^\ell$ and for the energy contained in the fluctuations $\mathbf{u}-\mathbf{u}^\ell$, as well as for the scalar product $\mathbf{u}^\ell \cdot (\mathbf{u}-\mathbf{u}^\ell)$. These equations involve both the Duchon-Robert term Π^ℓ_{DR} and the inter-scale energy transfer term appearing in the LES equations Π^ℓ_{LES}.

Let $\mathbf{u}$ be a smooth solution of the 3D incompressible Navier-Stokes equations :

$$\partial_t u_i + \partial_j(u_j u_i) = -\partial_i p + \Delta u_i \tag{F.1}$$
$$\partial_i u_i = 0 \tag{F.2}$$

Filtering these equations leads to the transport equations of the filtered velocity components u_i^ℓ, i.e. te filtered Navier-Stokes equations :

$$\partial_t u_i^\ell + \partial_j(u_j u_i)^\ell = -\partial_i p^\ell + \Delta u_i^\ell \tag{F.3}$$
$$\partial_i u_i^\ell = 0 \tag{F.4}$$

Multiplying the filtered Navier-Stokes equations by the filtered velocity, we get :

$$\partial_t \frac{{u_i^\ell}^2}{2} + u_i^\ell \partial_j[(u_j u_i)^\ell] = -\partial_i[u_i^\ell p^\ell] + \nu u_i^\ell \Delta u_i^\ell \tag{F.5}$$

Introducing the so-called subgrid scale tensor $\tau_{ij}^\ell = (u_i u_j)^\ell - u_i^\ell u_j^\ell$, we obtain :

$$\partial_t \frac{{u_i^\ell}^2}{2} + u_i^\ell \partial_j[u_j^\ell u_i^\ell + \tau_i j^\ell] = -\partial_i[u_i^\ell p^\ell] + \nu u_i^\ell \Delta u_i^\ell \tag{F.6}$$

After few steps we obtain :

$$\partial_t \frac{{u_i^\ell}^2}{2} + \partial_j[u_j^\ell \frac{{u_i^\ell}^2}{2} + u_i^\ell \tau_{ij}^\ell] = -\partial_i[u_i^\ell p^\ell] + \nu \Delta \frac{{u_i^\ell}^2}{2} - \nu \partial_j u_i^\ell \partial_j u_i^\ell + \tau_{ij}^\ell \partial_j u_i^\ell \tag{F.7}$$

i.e. :

$$\partial_t \frac{u_i^{\ell 2}}{2} + \partial_j [u_j^\ell \frac{u_i^{\ell 2}}{2} + u_i^\ell \tau_{ij}^\ell + u_j^\ell p^\ell] = \nu \Delta \frac{u_i^{\ell 2}}{2} - \mathscr{D}_{\nu,LES}^\ell - \Pi_{LES}^\ell \tag{F.8}$$

The equations for $u_i - u_i^\ell$ are :

$$\partial_t (u_i - u_i^\ell) + \partial_j [u_j u_i - (u_j u_i)^\ell] = -\partial_i (p - p^\ell) + \nu \Delta (u_i - u_i^\ell) \tag{F.9}$$

$$\partial_i (u_i - u_i^\ell) = 0 \tag{F.10}$$

Multiplying it by $u_i - u_i^\ell$, we get :

$$\partial_t \frac{(u_i - u_i^\ell)^2}{2} + (u_i - u_i^\ell) \partial_j [u_j u_i - (u_j u_i)^\ell] = -\partial_i [(u_i - u_i^\ell)(p - p^\ell)] + \nu (u_i - u_i^\ell) \Delta (u_i - u_i^\ell) \tag{F.11}$$

And then :

$$\partial_t \frac{(u_i - u_i^\ell)^2}{2} + u_i \partial_j [u_j u_i - (u_j u_i)^\ell] - u_i^\ell \partial_j [u_j u_i - (u_j u_i)^\ell] \tag{F.12}$$

$$= -\partial_i [(u_i - u_i^\ell)(p - p^\ell)] + \nu (u_i - u_i^\ell) \Delta (u_i - u_i^\ell) \tag{F.13}$$

We have :

$$u_i^\ell \partial_j [u_j u_i - (u_j u_i)^\ell] = u_j [\partial_j (u_i^\ell u_i) - u_i \partial_j u_i^\ell] - u_i^\ell \partial_j [\tau_{ij}^\ell + u_i^\ell u_j^\ell] \tag{F.14}$$

$$= \partial_j [u_j u_i^\ell u_i] - u_i \partial_j (u_j u_i^\ell) - \partial_j [u_i^\ell \tau_{ij}^\ell] + \tau_{ij}^\ell \partial_j u_i^\ell - \partial_j [u_j^\ell \frac{u_i^{\ell 2}}{2}] \tag{F.15}$$

Replacing in F.13, we get :

$$\partial_t \frac{(u_i - u_i^\ell)^2}{2} + \partial_j [u_j \frac{u_i^2}{2}] - u_i \partial_j (u_j u_i)^\ell \tag{F.16}$$

$$-\partial_j [u_j u_i^\ell u_i] + u_i \partial_j (u_j u_i^\ell) + \partial_j [u_i^\ell \tau_{ij}^\ell] - \tau_{ij}^\ell \partial_j u_i^\ell + \partial_j [u_j^\ell \frac{u_i^{\ell 2}}{2}] \tag{F.17}$$

$$= -\partial_i [(u_i - u_i^\ell)(p - p^\ell)] + \nu (u_i - u_i^\ell) \Delta (u_i - u_i^\ell) \tag{F.18}$$

or :

$$\partial_t \frac{(u_i - u_i^\ell)^2}{2} + \partial_j [u_j \frac{u_i^2}{2} - u_j u_i^\ell u_i + u_i^\ell \tau_{ij}^\ell + u_j^\ell \frac{u_i^{\ell 2}}{2} + (u_j - u_j^\ell)(p - p^\ell)] \tag{F.19}$$

$$= \nu (u_i - u_i^\ell) \Delta (u_i - u_i^\ell) + \tau_{ij}^\ell \partial_j u_i^\ell + u_i \partial_j [(u_j u_i)^\ell] - u_j u_i^\ell] \tag{F.20}$$

i.e. :

$$\partial_t \frac{(u_i - u_i^\ell)^2}{2} + \partial_j [u_j \frac{(u_i - u_i^\ell)^2}{2} - (u_j - u_j^\ell) \frac{u_i^{\ell 2}}{2} + u_i^\ell \tau_{ij}^\ell + (u_j - u_j^\ell)(p - p^\ell)] \tag{F.21}$$

$$= \nu \Delta \frac{(u_i - u_i^\ell)^2}{2} - \mathscr{D}_{\nu,LES}^\ell - \Pi_{LES}^\ell + u_i \partial_j [(u_j u_i)^\ell] - u_j u_i^\ell] \tag{F.22}$$

We used the definitions $\Pi^\ell_{LES} = -\tau^\ell_{ij}\partial_j u^\ell_i$ and $\mathscr{D}^\ell_{\nu,LES} = \nu\partial_i u^\ell_j \partial_i u^\ell_j$. We know that the Duchon-Robert term can be splitted as :

$$2\Pi^\ell_{DR} = u_i\partial_j(u_j u_i)^\ell - u_j u_i \partial_j u^\ell_i - \frac{1}{2}\partial_j(u_j u_i u_i)^\ell + \frac{1}{2}u_j\partial_j(u_i u_i)^\ell \tag{F.23}$$

$$= u_i\partial_j(u_j u_i)^\ell - u_i\partial_j(u_j u^\ell_i) - \frac{1}{2}\partial_j(u_j u_i u_i)^\ell + \frac{1}{2}u_j\partial_j(u_i u_i)^\ell \tag{F.24}$$

$$\tag{F.25}$$

We recognize the last two terms of the previous equation, hence :

$$\partial_t\frac{(u_i - u^\ell_i)^2}{2} + \partial_j[u_j\frac{(u_i - u^\ell_i)^2}{2} - (u_j - u^\ell_j)\frac{u^{\ell 2}_i}{2}] \tag{F.26}$$

$$+\partial_j[u^\ell_i\tau^\ell_{ij} - \frac{1}{2}(u_j u_i u_i)^\ell + \frac{1}{2}u_j(u_i u_i)^\ell + (u_j - u^\ell_j)(p - p^\ell)] \tag{F.27}$$

$$= \nu\Delta\frac{(u_i - u^\ell_i)^2}{2} - \nu\partial_j(u_i - u^\ell_i)\partial_j(u_i - u^\ell_i) - \Pi^\ell_{LES} + 2\Pi^\ell_{DR} \tag{F.28}$$

Noticing that the total energy is equal to :

$$\frac{{u_i}^2}{2} = \frac{u^{\ell 2}_i}{2} + \frac{(u_i - u^\ell_i)^2}{2} + u^\ell_i(u_i - u^\ell_i) \tag{F.29}$$

We can use the following transport equation of the total energy :

$$\partial_t\frac{{u_i}^2}{2} + \partial_j[u_j\frac{u^2_i}{2} + u_j p] = \nu\Delta\frac{u^2_i}{2} - \partial_j u_i\partial_j u_i \tag{F.30}$$

as well as equations F.8 and F.28 to get the transport equation for the scalar product $u^\ell_i(u_i - u^\ell_i)$:

$$\partial_t u^\ell_i(u_i - u^\ell_i) + \partial_j[u_j u_i u^\ell_i - u^\ell_j u^\ell_i u^\ell_i + 2\tau^\ell_{ij}] \tag{F.31}$$

$$+\partial_j[\frac{1}{2}(u_j u_i u_i)^\ell - \frac{1}{2}u_j(u_i u_i)^\ell + u^\ell_j(p - p^\ell) + (u_j - u^\ell_j)p^\ell] \tag{F.32}$$

$$= \nu\Delta(u^\ell_i(u_i - u^\ell_i)) - \nu\partial_j u^\ell_i\partial_j(u_i - u^\ell_i) + 2\Pi^\ell_{LES} - 2\Pi^\ell_{DR} \tag{F.33}$$

Appendix G

Design of the GvK experiment

In this thesis, we probed the inertial range and the beginning of the dissipative range in order to find prints of singularities, characterized by a very large inter-scale transfer or a very large ratio of inter-scale transfer to viscous dissipation. We showed that there were very intense events of inter-scale transfer even in the beginning of the dissipative range, whereas in the classical phenomenology of turbulence, viscous effects are assumed to overwhelm non-linear effects in this range. This suggests that the Kolmogorov scale is not the smallest scale in a turbulent flow and therefore makes the case for the existence of Euler-type singularities (see chapter 2). In order to confirm these results, measurements in the far dissipative range should be done. This could be achieved by improving the spatial resolution of PIV ; however, we showed in chapter 4 that it was limited by the particle density and by optical constraints such as the size of the diffraction spot and the focal depth which should be large enough in 3D measurements. Currently, the resolution of our TPIV set-up is around 0.5 mm, which is close to the Kolmogorov scale at the smallest Reynolds number in our VK2 set-up. Instead of improving the resolution, we can increase the Kolmogorov scale. This is the ground idea of the EXPLOIT project funded by ANR whose goal is to build a set-up similar to VK2 but five times bigger : the GvK set-up. A part of this thesis was dedicated to the design of this new set-up ; it is reported in this chapter. The first step consisted in designing and dimensioning the set-up in order to be able to resolve the Kolmogorov length- and time-scales in good experimental conditions ; mainly physical and experimental issues were adressed. As the designed set-up was too big to be made at the mechanical workshop of the laboratory, we then wrote specifications in order to have the mechanical conception and the manufacturing realized by an external company, GP Concept.

1 Choice of the size

The goal of the EXPLOIT project is to observe very small scales in turbulence. Rather than improving the spatial resolution of the measurement technique (PIV), the strategy is to increase the size of the small scales. Usually, the smallest scale of a turbulent flow is considered to be the Kolmogorov scale η. In the case of the von Kármán flow described in chapter 3, the Kolmogorov scale is given by :

$$\eta = R(Re^3\epsilon^*)^{-1/4} \tag{G.1}$$

where R is the tank radius, Re the Reynolds number and ϵ^* the dimensionless average energy dissipation rate (which is constant at large Reynolds numbers, see chapter 3).
This formula clearly shows that for a given Reynolds number, the Kolmogorov scale increases linearly with the set-up size. In the VK2 set-up, our resolution is equal to the Kolmogorov scale

for $Re = 6000$. Building a set-up bigger than the VK2 set-up would therefore allow us to observe scales smaller than the Kolmogorov scale, at least at $Re = 6000$.
For instance, tables G.1 and G.2 give the values of the Kolmogorov scale for the three kinds of flows described in chapter 3 (contra ; anti, symmetrical and anti, bifurcated) for R=10 cm and R=50 cm respectively.

	Flow type		
Reynolds number	Contra	Anti, symmetrical	Anti, bifurcated
6.3×10^3	0.39 mm	0.30 mm	0.21 mm
3.1×10^4	0.11 mm	91 μm	64 μm
6.3×10^4	70 μm	54 μm	38 μm
3.1×10^5	21 μm	16 μm	11 μm
1.6×10^6	6.4 μm	4.8 μm	3.4 μm

Table G.1: Kolmogorov scale in the von Kármán flow for R=10 cm (VK2 set-up) at different Reynolds numbers and for different flow types.

	Flow type		
Reynolds number	Contra	Anti, symmetrical	Anti, bifurcated
6.3×10^3	2.0 mm	1.5 mm	1.1 mm
3.1×10^4	0.59 mm	0.45 mm	0.32 mm
6.3×10^4	0.35 mm	0.27 mm	0.19 mm
3.1×10^5	0.1 mm	81 μm	57 μm
1.6×10^6	31 μm	24 μm	17 μm

Table G.2: Kolmogorov scale in the von Kármán flow for R=50 cm (GvK set-up) at different Reynolds numbers and for different flow types.

In chapter 4, we showed that our current resolution was around 0.1 mm for 2D PIV and around 0.5 mm for 3D PIV. The improvement due to the increase of the set-up radius is clear from tables G.1 and G.2 : for the VK2 set-up, the Kolmogorov scale is hardly resolved at $Re = 3.1 \times 10^4$ for 2D PIV and $Re = 6.3 \times 10^3$ for 3D PIV whereas for GvK set-up, the Kolmogorov scale is resolved up to almost $Re = 3.1 \times 10^5$ with 2D PIV and $Re = 6.3 \times 10^4$ for 3D PIV.
Increasing the cylinder radius by a factor 5 compared to the VK2 set-up is enough to obtain a resolution smaller than the Kolmogorov scale, but one could be tempted to increase it even more. Nevertheless, we chose to limit to a factor 5 for quite practical issues : we could already plan that a five times bigger set-up would be heavy and would need a large room ; also we had a limited budget and even if we did not foresee all the difficulties, we could guess that they would increase at least linearly with R. We therefore preferred to be careful ; we did not regret this choice retrospectively.

2 Choice of the fluid

In the VK2 set-up, the fluid used is either water or a water-glycerol mixture. This allows to play either on the fluid viscosity or on the impeller rotation frequency in order to vary the Reynolds number ; this is particularly useful to avoid small rotation frequencies for which the frequency regulation

is less accurate, the particles settle and a low acquisition frequency is required to get independent frames (resulting in long acquisition times). However, this has drawbacks like leaks, or bubbles and dirts in the flow hindering the PIV measurements. Therefore, we asked ourselves whether we should use a different fluid, i.e. air or other gases, in the new set-up. We then investigated the different aspects of the experiment impacted by the choice of the fluid before taking a decision.

2.1 Range of working parameters

For a given set-up size, the working parameters (rotation frequency, torque and power) depend on the studied Reynolds number and on the fluid. The range of working parameters is finite due to some constraints ; therefore the range of Reynolds numbers that can be reached depends on the fluid.

The rotation frequency F of the impellers, the average torque T applied by one impeller on the flow and the total power P_{tot} injected by the two of them in the flow are given by the following formulas, deduced from chapter 3 :

$$F = \frac{\nu \cdot Re}{2\pi R^2} \tag{G.2}$$

$$T = \rho K_p R^5 (2\pi F)^2 = \rho K_p R \nu^2 Re^2 \tag{G.3}$$

$$P_{tot} = 2\rho K_p R^5 (2\pi F)^3 = \frac{2\rho K_p \nu^3 Re^3}{R} \tag{G.4}$$

where :

- Re is the Reynolds number,
- ν is the fluid viscosity,
- K_p is the dimensionless torque, depending on the type of flow. For a bifurcated flow, it is the average of the dimensionless torques applied by the two impellers.

Note that these are average values in stationary state ; in practice, there are fluctuations. Tables G.3 to G.6 give the values of the impeller working parameters for different Reynolds numbers and for the three different types of flow, in the case of water, pure glycerol, air and helium filling the tank.

There are simple relations between the working parameters of the engines and those of the impellers : the power supplied by the engines is equal (up to the mechanical losses) to the power injected by the impellers into the flow ; the rotation frequency of the engines is equal to the rotation frequency of the impellers, or proportional to it if there is a reduction ratio ; the torques of the engines and of the impellers are also equal or proportional to each other.
The constraints on the range of working parameters are the following :

- finite resolution of the control of the rotation frequency or of the torque by the engines : the rotation frequency and the torque applied cannot be too small. For instance, the engines of the VK2 set-up cannot control the rotation frequency below 0.2 Hz with an accuracy higher than 1%.
- finite range of rotation frequencies and torques handled by the engines. A reduction gear can help increasing this range. For instance, the maximum rotation frequency allowed for the engines of the VK2 set-up is 50 Hz. The frequency range is then $50/0.2 = 250$.

- finite resolution of the torquemeters (we wish to perform torque measurements). The best torquemeter we found is sold by HBM and has a resolution of 0.01 N.m. It cannot measure torques higher than 100 N.m.
- finite measurement range of the torquemeters. Several torquemeters with different measurement ranges are needed if the required torque range is too large.
- additional torques due to the transmission between the engine and the impeller which prevent measurement or accurate control for torques that are too small.
- limited power of the cooling system which should be able to keep a constant temperature in the flow. The power of the cooling system is related to the power injected in the flow ; it is equal (up to the losses) to the power provided to the engine, see next point.
- limited electricity power supply : we decided to use a total power P_{tot} smaller than 10 kW.

Based on these constraints, a first comparison can be made between the different fluids.
In the case of pure water, it will be difficult to study low Reynolds numbers as the corresponding rotation frequencies and torques are very low, preventing accurate control and measurement. For an anti bifurcated flow, the maximum Reynolds number that can be reached is around 1.6×10^6 because of the required power, for a contra or anti symmetrical flow it can be higher.
For pure glycerol, all the considered Reynolds numbers require a total power higher than 10 kW. $Re = 6000$ being considered as the lowest turbulent Reynolds number in this flow, pure glycerol will not be used in the GvK set-up. However, working with a water-glycerol mixture would allow to study Reynolds numbers down to 6.3×10^3 as the required power would be smaller than in the case of pure glycerol and the required frequency and torque larger than in the case of pure water.
For air, smaller Reynolds numbers than in the case of water can be reached : the lower limit is smaller and the higher limit is closer to 1.6×10^6. At $Re = 6.3 \times 10^3$, the frequency and the torque are a bit small but if we give up on the torque measurement and use a reduction gear to achieve an accurate frequency control, this Reynolds number could be reached.
For helium, the upper limit on the Reynolds number due to the limited power is between $Re = 3.1 \times 10^5$ and $Re = 1.6 \times 10^6$. At $Re = 6.3 \times 10^3$, accurate frequency control is possible but not torque measurement.

Based on the analysis of the working parameters of the engines, it seems that a set-up allowing to use both water and water-glycerol mixtures is the best solution. A set-up filled with air could also allow to reach Reynolds numbers between 6.3×10^3 and 1.6×10^6, using a reduction gear and at the cost of giving up on the torque measurement at lower Reynolds. Using helium, alone or in addition to air, is not convincing because higher Reynolds cannot be reached and at lower Reynolds, the problem is the same as in air. Therefore, we will stop considering this gas in the following.

Reynolds number		6.3×10^3	3.1×10^4	6.3×10^4	3.1×10^5	1.6×10^6
Impeller rotation frequency (Hz)		4.0×10^{-3}	2.0×10^{-2}	4.0×10^{-2}	2.0×10^{-1}	1.0×10^0
T (N.m)	Contra	9.3×10^{-4}	2.3×10^{-2}	9.3×10^{-2}	2.3×10^0	5.8×10^1
	Anti, symmetrical	2.7×10^{-3}	6.7×10^{-2}	2.7×10^{-1}	6.7×10^0	1.7×10^2
	Anti, bifurcated	1.1×10^{-2}	2.7×10^{-1}	1.1×10^0	2.7×10^1	6.7×10^2
P_{tot} (W)	Contra	4.7×10^{-5}	5.8×10^{-3}	4.7×10^{-2}	5.8×10^0	7.3×10^2
	Anti, symmetrical	1.3×10^{-4}	1.7×10^{-2}	1.3×10^{-1}	1.7×10^1	2.1×10^3
	Anti, bifurcated	5.4×10^{-4}	6.7×10^{-2}	5.4×10^{-1}	6.7×10^1	8.4×10^3

Table G.3: Working parameters for the GvK set-up filled with pure water ($\rho = 1000$ kg/m^3 and $\nu = 1.6 \times 10^{-6}$ m^2/s).

Reynolds number		6.3×10^3	3.1×10^4	6.3×10^4	3.1×10^5	1.6×10^6
Impeller rotation frequency (Hz)		4.5×10^0	2.2×10^1	4.5×10^1	2.2×10^2	1.1×10^3
T (N.m)	Contra	1.5×10^3	3.7×10^4	1.5×10^5	3.7×10^6	9.2×10^7
	Anti, symmetrical	4.2×10^3	1.1×10^5	4.2×10^5	1.1×10^7	2.6×10^8
	Anti, bifurcated	1.7×10^4	4.2×10^5	1.7×10^6	4.2×10^7	1.1×10^9
P_{tot} (W)	Contra	8.3×10^4	1.0×10^7	8.3×10^7	1.0×10^{10}	1.3×10^{12}
	Anti, symmetrical	2.4×10^5	3.0×10^7	2.4×10^8	3.0×10^{10}	3.7×10^{12}
	Anti, bifurcated	9.5×10^5	1.2×10^8	9.5×10^8	1.2×10^{11}	1.5×10^{13}

Table G.4: Working parameters for the GvK set-up filled with pure glycerol ($\rho = 1260$ kg/m^3 and $\nu = 1.12 \times 10^{-3}$ m^2/s).

Reynolds number		6.3×10^3	3.1×10^4	6.3×10^4	3.1×10^5	1.6×10^6
Impeller rotation frequency (Hz)		6.0×10^{-2}	3.0×10^{-1}	6.0×10^{-1}	3.0×10^0	1.5×10^1
T (N.m)	Contra	2.5×10^{-4}	6.3×10^{-3}	2.5×10^{-2}	6.3×10^{-1}	1.6×10^1
	Anti, symmetrical	7.2×10^{-4}	1.8×10^{-2}	7.2×10^{-2}	1.8×10^0	4.5×10^1
	Anti, bifurcated	2.9×10^{-3}	7.2×10^{-2}	2.9×10^{-1}	7.2×10^0	1.8×10^2
P_{tot} (W)	Contra	1.9×10^{-4}	2.4×10^{-2}	1.9×10^{-1}	2.4×10^1	3.0×10^3
	Anti, symmetrical	5.4×10^{-4}	6.8×10^{-2}	5.4×10^{-1}	6.8×10^1	8.5×10^3
	Anti, bifurcated	2.2×10^{-3}	2.7×10^{-1}	2.2×10^0	2.7×10^2	3.4×10^4

Table G.5: Working parameters for the GvK set-up filled with air ($\rho = 1.2$ kg/m^3 and $\nu = 1.5 \times 10^{-5}$ m^2/s).

Reynolds number		6.3×10^3	3.1×10^4	6.3×10^4	3.1×10^5	1.6×10^6
Impeller rotation frequency (Hz)		4.8×10^{-1}	2.4×10^0	4.8×10^0	2.4×10^1	1.2×10^2
T (N.m)	Contra	2.3×10^{-3}	5.7×10^{-2}	2.3×10^{-1}	5.7×10^0	1.4×10^2
	Anti, symmetrical	6.5×10^{-3}	1.6×10^{-1}	6.5×10^{-1}	1.6×10^1	4.1×10^2
	Anti, bifurcated	2.6×10^{-2}	6.5×10^{-1}	2.6×10^0	6.5×10^1	1.6×10^3
P_{tot} (W)	Contra	1.4×10^{-2}	1.7×10^0	1.4×10^1	1.7×10^3	2.1×10^5
	Anti, symmetrical	3.9×10^{-2}	4.9×10^0	3.9×10^1	4.9×10^3	6.1×10^5
	Anti, bifurcated	1.6×10^{-1}	2.0×10^1	1.6×10^2	2.0×10^4	2.5×10^6

Table G.6: Working parameters for the GvK set-up filled with helium ($\rho = 0.17$ kg/m^3 and $\nu = 1.2 \times 10^{-4}$ m^2/s).

2.2 Seeding

The kind of seeding particles is not the same in the case of water or water-glycerol mixture filling the cylinder and in the case of air ; each case has its own advantages and drawbacks. In both cases, particles must follow the flow and have a low velocity shift.

Seeding for liquid In the case of water or water-glycerol mixture filling the cylinder, solid seeding particles will be used, as in the VK2 set-up. In this case we used Dantec silver-coated glass hollowspheres of average diameter 15 μm and density 1.4, and Lavision non-silver-coated hollowspheres of average diameter 10 μm and density 1.1. Typical price is a few hundreds euros for 200 g of particles, and fillling the whole GvK tank will require around 100 g. We are used to work with these kinds of particles in the VK2 set-up, but the Stokes number and the velocity shift must be computed for the GvK set-up to be sure that the particles will follow the flow (indeed, time scales are different for a given Reynolds number in the VK2 set-up and in the GvK set-up). Also, as the cylinder radius is 5 times bigger, the laser will have to cross a length 5 times longer before reaching the measurement volume at the center of the tank, there will probably be intensity losses at high concentration and a more powerful laser will be required.

Seeding for air In the case of air, the seeding is usually achieved with a fog generator that generates a fog made of droplets of a water-glycol or water-glycerol mixture (around 1% of glycol or glycerol, and other secret components). These droplets have a diameter of a few micrometers and a density close to 1 g/cm^3. The price of a fog generator is around 4000 euros, and the price of the fog liquid is around 8 euros per liter. Droplets have a finite life time so the fog generator has to produce droplets continuously. As the von Kármán flow is a closed flow, it is not possible to renew the seeding, so the droplets may clog the walls of the tank, which is a real problem when observing the flow through them.
Also, as particles are smaller than in water, they scatter less light. Therefore, there will be less losses while crossing the fluid but a high power is still required so that cameras receive enough light. This last point should not be a major problem as this kind of seeding is known to be widely used.

Stokes number To ensure that the particles properly follow the flow, the Stokes number can be computed (see chapter 4). Tables G.7 to G.9 give the Stokes number based on the Kolmogorov time scale for the GvK set-up in the case of water, glycerol and air filling the tank. For tables G.7 and G.8, the particles considered have a diameter of 15 μm and a density of 1400 kg/m^3 ; this is a quite conservative case. For table G.9, particles have a diameter of 1 μm and a density of 1050 kg/m^3, which are typical values for the seeding in air.
In all cases, the Stokes number based on the Kolmogorov time scale τ_k is much smaller than 1 ; at most it reaches a few percents (in the anti, bifurcated case when the set-up is filled with air the value is too high but we saw in the previous section that the power required for this case is too high and that we would not be able to achieve it). For a water-glycerol mixture, the values are of the same order.

Velocity shift The velocity shift of the particles can be computed according to the formula given in chapter 4. It is given in table G.10. The total root mean square (rms) of the fluctuations u_{rms}^{tot} (see chapter 5) at the smallest turbulent Reynolds number ($Re = 6000$) are given in table G.11 for the GvK set-up (R=50 cm). The u_{rms}^{tot} at higher Reynolds numbers are higher.

Reynolds number		6.3×10^3	3.1×10^4	6.3×10^4	3.1×10^5	1.6×10^6
Impeller rotation frequency (Hz)		4.0×10^{-3}	2.0×10^{-2}	4.0×10^{-2}	2.0×10^{-1}	1.0×10^{0}
τ_k	Contra	3.9×10^{0}	3.5×10^{-1}	1.2×10^{-1}	1.1×10^{-2}	9.8×10^{-4}
	Anti, symmetrical	2.3×10^{0}	2.1×10^{-1}	7.3×10^{-2}	6.5×10^{-3}	5.8×10^{-4}
	Anti, bifurcated	1.1×10^{0}	1.0×10^{-1}	3.6×10^{-2}	3.2×10^{-3}	2.9×10^{-4}
$St = \frac{\rho_p d_p^2}{18\mu\tau_k}$	Contra	4.5×10^{-6}	5.0×10^{-5}	1.4×10^{-4}	1.6×10^{-3}	1.8×10^{-2}
	Anti, symmetrical	7.6×10^{-6}	8.5×10^{-5}	2.4×10^{-4}	2.7×10^{-3}	3.0×10^{-2}
	Anti, bifurcated	1.5×10^{-5}	1.7×10^{-4}	4.8×10^{-4}	5.4×10^{-3}	6.0×10^{-2}

Table G.7: Stokes number for the GvK set-up filled with pure water, in the case of seeding particles of diameter 15 μm and density 1400 kg/m^3.

Reynolds number		6.3×10^3	3.1×10^4	6.3×10^4	3.1×10^5	1.6×10^6
Impeller rotation frequency (Hz)		4.5×10^{0}	2.2×10^{1}	4.5×10^{1}	2.2×10^{2}	1.1×10^{3}
τ_k	Contra	3.5×10^{-3}	3.1×10^{-4}	1.1×10^{-4}	9.8×10^{-6}	8.8×10^{-7}
	Anti, symmetrical	2.1×10^{-3}	1.8×10^{-4}	6.5×10^{-5}	5.8×10^{-6}	5.2×10^{-7}
	Anti, bifurcated	1.0×10^{-3}	9.2×10^{-5}	3.2×10^{-5}	2.9×10^{-6}	2.6×10^{-7}
$St = \frac{\rho_p d_p^2}{18\mu\tau_k}$	Contra	3.6×10^{-6}	4.0×10^{-5}	1.1×10^{-4}	1.3×10^{-3}	1.4×10^{-2}
	Anti, symmetrical	6.0×10^{-6}	6.8×10^{-5}	1.9×10^{-4}	2.1×10^{-3}	2.4×10^{-2}
	Anti, bifurcated	1.2×10^{-5}	1.4×10^{-4}	3.8×10^{-4}	4.3×10^{-3}	4.8×10^{-2}

Table G.8: Stokes number for the GvK set-up filled with pure glycerol, in the case of seeding particles of diameter 15 μm and density 1400 kg/m^3.

Reynolds number		6.3×10^3	3.1×10^4	6.3×10^4	3.1×10^5	1.6×10^6
Impeller rotation frequency (Hz)		6.0×10^{-2}	3.0×10^{-1}	6.0×10^{-1}	3.0×10^{0}	1.5×10^{1}
τ_k	Contra	2.6×10^{-1}	2.3×10^{-2}	8.2×10^{-3}	7.3×10^{-4}	6.6×10^{-5}
	Anti, symmetrical	1.5×10^{-1}	1.4×10^{-2}	4.8×10^{-3}	4.3×10^{-4}	3.9×10^{-5}
	Anti, bifurcated	7.7×10^{-2}	6.8×10^{-3}	2.4×10^{-3}	2.2×10^{-4}	1.9×10^{-5}
$St = \frac{\rho_p d_p^2}{18\mu\tau_k}$	Contra	1.2×10^{-5}	1.4×10^{-4}	3.9×10^{-4}	4.4×10^{-3}	4.9×10^{-2}
	Anti, symmetrical	2.1×10^{-5}	2.4×10^{-4}	6.7×10^{-4}	7.5×10^{-3}	8.4×10^{-2}
	Anti, bifurcated	4.2×10^{-5}	4.7×10^{-4}	1.3×10^{-3}	1.5×10^{-2}	1.7×10^{-1}

Table G.9: Stokes number for the GvK set-up filled with air, in the case of seeding particles of diameter 1 μm and density 1050 kg/m^3.

The velocity shift is negligible compared to the rms of the velocity fluctuations in all cases, as it was the case in the VK2 set-up. Therefore, the sedimentation will not affect the measurement in any case ; the problem is rather the sedimentation of the particles over time scales longer than the interframing time. This sedimentation implies to stir the fluid regularly and strongly to re-suspend the particles. In the VK2 set-up, sedimentation was observed in pure water at all Reynolds numbers. For a water-glycerol mixture having a density close to the particle density, sedimentation

Particles	$\rho_p = 1100$ kg/m^3, $d_p = 10$ μm		$\rho_p = 1400$ kg/m^3, $d_p = 15$ μm		$\rho_p = 1050$ kg/m^3, $d_p = 1$ μm
Liquid	Pure water	Pure glycerol	Pure water	Pure glycerol	Air
Velocity shift	5 μm/s (downward)	6 nm/s (upward)	60 μm/s (downward)	10 nm/s (downward)	30 μm/s (downward)

Table G.10: Velocity shift for different particles and fluids

Fluid	Pure water	Pure glycerol	Air
u_{rms}^{tot}	4 mm/s	4 m/s	6 cm/s

Table G.11: u_{rms}^{tot} at $Re = 6.3 \times 10^3$ for different fluids and for the GvK set-up (R=50 cm)

was not observed. Extrapolating this observation, we can reasonably assume that there will also be sedimentation in air.

Based on the seeding issue, the option of using water or a water-glycerol mixture seems better than using air. In all cases, the seeding particles will properly follow the flow. Costs are comparable. However, using a water-glycerol mixture seems to be the only way to avoid a velocity shift. The drawback of the seeding in water or water-glycerol mixture is the attenuation of light over a radius of 50 cm. This can be compensated by a higher laser power though. We are used to performing PIV in water or water-glycerol mixtures in the von Kármán flow whereas we have no experience of PIV in air in a closed flow ; in particular, we expect a risk of clogging the tank walls, which will hinder image acquisition.

2.3 Time-resolved measurements of the flow

One of the goals of building the GvK experiment is to perform time-resolved velocity measurements. Such measurements can be achieved with high-speed laser and cameras whose working frequency is high but finite. The time scales of the flow for a given Reynolds number depend on the fluid viscosity, and so does the acquisition frequency. We compute here the required acquisition frequency for a set-up filled with either water, glycerol or air.

The acquisition frequency must be set such that the average displacement on the camera sensors is around 5 pixels. This average displacement in pixels d_{pix} depends on the rms of the velocity u_{rms}^{tot}, on the magnification $|M|$, on the camera pixel size c and on the acquisition frequency f_{acq} :

$$d_{pix} = \frac{u_{rms}^{tot} \cdot |M|}{f_{acq} \cdot c} \tag{G.5}$$

In the von Kármán flow, $u_{rms}^{tot} = a * (2\pi RF)$, R being the tank radius and F the impeller rotation frequency. At the center of the flow, $a \approx 0.35$ for the contra direction of rotation, and $a \approx 0.4$ for the anti direction of rotation (symmetrical flow). For an average displacement of 5 pixels, f_{acq} should be equal to :

$$f_{acq} = \frac{2\pi a RF|M|}{5c} \tag{G.6}$$

Tables G.12 to G.14 give the values of f_{acq} respectively for pure water, pure glycerol and air, for contra and anti (symmetrical) directions of rotation, several Reynolds numbers and several magnifications. The camera pixel size c is equal to 10 μm.

Reynolds number		6.3×10^3	3.1×10^4	6.3×10^4	3.1×10^5	1.6×10^6
Contra	|M|=0.1	8.8×10^0	4.4×10^1	8.8×10^1	4.4×10^2	2.2×10^3
	|M|=0.3	2.6×10^1	1.3×10^2	2.6×10^2	1.3×10^3	6.6×10^3
	|M|=0.5	4.4×10^1	2.2×10^2	4.4×10^2	2.2×10^3	1.1×10^4
	|M|=0.7	6.2×10^1	3.1×10^2	6.2×10^2	3.1×10^3	1.5×10^4
	|M|=0.9	7.9×10^1	4.0×10^2	7.9×10^2	4.0×10^3	2.0×10^4
	|M|=1.1	9.7×10^1	4.8×10^2	9.7×10^2	4.8×10^3	2.4×10^4
	|M|=1.3	1.1×10^2	5.7×10^2	1.1×10^3	5.7×10^3	2.9×10^4
	|M|=1.5	1.3×10^2	6.6×10^2	1.3×10^3	6.6×10^3	3.3×10^4
Anti	|M|=0.1	1.0×10^1	5.0×10^1	1.0×10^2	5.0×10^2	2.5×10^3
	|M|=0.3	3.0×10^1	1.5×10^2	3.0×10^2	1.5×10^3	7.5×10^3
	|M|=0.5	5.0×10^1	2.5×10^2	5.0×10^2	2.5×10^3	1.3×10^4
	|M|=0.7	7.0×10^1	3.5×10^2	7.0×10^2	3.5×10^3	1.8×10^4
	|M|=0.9	9.0×10^1	4.5×10^2	9.0×10^2	4.5×10^3	2.3×10^4
	|M|=1.1	1.1×10^2	5.5×10^2	1.1×10^3	5.5×10^3	2.8×10^4
	|M|=1.3	1.3×10^2	6.5×10^2	1.3×10^3	6.5×10^3	3.3×10^4
	|M|=1.5	1.5×10^2	7.5×10^2	1.5×10^3	7.5×10^3	3.8×10^4

Table G.12: f_{acq} (Hz) for contra and anti (symmetrical) rotation directions, several Reynolds numbers and several magnifications in the case of pure water filling the tank. $c = 10$ μm.

The fast cameras we use (Phantom Miro m340, see chapter 5) have a maximum acquisition frequency of 800 Hz at full resolution. They can also acquire images at higher frequency but the resolution is decreased. We consider here that the maximum acquisition frequency is 4 kHz. At this frequency, the resolution is 512 × 512 pixels. The acquisition frequency is increasing with $|M|$, but a high value of $|M|$ is not required as we showed in chapter 4 that a magnification $|M|$ between 0.3 and 0.4 is a good setting.
In the case of pure water filling the tank, the flow can be time-resolved with full camera resolution up to $Re = 6.3 \times 10^4$ with optimal $|M|$, and at higher Reynolds number with lower $|M|$ or lower camera resolution. In the case of pure glycerol filling the tank, the flow cannot be time-resolved at a fullly turbulent Reynolds number with our cameras. For a water-glycerol mixture, the highest Reynolds number at which the flow can be time-resolved is therefore between $Re = 6.3 \times 10^3$ and $Re = 1.6 \times 10^6$.
In the case of air filling the tank, the flow can be time-resolved only at $Re = 6.3 \times 10^3$ at full resolution and up to $Re = 6.3 \times 10^4$ with lower resolution.

In the case of water or water-glycerol mixture filling the GvK set-up, the flow can be time-resolved up to higher Reynolds numbers than in the case of air.

Reynolds number		6.3×10^3	3.1×10^4	6.3×10^4	3.1×10^5	1.6×10^6
Contra	|M|=0.1	9.9×10^3	4.9×10^4	9.9×10^4	4.9×10^5	2.5×10^6
	|M|=0.3	3.0×10^4	1.5×10^5	3.0×10^5	1.5×10^6	7.4×10^6
	|M|=0.5	4.9×10^4	2.5×10^5	4.9×10^5	2.5×10^6	1.2×10^7
	|M|=0.7	6.9×10^4	3.4×10^5	6.9×10^5	3.4×10^6	1.7×10^7
	|M|=0.9	8.9×10^4	4.4×10^5	8.9×10^5	4.4×10^6	2.2×10^7
	|M|=1.1	1.1×10^5	5.4×10^5	1.1×10^6	5.4×10^6	2.7×10^7
	|M|=1.3	1.3×10^5	6.4×10^5	1.3×10^6	6.4×10^6	3.2×10^7
	|M|=1.5	1.5×10^5	7.4×10^5	1.5×10^6	7.4×10^6	3.7×10^7
Anti	|M|=0.1	1.1×10^4	5.6×10^4	1.1×10^5	5.6×10^5	2.8×10^6
	|M|=0.3	3.4×10^4	1.7×10^5	3.4×10^5	1.7×10^6	8.4×10^6
	|M|=0.5	5.6×10^4	2.8×10^5	5.6×10^5	2.8×10^6	1.4×10^7
	|M|=0.7	7.9×10^4	3.9×10^5	7.9×10^5	3.9×10^6	2.0×10^7
	|M|=0.9	1.0×10^5	5.1×10^5	1.0×10^6	5.1×10^6	2.5×10^7
	|M|=1.1	1.2×10^5	6.2×10^5	1.2×10^6	6.2×10^6	3.1×10^7
	|M|=1.3	1.5×10^5	7.3×10^5	1.5×10^6	7.3×10^6	3.7×10^7
	|M|=1.5	1.7×10^5	8.4×10^5	1.7×10^6	8.4×10^6	4.2×10^7

Table G.13: f_{acq} (Hz) for contra and anti (symmetrical) rotation directions, several Reynolds numbers and several magnifications in the case of pure glycerol filling the tank. $c = 10$ μm.

Reynolds number		6.3×10^3	3.1×10^4	6.3×10^4	3.1×10^5	1.6×10^6
Contra	|M|=0.1	1.3×10^2	6.6×10^2	1.3×10^3	6.6×10^3	3.3×10^4
	|M|=0.3	4.0×10^2	2.0×10^3	4.0×10^3	2.0×10^4	9.9×10^4
	|M|=0.5	6.6×10^2	3.3×10^3	6.6×10^3	3.3×10^4	1.6×10^5
	|M|=0.7	9.2×10^2	4.6×10^3	9.2×10^3	4.6×10^4	2.3×10^5
	|M|=0.9	1.2×10^3	5.9×10^3	1.2×10^4	5.9×10^4	3.0×10^5
	|M|=1.1	1.5×10^3	7.3×10^3	1.5×10^4	7.3×10^4	3.6×10^5
	|M|=1.3	1.7×10^3	8.6×10^3	1.7×10^4	8.6×10^4	4.3×10^5
	|M|=1.5	2.0×10^3	9.9×10^3	2.0×10^4	9.9×10^4	4.9×10^5
Anti	|M|=0.1	1.5×10^2	7.5×10^2	1.5×10^3	7.5×10^3	3.8×10^4
	|M|=0.3	4.5×10^2	2.3×10^3	4.5×10^3	2.3×10^4	1.1×10^5
	|M|=0.5	7.5×10^2	3.8×10^3	7.5×10^3	3.8×10^4	1.9×10^5
	|M|=0.7	1.1×10^3	5.3×10^3	1.1×10^4	5.3×10^4	2.6×10^5
	|M|=0.9	1.4×10^3	6.8×10^3	1.4×10^4	6.8×10^4	3.4×10^5
	|M|=1.1	1.7×10^3	8.3×10^3	1.7×10^4	8.3×10^4	4.1×10^5
	|M|=1.3	2.0×10^3	9.8×10^3	2.0×10^4	9.8×10^4	4.9×10^5
	|M|=1.5	2.3×10^3	1.1×10^4	2.3×10^4	1.1×10^5	5.7×10^5

Table G.14: f_{acq} (Hz) for contra and anti (symmetrical) rotation directions, several Reynolds numbers and several magnifications in the case of air filling the tank. $c = 10$ μm.

2.4 Bubbles and cavitation

In the VK2 set-up, before doing any PIV measurement, air bubbles corresponding to air trapped in the mechanical parts have to be removed by stirring the fluid for some time. Also, the tank is pressurized to avoid cavitation, i.e. the formation of bubbles due to local decrease in pressure.
In the case of a set-up filled with air, this problem does of course not occur. In the case of a set-up filled with water or with a water-glycerol mixture, we can discuss the impeller rotation frequency f_{cav} at which cavitation occurs based on the formula proposed in [Marié, 2003] :

$$f_{cav} = \frac{1}{2\pi R}\sqrt{\frac{P_{surf} - P_{sat}}{C\rho}} \approx \frac{1}{2\pi R}\sqrt{\frac{P_{surf}}{C\rho}} \tag{G.7}$$

where R is the tank radius, ρ the fluid viscosity, P_{surf} the pressure at the top of the tank, P_{sat} the vapor pressure, considered negligible and C a coefficient depending on the geometry and weakly on the Reynolds number.
According to this formula, when multiplying the tank radius by five, f_{cav} will be divided by 5. However, when multiplying the tank radius by five, the impeller rotation frequency must be divided by 25 to keep the Reynolds number constant (considering C constant). Therefore, the Reynolds number at which cavitation will appear will roughly be 5 times larger for the GvK set-up than for VK2. In VK2 in water, pressure was required to prevent bubble formation around $Re = 3 \times 10^5$. This corresponds to $Re = 1.5 \times 10^6$ in GvK for water, a Reynolds number that we would like to study.

Considering the problem of bubbles, using air is clearly better as water or water-glycerol mixture as the problem does not exist with air. For water or water-glycerol mixture, the tank should be pressurized to avoid bubble formation at high Reynolds.

2.5 Other practical issues related to the properties of the fluid

Here, we discuss other issues that should be considered before chosing the fluid.

Optical index Water or a water-glycerol mixtures have a larger optical index than air. This may result in larger distortions, handled to some extent by the 3D calibration map in TPIV. This also allows larger focal depths, as shown in chapter 4.

Price Air and water are free, whereas glycerol must be bought. For instance, the cost of 2 m^3 of glycerol (containing more than 98 % of glycerol) is 4500 euros.

Fluid handling Handling air is of course much easier than handling water or water-glycerol mixture as there is nothing to do. In the case of a liquid, the tank must be filled and unfilled ; this will take quite a long time with a set-up of 1 m diameter, especially for viscous mixtures.
Glycerol is not very convenient to use because it makes everything sticky.
Considering the cost of glycerol and of seeding particles, it may be convenient to store the liquids used. This requires further equipments.
Also, another problem of VK2 is the dirts producing big bright spots on the camera images. These dirts enter the tank when opening it or handling the liquid. In the case of air filling the tank, it would not be a problem as they are probably too heavy to be carried by the air.

Tightness In the case of a liquid, tightness is an important issue, especially for a pressurized set-up containing more than 1 m^3 of water. There were often leaks on the VK2 set-up because a proper tightness could not be achieved. Also, ensuring tightness at the shaft is often done at the expense of the reproducibility and accuracy on torque measurements, because the device (joint or sealings) achieving it produces an additional torque. In the VK2 set-up, this was partly addressed by implementing mechanical sealings, but tuning them was quite difficult (see [Saint-Michel, 2013]). Of course, in the case of air filling the tank, tightness is not required.

From a practical point of view, using air for the GvK set-up seems to be a better solution.

2.6 Conclusion

We finally decided to use water or water-glycerol mixtures rather than air. The main reasons are :

- the flexibility : we can play either on the impeller rotation frequency or in the fluid viscosity to set the Reynolds number. In particular, this allows to perform torque and time-resolved measurements over a wider range of Reynolds numbers.
- the unknown behaviour of the seeding in air in a closed flow which could hinder proper PIV measurements.

3 Other choices

Before writing the specifications, we had to choose the geometry of the set-up as well as the measurement areas.

3.1 Shape

The VK2 set-up has a cylindrical tank which is vertical ; this could have been different for the GvK set-up as the goal was not to build exactly the same set-up as VK2 with a larger radius but to generate turbulence with larger length scales. For example, a tank with a polygonal section could have been chosen as it is a priori easier to build. However, we preferred to keep on with a cylindrical tank as the corresponding flow has been widely studied : we know for instance the statistics of the velocity field, the behaviour of the dimensionless torque with respect to the Reynolds number, and the different states of the flow. Also, as we had chosen to use a liquid, we decided to let the tank vertical so that the calibration plate can be put in it without emptying it completely.

3.2 Measurement areas

In the VK2 set-up, the velocity is usually measured at the center of the flow, i.e. around the cylinder axis at the same distance from both impellers. Some measurements have also been made next to the walls, also at the same distance from both impellers. Actually, there is no mechanical structure around the cylindrical tank so that any point in the flow can be observed ; there may be distortions if the observation axis does not cross the cylinder perpendicularly though.
In the case of GvK, it was unlikely that there would not be any structure around the cylindrical tank, or even that the cylindrical tank would be fully transparent. Therefore, we needed to specify the observation directions, which should be kept free from any non-transparent obstacle. Based on the TPIV tests (see chapter 4), we decided to keep only horizontal observation directions. We decided to be able to perform measurements at the center of the flow and at a point next to

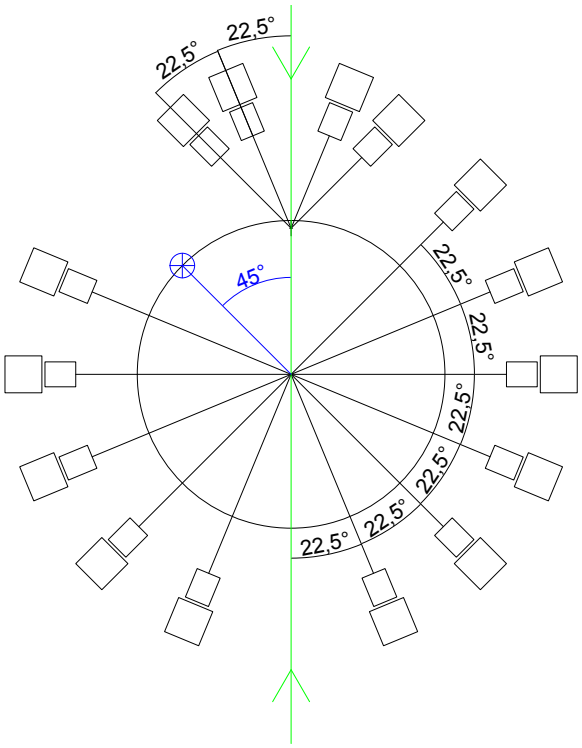

Figure G.1: Required directions that should be kept free from non-transparent obstacles and location of the openings for temperature, pressure or hot wire anemometry measurements. The green line corresponds to the laser beam direction.

the cylindrical tank. The required observation directions corresponding to these two locations are depicted on figure G.1 (we did not plan to use as many cameras, but we wanted to be able to try different configurations, hence the large number of directions specified). Concerning the height of the measurement areas, we chose to let several possibilities, and we specified that we would need the measurement areas at 5 different heights, including the mid-height of the set-up (same distance from both impellers).

Also, we decided to let the possibility to perform temperature, pressure or hot wire anemometry measurements. The blue circle on figure G.1 corresponds to the specified location of the corresponding sensors. Again, we specified that we would need to put such sensors at nine different heights, including the mid-height of the set-up.

4 Dimensioning

4.1 Dimensioning of the room for the set-up

Along with the realization of the experimental set-up, a room had to be chosen and adapted to host the set-up. We had to estimate the size and weight of the set-up to this aim.

4.1.1 Height

The VK2 set-up is 1 m high from the bottom torquemeter to the top torquemeter (see chapter 3). It fits in a room of normal height, even accounting for the space required to lift and remove the top. The size of the GvK set-up cannot be estimated simply by multiplying by 5 the size of the VK2 set-up because only the lengths related to the flow geometry have to be multiplied by 5. The heights indicated on figure G.2 are estimated as follows :

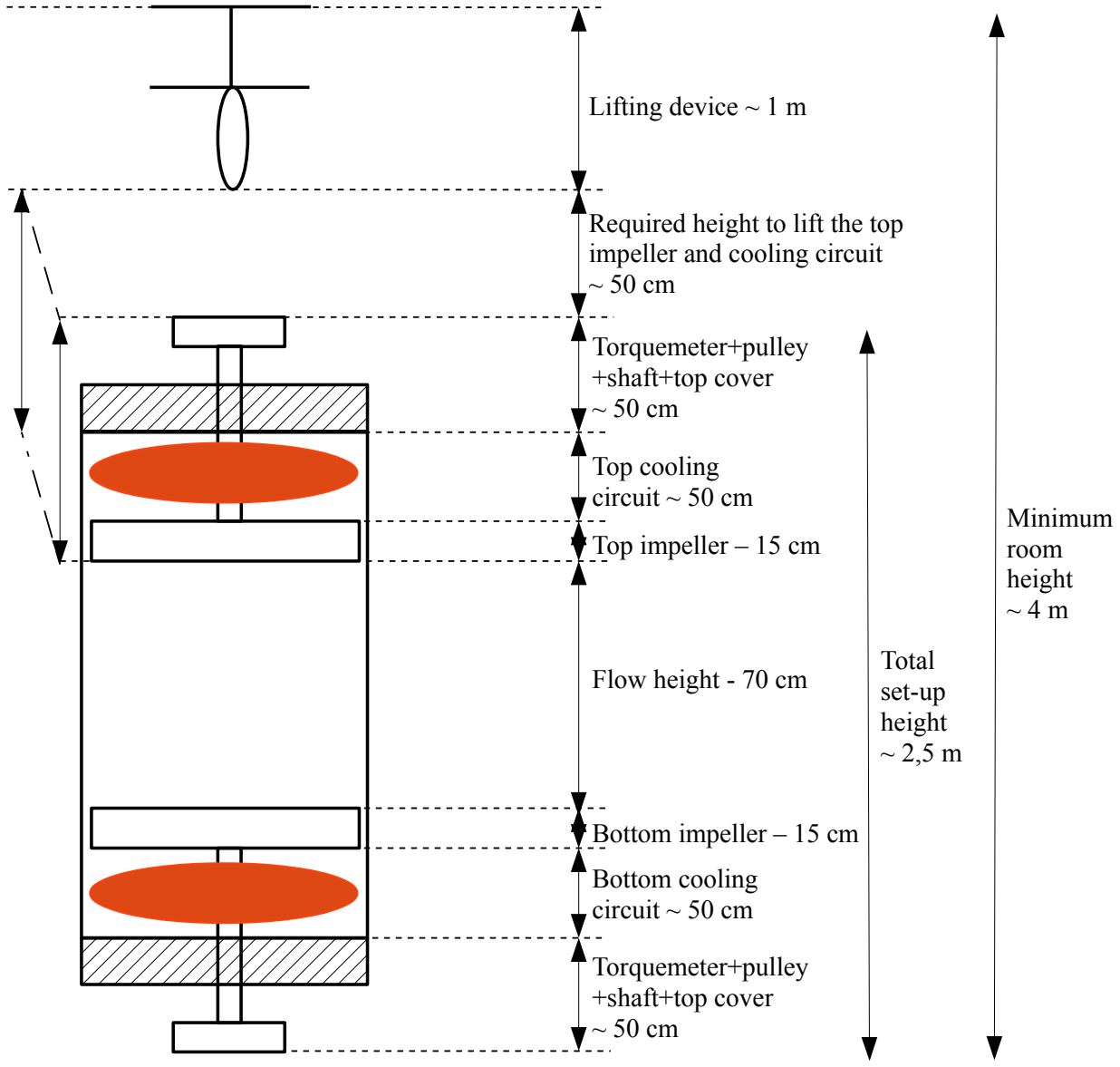

Figure G.2: Scheme of the GvK set-up with the estimated heights.

- the height of the impellers and of the space between them are multiplied by 5 giving a total height of 1 m
- the height of the torquemeters is not modified, each of them measures 12 cm

- the height of the pulleys and of the shaft is multiplied by 2, giving a height of 20 cm at the bottom and at the top
- the height of the top cover and of the bottom is multiplied by 2, giving a height of 15 cm each
- the height of the top and bottom cooling circuits is multiplied by 2 only because its radius is multiplied by 5 so its exchange surface is already multiplied by $5^2 = 25$; it is therefore 20 cm
- the height required to remove the top cooling circuit and impellers is equal to 1.5 times the total height of the impeller and of the cooling circuit, i.e. 50 cm
- the height of the lifting device is estimated to be 1 m

The estimated total height of the set-up itself is then around 2.5 m and it requires a room of at least 4 m high.

4.1.2 Width

The width of the experimental device itself will be a bit larger than 1 m because the inner diameter of the cylinder is 1 m, and there will be probably an outer tank around it. On top of that, additional space is needed to place the cameras around the set-up. The distance between the cameras and the set-up can be estimated by the distance p_e defined in appendix A, where the optical configuration is approximated by a 2-optical media configuration (see chapter 4). p_e is related to the magnification M, the optical indices n_i and n_e and the focal length of the lens f' (same notations as in appendix A) by the formula (derived from A.6) :

$$p_e = f'(\frac{1}{M} - 1) - \frac{n_e}{n_i} p_i \tag{G.8}$$

In the case of the VK2 set-up, this formula allows to find the distance between the outer tank and the cameras with 10% accuracy. Table G.15 gives values of p_e for the GvK set-up for $n_i = 1$, $n_i = 1.4$ and few values of $|M|$ and f'. p_i is set to the sum of the cylindrical tank inner radius and 12 cm which is the approximate width of both tanks and of the distance between the them. n_e is set to 1 (the external medium will be air). $n_i = 1$ corresponds to the case where the tank is filled with a gas, $n_i = 1.4$ to the case where it is filled with a water-glycerol mixture ($n_i = 1.33$ for water and $n_i = 1.47$ for pure glycerol, p_e does not vary much between these values).

n_i		1			1.4			
f' (mm)		100	200	300	70	100	200	300
$\|M\|$	0.1	48	160	270	33	66	180	290
	0.3	/	25	68	/	/	42	86
	0.5	/	/	28	/	/	16	46
	0.7	/	/	11	/	/	4	29
	0.9	/	/	1	/	/	/	20

Table G.15: Distance $|p_e|$ in cm between cameras and the outer tank for the GvK set-up for several values of n_i and f'. The / corresponds to values of f' that are too small allow the considered magnification.

According to table G.15, the maximum distance between the tank and the cameras is less than 1 m, whatever n_i (according to chapter 4, optimal $|M|$ are larger than 0.3). Therefore, the GvK set-up with the cameras around it will occupy an area comprised in a disk of 3.5 m diameter. In addition

to the tank and the camera, additional space is needed for the thermocooler, the engines, the laser, the desks, etc.

4.1.3 Weight

The total weight of the set-up can be estimated with typical densities and the estimated lengths. The cylinder is filled with the fluid, whose density is 1 kg/m^3 for air, 1000 kg/m^3 for water and 1260 kg/m^3 for pure glycerol. The height of the cylinder is 2 m. Therefore, the weight of fluid is 1.6 kg in the case of air, 1600 kg in the case of water and 2000 kg in the case of pure glycerol.
Considering that the cylinder has a thickness of 1 cm and is made of PMMA of density around 1200 kg/m^3, its weight is around 75 kg.
Considering that the outer tank is a cylinder of radius 0.6 m and of height 2 m, made of aluminium (density around 2700 kg/m^3), its weight will be around 200 kg.
The metallic impellers of the VK2 set-up weight 2.8 kg each. Multiplying this weight by $5^3 = 125$ gives a weight of 350 kg.
The top cover and the bottom of the tank can be approximated by plain cylinders of radius 0.5 m and height 15 cm. If they are made of steel (density around 8000 kg/m^3), the corresponding weight will be around 1000 kg each. This is probably overestimated but will also account for the metal structure holding the whole set-up.
With these estimations, the total weight is around 3 t if it is filled with air (or another gas, the weight of a gas is negligible compared to other components) and 5 t if it is filled with liquid.

4.2 Engines, torquemeters and cooling system dimensioning

After the liquid had been chosen, we defined more accurately the range of working parameters of the engines, as well as the corresponding working ranges for the torquemeters and the cooling system.

4.2.1 Engines

The maximum allowed power was decided to be 10 kW ; this would fix the upper limits on the frequency and torque ranges. The lower limit was going to be limited by the velocity regulation resolution and torquemeter resolution. Proceeding by trial and error, we found that a range of frequencies of $[0.1, 2]$ Hz allowed to reach all the Reynolds numbers with high enough torques and small enough power. Note that 0.1 Hz is the lowest frequency we could reach in the VK2 set-up. We then chose three target cases that we were interested to study and which had extreme frequencies and torques. We computed the corresponding frequencies and torques for each of them. This defined a frequency range and a torque range that were acceptable, so we adopted these ranges. The working parameters of these target cases are given in table G.16.
The first case (mixture containing 68.6% of glycerol in volume) corresponds to the smallest turbulent Reynolds number and to the lowest frequency we will have to use. The second case (mixture containing 95.3% of glycerol in volume) corresponds to the smallest turbulent Reynolds number and to the highest frequency of the chosen range. Note that the required power is higher than 10 kW for the anti symmetrical and bifurcated cases. The third case corresponds to the highest Reynolds number with pure water filling the tank. If the engines can implement these three cases, then the lowest and the highest Reynolds numbers can be reached and according to tables G.3 and G.4, intermediary Reynolds can be reached too with different water-glycerol mixtures.
The required range of working parameters for the engines are therefore the following : [0.1, 2] Hz for the frequency ; [1, 700] N.m for the torque and [0, 10] kW for the power.

Percentage of glycerol in volume		68.6%	95.3%	0%
Kinematic viscosity at 20°C (m^2/s)		2.6×10^{-5}	5.2×10^{-4}	1.0×10^{-6}
Density at 20°C (m^2/s)		1.19×10^3	1.25×10^3	9.98×10^2
Reynolds number		6000	6000	1.6×10^6
Impeller rotation frequency (Hz)		0.1	2.0	1.0
T (N.m)	Contra	1.4	5.8×10^2	1.2×10^2
	Anti, symmetrical	4.0	$P_{tot} > 10$ kW	3.4×10^2
	Anti, bifurcated	1.6×10^1	$P_{tot} > 10$ kW	1.4×10^3
P_{tot} (W)	Contra	8.6×10^{-1}	7.2×10^3	7.7×10^2
	Anti, symmetrical	2.4	$P_{tot} > 10$ kW	2.2×10^2
	Anti, bifurcated	1.0×10^1	$P_{tot} > 10$ kW	8.8×10^3

Table G.16: Working parameters for the GvK set-up for the three chosen target cases.

Note that in bifurcated state, the 700 N.m value corresponds to the average of the torques applied by the two impellers, therefore one impeller will apply a larger torque and the other impeller a lower one. Therefore, this value should be considered as a conservative upper bound for the torque fluctuations in the anti symmetrical state (torques fluctuate aroud their average value which is given in table G.16) rather than the largest average value that will be reached in the anti bifurcated state.

4.2.2 Torquemeters

Torquemeters should therefore have a measurement range of [1, 700] N.m.

4.2.3 Cooling system

The cooling system should be able to dissipate a power of 10 kW.

5 Results of the mechanical conception design

After we completed the preliminary design, we wrote the specifications. They were sent to three different companies ; finally, GP Concept was chosen to carry out the mechanical conception of GvK. The mechanical conception lasted 4 months during which we gave a regular feedback on the propositions of the chosen engineering desk. In this section, we present the main features of the final design.

5.1 Overview

An overview of the designed set-up is shown in figures G.3 and G.4. It is made of a cylindrical tank of PMMA (not very visible in the figures) surrounded by an outer tank of aluminium which holds the top of the set-up and the top impeller. There are openings for the laser beam and image acquisition. A metal structure holds the tank and another one holds the bottom and the top engines. Transmission is ensured by belts. Protections are placed around the belts in case they break. The total height (when it is closed) is 2.2 m, the length is 3 m and the width is 1.3 m.

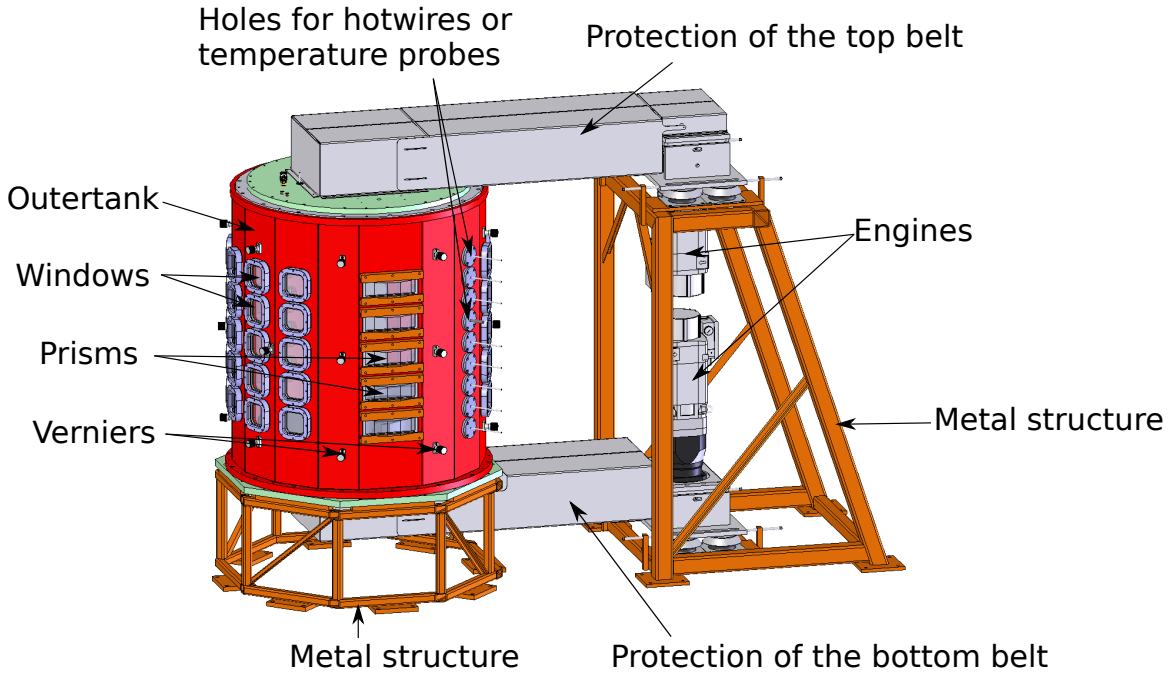

Figure G.3: 3D view of the GvK set-up designed by GP Concept.

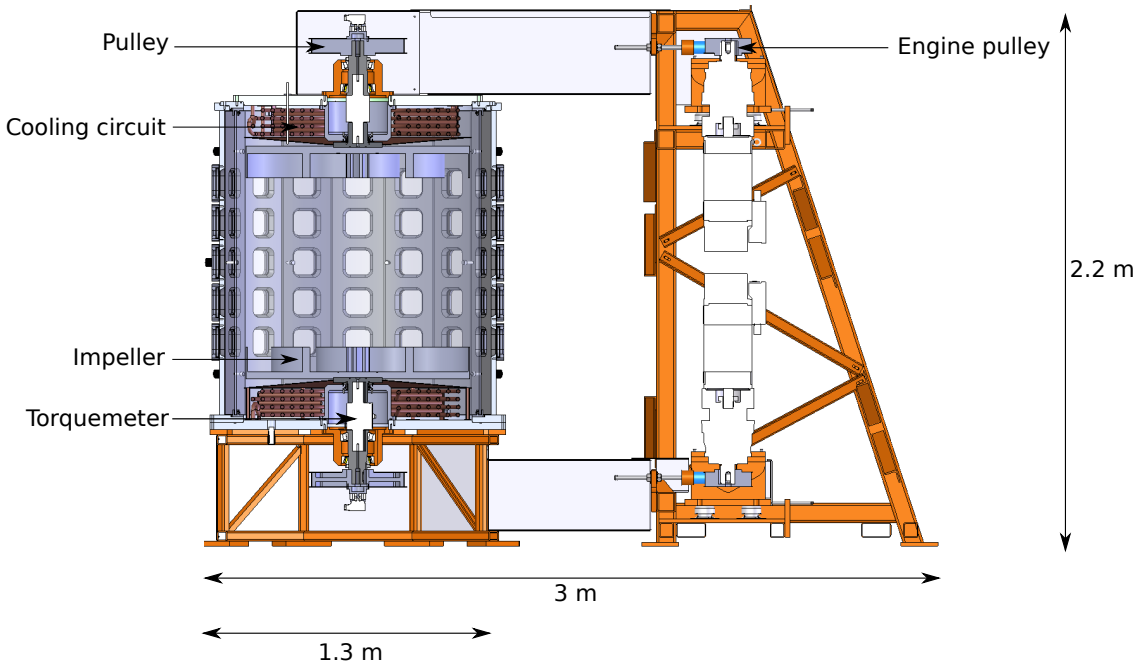

Figure G.4: Vertical cross-section of the GvK set-up designed by GP Concept.

5.2 Outer tank

The outer tank is made of aluminium. It holds the cylindrical tank and connects the bottom and the top of the set-up so that there is no stress on the cylindrical tank which is made of PMMA. The

distance between the inner and the outer tank is 4 cm. The tightness is ensured by O-rings and the outer tank can be pressurized.
There are two kinds of openings in the outer tank : windows and prisms. Both are made of optical anti-reflective glass and can be removed. The windows will be used to observe a measurement volume at the center of the tank, at several possible heights. The prisms will be used to observe a measurement volume close to the wall, at several possible heights too. Thanks to the prisms, the lines of sight of the cameras are perpendicular to the optical interface between air and glass. They are not perpendicular to the optical interface between liquid and PMMA but as the corresponding optical indices are close to each other, the resulting distortions will be less important and more easily corrected by the camera calibration.
There are also holes allowing to put hotwires, or temperature or pressure probes for alternative measurements.
To avoid bubbles, the openings for the windows have chamfers which limit the trapping of the bubbles. Also, elbow connectors have been added to the outer tank to force a flow in the space between the inner and the outer tank in order to remove bubbles. As the outer tank is tight, it can also be depressurized during its filling in order to avoid bubbles.

5.3 Cylindrical tank

The cylindrical tank is made of two plates of PMMA which are thermoformed and glued together. This technique allows a better optical quality than casted PMMA. The only drawback is the roughness along the bonding line, but a proper polishing will fix this problem.
The final cylinder has a thickness of 1 cm, as in the VK2 set-up and an inner diameter of 0.98 m. As the PMMA may deform, verniers are used. They are big screws fixed in the outer tank (which is made of aluminium and therefore much less prone to deformation) and which push on the cylindrical tank via pads. Screwing or unscrewing them allows to adjust the shape of the cylinder with a good accuracy, as the cylinder diameter and the shape of the outer tank are known accurately. Anyway, there are small spaces above and below the cylindrical tank which allow the liquid to flow from the cylindrical tank to the outer one ; therefore, there is no pressure difference between the inside and the outside of the cylindrical tank.
Small holes in the cylindrical tank allow to put the possible hotwires or pressure or temperature probes.

5.4 Engines

The chosen engines are electrical asynchronous engines made by Siemens. The rated power is 7 kW (each), the rated torque is 45 N.m and the rated rotation frequency is 1500 rpm. They will be used with Neugart reduction gears which have a reduction ratio of 20. For each engine, two pulleys of different sizes are provided ; this allows to achieve the whole requested range of working parameters.

5.5 Tightness at the shafts

The tightness at each shaft is ensured by two lip seals placed symmetrically as shown on figure G.5. There are two of them out of precaution and also because placing them in opposite directions ensures the tightness in both cases of over- and under- pressure. The shaft can be lubricated around the lip seals with a special grease in order to limit the fatigue of the seals. In addition to these lip seals, a V-seal is used, which aims at preventing the seeding particles from reaching the lip seals and wearing them out.

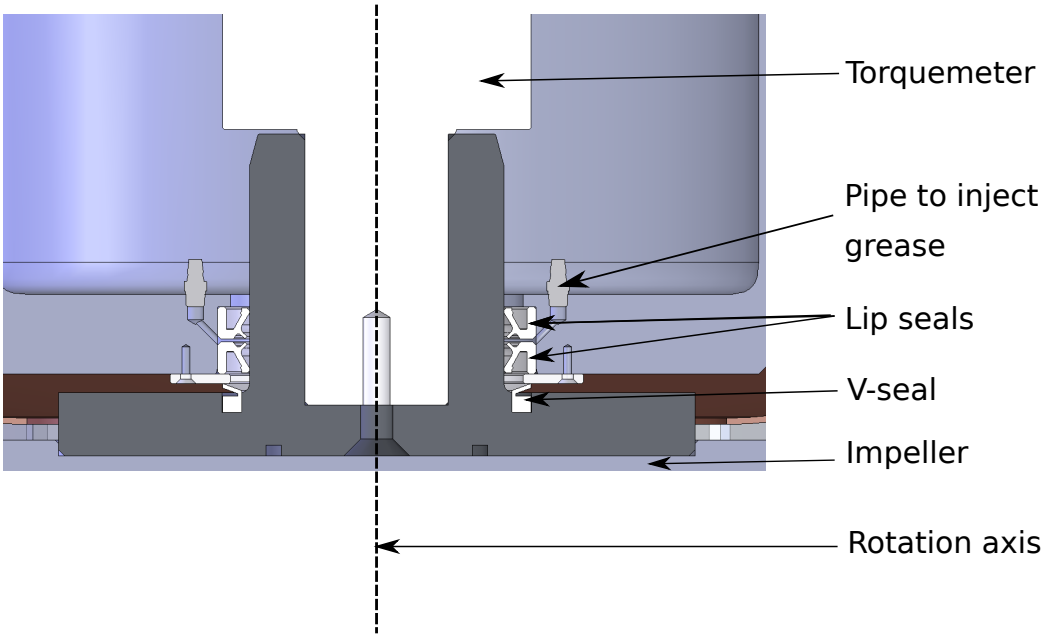

Figure G.5: Close-up on the seals ensuring the tightness at the shaft.

5.6 Impellers

The impellers are made of aluminium. The stresses on the impellers due to the dynamic pressure have been computed based on pressure fields obtained from LES simulations by Caroline Nore's team, such as those on figure G.6. These computations allowed to validate the choice of aluminium and to reject polycarbonate and delrin.

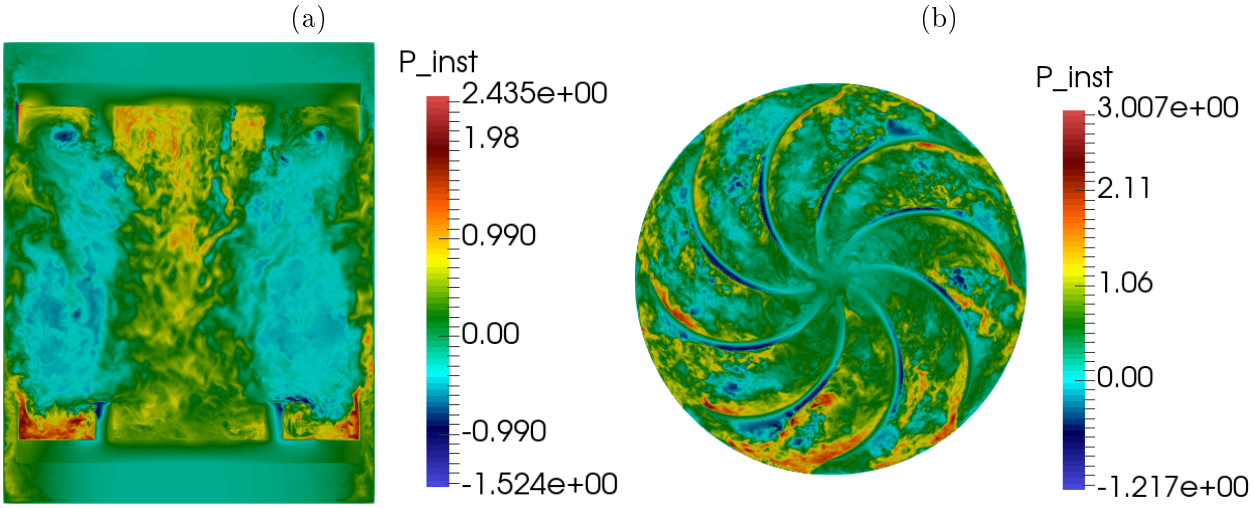

Figure G.6: Instantaneous pressure field in a bifurcated von Kármán flow at $Re = 10^5$ obtained by LES (courtesy of Caroline Nore). (a) Vertical meridian plane. (b) Horizontal plane at the mid-height of the blades of the impellers.

5.7 Torquemeters

The torquemeters are made by ETH Messtechnik. They have two measurement ranges : they can measure torques up to 100 N.m with an accuracy of 0.1 N.m and torques up to 1000 N.m with an accuracy of 1 N.m.
These torquemeters are placed between the mechanical bearings and the lip seals. Therefore, the measured torques will not be affected by the contribution of the bearings.
These torquemeters do not allow an accurate measurement of the rotation frequency ; therefore, additional sensors with a resolution of $1/10000^{\text{th}}$ of round are added on the pulleys.

5.8 Cooling system

The cooling circuit, rather similar to the one in VK2, is made of two copper windings : one above the top impeller and one below the bottom impeller. Such a winding is shown on figure G.7. Each winding has four levels and is made with a copper pipe which has a diameter of the order of 1 cm and is 50 m long. It was dimensioned with a 0D model and slightly oversized out of precaution. It is connected to a Huber thermocooler, itself connected to the cooling circuit of the building.

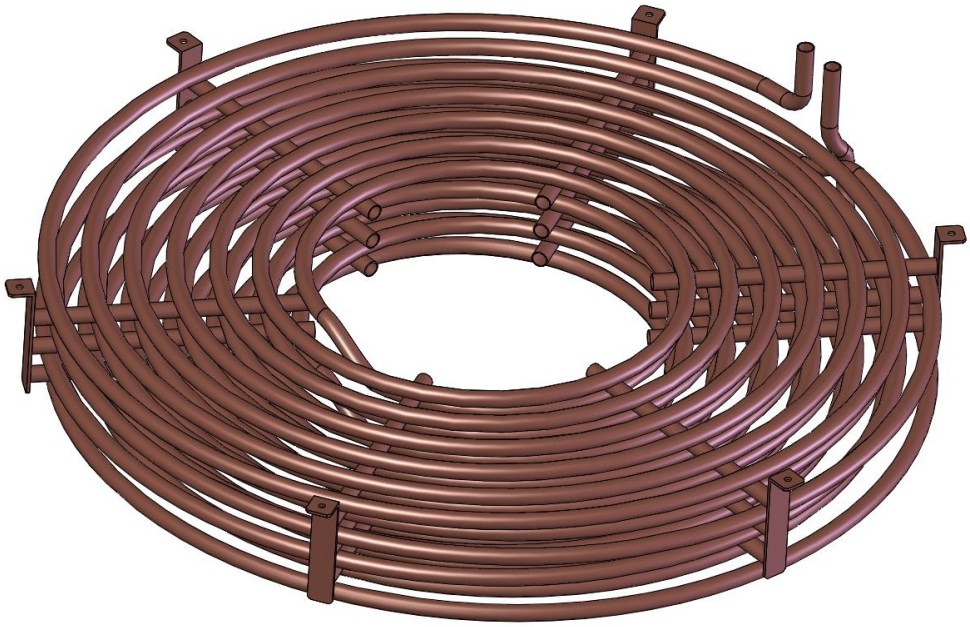

Figure G.7: 3D view of one of the windings of the cooling circuit.

5.9 Numerical assessment of the eigen frequencies

GP Concept computed the eigen frequencies of the different parts of the experiment to ensure that they were much higher than the impeller and engine rotation frequencies. This condition was fullfilled except for the metal structure which was then modified accordingly.

Appendix H

French summary

L'objectif de cette thèse est de chercher, dans un écoulement turbulent réel, d'éventuelles traces des singularités que pourraient développer les solutions des équations d'Euler ou de Navier-Stokes incompressibles 3D. En effet, la question de leur régularité est toujours en suspens. Dans cette thèse, on part du principe que l'existence de singularités dans les équations d'Euler ou de Navier-Stokes aurait, le cas échéant, un impact observable sur les écoulements turbulents réels, et on cherche des traces de ces singularités dans des champs de vitesse tridimensionnels mesurés dans un écoulement turbulent tourbillonnaire modèle, l'écoulement de von Kármán. La distribution, la structure de l'écoulement autour de ces possibles empreintes de singularités ainsi que leur évolution temporelle sont étudiées.

Les équations de Navier-Stokes sont des équations aux dérivées partielles permettant de décrire le mouvement des fluides. Elles ont été établies vers le milieu du XIXème siècle. Dans le cas particulier des écoulements incompressibles, c'est-à-dire pour lesquels la vitesse du fluide est négligeable devant la vitesse du son dans ledit fluide, ces équations se simplifient en équations de Navier-Stokes incompressibles. Ces équations simplifiées sont néanmoins représentatives d'un grand nombre d'écoulements, en particulier turbulents. La turbulence est le phénomène qui se développe quand les effets inertiels, liés aux termes non-linéaires des équations de Navier-Stokes, deviennent prépondérants par rapport aux effets visqueux. Les écoulements turbulents se caractérisent notamment par une grande complexité et une multiplicité d'échelles spatiales et temporelles. Pour expliquer ces caractéristiques, l'image d'une cascade d'énergie des grandes échelles vers les petites est souvent invoquée : quand on met en mouvement un fluide, des structures de plus en plus fines sont générées. Ce raffinement s'arrête autour d'une échelle, appelée échelle de Kolmogorov, à laquelle les effets visqueux reprennent le pas sur les effets inertiels. Cette image est en adéquation avec nombre d'observations numériques et expérimentales, en particulier les spectres d'énergie qui présentent une large gamme d'échelles dans laquelle le spectre décroit algébriquement comme le nombre d'onde à la puissance -5/3, avant de chuter brusquement quand le nombre d'onde se rapproche de l'inverse de l'échelle de Kolmogorov. Cependant, la réalité est plus complexe qu'un transfert homogène de l'énergie des grandes vers les petites échelles : la turbulence se caractérise par de l'intermittence en espace et en temps ; des zones de forte activité (forte vitesse, dissipation ou vorticité par exemple) surgissent localement ou sporadiquement au milieu de zones plus calmes. Cela se traduit par une non-invariance d'échelle des fonctions de structure. Plusieurs tentatives de modélisation existent, qui essaient d'expliquer la forme de ces fonctions de structure. On compte parmi elles le modèle multifractal, qui, sans toutefois en nécessiter, est compatible avec l'existence de singularités dans les solutions des équations d'Euler, voire de Navier-Stokes (incompressibles). Outre l'intérêt purement

mathématique de savoir si les solutions des équations d'Euler et de Navier-Stokes sont régulières ou non, le problème des singularités a donc aussi un intérêt dans la compréhension de la turbulence.

Face à une équation aux dérivées partielles, la stratégie des mathématiciens est généralement de reformuler l'équation dans un espace plus large de fonctions non nécessairement régulières, puis d'essayer de prouver existence, unicité et régularité de la solution. En effet, les équations de la physique sont généralement exprimées à l'aide de dérivées qui ne sont pas bien définies dans le cas de solutions singulières. Dans le cas des équations de Navier-Stokes, le travail a été amorcé par Jean Leray qui a établi la formulation plus générale, dite faible, des équations de Navier-Stokes et prouvé l'existence de solutions. Duchon et Robert ont poursuivi le travail en établissant un bilan d'énergie valable pour toute solution faible, régulière ou non. Ce bilan d'énergie a la particularité de mettre en jeu un deuxième terme de dissipation, en plus de la dissipation visqueuse. Ce deuxième terme, appelé dissipation inertielle, égal à zéro dans le cas d'une solution régulière, pourrait devenir non-nul si une singularité se développait.

Dans cette thèse, nous nous basons sur le travail de Duchon et Robert pour chercher des traces de singularités dans un écoulement turbulent réel. En effet, le terme de dissipation inertielle est la limite quand l'échelle tend vers 0 d'une quantité dépendant de l'échelle. Cette quantité, que nous appelons terme de Duchon-Robert, est liée au terme non-linéaire d'advection des équations de Navier-Stokes. Le travail de Duchon et Robert suggère que dans le cas d'une singularité, ce terme reste non-nul même quand l'échelle tend vers 0, puisqu'il tend vers une dissipation inertielle. Ce terme de Duchon-Robert peut aussi être interprété comme du transfert inter-échelles, et le fait qu'il ne s'annule pas quand l'échelle tend vers 0 correspond alors à l'apparition d'échelles caractéristiques infiniment fines, c'est-à-dire d'une singularité. On peut aussi voir un tel événement comme l'incapacité des effets visqueux à absorber le transfert inter-échelles. Nous cherchons donc des points où le terme de Duchon-Robert, calculé à une échelle toute petite, prend des valeurs très grandes, par rapport à ses valeurs habituelles ou par rapport aux effets visqueux à la même échelle. C'est ce que nous appelons des traces de singularités. Expérimentalement, nous n'avons pas accès à des échelles infiniment petites, donc nous nous limitons à l'échelle de Kolmogorov, qui est généralement considérée comme la plus petite échelle caractéristique d'un écoulement. Cette approche peut bien sûr être menée sur des champs de vitesse obtenus par simulation numérique, mais l'approche expérimentale a l'avantage de ne faire aucune hypothèse, modélisation ou coupure sur les petites échelles, contrairement à la simulation numérique qui ne peut simuler une gamme infinie d'échelles.

Les champs de vitesse turbulents utilisés pour notre étude sont mesurés par vélocimétrie par image de particules tomographique (TPIV) au centre d'un écoulement de von Kármán. Cet écoulement est généré par deux turbines contrarotatives dans un cylindre. Le cylindre a un diamètre de 20 cm et les turbines, des disques sur chacun desquels sont montées huit pales courbes de 2 cm de haut, sont distantes de 14 cm. Les champs de vitesse sont mesurés dans un volume de 4 cm x 4 cm x 0.5 cm au centre de l'écoulement ; à cet endroit la vitesse moyenne est très faible. Le liquide remplissant le cylindre est de l'eau ou un mélange d'eau et de glycérol, en fonction de la viscosité souhaitée. En faisant varier la viscosité du liquide ou la fréquence de rotation des turbines, on peut balayer une large gamme de nombres de Reynolds turbulents. On peut ainsi régler l'échelle Kolmogorov, et, à résolution constante, faire varier la gamme d'échelles étudiées. Typiquement, pour un nombre de Reynolds de 6000, l'échelle de Kolmogorov est de 0.4 mm (de l'ordre de notre résolution spatiale) ; elle diminue à 15 microns pour un nombre de Reynolds de 300000. Dans cette thèse, nous avons réutilisé un dispositif déjà existant, et l'avons adapté à la TPIV qui requiert plusieurs caméras (4 ou

5 dans notre cas) orientées dans différentes directions. Il a fallu élargir le châssis existant et fabriquer de nouvelles contre-cuves, des cuves à faces droites placées autour de la cuve cylindrique et remplies du même liquide afin de réduire les distorsions optiques. Nous en avons fabriqué deux différentes, une permettant de placer les caméras dans deux plans différents, et une ne permettant de les placer que dans un seul plan. A priori, la première permettait une meilleure reconstruction volumique mais les caméras dont les axes optiques ne croisaient pas perpendiculairement la cuve cylindrique souffraient d'un problème d'astigmatisme. La deuxième contre-cuve évitait ce problème et permettait d'obtenir une qualité de reconstruction volumique similaire ; nous l'avons donc adoptée. Un miroir a également été placé au bout du faisceau laser afin de le réfléchir et réduire les différences d'intensité lumineuse sur les caméras placées en diffusion avant et celles placées en diffusion arrière.

Durant cette thèse, trois campagnes de TPIV ont été réalisées, en collaboration avec le Laboratoire de Mécanique des Fluides de Lille. Les deux premières ont permis de mesurer des champs de vitesse décorrellés, afin d'engranger assez de statistiques et d'observer des événements rares. Durant la troisième campagne, des mesures par TPIV résolue en temps ont été réalisées afin de pouvoir étudier l'évolution temporelle du champ de vitesse au niveau des extrêmes du terme de Duchon-Robert. Les champs de vitesse ont été reconstruits à partir des images par TPIV en utilisant le logiciel Davis de Lavision. Par rapport à la PIV 2D, la TPIV nécessite, outre les caméras additionnelles, une étape de reconstruction volumique consistant à reconstruire un champ 3D d'intensité lumineuse des particules, auquel l'algorithme de corrélation est appliqué afin d'obtenir le champ de vitesse 3D. Cette étape additionnelle, ainsi que la corrélation tridimensionnelle sont coûteuses en ressources de calcul, et nous en avons réalisé une bonne part sur un cluster.

Le premier volet de résultats consiste en une étude de la distribution statistique du terme de Duchon-Robert et de ses extrêmes, que nous avons comparée d'une part à celle de la dissipation visqueuse, et d'autre part à celle du terme de transfert inter-échelles utilisé dans les équations LES.

En moyenne, le terme de Duchon-Robert croît avec l'échelle à laquelle il est mesuré : il est faible dans la zone dissipative et fort dans la zone inertielle. De plus, il semble constant dans la zone inertielle. La dissipation visqueuse a un comportement inverse : en moyenne, elle est forte dans la zone dissipative alors qu'elle décroît comme l'échelle de mesure à la puissance -4/3 dans la zone inertielle. On observe un comportement semblable pour les écart-types du terme de Duchon-Robert et de la dissipation visqueuse. Ceci est en accord avec la théorie de Kolmogorov et l'image traditionnelle de la cascade : les effets visqueux, négligeables devant les effets inertiels ou le transfert inter-échelles dans la zone inertielle, deviennent prépondérants dans la zone dissipative, mettant fin au transfert inter-échelles qui devient très faible.

Cependant, l'étude des distributions et des valeurs extrêmes du terme de Duchon-Robert et de la dissipation visqueuse à une échelle donnée révèle des différences plus subtiles. En effet, la distribution de la dissipation visqueuse ne semble être pilotée que par la moyenne et l'écart-type, sa forme (assez proche d'une gaussienne mais pas exactement) étant la même d'une échelle à l'autre. Cela apparaît clairement quand on trace les distributions centrées réduites de la dissipation visqueuse obtenues à plusieurs échelles : elles se superposent. Au contraire, pour le terme de Duchon-Robert, alors que la moyenne et l'écart-type diminuent quand l'échelle diminue, la distribution devient plus asymétrique (les valeurs positives étant favorisées) et aussi plus intermittente : les extrêmes sont plus forts, en termes de nombre d'écart-types. Ce phénomène est confirmé par l'analyse des extrêmes : alors que le maximum de la dissipation visqueuse à échelle finie, normalisé par l'écart-type de la distribution, est indépendant de l'échelle, le maximum du terme de Duchon-Robert normalisé par l'écart-type de la distribution correspondante augmente quand l'échelle diminue, alors qu'en

valeur absolue il diminue.

Nous avons également étudié le comportement conjoint du terme de Duchon-Robert et de la dissipation visqueuse via les distributions jointes et la distribution du ratio entre les deux termes. La distribution jointe de ces deux grandeurs, tracée en coordonnées doublement logarithmique, a la forme d'un triangle inversé, ce qui signifie que les fortes valeurs du terme de Duchon-Robert s'accompagnent de fortes valeurs du terme de dissipation visqueuse, tandis que la réciproque n'est pas vraie. Cela montre que les extrêmes du terme de Duchon-Robert et les extrêmes du ratio entre le terme de Duchon-Robert et la dissipation visqueuse ne sont pas les mêmes et cela encourage à étudier les deux. Ce résultat est confirmé par l'analyse de la distribution du rapport entre terme de Duchon-Robert et la dissipation visqueuse à échelle finie.

De plus, l'analyse de ces distributions montre une différence, dans la zone dissipative, de comportement entre les distributions conditionnées aux valeurs positives du terme de Duchon-Robert et celles conditionnées aux valeurs négatives ; cette différence se résorbe dans la zone inertielle. Enfin, la distribution centrée-réduite du ratio montre qu'il est moins intermittent dans la zone dissipative que dans la zone inertielle, au contraire du terme de Duchon-Robert.

Nous avons terminé les études statistiques par une comparaison entre le terme de Duchon-Robert et celui de transfert inter-échelles qui apparaît dans les équations LES. Le comportement en fonction de l'échelle des moyennes, écart-types et distributions des deux termes est similaire. Le comportement joint avec la dissipation visqueuse à échelle finie présente deux légères différences. Premièrement, la pdf centrée-réduite du ratio entre terme de transfert LES et dissipation visqueuse est indépendante de l'échelle, il n'est donc pas moins intermittent dans la zone dissipative. Deuxièmement, ces pdfs centrées-réduites conditionnées aux valeurs positives et négatives du terme de transfert LES ne se recouvrent pas dans la zone inertielle. Nous avons achevé cette comparaison avec l'étude des pdfs jointes entre le terme de Duchon-Robert et le terme de transfert LES, ainsi que du ratio correspondant. Le ratio le plus probable est autour de 0.5 dans la zone dissipative et tend vers 1 dans la zone inertielle. Les ratios des valeurs moyennes sont aussi de cet ordre. Nous tentons de l'expliquer par une analyse des équations de transport de l'énergie contenue dans les composantes du champ de vitesse correspondant aux échelles supérieures ou inférieures à l'échelle étudiée. Les pdfs jointes du terme de Duchon-Robert et de celui de transfert LES sont orientées selon les droites correspondant aux ratios les plus probables. Elles présentent néanmoins une certaine dispersion autour de ces droites, indiquant qu'utiliser l'un ou l'autre de ces deux termes mènerait à la détection d'événements différents.

Ces études statistiques sont complétées par des analyses menées sur des champs de vitesse 2D-3C obtenus par SPIV et qui montrent que le terme de Duchon-Robert a un rôle important dans les statistiques de la turbulence. En effet, les fonctions de structure conditionnées à un terme de Duchon-Robert de faible valeur présentent une loi d'échelle auto-similaire alors que celles conditionnées à un terme de Duchon-Robert élevé suivent la même loi d'échelle que les fonctions de structure non conditionnées. Cela montre que ce que nous appelons traces de singularités correspond aux zones de forte activité responsables des lois d'échelles intermittentes.

Le deuxième volet de résultats concerne la structure du champ de vitesses autour des traces de singularités, i.e. des valeurs extrêmes du terme de Duchon-Robert ou du rapport entre le terme de Duchon-Robert et le terme de dissipation visqueuse à échelle finie. Cette étude a été divisée en deux parties : une première utilisant le gradient du vecteur vitesse, et une deuxième se basant sur l'observation directe des champs de vitesse au niveau des extrêmes. Analyser le gradient du vecteur vitesse en un point revient à étudier la forme des lignes de courant très localement autour

de ces points. Pour un écoulement incompressible, quatre configurations différentes sont possibles en fonction des invariants du gradient de la vitesse : l'étirement de vorticité (vortex stretching, VS), la compression de vorticité (vortex compressing, VC), le filament (F) et la nappe (sheet, S). Le calcul du gradient de la vitesse peut être réalisé par un ordinateur, ce qui permet d'analyser un grand nombre de champs.

Nous avons d'abord étudié la répartition des différentes structures dans tout l'écoulement, en traçant la distribution jointe des deuxième et troisième invariants Q et R du gradient du vecteur vitesse. Celle-ci présente une forme de goutte, déjà largement observée dans la littérature. Cette forme devient floue quand l'échelle de Kolmogorov devient plus petite que la résolution spatiale.

Nous avons ensuite calculé les moyennes conditionnelles du terme de Duchon-Robert et de la dissipation visqueuse à échelle donnée, conditionnées à Q et R. Quand la résolution est de l'ordre de l'échelle de Kolmogorov, la moyenne conditionnelle du terme de Duchon-Robert est négative dans une sous-partie du domaine VC, avec $Q>0$. Quand la résolution augmente par rapport à l'échelle de Kolmogorov, la zone où la moyenne conditionnelle du terme de Duchon-Robert est négative se déplace au sein du domaine VC vers la sous-partie où $Q<0$, et s'étend sur une partie du domaine VS. Cela suggère que la topologie à un point donné ne détermine pas seule le signe du terme de Duchon-Robert. Concernant la moyenne conditionnelle du terme de dissipation visqueuse, il est remarquable que ses isoplèthes soient très proches de celles de la distribution jointe de Q et R, ce qui laisse supposer que l'une est fonction de l'autre. Les moyennes conditionnelles donnent une idée des topologies élémentaires menant aux extrêmes : par exemple, la moyenne conditionnelle du terme de Duchon-Robert est la plus élevée dans le domaine S avec Q et R très grands en valeur absolue tandis que la moyenne conditionnelle de la dissipation visqueuse à échelle finie est la plus élevée dans les domaines de VS et VC avec Q très grand. Cela laisse supposer que les traces de singularités correspondent plutôt à des nappes.

Finalement, nous avons directement calculé les topologies élémentaires correspondant aux mille plus fortes valeurs du terme de Duchon-Robert. En contradiction avec la moyenne conditionnelle, il semble que les extrêmes du terme de Duchon-Robert favorisent l'étirement de vorticité comme topologie élémentaire. Les extrêmes du ratio entre terme de Duchon-Robert et terme de dissipation visqueuse favorisent à la fois l'étirement de vorticité et la nappe. Ceci est vrai à la fois dans la zone dissipative et la zone inertielle, mais plus accentué dans la zone dissipative.

Utiliser le gradient de la vitesse est pratique puisque la méthode peut être automatisée et appliquée à un grand nombre de points. Cependant, elle ne rend pas compte de la complexité de l'écoulement autour d'un point donné. Nous avons donc également caractérisé les champs de vitesse autour des extrêmes en décrivant directement le champ de vitesses et certaines grandeurs comme le terme de Duchon-Robert et celui de dissipation visqueuse, les normes de la vorticité et de la vitesse ou encore la divergence.

Nous avons principalement observé trois types de structures autour des traces de singularités : le tourbillon-vis, le tourbillon-rouleau et le demi-tour. Concernant les extrêmes du ratio entre terme de Duchon-Robert et terme de dissipation visqueuse, nous avons également observé quelques structures moins nettes comme des changements de direction abrupts des lignes de courant ou une forte torsion de ces lignes. La plupart du temps, le point où le terme de Duchon-Robert ou le ratio est le plus fort ne semble pas occuper de point central ou particulier de la structure observée. Dans la plupart des structures observées, le terme de Duchon-Robert prend des valeurs positives et négatives. Les traces de singularités s'accompagnent également de valeurs très fortes de la dissipation et des normes de la vitesse et de la vorticité. Pour les tourbillons, la vorticité est la plus forte au centre du tourbillon, et ses isosurfaces sont des tubes. La dissipation visqueuse est importante en périphérie du tourbillon,

plus à l'extérieur que le terme de Duchon-Robert. Pour les demi-tours, soit les isosurfaces de vorticité sont des tubes, soit elles sont plus aplaties. Les demi-tours n'ont été observés que parmi les extrêmes négatifs du terme de Duchon-Robert.
Dans la zone inertielle, nous avons observé les mêmes structures, mais plus déformées et plus complexes, probablement à cause des effets inertiels plus forts qui les perturbent.
Nous avons comparé les extrêmes du terme de Duchon-Robert à ceux de la dissipation visqueuse et de la vorticité, dans la zone dissipative et dans la zone inertielle. Ces extrêmes correspondent aux mêmes types de structures. Dans certains cas, les extrêmes de dissipation ou de vorticité étaient dans la même structure qu'un extrême du terme de Duchon-Robert. Cela était particulièrement le cas dans la zone dissipative.
Nous avons également observé que la divergence était plus forte au niveau des extrêmes qu'ailleurs, son signe étant positif ou négatif, alors qu'elle est censée être nulle. En fait, pour un écoulement incompressible mesuré par TPIV, la divergence donne plutôt une idée de l'erreur de mesure. Ici, l'existence de divergences très grandes s'explique probablement par l'accumulation de particules à certains endroits, en particulier au centre des tourbillons. Les champs de vitesse observés sont donc ceux des particules et non du fluide, mais s'approchent de ceux du fluide et révèlent tout de même des événements extrêmes.
Il se pourrait que les trois types de structure observées correspondent à une ou deux structures seulement, observées à différents instants ou dans des référentiels différents. En effet, nos observations sont basées sur les champs de vitesse mesurés dans le référentiel du laboratoire ; leur aspect est parfois assez différent dans le référentiel allant à la vitesse au niveau de l'extrême par exemple. Nos observations sont en bon accord avec des travaux précédents, étudiant soit les extrêmes du terme de Duchon-Robert, soit les structures de forte vorticité.

Au cours de cette thèse, nous avons appliqué la technique de TPIV, résolue en temps ou non, à la mesure des petites échelles du champ de vitesse dans un écoulement de von Kármán. Ces champs de vitesse ont ensuite été analysés à la recherche de traces de possibles singularités pouvant survenir dans les équations d'Euler ou de Navier-Stokes. Ces singularités potentielles se caractériseraient, le cas échéant, par un terme de Duchon-Robert très fort à des échelles très petites, c'est-à-dire aux échelles dissipatives. Nous avons de fait observé de tels événements, le terme de Duchon-Robert étant plus intermittent à petite échelle. Cependant, nous n'avons pas observé de structures du champ de vitesse nouvelles par rapport aux travaux précédents. Cela est peut-être dû à notre résolution expérimentale encore trop élevée. Pour pallier ce problème, un nouveau dispositif expérimental, cinq fois plus gros que le dispositif actuel et conçu en partie pendant cette thèse, est en cours de fabrication. Il permettra d'observer des échelles cinq fois plus petites qu'actuellement, non en améliorant la résolution de la TPIV, mais en agrandissant les échelles de l'écoulement.

Bibliography

[Adrian, 1997] Adrian, R. (1997). Dynamic ranges of velocity and spatial resolution of particle image velocimetry. *Measurement Science and Technology*, 8:1393.

[Atkinson et al., 2011] Atkinson, C., Coudert, S., Foucaut, J.-M., Stanislas, M., and Soria, J. (2011). The accuracy of tomographic particle image velocimetry for measurements of a turbulent boundary layer. *Experiments in Fluids*, 50:1031–1056.

[Beale et al., 1984] Beale, J. T., Kato, T., and Majda, A. (1984). Remarks on the breakdown of smooth solutions for the 3D Euler equations. *Communications in Mathematical Physics*, 94:61–66.

[Boutier, 2012] Boutier, A. (2012). *Laser velocimetry in fluid mechanics.*

[Brachet, 1991] Brachet, M.-E. (1991). Direct simulation of three-dimensional turbulence in the Taylor-Green vortex. *Fluid Dyn. Res.*, 8:1.

[Brachet et al., 1992] Brachet, M.-E., Meneguzzi, M., Vincent, A., Politano, H., and Sulem, P.-L. (1992). Numerical evidence of smooth self-similar dynamics and possibility of subsequent collapse for three-dimensional ideal flows. *Phys. Fluids. A*, 4:12.

[Burgers, 1948] Burgers, J. M. (1948). A mathematical model illustrating the theory of turbulence. *Advances in Applied Mechanics*, 1:171–199.

[Cafarelli et al., 1982] Cafarelli, L., Kohn, R., and Nirenberg, L. (1982). Partial regularity of suitable weak solutions of the Navier-Stokes equations. *Comm. Pure and Appl. Math*, 35:771–831.

[Campolina and Mailybaev, 2018] Campolina, C.-S. and Mailybaev, A.-A. (2018). Chaotic blowup in the 3D incompressible Euler equations on a logarithmic lattice. *Physical Review Letters*, 121:064501.

[Cappanera et al., 2019] Cappanera, L., Debue, P., Faller, H., Kuzzay, D., Saw, E.-W., Nore, C., Guermond, J.-L., Daviaud, F., Wiertel-Gasquet, C., and Dubrulle, B. (2019). Turbulence in realistic geometries with moving boundaries : when simulations meet experiments. *submitted to Physical Review Fluids.*

[Chevillard and Meneveau, 2006] Chevillard, L. and Meneveau, C. (2006). Lagrangian dynamics and statistical geometric structure of turbulence. *Physical Review Letters*, 97:174501.

[Chevillard et al., 2008] Chevillard, L., Meneveau, C., Biferale, L., and Toschi, F. (2008). Modeling the pressure Hessian and viscous Laplacian in turbulence : comparisons with direct numerical simulation and implications on velocity gradient dynamics. *Physics of Fluids*, 20:101504.

[Chong et al., 1990] Chong, M. S., Perry, A. E., and J, C. B. (1990). A general classification of three-dimensional flow fields. *Phys. Fluids A*, 2:5.

[Constantin, 2008] Constantin, P. (2008). Euler and Navier-Stokes equations. *Publicacions Matemàtiques*, 52(2):235–265.

[Cuvier and Foucaut, 2018] Cuvier, C. and Foucaut, J.-M. (2018). PIV noise estimation derived from spectrum analyses. *Proceedings of the 5th International Conference on Experimental Fluid Mechanics*, pages 247–252.

[Danish and Meneveau, 2018] Danish, M. and Meneveau, C. (2018). Multiscale analysis of the invariants of the velocity gradient tensor in isotropic turbulence. *Physical Review fluids*, 3:044604.

[Debue et al., 2018a] Debue, P., Kuzzay, D., Saw, E.-W., Daviaud, F., Dubrulle, B., Canet, L., Rossetto, V., and Wschebor, N. (2018a). Experimental test of the crossover between the inertial and the dissipative range in a turbulent swirling flow. *Phys. Rev. Fluids*, 3:024602.

[Debue et al., 2018b] Debue, P., Shukla, V., Kuzzay, D., Faranda, D., Saw, E.-W., Daviaud, F., and Dubrulle, B. (2018b). Dissipation, intermittency, and singularities in incompressible turbulent flows. *Physical Review E*, 97:053101.

[Douady et al., 1991] Douady, S., Couder, Y., and Brachet, M.-E. (1991). Direct observation of the intermittency of intense vorticity filaments in turbulence. *Phys. Rev. Lett.*, 67:983–986.

[Dubrulle, 2019] Dubrulle, B. (2019). Beyond Kolmogorov cascades. *JFM Perspectives*, 867:P1.

[Duchon and Robert, 2000] Duchon, J. and Robert, R. (2000). Inertial energy dissipation for weak solutions of incompressible Euler and Navier-Stokes equations. *Nonlinearity*, 13:249–255.

[Elsinga and Marusic, 2010] Elsinga, G. E. and Marusic, I. (2010). Universal aspects of small-scale motions in turbulence. *J. Fluid Mech.*, 662:514–539.

[Elsinga et al., 2006] Elsinga, G. E., Scarano, F., Wieneke, B., and Van Oudheusden, B. W. (2006). Tomographic particle image velocimetry. *Exp Fluids*, 41:933–947.

[Eyink, 2005] Eyink, G. L. (2005). Locality of turbulent cascades. *Physica D*, 207:91–116.

[Eyink, 2008] Eyink, G. L. (2007-2008). *Turbulence theory, course notes.* The John Hopkins University, http://www.ams.jhu.edu/ eyink/Turbulence/notes.html.

[Foucaut et al., 2004] Foucaut, J.-M., Carlier, J., and Stanislas, M. (2004). PIV optimization for the study of turbulent flow using spectral analysis. *Measurement Science and Technology*, 15:1046–1058.

[Frisch, 1995] Frisch, U. (1995). *Turbulence : the legacy of A. N. Kolmogorov.* Cambridge University Press, Cambridge.

[Frisch and Morf, 1981] Frisch, U. and Morf, R. (1981). Intermittency in nonlinear dynamics and singularities at complex times. *Phys. Rev. A*, 23:2673–2705.

[Gan et al., 2016] Gan, L., Baqui, Y. B., and A, M. (2016). An experimental investigation of forced steady rotating turbulence. *European Journal of Mechanics B/Fluids*, 58:59–69.

[Germano, 1992] Germano, M. (1992). Turbulence : the filtering approach. *J. Fluid Mech.*, 238:325–336.

[Gomit et al., 2018] Gomit, G., Beaulieu, C., Braud, P., and David, L. (2018). Démarche d'estimation des incertitudes en PIV basée sur la méthode GUM. *Conference paper of the 16th CFTL, Dourdan.*

[Hou and Li, 2008] Hou, T. and Li, C.-M. (2008). Dynamic stability of the 3D axisymmetric Navier-Stokes equations with swirl. *Comm. Pure Appl. Math.*, 61:661.

[Joint Committee for Guides in Metrology-Working Group 1, 2008] Joint Committee for Guides in Metrology-Working Group 1 (2008). *Evaluation of measurement data - Guide to the expression of uncertainty in measurement.*

[Keane and Adrian, 1992] Keane, R. and Adrian, R. (1992). Theory of cross-correlation analysis of PIV images. *Applied Scientific Research*, 49:191–215.

[Kolmogorov, 1941] Kolmogorov, A. N. (1941). Dissipation of energy in locally isotropic turbulence. *Dokl. Akad. Nauk SSSR*, 32:16–18.

[Kolmogorov, 1962] Kolmogorov, A. N. (1962). A refinement of previous hypotheses concerning the local structure of turbulence in a viscous incompressible fluid at high Reynolds number. *J. Fluid. Mech.*, 13:82–85.

[Kuzzay et al., 2017] Kuzzay, D., Saw, E. W., Martins, J. W. A., Faranda, D., Foucaut, J. M., Daviaud, F., and Dubrulle, B. (2017). New method for detecting singularities in experimental incompressible flows. *Nonlinearity*, 30(6):2381–2402.

[Ladyzhenskaya, 1968] Ladyzhenskaya, O. (1968). Unique global solvability of the three-dimensional Cauchy problem for the Navier-Stokes equations in the presence of axial symmetry. *Zap. Nauecn. Sem. Leningrad. Otdel. Mat. Inst. Steklov.*, 7:155.

[Ladyzhenskaya, 1969] Ladyzhenskaya, O. (1969). *The Mathematical Theory of Viscous Incompressible Flows.* New York.

[Leray, 1934] Leray, J. (1934). Sur le mouvement d'un liquide visqueux emplissant l'espace. *Acta Math. J.*, 63:193–248.

[Li et al., 2018] Li, L., Li, Y., and Yan, X. (2018). Homogeneous solutions of stationary Navier-Stokes equations with isolated singularities on the unit sphere. *Archive for Rational Mechanics and Analysis*, 227:1091–1163.

[Lynch and Scarano, 2014] Lynch, K. P. and Scarano, F. (2014). Experimental determination of tomographic PIV accuracy by a 12-camera system. *Measurement Science and Technology*, 25:084003.

[Marié, 2003] Marié, L. (2003). *Transport de moment cinétique et de champ magnétique par un écoulement tourbillonnaire turbulent : influence de la rotation.* Ph.D. thesis, Université Paris VII.

[Martins, 2016] Martins, F. (2016). *Caractérisation des écoulements turbulents à proximité d'une paroi par PIV tomographique.* Ph.D. thesis, Université de Lille.

[Monchaux, 2007] Monchaux, R. (2007). *Mécanique statistique et effet dynamo dans un écoulement de von Kármán turbulent.* Ph.D. thesis, Université Paris Diderot.

[Nobach and Bodenschatz, 2009] Nobach, H. and Bodenschatz, E. (2009). Limitations of accuracy in PIV due to individual variations of particle image intensities. *Exp Fluids*, 47:27–38.

[Nogueira et al., 2001] Nogueira, J., Lecuona, A., and Rodríguez, P. A. (2001). Local field correction PIV, implemented by means of simple algorithms, and multigrid versions. *Measurement Science and Technology*, 12:1911–1921.

[Nogueira et al., 2004] Nogueira, J., Lecuona, A., and Rodríguez, P. A. (2004). Limits on the resolution of correlation PIV iterative methods. *12th international symposium on applications of laser techniques to fluid mechanics.*

[Nogueira et al., 2005] Nogueira, J., Lecuona, A., and Rodríguez, P. A. (2005). Limits on the resolution of correlation PIV iterative methods. Fundamentals. *Experiments in Fluids*, 39:305–313.

[Nogueira et al., 2002] Nogueira, J., Lecuona, A., Ruiz-Rivas, U., and Rodríguez, P. A. (2002). Analysis and alternatives in two-dimensional multigrid particle image velocimetry methods : application of a dedicated weighting function and symmetric direct correlation. *Measurement Science and Technology*, 13:963–974.

[Novara et al., 2010] Novara, M., Batenburg, K. J., and Scarano, F. (2010). Motion tracking-enhanced MART for tomographic PIV. *Measurement Science and Technology*, 21(3):035401.

[Onsager, 1949] Onsager, L. (1949). Statistical hydrodynamics. *Nuovo Cimento (Suppl.)*, 6:279–287.

[Ouellette et al., 2006] Ouellette, N., Xu, H., Bourgoin, M., and Bodenschatz, E. (2006). Small-scale anisotropy in Lagrangian turbulence. *New. J. Phys.*, 8:102.

[Parisi and Frisch, 1985] Parisi, G. and Frisch, U. (1985). On the singularity structure of fully developed turbulence. *Turbulence and Predictability in Geophysical Fluid Dynamics, Proceed. Intern. School of Physics 'E. Fermi', 1983, Varenna, Italy*, pages 84–87.

[Prasad et al., 1992] Prasad, A. K., Adrian, R. J., Landreth, C. C., and Offutt, P. W. (1992). Effect of resolution on the speed and accuracy of particle image velocimetry interrogation. *Exp. Fluids*, 13:105–116.

[Pumir and Siggia, 1990] Pumir, A. and Siggia, E.-D. (1990). Collapsing solutions in the 3D Euler equations. *Topological Fluid Mechanics*, pages 469–411.

[Ravelet, 2005] Ravelet, F. (2005). *Bifurcations globales hydrodynamiques et magnétohydrodynamiques dans un écoulement de von Kármán turbulent.* Ph.D. thesis, Ecole doctorale de l'Ecole Polytechnique.

[Ravelet et al., 2008] Ravelet, F., Chiffaudel, A., and Daviaud, F. (2008). Supercritical transition to turbulence in an inertially driven von Kármán closed flow. *J. Fluid. Mech.*, 601:339–364.

[Ravelet et al., 2004] Ravelet, F., Marié, L., Chiffaudel, A., and Daviaud, F. (2004). Multistability and memory effect in a highly turbulent flow : experimental evidence for a global bifurcation. *Physical Review Letters*, 93:164501.

[Reynolds, 1883] Reynolds, O. (1883). An experimental investigation of the circumstances which determine whether the motion of water shall be direct or sinuous, and of the law of resistance in parallel channels. *Proceedings of the Royal Society of London*, 35:224–226.

[Rhodes, 2008] Rhodes, M. (2008). *Introduction to particle technology.*

[Saint-Michel, 2013] Saint-Michel, B. (2013). *L'écoulement de von Kármán comme paradigme de la physique statistique hors-équilibre.* Ph.D. thesis, Université Pierre et Marie Curie.

[Saint-Michel et al., 2014] Saint-Michel, B., Herbert, E., Salort, J., Baudet, C., Bon Mardion, M., Bonnay, P., Bourgoin, M., Castaing, B., Chevillard, L., Daviaud, F., Diribarne, P., Dubrulle, B., Gagne, Y., Gibert, M., Girard, A., Hébral, B., Lehner, T., and Rousset, B. (2014). Probing quantum and classical turbulence analogy in von Kármán liquid helium, nitrogen, and water experiments. *Physics of Fluids*, 26:125109.

[Saw et al., 2016] Saw, E. W., Kuzzay, D., Faranda, D., Guittonneau, A., Daviaud, F., Wiertel-Gasquet, C., Padilla, V., and Dubrulle, B. (2016). Experimental characterization of extreme events of inertial dissipation in a turbulent swirling flow. *Nature Communications*, 7:12466.

[Saw et al., 2018] Saw, E. W., P, D., Kuzzay, D., Daviaud, F., and Dubrulle, B. (2018). On the universality of anomalous scaling exponents of structure functions in turbulent flows. *J. Fluid Mech.*, 837:657–669.

[Scarano, 2013] Scarano, F. (2013). Tomographic PIV : principles and practice. *Measurement Science and Technology*, 24.

[Schanz et al., 2016] Schanz, D., Gesemann, S., and Schröder, A. (2016). Shake-the-box : Lagrangian particle tracking at high particle image densities. *Exp. Fluids*, pages 57–70.

[Sciacchitano et al., 2015] Sciacchitano, A., Neal, D. R., Smith, B. L., Warner, S. O., Vlachos, P. P., Wieneke, B., and Scarano, F. (2015). Collaborative framework for PIV uncertainty quantification : comparative assessment of methods. *Measurement Science and Technology*, 26:074004.

[Sciacchitano and Wieneke, 2016] Sciacchitano, A. and Wieneke, B. (2016). PIV uncertainty propagation. *Measurement Science and Technology*, 27:084006.

[She et al., 1990] She, Z.-S., Jackson, E., and Orszag, S.-A. (1990). Intermittent vortex structures in homogeneous isotropic turbulence. *Nature*, 344:226–228.

[Shnirelman, 1997] Shnirelman, A. (1997). On the non-uniqueness of weak solutions of the Euler equation. *Comm. Pure and Appl. Math*, 50:1260–1286.

[Soloff et al., 1997] Soloff, S., Adrian, R., and Liu, S.-C. (1997). Distortion compensation for generalized stereoscopic particle image velocimetry. *Measurement Science and Technology*, 8(12):1441.

[Sulem et al., 1983] Sulem, C., Sulem, P.-L., and Frisch, H. (1983). Tracing complex singularities with spectral methods. *J. Comput. Phys.*, 50:138–161.

[Tsai, 1986] Tsai, R. (1986). An efficient and accurate camera calibration technique for 3D machine vision. *Proceedings of the IEEE Computer Society Conference on Computer Vision and Pattern Recognition.*

[Vieillefosse, 1983] Vieillefosse, P. (1983). Internal motion of a small element of fluid in an inviscid flow. *Physica*, 125A:150–162.

[Vincent and Meneguzzi, 1991] Vincent, A. and Meneguzzi, M. (1991). The spatial structure and statistical properties of homogeneous turbulence. *J. Fluid Mech.*, 225:1–20.

[Vincent and Meneguzzi, 1994] Vincent, A. and Meneguzzi, M. (1994). The dynamics of vorticity tubes in homogeneous turbulence. *J. Fluid Mech.*, 258:245–254.

[Westerweel et al., 2013] Westerweel, J., Elsinga, G. E., and J, A. R. (2013). Particle image velocimetry for complex and turbulent flows. *Annu. Rev. Fluid. Mech.*, 45:409–36.

[Westerweel and Scarano, 2005] Westerweel, J. and Scarano, F. (2005). Universal outlier detection for PIV data. *Experiments in Fluids*, 39:1096–1100.

[Wieneke, 2008] Wieneke, B. (2008). Volume self-calibration for 3D particle image velocimetry. *Exp Fluids*, 45:549–556.

[Wieneke, 2015] Wieneke, B. (2015). PIV uncertainty quantification from correlation statistics. *Measurement Science and Technology*, 26:074002.

[Wieneke, 2018] Wieneke, B. (2018). Improvements for volume self-calibration. *Measurement Science and Technology*, 29:084002.

[Willert and Gharib, 1991] Willert, C. E. and Gharib, M. (1991). Digital particle image velocimetry. *Experiments in Fluids*, 10:181–193.

[Worth et al., 2010] Worth, N. A., Nickels, T. B., and Swaminathan, N. (2010). A tomographic PIV resolution study based on homogeneous isotropic turbulence DNS data. *Experiments in Fluids*, 49:637–656.

[Yeung et al., 2018] Yeung, P. K., Sreenivasan, K. R., and Pope, S. B. (2018). Effects of finite spatial and temporal resolution in direct numerical simulations of incompressible isotropic turbulence. *PRF*, 3:064603.

[Yeung et al., 2015] Yeung, P. K., Zhai, X. M., and Sreenivasan, K. R. (2015). Extreme events in computational turbulence. *PNAS*, 112:12633–12638.

[Yudovich, 1963] Yudovich, Y. (1963). Non-stationary flow of an ideal incompressible liquid. *Zh. Vych. Mat*, 3:1032–1066.

[Zhang et al., 1997] Zhang, J., Tao, B., and Katz, J. (1997). Turbulent flow measurement in a square duct with hybrid holographic PIV. *Experiments in Fluids*, 23:373–381.

université PARIS-SACLAY
ÉCOLE DOCTORALE
Physique en île-de-France (EDPIF)

Titre : Approche expérimentale du problème des singularités de Navier-Stokes

Mots clés : Turbulence, singularités, TPIV, Navier-Stokes, anomalie de dissipation

Résumé : L'objectif de cette thèse est de chercher, dans un écoulement turbulent réel, d'éventuelles traces des singularités que pourraient développer les solutions des équations d'Euler ou de Navier-Stokes incompressibles 3D. En effet, la question de leur régularité mathématique est toujours ouverte. Dans cette thèse, on postule l'existence de singularités dans les équations d'Euler ou de Navier-Stokes, et on cherche des traces de ces singularités dans des champs de vitesse 3D mesurés dans un écoulement turbulent tourbillonnaire modèle, l'écoulement de von Kármán. La répartition de ces possibles empreintes de singularités, la structure de l'écoulement en leur voisinage ainsi que leur évolution temporelle sont étudiées. Nous nous appuyons sur le travail des mathématiciens Duchon et Robert pour chercher des traces de singularités et cherchons des valeurs extrêmes du terme de Duchon-Robert calculé à toute petite échelle, c'est-à-dire dans la zone dissipative : c'est ce que l'on appelle « traces de singularités ».
Nous calculons le terme de Duchon-Robert à partir de champs de vitesse obtenus expérimentalement au centre d'un écoulement de von Kármán turbulent. Les champs de vitesse sont mesurés par vélocimétrie par image de particules tomographique (TPIV), résolue en temps ou non. Dans un premier temps, nous analysons les statistiques du terme de Duchon-Robert échelle par échelle et les comparons à celles de la dissipation visqueuse et à celles du terme de transfert inter-échelles apparaissant dans les équations LES. Dans un deuxième temps, nous analysons la topologie du champ de vitesse autour des événements extrêmes du terme de Duchon-Robert, d'abord à partir des invariants du gradient de la vitesse, puis par observation directe des champs de vitesse. Dans un troisième temps, nous présentons les résultats préliminaires d'une étude eulérienne de l'évolution temporelle des événements extrêmes du terme de Duchon-Robert.

Title : Experimental approach to the problem of the Navier-Stokes singularities

Keywords : Turbulence, singularities, TPIV, Navier-Stokes, dissipation anomaly

Abstract : This thesis is devoted to the experimental search for prints of the singularities that might occur in the solutions of the 3D incompressible Euler or Navier-Stokes equations. Indeed, the existence of solutions to these partial differential equations has been proven but it is still unknown whether these solutions are regular, i.e. whether they blow up in finite time or not. In this thesis, we postulate the existence of such singularities and look for prints of them in 3D velocity fields acquired experimentally in a turbulent swirling flow. The distribution, 3D structure and time evolution of these prints are detailed.
Our detection of prints of possible singularities is based on the work of the mathematicists Duchon and Robert. We look for extreme values of the Duchon-Robert term at small scales, i.e. in the dissipative range. That is what we call prints of singularities.
We compute the Duchon-Robert term on velocity fields which are acquired experimentally at the center of a von Kármán turbulent swirling flow. The velocity field is measured by tomographic particle image velocimetry (TPIV), either time-resolved or not.
In a first part we perform a scale-by-scale analysis of the statistics of the Duchon-Robert term and compare them to the statistics of the viscous dissipation and of the inter-scale energy transfer terms involved in the LES equations.
In a second part, we analyze the topology of the velocity field around the extreme events of the Duchon-Robert term. We first use a method based on the invariants of the velocity gradient tensor (VGT) and then observe directly the velocity fields.
A third part presents preliminary results of an Eulerian study of the time-evolution of the extreme events of the Duchon-Robert term.

Université Paris-Saclay
Espace Technologique / Immeuble Discovery
Route de l'Orme aux Merisiers RD 128 / 91190 Saint-Aubin, France